Philipps Universität Marburg

Synthesis and applications of nanoparticles in polymer matrix

Dissertation
zur
Erlangung des Doktorgrades
der Naturwissenschaften
(Dr. rer. nat.)

dem

Fachbereich Physik
der Philipps-Universität Marburg

vorgelegt von

Azhar Zahoor Abbasi

aus

Pakistan

Marburg/Lahn, 2010

Vom Fachbereich Physik der Philipps-Universität

Als Dissertation angenommen am

Erstgutachter: Prof. Dr. Wolfgang J. Parak

Zweitgutachter: Prof. Dr. Kerstin Volz

Tag der mündlichen Prüfung: 25.11.2010

Zusammenfassung

Thema der vorliegenden Dissertation ist die Synthese von Nanopartikeln und deren Einbettung in Polymerschichten. Nanopartikel haben definitionsgemäß einen Durchmesser von 1 bis 100 nm. Aufgrund ihrer geringen Größe und verhältnismäßig großen Oberfläche weisen solche Teilchen einzigartige optische, magnetische und reaktive Eigenschaften auf. Aufgrund dieser Eigenschaften finden Nanopartikel in vielen Forschungsbereichen Anwendung. So können sie als fluoreszente Marker, als magnetische Kontrastverstärker oder als Reaktionsgruppe zur Bindung anderer Moleküle eingesetzt werden.

Die Forschungsarbeit gliedert sich in zwei Schwerpunkte: 1. Nanopartikel mit unterschiedlichen optischen, magnetischen und reaktiven Eigenschaften wurden synthetisieren. 2. diese Nanopartikel wurden in eine Polymermatrix (hier Polyelektrolytkapseln) für biomedizinische Anwendungen wie Drug-Delivery oder Bio-Sensorik eingebettet.

Die Synthese der Nanopartikel wurde in Lösungsmitteln in Gegenwart von organischen Tensiden durchgeführt. Diese Tenside dienen zur Kontrolle des Wachstums der Partikel während der Synthese. Desweiteren stabilisieren sie die Nanopartikel in der Lösung und verhindern so die Aggregation der spherischen Teilchen. Durch die Variation der Wachstumsparameter während der Synthese kann der Entstehungsprozess untersucht werden. Für sehr kleine Partikel konnte ein diskontinuierliches Wachstum, d.h. eine sprunghafte Größenanderung beobachtet werden.

Im zweiten Teil der Forschungsarbeit wurden Nanopartikel in eine Polymermatrix eingebettet. Ziel war es, aus dem Verband von Nanopartikeln und Polymer-Molekülen, stabile Polyelektrolytkapsen in der Größenordnung von Mikrometern herzustellen. Solche Polyelektrolytkapseln können als Kontainer für eine Vielzahl anderer Moleküle in biomedizinischen Untersuchungen Anwendung finden. So können durch Funktionalisierung der Kavität oder der Polymerhülle multifunktionale Kapseln als Transportmittel für Drug-Delivery oder bio-kompatible Sensoren eingesetzt werden.

Die Kapseln wurden mit der so genannten Layer-by-Layer (LbL) Technik hergestellt, die von Decher et. al in den 1990ern vorgestellt wurde. Das Prinzip beruht auf der Deposition von geladenen Polymeren auf einem entgegengesetzt geladenen Templat. Hierzu dienten mit Makromolekülen angereicherte, spherische Kalziumkarbonat-Partikel. Durch die abwechselnde Anlagerung von entgegengesetzt geladenen Polymeren auf der Oberfläche der $CaCO_3$ Partikel entsteht durch die elektrostatischen Kräfte eine teilweise durchlässige Hülle, welche nach dem Auflösen des Kerns als Kapselwand dient. Sie hindert die im Innern der Kapsel eingeschlossenen Makromoleküle daran, herauszudiffundieren und gibt der Struktur ihre sphärische Form.

Während der Forschungsarbeiten wurden verschiedener Nanopartikel in der Wand der Kapseln eingebettet. Zu ihnen gehörten fluoreszierende Nanopartikel (QDs), magnetische (FePt & Fe_2O_3) und metallischen Nanopartikeln (Au). In einigen Experimenten wurde die Wand der Kapseln auch mit fluoreszierenden organischen Farbstoffen Funktionalisiert. Der Hohlraum der Kapseln wurde mit verschiedenen Molekülen gefüllt. Um als Ionensensoren für Zellulare Anwendungen zu dienen, wurden die Kavitäten der Kapseln mit Ionen-sensitiven Farbstoffen gefüllt.

Abstract

Subject of this cumulative dissertation is the synthesis of nanoparticles and their applications in polymer matrix. Nanoparticles have diameter from 1 to 100 nm. Due to their small size and high surface area these particles show unique optical, magnetic and metallic properties. Because of these properties, nanoparticles exhibit interesting applications in biology, as sensors and electronics fields.

There were two main goals of the research work: firstly to synthesize nanoparticles having different properties such as optical, magnetic and metallic, and secondly to embed these nanoparticles in polymer matrix (i.e polyelectrolyte capsules) for biomedical applications such as drug delivery and sensing.

The synthesis of nanoparticles was performed in solution in the presence of organic molecules. These molecules so called "surfactant molecules" control the growth of particles during synthesis. For this purpose surfactant molecules bind to and unbind from the surface of growing nanoparticles. These molecules also stabilize the nanoparticles in solution against aggregation and allow one to get particles dispersed in solution; which could be further used in experiments. It was observed that the control of the synthesis parameters could allow one to study the mechanism of particle formation. For very small particles discontinuous growth of nanoparticles was observed where particles were growing from one stable configuration to the next one.

In second part of the research work nanoparticles were embedded in polymer matrix. The objective of this was to understand and control the assembly of charged nanoparticles and polymer to form functional polyelectrolyte capsules of micrometer size. Such polyelectrolyte capsules find applications in biomedical for drug delivery and sensing by serving as micro container to store, deliver and/or release cargo materials.

Polyelectrolyte capsules were fabricated by so called layer-by-layer (LbL) technique introduced by Decher in 1990s. Using this technique oppositely charged polymers were assembled around a spherical charged template (made of $CaCO_3$) containing the macromolecules. A polymer layers were held together due to their electrostatic interaction, it was possible to introduce charged nanoparticles during the LbL assembly. After the LbL assembly the template was removed to get the polyelectrolyte capsules containing only macromolecules in their cavity.

During the research work different nanoparticles were embedded in the walls of the capsules such as fluorescent nanoparticles (e.g QDs), magnetic (e.g FePt & Fe_2O_3) and metallic nanoparticles (e.g Au). In some experiments walls of capsules were also made fluorescent using organic fluorophores. The cavity of the capsules was filled with different molecules. For sensing applications the cavity of the polyelectrolyte capsules was filled with different ion sensitive fluorophores.

This thesis is dedicated to my loving parents and especially my father whose dream pushed me to strive and be the best to reach the goals. You both are truly missed.

Table of Contents

List of figures & tables

List of abbreviations

Quantum dots	QDs
Tri-n-octylphosphine oxide	TOPO
Tri-n-butylphosphine	TBP
Tri-octylphosphine	TOP
Dioctyl sodium sulfosuccinate	AOT
Physical vapor deposition	PVD
Chemical vapor deposition	CVD
Light emitting-diodes	LEDs
Magic size crystals	MSCs
Layer by layer	LbL
Dimethyl sulfoxide	DMSO
Ethylenediaminetetraacetic acid	EDTA
Poly (allylamine hydrochloride)	PAH
Poly(diallyldimethylammonium chloride)	PDADMAC
Poly(ethyleneimine)	PEI
Polyvinylpyrrolidone	PVP
Poly(styrene sulfonate)	PSS
Poly(acrylic acid)	PAA
Poly(methacrylic acid)	PMA
Polyphosphoric acid	PPA
Poly($_L$-arginine)	pARG
Poly($_L$-aspartic acid)	PLA
Poly($_L$-lysine)	PLL
Chitosan	CT
Dextran sulfate	DEXS

Fluorescein isothiocyanate	FITC
Sodium-binding benzofuran isophthalate	SBFI
Potasium-binding benzofuran isophthalate	PBFI
Seminaphtharhodafluor	SNARF
Rhodamine isothiocyanate	RITC
Polyethylene glycol	PEG
High frequency magnetic field	HFMF
Transmission electron microscope	TEM
Scanning electron microscope	SEM
Confocal laser scanning microscope	CLSM
Dynamic light scattering	DLS

Nanotechnology and its applications

Nanotechnology is science of creation and utilization of materials, devices and systems through the control of matter on nanometer scale. As an emerging field of research, its multiple functions and potential applications turned it into a necessary and powerful tool in the day-to-day scientific work. It is a broad and interdisciplinary field, involving physics, chemistry, biology, medicine, materials science and the full range of engineering disciplines. For instance, electronic engineering has shown an increasing interest in the design of micro/nanoelectronic devices due to their continuously miniaturization. Several efforts have been focused on the fabrication of new electronic circuits and their interconnections[1-5]. In chemical catalysis, nanotechnology plays already an important role in the synthesis of novel materials with tailored features and chemical properties[6-8]. Additionally, advances in nanoscale particle design provide new options for drug delivery and drug therapies[9-12].

Use of nanoparticles in biomedical applications such as biosensing, observation in living cells and in drug/gene delivery is a key topic of today's research. The fluorescent semiconductor nanoparticles (also known as quantum dots or QDs) have been used for imaging inside the living cells[13-15], magnetic nanoparticles have been used as magnetic resonance imaging (MRI) contrast agent[16], while metal nanoparticles (e.g gold nanoparticles) have been widely used in cancer research[17]. For drug delivery applications many carrier systems have been developed based on verity of functionalization and preparation techniques. Structures consisting of nano-materials (like carbon nanotubes[18], nanoparticles[19-22] and nanocomposites[23]) or biomaterials (i.e. dendrimers,[24], liposomes[25, 26], block co-polymer micelles[27] or bio-degradable polymers[28]) have been developed.

In the recent year's great interests have been focused to develop multifunctional systems combining the properties of different nanoparticles for drug delivery applications. The aim of research is to build new delivery systems that are able to navigate within living organisms using remote guidance and activation for the local release of their cargo. Such carrier systems can be used to improve cargo stability, to sustain and control their release rates, to increase the bioavailability of cargo substances, and to target them to specific sites within the body. One important step in this direction is the fabrication of multilayer polyelectrolyte capsules[29].

Multilayer polyelectrolyte capsules are spherical microcontainers based on layer-by-layer (LbL) adsorption of oppositely charged polymers onto a sacrificial template followed by decomposition of these templates[30]. Compared to other composite carrier systems (such as liposomes, block copolymers, and dendrimers) polymer capsules have many advantageous properties which make them attractive candidates for medical applications including biosensing and drug delivery. Firstly, they can be synthesized under mild conditions by using numerous materials. Secondly the wall of the polyelectrolyte capsules can be functionalized by incorporating different types of charged inorganic nanoparticles. Thirdly, they can efficiently host (biological) macromolecules within their cavity for numerous biomedical applications. Finally, they can be composed of biocompatible materials for the delivery of encapsulated materials into cells[29].

1.1 Synthesis of nanoparticles

Methods for the fabrication of nanoparticles are of key importance in inorganic and physical chemistry. Two main approaches commonly known to develop materials on the nanoscale are: top down and bottom up[31].

Top down methods start with patterns made on a large scale and reduce its lateral dimension before forming the nanostructures. Lithographic techniques are one example for the top down approach[32]. Bulk materials like semiconductors are selectively degraded until small, often nanoscopic patterns appear. For example, in the case of microlithography light is used to etch either a positive or negative pattern on a surface. In top down approach nanostructures can also be fabricated through chemical etching, although this method relies much more on the initial properties of the bulk material. On the other hand, the bottom up methods begins with atoms and molecules[32]. In this approach the atoms and molecules are assembled to build smallest nanoparticles by carefully controlled chemical reaction. Herein lies the reason why this technique is cheaper as compare to the lithographic methods. This technique involves many sub-methods like, wet chemical synthesis, reverse micelles, hydrothermal processes, chemical and physical vapor deposition, arrested precipitation or the sol gel method.

In the next paragraphs some of the most important methodologies to synthesize the nanoparticles are described.

1.1.1 Wet chemical synthesis

In general wet chemical synthesis involves reacting atomic or molecular species in a coordinating solvent. The coordinating solvent can be organic solvent or aqueous solution[33, 34]. In most of the synthesis recipes organic solvents are used as reaction mixture. The advantage of using the organic solvent is that one can tune the reaction temperature over a wide range. The composition and temperature of the solvent strongly affect the shape and size of final nanoparticles. In general solvent serves for two main steps of the synthesis. Firstly it acts as solvent to prevent appearing particles from precipitation. Secondly it controls the speed of reaction and regulates the size and shape of growing nanoparticles. For this purpose solvent molecules interact dynamically with the surface of growing nanoparticles. This characteristic function during the synthesis gives them the name “surfactants”. The surfactant molecules also act as stabilizer preventing the agglomeration of the nanoparticles by capping their surface. The surfactant molecules most frequently used for such a purpose are for instance phosphine oxides (tri-n-octylphosphine oxide (TOPO), phosphines (e.g. tri-n-butylphosphine (TBP), tri-octylphosphine (TOP)), phosphonic acids, amines and carboxylic acids[35].

In general, nanoparticles of different materials require different surfactants for growing in a controlled and reproducible way. For example, semiconductor nanoparticles made of CdSe are frequently grown in a mixture of TOPO and TOP, whereas oleic acid is used as surfactant for the synthesis of magnetic nanoparticles such as Fe_2O_3 and FePt[35]. Fig.1.1.1 shows the schematic diagram for the formation of CdSe nanoparticles in the presence of surfactant molecules.

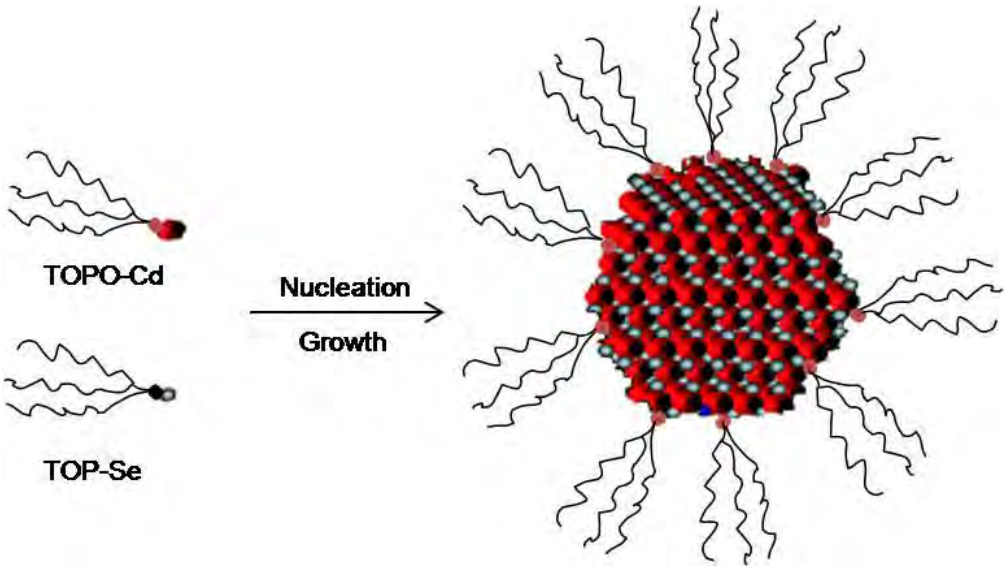

Fig. 1.1.1: *Schematic diagram for the formation of CdSe nanoparticle. The cadmium (red) and selenium (gray) atoms connected to organic molecules react, after nucleation and growth CdSe nanoparticle is stabilized by surfactant molecules which stick to the surface.*

Reaction performs inside a three necks flask connected to Schlenk line fig. 1.1.2. The other two necks of the flask are sealed with rubber septa and can be used for the measurement of reaction temperature and for the injection of precursors. A heating mantel is used to control the temperature of the reaction. At a certain temperature, precursors (which contain the atoms of which the final particle will consist) are introduced into the reaction by injection. The precursors can be introduced in different ways, by quick injection or drop wise depending on the synthesis. The addition of precursors raises their concentration in the organic solvent above a value called "nucleation threshold" and initializes the nucleation of crystals. After nucleation, crystals start to grow by using the precursors left in solution. The shape and size of nanoparticles can be controlled by controlling the growth conditions such as the amount of injected precursors, growing time in the solvent and reaction temperature. When the nanoparticles have desired size and properties, reaction can be stopped by simply removing the heating mantel and cooling down the solution. At room temperature the particles can be isolated by adding a compatible solvent. It should be capable of separating the particles from reaction mixture to perform precipitation. Addition of such solvent reduces the interaction between surfactant coated nanoparticles and solvent in which they grow and cause the aggregation of nanoparticles which can be then precipitated by centrifuge. After the centrifugation, the precipitate can be redissolved in solvent which is compatible with the surfactant of nanoparticles leading to stable colloidal in solution.
In the present work all the nanoparticles were synthesized using wet chemical synthesis. But to have the understanding of other possible methods which are widely used for the synthesis of nanoparticles few of them are described in next pages.

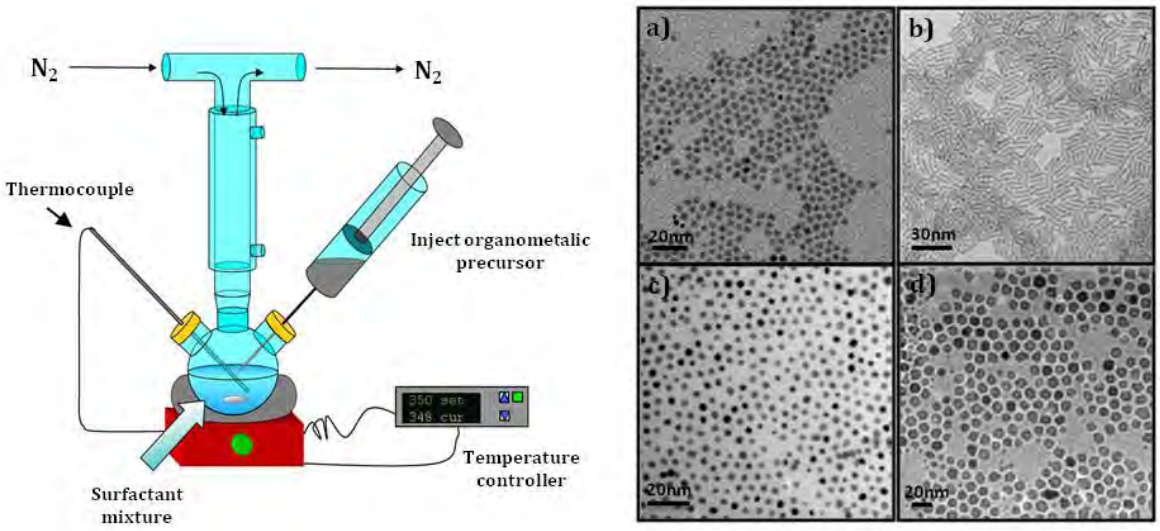

Fig. 1.1.2: *(left) Sketch of apparatus used for the synthesis of nanoparticles. (right) Transmission electron microscope (TEM) images of a) CdSe nanoparticles, b) CdSe nanorods, c) FePt nanoparticles and d) iron oxide (Fe_2O_3) nanoparticles.*

1.1.2 Reverse micelles

Nanoparticles can also be synthesized in the so-called reverse micelles mode. This technique is based on the natural structures created by the water-in-oil mixtures upon adding an amphiphilic surfactant, such as dioctyl sodium sulfosuccinate (AOT). Normally oil and water are immiscible but with the addition of a surfactant, the oil and water become miscible because the surfactant is able to bridge the interfacial tension between the two fluids. Surfactants consist of two main entities, a hydrophilic head group, which prefers an aqueous environment and a hydrophobic tail group, which prefers an organic, non-polar environment. The layer of surfactant molecule encapsulates the water with hydrophilic head group preferentially oriented at the water surface and by keeping hydrophilic tails in the direction of oil. By varying the water content of the mixture, the size of the water droplets suspended in the oil phase could be varied systematically. This led to the idea of using these self enclosed water pools as micro-reactors for carrying out sustained nanoscale chemical reactions. CdS nanoparticles have been synthesized using this technique[36, 37].

1.1.3 Hydrothermal synthesis

In hydro thermal method crystal growth is performed in an autoclave, in which nutrient is present in aqueous solution. A gradient of temperature is maintained at the opposite ends of the growth chamber so that the nutrient is dissolved at the hot part and crystallizing at the cooler one due to a concentration gradient. Possible advantages of the hydrothermal method over the other types of crystal growth include the ability to create crystalline phases which are not stable at the melting point. Also, materials which have a high vapor pressure near their melting points can also be grown by the hydrothermal method. This method is also particularly suitable for the growth of large crystals while maintaining control over their composition and size.

1.1.4 Physical and chemical vapor deposition

Nanoparticles can also be synthesized by gas phase methods. These methods are generally considered to create nanoparticles of high purity. Through the gas phase methods particles are obtained by homogeneous nucleation of atoms, molecules or fragments, using physical vapor deposition (PVD) or chemical vapor deposition (CVD).
The synthesis of nanoparticles in PVD can be obtained by evaporation of atoms from a solid target in vacuum. The reaction normally takes place in horizontal furnace one end contains the target material which is heated to evaporate the atoms and other end of furnace contains a substrate which is at low temperature to condense the atoms. Material can be heated by using several sources, such as thermal, pulsed laser or plasma source.
The CVD method is widely used in the synthesis of nanoparticles and nano structures. It is more complex than PVD due to chemical reaction in gas phase. In this technique reaction take place between materials in gas phase on the substrate surface held at high temperature. This method has good reproducibility and creates uniform and pure materials. The simplest CVD technique to produce nanoparticles is thermally assisted CVD using an oven to decompose and chemically react the introduced gaseous precursors. Other heat sources like plasma source and laser source can also be used to produce heat to start reaction between precursors.

1.2 Nucleation and growth processes

During the synthesis of nanoparticles there are three main processes which are occurring,

1) Nucleation
2) Growth
3) Ostwald ripening mechanism

In this part detail of these processes and some factor governing the rate of these processes are described. Lot of efforts have been made to explain the nucleation and growth of nanoparticles but still there is no analytical model which can explain these processes. La Mer and co-workers[38, 39] studied extensively nucleation and growth in sulfur sols, from which they developed a theory about the formation of colloids or nanostructure from a homogenous and supersaturated medium. According to their classical theory, synthesis of a colloid should be designed in such a way that the concentration of precursors increases rapidly rising above the threshold value, when a short burst of nucleation occurs with the formation of large number of nuclei in a short period of time. These particles grow rapidly and lower the monomer concentration below the nucleation threshold, allowing the further growth of these particles. The schematic diagram depicting the La Mer's mechanism is shown in fig. 1.2.1.
In many synthesis protocols the concentration of precursor increases after their injunction at certain temperature (depending on the material which is to be synthesized). This sudden increase in precursor concentration then causes a nucleation and growth f particles. Rapid injection of precursor does not necessary lead to fast nucleation and growth. This can be explained by the example of the synthesis protocols of QDs (CdSe) and iron oxide

nanoparticles (Fe_2O_3). In the case of CdSe nanoparticles the rapid injection of Se precursors (Se dissolved in TOP) at 270 ^{0}C initiates rapid nucleation for a short time followed by the growth process. Whereas in the case of Fe_2O_3 nanoparticles after injection of precursors (iron pentacarbonyl) at 100 ^{0}C a long incubation time is required to start the nucleation.

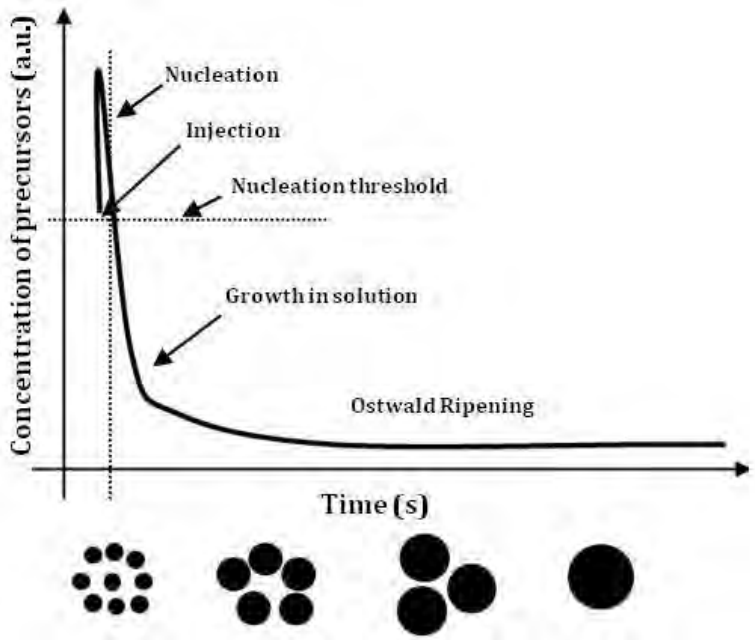

Fig. 1.2.1: *Schematic diagram illustrating La Mer's condition for nucleation and growth of nanostructures taken from reference[40].*

Nucleation occurs over some time with constant monomer concentration. Eventually surface growth of particles begins. The growth stage of crystals is more readily examined. Sugimoto[41] derived a model to understand the diffusion growth rate of crystals by using the Gibbs Thomphson equation as starting point. The Gibbs Thomphson equation is basis of classic crystallization theory to quantify the equilibrium of water droplet in surrounding vapor. The Gibbs Thomphson equation for a solid crystal of radius *r* is written as,

$$S_r = S_b exp\left(\frac{2\sigma V_m}{rRT}\right) \qquad \text{eq. 1.2.1}$$

Where S_r and S_b are the solubility of nanoparticles of radius *r* and corresponding bulk material respectively; σ is the specific surface energy; *r* is the radius of the nanocrystal; V_m is the volume of the material; *R* the gas constant and *T* the absolute temperature.
Using eq. 1.2.1 Sugimoto developed a model to understand the growth of crystals. In his model he considered that monomers are taken up by the nuclei through diffusion control mechanism. Using this consideration he calculated the growth rate of crystal which is given by the equation,

$$\frac{dr}{dt} = \frac{2\sigma D V_m^2 S_b}{rRT}\left(\frac{1}{r_c} - \frac{1}{r}\right) \qquad \text{eq. 1.2.2}$$

Here D is diffusion constant and r_c is critical radius of the crystal (explained in next paragraph). Fig. 1.2.2 shows the variation of growth rate versus size according to the model of Sugimoto.

From fig. 1.2.2 one can see that the growth rate can be negative. This can be explained on the basis of surface energy of crystals. After the nucleation process solution contains a large number of small particles. Due to high surface to volume ratio the small particles are much more soluble than the large particles. For the particles below the critical radius the dissociation of monomer is more favorable then addition of new monomers therefore these particles dissolve and feed the particles which have size greater than critical radius. At this stage smaller particles act as nutrients for bigger particles. The rate of this process, called "Ostwald-ripening" decreases with the increase of particle size[42]. This process explains the left hand side of the figure which shows the negative growth rate. The growth rate has a maximum for the size twice the critical radius. When most of nanoparticles present in the solution have size larger then $2r_c$ the smallest particles grow fast and the size distribution becomes narrow with time. The critical radius can be defined as "the size at which the growth rate is zero" at this radius the particles neither grow nor shrink[43]. The critical radius strongly depends on the monomer concentration. At high monomer concentration critical radius will be small and the entire crystals will grow and growth is said to be in focusing regime. That is the reason to get the small particle size it is better to start with high monomer concentration. When the concentration of monomers is low the critical radius shift to the bigger size and size distribution will be broad. During the growth of nanoparticles the monomer concentration decreases and critical radius shift to large size. If monomer concentration is too low the critical radius lies in the size distribution of nanoparticles and growth enters again into the Ostwald-ripening regime where again the smaller particles start to dissolve and the size distribution become's broader.

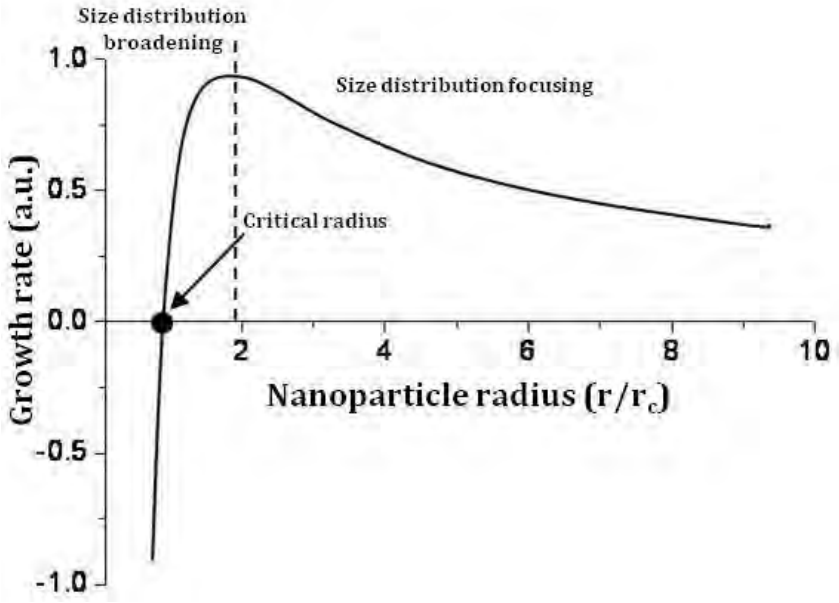

Fig. 1.2.2: *Figure of growth rate versus nanoparticle radius, according to the Sugimoto model. Taken from reference[43].*

To get a narrow size distribution it is better to stop the reaction before it reaches the Ostwald-ripening regime. But still if this happens it is possible to recover a monodisperse sample by separating out the fractions of particles with a narrow size distribution from the original broad size distribution using different techniques. One of these techniques is size-selective precipitation which is generally more applicable[44]. In this method aggregates of nanoparticles are obtained by adding the poor solvent to the stable solution of nanoparticles which gradually reduces their solvating power. The big particles with greater attractive van der waal and dipolar forces will then precipitate first. Using this method one can recover the narrow size distribution of nanoparticles but this is time consuming and final quantity of desired material will be small.

1.3 Discontinuous growth of semiconductor nanoparticles

Semiconductor nanoparticles or quantum dots (QDs) are luminescent particles. These particles have unique physical and chemical properties due to their size and compact structure. Depending on their size they emit light of different wavelength over a broad range from visible to infrared region. These particles can be made of nearly every semiconductor metal (e.g., CdS, CdSe, CdTe, ZnS, PbS), but alloys can also be used[45, 46].

The optical properties (absorbance and fluorescence) of these materials depend on their band gap which is size dependent. As the size of the QDs increases the band gap decreases which means the maximum of their absorbance and fluorescence spectra shift to higher wavelength. So optical properties of these materials can be tuned by simply varying their size. Furthermore growth of these materials in solution can be easily monitored by simply detecting their optical properties. One can also grow a shell of another material on the core to increase its quantum yield. The fig. 1.3.1 shows the absorbance and fluorescence spectra of four different families of CdSe/ZnS nanoparticles. In this case a shell of ZnS is grown on CdSe cores.

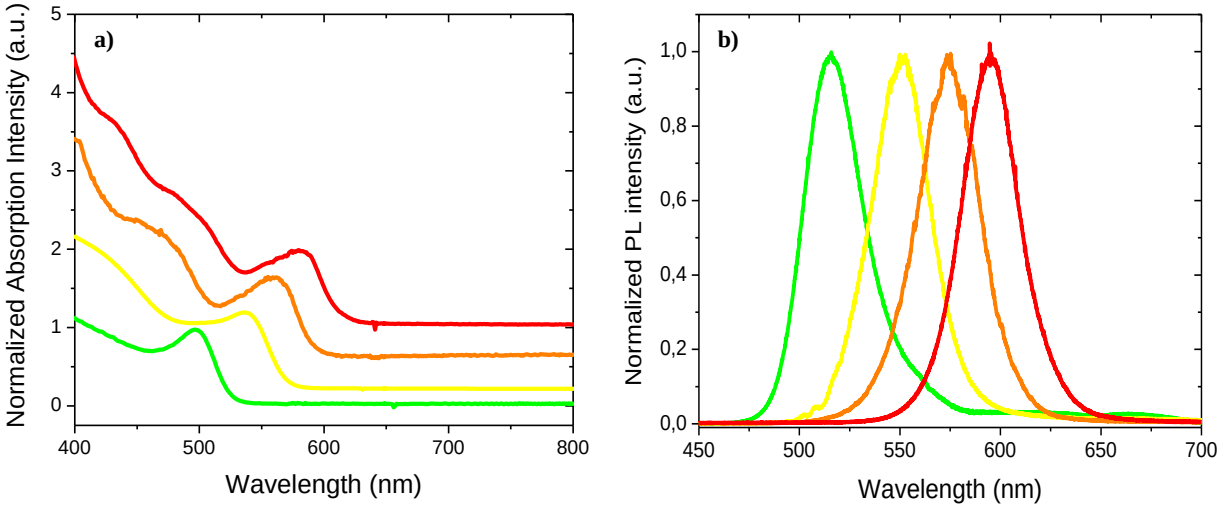

Fig. 1.3.1: *a) absorbance spectra, b) fluorescence spectra of four different sizes of CdSe/ZnS core shell nanoparticles.*

Due to unique optoelectronic properties these nanoparticles are used for many applications, ranging from light emitting-diodes (LEDs)[47], lasers[48], solar cells[49] and as bio medical labeling for imaging, detection and targeting[13, 15]. For some applications it is necessary to synthesize QDs with very reproducible properties. When we talk about reproducible properties it means QDs with same size having similar optical properties. The most common synthesis protocols for QDs are at high temperature. At high temperature the nucleation and growth of particles is very fast. Due to the fast growth of the particles, reproducibility is difficult to obtain during different synthesis. One can also synthesize nanoparticles at low temperature in which it is much easy to stop the reaction when the desired size of nanoparticles is achieved. Further changes of the synthesis conditions such as precursor concentration, type of surfactant and synthesis temperature can favor special families of nanoparticles characterized by having fixed electronic and structural properties. Such families of nanoparticles named as "magic size" by Teo and Sloane[50]. During their studies they showed that clusters consisting of specific numbers of atoms are more stable than those in which this feature is not present.

As described before in section 1.2, in a general wet chemical synthesis, after the precursors injection, nanoparticles start to nucleate in solution forming the fundamental seeds to which the remaining monomers attach during the nanoparticles growth. This is the typical growth scheme also known as continuous growth, but under certain conditions (type of monomers, their amount and the amount and type of surfactants) this kind of growth mechanism is turned into another kind in which after the nucleation, particularly stable crystal structures are formed. The growth then proceeds not in a continuous way but with the formation of other very stable crystal configurations. Each one of these crystal structures constitutes a family of nanoparticles with peculiar properties. In fact the nanoparticles belonging to each one of these families are characterized by having almost the same size and number of atoms. As we are talking about semiconductor nanoparticles this means that all the nanoparticles of a given family are characterized by having almost the same band gap. Thanks to these peculiar characteristics the nanocrystals belonging to these families are known as magic size crystals (MSCs).

Different families of almost monodisperse CdS and CdSe MSCs have been synthesized by high pressure and high temperature methods[51], inverse micelle approach[52], but none of these nanoparticles present comparable optical properties as those synthesized in solution. The sequential synthesis of these materials in solution allows to study the mechanism which drives their nucleation and growth kinetics. Recently different families of CdSe[53, 54] and CdTe[55] have been synthesized in solution. A simple way to detect the presence of semiconductive MSCs formation is through absorbance spectroscopy measurements. In the case of a continuous growth of semiconductor nanoparticles the exciton peak in the absorbance spectra simply red shifts with the particle size. When MSCs are formed we do not find just one exciton peak but as many as the families of MSCs present in solution. These peaks, in the case of sequential growth of MSCs, show an evolution over time which is completely different from those observed in a normal growth. In this time evolution of the absorbance spectrum it is possible to observe a different growth mechanism which involves not only the monomers but even the particles present in solution.

Fig. 1.3.2 shows different families of CdS and CdTe MSCs synthesized in solution. Six different families of MSCs were observed in the case of CdS, while three in the case of CdTe. Absorption spectra of aliquots were taken during the synthesis of MSCs each family of MSCs is shown by dotted line. In the case of CdTe MSCs 10min. after precursor injection MSC growth turned into regular particle growth with continuous shift of absorbance peak (indicated by the arrow).

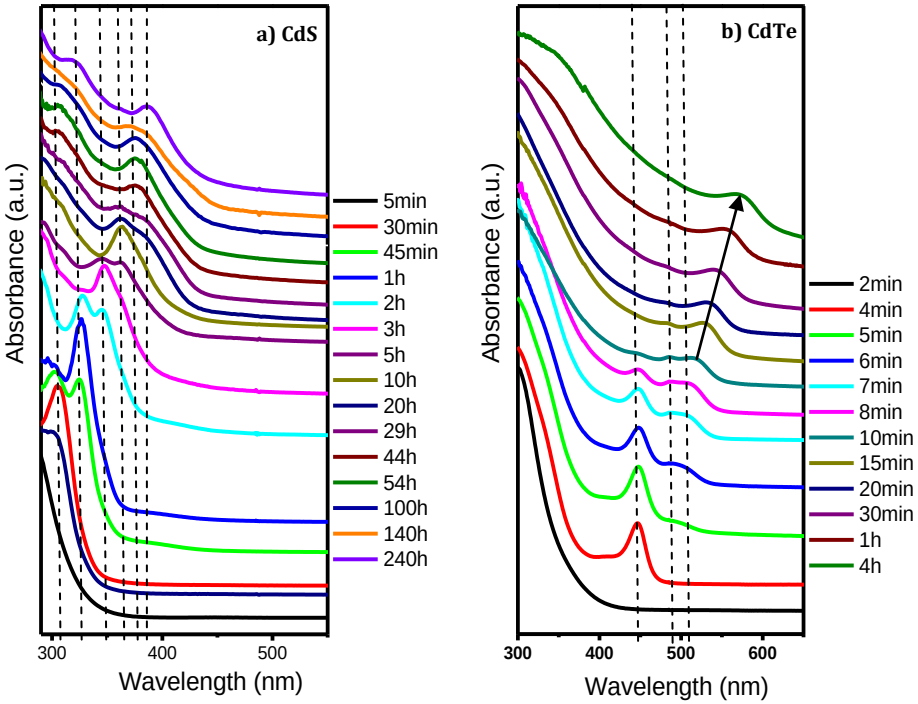

Fig. 1.3.2: *Absorbance spectra time evolution of different a)CdS and b)CdTe MSCs in solution. The zero time correspond to the time of precursor injection. Taken from reference*[56]

The growth of nanoparticles depends on binding and unbinding rate of free monomers present in solution. In normal growth model the binding rate dominates for all the particles above the critical size so that the particles grow continuously. As in the case of MSCs the growth of particles is different from the regular sized particles, growth kinetics undergoes stages of appearance and disappearance. A different growth model has been proposed to understand the growth mechanism involved during MSCs formation.

Kudera et al.[53] proposed a model for the growth of CdSe MSCs based upon their experimental results. In their model they reported that MSCs are so stable that when a family of these MSCs grows in solution no atom detach from them. So these MSCs only grow but they cannot shrink to smaller size. Particles present in between the two families of MSCs are unstable and their lifetime will be short. If these intermediate particles are slightly larger than a MSC family the release of the outer most atoms will be more probable than the deposition of new monomer and particles tend to enter MSCs of smaller size, where as if the particles are slightly smaller than a MSC family the binding of monomer will be more favorable to enter the MSCs of larger size.

For the growth of CdTe MSCs Dagtepe and coworkers[55] reported a mechanism involved during the growth of CdTe MSCs. According to Dagtepe the mechanism for the growth of CdTe MSCs was the aggregation of MSCs which may or may not involved the addition of

monomers. The High resolution TEM images confirmed their growth model in which they observed different orientations in the crystal structure of nanoparticles which according to them is due to the different orientation of MSCs in which they attach with each other.
The most suitable model for the growth of MSCs was reported by Peng et al.[57]. In their model Peng et al. used the Gibbs Thomphson eq. 1.2.1 as a starting point to describe the chemical potential. A simple mathematical treatment changes the eq. 1.2.1,

$$RTlnS_r = RTlnS_b + \left(\frac{2\sigma V_m}{rRT}\right) \qquad \text{eq. 1.3.1}$$

If μ_r and μ_b represent the chemical potential of the crystal of radius r and crystal of infinite size the equation change into,

$$\mu_r = \mu_b + \left(\frac{2\sigma V_m}{rRT}\right) \qquad \text{eq. 1.3.2}$$

By setting the relative chemical potential of crystal of infinite size as the relative standard eq. 1.3.2 gives,

$$\mu_r \propto \frac{1}{r} \qquad \text{eq. 1.3.3}$$

In the case of spherical crystal the ratio of surface atom and total atoms should be proportional to the surface area of crystal and volume of crystal. If δ denotes the surface atoms ratio then in case of spherical crystal,

$$\delta = \left(\frac{A_1 \pi r^2}{A_2 \frac{4}{3}\pi r^3}\right) = \frac{A_3}{r} \qquad \text{eq. 1.3.4}$$

Where A_1, A_2 and A_3 are proportionality constants,

$$\delta \propto \frac{1}{r} \qquad \text{eq. 1.3.5}$$

Comparing equation (1.3.3) and equation (1.3.5) we can see that relative chemical potential of a crystal of finite size is proportional to the surface atom ratio,

$$\mu_r \propto \delta \qquad \text{eq. 1.3.6}$$

In this model they proposed two basic assumptions. Firstly all the surface atoms bear same chemical potential independent of their position in the crystal. Secondly relative chemical potential is an average value over all the atoms in the crystal.
Chemical potential of the crystals depends on their size. For the small sized crystals the chemical potential is high. As discussed before the size of the particles depends on the critical radius, to get the small sized particles one has to start with high monomer concentration so that the critical radius lies at very low values. Peng et al. reported that such a high monomer concentration will complicate the nucleation process. At this monomer

concentration the critical radius will be extremely small as compared to the synthesis of regular sized particles. In this small size range the relative chemical potential is extremely size dependent and very sensitive to the configuration of nuclei. And one can observe the formation of MSCs. Peng et al. showed that in such a small size range the Gibbs Thomphson equation is no longer valid. They introduced wells in the chemical potential curve and proposed tunneling mechanism for the formation of bigger MSCs.
Schematic diagram for the relative chemical potential versus the number of atoms in the particles according to Peng et al. is shown below.

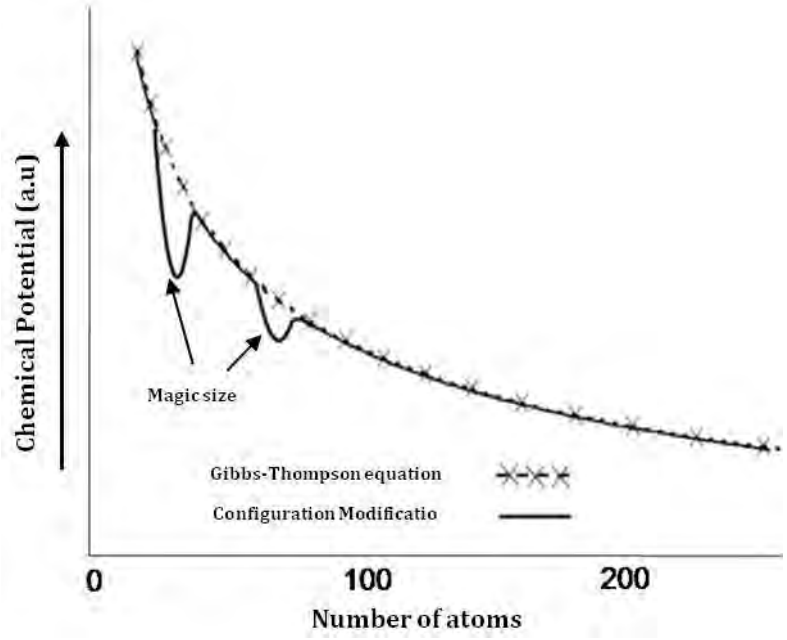

Fig. 1.3.3: *Schematic diagram showing dependence of relative chemical potential on size of crystal in extremely small sized regime taken from reference*[57].

Study of these small stable structures could help to understand processes involved during the initial stages of nanoparticles formation. Such stable nanoparticles are very promising for the application where high reproducibility is required.

References

[1] N. J. Tao, *Nature Nanotechnology* **2006**, *1*, 173.
[2] G. Eda, G. Fanchini, M. Chhowalla, *Nature Nanotechnology* **2008**, *3*, 270.
[3] D. Zhang, K. Ryu, X. Liu, E. Polikarpov, J. Ly, M. E. Tompson, C. Zhou, *Nano Letters* **2006**, *6*, 1880.
[4] S. Kan, T. Mokari, E. Rothenberg, U. Banin, *Nature Materials* **2003**, *2*, 155.
[5] S. Kumar, T. Nann, *Small* **2006**, *2*, 316.
[6] M. C. Daniel, D. Astruc, *Chemical Reviews* **2004**, *104*, 293.
[7] J. G. Gibbs, Y. P. Zhao, *Small* **2009**, *5*, 2304.
[8] Z. G. Wang, O. I. Wilner, I. Willner, *Nano Letters* **2009**, *9*, 4098.
[9] N. A. Peppas, J. Z. Hilt, A. Khademhosseini, R. Langer, *Advanced Materials* **2006**, *18*, 1345.
[10] T. M. Allen, P. R. Cullis, *Science* **2004**, *303*, 1818.
[11] D. A. LaVan, T. McGuire, R. Langer, *Nature Biotechnology* **2003**, *21*, 1184.
[12] J. Panyam, V. Labhasetwar, *Advance Drug Delivery Reviews* **2003**, *55*, 329.
[13] M. J. Bruchez, M. Moronne, P. Gin, S. Weiss, A. P. Alivisatos, *Science* **1998**, *281*, 2013.
[14] W. J. Parak, D. Gerion, T. Pellegrino, D. Zanchet, C. Micheel, S. C. Williams, R. Boudreau, M. A. L. Gros, C. A. Larabell, A. P. Alivisatos, *Nanotechnology* **2003**, *14*, R15.
[15] W. J. Parak, T. Pellegrino, C. Plank, *Nanotechnology* **2005**, *16*, R5.
[16] R. Weissleder, G. Elizondo, J. Wittenberg, C. A. Rabito, H. H. Bengele, L. Josephson, *Radiology* **1990**, *175*, 489.
[17] W. Cai, T. Gao, H. Hong, J. Sun, *Nanotechnology, Science and Applications* **2008**, *1*, 17.
[18] S. J. Son, X. Bai, S. B. Lee, *Drug Discovery Today* **2007**, *12*, 650.
[19] E. Boisselier, D. Astruc, *Chemical Society Reviews* **2009**, *38*, 1759.
[20] M. Arruebo, R. Fernandez-Pacheco, M. R. Ibarra, J. Santamaria, *Nano Today* **2007**, *2*, 22.
[21] L. Zhang, F. X. Gu, J. M. Chan, A. Z. Wang, R. S. Langer, O. C. Farokhzad, *Clinical Pharmacology & Therapeutics* **2008**, *83*, 761.
[22] R. A. Sperling, P. Rivera_Gil, F. Zhang, M. Zanella, W. J. Parak, *Chemical Society Reviews* **2008**, *37*, 1896.
[23] J. H. Adair, T. Li, T. Kido, K. Havey, J. Moon, J. Mecholsky, A. Morrone, D. R. Talham, M. H. Ludwig, L. Wang, *Materials Science & Engineering R-Reports* **1998**, *23*, 139.
[24] H. L. Crampton, E. E. Simanek, *Polymer International* **2007**, *56*, 489.
[25] Y. Malam, M. Loizidou, A. M. Seifalian, *Trends in Pharmacological Sciences* **2009**, *30*, 592.
[26] A. Samad, Y. Sultana, M. Aqil, *Current Drug Delivery* **2007**, *4*, 297.
[27] K. Kataoka, A. Harada, Y. Nagasaki, *Advanced Drug Delivery Reviews* **2001**, *47*, 113.
[28] Y. Yang, W. Jia, X. Qi, C. Yang, L. Liu, Z. Zhang, J. Ma, S. Zhou, X. Li, *Macromolecular Bioscience* **2004**, *4*, 1113.
[29] P. Rivera Gil, L. L. del Mercato, P. del Pino, A. Munoz Javier, W. J. Parak, *Nano Today* **2008**, *3*, 12.
[30] A. Antipov, G. B. Sukhorukov, *Advances in Colloid and Interface Science* **2004**, *111*, 49.
[31] A. P. Alivisatos, K. P. Johnsson, X. Peng, T. E. Wilson, C. J. Loweth, M. P. Bruchez, P. G. Schultz, *Nature* **1996**, *382*, 609.
[32] M. E. Stewart, M. J. Motala, J. Yao, L. B. Thompson1, R. G. Nuzzo, *Journal of Nanoengineering and Nanosystems* **2006**, *220*, 81.

[33] T. Vossmeyer, L. Katsikas, M. Giersig, I. G. Popovic, K. Diesner, A. Chemseddine, A. Eychmüller, H. Weller, *Journal of Physical Chemistry* **1994**, *98*, 7665.
[34] A. L. Rogach, A. Kornowski, M. Y. Gao, A. Eychmuller, H. Weller, *Journal of Physical Chemistry B* **1999**, *103*, 3065.
[35] S. Kudera, L. Carbone, M. Zanella, R. Cingolani, W. J. Parak, L. Manna, *Physica Staus Solidi (c)* **2006**, *203*, 1329.
[36] N. Pinna, K. Weiss, H. Sack-Kongehl, W. Vogel, J. Urban, M. P. Pileni, *Langmuir* **2001**, *17*, 7982.
[37] N. Pinna, K. Weiss, J. Urban, M.-P. Pileni, *Advanced Materials* **2001**, *13*, 261.
[38] V. K. Lamer, R. H. Dinegar, *Journal of the American Chemical Society* **1950**, *72*, 4847.
[39] V. K. Lamer, *Industrial and Engineering Chemistry* **1952**, *44*, 1270.
[40] C. B. Murray, C. R. Kagan, M. G. Bawendi, *Annual Review Material Science* **2000**, *30*, 545.
[41] T. Sugimoto, *Advances in Colloid and Interface Science* **1987**, *28*, 65.
[42] H. Weller, *Philosophical Transactions of the Royal Society A* **2003**, *361*, 229.
[43] X. Peng, J. Wickham, A. P. Alivisatos, *Journal of the American Chemical Society* **1998**, *120*, 5343.
[44] Y. Yin, A. P. Alivisatos, *Nature* **2005**, *437*, 664.
[45] A. P. Alivisatos, *Science* **1996**, *271*, 933.
[46] R. E. Bailey, S. Nie, *Journal of the American Chemical Society* **2003**, *125*, 7100.
[47] P. O. Anikeeva, J. E. Halpert, M. G. Bawendi, V. Bulovic, *Nano Letters* **2007**, *7*, 2196.
[48] Y. Chan, P. T. Snee, J. M. Caruge, B. K. Yen, G. P. Nair, D. G. Nocera, M. G. Bawendi, *Journal of the American Chemical Society* **2006**, *128*, 3146.
[49] P. V. Kamat, *Journal of physical chemistry C* **2008**, *112*, 18737.
[50] B. K. Teo, N. J. A. Sloane., *Inorganic chemistry* **1985**, *24*, 4545.
[51] N. Herron, J. C. Calabrese, W. E. Farneth, Y. Wang, *Science* **1993**, *259*, 1426.
[52] A. Kasuya, R. Sivamohan, Y. A. Barnakov, I. M. Dmitruk, T. Nirasawa, V. R. Romanyuk, V. Kumar, S. V. Mamykin, K. Tohji, B. Jeyadevan, K. Shinoda, T. Kudo, O. Terasaki, Z. Liu, R. V. Belosludov, V. Sundararajan, A. Y. Kawazoe, *Nature Materials* **2004**, *3*, 99.
[53] S. Kudera, M. Zanella, C. Giannini, A. Rizzo, Y. Li, G. Gigli, R. Cingolani, G. Ciccarella, W. Spahl, W. J. Parak, L. Manna, *Advanced Materials* **2007**, *19*, 548.
[54] F. S. Riehle, R. Bienert, R. Thomann, G. A. Urban, M. Krüger, *Nano Letters* **2009**, *9*, 514.
[55] P. Dagtepe, V. Chikan, J. Jasinski, V. J. Leppert, *Journal Of Physical Chemistry C* **2007**, *111*, 14977.
[56] M. Zanella, A. Z. Abbasi, A. K. Schaper, W. J. Parak, *Journal Of Physical Chemistry C* **2010**, *114*, 6205.
[57] Z. A. Peng, X. Peng, *Journal of the American Chemical Society* **2002**, *124*, 3343.

Contribution

- **Discontinuous growth of semiconductor nanoparticles**

Synthesis of different families of MSCs from different semiconductor materials such as CdS, CdTe, ZnSe and ZnO were performed.
In case of CdS, six different families of MSCs were observed; synthesis was performed at low temperature 60 ^{0}C. Cadmium oxide (CdO) was used as Cd precursor where as selenium (Se) precursors were obtained by dissolving the Se metal powder in TOP. Growth of particles was observed by measuring the absorption spectrum of reaction solution with time. Different families of these MSCs were found at 303nm, 326nm, 347nm, 362nm, 377nm and 387nm in absorption spectra.
For CdTe MSCs three different families were observed. Synthesis was carried out at 130 ^{0}C using CdO as a Cd precursor where as tellurium (Te) precursors were obtained by dissolving tellurium powder in TOP. MSCs were observed at 445nm, 487nm and at 506nm in absorption spectra during the growth of these particles.
In case of ZnSe MSCs three different families were observed. Zinc oxide (ZnO) was used as Zn precursors whereas the selenium precursors were obtained using same approach as in case of CdS MSCs synthesis. Synthesis was performed at relatively high temperature 180 ^{0}C. Three different families of MSCs were observed at 328nm, 346nm and at 378nm.
Synthesis of ZnO MSCs was performed at 180^{o}C. Only one family of MSCs was observed at 365nm.
Furthermore the doping of mercury (Hg) atoms was carried out on the CdS MSCs. The Hg atoms were introduced during the synthesis of CdS MSCs. Four families of CdS MSCs were found when doping of Hg atoms was performed. It was observed that by incorporating these impurity atoms the optical properties of the CdS MSCs can be changed. The fluorescence of the CdS MSCs was shifted to near infra red region due to the presence of Hg atoms in the crystal structure.
Each MSCs family of different materials was collected for further investigation by simply stopping the reaction and precipitation of nanoparticles when most of these particles were belonging to the same family i.e having same absorption spectra.

- **Synthesis of fluorescent nanoparticles**

Fluorescent nanoparticles CdSe were synthesized using the wet chemical synthesis technique. To enhance the optical properties of these particles the shell of ZnS was grown on top of these particles. These particles were further used in different experiments such as by embedding these particles in the walls of the capsules it was possible to detect the capsule under fluorescence microscope and to get the information about their structure.

- **Synthesis of magnetic nanoparticles**

Magnetic nanoparticles such as iron oxide (Fe_2O_3) and iron platinum (FePt) were synthesized. Magnetic properties of these particles were investigated by embedding them in the walls of the capsules.

2.1 Polyelectrolyte and layer by layer technique

Any substance which is dissociated into free ions when dissolved is called an electrolyte, whereas a polymer whose repetitive units contain an electrolyte is called a polyelectrolyte[1]. By dissolving such polymers in aqueous solution, electrolytes present in its chains will disassociate leaving a charge on the polyelectrolyte. The charge is compensated by counter ions present in solution. Depending on their charge polyelectrolytes are divided into two groups. If after dissolving in an aqueous solution the resulting polyelectrolyte is positive, it is referred as polycation. Conversely, if a polyelectrolyte is negative upon dissolution it is referred as polyanion. Also depending on their charge density polyelectrolytes can be classified as "strong" or "weak" polyelectrolyte. If a polyelectrolyte completely dissociate within the normal pH range it is called strong polyelectrolyte. Whereas if a polyelectrolyte partially dissociate when dissolved in aqueous solution it is referred as weak polyelectrolyte. The Henderson–Hasselbalch[2] equation is used to describe the dependence of pH value on the dissociation constant which is written as,

$$pH = pK_a + log\left(\frac{[conj.\ base]}{[acid]}\right) \qquad \text{eq. 2.1.1}$$

Here pK_a is dissociation constant, [conju. base] is molar concentration of conjugated base, and [acid] is molar concentration of acid. As we know that charge of polyelectrolyte depends on the dissociation of electrolyte present in each of its units, so we can say that a polyelectrolyte is fully charged when its electrolyte is completely dissolved. Eq. 2.1.1 is also used to determine the percentage of polyelectrolyte in, protonated, neutral or deprotonated state at a given pH value.

As polyelectrolytes can be positive or negative, two oppositely charged polymers in a mixture will bind and form a complex due to electrostatic attraction. Same phenomena will happen if we give a charged surface in a polyelectrolyte solution whose charge is opposite to that of the surface. The polyelectrolyte will start to adsorb on the surface until it covers the whole surface or the surface charge is compensated. So at the end of polyelectrolyte adsorption the surface will carry the charge of the polyelectrolyte. This is called a charge reversal. If now the surface is washed to get rid of unreacted polyelectrolyte and placed in a solution of an oppositely charged polyelectrolyte, again the adsorption will take place and the charge of the surface will reverse. This process can be repeated as many times as required, and is called layer-by-layer (LbL) assembly. This technique was first introduced by Decher et al. [3, 4] (in the 1990s) to fabricate thin films. To study the structure of films X-ray and neutron reflectivity measurements were performed. The experiments showed that structure of films is continuous, striated and interdigitated[5, 6]. After the work of Decher et al. in 1992 large increase was observed in the field of thin films using LbL technique due to ease and versatility of this method. Zhai and co-workers[7] have reported a thin film made of 200 layer of poly(allylamine hydrochloride) (PAH) and poly(acrylic acid)(PAA) polyelectrolytes. Substrates made of different materials such as glass[8], silicon wafer[9], mica[10] and gold[11] have been used to fabricate thin films applying LbL assembly. Multilayer films are mostly formed due to electrostatic interaction of oppositely charged polyelectrolytes, but this technique is not limited to only this interaction of layers.

Assemblies based on hydrogen bonding[12], charge transfer[13], covalent bonding[14], biological recognition[15] and hydrophobic interaction[16] have also been demonstrated.

2.2. Polyelectrolyte capsules based on layer by layer technique

Synthesis of polyelectrolyte capsules is based on the same LbL technique used by Decher et al. [3, 4] on the flat surface. A sacrificial charged spherical particle is used as template for the LbL adsorption of polyelectrolytes onto its surface[17]. During each layer the template particles are given to the excess of a polyelectrolyte solution. After the adsorption the excess of polyelectrolyte has to be removed and core particles should be washed at least three times before adding the next polyelectrolyte of opposite charge. This avoids the formation of aggregates and polymer sediments in the solution. The template particles can be separate from the bulk solution by centrifugation or filtration[18]. After the desired number of layers the sacrificial template can be removed by decomposition or dissolution of its components, resulting in spherical and defined hollow capsules. Fig. 2.2.1 shows the schematic diagram of polyelectrolyte capsule fabrication based on LbL-assembly of polyelectrolytes onto solid template.

This technique was first reported by Sukhorukov and co-workers in 1998[19]. Initially lot of work was done to investigate the basic properties of these hollow structures, such as thickness of the capsule wall, and its sensitivity upon changing pH[20], salt concentration[21] or temperature[22, 23]. Afterwards polyelectrolyte capsules have been used as micro containers for several purposes [24, 25]. Different materials like proteins[26], enzymes[27, 28] and inorganic salts[29] have been encapsulated in such carrier systems using different techniques which are described in section (2.4).

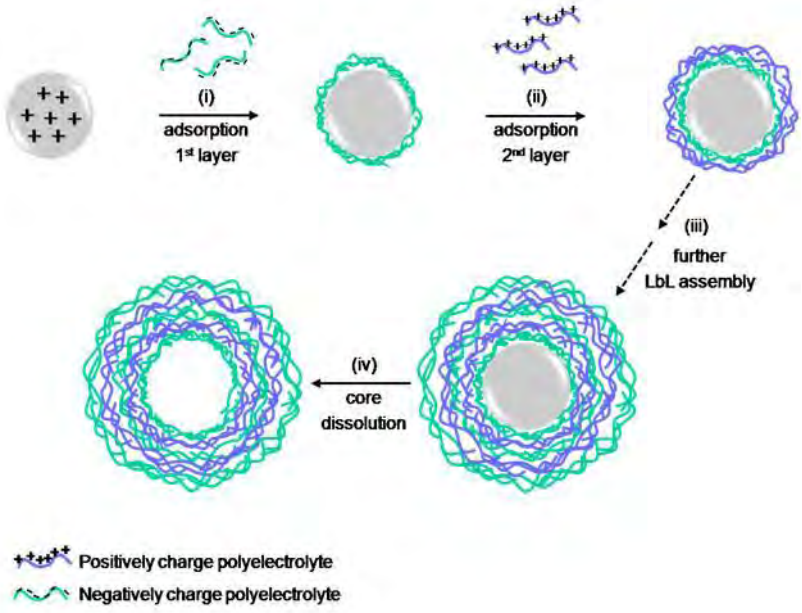

Fig. 2.2.1: *Schematic diagram for the fabrication of polyelectrolyte capsules by LbL assembly. i) negatively charged polymer is adsorbed on positively charged template core, ii)adsorption of second positively charged polymer, iii) further LbL assembly, iv) removal of template to obtain empty cavity. Figure taken from reference[17] .*

2.3 Templates and wall materials

There are two main compartments of the capsule: The cavity and the wall. Size and shape of the cavity depend on the template core whereas the properties of the wall depend on the polyelectrolytes used to build up the capsule. In this section details about different materials widely used as template and for wall formation are given.

The template core is used as sacrificial support which is removed by decomposition or dissolution after the capsule synthesis. The template material has to fulfill certain requirements: First of all it should be stable during the LbL assembly, secondly the wall of the capsules should be stable during the core removal and last the core material has to be removed completely without disturbing or interacting with the cargo material loaded in the arising cavity. As shape and size of final capsules depend on the template cores, these particles should be monodisperse and spherical in shape. Wide variety of materials ranging from nanometer size to micrometer size have been used to fabricate such polyelectrolyte capsules. The spherical melamine formaldehyde (MF) particles were initially used as template core and later studied extensively[30]. These particles can be dissolved in organic solvent such as dimethyl sulfoxide (DMSO). Major drawbacks of these particles are: it is difficult to dissolve and remove the MF completely from the cavity and they are not biocompatible[31]. Poly styrene (PS) particles are also used as template core. These particles suffer from aggregation during the core removal[32]. Silicon dioxide (SiO_2) particles are promising candidates as templates. These particles are available in broad range of size with polydispersity. The drawback of these particles is the core removal step. One has to work with strong acids like hydrofluoric acid to dissolve silicon-oxide completely[23]. This requires lot of care and specialized laboratory equipments. One common drawback of all template cores listed above is the impossibility of loading of material inside the cavity before the core removal. As these particles are not porous the loading of cavity occurs after the dissolution process by varying the different conditions to make the wall permeable for macromolecules. This method is called post-loading[32]. Detail about different loading process is given in the encapsulation part (section 2.4). Spherical carbonate crystals such as porous calcium carbonate ($CaCO_3$) are also widely used as template cores [26, 30]. These particles have some advantages over other template materials, such as one can easily encapsulate macromolecules during the synthesis of these particles which is called co-precipitation method or pre loading technique. Second advantage of these particles is they can be dissolved under mild condition such as by lowering the pH or by using ethylenediaminetetraacetic acid (EDTA) as complexing agent. Furthermore, toxic side effects play minor roles when working with $CaCO_3$ particles[33]. The disadvantage of these particles is polydispersity of particles. Techniques to fabricate these particles with a narrow size distribution in micrometer scale are not published yet. In the present work all the capsules were fabricated using $CaCO_3$ particles as template.

A Large variety of polyelectrolytes have been used for the fabrication of capsules. Different polyelectrolytes have varying properties in structure (linear or branched), charge density, strength and type of electrolyte. Most commonly used polycations for the fabrication of microcapsules are poly (allylamine hydrochloride) (PAH), poly(diallyldimethylammonium chloride) (PDADMAC), poly(ethyleneimine) (PEI) and polyvinylpyrrolidone (PVP), the most

commonly used polyanions are poly(styrene sulfonate) (PSS), poly(acrylic acid) (PAA), poly(methacrylic acid) (PMA) and polyphosphoric acid (PPA). Biological materials/molecules like nucleic acids, proteins and polysaccharides, as well as charged supramolecular biological assemblies, such as viruses or membrane fragments [34], are gaining significant interest for the fabrication of biodegradable and bio-functionalized capsule wall. In the present work most of the capsules were fabricated using PAH as polycation and PSS as polyanion.

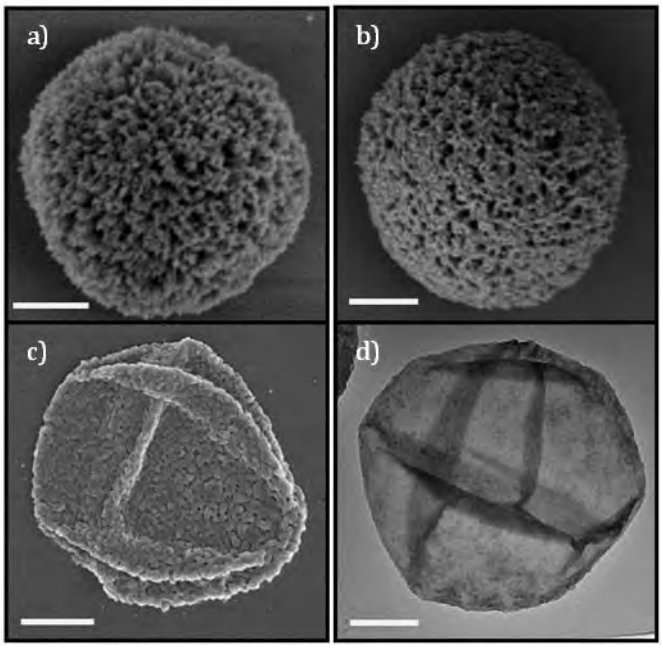

Fig. 2.3.1: *a) Scanning electron microscope (SEM) image of porous plane $CaCO_3$ template before LbL assembly, b) SEM image after $(PSS/PAH)_5$ polyelectrolyte layers, c) SEM image of $(PSS/PAH)_5$ capsule after core removal, d) Transmission electron microscope (TEM) image of $(PSS/PAH)_5$ capsule after core removal. In figure c & d capsules collapse after core removal. Scale bar corresponds to 1µm.*

2.4 Encapsulation of cargo molecules

The cavity of polyelectrolyte capsules can be loaded by two different methods: One is called the co-precipitation or direct loading technique and other is called post loading or indirect loading[35].

In the direct loading technique material is either entrapped within or adsorbed onto the template cores before the LbL assembly. For this technique the porous $CaCO_3$ particles are an interesting candidate and most widely used[35]. The materials or macromolecules of interest can be added during the synthesis of the templates or particles can be incubated in the solution of macromolecules after their synthesis[30]. The $CaCO_3$ are porous particles macro molecules stay inside the pores during the LbL assembly, after the dissolution of cores the entrapped material is released into the cavity of the polyelectrolyte capsules. The filling rate of macromolecules depends on the pore size of $CaCO_3$ and on the nature of the

materials. Nowadays this method is widely used to encapsulate different material (e.g. DNA, proteins, dextran, nanoparticles, etc).

Post-loading of macromolecules can be achieved by loading hollow capsules after removal of their templates. In this method after the LbL assembly the core of the capsule is dissolved leaving behind an empty cavity[35]. The macromolecules are then driven into the cavity by using physicochemical forces such as, ionic strength, pH, temperature or using the external stimuli like light, magnetic field or ultra sound. By applying such methods wall of the capsules could be made permeable so that cargo material can diffuse through the polyelectrolyte wall and being entrapped in the capsules cavity. Once the molecules are in the cavity the environmental conditions are reversed again resulting in an impermeable wall. In present work only co-precipitation was used to embed macromolecules in polymer capsules. In next paragraphs explanation of some other methods are given which are reported in literature and widely used for the encapsulation of molecules.

The wall of the polyelectrolyte capsules can be modified to show pH sensitive behavior by introducing a polyelectrolyte with weak acid and weak base functionalities[36]. In these kinds of capsules the average charge and interaction between the wall constituents can be controlled by adjusting the pH of the surrounding medium. As the charge of polyelectrolytes depends on pH, the change in pH value induces an imbalance of charge which leads to the change in the wall structure. The stability of capsules made of weak polyelectrolytes such as poly(allylamine hydrochloride) (PAH), poly(acrylic acid) PAA, and poly(methacrylic acid) (PMA) was found to be pH dependent.

It was observed that PSS/PAH capsules are in open sate (permeable) when the pH<6.5 while the wall of capsules are in closed state (impermeable) when pH>6.5. Sukhorukov and co-workers[37] used this pH dependent reversible pore formation method for PSS/PAH polyelectrolyte capsules to encapsulate 75kDa FITC-dextran molecule. They found that these polyelectrolyte capsules were permeable for FITC-dextran at pH values up to 6 while for pH 8 upwards most of the capsules were in closed state. It has been shown that PSS/PAH capsules can be used to encapsulate urea[38], and high molecular weight compounds such as rhodamine-labeled PSS[24] using pH-switchable permeability of capsules wall. It was observed that capsules made of weak polyelectrolytes PAH and PMA have dual pH response, because swelling was observed at both low and high pH. This reversible swelling of capsules can be used to encapsulate cargo molecules in the cavity[20]. The pH response of polyelectrolyte capsules made of chitosan (CT) and dextran sulfate (DEXS) has also been reported[39]. Results showed that the wall of these types of capsules was impermeable for dextran 4kDa-250kDa at pH<6.8 while it was permeable at higher pH.

The high molecular weight compound can also be encapsulated by switching the permeability of polyelectrolyte capsules by variation of salt concentration. This changes the ionic strength, which leads to increased permeability of the capsule wall. Diffusion of these charged species through the wall of the capsule cause a change in electrostatic interaction between the oppositely charged polyelectrolytes. The ionic strength influences both the range and magnitude of electrostatic interaction. High salt concentration can also lead to the destruction of polyelectrolyte capsules[25].

The permeability of PSS/PAH capsules depending on salt concentration was already studied[25]. Results showed that at low NaCl concentration the wall of the capsules was in

closed state while at high salt concentration the wall was in open state. It was shown that capsules were permeable for PAH (70kDa) conjugated with rodamine B above $2x10^{-2}$M of NaCl. It was also observed that this permeability of wall is reversible.

Polyelectrolyte capsules can be also fabricated to behave temperature sensitive by introducing different thermo-sensitive compounds as wall materials. Polyelectrolyte multi-layers are kinetically stable structures, so one can expect that a temperature increase can provide enough thermal energy to surpass the energy barrier necessary for polymeric film rearrangement. The most widely used thermo-sensitive polyelectrolyte is poly(diallydimethylammonium chloride) (PDADMAC). Encapsulation of macromolecules in PDADMAC/PSS polyelectrolyte capsules have been studied[40]. For this purpose the hollow capsules were incubated in a solution of the respective compound followed by heating step. It was observed that PDADMAC/PSS polyelectrolyte capsules start to shrink when they are heated. Resulting capsule diameter was reduced to 3.3μM (initial 4.5μM) after incubation at 50 ^{0}C for 20 min. This shrinking of PSS/PDADMAC capsules was successively used for the encapsulation of FITC-dextran 10kDa and 70kDa. The shrinking caused impermeability for entrapped molecules.

Another way of changing capsules permeability is applying external stimuli, e.g. strong magnetic fields can be used to manipulate the polymer structure of the wall. For this purpose magnetic particles have to be embedded into the wall of the capsules. By exposing them to a magnetic field the particles in the wall are stimulated which leads to partially or total decomposition of the wall. This approach has been studied by Lu et al.[41] on magnetic nanoparticles containing PSS/PAH capsules. In their study they used oscillating magnetic field on the hollow PSS/PAH capsules with one layer of gold coated cobalt particle Co@Au. They observed that due to the magnetic field the Co@Au particles start to spin and disturb the wall of polyelectrolyte capsules. Obviously no thermo-sensitive drugs (protein and DNA) can be loaded into such capsules due to massive heat production during the long exposure to strong magnetic fields.

Another easy way to encapsulate material is the entrapment due to electrostatic interaction. Charged molecules can stick to an oppositely charged matrix present inside the capsules[42-44].

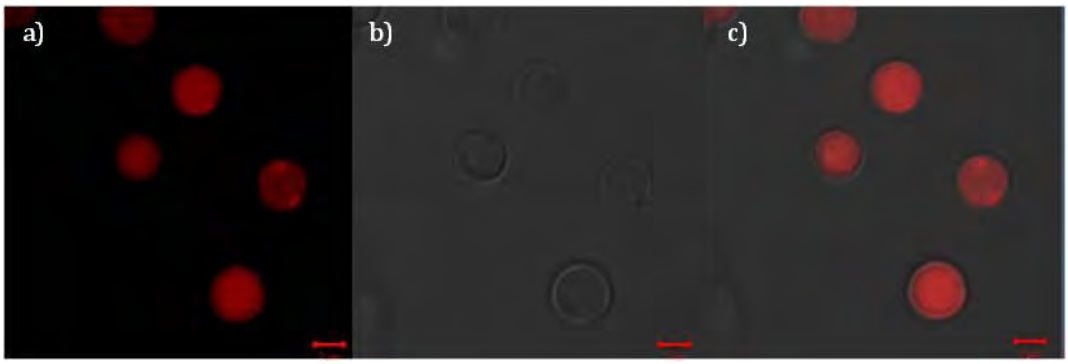

Fig. 2.4.1: *Confocal laser scanning microscope (CLSM) image of $(PSS/PAH)_5$ capsules containing RITC-dextran in cavity. a) Fluorescence & b) transmission channels, c) overlay of two channels. He-Ne laser with wave length 543nm was used to excite the RITC. Scale bar corresponds to 2μm.*

2.5 Functionalization of polyelectrolyte capsules

2.5.1 Functionalization of capsules wall

The main advantage of multilayer polyelectrolyte capsules is that the wall of the capsules can be functionalized with different substances (e.g. fluorophores or nanoparticles). Nanoparticles having different properties such as fluorescence (i.e. quantum dots), magnetic behavior or metallic character (i.e. gold nanoparticles) can be incorporated in the wall of the capsules to get a multifunctional system[17]. Using fluorophores and fluorescent nanoparticles in the wall of capsules allows a facile analysis and detection with a fluorescence microscope. Magnetic particles can be used to mobilize the capsules in desired direction by applying the external magnetic field gradient. Metallic particles in the capsules wall enable the release of encapsulated materials by stimulation with laser light. These different kind of nanoparticles can be introduced in the wall of polyelectrolyte capsules due to the electrostatic interaction of nanoparticles and oppositely charged polyelectrolyte layers[45, 46]. Fig. 2.5.1 shows a scheme for the synthesis of polyelectrolyte capsules using different kinds of nanoparticles in the wall and macromolecules in the cavity

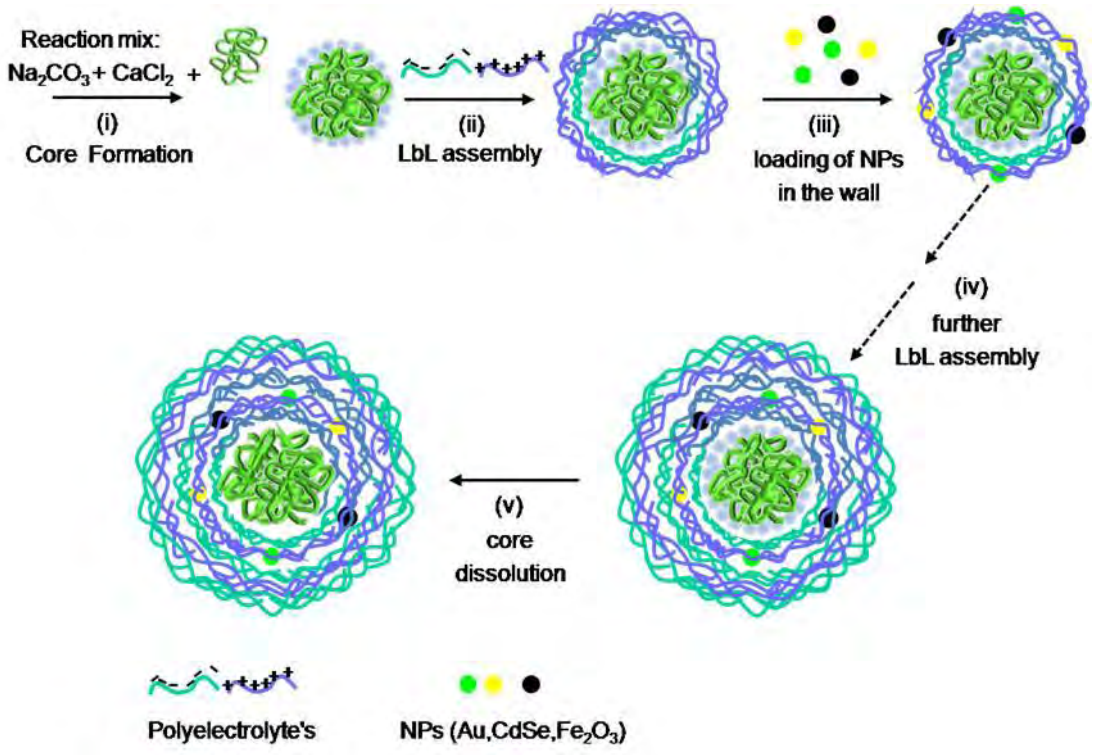

Fig. 2.5.1: *Schematic formation and functionalization of polyelectrolyte multilayer capsules based on filled $CaCO_3$ particles. i) precipitation of the template material in the presence of cargo molecules, ii) LbL assembly of oppositely charged polyelectrolytes onto the $CaCO_3$ template, iii) functionalization of the wall with different nanoparticles , iv)LbL assembly is repeated to obtain the stable structure, v) core removal to obtain hollow multilayer capsule with cargo molecules inside the cavity.*

Alternatively to organic fluorophores, colloidally synthesized semiconductor nanoparticles, QDs are widely used as fluorescent indicators for optical detection. As discussed in chapter one (section 1.3) these particles are available with high-intensity band gap and their wavelength can be adjusted by controlling the nanoparticle size due to quantum confinement effect[47]. An advantage of using QDs as fluorescent indicators is that differently emitting QDs can be excited simultaneously with light of a single wavelength[48]. In addition to this less photo bleaching is observed than in case of most organic fluorophores, which makes QDs suitable for measurements over long time periods[49, 50]. Most frequently used QDs are CdTe and CdSe[51, 52]. However these particles have the disadvantage that they might release Cd ions which can cause cytotoxic effects[52-54].

By using the magnetic nanoparticles it is easy to direct the capsules in a desired direction by applying the external magnetic field gradient. The magnetic Fe_3O_4 nanoparticles were used in the wall[55-57] as well as in the cavity of microcapsules[58]. Research showed that magnetic nanoparticles can also be used as contrast agent for magnetic resonance imaging (MRI)[59]. Embedding magnetic nanoparticles in the wall of the capsules turns this system into an interesting candidate for the magnetic resonance imaging. One can control the inter particle distance in the capsules wall by embedding different concentration of nanoparticles which could affect the relaxation time of these particles. FePt nanoparticles have been used in the wall of the polyelectrolyte capsules to study the dependence of relaxation time on the inter particle distance inside a polymer matrix[60]. It was observed that by decreasing the inter particle distance, inside a carrier matrix such as wall of the capsules drastically increases the r1 and r2 relaxivities in MRI. As discussed in detail in section 2.4 the permeability of the capsule wall can be enhanced by using the magnetic particles in the wall of capsules. Applying a radio frequency field on capsules containing magnetic nanoparticles results in heat generation which then affects the permeability of the capsule wall[61, 62].

There are also some studies where walls of the capsule were made light sensitive by doping then with metal nanoparticles[63]. Noble metal gold and silver nanoparticles absorb light, major part of this light simply change into heat so collective effect of several nanoparticles cause an increase of the temperature in surrounding[64, 65]. By embedding these nanoparticles in the wall of the capsules permeability of the individual capsule can be perturbed due to change in temperature. In conclusion incorporation of metallic nanoparticles can help to release cargo molecules from polyelectrolyte multilayer capsules for drug delivery applications.

Explanation about the opening of polyelectrolyte capsules using different metallic nanoparticles in the walls of the capsules for the release of cargo molecules is given in section (2.6).

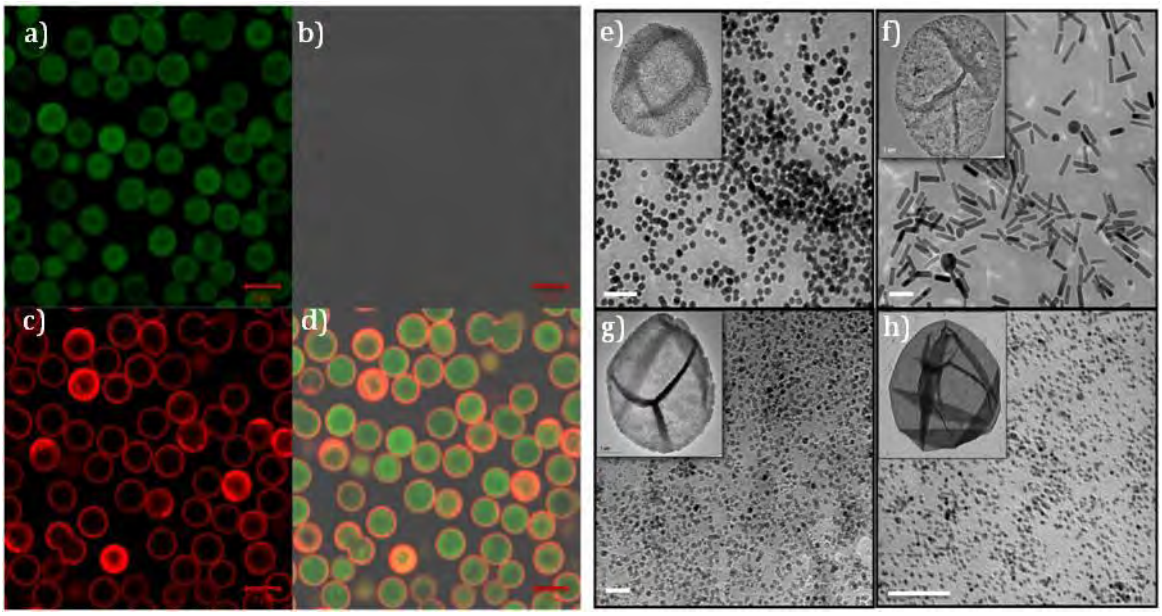

Fig. 2.5.2: *Functionalization of polyelectrolyte capsules with fluorophores and inorganic nanoparticles incorporated in the multilayer wall. (Left) Confocal laser scanning microscope (CLSM) image (CLSM) of $(PSS/PAH)_5$ with FITC-dextran in cavity and red QDs (CdSe/ZnS) in the wall a) green channel: FITC-dextran, b) transmission channel, c) red channel: red QDs, d) overlay of all three channels (Scale bar 5 µm). (Right) Typical TEM images of e) Au nanoparticles , f) Au nano rods, g) Fe_2O_3 nanoparticles and h) FePt nanoparticles embedded inside the multilayer wall of hollow $(PSS/PAH)_5$ capsules (scale bar 50nm). Insets show the single nanoparticles-modified capsule.*

2.5.2 Surface modification for targeted delivery

It is well known that surface chemistry of particles plays an important role in the interaction between cells and particles[66, 67].

For drug delivery applications of capsules it is important to understand the interaction of the capsules with cells and possibilities to enhance the specific uptake by target sites (cells) but also to reduce the non-specific uptake of the drug carrier. The control on uptake mechanisms can be achieved by modifying the surface of the capsules. It is known that cell uptake the capsules[57]. The rate of internalization depends on the surface charge of the capsules. Studies showed that capsules with a positive surface charge are ingested at a higher rate than the negatively charged ones[68]. One of the main problems of charged systems is that proteins start to adsorb on the surfaces[69]. The adsorption of proteins leads to a change in the surface charge and a change in the cell uptake. This adsorption of protein can be controlled by modifying the outer surface of the capsules. Different coating systems including the polyethylene glycol (PEG)[70] and lipids[71] have been applied to the surface of capsule in order to limit their non specific uptake. PEG and other hydrophobic materials such as poly(2-methyloxazoline) are frequently deposited to impart the protein resistance to the surfaces due to their stealth like properties[72]. Since the main stabilizing forces in polyelectrolyte capsules are electrostatic interactions, the efficient binding of PEG molecules to the surface of the capsule has to be carried out by previous linkage of PEG to highly

charged substances like polyelectrolytes. In this way, PEG modified polyelectrolytes can be strongly and stably attached to charged surfaces by electrostatic interactions. It has been reported that the surface modification of PAH/PSS capsules with a layer of poly($_L$-lysine)-graft-PEG (PLL-g-PEG) decrease the adsorption of protein three times as compared to standard PAH/PASS capsules[73]. It is also reported that the ratio of PEG graft on copolymer also effect the cell uptake. Hua et al.[69] showed that the uptake by cells is much higher for capsules which were modified with poly(ethyleneimine)-PEG (PEI-PEG) with low PEG grafting ratios compared to capsules with high PEG grafting ratios. The PEG molecule can be used on the surface of the capsules to prolong the blood circulating time of these micro containers for drug delivery applications.

Furthermore the specific uptake of the capsules can be achieved by biologically designing the surface properties of capsules. One possibility in this context is ligand-receptor interaction. A ligand can be a surface molecule that exhibits specific binding to a receptor molecule, whereas a receptor is a complementary macromolecular (e.g. protein) binding site on a cell surface that binds to ligand. By attaching a ligand onto the surface of a capsule the specific uptake of the capsules to the targeted cells can be enhanced. Heuberger et al.[73] reported one possible way to use the polyelectrolyte capsules for such specific targeting based on well know biological interaction between biotin/streptavidin. The bio-functionalized capsules were prepared by coating the PAH/PSS capsules with last layer of poly($_L$-lysine)-graft-PEG/PEG-biotin (PLL-g-PEG/PEG-biotin). To test the interaction of the capsules, fluorescent strepavidin was exposed to the micro capsules and examined using confocal microscope. The result showed the high fluorescent intensity in the wall of the capsules due to the binding of streptavidin with biotin present on the surface of the capsules. This approach can be used for the specific uptake of the capsules. Fig. 2.5.3 shows the schematic diagram for the targeted delivery through ligand-receptor interaction.

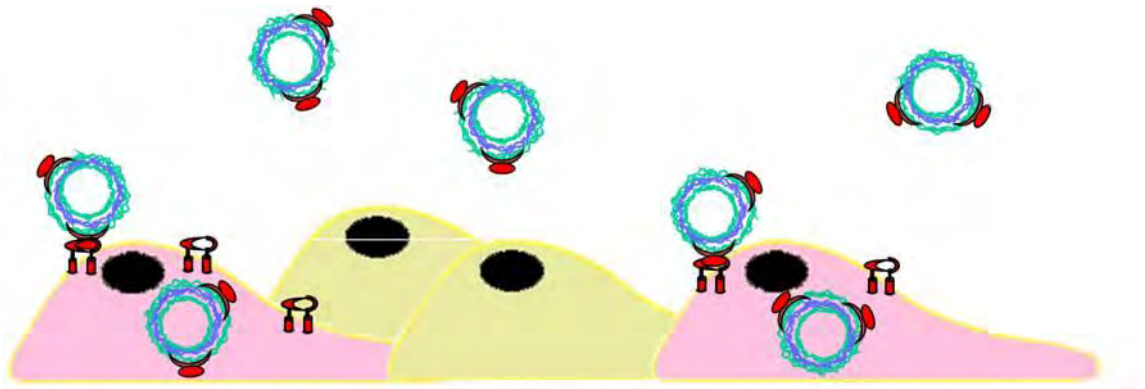

Fig. 2.5.3: *Scheme of targeted delivery of polyelectrolyte capsules through ligand-receptor interaction.*

2.6 Release of cargo from the cavity of polyelectrolyte capsules

A possible application of polyelectrolyte capsules in medicine is the delivery of cargo molecules like drugs, toxins, or oligonucleotides (DNA or RNA) to living cells[17]. It is known, that multilayer capsules of different sizes (from nanometer to micrometer scale) can be taken up by living cells[74, 75]. Thus transport into living organisms is possible, but releasing the cargo from the cavity of the capsules is challenging. The encapsulated molecules can be released at the targeted sites by two ways, through burst release or through sustained release. A burst release or instantly release is typically desired when the capsules are used for targeted drug delivery (i.e anti cancer drugs). Whereas a sustained release is desired when capsules remain in extracellular (i.e in blood circulation) and high doses of drug may be dangerous or in case when it is necessary to keep the drug level constant.

Among the release mechanisms, methods with remote functionalities such as by using the external stimuli for example light[63, 76-81], ultrasound[82, 83], hydrolysis[84, 85], or magnetism[41], show interesting strategies for control drug release after they reach the targeted tissue. In these methods various types of nanoparticles, including gold, silver and iron oxide, were embedded inside the wall of capsules during the LbL assembly procedure as discussed before. The optical properties of the material were suited to induce the disassembly of the multi layer wall or the formation of pores inside the capsules walls.

Numerous studies have demonstrated the possibility to remotely control the opening of the capsules under laser irradiation of silver[86] and gold[74] nanoparticles in the wall outside and inside living cells. The near infrared window is very advantageous when operating in the tissue environment to minimize the side effects because most of tissues show negligible absorption in the 800-1200nm region. For this reason, gold nanorods functionalized polyelectrolyte capsules can be opened by using the near infra-red laser 830nm[87]. Recently the aggregates of gold nanoparticles have also been used for the remote release experiments using the near infrared laser with an incident intensity of 65 mW[88]. It was observed that polyelectrolyte capsules containing gold nanoparticles could not be opened using the near infrared laser while the encapsulated materials were entirely released from the capsules functionalized with aggregates of gold nanoparticles.

Remote release of encapsulated material can also be achieved by ultra sound irradiation. It has been observed that such irradiation effect dramatically the integrity of multilayer capsules. When ultrasonic shock waves originating from ultrasound probe propagate through the liquid, they cause shear forces between the liquid successive layers. When such shear forces pass through the capsule membrane they can damage the capsule wall resulting the release of encapsulated materials. The wall of four bi-layer of PSS/PAH polyelectrolyte capsules were successively destroyed and release of FITC-dextran 2000kDa was observed[89].

As discussed in section 2.4 the permeability of capsules can also be changed by embedding magnetic nanoparticles into the capsules wall. Systems which can be magnetically controlled are attracting lot of interest in the field of drug delivery research. Shang et al.[90] reported rupturing of magnetic polyelectrolyte capsules for drug delivery applications. Magnetic polyelectrolyte capsules were fabricated by LbL assembly, using citric acid modified Fe_3O_4 as negative layer and PAH as positive layer on FITC-dextran loaded $CaCO_3$ templates. The

release of FITC-dextran was observed after applying a high frequency magnetic field (HFMF). The authors reported that HFMF cause two effects which were responsible for the capsule degradation. Firstly HFMF causes the local heating of the micro structure of the polyelectrolyte layers which further produced pores in the wall of capsules followed by the rupture of the wall. Secondly the magnetic nanoparticles tend to align in the direction of applied magnetic field which causes stress in the wall of the capsule. Such stress also plays a role in the pore formation. The combined effect of both heating and stress causes the rupturing of the magnetic polyelectrolyte capsules.

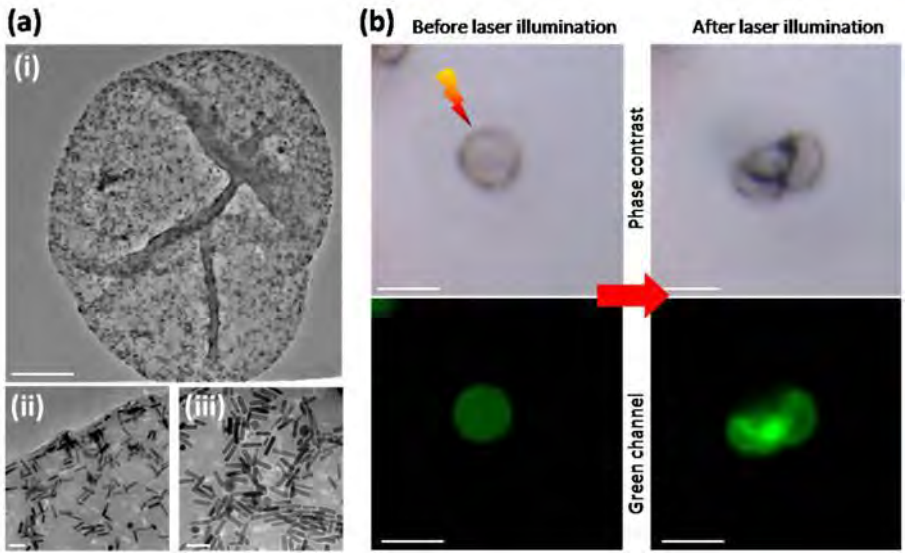

Fig. 2.6.1: *Laser-opening of FITC-dextran loaded $(PSS/PAH)_5$ capsule with Au NRs embedded in the capsules wall. (a) i) Representative TEM image of a single Au nanorods (NRs)-capsule (Scale bar 1 µm). (ii-iii) Two high-resolution images of the multilayer wall of the capsule (Scale bars 50 nm). (b) Effect of near-IR laser irradiation (830 nm) of a single Au NRs-capsule loaded with FITC-dextran. Before laser illumination: the capsule retains the green cargo inside the cavity. After laser illumination: the multilayer wall of the capsule is damaged (phase contrast) and the partial release of the green cargo throughout the small pores of the wall is observed (green channel) (Scare bars 5 µm).Figure taken from reference [91].*

As explained before, external stimuli such as pH, ionic strength and temperature affect the permeability of polyelectrolyte capsules by creating tiny pores in the wall of the capsules. Such conditions can also be used for the release of the encapsulated materials, but these methods are useful for the encapsulation and release of material under in vitro conditions. However these methods show some limitations for the drug release under in vivo conditions.

Sustained release of encapsulated material can be achieved by the slow diffusion through the walls of the capsules or by gradually decomposition of capsules wall. Such release of protein was achieved from the biodegradable capsules made of chitosan (CT) and dextran sulfate (DEXS) using LbL technique[92]. It was observed that with the passage of time, due to the presence of the enzyme chitosanase the chitosan part of the capsules wall can be degraded and the capsules begin to deform and are finally completely ruptured. Thus the

encapsulated proteins were released in a sustained manner. Borodina et al.[93] studied the enzymatic decomposition of polyelectrolyte capsules. These self-disintegrating microcapsules were synthesized by encapsulating the highly active mixture of proteases in the cavity of capsules. The co-precipitation method was used to entrap the pronase in the $CaCO_3$ microparticles. Poly($_L$-arginine)/poly($_L$-aspartic acid) (pARG/PLA) were assembled alternating onto the pronase containing templates. After the core removal the enzyme was released in the cavity of the microcapsules and started to digest the wall of the capsules. The life time of these self-disintegrating capsules could be adjusted by changing the amount of encapsulated pronase from seconds and hours to days which has the main advantage for the sustained release of the co-encapsulated DNA.

Polyelectrolyte capsules made of bio-degradable polymers are another way to deliver the drug inside the cell without any external stimuli. When such capsules are taken up by cells they can be destroyed by the enzymes present inside the cell. Most widely used bio-degradable polyelecctrolytes are poly($_L$-arginine) (pARG) and dextran sulfate (DEXS). De_Geest and co-workers[33] used these polyelectrolytes to synthesize bio-degradable capsules containing FITC-dextran in the cavity. When these capsules were supplied to the cells they were taken up by the cells, subsequently degraded and FITC-dextran was released inside the cell. Such capsules have high potential for the intracellular delivery of therapeutic nucleic acids (DNA, siRNA) and proteins.

2.7 Polyelectrolyte capsules as sensors

Polyelectrolyte capsules are also promising in the area of sensing[68, 94]. Due to diverse encapsulation method of assay elements and easy functionalization, this system is an interesting candidate for sensing application in biomedical field[17, 72]. In cells there are different concentration of ions such as Na^+, K^+, H^+, and Cl^- across the plasma membrane see table (2.7.1). The concentration of these ions across the cell membrane is very important because the functions of every cell in the body depend on the maintenance of a negative potential inside the cell. This negative potential depends upon the relative concentrations of these ions inside and outside the cell. The ionic pump present in the cell membrane maintains this ionic concentration by moving ions across the cell membrane against their concentration gradient[95]. In cellular and clinical research, accurate quantification of these ions with both high spatial and temporal resolution but negligible cell perturbation is an extremely challenging task.

One can investigate the intra/extra cellular ion concentration by optical measurements. Numerous fluorescent indicators are commercially available which are sensitive to the mentioned ions. These fluorophores change their optical properties upon interaction with the corresponding ion such as change in fluorescent intensity or shift in absorption or fluorescence spectra. These fluorophores can be conjugated to the high molecular weight molecules (i.e dextran) and could be embedded into the capsules cavity. An advantage of using polyelectrolyte capsules as sensors is that the wall of the capsule prevents the dyes from strong dilution and retains the high concentration inside the cavity thus the detection of the fluorescence signal can be significantly improved compared to the free dyes injected into the cells. Furthermore the sensor dye is protected from the surrounding environment

which might degrade or reduce its activity, and finally due to the porous nature of polyelectrolyte capsules wall the ions can move freely through the wall of the capsules and can interact with the fluorescent indicators[36, 94]. Another advantage of using polyelectrolyte capsules is the possibility to perform a ratiometric measurement by incorporating a reference dye which is not sensitive to the ion concentration along with the sensitive dye. Additionally capsules provide the facility to functionalize the wall of different sensor capsules with different colors. This can be helpful for the sensing of different ions at a same time.

ion	extra cell. Concentration(mM)	intra cell. Concentration(mM)
Na^+	~150	~15
K^+	~5	~150
Ca^{2+}	~1	~0,0001
Mg^{2+}	~1,5	~12
Cl^-	~110	~7
H^+	Generally known: intracellular pH level is lower than extracellular one.	

Table 2.7.1: *Composition of extracellular and intracellular Fluids (ion concentrations)[96]*

Polyelectrolyte capsules have also been used as oxygen sensor[97]. It was observed that the embedded dyes were stable and retained their properties. LbL assembled microcapsules can also be used as sensors for biomolecules (e.g. DNA) by embedding a molecular device that shows fluorescence upon binding of complementary DNA[98]. pH sensitive polyelectrolyte capsules have been fabricated by embedding the pH sensitive fluorophore SNARF conjugated to high molecular weight molecule dextran (70kDa)[99]. It was observed that SNARF retained its properties when embedded in the capsules cavity. The pH change was observed in the local environment of SNARF capsules upon their transition from alkaline cell medium to the acidic endosomal/lysosomal compartments. Uta et al.[100] reported that it is possible to locate the polyelectrolyte capsules inside the cell compartment by using the pH sensitive fluorophore. Such a system could allow the investigation of the uptake mechanism of capsules by cells in detail.

References

[1] H. Masanori, *Science and Tecnology* **1993**, 399.
[2] P. Atkins, J. de Paula, *Physical Chemistry* **2002**, *7th Edition*, 1149.
[3] G. Decher, J. D. Hong, J. Schmitt, *Thin Solid Films* **1992**, *210*, 831.
[4] G. Decher, *Science* **1997**, *277*, 1232.
[5] J. Schmitt, T. Griinewald, G. Decher, P. S. Perahan, K. Kjaer, M. Lösche, *Macromolecules* **1993**, *26*, 7098.
[6] M. Losche, J. Schmitt, G. Decher, W. G. Bouwman, K. Kjaer, *Macromolecules* **1998**, *31*, 8893.
[7] L. Zhai, F. C. Cebeci, R. E. Cohen, M. F. Rubner, *Nano Letters* **2004**, *4*, 1349.
[8] Yan-Lei Su, C. Li, *Applied Surface Science* **2008**, *254*, 2003.
[9] J. W. Ostrander, A. A. Mamedov, N. A. Kotov, *Journal of the American Chemical Society* **2001**, *123*, 1101.
[10] K. Katagiri, R. Hamasaki, K. Ariga, J. I. Kikuchi, *Langmuir* **2002**, *18*, 6709.
[11] R. N. Vyas, B. Wang, *International Journal of Molecular Science* **2010**, *11*, 1956.
[12] W. B. Stockton, M. F. Rubner, *Macromolecules* **1997**, *30*, 2717.
[13] Y. Shimazaki, M. Mitsuishi, S. Ito, M. Yamamoto, *Langmuir* **1997**, *13*, 1285.
[14] E. Brynda, M. Houska, *Journal of Colloid and Interface Science* **1996**, *183*, 18.
[15] J. I. Anzai, Y. Kobayashi, N. Nakamura, M. Nishimura, T. Hoshi, *Langmuir* **1999**, *15*, 221.
[16] E. Lojou, P. Bianco, *Langmuir* **2004**, *20*, 748.
[17] P. Rivera Gil, L. L. del Mercato, P. del Pino, A. Munoz Javier, W. J. Parak, *Nano Today* **2008**, *3*, 12.
[18] A. Voigt, H. Lichtenfeld, G. B. Sukhorukov, H. Zastrow, E. Donath, H. Baumler, H. Mohwald, *Industrial & Engineering Chemistry Research* **1999**, *38*, 4037.
[19] G. B. Sukhorukov, E. Donath, S. Davis, H. Lichtenfeld, F. Caruso, V. I. Popov, H. Möhwald, *Polymers for Advanced Technologies* **1998**, *9*, 759.
[20] T. Mauser, C. Dejugnat, G. B. Sukhorukov, *Macromolecular Rapid Communications* **2004**, *25*, 1781.
[21] A. A. Antipov, G. B. Sukhorukov, H. Mohwald, *Langmuir* **2003**, *19*, 2444.
[22] K. Köhler, D. G. Shchukin, G. B. Sukhorukov, H. Möhwald, *Macromolecules* **2004**, *37*, 9546.
[23] K. Köhler, D. G. Shchukin, H. Mohwald, G. B. Sukhorukov, *Journal Of Physical Chemistry B* **2005**, *109*, 18250.
[24] C. Dejugnat, D. Halozan, G. B. Sukhorukov, *Macromolecular Rapid Communications* **2005**, *26*, 961.
[25] G. Ibarz, L. Dähne, E. Donath, H. Möhwald, *Advanced Materials* **2001**, *13*, 1324.
[26] A. P. Petrov, D. V. Volodkin, G. B. Sukhorukov, *Biotechnology Progress* **2005**, *21*, 918.
[27] F. Caruso, D. Trau, H. Möhwald, R. Renneberg, *Langmuir* **2000**, *16*, 1485.
[28] O. P. Tiourina, A. A. Antipov, G. B. Sukhorukov, N. I. Larionova, Y. Lvov, H. Möhwald, *Macromolecular Bioscience* **2001**, *1*, 209.
[29] G. B. Sukhorukov, A. S. Susha, S. Davisc, S. Leporatti, E. Donath, J. Hartmann, H. Möhwald, *Journal of Colloid and Interface Science* **2002**, *247*, 251.

[30] G. B. Sukhorukov, D. V. Volodkin, A. M. Günther, A. I. Petrov, D. B. Shenoy, H. Möhwald, *Journal of Materials Chemistry* **2004**, *14*, 2073.
[31] C. Y. Gao, S. Moya, H. Lichtenfeld, A. Casoli, H. Fiedler, E. Donath, H. Möhwald, *Macromolecular Materials And Engineering* **2001**, *286*, 355.
[32] G. B. Sukhorukov, *Studies in Interface Science* **2001**, *11*, 383.
[33] B. G. De_Geest, R. E. Vandenbroucke, A. M. Guenther, G. B. Sukhorukov, W. E. Hennink, N. N. Sanders, J. Demeester, S. C. d. Smedt, *Advanced Materials* **2006**, *18*, 1005.
[34] M. Fischlechner, O. Zschörnig, J. Hofmann, E. Donath, *Angewandte Chemie International Edition* **2005**, *44*, 2892.
[35] B. G. De_Geest, N. N. Sanders, G. B. Sukhorukov, J. Demeestera, S. C. D. Smedt, *Chemical Society Reviews* **2007**, *36*, 636.
[36] A. A. Antipov, G. B. Sukhorukov, S. Leporatti, I. L. Radtchenko, E. Donath, H. Möhwald, *Colloids and Surfaces, A: Physicochemical and Engineering Aspects* **2002**, *198*, 535.
[37] G. B. Sukhorukov, A. A. Antipov, A. Voigt, E. Donath, H. Mohwald, *Macromolecular Rapid Communications* **2001**, *22*, 44.
[38] Y. Lvov, A. A. Antipov, A. Mamedov, H. Möhwald, G. B. Sukhorukov, *Nano Letters* **2001**, *1*, 125.
[39] Y. Itoh, M. Matsusaki, T. Kida, M. Akashi, *Biomacromolecules* **2008**, *9*, 2202.
[40] K. Köhler, G. B. Sukhorukov, *Advanced Functional Materials* **2007**, *17*, 2053.
[41] Z. Lu, M. D. Prouty, Z. Guo, V. O. Golub, C. S. Kumar, Y. M. Lvov, *Langmuir* **2005**, *21*, 2042.
[42] A. J. Khopade, F. Caruso, *Biomacromolecules* **2002**, *3*, 1154.
[43] W. Tong, W. Dong, C. Gao, H. Mohwald, *Journal of Physical Chemistry B* **2005**, *109*, 13159.
[44] H. Zhu, R. Srivastava, M. J. McShane, *Biomacromolecules* **2005**, *6*, 2221.
[45] A. S. Susha, F. Caruso, A. L. Rogach, G. B. Sukhorukov, A. Kornowski, H. Möhwald, M. Giersig, A. Eychmüller, H. Weller, *Colloids and Surfaces A* **2000**, *163*, 39.
[46] F. Caruso, A. S. Susha, M. Giersig, H. Möhwald, *Advanced Materials* **1999**, *11*, 950.
[47] A. L. Rogach, D. V. Talapin, H. Weller, *"Colloids and Colloid Assemblies", Ed. F. Caruso. WILEY-VCH, Weinheim* **2004**, 52.
[48] M. Han, X. Gao, J. Z. Su, S. Nie, *Nature Biotechnology* **2001**, *19*, 631.
[49] D. Gerion, F. Pinaud, S. C. Williams, W. J. Parak, D. Zanchet, S. Weiss, A. P. Alivisatos, *Journal of Physical Chemistry B* **2001**, *105*, 8861.
[50] M. Dahan, S. Levi, C. Luccardini, P. Rostaing, B. Riveau, A. Triller, *Science* **2003**, *302*, 442.
[51] A. Rogach, A. Susha, F. Caruso, G. Sukhorukov, A. Kornowski, S. Kershaw, H. Möhwald, A. Eychmüller, H. Weller, *Advanced Materials* **2000**, *12*, 333.
[52] D. Wang, A. L. Rogach, F. Caruso, *Nano Letters* **2002**, *2*, 857.
[53] A. M. Derfus, W. C. W. Chan, S. N. Bhatia, *Nano Letters* **2004**, *4*, 11.
[54] C. Kirchner, T. Liedl, S. Kudera, T. Pellegrino, A. M. Javier, H. E. Gaub, S. Stölzle, N. Fertig, W. J. Parak, *Nano Letters* **2005**, *5*, 331.
[55] F. Caruso, M. Spasova, A. Susha, M. Giersig, R. A. Caruso, *Chemistry of Materials* **2001**, *13*, 109.
[56] N. Gaponik, I. L. Radtchenko, G. B. Sukhorukov, A. L. Rogach, *Langmuir* **2004**, *20*, 1449.
[57] B. Zebli, A. S. Susha, G. B. Sukhorukov, A. L. Rogach, W. J. Parak, *Langmuir* **2005**, *21*, 4262.

[58] J. F. Pereira da Silva Gomes, A. Rank, A. Kronenberger, J. Fritz, M. Winterhalter, Y. Ramaye, *Langmuir* **2009**, *25*, 6793.
[59] E. P. A. M. Bakkers, E. Reitsma, J. J. Kelly, D. Vanmaekelbergh, *Journal of Physical Chemistry B, 103 (14)* **1999**, *103*, 2781.
[60] M. P. Morales, M. F. Bedard, A. G. Roca, P. de la Presa, A. Hernando, F. Zhang, M. Zanella, A. A. Zahoor, G. B. Sukhorukov, L. L. del Mercato, W. J. Parak, *Journal of Materials Chemistry* **2009**, *19*, 6381.
[61] Noriyasu Kawai, A. Ito, Y. Nakahara, M. Futakuchi, T. Shirai, H. Honda, T. Kobayashi, K. Kohri, *The Prostate* **2005**, *64*, 373.
[62] S. Mornet, S. Vasseur, F. Grasset, E. Duguet, *Journal of Materials Chemistry* **2004**, *14*, 2161.
[63] A. G. Skirtach, C. Dejugnat, D. Braun, A. S. Susha, W. J. Parak, H. Möhwald, G. B. Sukhorukov, *Nano Letters* **2005**, *5*, 1371.
[64] A. O. Govorov, W. Zhang, T. Skeini, H. Richardson, J. Lee, N. A. Kotov, *Nanoscale Research Letters* **2006**, *1*, 84.
[65] A. O. Govorov, H. H. Richardson, *Nano Today* **2007**, *2*, 30.
[66] G. B. Sukhorukov, H. Mohwald, *Trends In Biotechnology* **2007**, *25*, 93.
[67] C. Brandenberger, C. Mühlfeld, Z. Ali, A.-G. Lenz, O. Schmid, W. J. Parak, P. Gehr, B. Rothen-Rutishauser, *Small* **2010**, *6*, 1669.
[68] G. B. Sukhorukov, A. L. Rogach, M. Garstka, S. Springer, W. J. Parak, A. Muñoz-Javier, Oliver Kreft, A. G. Skirtach, A. S. Susha, Y. Ramaye, R. Palankar, M. Winterhalter, *Small* **2007**, *3*, 944.
[69] H. Ai, J. J. Pink, X. Shuai, D. A. Boothman, J. Gao, *Journal Of Biomedical Materials Research Part A* **2005**, *73A*, 303.
[70] A. J. Khopade, F. Caruso, *Langmuir* **2003**, *19*, 6219.
[71] S. Moya, E. Donath, G. B. Sukhorukov, M. Auch, H. Baumler, H. Lichtenfeld, H. Mohwald, *Macromolecules* **2000**, *33*, 4538.
[72] B. G. De_Geest, S. De Koker, G. B. Sukhorukov, O. Kreft, W. J. Parak, A. G. Skirtach, J. Demeester, S. C. De Smedt, W. E. Hennink, *Soft Matter* **2009**, *5*, 282.
[73] R. Heuberger, G. Sukhorukov, J. Vörös, M. Textor, H. Möhwald, *Advanced Functional Materials* **2005**, *15*, 357.
[74] A. Muñoz_Javier, O. Kreft, M. Semmling, S. Kempter, A. G. Skirtach, O. Bruns, P. d. Pino, M. F. Bedard, J. Rädler, J. Käs, C. Plank, G. Sukhorukov, W. J. Parak, *Advanced Materials* **2008**, *20*, 4281.
[75] S. De_Koker, B. G. De_Geest, C. Cuvelier, L. Ferdinande, W. Deckers, W. E. Hennink, S. De_Smedt, N. Mertens, *Advanced Functional Materials* **2007**, *17*, 3754.
[76] X. Tao, J. Junbai Li, H. Möhwald, *Chemistry a European Journal* **2004**, *10*, 3397.
[77] A. G. Skirtach, A. A. Antipov, D. G. Shchukin, G. B. Sukhorukov, *Langmuir* **2004**, *20*, 6988.
[78] A. S. Angelatos, B. Radt, F. Caruso, *Journal of Physical Chemistry B* **2005**, *109*, 3071.
[79] B. Radt, T. A. Smith, F. Caruso, *Advanced Materials* **2004**, *16*, 2184.
[80] A. G. Skirtach, A. M. Javier, O. Kreft, K. Köhler, A. P. Alberola, H. Möhwald, W. J. Parak, G. B. Sukhorukov, *Angewandte Chemie International Edition* **2006**, *45*, 4612.
[81] B. G. De_Geest, A. G. Skirtach, T. R. M. De Beer, G. B. Sukhorukov, L. Bracke, W. R. G. Baeyens, J. Demeester, S. C. De Smedt, *Macromolecular Rapid Communications* **2007**, *28*, 88.

[82] A. G. Skirtach, B. G. De_Geest, A. Mamedov, A. A. Antipov, N. A. Kotov, G. B. Sukhorukov, *Journal Of Materials Chemistry* **2007**, *17*, 1050.
[83] D. G. Shchukin, D. A. Gorin, H. Möhwald, *Langmuir* **2006**, *22*, 7400.
[84] B. G. De Geest, C. Déjugnat, M. Prevot, G. B. Sukhorukov, J. Demeester, S. C. De Smedt, *Advance Functional Materials* **2007**, *17*, 531.
[85] B. G. De_Geest, C. Dejugnat, G. B. Sukhorukov, K. Braeckmans, S. C. De_Smedt, J. Demeester, *Advanced Materials* **2005**, *17*, 2357.
[86] D. Radziuk, D. G. Shchukin, A. Skirtach, H. Mohwald, G. Sukhorukov, *Langmuir* **2007**, *23*, 4612.
[87] A. G. Skirtach, P. Karageorgiev, B. G. De_Geest, N. Pazos-Perez, D. Braun, G. B. Sukhorukov, *Advanced Materials* **2008**, *20*, 506.
[88] M. F. Bedard, D. Braun, G. B. Sukhorukov, A. G. Skirtach, *Acs Nano* **2008**, *2*, 1807.
[89] B. G. De_Geest, A. G. Skirtach, A. A. Mamedov, A. A. Antipov, N. A. Kotov, S. C. De Smedt, G. B. Sukhorukov, *Small* **2007**, *3*, 804.
[90] S. H. Hu, C. H. Tsai, C. F. Liao, D. M. Liu, S. Y. Chen, *Langmuir* **2008**, *24*, 11811.
[91] L. L. del_Mercato, P. Rivera-Gil, A. Z. Abbasi, M. Ochs, C. Ganas, I. Zins, C. Sönnichsen, W. J. Parak, *Nanoscale* **2010**, *2*, 458.
[92] Yuki Itoh, Michiya Matsusaki, Toshiyuki Kida, M. Akashi, *Biomacromolecules* **2006**, *7*, 2715.
[93] T. Borodina, E. Markvicheva, S. Kunizhev, H. Moehwald, G. B. Sukhorukov, O. Kreft, *Macromolecular Rapid Communications* **2007**, *28*, 1894.
[94] J. Q. Brown, M. J. McShane, *Ieee Engineering in Medicine and Biology Magazine* **2003**, *22*, 118.
[95] D. C. Gadsby, *Nature* **2007**, *450*, 957.
[96] A. Friedman, *Pediatr Nephrol* **2010**, *25*, 843.
[97] M. J. Mc_Shane, J. Q. Brown, K. B. Guice, Y. M. Lvov, *Journal of Nanoscience and Nanotechnology* **2002**, *2*, 411.
[98] A. P. R. Johnston, C. Cortez, A. S. Angelatos, F. Caruso, *Current Opinion in Colloid & Interface Science* **2006**, *11*, 203.
[99] O. Kreft, A. Muñoz_Javier, G. B. Sukhorukov, W. J. Parak, *Journal Of Materials Chemistry* **2007**, *17*, 4471.
[100] U. Reibetanz, D. Haloan, M. Brumen, E. Donath, *Biomacromolecules* **2007**, *8*, 1928.

Contribution

- **Polyelectrolyte capsules for NMR imaging and targeted delivery**

Polyelectrolyte capsules were fabricated by embedding magnetic iron oxide (Fe_2O_3) nanoparticles in the walls of the capsules. Such capsules could be used for the targeted drug delivery, beside targeted drug delivery this system can also be used as contrast agent for nuclear magnetic resonance imaging (NMR). Magnetic particles provide good imaging contrast capabilities for NMR because the relaxitivities r_1 and r_2 of nanoparticles are very sensitive to changes in local field gradients. To study the dependence of relaxivities r_1 and r_2 on inter particle distance, wall of the capsule was used as a matrix containing different number of magnetic nanoparticles. For these studies iron oxide nanoparticles (Fe_2O_3) were synthesized. Different concentrations of nanoparticles were embedded in the walls of the capsules. After the synthesis of microcapsules confocal laser scanning microscopy (CLSM), scanning electron microscopy (SEM), transmission electron microscopy (TEM) were performed to study the morphology of the capsules.

- **Ratiometric polyelectrolyte capsules as sensor**

Sensor polyelectrolyte capsules were fabricated for detection of intracellular concentrations of several ions, such as Na^+, K^+, H^+ and Cl^-. These sensor capsules were fabricated using commercially available fluorophores such as sodium-binding benzofuran isophthalate (SBFI), potasium-binding benzofuran isophthalate (PBFI), fluorescein isothiocyanate (FITC) and seminaphtharhodafluor dye (SNARF), whereas chloride sensitive capsules were produced by using a homemade chloride sensitive fluorophore (MQAE). The sensor activity of SBFI, PBFI, FITC and MQAE fluorophores is based either on the increase or decrease of their fluorescence signal upon increasing concentration of the corresponding ion. Whereas the pH sensitive fluorophore SNARF shifts the fluorescence maximum from green to red with the change of pH from acidic to alkaline ranges respectively. For the ratiometric measurements, red emitting fluorophore alexa 594 (AF594) was used as reference dye (non sensitive to ion concentration). All the ion sensitive fluorophores and reference fluorophore were conjugated to the cargo molecule dextran (500kDa) before embedding them into the capsules cavity.

The fabrication of polyelectrolyte capsules was performed by using spherical porous calcium carbonate ($CaCO_3$) templates. Co-precipitation method was used to encapsulate the fluoropores during the synthesis of $CaCO_3$ particles. After the core synthesis, the wall of the capsules was build using LbL technique. Commercially available polyelectrolyte PSS was used as anionic layer whereas PAH was used as cationic layer to build the walls of the capsules. After assembly of five bi-layers, the $CaCO_3$ cores were removed by complexation with EDTA.

The response of the fluorophores under different corresponding ion concentration was investigated by recording the emission spectra of free fluorophores, fluorophores conjugated to the dextran molecule and finally fluorophores embedded into the capsules cavity. The response of sensor capsules for different corresponding ion concentration was also observed using fluorescence microscope. Results showed that the fluorophores were

stable and retained their properties upon conjugation with dextran molecule and encapsulation in polyelectrolyte capsules.
Furthermore to use these polyelectrolyte capsules as multiplex sensor (i.e to measure the concentration of different ions at a same time) walls of the capsules were labeled. For this purpose fluorescent nanoparticles (CdSe/ZnS) of different color were embedded in the walls of the capsules containing different ion sensitive fluorophores in the cavity. By giving different colors to the wall of sensor capsules it was possible to identify different sensor system under different concentrations of ions.

- **Capsules made of proteins**

Proteins are naturally occurring polymers, having high potential for biomedical applications due to their intrinsic biocompatibility. To increase the biocompatibility of microcapsules instead of using standard synthetic charge polyelectrolytes supercharged elastin-like peptides (ELPs) were used to build the wall around the spherical $CaCO_3$ particles by using LbL technique. The multilayer wall was held together only by electrostatic interaction of these oppositely charged proteins. Such protein based capsules are less cytotoxic as compared to the other microcapsules based on PSS, PAH, PDADMAC, and PLL polyelectrolytes because these supercharged proteins can degrade into non toxic amino acids and do not contain toxic solvents or monomer residues. The structural properties of protein based capsules were compared to capsules based on synthetic polyelectrolytes such as capsules based on PSS/PAH and DEXS/pARG. Structural investigations were performed using TEM, SEM and CLSM. Results showed that such charged proteins could be used to fabricate the biodegradable microcapsules. One possible application of such capsules is in drug delivery.

- **Capsules for controlled release of cargo molecules**

For the controlled release of the cargo molecules gold (Au) nanoparticles were embedded in the multilayer walls of the capsules and effect of microwaves on capsules structure was studied. For the control experiment capsules without Au nanoparticles were also fabricated. The effect of microwave irradiation was investigated by comparing data obtained from TEM and dynamic light scattering (DLS) before and after the microwave irradiation. The wall damage was observed in both types of capsules. A rapid damage of wall was observed in the case of capsules having Au nanoparticles in their walls. Such method could be used for the simultaneous opening of numerous capsules containing the cargo molecules.

Conclusions and future perspectives

Nanoparticles of different shape and size could be synthesized from wide verity of materials. It is demonstrated that size and shape of the particle can be tuned by varying the synthesis condition. These small particles from different material can be incorporated in polymer matrix, such as in the walls of polyelectrolyte capsules. Such multifunctional system is promising for drug delivery and sensing application.

Layer-by-layer technique can be used to fabricate hollow microcapsules using different charged polymers. The two main compartments of the capsules are wall and cavity. The walls of the capsules can be functionalized with nanoparticles having different properties, size and shape. It is possible to encapsulate macromolecules in the cavity of the capsules. Calcium carbonate ($CaCO_3$) particles are interesting candidate for the template; small molecules can be easily encapsulated during synthesis of these particles.

Capsules containing magnetic nanoparticles in the wall could be used for nuclear magnetic resonance imaging (NMR). Further more such a system could also be used for drug delivery application where magnetic field can be used to produce the local heat to change the permeability of the capsule wall. Presence of magnetic nanoparticles also makes this system an interesting candidate for targeted delivery.

Polyelectrolyte capsules can also be used as sensors. Different ion sensitive fluorophores can be embedded in the cavity of the capsule. For ratiometric measurement it is possible to encapsulate reference dye along with the sensor dyes. It is demonstrated that fluorophores retained their properties. Experiments performed confirmed that such a system can be used to measure the ion concentration. These ion sensitive capsules could be used for in vivo ratiometric measurement of ions. Further it is possible to give different color to the walls of sensor capsules. This could help to distinguish different ion sensitive capsules localized in different compartment of the cells.

The wall of the capsule can be made with wide verity of synthetic as well as naturally occurring polymers. Charged elastic like protein can be used to make the wall of the capsules. Such biocompatible capsules could be used for drug delivery application and can be less toxic compare to other possible system because these supercharged proteins can degrade into non toxic amino acids and do not contain toxic solvents or monomer residues, they might be promising alternative building blocks for the synthesis of biocompatible and biodegradable capsules.

By embedding metal nanoparticles (e.g Au, Ag) it is possible to remotely open the capsule walls by using the external stimuli. It was observed that microwave irradiation affect the wall of the capsules. Capsules containing Au nanoparticles degrade rapidly under microwave irradiation. Such a system can be used to deliver high dose because by using microwave it could be possible to simultaneously open the large number of capsule to release the cargo material.

Publications

[A1] Discontinuous growth of II-VI Semiconductor nanocrystals from different materials
Marco Zanella, Azhar Z. Abbasi, Andreas K. Schaper, Wolfgang J. Parak,
Journal of Physical Chemistry C 2010, 114, 6205.

[A2] Magnetic microcapsules for NMR imaging and drug delivery: Effect of magnetic nanoparticles spatial distribution and aggregation
Azhar Zahoor Abbasi, Lucía Gutiérrez, Loretta L. del Mercato, Fernando Herranz, Oksana Chubykalo-Fesenko, Sabino Veintemillas-Verdaguer, Wolfgang J. Parak, M. Puerto Morales, Jesús M González, Antonio Hernando and Patricia de la Presa.
Submitted to Journal of Material Chemistry, 2010.

[A3] Synthesis and characterization of ratiometric ion sensitive polyelectrolyte capsules
L. L. del Mercato, Azhar Z. Abbasi, Wolfgang. J. Parak, SMALL, In revision, 2010.

[A4] De Novo Design of Supercharged, Non-folded Proteins and their Assembly into Supramolecular Aggregates
A. Kolbe, L. L. del Mercato, A. Z. Abbasi, P. Rivera Gil, S. J. Gorzini, W. H. C. Huibers, B. Poolman, Wolfgang J. Parak, A. Herrmann, Macromolecular Rapid Communications, accepted, 2010.

[A5] Synthesis and evaluation of gold nanoparticle-modified polyelectrolyte capsules under microwave irradiation for remotely controlled release for cargo
Loretta L. del Mercato, Edgar Gonzalez, Azhar Z. Abbasi, Wolfgang J. Parak, Victor Puntes,
In preparation.

[A6] Relaxation times of colloidal iron platinum in polymer matrixes
Maria Puerto Morales, Matthieu F. B_edard, Alejandro G. Roca, Patricia de la Presa, Antonio Hernando, Feng Zhang, Marco Zanella, Azhar Zahoor Abbasi, Gleb B. Sukhorukov, Loretta del Mercato and Wolfgang J. Parak, Journal of Material Chemistry 2009, 19, 6381.

[A7] Multilayer Capsules: recent progress and future outlook for their use in life sciences
L. L. del Mercato, Pilar Rivera Gil, Azhar Z. Abbasi, M. Ochs, C. Ganas, I. Zins, C. Sönnichsen, W. J. Parak, Nanoscale 2010, 2, 458.

[A8] Evaluation of quantum dots applied as switchable layer in a light-controlled electrochemical sensor
Z. Yue, W. Khalid, M. Zanella, Azhar Z. Abbasi, A. Pfreund, P. Rivera Gil, K. Schubert, F. Lisdat, Wolfgang J. Parak, Analytical and Bioanalytical Chemistry 2010, 396, 1095.

[A9] Wrapping Nanocrystals with an Amphiphilic Polymer Pre-loaded with Fixed Amounts of Fluorophore Generates FRET-based Nanoprobes with a Controlled Donor/Acceptor Ratio
Yakovlev Aleksey, Zhang Feng, Zulqurnain, Ali, Azhar Z. Abbasi, Luccardini Camilla, Gaillard Stéphane, Mallet Jean-Maurice, Tauc Patrick, Brochon Jean-Claude, Parak, Wolfgang, Feltz Anne, Oheim Martin, Langmuir 2009, 25, 3232.

Discontinuous Growth of II−VI Semiconductor Nanocrystals from Different Materials

Marco Zanella,[†] Azhar Z. Abbasi,[†] Andreas K. Schaper,[‡] and Wolfgang J. Parak*[,†]

Department of Physics and WZMW, Philipps University Marburg, Renthof 7, 35037 Marburg, Germany, and Material Sciences Centre, EM&M Laboratory, Philipps University Marburg, Hans-Meerwein-Str., 35032 Marburg, Germany

Received: July 18, 2009; Revised Manuscript Received: February 4, 2010

We report about the synthesis of II−VI semiconductor nanocrystals (NCs) that grow in discrete steps. CdS, CdTe, ZnSe, and ZnO NCs were synthesized in analogy to a method we recently developed for the discontinuous growth of CdSe NCs. Because of the similar growth conditions, the NCs of these different materials can be directly compared. Also, CdS NCs with Hg impurities showed discontinuous growth. From all materials, we could isolate fractions of NCs of different sizes via size-selective precipitation and characterize their optical and structural properties.

Introduction

Small nanocrystals (NCs) can show discontinuous growth behavior. This involves that such NCs have certain stable configurations and thus, instead of growing continuously, are growing from one stable configuration to the next one. All NCs of the same stable configuration have almost the same size, which means they have well-defined and reproducible properties. Sometimes, such configurations of NCs are also called magic size clusters. Discontinuous stepwise growth is well-known for metal clusters,[1−4] and in the past few years, the interest in these structures and their exclusive properties moved to other materials, such as semiconductors[5−16] and oxides.[17] Theoretical studies about nucleation, stability, and electronic and structural properties of NCs at the first stages of the discontinuous growth have been reported.[17−30] Concerning semiconductor materials, different stable configurations of almost monodisperse CdS and CdSe NCs have been synthesized by high-pressure and high-temperature methods[31] and the inverse micelle approach.[10] Also, wet-chemistry approaches have been reported recently about the sequential growth of CdSe, CdTe, PbSe, InAs, and CdTeSe NCs.[32−38] However, the mechanism is still under discussion.[39,40] Looking at the reports in the literature dealing with discontinuous growth of NCs, comparison of results is complicated by the fact that NCs from different materials are typically synthesized with different methods. Thus, it is hard to compare the NC growth and their properties between the studies of the different groups.

In this work, we report a unified synthesis of NCs of different II−VI semiconductor materials based on a protocol developed for the discontinuous growth of CdSe NCs.[32] Because of the similar synthesis techniques, the NCs of the different materials can be directly compared. In this way, it is possible to see whether similar NCs are obtained for a variety of different materials. For further understanding the growth mechanism, we also attempted to dope NCs by introducing impurities during their growth. Incorporation of mercury atoms to CdS NCs leads to NIR fluorescent NCs having the same size and structural properties as the corresponding undoped NCs, but completely different optical properties.

* To whom correspondence should be addressed. E-mail: wolfgang.parak@physik.uni-marburg.de.
[†] Department of Physics and WZMW.
[‡] Material Sciences Centre, EM&M Laboratory.

Materials and Methods

Synthesis of CdSe NCs. Synthesis was performed according to our previous report[32] (for more information, see the Supporting Information).

Synthesis of CdS NCs. CdS NCs were synthesized in a three-neck flask by reacting, at low temperature, a complex made of cadmium and nonanoic acid with a S/TOP solution in the presence of decylamine: 514 mg of cadmium oxide, 2 g of decylamine, and 2 g of nonanoic acid were mixed in a three-neck flask. The flask was evacuated under vacuum at 100 °C for 15 min and then heated to 200 °C under nitrogen atmosphere to decompose the CdO. The temperature was then lowered to 60 °C, and S/TOP stock (10% in weight of sulfur) was injected. The temperature dropped after the injection and was allowed to recover and increase to 80 °C. During the growth, 0.1 mL of the growth solution was extracted at time intervals ranging from 3 to 5 min (at the early stages of growth) to several hours (after several hundred minutes of growth) and diluted in 1−2 mL of toluene.

Synthesis of CdTe NCs. CdTe NCs were synthesized following a procedure similar to that one used for the synthesis of CdSe NCs. The cadmium nonanoic acid complex was allowed to react at 130 °C with a Te/TOP stock solution. At constant time intervals, 0.1 mL aliquots of NC solution were dissolved in 1−2 mL of toluene.

Synthesis of ZnSe NCs. ZnSe NCs were synthesized following the same procedure as described above for the synthesis of CdS and CdTe NCs. The zinc nonanoic acid complex was allowed to react with Se/Top stock solution at 170 °C. At constant time intervals, 0.1 mL aliquots of NC solution were dissolved in 1−2 mL of toluene.

Synthesis of ZnO NCs. ZnO NCs were synthesized following a procedure similar to those reported here for the synthesis of all the other NCs. The zinc nonanoic acid complex was allowed to react at 180 °C without addition of another precursor. At constant time intervals, 0.1 mL aliquots of NC solution were dissolved in 1−2 mL of toluene.

Synthesis of CdHgS NCs. NCs were synthesized in a 100 mL three-neck flask by reacting at low temperature a complex

10.1021/jp906812t
Published on Web 03/19/2010

made of cadmium and nonanoic acid with a S/TOP solution in the presence of decylamine. The injection of sulfur precursor was followed by the dropwise continuous injection of a mercury chloride stock solution at a constant rate during the whole synthesis. At constant time intervals, 0.1 mL aliquots from the growth solution were taken and dissolved in 1−2 mL of toluene.

Size-Selective Precipitation. After the synthesis of all NCs of different materials, the heating mantel was removed and the solution was left cooling to room temperature. Two milliliters of toluene was added to this solution, followed by methanol until a persistent cloudiness was observed. This solution was centrifuged, and the precipitate was washed again by addition of a few milliliters of toluene and methanol. The final precipitate was redissolved in toluene. By this procedure, the largest configurations of NCs were almost quantitatively separated from the smaller present configurations. We want to point out that the as-synthesized NCs had very good colloidal stability. However, in the case of repetitive precipitation and redissolution, the colloidal stability of the particles suffered and solutions turned cloudy. We attribute this partial agglomeration after repetitive precipitation and redissolution to loss of surfactant molecules from the NC surface.

Optical Characterization for Analysis and Controlled Growth. For each synthesis, UV/vis absorption spectra were recorded from all aliquots taken at different times of growth. Each set of absorbance spectra of one synthesis is characterized by several peaks whose positions do not change over time, though their intensity does. This intensity enhancement suggests the formation of stable configurations of NCs characterized by a specific absorbance wavelength. The growth of these peaks is sequential; for example, the NCs grow from one stable configuration to the next bigger stable one. To isolate NCs with predominantly only one stable configuration, the synthesis was stopped by cooling when the absorption peak associated with this stable configuration reached a maximum in intensity. The respective NCs were then extracted with size-selective precipitation. In this way, it was possible to grow and separate different samples of NCs in which most of the NCs belong to just one stable configuration.

Transmission Electron Microscopy (TEM). TEM investigations were performed using a JEM 3010 high-resolution electron microscope (Jeol Ltd., Tokyo, Japan) operated at 300 kV. For image acquisition, a 2 k × 2 k slow scan CCD camera (Mega Scan 794, Gatan Inc., Pleasanton, CA) was used along with the Digital Micrograph software. All samples were prepared by depositing the NCs on 300 mesh copper grids covered with a thin carbon supporting film. Image processing and Fourier analysis of individual NCs were done by making use of the CRISP (Calidris, Sollentuna, Sweden) software and the electron diffraction program by J.-P. Morniroli (Université de Lille, France).

Energy-Dispersive X-ray Spectroscopy (EDX). EDX graphs were recorded with an SEM CamScan IV. Nanocrystals were precipitated three times, and the powder was left drying under nitrogen atmosphere before being spread on a silicon wafer. Alternatively, in some cases, the composition of the NCs was determined by inductively coupled plasma mass spectrometry (ICP-MS).

Results and Discussion

As reported previously in the case of CdSe NCs,[32,41,42] the absorbance spectrum of the growth solution of very small NCs evolves over time, showing several characteristic peaks centered around precise wavelength values. In Figure 1, the temporal evolution of the absorbance spectra of CdSe, CdS, CdTe, ZnSe and ZnO NCs is shown. The temporal evolution of all spectra shows discontinuous growth. For continuous growth, the first exciton peak in the absorption spectrum of semiconductor NCs would continuously shift to higher wavelengths. On the other hand, the peaks at short wavelengths in the spectra shown in Figure 1 do not shift but stay at a fixed position. Upon discontinuous growth, the intensity of the peaks at short wavelengths is decreased, whereas the intensity of peaks at higher wavelengths is increased. For claiming peaks at constant positions, of course, multiple experiments have to be performed; that is, the same peak positions must have been observed in multiple syntheses. If NCs were grown further, the discrete absorption peaks would vanish and the absorption peak at the highest wavelength would, from now on, continuously shift toward higher wavelengths. Such transition to regular continuous growth has been shown before.[32] In this way, a clear separation between discontinuous and continuous growth can be obtained. Upon discontinuous growth, the position of the absorption peaks does not change; only their intensity shifts. For continuous growth, the position of the absorption peak shifts toward higher wavelengths upon growing. In all our experiments, discontinuous growth smoothly changed over to continuous growth, as has been already shown for the case of CdSe in a previous study.[32] In the present work, an example for the transition of discontinuous to continuous growth can be seen in Figure 1c (and in the following figures in the Supporting Information, S22 and S25) and will be explained below in the case of CdTe.

CdSe NCs. We recently published the temporal evolution of the absorbance spectra of CdSe NCs.[32] In the present study, CdSe NCs were grown as a reference system; see Figure 1a (and the Supporting Information for a more detailed description).

CdS NCs. The temporal evolution of the absorbance spectra of aliquots taken during the growth of CdS NCs is reported in Figure 1b. In the following, all times will refer to the duration of growth after sulfur injection of the stock solution. After 15 min of growth, a first shoulder around 303 nm is visible in the absorbance spectrum (Figure 1b, dark blue curve). This suggests the formation of a first stable configuration of CdS NCs in solution, which we will call CdS I. As the NCs grew over time in solution, the shoulder turned into a sharp peak after some more minutes of growth (Figure 1b, red curve), demonstrating the existence of more and more CdS I species. After 45 min of growth, an additional peak centered at about 326 nm appeared in the absorbance of the solution. This indicates formation of the next bigger stable configuration of NCs. We call this new configuration CdS II. Over time, the intensity of the peak associated with the CdS II species gains in intensity compared with the one of the peak associated with CdS I. After around 60 min of growth time, the absorption spectrum displays almost exclusively the peak at 326 nm (Figure 1b, blue line). This suggests that most of the NCs present in solution belonged to the CdS II species and just a little fraction of them still belonged to the CdS I species. When the synthesis was stopped at this point, followed by subsequent isolation of the NCs with size-selective precipitation with methanol and redissolution, a solution could be obtained that showed only the absorbance peak that is associated with the CdS II species. By carrying on the synthesis instead, sequential appearance of four more peaks centered at about 347, 362, 377, and 387 nm occurred. We associate these peaks with additional bigger stable configurations of CdS NCs, which we refer to as CdS III, IV, V, and VI. Again, our criterion for considering growth as discontinuous was based on the observation of peaks in the absorption spectra at fixed

[A1]

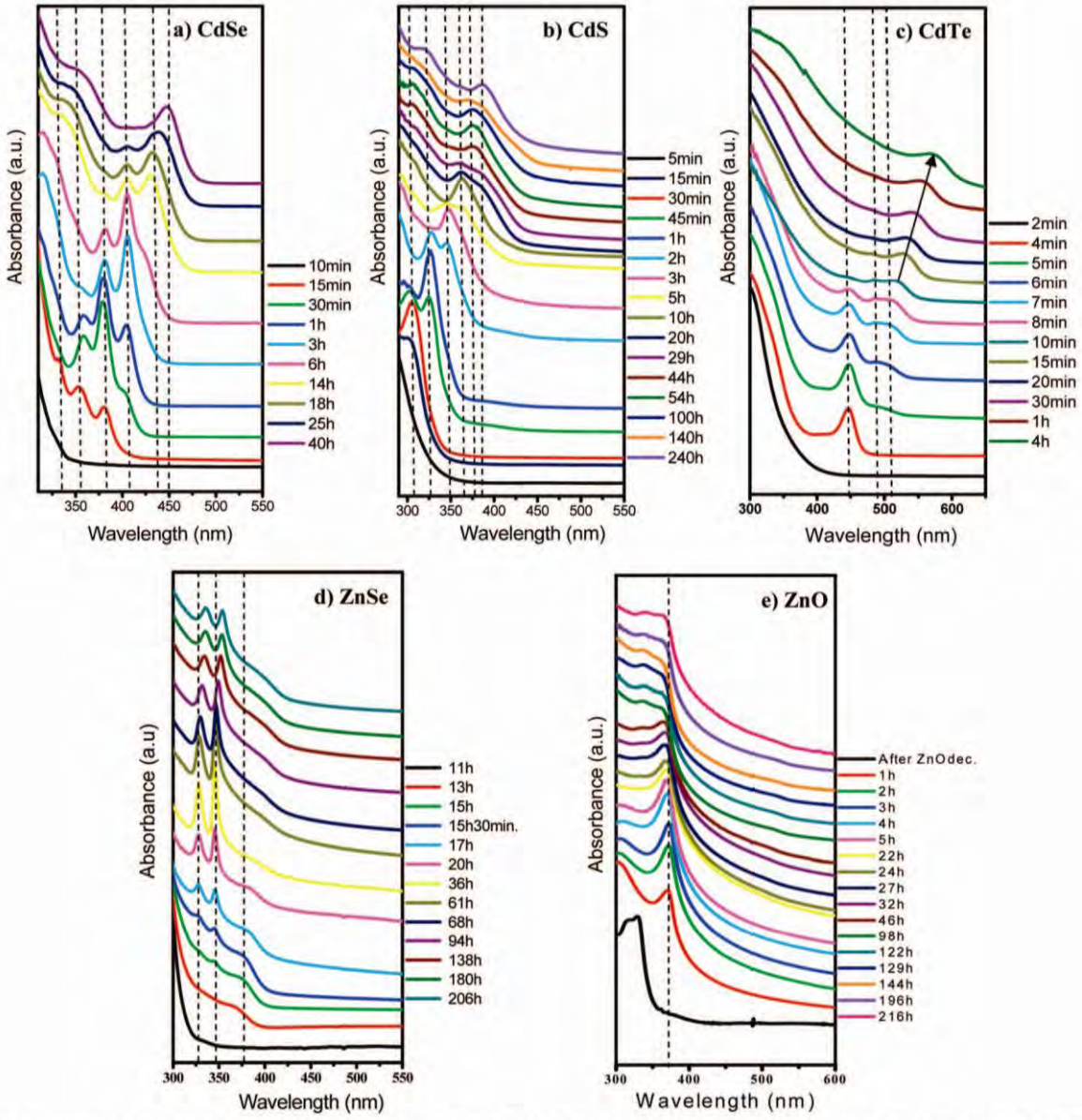

Figure 1. Absorbance spectra recorded at different stages of growth. The zero point of the time axis corresponds to the injection time of the Se, S, and Te precursor solutions: (a) CdSe, (b) CdS, (c) CdTe, (d) ZnSe, and (e) ZnO. The dotted lines indicate the absorption peaks of the different species of NCs. In the case of CdTe, the transition between discontinuous and continuous growth can be seen (arrow). For discontinuous growth, absorption peaks remain at fixed wavelengths while their respective intensities change, whereas for continuous growth, the absorption peaks shift to higher wavelengths.

positions, which did not shift during growth but, instead, changed their intensity. Obviously, for claiming peaks at constant positions, multiple experiments had to be performed. In the Supporting Information (cf. Figure S21), the temporal evolution of absorption spectra upon discontinuous growth of CdS NCs is shown for several experiments. Positions of peaks were the same in different experiments. The positions of the peaks are in relatively good agreement with values reported by Yu et al.[43] Yu et al. and Pan et al. have previously discussed the synthesis of CdS NCs.[43−46] In these studies, peaks in the absorption spectra were found at 309, 323, and 348 nm, which correspond reasonably with the peaks found in the present study at 303, 326, and 347 nm (cf. Table 1). Yu et al. argue that higher wavelength peaks in the absorption spectra are related to continuous growth.[43] However, as some of the peaks at higher wavelengths were found during several syntheses, we think that there is evidence that discontinuous growth might still occur until bigger particle sizes, before it eventually merges into continuous growth. The characteristic changes in the absorption spectra during growth of CdS are highly similar to those observed during the growth of CdSe.[32] The absorbance peaks are sharp and well-distinguishable. In the case where the synthesis was slow enough (i.e., the synthesis temperature is not too high), it was possible to stop the reaction at the points when the majority of NCs present in solution could be associated with one particular stable configuration. By precipitating these NCs, it was possible to prepare solutions in which basically just one stable configuration of NCs was present. This means that it is possible to obtain solutions with only one single peak at a fixed wavelength in the absorption spectrum. In Figure 2, the absorbance, fluorescence, and excitation spectra of solutions that have been extracted during growth and that predominantly comprise only one stable configuration of NCs (CdS I−CdS VI) are reported.

[A1]

TABLE 1: Summary of the Properties Recorded from CdS and CdTe NCs

material	CdS I	CdS II	CdS III	CdS IV	CdS V	CdS VI	CdTe I	CdTe II−III
wavelength of absorption peak (nm)[a]	303.7 ± 0.5	326.7 ± 0.5	347 ± 1	362.7 ± 0.6	377 ± 0.5	387 ± 1	445.3 ± 1.5	487.6 ± 2.5 506 ± 1.5
composition (EDX)[b,c]	Cd 53% S 47% $\chi^2 = 1.11$	Cd 53% S 47% $\chi^2 = 0.88$	Cd 52% S 48% $\chi^2 = 0.8$	Cd 51% S 49% $\chi^2 = 1.28$	Cd 49% S 51% $\chi^2 = 1.8$	Cd 49% S 51% $\chi^2 = 1.13$	Cd 53% Te 47% $\chi^2 = 0.89$	Cd 53% Te 47% $\chi^2 = 0.89$
composition (ICP-MS)[b]							Cd 55% Te 45%	Cd 58% Te 42%
crystalline structure[d]	both ZB and W	both ZB and W	both ZB and W	both ZB and W	both ZB and W	both ZB and W	both ZB and W	both ZB and W
size distribution from TEM (nm)[e]	2.3 ± 0.3	2.7 ± 0.5	2.9 ± 0.8	3.5 ± 0.7	3.6 ± 0.2	3.9 ± 0.1	2.4 ± 0.3	3.1 ± 0.8
QY[f]							29%	33%

[a] The wavelength of absorption refers to the center of the absorbance peak before size-selective precipitation. [b] The composition of the NCs was determined with EDX and ICP-MS analyses. [c] χ^2 denotes how well the composition of the NCs could be determined from the EDX analysis. [d] The crystalline structure can be either ZB = zinc blende or cubic, or W = wurtzite or hexagonal. [e] Average sizes of NCs were estimated by measuring the long axes of 10−25 NCs from TEM images. Because of the weak contrast, only the inorganic core of the NC, but not the organic surfactant shell, contributes to this value. [f] QY is the fluorescent quantum yield of the NCs.

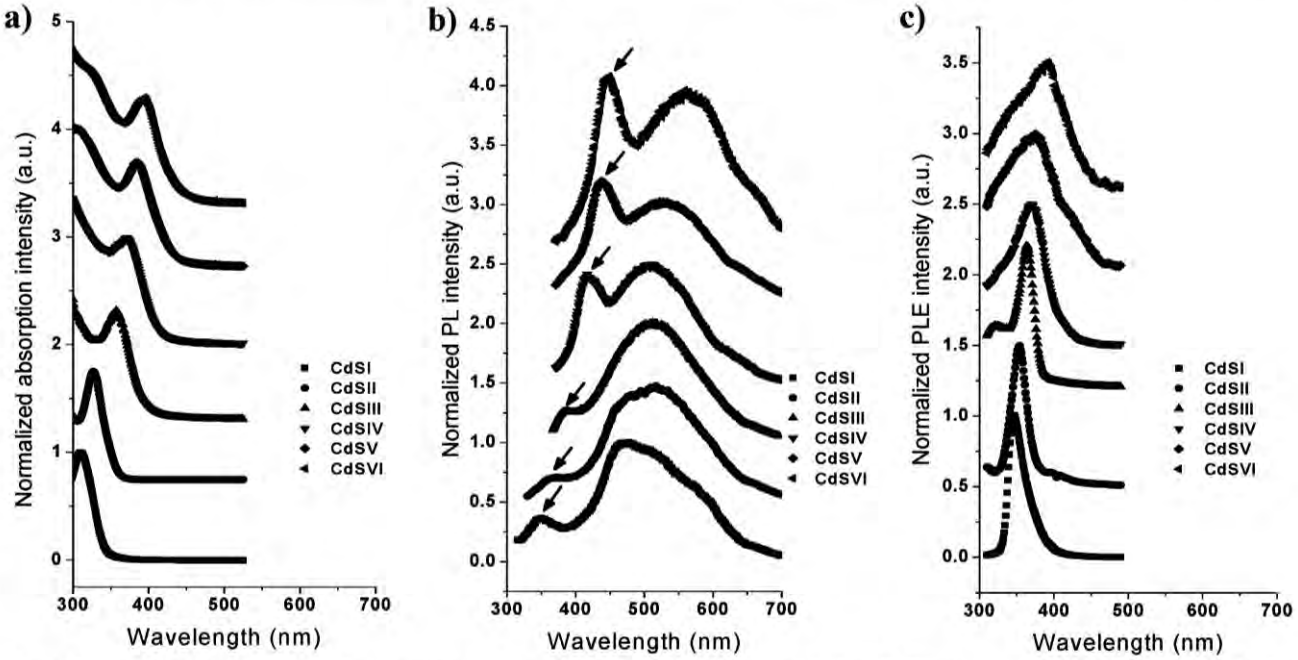

Figure 2. (a) Absorbance, (b) photoluminescence (PL), and (c) photoluminescence excitation (PLE) spectra of CdS NCs after size-selective precipitation. The PL spectra were collected with an excitation wavelength of 300 nm for CdS I, 310 nm for CdS II, 330 nm for CdS III, 345 nm for CdS IV, and 350 nm for CdS V and CdS VI. The fluorescence due to recombination of photoexcited electron−hole pairs is marked by arrows in the PL spectrum. The broad fluorescence peak is due to trap state emission. PLE spectra were recoded at the emission wavelength of the emission maximum of the peak at higher wavelength in the respective PL spectra. For better comparability between the graphs, data for wavelengths between 300 and 700 nm are displayed.

Compared with the absorption spectra recorded during growth (Figure 1b), the positions of the absorbance peaks in the absorption spectra recorded after size-selective precipitation of individual species of NCs (Figure 2a) are a few nanometers (1−10 nm) red shifted and their full width at half-maximum (fwhm) has become broader. We ascribe this to the size-selective precipitation. The fluorescence of the isolated species of NCs is prevalently dominated by trap state emission. We assume this to be due to stripping off of surfactant molecules during the washing/precipitation procedure. In fact, after repetitive precipitation and redissolution, the colloidal stability of the NCs suffered and aggregation occurred, which agrees well with the assumption of loss of surfactant molecules from the NC surface. The fluorescence peaks originating from the different species of CdS NCs are centered at about 351 nm for CdS I, 361 nm for CdS II, 387 nm for CdS III, 417 nm for CdS IV, 438 nm for CdS V, and 448 nm for CdS VI. The excitation spectra were recorded at the emission maximum of the peak in the fluorescence spectra (i.e., the trap state emission peak) for each family of NCs (475 nm for CdS I, 505 nm for CdS II, 510 nm for CdS III, 515 nm for CdS IV, 532 nm for CdS V, and 565 nm for CdS VI). The peak in the PLE spectra obtained from each family of NCs is centered at 346 nm for CdS I, 353 nm for CdS II, 364 nm for CdS III, 370 nm for CdS IV, 377 nm for CdS V, and 391 nm for CdS VI.

EDX analysis of the samples (see Table 1 and the Supporting Information, Figure S16) shows that the first stable configurations of CdS NCs (e.g., the species with absorption at short

[A1]

wavelenths) are richer in cadmium than in sulfur, although, for their synthesis, a higher amount of sulfur than of cadmium was required. The fact that a large amount of sulfur is required for the formation of the CdS NCs suggests that it is the presence of sulfur atoms that triggers nucleation of the NCs. The fact that the NCs are richer in cadmium than in sulfur suggests to us that their surface should be mainly composed of cadmium atoms. This interpretation is based on the assumption of a high surface-to-volume ratio. The atomic species that is most present in the NCs should be on the surface, as the next inner layer is only composed of fewer atoms. From the analysis of the HRTEM micrographs obtained on NCs (see the Supporting Information, Figure S3), it is possible to see that CdS NCs mainly come in a cubic crystalline structure. SAED (selected area electron diffraction) of the NCs did not lead to any conclusive data because of the broadness of the peaks due to the small size of the NCs. As the analysis of the HRTEM images (see the Supporting Information, Figures S1, S2, S4, and S5) does not provide an exhaustive answer to the determination of the crystalline structure of the NCs, we cannot exclude the hypothesis that some NCs may have a wurtzite structure. From TEM picture analysis, it was possible to estimate the mean size of the different stable configurations of NCs with values from about 2 to 4 nm (Table 1). Comparing our data with those reported by Yu et al.,[47] we can see that our average size is a little larger (cf. Table T3 in the Supporting Information). This is probably due to the different ligands used for the synthesis. Furthermore, the presence of agglomerates in the TEM images cannot be excluded, for which reason they have to be considered with care.

Comparison of our results obtained with CdS NCs with previous studies point out fundamental differences. Herron et al. report the synthesis of $Cd_{32}S_{14}(SC_6H_5)_{36}$-$(DMF)_4$ NCs that were synthesized with a high-temperature and high-pressure process starting from $Cd_{10}S_4(SC_6H_5)_{12}$ NCs as precursors.[31] The stoichiometry, the size, and the shape of those CdS NCs are different from the ones reported in our present study. However, the absorbance of 358 nm reported by Herron for NCs dissolved in THF is very close to the one we observed for NCs belonging to the CdS IV species (362 nm). Likewise, the absorbance of 346 nm of $Cd_{20}S_{13}(SPh)_{22})^{-8}$ NCs reported by Farneth et al.[48] is very similar to the NCs of the CdS III species (347 nm), although, again, the size and shape are different from our findings. In the same paper, Farneth et al. ascribe the peak at 346 nm as the absorbance peak of NCs formed by the agglomerations of $Cd_{10}S_{16}Ph_{12}$ NCs that present an absorbance maximum at 300 nm. This is similar to the value we attribute to NC species CdS I. Vossmeyer et al.[49] report absorbance spectra of $Cd_{32}S_{14}(SCH_2CH(OH)CH_3)_{36}\cdot 4H_2O$ NCs dissolved in DMF with a main peak centered at 325 nm along with a less intense peak centered at about 305 nm. These values are very close to the ones ascribed to the CdS II (326 nm) and CdS I (303 nm) species found in our study. The NCs reported by Vossmeyer[49] and Herron[31] have an entirely identical core but a different absorbance peak position. This fact is justified by Herron by considering the presence of different surfactants on the NCs' surfaces.[31] The surfactant molecules used in our study and that are, therefore, present on the surface of species CdS I−CdS VI are different from both Vossmeyer's[49] and Herron's[31] reports. We argue that this is the reason why our particles are different in size, shape, and stoichiometry. Surprisingly, absorption peaks of CdS NCs obtained by different synthesis routes display similar wavelengths of the absorption peaks, though their morphology (size, shape, stoichiometry) varies significantly between the different synthesis routes. One explanation might be that part of the NCs refer to agglomerates of NCs rather than dispersed NCs, as already had been suggested by Farneth et al.[48]

CdTe NCs. In Figure 1c, the evolution over time of a series of absorbance spectra of CdTe NCs in solution is shown. Again, in the following, all times will refer to the duration of growth after injection of the tellurium stock solution. After 4 min (Figure 1c, red curve), a narrow peak centered at about 445 nm was clearly visible in the solution absorbance spectrum, suggesting the formation of the first stable configuration of CdTe NCs (CdTe I). After 1 additional min, a second shoulder became clearly visible in the absorbance spectrum (Figure 1c, green curve). This shoulder increased in intensity and broadness over time, while the first peak started to disappear (Figure 1c, fuchsia curve). Subsequently, the absorbance spectrum presented two new peaks (one centered at about 488 nm (CdTe II) and the other one around 506 nm (CdTe III) having a comparable intensity. A detailed zoom showing the presence of two distinct peaks for CdTe II and CdTe III is shown in the Supporting Information (Figure S24). In this case, we cannot claim sequential growth because the formation of CdTe II and III NCs could not be observed separately. Consecutively, the peak structure in the absorbance spectra became less pronounced by peak broadening. Nevertheless, Figure 1c shows discontinuous growth for the CdTe I and CdTe II & CdTe III species. This is manifested by that the peaks associated with the different species are at a fixed position and only their intensity changes upon growth (cf. the derivative of the absorption spectrum in the Supporting Information, Figure S23). The same peak positions were observed in several experiments, as is shown in the Supporting Information (Figure S22). Upon longer times of growth, NCs started to grow continuously, as commonly reported in literature, which can be seen in the typical red shift of the first exciton peak over time. This can be, again, seen by comparing the absorption spectra of different syntheses. In the case of continuous growth, there is no fixed wavelength and, upon further growth, the peaks in the absorption spectrum shifts continuously. Our data are in relatively good agreement with the findings of Dagtepe et al., who observed peaks in their absorption spectra at 425, 470, 505, 557, and 606 nm for the synthesis of CdTe NCs using hexylphosphonic acid for the cadmium oxide decomposition.[34] The first of these peaks would correspond to our peaks at 445, 488, and 506 nm (cf. Table 1). The last two peaks observed by Dagpete et al. refer to a wavelength region that, in our case, already accounts for continuous growth of the NCs.[34] This is probably due to the different molecules used for the cadmium oxide decomposition, which is carboxylic acid in our case and phosphonic acid in Dagpete's synthesis, as they control the surface reactivity of the NCs. We applied size-selective precipitation on the solution in which just CdTe I was present, on the solution in which CdTe II and III were both present, and on the solution with only CdTe III. The absorbance and the fluorescence spectra of these two samples after precipitation and redissolution in toluene are shown in Figure 3.

The absorption and PL spectra of the CdTe I NCs present narrow peaks centered at 445 (fwhm ≈ 35 nm) and 506 nm (fwhm ≈ 35 nm). In the PL spectrum, some trap state emission is present with a small peak at 650 nm. All data are summarized in Table 1. In the solution containing CdTe II and III NCs, the broad absorption peak can be resolved in two strongly overlapping absorption peaks centered at about 488 and 506 nm (cf. Figure S24 in the Supporting Information). The fluorescence

[A1]

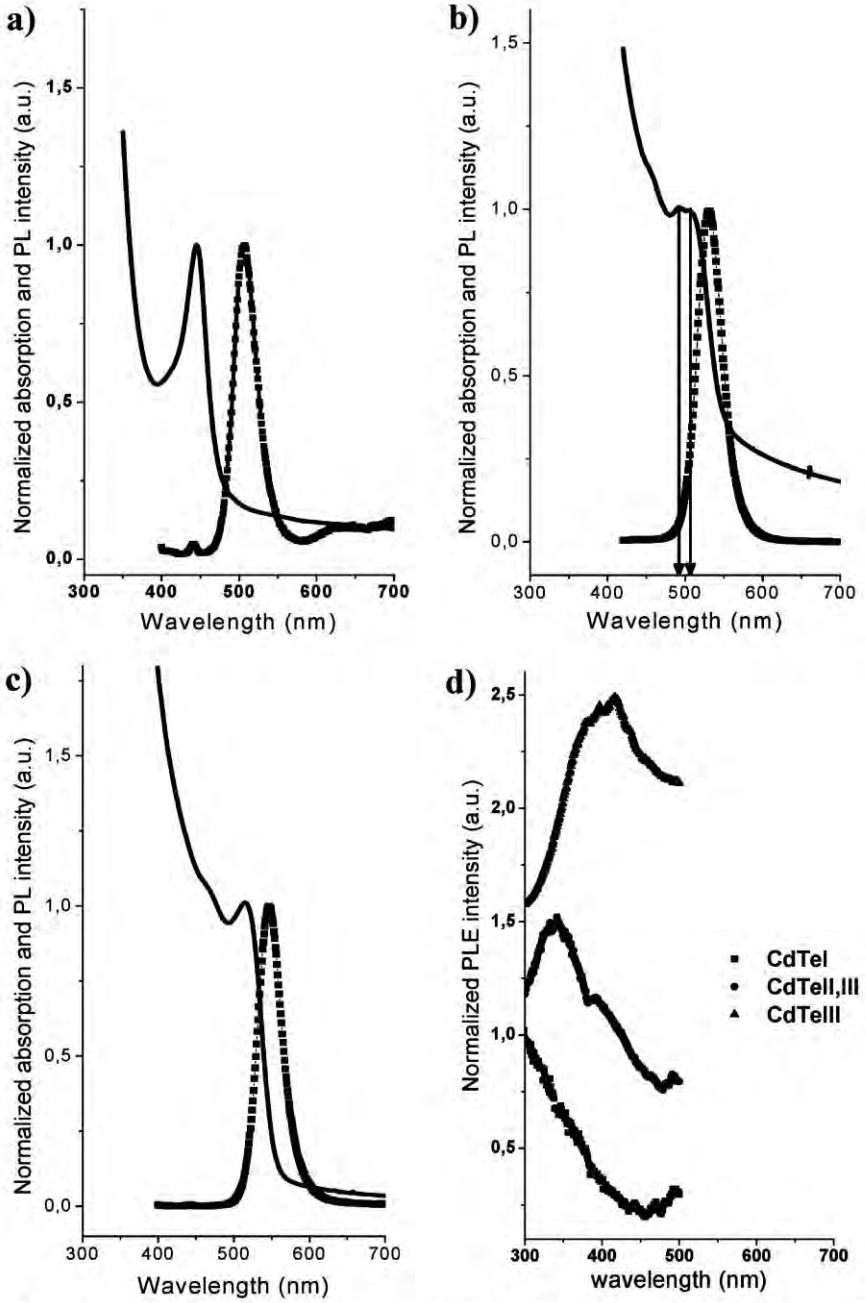

Figure 3. (a) Normalized absorbance and fluorescence (PL) spectra of CdTe I NCs. (b) Normalized absorbance and fluorescence spectra of a sample containing CdTe II and CdTe III NCs. (c) Normalized absorbance and fluorescence spectra of a sample containing CdTe III NCs. (d) Normalized photoluminescence excitation (PLE) spectra of samples containing CdTe I, CdTe II + CdTe III, and CdTe III NCs. The solutions had been obtained by size-selective precipitation and redissolution in toluene. The excitation wavelength used for the PL measurements was 390 nm. The presence of two absorbance peaks in the CdTe II & CdTe III spectrum (panel b) is displayed with arrows. The PLE spectra were recorded at an emission wavelength of 506, 535, and 547 nm in the case of CdTe I, CdTe II & CdTe III, and CdTe III, respectively. For better comparability between the graphs, data for wavelengths between 300 and 700 nm are displayed.

peak does not show a substructure, and we do not have any evidence if the peak originates only from one of the stable configurations (CdTe II, CdTe III) or from both. At any rate, the fluorescence is rather trap state free and centered at about 535 nm (Figure 3b). The fluorescence and absorbance spectra of the solution containing CdTe III after size-selective precipitation is shown in Figure 3c. The absorption peak for CdTe III is centered at 514 nm (which is red shifted in comparison with the peak before size-selective precipitation), while the fluorescence peak maximum is about 547 nm. The excitation spectra of solutions containing CdTe I, CdTe II & CdTe III, and CdTe III are shown in Figure 3d. Again, our main criterion for discontinuous growth is the fact that wavelengths of the peaks associated with the species CdTe I, CdTe II, and CdTe III were reproducible in several experiments (see the Supporting Information, Figure S22). In the case where CdTe particles were left growing for long enough times, the transition to continuous growth can be observed; see Figure 1c and Figure S22 in the Supporting Information. For continuous growth, the exciton peak shifts continuously to higher wavelengths. The composition of the samples, as determined by EDX and ICP-MS analyses, is reported in Table 1 (see also the Supporting Information, Figure

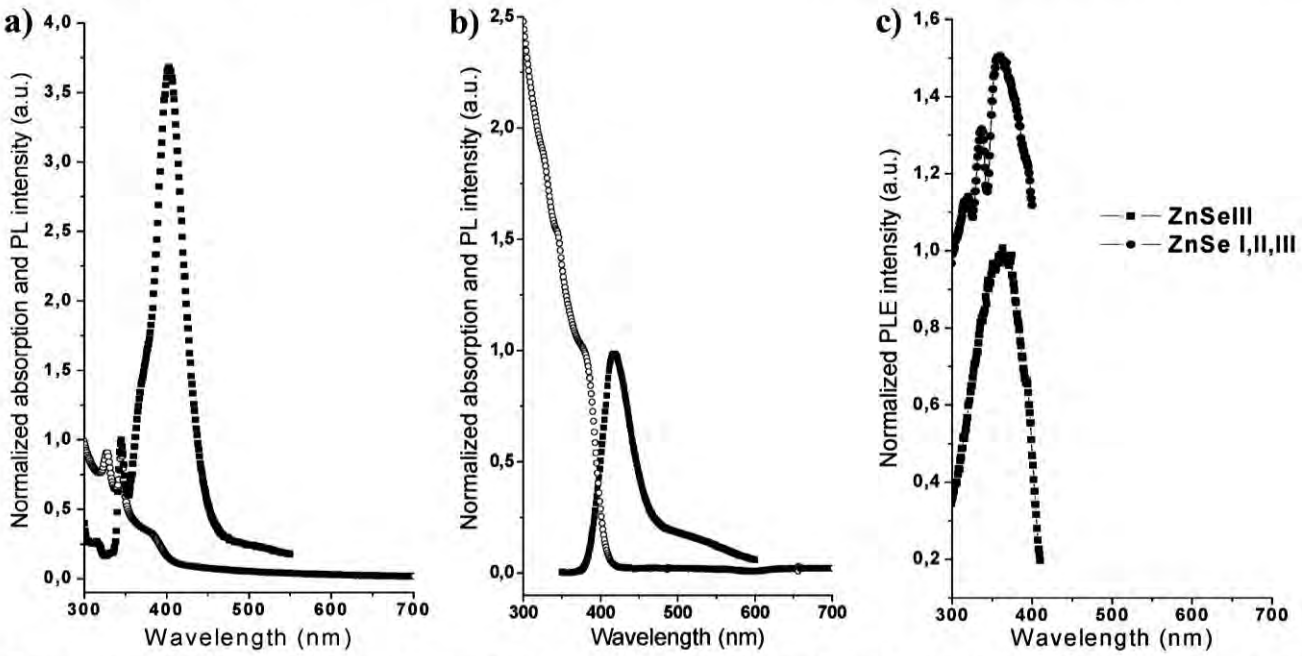

Figure 4. (a) Normalized absorption and fluorescence spectra of an aliquot containing all three families of ZnSe NCs. The aliquot was taken directly from the growth solution, and the spectra were taken without any previous purification step. Thus, the sample comprises all three species. (b) Absorption and fluorescence of ZnSe III NCs dissolved in toluene after size-selective precipitation. (c) Normalized PLE spectra of samples containing all three species and only containing ZnSe III NCs. For the sample containing all three species, the emission at 405 nm, for the sample containing ZnSe III, the emission at 415 nm was recorded. For better comparability between the graphs, data for wavelengths between 300 and 700 nm are displayed.

S17). All the tested configurations were richer in cadmium than in tellurium. This supports the hypothesis that their surface is mainly composed of cadmium atoms, and due to the high surface-to-volume ratio, the atomic species with the highest content should be present in the outermost layer. The synthesis of CdTe NCs has been performed with different Cd/Te ratios: 1:1, 1:2, 2:1, and 3:1[50] (see the Supporting Information, Figure S25). Even if, in almost all the synthesis, it was possible to see the growth of the peak attributed to CdTe I, only in those with a ratio between cadmium and tellurium of 2:1 was good discrimination of the different peaks possible. The analysis of HRTEM pictures (see the Supporting Information, Figure S6) confirmed the wurtzite structure already reported by Peng et al. for the synthesis of CdTe NCs in the presence of oleic acid,[51] but some crystals having a zinc blende structure have been observed too. Estimation of the NC diameters from the TEM images leads to values around 2.4 nm for CdTe I and about 3 nm for CdTe II and III (see Table 1). Again, we have to point out the possibility of aggregates in the particles, for which reason the determined diameters have to be interpreted with great care.

ZnSe NCs. In Figure 1d, the temporal evolution of typical ZnSe NC absorbance spectra is shown. All times refer to the duration of growth after selenium injection. After 13 h, a peak centered at about 378 nm appeared and kept growing slowly for several more minutes (Figure 1d, red curve). This peak is actually quite broad compared with the typical peaks characterizing NCs. However, its intensity keeps on growing without shifting to other wavelengths, which we regard as a typical feature of one stable configuration during discontinuous growth of NCs. We, therefore, refer to this peak as ZnSe III. Again, the peak position was reproducible in several syntheses (cf. the Supporting Information, Figure S26). However, experimental evidence is not strong enough to strictly claim this peak as a stable configuration during discontinuous growth. After 15 h (Figure 1d, green curve), two more peaks started growing, though surprisingly at lower wavelengths. Both of these two peaks were not present in the absorbance spectra before this point of growth. They are centered at 328 and 346 nm and are extremely sharp (fwhm ≈ 22 nm). We refer to them as ZnSe I and ZnSe II, respectively. Both peaks kept on growing in intensity over several days, while the third peak associated with ZnSe III became broader and eventually slowly red shifted. Broadening and red shifting of the absorption peaks eventually occurred, also to the particles associated with ZnSe I and II NCs. This suggests that, at this stage, conditions are that NC nucleation is stopped in favor of continuous growth of all NCs in solution. The mechanism that governs this peculiar nucleation of NCs of different sizes in solution is definitely fascinating, though for us, it was not straightforward to understand it. Fluorescence spectra of solutions containing ZnSe NCs of the different configurations, as obtained by size-selective precipitation, have peaks centered at about 345 nm (fwhm ≈ 20 nm), 368 nm (fwhm ≈ 24 nm), and 403 nm (fwhm ≈ 46 nm); see Figure 4. We also want to point out that these peaks, in fact, correspond to particles, as the presence of NCs in solution was confirmed by TEM images (Supporting Information, Figure S7). We, therefore, can exclude molecular species in the solution that could have been responsible for one of the absorption peaks. However, our data do not permit us to fully unravel the different nucleation and growth behaviors.

Because of the unexpected growth that first led to the ZnSe III configuration and only then to the subsequent simultaneous appearance of the ZnSe I and ZnSe II species, we were not able to extract samples enriched only in ZnSe I and ZnSe II. However, by stopping the growth already during the initial stage when only ZnSe III was present, we were able to obtain an aliquot with ZnSe III only (Figure 4b). From HRTEM micrographs (see the Supporting Information, Figure S7), the NCs' crystalline structure was found to be wurtzite, though we are not able to exclude that some NCs present a cubic lattice, as

TABLE 2: Summary of the Properties of ZnSe, ZnO, and CdHgS NCs

material	ZnSe I	ZnSe II	ZnSe III	ZnO	CdHgSI	CdHgSII	CdHgSIII	CdHgSIV	CdHgS final
wavelength of absorption peak (nm)[a]	328.2 ± 0.9	346.0 ± 1.1	378.0 ± 1.8	365.0 ± 2.0	306.0 ± 1.0	326.0 ± 1.0	349.8 ± 2.0	367.0 ± 2.0	393.0 ± 3.0
composition (EDX)[b,c]		Zn 49% Se 51% $\chi^2 = 1.11$		Zn 49% O 51% $\chi^2 = 2.05$	Cd 25% Hg 22% Cl 3% S 50% $\chi^2 = 1.42$	Cd 50% Hg 5% Cl 4% S 41% $\chi^2 = 1.5$	Cd 38% Hg 13% Cl 7% S 42% $\chi^2 = 1.11$	Cd 36% Hg 13% Cl 8% S 43% $\chi^2 = 1.93$	Cd 31% Hg 16% Cl 7% S 46% $\chi^2 = 2.15$
composition (ICP-MS)[b]		Zn 47% Se 53%	Zn 45% Se 55%						
crystalline structure[d]		both ZB and W		both ZB and W	both ZB and W	both ZB and W	both ZB and W	bothZB and W	both ZB and W
size distribution from TEM (nm)[e]	2 ± 0.2	2.4 ± 0.2	3.2 ± 0.4	6 ± 0.7	2.5 ± 0.5	2.67 ± 0.35	3.1 ± 0.4	3.7 ± 0.6	4.1 ± 0.8

[a] The peak position values refer to the center of the absorbance peak associated with this NC configuration before the size-selective precipitation. [b] Composition of the NCs was determined by EDX or ICP-MS. [c] χ^2 denotes how well the composition of the NCs could be determined from the EDX analysis. [d] The crystal structure is either ZB = zinc blende or cubic, or W = wurtzite or hexagonal. [e] The mean diameter of NCs was estimated by measuring the long axes of 10−25 NCs in TEM images.

suggested by SAED measurements (see the Supporting Information, Figure S8). NCs including both phases in their lattice were never directly observed. In aliquots such as the one shown in Figure 4a, in which the ZnSe I and ZnSe II species were present together with the ZnSe III species, the HRTEM micrographs gave evidence of the presence of three NC sizes centered at about 2, 2.4, and 3.2 nm (Table 2). As the statistics in determining the particle diameters with TEM is limited and the widths of the size distributions are comparable to the difference in average size between the different configurations, this analysis has naturally to be regarded with care, in particular, as we cannot claim having imaged always single NCs. EDX and ICP-MS measurements (see the Supporting Information, Figure S18) displayed a higher presence of selenium, which is likely to compose the surface of the NCs.

ZnO NCs. In Figure 1e, temporal evolution of a typical ZnO NC solution absorption spectrum is shown. Just after decomposition of the ZnO precursors, a small broad shoulder appeared (Figure 1e, black curve), which suggests the formation of some sort of NC. At this point, the solution was still completely clear and any attempt to precipitate the NCs was not successful. After the synthesis was run for about 1 h (Figure 1e, red curve), the solution turned gradually white in color and the absorption spectrum clearly showed the presence of a peak centered at about 365 nm. This peak grew over time. The peak did not shift in wavelength, and it presented a sharp top and a quite broad base. Similar behavior has been reported for Cd_3P_2.[52] This is probably due to the weakness of nonanoic acid as a surfactant for this kind of material, which could have led to the formation of agglomerates whose optical properties vary, depending on the agglomerate size. Agglomerate formation has been previously reported by Reiss et al.[53] for ZnO NCs that presented an absorption peak centered at 360 nm, which is close to the value of 365 observed in our present study. The absorption peak kept on growing for several hours, and as it did not shift, we refer to it as NC configuration and was found at the same position in several syntheses (Supporting Information, Figure S27). TEM imaging of particles obtained by precipitation of aliquots taken at this point of growth showed the presence of agglomerates that are composed of NCs (see the Supporting Information, Figure S9). We attribute the peak in the absorption spectra to these individual NCs. After several days of further growth, the peak intensity started to decrease and formation of a broad and weak shoulder in the absorption spectra began together with a red tail. We believe that, at this point, agglomerated NCs transfer to a bulklike configuration. In Figure 5, the absorption and fluorescence spectra of ZnO NCs after selective precipitation and redispersion in toluene are shown. The main peak in the absorption spectrum is centered at about 368 nm, whereas the fluorescence peak is centered at 376 nm (fwhm = 20 nm). There is also a high degree of trap state emission. The obtained wavelength of ZnO NC absorption of 360−365 nm, as reported here and in the work of Reiss,[53] is only slightly shorter than the bulk absorption values (378 nm, 3.3 eV), which might be affected by the measurement technique used.[54] EDX analysis of the ZnO NCs showed that these particles are richer in oxygen than in zinc, but this could be easily due to the presence of the carboxylic acid on the surface. SAED results (see the Supporting Information, Figure S10) suggest that their crystalline structure is either cubic or hexagonal. HRTEM image analysis leads to an average diameter of the NCs (or of their small aggregates) of about 6 nm (see the Supporting Information, Figure S9). We also want to point out that our original aim was the synthesis of ZnTe MScs. However, injection of Te/TOP stock solution to the zinc−nonanoic acid complex did not led to ZnTe NCs but, instead, to ZnO NCs. EDX analysis clearly demonstrated the presence of oxygen, but the absence of Te; cf. Table 2 (see the Supporting Information, Figure S18). This result is, therefore, in contrast to the other syntheses described in this manuscript, in which oxygen incorporation did not play a major role:

CdHgS NCs. The temporal evolution of the absorption spectra of CdHgS NCs is reported in Figure 6. All times refer to the duration of growth after injection of the selenium precursor stock solution. After 2 min, the solution turned from yellow to dark brown, which suggests that, from this time on, mercury is included in the growing particles due to its high reactivity with sulfur. After 10 min (Figure 6a, black curve), a pronounced shoulder at about 305 nm showed up in the absorption spectrum, which we associate with the first stable configuration of NCs (CdHgS I). Stopping the synthesis at this point allowed for size-selective precipitation of the NCs belonging to the CdHgS I species via centrifugation with methanol. By continuing the growth, on the other hand, three more peaks appeared that were detected at about 326, 349, and

[A1]

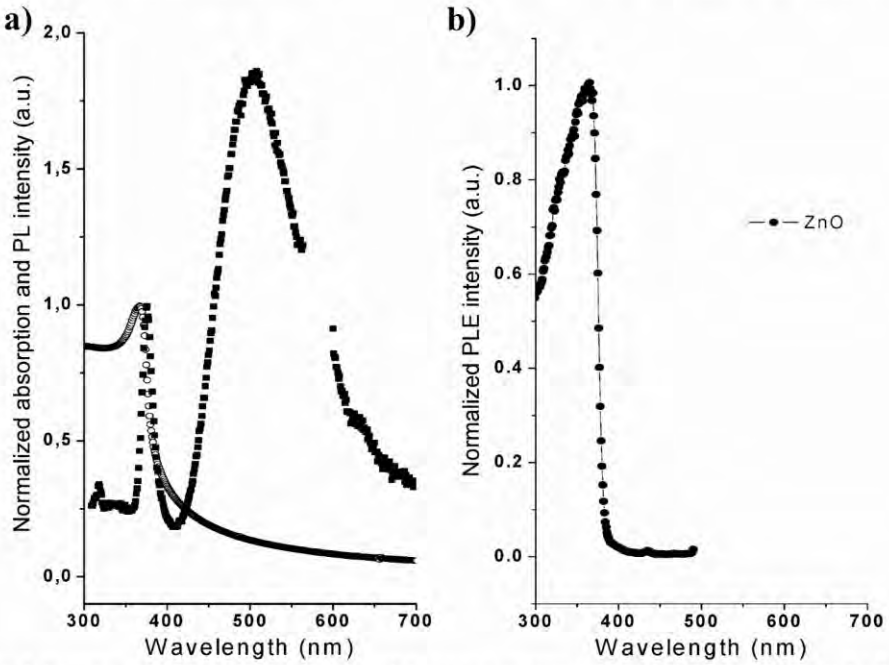

Figure 5. (a) Normalized absorption (circles) and fluorescence (solid squares) spectra of ZnO NCs in toluene. For all the fluorescence spectra, the excitation wavelength was 290 nm. (b) PLE spectrum taken for an emission wavelength of 505 nm. For better comparability between the graphs, data for wavelengths between 300 and 700 nm are displayed.

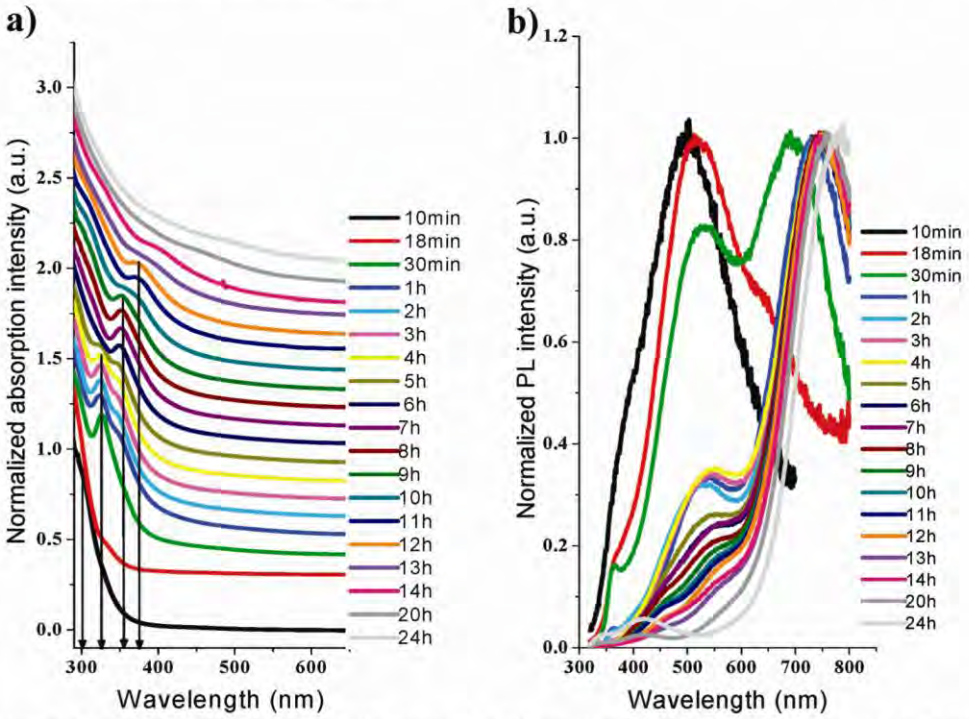

Figure 6. Absorption and fluorescence spectra of CdHgS NCs recorded at different times of growth. For simplicity, all the fluorescent spectra have been normalized. Whereas the very broad peak around 500 nm is attributed to trap state emission, the peak around 750 nm is attributed to the contribution of mercury.

367 nm. As these peaks present the characteristic intensity increment upon their appearance, followed by an intensity decrease as soon as the next peak appears at a higher wavelength, we consider them as CdHgS NCs belonging to the species CdHgS II, III, and IV. In comparison to the CdS NCs that have been obtained without the presence of Hg, the absorption peaks of the CdHgS NCs are less pronounced, though they are clearly notable and centered at wavelengths similar to that of the CdS NCs (cf. Figures 1b and 6a and Table 2). In contrast, the temporal evolution of the fluorescence of the CdHgS particles is completely different from that of the CdS particles (cf. Figures 2b and 6b). Though initially, at the start of growth, fluorescence was as in the case of CdS mainly due to trap state emission (very broad peak around 500 nm), fluorescence started to shift to the red/near infrared (NIR) upon prolonged growth. This can be attributed to incorporation of mercury.

[A1]

As done with the other samples also, the different species of NCs of CdHgS were extracted by size-selective precipitation and analyzed. Also, the final particles after 24 h of growth were purified by size-selective purification (see the Supporting Information, Figure S20, for the respective fluorescence and absorption spectra). However, from the absorption spectrum, it is obvious that the latter particles do not belong to a distinct species of NCs but already are in the region of continuous growth. We refer to these particles as "$CdHgS_{final}$". In Table 2, the mean diameters of different species of CdHgS NCs, as determined by TEM analysis (see the Supporting Information, Figures S11−S14), are listed. They are comparable to the values obtained for CdS NCs; cf. Table 1. The crystalline structure of the CdHgS NCs is both zinc blende and wurtzite, as for CdS NCs.

In Table 2 also, the composition of each configuration of CdHgS NCs, as determined with EDX, is reported (cf. the Supporting Information, Figure S19). Clearly, the presence of Hg in the NCs can be observed. It has to be pointed out that the samples had been purified with size-selective precipitation, which makes the presence of excess mercury in unreacted precursors unlikely, and the detected Hg has to be actually part of the particles. In the literature, there is an ongoing discussion about the doping of semiconductor NCs and, in particular, about the location of the dopant atoms within the particles.[55,56] Though the presence of an additional species of atoms in NCs is by several authors claimed as doping, several authors point out that doping, in fact, is complicated to prove.[57] Though we can see the presence of mercury atoms in the particles by the EDX results and by the change in the fluorescence spectra, we cannot prove doping. In fact, our data do not provide any information about the location of the mercury, which might be integrated in the core of the particles or just present on the particle surface. However, we can clearly exclude formation of conucleated HgS NCs, as in energy-filtered TEM images, Cd and Hg are found in the same NCs (see the Supporting Information, S15). For obtaining information about the local environment of the Hg atoms, other techniques, such as nuclear magnetic resonance (NMR), would be required.

Correlation of Absorption and Size. Though, in our paper, we have referred to particular NC sizes that are stable during discontinuous growth, we want to clearly point out that most of our raw data are based on absorption measurements. Yu et al. have demonstrated that an increase in NC size for several II−VI semiconductors correlates with an increase in the wavelength of the first exciton peak in the absorption spectrum.[47] Our interpretation of having increased NC sizes for NCs species that show a peak in the absorption spectrum at a higher wavelength is based on the direct correlation of absorption wavelength and size of the NC cores reported by Yu et al. Note that the correlation is described for the wavelengths of the absorption peak (which corresponds to the excitation of the first exciton), not to the wavelength of the PL emission peak. In our NC preparations, massive trap emission was found. In contrast to the PL spectra that are changed by trap emission, to our knowledge, the existence of trapped states does not significantly shift the wavelength of the first exciton peak in the absorption spectrum. Thus, the existence of trapped states does not change the correlation between the wavelength of the absorption peak and the NC size, as reported by Yu et al. However, we also want to point out that the correlation reported from Yu et al. has been obtained for NCs of larger sizes, as the ones synthesized in our study. Therefore, the Yu data cannot be reasonably extrapolated to fit our NCs (cf. the Supporting Information, Table T4). We have performed a TEM study corresponding to the absorption measurements. These data indicate that NC species that had an absorption peak at higher wavelengths, in fact, also had a bigger size. However, resolution of our TEM data is not good enough to make any statement about discontinuous growth from them. This is, in particular, due to the fact that we cannot exclude having partially imaged aggregates, as this has been shown by other authors.[50] Our argument for discontinuous growth is solely based on absorption measurements, in which we postulate stable configurations of NCs in the case where the absorption peak stays at fixed. From the TEM images (see the Supporting Information, Figures S1−S7, S9, and S11−S14), it is obvious that NCs associated with one absorption peak during discontinuous growths, and thus with a stable configuration, are not identical. Though NCs associated with one peak in the absorption spectrum clearly are not identical (as it is obvious from the TEM images), nevertheless, discontinuous growth for small NC sizes is obvious due to fixed peaks in the absorption spetra.

Conclusions

We have reported discontinuous, sequential stepwise growth of CdSe, CdS, CdTe, ZnSe, and ZnO NCs. The similar procedures and employed chemicals allow for comparison between the reactivity of the monomers in similar synthesis conditions. The synthesis could be stopped when the desired species of NCs was populated highest in solution, and via size-selective precipitation, it was possible to obtain a purified colloidal solution enriched in this species of NCs. In this way, we could associate species of NCs with discrete peaks in the absorption spectrum with NCs. This allowed for the structural and optical characterization of the different NCs species and their direct comparison. Dropwise injection of mercury chloride during the growth of CdS NCs led to NCs with integrated mercury, which resulted in a complete change in the fluorescent properties. Though we were not able to get information of the position of the Hg atoms in these particles, it is interesting to see that incorporation of Hg did not interfere with the stepwise growth of the NCs. Due to their discrete nature, NCs of different materials might develop as interesting standards for devices.[58]

Acknowledgment. The project was funded by the BMBF (project BiCIRTS). M.Z. is grateful for a fellowship from the International Graduate School at the Center for Nanoscience at the Ludwig Maximilians Universität München.

Supporting Information Available: Synthesis details; characterization of structural and compositional properties by TEM, EFTEM, and EDX; and characterization of optical properties. This material is available free of charge via the Internet at http://pubs.acs.org.

References and Notes

(1) Briant, C. E.; Theobald, B. R. C.; White, J. W.; Bell, L. K.; Mingos, D. M. P. *J. Chem. Soc., Chem. Commun.* **1981**, 201.
(2) Sotelo, A. F.; Felicissimo, A. M. P.; Sal, P. G. *Inorg. Chim. Acta* **2003**, *348*, 63.
(3) Copley, R. C. B.; Hill, C. M.; Mingos, D. M. P. *J. Cluster Sci.* **1995**, *6*, 71.
(4) Mingos, D. M. P. *J. Cluster Sci.* **1992**, *3*, 397.
(5) Soloviev, V. N.; Eichhofer, A.; Fenske, D.; Banin, U. *J. Am. Chem. Soc.* **2000**, *122*, 2673.
(6) Soloviev, V. N.; Eichhöfer, A.; Fenske, D.; Banin, U. *J. Am. Chem. Soc.* **2001**, *123*, 2354.
(7) Soloviev, V. N.; Eichhöfer, A.; Fenske, D.; Banin, U. *Phys. Status Solidi B* **2001**, *224*, 285.

[A1]

(8) Wuister, S. F.; van Driel, F.; Meijerink, A. *Phys. Chem. Chem. Phys.* **2003**, *5*, 1253.
(9) Kasuya, A.; Noda, Y.; Dmitruk, I.; Romanyuk, V.; Barnakov, Y.; Tohji, K.; Kumar, V.; Belosludov, R.; Kawazoe, Y.; Ohuchi, N. *Eur. Phys. J. D* **2005**, *34*, 39.
(10) Kasuya, A.; Sivamohan, R.; Barnakov, Y. A.; Dmitruk, I. M.; Nirasawa, T.; Romanyuk, V. R.; Kumar, V.; Mamykin, S. V.; Tohji, K.; Jeyadevan, B.; Shinoda, K.; Kudo, T.; Terasaki, O.; Liu, Z.; Belosludov, R. V.; Sundararajan, V.; Kawazoe, A. Y. *Nat. Mater.* **2004**, *3*, 99.
(11) Kuzuya, T.; Tai, Y.; Yamamuro, S.; Sumiyama, K. *Chem. Phys. Lett.* **2005**, *407*, 460.
(12) Xie, R. H.; Bryant, G. W.; Zhao, J. J.; Kar, T.; Smith, V. H. *Phys. Rev. B* **2005**, *71*, 125422.
(13) Dance, I. G.; Choy, A.; Scudder, M. L. *J. Am. Chem. Soc.* **1984**, *106*, 6285.
(14) Behrens, S.; Bettenhausen, M.; Eichhofer, A.; Fenske, D. *Angew. Chem., Int. Ed.* **1997**, *36*, 2797.
(15) Behrens, S.; Bettenhausen, M.; Deveson, A. C.; Eichhofer, A.; Fenske, D.; Lohde, A.; Woggon, U. *Angew. Chem., Int. Ed. Engl.* **1996**, *35*, 2215.
(16) Behrens, S.; Fenske, D. *Ber. Bunsen−Ges.* **1997**, *101*, 1588.
(17) Aguado, A.; Lopez, J. M. *J. Phys. Chem. B* **2000**, *104*, 8398.
(18) Bhattacharya, S. K.; Kshirsagar, A. *Phys. Rev. B* **2007**, *75*, 035402.
(19) Botti, S.; Marques, M. A. L. *Phys. Rev. B* **2007**, *75*, 035311.
(20) Goswami, B.; Pal, S.; Sarkar, P. *Phys. Rev. B* **2007**, *76*, 045323.
(21) Goswami, B.; Pal, S.; Sarkar, P.; Seifert, G.; Springborg, M. *Phys. Rev. B* **2006**, *73*, 205312.
(22) Jose, R.; Zhanpeisov, N. U.; Fukumura, H.; Baba, Y.; Ishikawa, M. *J. Am. Chem. Soc.* **2006**, *128*, 629.
(23) Joswig, J.-O.; Springborg, M.; Seifert, G. *J. Phys. Chem. B* **2000**, *104*, 2617.
(24) Joswig, J. O.; Roy, S.; Sarkar, P.; Springborg, M. *Chem. Phys. Lett.* **2002**, *365*, 75.
(25) Joswig, J. O.; Seifert, G.; Niehaus, T. A.; Springborg, M. *J. Phys. Chem. B* **2003**, *107*, 2897.
(26) del Puerto, M. L.; Tiago, M. L.; Chelikowsky, J. R. *Phys. Rev. Lett.* **2006**, *97*, 096401.
(27) Puzder, A.; Williamson, A. J.; Gygi, F.; Galli, G. *Phys. Rev. Lett.* **2004**, *92*, 217401.
(28) Roy, S.; Springborg, M. *J. Phys. Chem. B* **2003**, *107*, 2771.
(29) Sarkar, P.; Springborg, M. *Phys. Rev. B* **2003**, *68*, 235409.
(30) Yu, M.; Fernando, G. W.; Li, R.; Papadimitrakopoulos, F.; Shi, N.; Ramprasad, R. *J. Comput.−Aided Mater. Des.* **2007**, *14*, 167.
(31) Herron, N.; Calabrese, J. C.; Farneth, W. E.; Wang, Y. *Science* **1993**, *259*, 1426.
(32) Kudera, S.; Zanella, M.; Giannini, C.; Rizzo, A.; Li, Y.; Gigli, G.; Cingolani, R.; Ciccarella, G.; Spahl, W.; Parak, W. J.; Manna, L. *Adv. Mater.* **2007**, *19*, 548.
(33) Dai, Q. Q.; Li, D. M.; Chang, J. J.; Song, Y. L.; Kan, S. H.; Chen, H. Y.; Zou, B.; Xu, W. P.; Xu, S. P.; Liu, B. B.; Zou, G. T. *Nanotechnology* **2007**, *18*, 405603.
(34) Dagtepe, P.; Chikan, V.; Jasinski, J.; Leppert, V. J. *J.Phys. Chem. C* **2007**, *111*, 14977.
(35) Evans, C. M.; Guo, L.; Peterson, J. J.; Maccagnano-Zacher, S.; Krauss, T. D. *Nano Lett.* **2008**, *8*, 2896.
(36) Xie, R. G.; Peng, X. G. *Angew. Chem., Int. Ed.* **2008**, *47*, 7677.
(37) Kucur, E.; Ziegler, J.; Nann, T. *Small* **2008**, *4*, 883.
(38) Wang, R.; Calvignanello, O.; Ratcliffe, C. I.; Wu, X.; Leek, D. M.; Zaman, M. B.; Kingston, D.; Ripmeester, J. A.; Yu, K. *J. Phys. Chem. C* **2009**, *113*, 3402.
(39) Chen, H. S.; Kumar, R. V. *Cryst. Growth Des.* **2009**, *9*, 4235.
(40) Sun, M.; Yang, X. R. *J. Phys. Chem. C* **2009**, *113*, 8701.
(41) Riehle, F. S.; Bienert, R.; Thomann, R.; Urban, G. A.; Krugert, M. *Nano Lett.* **2009**, *9*, 514.
(42) Yu, K.; Ouyang, J.; Zaman, M. B.; Johnston, D.; Yan, F. J.; Li, G.; Ratcliffe, C. I.; Leek, D. M.; Wu, X. H.; Stupak, J.; Jakubek, Z.; Whitfiel, D. *J. Phys. Chem. C* **2009**, *113*, 3390.
(43) Yu, Q. Y.; Liu, C. Y. *J. Phys. Chem. C* **2009**, *113*, 12766.
(44) Pan, D. C.; Jiang, S. C.; An, L. J.; Jiang, B. Z. *Adv. Mater.* **2004**, *16*, 982.
(45) Pan, D. C.; Ji, X. L.; An, L. J.; Lu, Y. F. *Chem. Mater.* **2008**, *20*, 3560.
(46) Yu, Q. Y.; Liu, C. Y.; Zhang, Z. Y.; Liu, Y. *J. Phys. Chem. C* **2008**, *112*, 2266.
(47) Yu, W. W.; Qu, L.; Guo, W.; Peng, X. *Chem. Mater.* **2003**, *15*, 2854.
(48) Farneth, W. E.; Herron, N.; Wang, Y. *Chem. Mater.* **1992**, *4*, 916.
(49) Vossmeyer, T.; Reck, G.; Schulz, B.; Katsikas, L.; Weller, H. *J. Am. Chem. Soc.* **1995**, *117*, 12881.
(50) Dagtepe, P.; Chikan, V. *J. Phys. Chem. A* **2008**, *112*, 9304.
(51) Yu, W. W.; Wang, Y. A.; Peng, X. *Chem. Mater.* **2003**, *15*, 4300.
(52) Wang, R. B.; Ratcliffe, C. I.; Wu, X. H.; Voznyy, O.; Tao, Y.; Yu, K. *J. Phys. Chem. C* **2009**, *113*, 17979.
(53) Quemard, G.; Reiss, P.; Carayon, S.; Bleuse, J. *J. Cryst. Growth* **2005**, *275*, e2395.
(54) Srikant, V.; Clarke, D. R. *J. Appl. Phys.* **1998**, *83*, 5447.
(55) Mikulec, F. V.; Kuno, M.; Bennati, M.; Hall, A. D.; Griffin, R. G.; Bawendi, M. G. *J. Am. Chem. Soc.* **2000**, *122*, 2532.
(56) Erwin, S. C.; Zu, L. J.; Haftel, M. I.; Efros, A. L.; Kennedy, T. A.; Norris, D. J. *Nature* **2005**, *436*, 91.
(57) Norris, D. J.; Efros, A. L.; Erwin, S. C. *Science* **2008**, *319*, 1776.
(58) Rizzo, A.; Li, Y. Q.; Kudera, S.; Della Sala, F.; Zanella, M.; Parak, W. J.; Cingolani, R.; Manna, L.; Gigli, G. *Appl. Phys. Lett.* **2007**, *90*, 051106.

JP906812T

Discontinuous growth of II-VI Semiconductor nanocrystals from different materials

Marco Zanella [1], A. Z. Abbasi [1], Andreas K. Schaper [2], and Wolfgang J. Parak [1]*

1 Department of Physics, Philipps University Marburg and WZMW, Renthof 7, 35037 Marburg, Germany
2 Material Sciences Centre, EM&MLaboratory, Philipps University Marburg, Hans-Meerwein-Str., 35032 Marburg, Germany

*corresponding author: wolfgang.parak@physik.uni-marburg.de

Supporting Information

I) Synthesis

I.1) Chemicals. Cadmium oxide (99.999%), Zinc Oxide (99.999%), Mercury(II) chloride (99.99%), nonanoic acid (97%), decylamine (98%), sulphur powder (99.9%, 100mesh), selenium powder (99.9%, 100mesh), tellurium powder (99.8%, 200mesh) and water free toluene and methanol were purchased from Sigma, TOP (97%) was purchased from Strem. All the chemicals were used as shipped.

I.2) CdSe NC synthesis. CdSe NCs were synthesized according to a previous protocol [1] in a 3 neck flask by reacting, at low temperature, a complex made of cadmium and nonanoic acid with a selenium:Trioctylphosphine (Se:TOP) solution in presence of decylamine. 500mg of Cadmium oxide, 2 g of decylamine and 2g of nonanoic acid were mixed in a three-neck flask. The flask was evacuated to vacuum at 100 ℃ for 15 minutes and then heated to 200 ℃ under nitrogen atmosphere to decompose the CdO. The temperature was then lowered to 80 ℃ and 10 g of a solution of selenium in Trioctylphosphine (10% in weight of selenium) was quickly injected. The temperature dropped after the injection and was allowed to recover to 80 ℃. During the growth, 0.1 ml of the growth solution were extracted at time intervals ranging from 3-5 minutes (at the early stages of growth) to several hours (after several hundreds of minutes of growth) and diluted in 1-2ml of toluene.

Size selective precipitation. After the synthesis of the desired size, the heating mantel was removed and the solution left cooling to room temperature. Two milliliters of toluene were added to the solution, followed by methanol until a persistent cloudiness is observed. The resulting solution was centrifuged and the precipitate was washed again by addition of a few milliliters of toluene and methanol. The final precipitate was redissolved in toluene. By this procedure the largest species of NCs was almost quantitatively separated from the smaller species of NCs.

I.3) CdS NC synthesis. In a typical synthesis 514mg of Cadmium oxide, 2 g of decylamine and 2g of nonanoic acid were mixed in a three-neck flask. The red slurry was left under vacuum at 100 ℃ for 15 minutes and then heated at 200 ℃ under nitrogen atmosphere. The solution turned transparent because of the formation of a complex between cadmium and the carboxylic acid. The temperature was then lowered to 60 ℃ and 10 g of a solution of S in Trioctylphosphine (10% in weight) was injected. After injection, the temperature dropped and was allowed to recover and increased to 80 ℃. The NCs growth was followed taking with a syringe 0.1ml of the growth solution at time intervals ranging from 3-5 minutes (at the early stages of growth) to several hours (after several hundreds of minutes of growth) and diluted with fresh toluene.

Size selective precipitation. After the synthesis of the desired size, the heating mantel was removed and the solution left cooling to room temperature. Two milliliters of toluene were added to the solution, followed by methanol until a persistent cloudiness is observed. The resulting solution was centrifuged and the precipitate was washed again by addition of a few milliliters of toluene and methanol. The final precipitate was redissolved in toluene. By this procedure the largest species of NCs was almost quantitatively separated from the smaller species of NCs. Data are shown in Figures S1, S2, S4, and S5.

I.4) CdTe NC synthesis. In a typical synthesis 514mg of Cadmium oxide, 1 g of decylamine and 1g of nonanoic acid were mixed in a three-neck flask. The flask was pumped to vacuum at 100 ℃ for 15 minutes and then heated at 200 ℃ under nitrogen to decompose the CdO. The temperature was then lowered to 90 ℃ and the tellurium stock solution (255mg of tellurium dissolved in 5g of Trioctylphosphine (TOP)) was injected. The temperature after the injection dropped and was allowed to recover and increased to 120 ℃. During the growth, 0.1 ml of the growth solution were extracted at time intervals ranging from 3-5 minutes (at the early stages of growth) to several hours (after several hundreds of minutes of growth) and diluted into toluene.

Size selective precipitation. After the synthesis, the heating mantel was removed and the solution left cooling to room temperature. Two milliliters of toluene were added to the solution, followed by methanol which was added until a persistent cloudiness was observed. This solution was centrifuged and the precipitate was washed again by addition of a few ml of toluene and methanol. The final precipitate was redissolved in toluene. By this procedure the largest species of NCs was almost quantitatively separated from the smaller species of NCs. Data are shown in Figure S6.

I.5) ZnSe NC synthesis. In a typical synthesis 488mg of Zinc oxide, 2 g of decylamine and 2g of nonanoic acid were mixed in a three-neck flask. The flask was pumped to vacuum at 100 ℃ for 15 minutes and then heated at 200 ℃ under nitrogen to decompose the ZnO. The temperature was then lowered to 130 ℃ and 10 g of a solution of Se in trioctylphosphine (10% in weight of Se) was injected. The temperature after the injection dropped and was allowed to recover and increased to 170 ℃. During the growth, 0.1 ml of the growth solution were extracted at time intervals ranging from 3-5 minutes (at the early stages of growth) to several hours (after several hundreds of minutes of growth) and diluted into toluene.

Size selective precipitation. After the synthesis, the heating mantel was removed and the solution left cooling to room temperature. Two milliliters of toluene were added to this solution, followed by methanol until a persistent cloudiness was observed. This solution was centrifuged and the precipitate was washed again by addition of a few ml of toluene and methanol. The final precipitate was redissolved in toluene. The injection of Te:TOP stock solution or just TOP with different molar ratios always led to ZnO NCs (Table T1 and Figure S9). In the case in which the Zn:Te molar ratio is in favor of the chalcogen no peak associated to a specific species of NCs was observed. Data are shown in Figures S7, and S8.

I.6) ZnO NC synthesis. In a typical synthesis 651mg of zinc oxide, 3 g of decylamine and 3g of nonanoic acid were mixed in a three-neck flask. The flask was pumped to vacuum at 100 ℃ for 15 minutes and then heated at 200 ℃ under nitrogen to decompose the ZnO. NC growth was performed at 180 ℃. During the growth, 0.1ml of the growth solution were extracted at time intervals ranging from 3-5 minutes (at the early stages of growth) to several hours (after several hundreds of minutes of growth) and diluted into 2-3ml of toluene.

Size selective precipitation. After the synthesis, the heating mantel was removed and the solution left cooling to room temperature. Two milliliters of toluene were added to this solution, followed by methanol until a persistent cloudiness was observed. This solution was centrifuged and the final precipitate was redissolved in toluene. Data are shown in Figures S9 and S10.

I.7) Comparison of the reaction conditions. Since the syntheses of all the NCs presented in this report have been performed using similar precursors and surfactants it is possible to make a comparison regarding the reactivity of different materials. The first remarkable difference concerns the decomposition of cadmium and zinc oxide powders. After pumping the vacuum at 100 ℃ for 15-20min ZnO and CdO are well decomposed when the temperature is raised to 200 ℃ and their complex with nonanoic acid seems to be stable. We had no possibility to check if little clusters of CdO were forming in solution during the decomposition of the cadmium precursor. However, when ZnO was dissolved in presence of nonanoic acid a slight shoulder in the ultraviolet region of the absorbance spectrum was observed (Figure 1e). The presence of this shoulder might suggest the formation of very small ZnO clusters which occurs just after the formation of the Zinc-nonanoic acid complex. Because of the small size of these NCs and the excess of solvent it was not possible to isolate them via precipitation. We therefore can not demonstrate their formation. The reactivity of the Zinc-nonanoic acid complex with selenium and tellurium was found to be extremely different. The injection of selenium precursor led to the formation of ZnSe NCs as is possible to see from the characteristic absorbance spectrum landscape (Figure1d), while the presence of tellurium was completely ignored by the complex which preferred to grow crystals incorporating oxygen atoms instead than tellurium as displayed by EDX measurements (Figure S18). Probably, since the reaction occurs always under air free conditions, the oxygen for the NC growth is taken away from the carboxylic acid present in solution. The decomposition procedure used here can be employed for the decomposition of lead oxide too, which would open the way to the synthesis of lead chalcogenide NCs. In the case of mercury, increasing the temperature to 200 ℃ most of the HgO decomposes into liquid mercury drops and just a little amount formed a complex with the nonanoic acid. Since for the nucleation of the NCs a high concentration of precursors is required, this kind of protocol is not the proper one for the synthesis of mercury chalcogenide NCs. Another difference between zinc and cadmium concerns their reactivity with the chalcogens solutions (see Table T1). For the synthesis of ZnSe and ZnO NCs the growth temperature could be held to 170-180 ℃ and still the crystals required several hours to appear, while for cadmium a temperature close to 100 ℃ led to the growth of the smallest families of clusters in a few minutes.

Precursor concentration and molar ratio appear to be paramount for the formation of the NCs. Generally a high concentration of precursors is required for the synthesis of small NCs. In the case of CdS, ZnSe (Table T1) and CdSe [1] it has been observed that small Cd:S, Cd:Se and Zn:Se ratios favor the NCs formation. This fact is very interesting in order to understand which, among the precursors, is responsible for triggering the nucleation. If S and Se concentration are able to trigger the nucleation of NCs for CdS, ZnSe and CdSe, for CdTe and ZnO it seems to be the opposite. Although we observed CdTe NCs even at synthesis with different molar ratios we observed that more peaks were visible with an higher Cd:Te ratio (Table T1, Figure 1c and Figure S25). In the case of ZnO (Figure 1e and Figure S27) the presence of a high concentration of zinc precursor always guaranteed the NCs nucleation. In general the NCs reported here can be grown at temperatures higher than those listed in Table T1 without affecting their properties (Absorption peak position and FWHM). At any rate a slow growth allows a better control of the synthesis evolution which maximizes the probability to isolate one family from the others. This can highly improve the quality of the precipitate and the yield of the synthesis.

I.8) CdHgS NC synthesis. In a general synthesis of CdHgS NCs 514mg of Cadmium oxide, 2 g of decylamine and 2g of nonanoic acid were mixed in a three-neck flask. The flask was pumped to vacuum at 100 ℃ for 15 minutes and then heated at 200 ℃ under nitrogen to

decompose the CdO. When the solution was totally transparent the temperature was lowered to 60 ℃ and 10 g of a solution of sulphur in Trioctylphosphine (10% by weight of S) was injected, which caused the temperature to drop. While the temperature was left recovering mercury precursor (Mercury stock solution was prepared by dissolving 2.16g of mercury(II) chloride (8mmol) in 40g of Trioctylphosphine at 110-120 ℃ for 1hour) was added dropwise using a syringe pump with a speed of 2.5ml/h. The injection continued during all the NC growth which was performed at 80 ℃. The growth of the particles was monitored by taking aliquots during the reaction, and recording their UV/visible absorption and fluorescence spectra. The aliquots were extracted at time intervals ranging from 3-5 minutes (at the early stages of growth) to several hours (after several hundreds of minutes of growth) and diluted with toluene.

Size selective precipitation. After the synthesis, 5-10mL toluene was added to the growth solution, followed by addition of methanol, until a persistent cloudiness was observed. An amount of methanol ranging from 50 to 100 mL was required, depending on the size of NCs present in the solution and their concentration. This solution was precipitated with centrifugation at 2500 rpm speed. The precipitate was washed several times with toluene and methanol. The final precipitate was redissolved in toluene. Data are shown in Figures S11, S12, S13, S14, and S20.

Cd:S molar ratio	CdO	S:TOP	NNA	DA	CdS NC formation
4,59:31,25 (≈1:6)	514mg	1g S: 10g TOP	2g	2g	Yes
4,46:12,65 (≈1:3)	500mg	405mg S: 10g TOP	2g	2g	No

Temperature of S:TOP injection: 60 ℃; growth temperature: 75-80 ℃;
precipitation with 2-3ml toluene+ 20ml methanol repeated 2 times for purification.

Cd:Te molar ratio	CdO	Te:TOP	NNA	DA	CdTe NC formation
1:1	257mg	255mg:5g	1g	1g	Yes
1:2	257mg	510mg:10g	1g	1g	Yes
2:1	514mg	255mg:5g	2g	2g	Yes best result
3:1	771mg	255mg:5g	3g	3g	Yes very fast

Temperature of Te:TOP injection: 90 ℃; temperature of growth: 120 ℃;
precipitation with 20ml methanol repeated 2 times for the purification.

Zn:Se molar ratio	ZnO	Se:TOP	NNA	DA	ZnSe NC formation
1:0,95	976,43mg	1g:10g	4,5g	4,5g	Yes
1:2	488.4mg	1g:10g	2g	2g	Yes
2:1	488.4mg	237mg:5g	2g	2g	No

Temperature of Se:TOP injection: 130 ℃; temperature of growth: 170 ℃;
precipitation with 2-3ml toluene+ 20ml methanol repeated 2 times for purification.

Zn:Te molar ratio	ZnO	Te:TOP	NNA	DA	ZnO NC formation
1:1	162,8mg	255mg:5g	2g	2g	Yes
1:2	81,4mg	255mg:5g	1g	1g	No
2:1	325mg	255mg:5g	2,5g	2,5g	Yes
4:1	651,2mg	255mg:5g	3g	3g	Yes
6:1	976,8mg	255mg:5g	4,5g	4,5g	Yes

Temperature of Te:TOP injection: 130 ℃; temperature of growth: 180 ℃; precipitation with 2-3ml Toluene+ 20ml methanol for the purification.

Table T1. *NC synthesis depending from the synthesis conditions. The last column indicates if NCs formed during this synthesis condition. NNA and DA are the amount of nonanoic acid and decylamine used for the synthesis. Below each chart the different reaction conditions, and the amounts of chemicals used for the purification are reported.*

Characterization of structural and compositional properties

II.1) Transmission electron microscopy (TEM).

Transmission electron microscopy (TEM) investigations were performed using a JEM 3010 high-resolution electron microscope (Jeol Ltd., Tokyo, Japan) operating at 300 kV. For image acquisition a 2 k x 2 k slow scan CCD camera (Mega Scan 794, Gatan Inc., Pleasanton, CA, USA) was used along with the Digital Micrograph software. All samples were prepared by depositing the NCs on 300mesh copper grids covered with a thin carbon supporting film. Image processing and Fourier analysis of individual NCs was done by making use of the CRISP (Calidris, Sollentuna, Sweden) software, and the Electron Diffraction program by J.-P. Morniroli (Universit é de Lille, France). All the samples were prepared by dropping the NCs solution on a TEM grid, and waiting for the solvent evaporation.

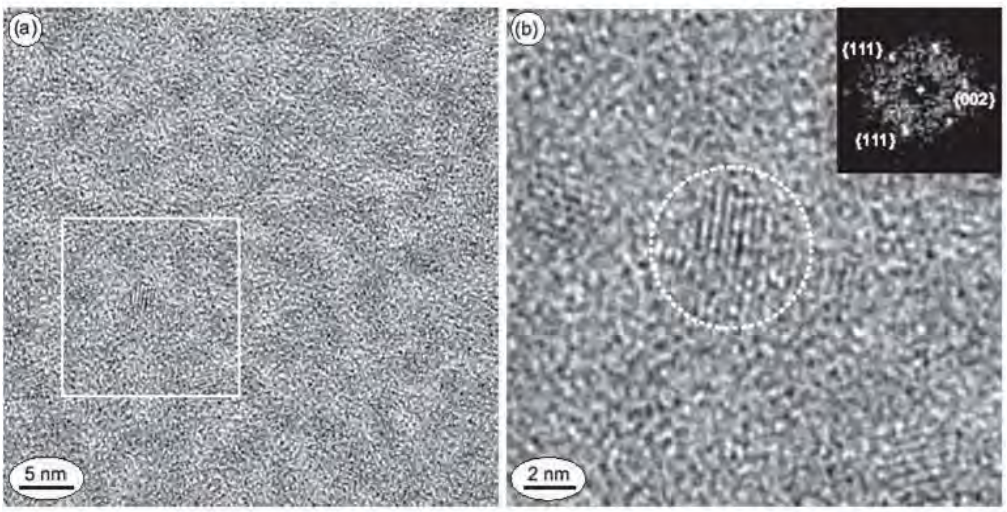

Figure S1. *TEM micrograph of cadmium sulfide NCs of species CdS I with cubic structure: (a) overview, (b) close-up of the square region marked in (a). The inset shows the Fourier transformation of the marked circular area revealing (110) zone axis orientation of the single particle.*

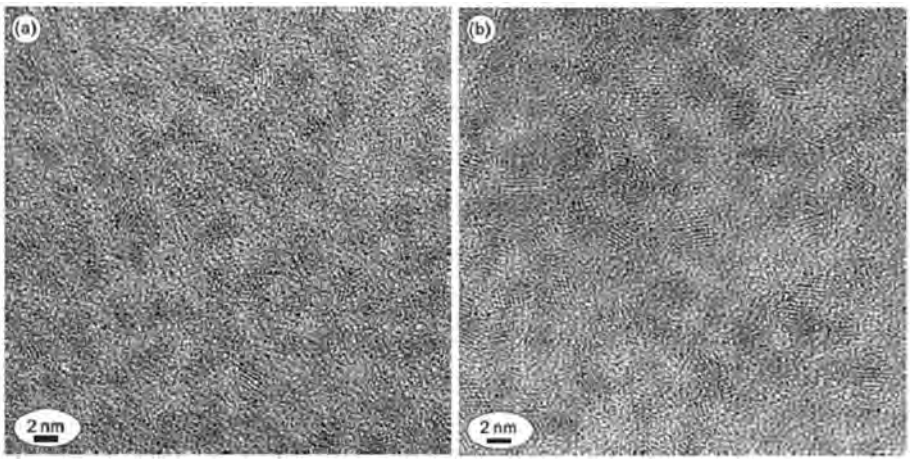

Figure S2. *Overview TEM images of cadmium sulfide NCs of species CdS II (a) and CdS IV (b).*

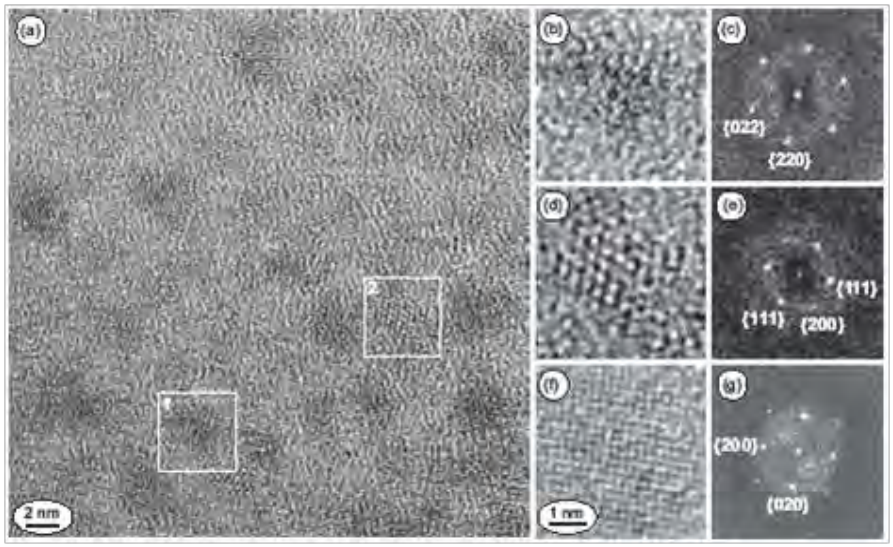

Figure S3. *TEM micrographs of cadmium sulfide NCs of sample CdS III with cubic structure: (a) overview; (b) close-up on one single particle in area 1 with (111) zone axis orientation; (d) close-up on one single particle in area 2 with (110) orientation; (f) single particle in (100) orientation; (c), (e) and (g) are the corresponding Fourier transformations.*

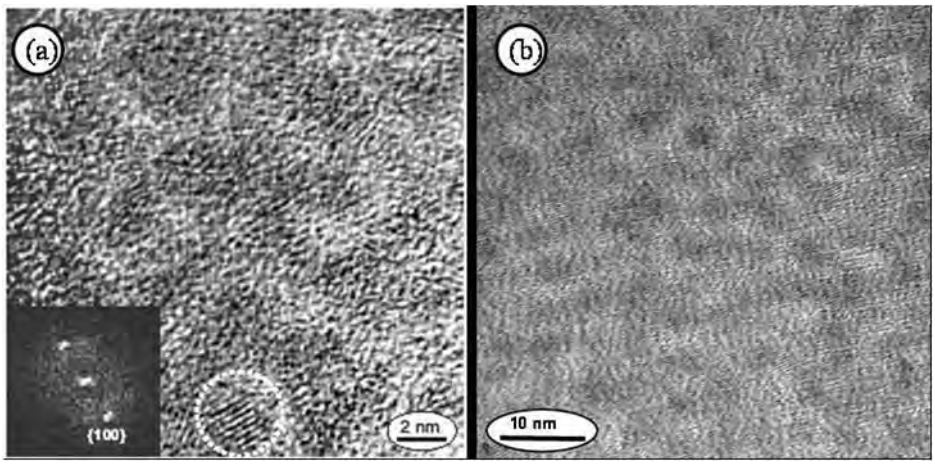

Figure S4. *(a) TEM micrograph of cadmium sulfide NCs of species CdS V. The inset shows the Fourier transformation of the marked area showing the (100) spacing. (b) TEM micrograph of cadmium sulfide NCs of species CdS VII.*

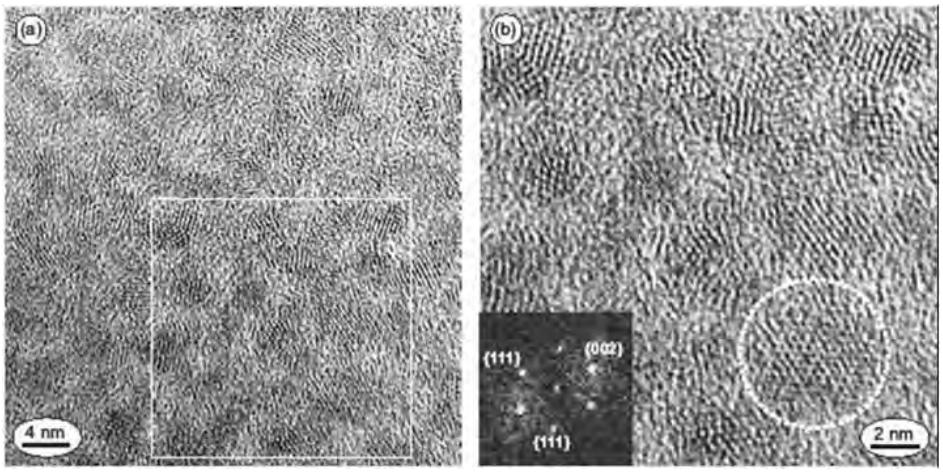

Figure S5. *TEM micrograph of cadmium sulfide NCs of species CdS VI: (a) overview, (b) close-up of the square region in (a). The inset shows the Fourier transformation of the marked circular area revealing a (110) zone axis orientation of the respective particle.*

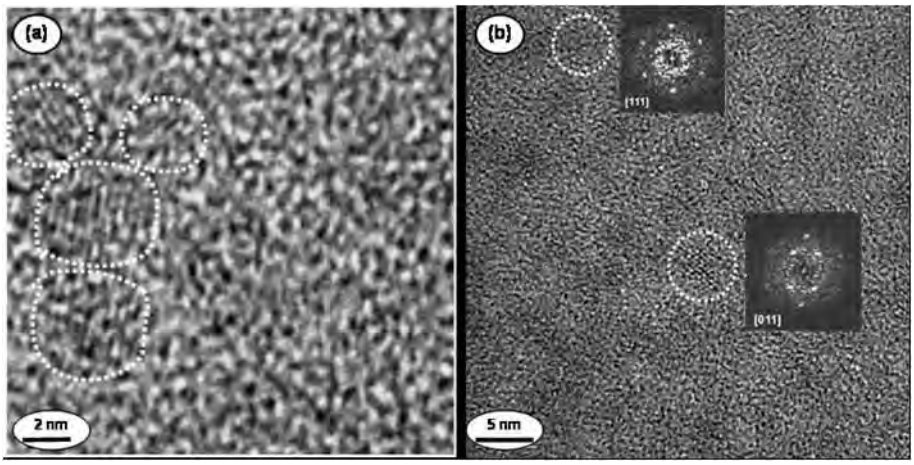

Figure S6. *TEM micrographs of cadmium telluride NCs species CdTe I (a) and species CdTe II-III (b). Particles are marked by dashed lines. The insets in (b) are the Fourier transformations of the marked circular areas revealing (111) and (011) zone axis orientation of the respective particles.*

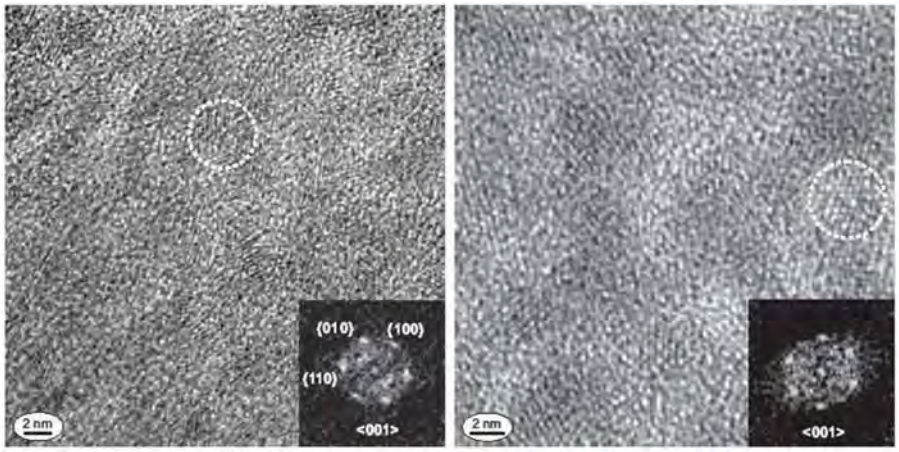

Figure S7. *TEM micrographs of zinc selenide NCs including all three species of NCs (left) and a sample with particles belonging just to the species ZnSe III (right). The insets show the Fourier transformations of the encircled areas in each image and reveal the hexagonal (001) zone axis orientation of the respective single particles.*

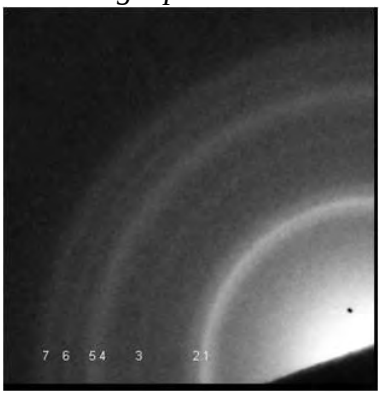

Figure S8. *SAED of ZnSe NCs. This picture was taken from a sample in which all the species of ZnSe NCs were present. In the picture the rings due to the hexagonal structure (1,2,3,4 (faint)) are clearly visible. However, the broadness of the rings due to the small particles size does not permit us to exclude the presence of some particles with cubic (zinc blende) structure.*

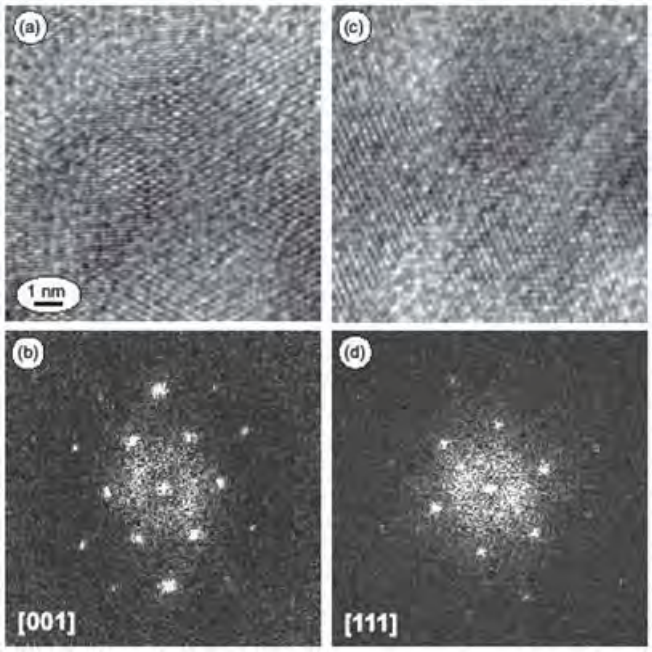

Figure S9. *TEM micrographs of two zinc oxide NCs (a) and (c), with their corresponding Fourier transformations indicating (b) (001) and (d) (111) zone axis orientation of the hexagonal structure.*

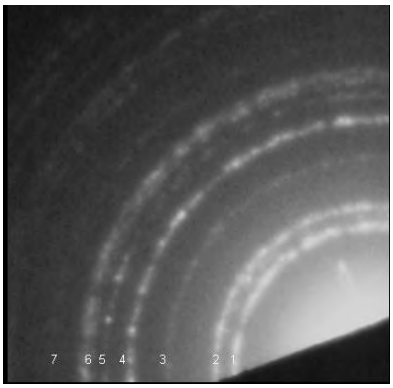

Figure S10. *SAED of ZnO NCs. In the picture the rings due to the hexagonal structure (1, 2, 3, 4, 6 and 7) are clearly visible but the presence of the ring 5 confirm the presence of same particles having a cubic structure as reported in Table T2*

.

Ring	hkl (hexagonal)	hkl (cubic)
1	100	none
2	002	111
3	110	220
4	200	311
5	None	400
6	210	331
7	300	422

Table T2. *Assignment of SAED rings to hexagonal and cubic structure.*

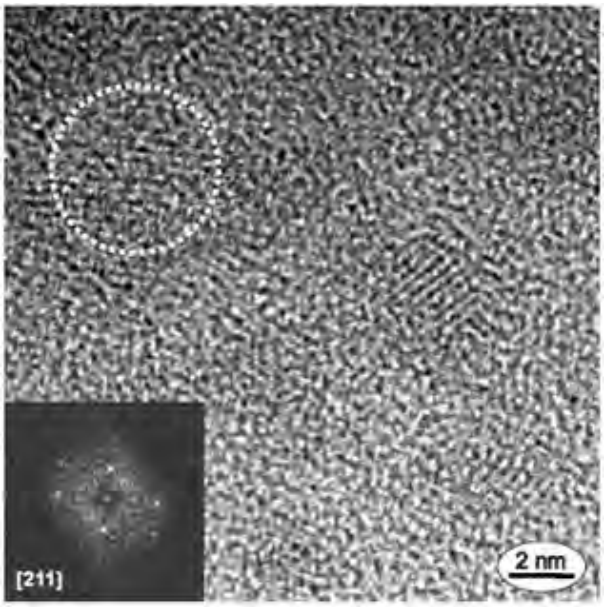

Figure S11. *TEM micrograph of CdHgS I NCs with cubic structure. The Inset shows the Fourier transformation indicating the (211) orientation of the selected particle.*

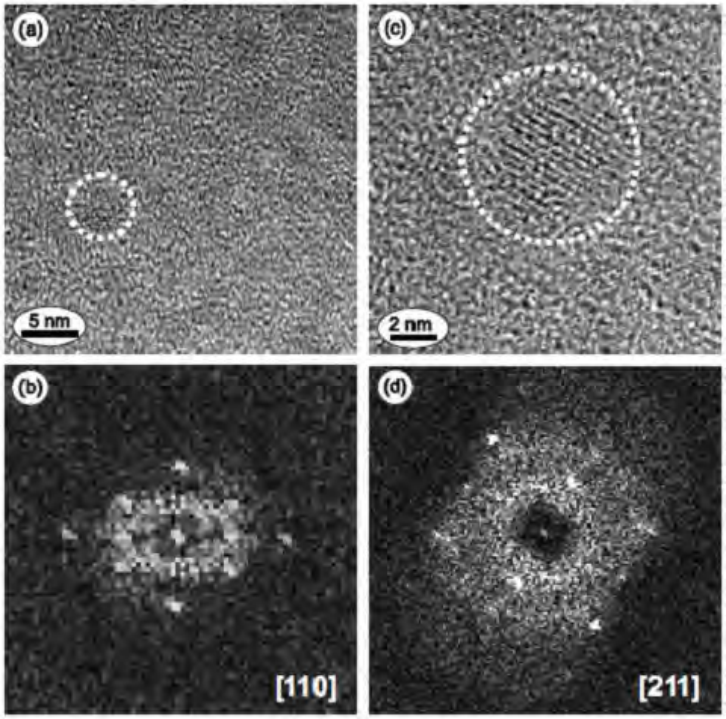

Figure S12. *TEM micrographs of CdHgS II NCs and the corresponding Fourier transformations of the selected areas, showing (110) and (211) orientation of the cubic structure.*

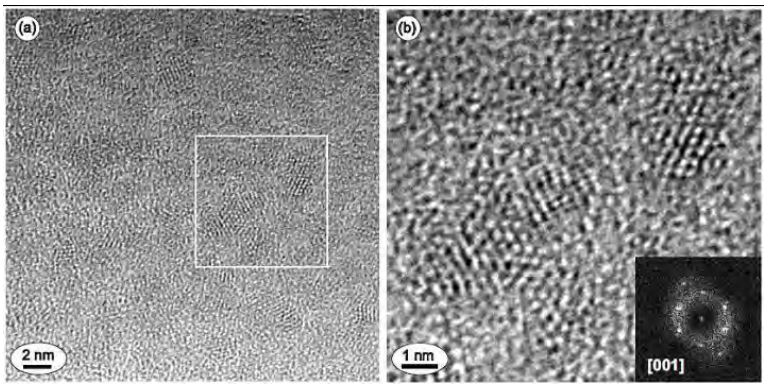

Figure S13. *CdHgS III NCs in the TEM overview (a), and in a close-up (b) with the Fourier transformation in the inset revealing a (111) orientation of the hexagonal structure.*

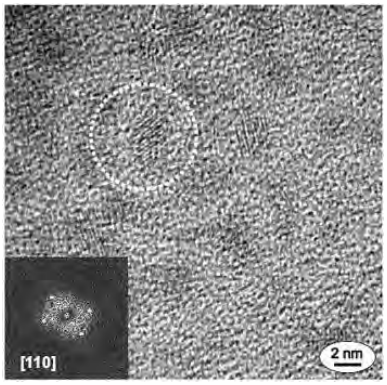

Figure S14. *TEM micrograph of CdHgS IV NCs with (110) orientation of the cubic structure as indicated by the Fourier transformation of the selected are.*

Material	**CdS I**	**CdS II**	**CdS III**	**CdS IV**	**CdS V**	**CdS VI**	**CdTe I**	**CdTe II-III**
Wavelength of Absorption Peak (nm)	303,7 ±0,5	326,7 ±0,5	347 ±1	362,7 ±0,6	377 ±0,5	387 ±1	445,3 ±1,5	487,6 ±2,5 506 ±1,5
Size distribution from TEM (nm)	2,3 ±0,3	2,7 ±0,5	2,9 ±0,8	3,5 ±0,7	3,6 ±0,2	3,9 ±0,1	2,4 ±0,3	3,1 ±0,8
Size as obtained from the absorption data using the Yu-correlation	1,4	1,7	2,0	2,3	2,7	3,0	0,0	1,9 2,5

Table T3. *Summary of the properties recorded from CdS and CdTe NCs. The wavelength of absorption (first exction peak) refers to the center of the absorbance peak before size selective precipitation. Average sizes of NCs were estimated measuring the long axes of 10-25 NCs from TEM images. The wavelength of the first exciton peak was also used to calculate the NC size based on extrapolation of a correlation curve by Yu et al. [2]. As the correlation curve absorption wavelength / NC diameter by Yu et al. had been obtained for NCs of larger size extrapolation to small NCs as synthesized in our study is problematic. Therefore the size data as derived from the Yu study do not match our size data as experimentally obtained with TEM. Furthermore we can't exclude that our TEM images display small aggregates of NCs instead of single NCs. This has been actually reported by Dagtepe et al. [3].*

II.2) Energy filtered transmission electron microscopy (EFTEM).

Energy Filtered images (EFTEM) were acquired on a JEOL JEM-2200FS equipped with an Omega in column energy filter, and a spherical aberration corrector in the objective lens. An aperture was used to further reduce chromatic aberration, so that the expected resolution is mainly due to the delocalization of inelastic scattering (about 0.5 nm at 100eV for a thin sample as calculated from Egerton et al. [4]. The elemental chemical maps for Hg O2,3 (58 eV), Cd N2,3 (67 eV), and S L2,3 (165 eV) are presented in Figure S15. They are obtained by using the three windows method at each element edge to subtract the inelastic background. A small energy slit of 5eV was used to reduce the superposition of the Hg-O edges and Cd-N signals. For S-L edge an energy slit of 20eV was used to improve the signal. The resulting maps show the presence of the three elements in the particles.

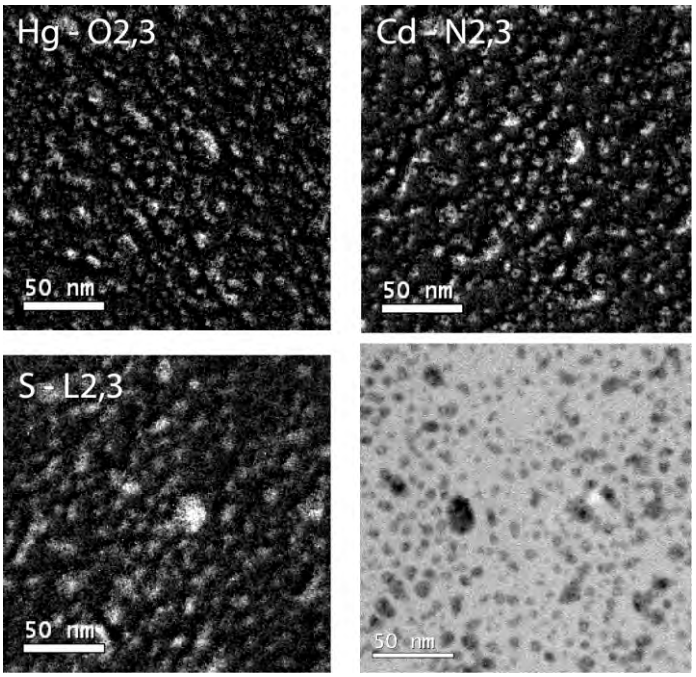

Figure S15. *Elemental maps for Hg-$O_{2,3}$, Cd-$N_{2,3}$, and S-$L_{2,3}$ obtained in EFTEM. The image on the right bottom is a filtered image of the elastic peak from a adjacent region shown as representation of the sample morphology.*

II.3) Energy dispersive X-ray spectroscopy (EDX).

EDX graphs were recorded with a SEM CamScan IV. NCs were precipitated 3 times and the powder was left drying under nitrogen atmosphere before being spread on a silicon wafer.

CdS NC EDX

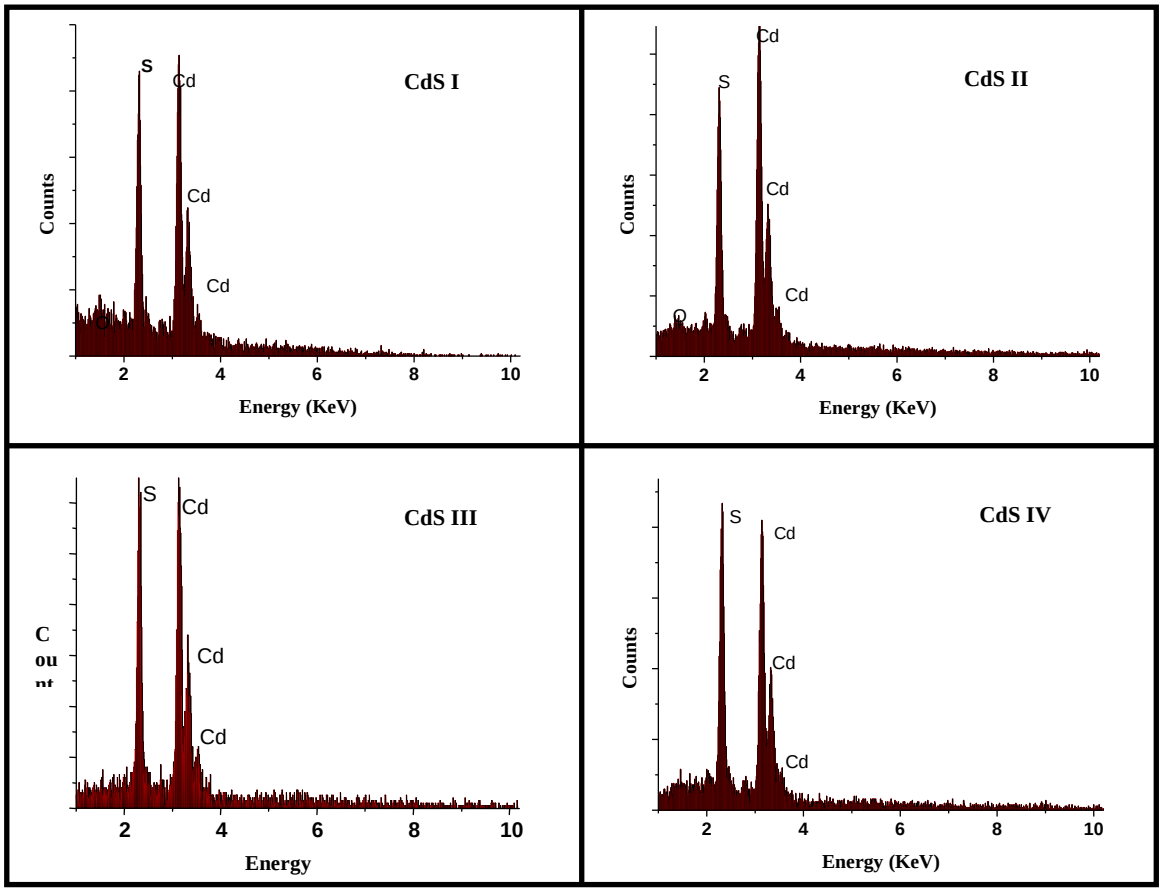

Figure S16. *EDX spectra of the first (CdS I), second (CdS II), third (CdS III) and forth (CdS IV) species cadmium sulphide NCs. The accelerating voltage was 15kV.*

The cadmium ($L_{\alpha 1}$ (3,129KeV), $L_{\beta 1}$ (3,295KeV)) and sulphur (K_{α} (2,299KeV), K_{β} (2,441KeV)) transitions are clearly visible in these spectra (Figure S16).

CdTe NC EDX

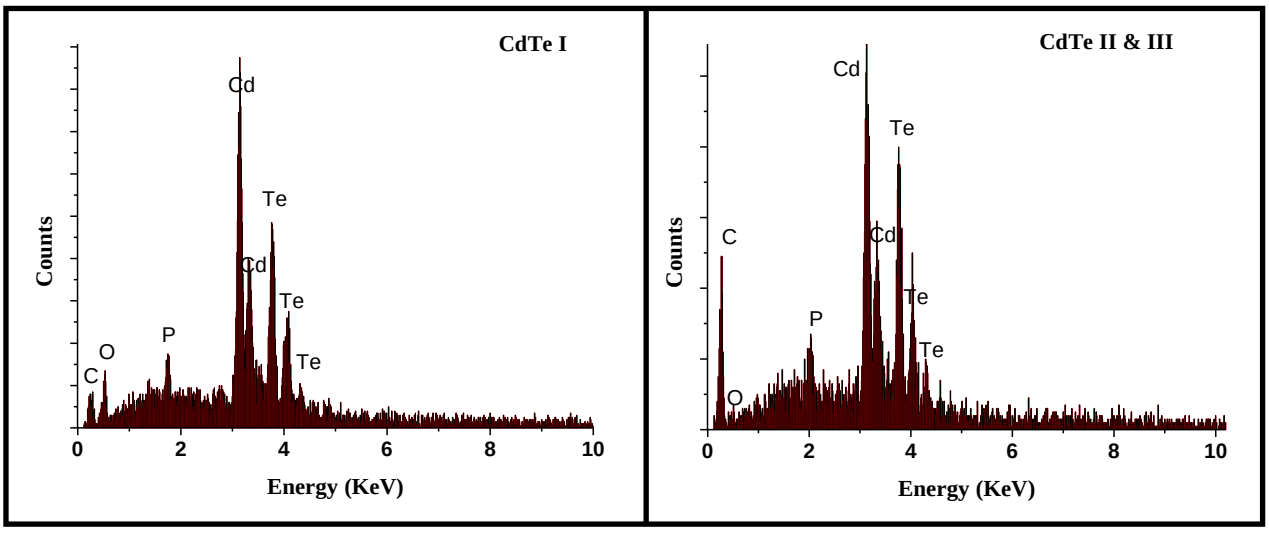

Figure S17. *EDX spectra of the first (CdTe I) and second (CdTe II) species of cadmium telluride NCs. The accelerating voltage was 15kV.*

The cadmium ($L_{\alpha 1}$ (3,129KeV), $L_{\beta 1}$ (3,295KeV)) and tellurium ($L_{\alpha 1}$ (3,796KeV), $L_{\beta 1}$ (4,006KeV), $L_{\beta 2}$ (4,29KeV)) transitions are clearly visible in these spectra (Figure S17). The presence of carbon, oxygen, and phosphorous are due to the surfactants still present on the particle surface after the washing procedure.

ZnSe and ZnO NC EDX

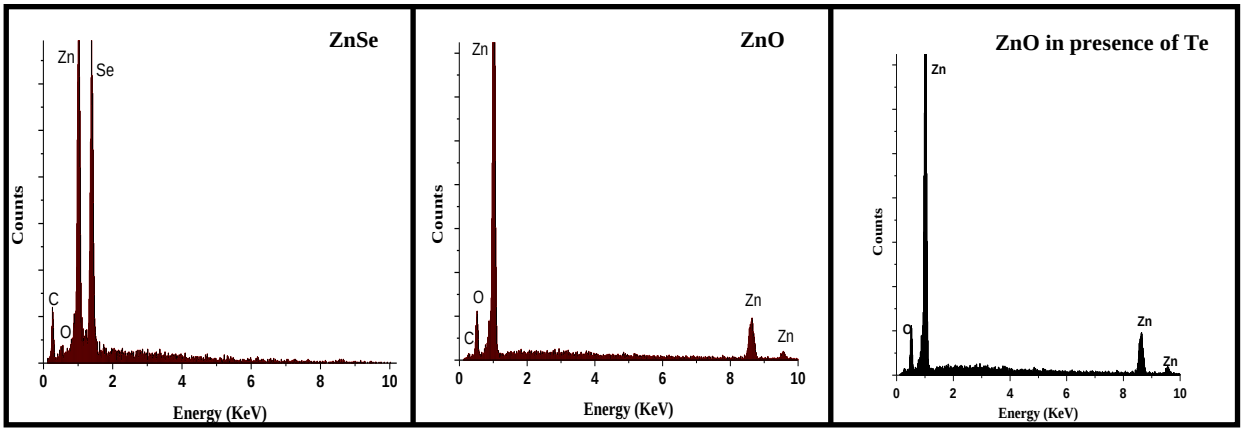

Figure S18. *EDX spectra of ZnSe and ZnO NCs without size selective precipitation. In the ZnSe sample all the three species of NCs were present. The acceleration voltage was 20kV.*

In case of ZnSe the zinc (L_1 (0,877KeV), $L_{\alpha 1}$ (0,996KeV), $K_{\alpha 1}$ (08,628KeV), $K_{\beta 1}$ (9,553KeV)), and selenium ($L_{\alpha 1}$ (1,375KeV)) transitions are clearly visible in the spectrum (Figure S18, on the left). In case of ZnO the zinc (L_1 (0,877KeV), $L_{\alpha 1}$ (0,996KeV), $K_{\alpha 1}$ (08,628KeV), $K_{\beta 1}$ (9,553KeV)) and oxygen (K_{α} (0,521KeV) transitions are clearly visible in Figure S18 in the center and right spectra. The presence of carbon, is due to the surfactants still present on the NC surface after the washing procedure.

CdHgS NC EDX.

In Figure S19 and Table T4 the normalized composition of each species of CdHgS NCs is reported. The particles belonging to the CdHgS I species are composed out of 50% of sulfur, whereas the percentages of cadmium and mercury are about 25% and 21%. The mercury precursor is very reactive with the sulphur atoms present in the surfaces of the small nuclei in solution and it is easily incorporated in the crystal lattice during the growth by replacing cadmium atoms. The presence of chlorine in a percentage of less than 2% shows that using mercury chloride as mercury precursor lead to a halogen-chalcogen co-incorporation already reported for semiconductor thin film doping [5]. Considering Figure S19, in the CdHgS I species the presence of transition metals is smaller than that of sulphur, which is the opposite of what is found in the case of undoped NCs (Cd:S≈1,13). This might be explained with the different nucleus surface reactivities due to the presence of mercury, which could favor the adhesion of sulfur leading to particles more rich in sulfur.

The particles of the CdHgS II species present an inverted Cd:S ratio. These particles are composed out of more than 50% by cadmium and just for 40% by sulfur. The amount of mercury present dropped to almost 5%. This fact is probably due to the low concentration of this element in solution which probably has been quickly consumed in the formation of the previous NC species. This fact supports the previous statement concerning the different sulfur adhesion driven by the presence of mercury. Since the mercury concentration quickly drops during the nucleation the NC growth proceed as in the case of undoped NCs leading again to NCs more rich in cadmium. Anyway while the NCs evolve into the next species the incorporated amount of mercury slowly increases cause the decreasing of cadmium precursor in solution. This fact justifies the higher amount of sulfur present in the larger NCs. Even the chlorine amount slowly keeps on growing along with the NCs showing an almost linear trend (Figure S19). This trend seems to be interrupted when the presence of mercury atoms on the NC surfaces overcomes a certain threshold over which the sulfur atoms replace the chlorine atoms from the NC surface.

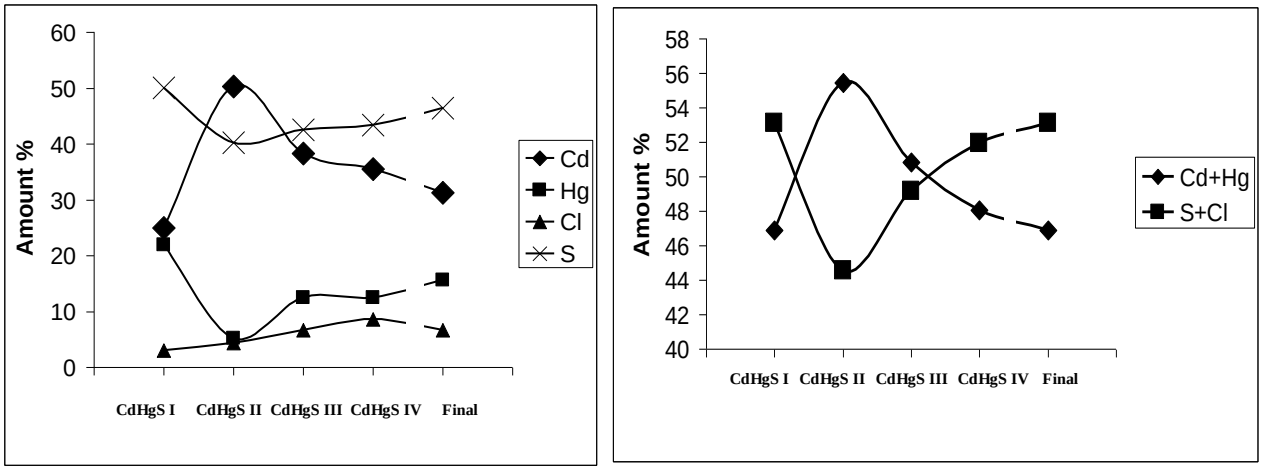

Figure S19. a*) Relative amounts of the elements which compose the different species of CdHgS NCs. b) Relative amounts of the transition metals (Cd+Hg) and the sum of the amount of sulphur and chlorine present in different species of CdHgS NCs.*

	CdHgS I	CdHgS II	CdHgS III	CdHgS IV	CdHgS final
Absorption peak position (nm)	306 ±1	326 ±1	349,8 ±2	367 ±2	393 ±3
Composition	Cd 25% Hg 22% Cl 3% S 50% χ^2= 1.42	Cd 50% Hg 5% Cl 4% S 41% χ^2= 1.5	Cd 38% Hg 13% Cl 7% S 42% χ^2= 1.11	Cd 36% Hg 13% Cl 8% S 43% χ^2= 1.93	Cd 31% Hg 16% Cl 7% S 46% χ^2= 2.15
Crystalline structure	Both W and ZB	Both W and ZB	Both W and ZB	Both W and ZB	Both W and ZB
Size distribution (nm)	2.51 ±0.5	2.67 ±0.35	3.1 ±0.4	3.7 ±0.6	4.1 ±0.8

Table T4. *Main characteristics of CdHgS NCs.*

The average size of CdHgS NCs was estimated by evaluating 10-25 NCs in the TEM images. The obtained values are compatible, within the statistical error, with those of the undoped NCs (Table T5) suggesting that the CdS NC size is independent from the presence of the incorporated Hg. The absorption peak positions of the doped NCs are very close to those reported for the undoped NCs (Table T5).

III) Characterization of optical properties

III.1) Absorption and fluorescence. All the absorption spectra were collected with an Agilent 8453 UV-vis absorption spectrometer, while a Fluoromax-3 (JOBIN YVON HORIBA) fluorescence spectrometer was used to record the fluorescence spectra. All the spectra were taken from NCs dissolved in toluene.

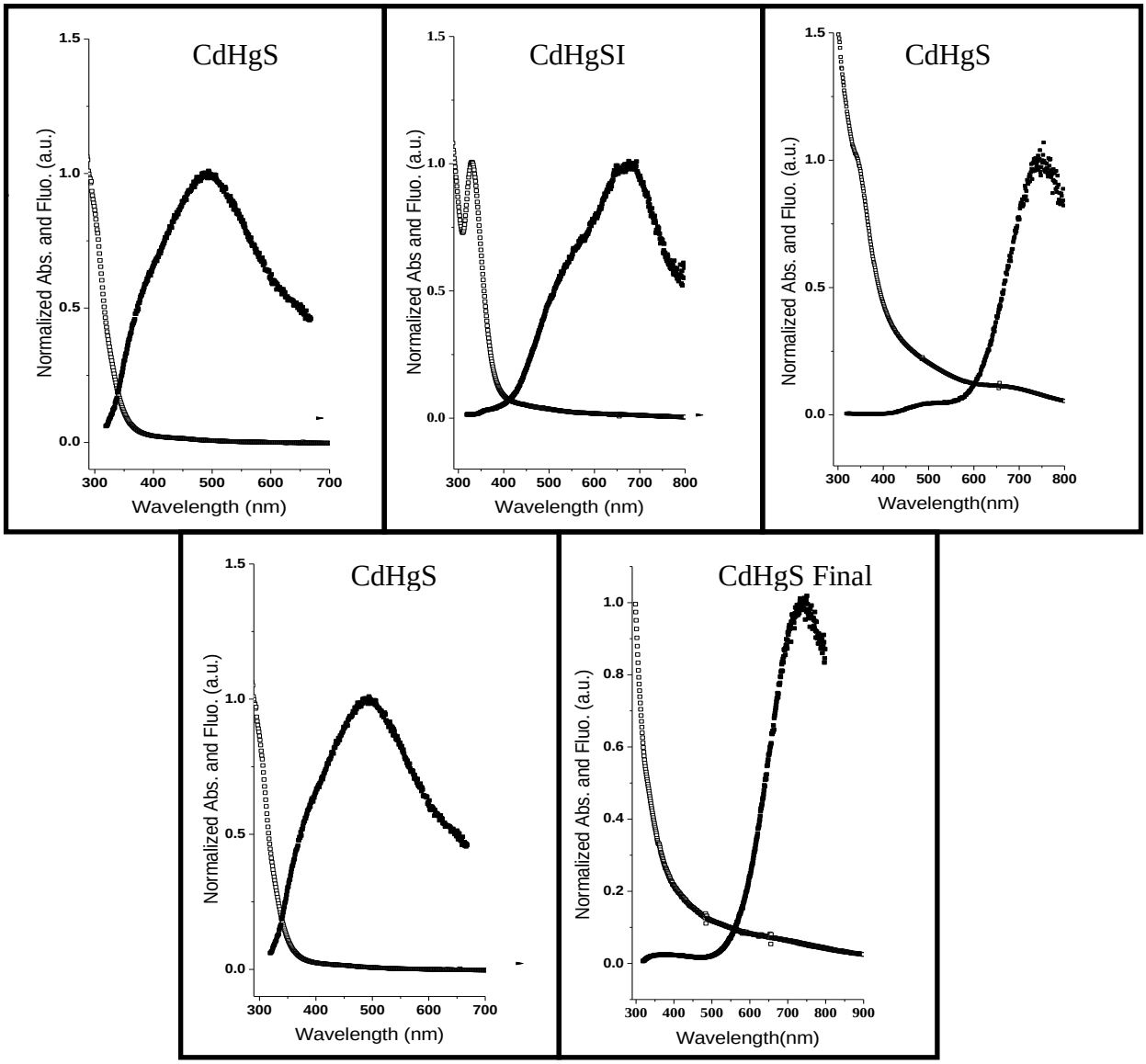

Figure S20. *Absorption (empty squares) and fluorescence (full squares) of CdHgS NCs after size selective precipitation.*

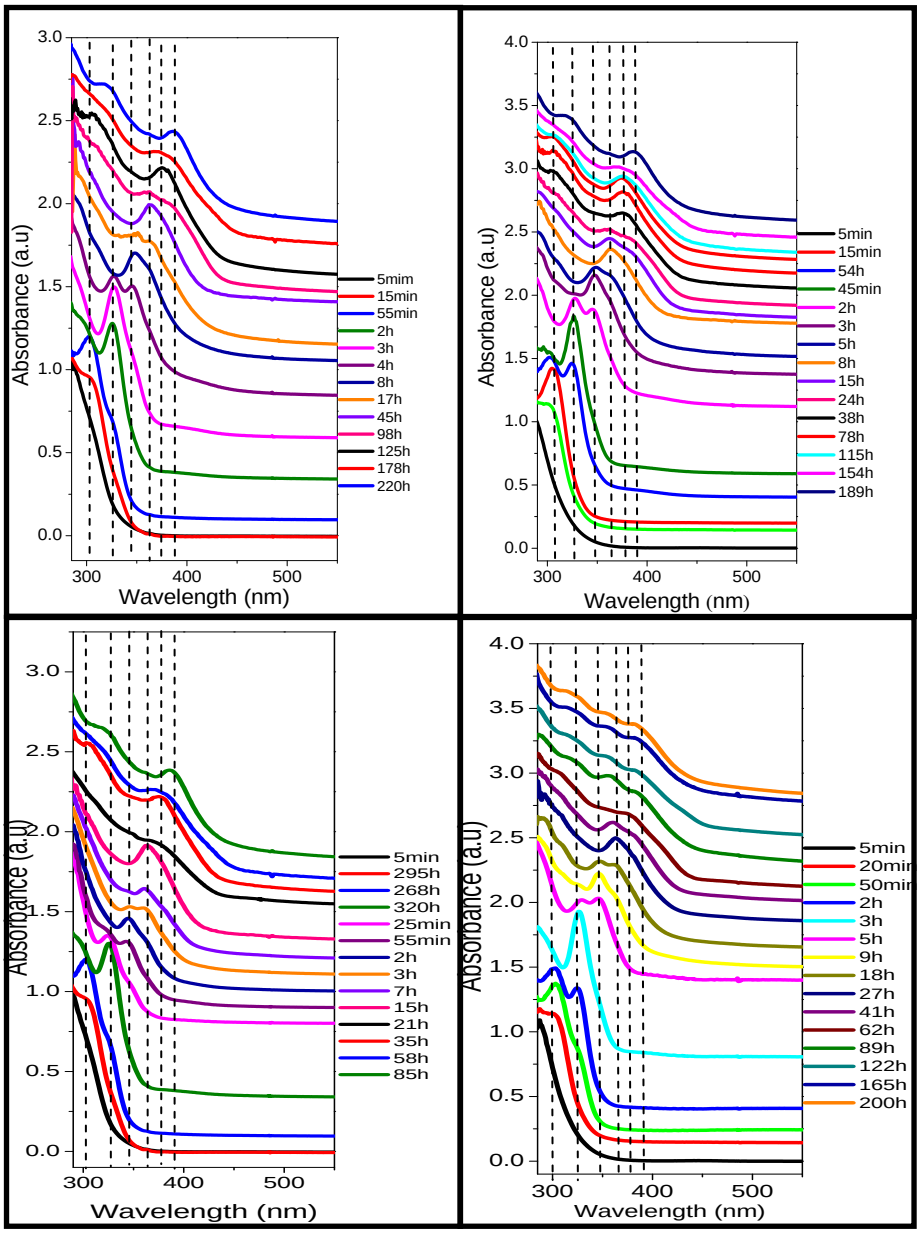

Figure S21. *Temporal evolution of the absorption spectra of a solution of CdS NCs of different experiments.*

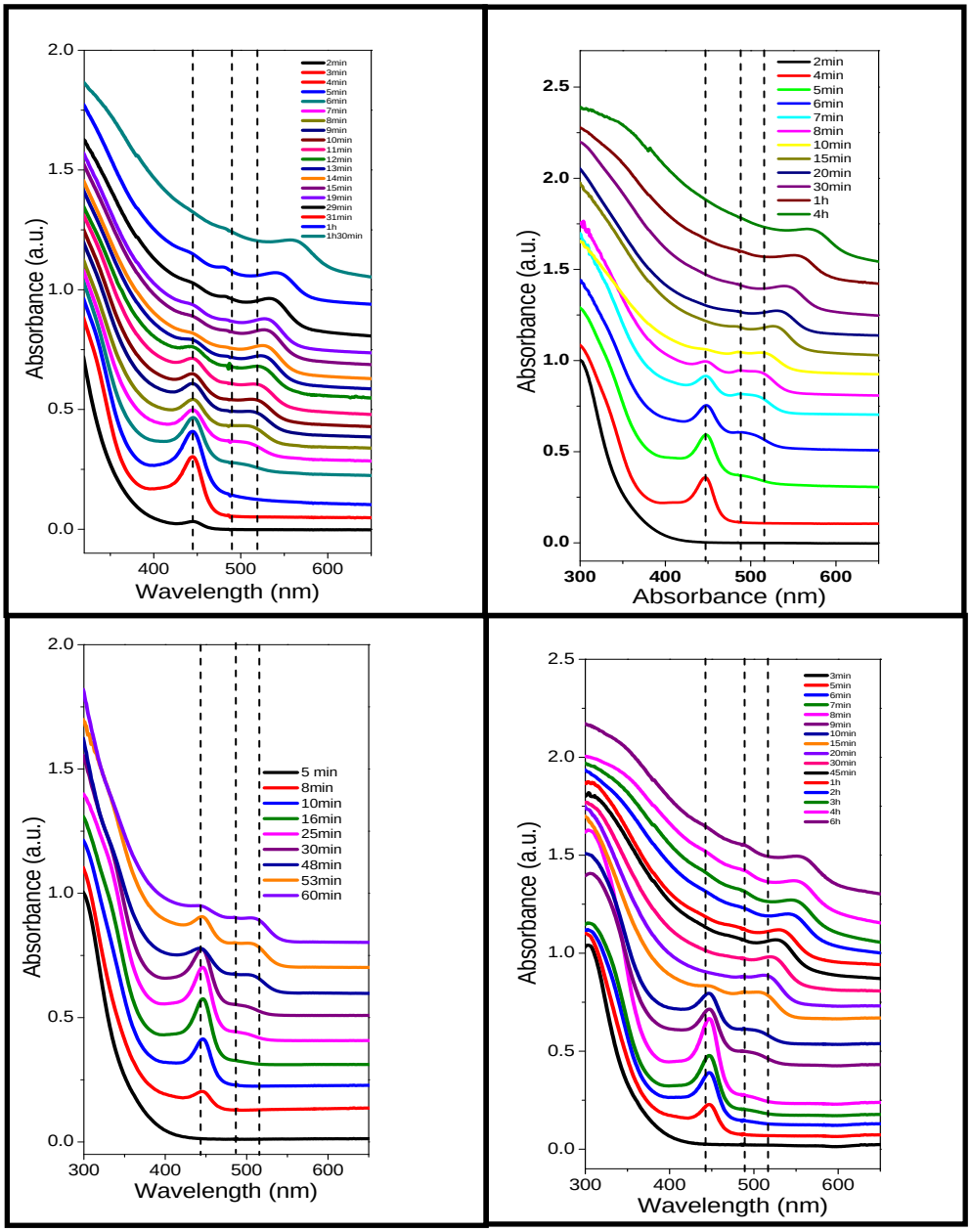

Figure S22. *Temporal evolution of the absorption spectra of solutions of CdTe NCs originating from different experiments. A zoom into the double-peak structure around 500 nm is displayed in Figure S24.*

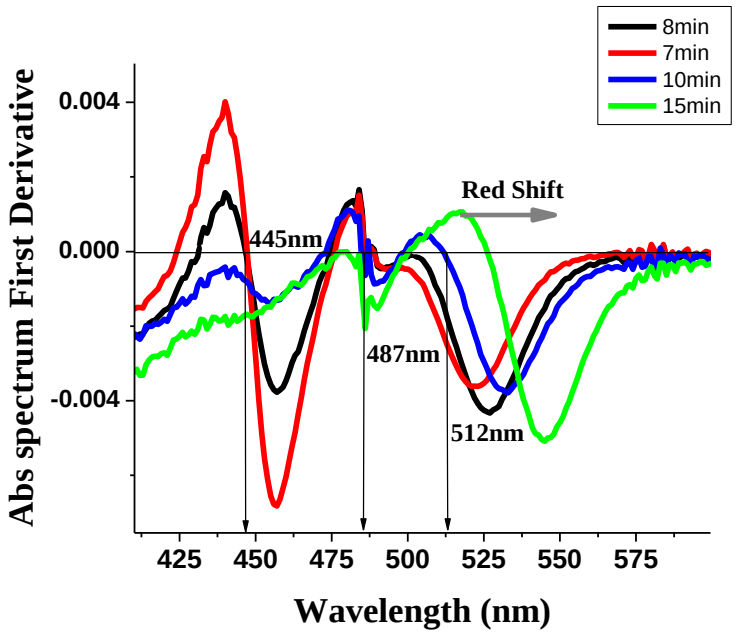

Figure S23. *Derivative of the absorption spectrum shown in Figure 1c. This graph shows that the absorption peak of the stable configurations does not shift over time. The peak at higher wavelength keeps on growing in intensity, while the intensity of the previous peak disappears. This indicates discontinuous growth.*

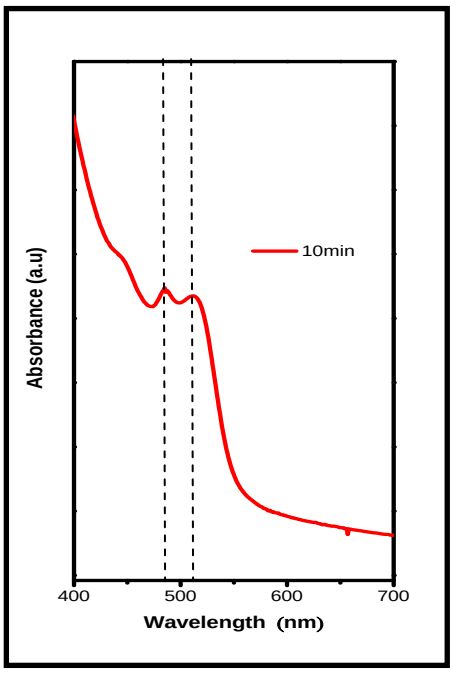

Figure S24. *Absorption spectra of a CdTe NCs solution at Cd:Te 2:1 ratio after 10min of Te precursor injection. Two peaks around 500 nm are clearly visible showing two families of CdTe NCs (485nm, 508nm).*

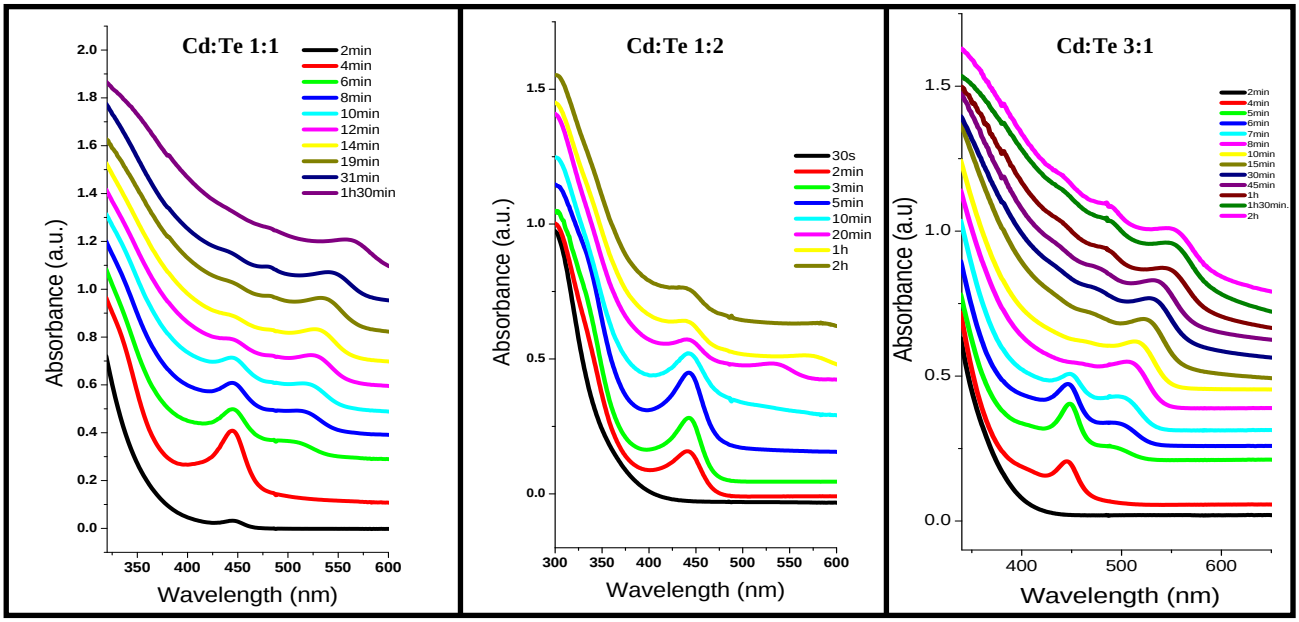

Figure S25. *Temporal evolution of the absorption spectra of a solution of CdTe NCs at different Cd:Te ratios. The Te:TOP stock solution was injected at 100 ℃ and the NCs were let growing at 130 ℃. In each Cd:Te molar ratio tried, the peak characteristic of CdTe I appeared but with different broadness. By Increasing the molar ratio this peak got sharper and even the other peaks became a little more distinguishable.*

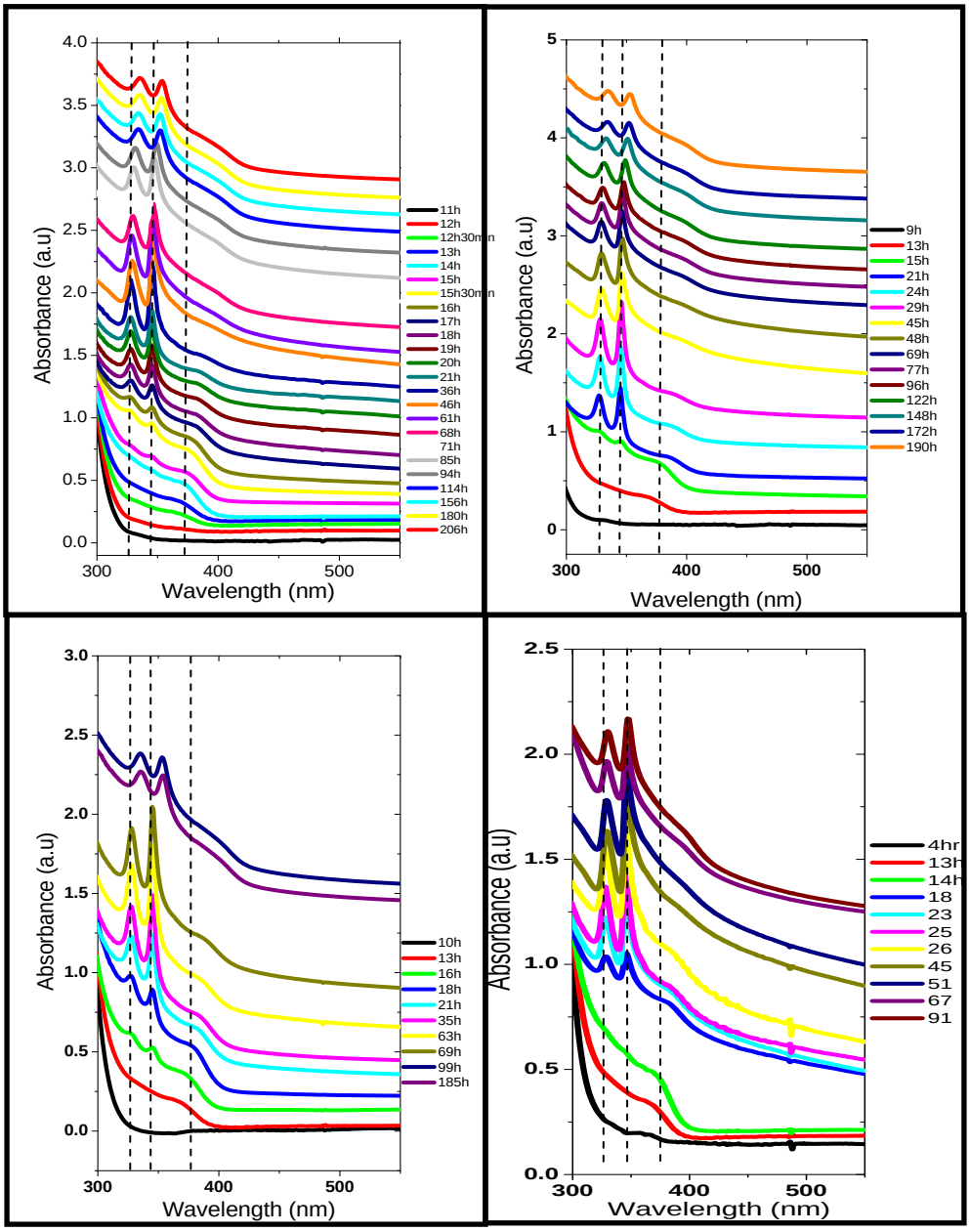

Figure S26. *Temporal evolution of the absorption spectra of a solution of ZnSe NCs of different experiments.*

[A1]

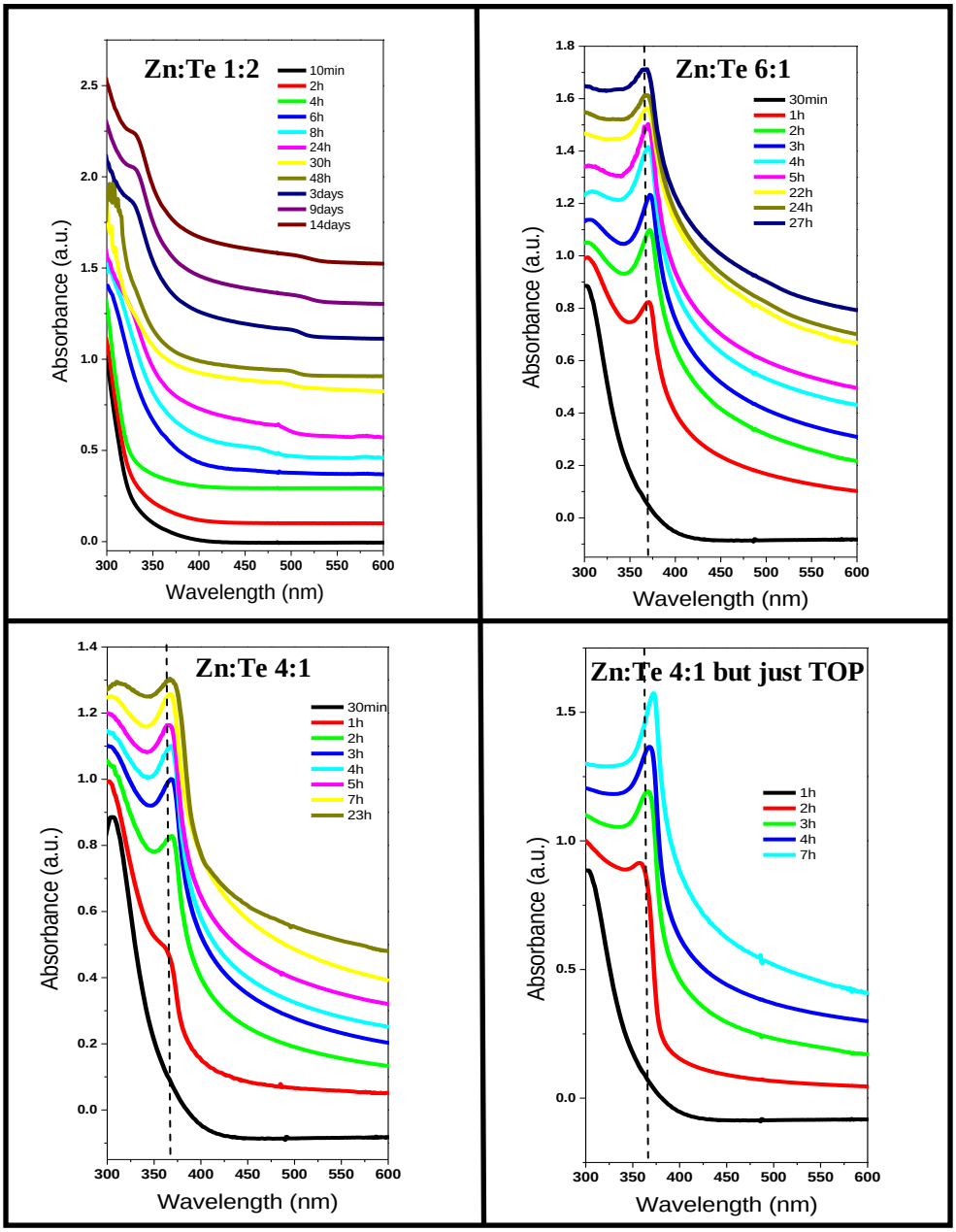

Figure S27. *Temporal evolution of the absorption spectra of a solution of ZnO NCs at different Zn:Te ratio. The Te:TOP stock solution was injected at 130 ℃ and the NCs were let growing at 180 ℃. a) Zn:Te ratio 1:2, b) Zn:Te ratio 6:1, c) Zn:Te ratio 4:1, d) Zn:Te ratio 4:1. In d) the solution the volume of TOP was the same of synthesis c) but no tellurium was present. Analysis showed that also in cases a), b), c) where Te was present in the growth solution, no Te was incorporated into the NCs. In fact ZnO instead of ZnTe was obtained.*

III.2) Discussion of CdSe NCs

In accordance with our previous report some minutes after the injection of the selenium precursor two well-defined absorption peaks appeared, one at higher energy centered at 330 nm and the other one at about 360nm. These two peaks disappeared over time and a new peak centred at about 380nm showed up. The intensity of this peak increased over time, supporting the hypothesis that it belongs to a new stable configuration of CdSe NCs, which arises by growth of the previously existing smaller stable configuration. As the synthesis proceeded, new peaks appeared at longer wavelengths centred at about 407, 431 and 447nm. This again suggests the formations of other stable configurations of bigger size of CdSe NCs (see Table T5). If only one stable configuration of NCs were present, and these clusters were steadily growing and thus increasing their size, then a single absorption peak would be seen, which should be shifting gradually towards longer wavelengths [1]. Instead, formation and increase in intensity of the new peaks always coincides by disappearing of the previous peaks. Again, this suggests that the particles at longer wavelength are formed to the detriment of those absorbing at shorter wavelength. In this way NCs increase their size step-wise from one to the next bigger stable configuration, until they finally reach the range of continuous growth. According to the width of the various absorption peaks the size distribution of each NCs configuration is quite narrow. We have identified 6 different discrete absorption peaks in the spectra for CdSe (see Table T5), whereby the values are in very good agreement with previously published ones [1]. For claiming peaks at constant positions multiple experiments have to be performed. If NCs were grown further, the discrete absorption peaks would vanish and the absorption peak at the highest wavelength would from now on continuously shift towards higher wavelengths. Such transition to regular continuous growth has been shown before [1]. In this way a clear separation between discontinuous and continuous growth can be obtained. Upon discontinuous growth the position of the absorption peaks does not change, only their intensity shifts. For continuous growth the position of the absorption peak shifts towards higher wavelengths upon grows. In all our experiments discontinuous growth smoothly went over to continuous growth, as has been already shown for the case of CdSe in a previous study [1].

Material	CdSe I	CdSe II	CdSe III	CdSe IV	CdSe V	CdSe VI
Wavelength of absorption peak (nm)	330	360	380	407	431	447
Composition (EDX)	-	-	-	Cd 54% Se 46%	Cd 56% Se 44%	Cd 56% Se 44%
Crystalline structure	Both ZB and W	Both ZB and W	Both ZB and W	Both ZB and W	Both ZB and W	Both ZB and W

Table T5. *Summary of the properties recorded from CdSe NCs, which are in good agreement with our previous study [1]. The wavelength of absorption refers to the center of the absorbance peak before size selective precipitation. The Cd:Se ratio has been measured using elemental analysis (EDX). In agreement with previous studies the CdSe NCs are richer in Cd than in Se [1,6]. The crystalline structure can be either ZB=zinc blende or cubic, W=wurtzite or hexagonal.*

IV) References

(1) Kudera, S.; Zanella, M.; Giannini, C.; Rizzo, A.; Li, Y.; Gigli, G.; Cingolani, R.; Ciccarella, G.; Spahl, W.; Parak, W. J.; Manna, L. *Advanced Materials* **2007**, *19*, 548.
(2) Yu, W. W.; Qu, L.; Guo, W.; Peng, X. *Chemistry of Materials* **2003**, *15*, 2854.
(3) Dagtepe, P.; Chikan, V.; Jasinski, J.; Leppert, V. J. *Journal Of Physical Chemistry C* **2007**, *111*, 14977.
(4) Egerton, R. F. *Ultramicroscopy* **2007**, *8*, 575.
(5) Bao, K.; Healey, P. D.; Gokhale, M.; Ayers, J. E.; Jain, F. C. *Applied Physics Letters* **1995**, *67*, 1098.
(6) Taylor, J.; Kippeny, T.; Rosenthal, S. J. *JOURNAL OF CLUSTER SCIENCE* **2001**, *12*, 571.

Magnetic microcapsules for NMR imaging and drug delivery: Effect of magnetic nanoparticles spatial distribution and aggregation.

Azhar Zahoor Abbasi, Lucía Gutiérrez, Loretta L. del Mercato, Fernando Herranz, Oksana Chubykalo-Fesenko, Sabino Veintemillas-Verdaguer, Wolfgang J. Parak, M. Puerto Morales, Jesús M González, Antonio Hernando and Patricia de la Presa.

Philipps Universität Marburg, Fachbereich Physik and WZMW, Renthof 7, 35037 Marburg (Germany)

Departamento de biomateriales y materiales bioinspirados, Instituto de Ciencia de Materiales de Madrid/CSIC, Sor Juana Inés de la Cruz 3, Campus de Cantoblanco, Madrid 28049, Spain

Instituto de Estudios Biofuncionales (UCM), Centro de Investigación Biomédica en Red de Enfermedades Respiratorias (CIBERES). Madrid (Spain)

Departamento de Nanoestructuras, Superficies y Recubrimientos, Instituto de Ciencia de Materiales de Madrid/CSIC, Sor Juana Inés de la Cruz 3, Campus de Cantoblanco, Madrid 28049, Spain

Instituto de Magnetismo Aplicado (ADIF-UCM-CSIC), P.O. Box 155, Las Rozas, Madrid 28230, Spain

Abstract

The magnetic and NMR relaxivity properties of γ-Fe_2O_3 nanoparticles embedded into the walls of polyelectrolyte multilayer capsules and freely dispersed in a sodium borate buffer solution have been investigated. The different geometric distribution of both configurations provides the opportunity to study the relationship of water accessibility and magnetic properties of the particles on the NMR relaxivity. Changes in their blocking temperature and average dipolar field were modeled as a function of packing faction in the ensemble of free and entrapped nanoparticles. For free NPs with relatively low concentration, the relaxivity values increases with packing fraction according to an increase in the dipolar field and larger water accessibility. However for embedded NPs in the capsule wall, the packing fraction should be limited to optimise the efficiency of this system as magnetic resonance imaging (MRI) contrast agent.

Introduction

Magnetic nanoparticles are interesting contrast agents for Magnetic Resonance Imaging (MRI) thanks to their ability to affect the relaxation rate of water protons, causing a decrease in signal intensity that results in a darkening effect in the corresponding MR image.[1-4] During the past decade an increasing number of works on the use of coated iron oxide nanoparticles (NPs) as MR contrast have been published.[5] Effectiveness of MR contrast agents is expressed as relaxivity, which represents the slope of dose-relaxation rate dependencies. As there are two relaxation times (T_1 and T_2), there are two relaxation rates (R_1 and R_2) and two relaxivities (r_1 and r_2). Relaxivities vary with magnetic field strength, temperature and biological environment. Particles synthesized by different procedures exhibit differences in their physicochemical characteristics and hence in their imaging efficacy which is not yet fully established and it will be analyzed in this paper. Magnetic NPs can also be used in cancer therapy, which is known as magnetic field hyperthermia, based on the local heating of the magnetic nanoparticles with an externally applied AC magnetic field and also as drug delivery.[6-10] Another field of interest in biomedicine is the treatment of iron deficiency anemia in humans and farm animals.[11] In addition to their technological significance as diagnostic and therapeutic agents, these systems are also very interesting for basic research owing to their large surface to volume ratio.[12]

Recently, the scientific interest in the field of magnetic carriers has been shifted from colloidal suspensions of coated iron oxide nanoparticles, forming aggregates sized between 7 and 200 nm, to multicomponent nanocapsules produced by self-assembly of molecular components in which magnetic nanoparticles constitute key components.[13] General aspects such as particle size, morphology, composition, chemical structure and processing methodology will determine the capsule performance as well as the new interactions that are expected to appear within the different components inside these systems and with the surroundings.[14] The most common nanocapsules are liposomes, in which the magnetic nanoparticles are confined in the aqueous liposome phase or in the liposomal hydrophobic wall.[15] In both cases by applying an AC magnetic field the whole system could become unstable releasing the therapeutic drug also present in the nanocapsule.[16]

Among the important parameters that influence the relaxivity, the distance between the magnetic particles and external water molecules plays a key role. For example, it has been proven that the presence of a double surfactant will go in detriment of the imaging contrast.[17] On the other hand, the aggregation of magnetic nanoparticles into micelles has been shown to enhance NMR relaxivity in spite of the fact that water accessibility is reduced due to the reduction in specific surface area.[18-22] Recently, MRI results of FePt nanoparticles encapsulated into the walls of polyelectrolyte multilayer capsules have shown that the relaxivity increases as the FePt concentration increases.[23] It has also been observed that relaxation of water molecules entrapped in a liposome cavity in the presence of magnetic Gd complexes are affected by size and shape of the internal compartment. Thus, liposome osmotic shrinking leads to an enhancement of both relaxation times.[24] Magnetic properties of nanoparticles has also been extensively studied to understand the relaxivity behavior. For moderate and large anisotropies, blocking temperature has been observed to decrease as the NP concentration increases. However, for sufficiently small anisotropy values, T_B shifts towards higher temperatures when the particle concentration increases.[25] Experimental data on ferrofluids consisting of magnetite or maghemite nanoparticles show a shift of the blocking temperature towards higher temperatures with increasing concentration. According to that, r_2 values increase with aggregate size for maghemite commercial samples such as Endorem, Resovit and Sinerem[26] and for uniform magnetite NPs prepared by thermal decomposition in organic media.[27]

In this work, iron oxide nanoparticles have been incorporated into the walls of polyelectrolyte multilayer capsules being preferentially located at the surface. This configuration is very different from most of the encapsulated particles in which NPs are embedded into a volume. In these capsules all the magnetic particles are virtually equivalent respect to their interaction with water protons, and this gives a unique opportunity for understanding the relationship between water accessibility and intrinsic relaxivity of the entrapped particles which depend finally on their magnetic properties. The information obtained will help us to understand the lack of correlation among the magnetic and relaxometric properties and to design more efficient contrast agents for MRI. We compare here magnetic and relaxivity properties of iron oxide NPs embedded in a capsule wall and dispersed in a sodium borate buffer solution (SBBS). Surprisingly whereas the magnetic response of both kinds of configurations is quite similar, their relaxivities differ markedly. Calculation of the average dipolar field and the blocking temperature is performed on the two geometrical layouts in order to understand the different behaviors.

Experimental section

Synthesis of hydrophobic magnetic NPs

The iron oxide NPs have been synthesized following the procedure reported by Hyeon *et al*.[28] The synthesis yielded nearly monodisperse γ-Fe_2O_3 NPs which were characterized by transmission electron microscopy (TEM) and X-ray diffraction. For more details see the Supporting Information Section I (SI-I). In a next step the hydrophobic NPs were transferred to aqueous solution by coating those with an amphiphilic polymer.

Synthesis of the amphiphilic polymer

The synthesis of the amphiphilic polymer and coating of the hydrophobic particles with it were done using a published protocol [29-30] and they are described in SI-II. The resulting hydrophilic particles are dispersed in SBBS and are called **FREE_NPs**.

Synthesis of the micro capsules containing hydrophilic γ-Fe_2O_3 NPs in the wall

Polyelectrolyte capsules were synthesized using the layer by layer (LbL) technique on calcium carbonate ($CaCO_3$) cores.[31] Those capsules consist of an empty cavity and the magnetic NPs in their polyelectrolyte wall. The wall of the capsules was made using poly(sodium 4-styrenesulfonate) (PSS) as anionic layer, whereas the poly(allylamine hydrochloride) (PAH) and poly(acrylamide-co-diallyl-dimethylammonium chloride) (P(Am-DDA)) were used as cationic layers. In total, two types of polymeric microcapsules were prepared at two different concentrations of γ-Fe_2O_3 NPs (low and high, named as **LCAP** and **HCAP**, respectively). Moreover one sample made of capsules without γ-Fe_2O_3 NPs was fabricated as control. Schematic illustration of the synthesis of a polyelectrolyte capsule with low and high packing fraction of γ-Fe_2O_3 embedded in the wall is shown is Fig. 1. For more details on the encapsulation of γ-Fe_2O_3 NPs in the wall of microcapsules see SI-III.

Structural characterization

The structural characterization was carried out with transmission electron microscopy (TEM), scanning electron microscopy (SEM) and confocal laser scanning microscopy (CLSM). Transmission electron microscopy was performed on JEM 3010 machine operated at 300kV. Samples for TEM analysis were prepared by putting a drop of low concentrated capsule solution onto a carbon coated TEM grid. The grid was dried in air prior to TEM measurements. SEM measurements were conducted using a JEOL JSM-7500F machine at an operation voltage of 2.0kV. For SEM analysis, samples were prepared by putting a drop of capsule solution to a glass slide and drying in vacuum. Confocal micrographs were taken with a confocal laser scanning microscope (CLSM 510 META, Zeiss) equipped with a 100x/1.45 oil immersion objective. The capsules were made fluorescent by adding a layer of poly(fluorescein isothiocyanate allylamine hydrochloride) (PAH_{-FITC}) as second last layer of the wall. The excitation wavelength was 488 nm for PAH_{-FITC}. The concentration of capsules was directly determined by counting the number of capsules with an optical microscope in phase-contrast mode (see SI-III).

Fe concentration

The Fe concentration was then measured with an Inductively Coupled Plasma Optical Emission Spectrometer (ICP-OES) Perkin Elmer Optima 2100 DV. For this purpose samples were digested with nitric acid to oxidize the organic coating and then, with hydrochloric acid to dissolve the particles (see SI-III).

Magnetic characterization

The magnetic characterization was performed in a Quantum Design MPMS-5S SQUID magnetometer. The magnetic characterization of the suspensions (0.1 ml) was carried out in special closed sample holders. The characterization consists of hysteresis loops at 5 Tesla and at 5 K and zero-field-cooled and field-cooled (ZFC-FC) curves from 5 to 250 K and 50 Oe applied field. Diamagnetic contribution from water and organic components was evaluated at high fields (larger than 1 T) and subtracted from the experimental data. In the case of ZFC-FC curves, the low value of the applied field (50 Oe) allows discarding the diamagnetic contribution, *i.e*. the magnetic contribution comes mainly from the iron oxide particles.

Magnetic resonance characterization

Relaxometric properties were also investigated for each aliquot by measuring T_1 and T_2 protons relaxation times at different dilutions. The relaxation time measurements were carried out in a Minispec MQ60 (Brucker) at 37 ℃ and a magnetic field of 1.5 T. From the graph of the Fe-concentration dependent relaxation times, the relaxivities r_1 and r_2 were determined for each type of sample. A control of hollow capsules was used to correct the relaxivity data.

Results

Iron oxide nanoparticle in maghemite phase, γ-Fe_2O_3, were obtained as revealed by X-ray diffraction and confirming previous results (See Fig. SI-3).[28] The mean particle size calculated from TEM images by measuring the size of 240 particles was 10.8 nm and the standard deviation was 16% (see Fig. SI-2). Particles are spherical and uniform in size, within the monodisperse limit (standard deviation lower than 20%).

Capsules containing different concentrations of γ-Fe_2O_3 were observed under TEM microscopy (Fig. 2). Such analysis confirmed the presence of low (Fig. 2a) and high (Fig. 2b) packing fraction of NPs embedded into the wall of the polyelectrolyte capsules. As expected, capsules collapse after core removal indicating the absence of the $CaCO_3$ cores in their cavities (see also Fig. SI-5). CLSM images of polyelectrolyte capsules with γ-Fe_2O_3 at high and low concentration are shown in Fig. 3a and 3b, respectively. Fluorescence images of green emitting dye (FITC) from the capsule walls can be seen in the first column. The second column shows the spherical shape of hollow polyelectrolyte capsules by optical transmission images. Finally the corresponding overlay of both fluorescence and transmission channels are shown in the third column, showing a perfect match (Fig. 3). The average diameter of capsules obtained from TEM and CLSM images was 3.8 ± 0.5 μm. The number of capsules per millilitre was of the order of 10^8 and it was determined using the microscope in phase contrast mode with a mean capsule diameter of 3.8 μm.

In order to determine the particle concentration per sample and per capsule, iron content was measured by ICP- OES, being 0.932, 0.227 and 0.0532 mg/mL for samples FREE_NPS, HCAP and LCAP, respectively. Taking into account that 2.61×10^4 Fe atoms are needed to form one γ-Fe_2O_3 nanoparticle of $\varnothing$ =11 nm and the number of capsules per milliliter in each sample determined with an optical microscope in phase-contrast mode (Figure SI-6) is 10^8,

then the number of particles per capsule is 7.15 10^4 for LCAP and 2.86 10^5 for HCAP. The methodology to determine the number of γ-Fe_2O_3 NPs per capsule is described in the Supporting Information (SI-III.7 and SI-III.8).

The study of the magnetic response and relaxivity of γ-Fe_2O_3 NPs in the capsule wall in comparison to those dispersed in SBBS has been done by comparing the samples behavior at the same particle concentration. If the particle concentration is constant, the distance between NPs is much smaller for those in the capsule wall than the ones dispersed in SBBS. To gauge these differences, it is better to define a local concentration or packing fraction. This packing fraction is defined as the total volume occupied by the NPs divided by the volume in which the NPs are distributed. In the case of γ-Fe_2O_3 NPs in the capsule wall, the available volume for the NPs is the $\mathbf{4\pi r^2 t}$, in which **r** is the radius of the capsule (r = 1.9 μm) and **t** the thickness of the wall. Thickness of one polyelectrolyte bi-layer is around 1.5 nm [32]; the wall of the capsule is made of six bi-layers so that the total thickness of the wall is 18 nm. Therefore, the volume in which the particle can be distributed is 8.16 $10^{-13}$$cm^3$. The total volume of the NPs was obtained by simply multiplying the volume of one γ-Fe_2O_3 nanoparticle by the total number of NPs in each sample. Packing fraction for sample LCAP was 5.8 % and for HCAP was 23 %. On the other hand, FREE_NPs can be distributed in the whole volume of the sample resulting in packing fractions of 0.02 %. As a result, the packing fraction for γ-Fe_2O_3 NPs in the capsule wall is 300-400 times larger than that for FREE_NPs at the same Fe total concentration.

The hysteresis loops of γ-Fe_2O_3 NPs in the capsule wall and in SBBS do not differ significantly as shown in Fig 4. However, the ZFC-FC measurements show slightly differences for these samples (Fig. 5). The blocking temperature (T_B) of FREE_NPS decreases for increasing particle concentration, while the contrary occurs for the NPs in capsule wall, in which T_B increases for increasing particle concentration, as shown in Fig 5. Table 1 shows the coercive field and T_B for each sample. Coercivity decreases as the NP concentration decreases independently on the particle spatial distribution.

Relaxivity characterization for particles with different spatial distribution either dispersed in SBBS or in the capsule walls, showed a marked decrease in the relaxivity values (r_1 and r_2) when particles are encapsulated. The r_1 and r_2 values go from 3.39 and 43.8 $(mM.s)^{-1}$ for FREE_NPS down to 0 and 1.8 $(mM.s)^{-1}$ for HCAP, respectively. Surprisingly, r_2 value increases as the NPs packing fraction in the capsule wall decreases, *i.e*. from sample HCAP to LCAP (Table 1). This trend is opposite to the one observed for FePt NPs in a similar capsule wall, where r_2 was observed to increase with NPs packing fraction.[23] However, for free nanoparticles it has been reported that r_2 values increase with the aggregate size and therefore with the packing fraction (see Fig. 6).[26 27]

The different behavior observed for maghemite NPs encapsulated in the capsule wall may be explained by the different magnetic anisotropy in comparison to FePt and the different distribution geometry when compared to the bibliography data for maghemite/magnetite NPs. Magnetic interactions in a many particle system and NP size distribution need to be taking

into account to understand the results; therefore, we perform theoretical modeling in these systems.

Discussion

The behaviour of the blocking temperature, which results in low or high values depending on magnetic anisotropy, agglomeration and particle size, can be visualized in a simple model of two magnetic NPs with large angle between their anisotropy axes. When the NPs are far away enough (low packing fraction), they can be considered as two non-interacting magnetic NPs and the blocking temperature is governed by the anisotropy field. As the distance between particles decreases (larger packing fraction), the magnetic interaction increases and produces a drop in the effective anisotropy that leads to a decrease in the blocking temperature. The blocking temperature decreases up to the moment when the magnetic interaction between particles becomes comparable to the anisotropy field. However, when the magnetic interaction is higher than the anisotropy field (even larger packing fraction), NPs behave as a cooperating system and the blocking temperature is ruled by their total volume, *i.e.*, the higher the magnetic interaction, the higher the blocking temperature. In our case -NPs dispersed in the volume of SBBS or located at the capsule wall- it is necessary to take into account the interactions in a many particle system and also the NPs size distributions; therefore, we perform calculations in this system to calculate the average dipolar field felt by the magnetic particles (affecting the blocking temperature) and the dipolar field created by the magnetic capsules averaged over the overall space (affecting r_2 values) as a function of NPs concentration and spatial distribution, *i.e.* packing fraction.

In what follows we present modeling results on ensembles of NPs with different spatial distributions. The complete modeling of the experimental situation is outside of our possibilities since one capsule contains 10^4 – 10^5 NPs. To get an inside into general tendencies of the magnetic behavior, we consider smaller capsules. More concretely, we generate an ensemble of NPs with a log-normal distribution having the most probable diameter D=10 nm and 10% of volume dispersion. The NPs are distributed inside a cube of 500x500x500 nm^3 in two geometries: (a) uniform volume distribution and (b) uniform distribution within a surface layer of 18 nm on a sphere with D=400 nm diameter (see Fig. SI-7). We consider NPs with saturation magnetization values M_s= 400 emu/cm^3, as corresponding to maghemite. The value of the crystalline anisotropy is not well known. Additionally, in our analysis we consider the macrospin approximation with the effective anisotropy which can be larger than the bulk magnetocrystalline anisotropy due to the surface anisotropy.[33] In the present study we have chosen to consider two possibilities, corresponding to weak and strong interaction cases. In the former case we take the anisotropy parameter corresponding to maghemite NPs as K= **4.6 10**^{4} erg/cm^3,[33] in the latter case we take the effective anisotropy as K= **3.3 10**^{5} erg/cm^3, which in the non-interacting case gives the blocking temperature similar to the experimentally measured. The anisotropy axes are considered distributed randomly. For detailed description of the model see the SI-IV.

Our estimation of T_B is based on the evaluation of the energy barrier distribution,[34-35] see SI-IV for details. The change in energy barrier distributions as a function of the number of NPs

per capsule (low packing fraction) is presented in Fig. 7. At low concentrations the main effects is the dispersion of the distribution as a function of the packing fraction. This is easy to understand in terms of the mean dipolar field acting on each nanoparticle. The nanoparticle with randomly distributed easy axes feels a randomly distributed local dipolar field. Depending on its value and the angle with the direction of the easy axis, this field may increase or decrease the NPs largest energy barrier in comparison to the non-interacting nanoparticle.[34] Since the absolute value of the dipolar field is larger for smaller interparticle distances, the dispersion of the energy barrier distribution increases with packing fraction. We define T_B as the temperature at which 90% of NPs are blocked. Figure 8 shows T_B as a function of packing fraction for FREE_NPS sample and capsules for the high anisotropy case. According to the general tendency for the behavior of the energy barrier distributions in Fig. 7, T_B decreases as a function of concentration in both cases, being the T_B values slightly lower for the uniform ensemble than for the capsule systems with the same packing fraction.

In the case considered above the relative strength of the dipolar interactions is not high. Since the energy barrier calculations in a multidimensional space are time consuming we have not been able to take into consideration very high packing densities. To consider the case with strong dipolar fields and high concentrations we present in Fig. 9 the results for a smaller capsule (D=200 nm) and two anisotropy values. At low packing densities the blocking temperature decreases in agreement with the results above. However, at high packing densities the blocking temperature increases. This different regime is due to the fact that at high concentrations the NPs magnetically couple one to another and their energy barriers become collective. Collective energy barriers are associated with volumes of several NPs and thus are large. The transition between the regime of individual energy barriers and collective ones depends on the strength of the dipolar interactions. Thus the corresponding minimum of the blocking temperature versus concentration occurs at larger concentrations in the high anisotropy case.

On the other hand, the measured value of r_2 is proportional to the strength of the dipolar field acting on the proton of the water in the system. In Fig. 10 we present the absolute value of the dipolar field, averaged over the whole volume, and evaluated for sample FREE_NPS and the capsules, assuming two anisotropy values as described above. The average dipolar field is smaller for the capsules as compared to the uniform distribution, in agreement with the experiment (see the Table 1). This effect has two contributions: (i) In the case of capsules, the average distances between the protons in the water and NPs are larger than for free distributed NPs. (ii) The spherical geometry leads to additional minimization of the dipolar energy, favoring the parallel-to the surface magnetization distribution in systems with high packing density. The latter effect is responsible for the differences observed between high and low anisotropy cases (Fig. 10). In the case of low anisotropy, the magnetostatic interactions are relatively stronger producing additional minimization of the dipolar field. The difference between the uniform ensemble and the capsule are much more pronounced if the results are re-plotted as a function of the local packing fraction (see Fig. 10b). As an example, for the modeled capsule with 4000 NPs, the packing fraction is around 3% for the uniform ensemble and 23% (as in the experimental sample) on the surface of the capsule. It should be noted that the experimental values of the averaged dipolar field in the case of capsules should be much

smaller than the ones obtained in modeling due to a smaller volume concentration of microcapsules.

Conclusions

To sum up, the absolute value of the dipolar field averaged over the overall space is smaller for the capsule than for the uniformly distributed ensemble leading to a smaller r_2 value for the former. The ensembles of FREE_NPs have low packing densities and are in the regime of individual energy barriers; therefore, the blocking temperature decreases as a function of packing fraction. The NPs on capsules have locally large packing densities and their behavior belongs to the regime of collective energy barriers. Consequently, the blocking temperature increases with concentration. The latter is also true for aggregated arrays of NPs as those present in commercial samples, where packing density is high; however, in these cases, the blocking temperature as well as the r_2 values increase with concentration, as observed in Fig. 6. Aggregation affects the spatially inhomogeneous particle distribution leading to collective magnetization.

From these results is clear that the geometrical layout of the magnetic NPs plays also a role as important as the magnetic, structural or colloidal properties of the particles (magnetic saturation, anisotropy, homogeneous size and aggregate size). For low NPs concentration relaxivity values are comparable for both geometrical layouts. However, for high NPs concentration, the NPs arrangement on the capsule wall leads to a minimization of the dipolar energy, favoring the parallel-to the surface magnetization distribution. This fact together with lower water accessibility due to the increase in the distance between magnetic capsules at the same Fe concentration, results in lower relaxivity values. The design of complex materials that serve simultaneously as diagnostic and therapeutic agents requires the optimization of each component. Thus, for example, capsules for drug delivery would be better containing large quantities of magnetic NPs to produce an efficient local heating under an AC magnetic field.[36] However, in the light of these results, the NMR imaging contrast produced by this system would be diminished if the particles are encapsulated at high packing density in the capsule wall. NPs with larger magnetic anisotropy could enhance the image contrast.

Acknowledgements

Azhar Zahoor Abbasi is thankful to Higher education commission of Pakistan (HEC) and Deutsche Akademischer Austtausch Dienst (DAAD) for the fellowship, LG and FH hold a Sara Borrel post-doctoral contract. This work was supported by grants from the Spanish Ministry of Science and Innovation (MAT2007-66719-C03-01, MAT2008-01489, CSD2007-00010, CS2008-023), the Madrid regional government CM (S009/MAT-1726), and the European Commission (project NAMDIATREAM).

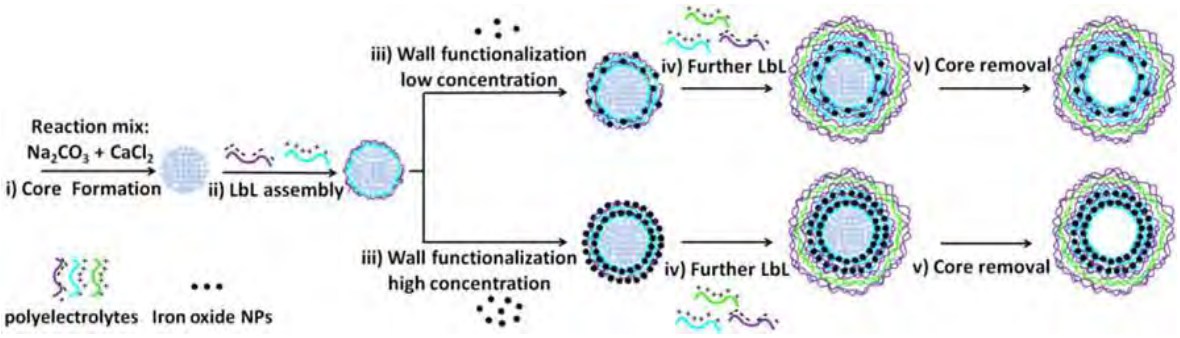

Figure 1: Schematic illustration of the synthesis of a polyelectrolyte capsule with low and high concentration of γ-Fe_2O_3 embedded in the wall. i) A spherical $CaCO_3$ porous template is synthesized by mixing two solutions of Na_2CO_3 and $CaCl_2$. ii) The $CaCO_3$ particle is then coated via consecutive LbL deposition of oppositely charged polyelectrolytes to grow a multilayer polymer wall around the template. iii) The wall is functionalized by loading low and high concentrations of charged γ-Fe_2O_3 NPs onto an oppositely charged layer during the LbL assembly. The NPs were added as seventh and tenth layer giving the following wall architecture: $(PSS/PAH)_2(PSS/P(Am\text{-}DDA)/\gamma\text{-}Fe_2O_3)_2(PSS/PAH_{\text{-}FITC})(PSS/PAH)$. iv) LbL of polyelectrolytes is repeated to obtain a stable multilayer wall on both capsules with loading low and high concentrations of NPs. A green fluorescent layer was also added to make the wall fluorescent. v) The spherical template is removed to obtain a multilayer capsule with loading low and high concentration of charged γ-Fe_2O_3 NPs in the walls. Capsules are not drawn to scale.

Sample	[Fe] (mg ml^{-1})	H_c (Oe)	T_B (K)	r_2 ($(mM\ s)^{-1}$)
FREE_NPS	0.2	210	45	43.8
FREE_NPS	0.05	200	55	-
HCAP	0.2	230	65	1.8
LCAP	0.05	200	55	46.1

Table 1: Iron concentration, coercive field (H_c), Blocking temperature (T_B) and transversal relaxivity values (r_2) for maghemite nanoparticles freely dispersed (sample FREE_NP) and entrapped at the capsule wall (HCAP and LCAP).

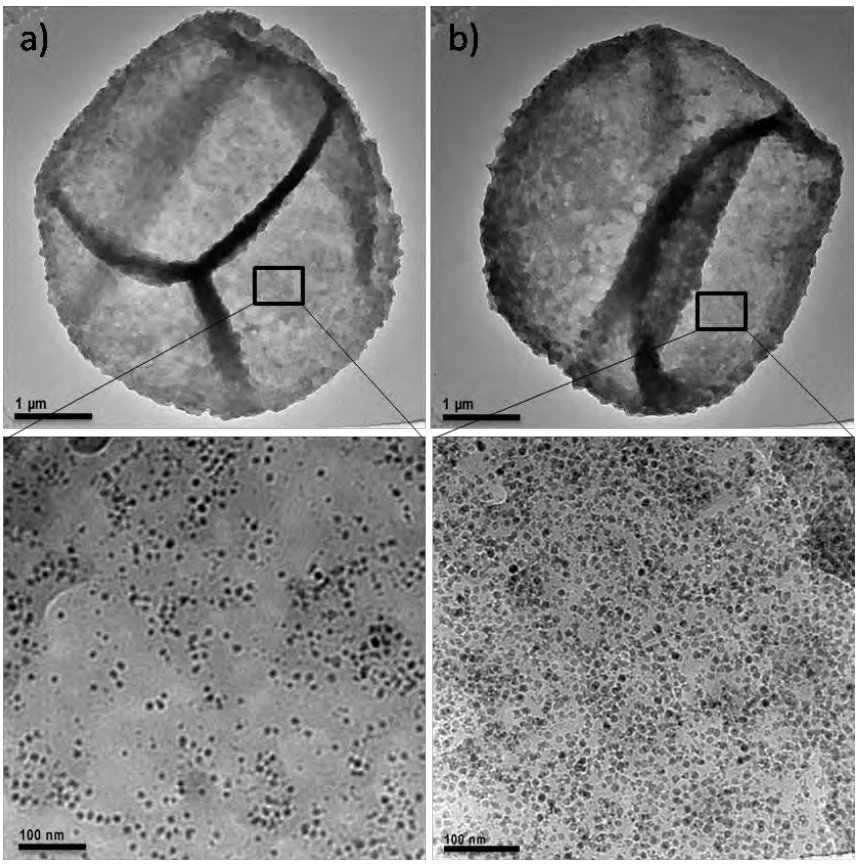

Figure 2: TEM images of $(PSS/PAH)_2(PSS/P(Am\text{-}DDA)/\gamma\text{-}Fe_2O_3)_2(PSS/PAH_{FITC})(PSS/PAH)$ polyelectrolyte capsules after core removal. a) Capsules with low concentration of $\gamma\text{-}Fe_2O_3$ nanoparticles. b) Capsules with high concentration of $\gamma\text{-}Fe_2O_3$ nanoparticles. The upper row shows low magnification images of individual capsule. The lower row shows high resolution images zoomed into the capsule wall showing the distribution of the $\gamma\text{-}Fe_2O_3$ particles in the capsule wall. The scale bars in the upper and lower row correspond to 1 µm and 100 nm, respectively.

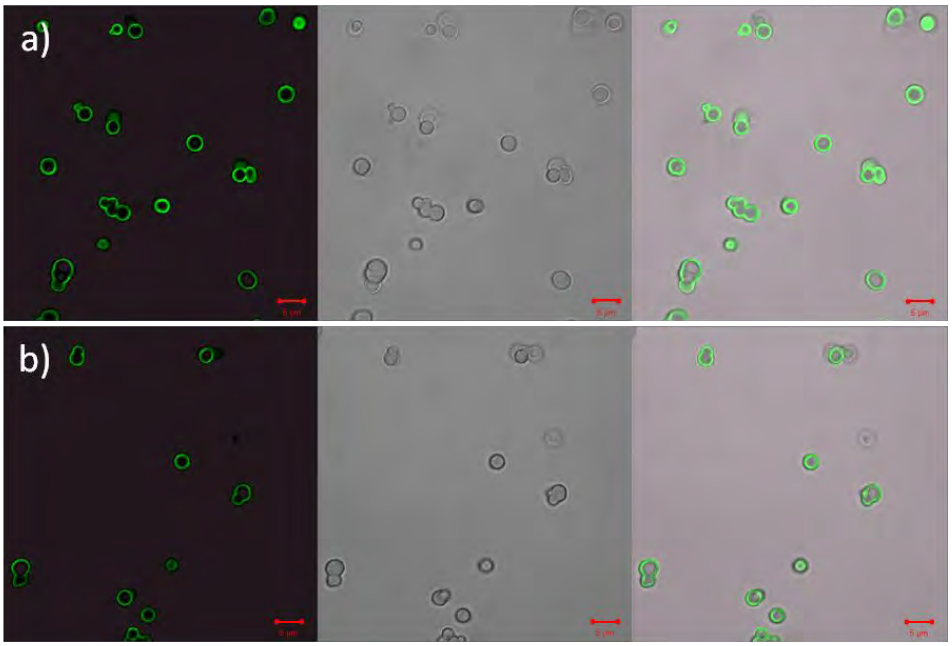

Figure 3: CLSM images of $(PSS/PAH)_2(PSS/P(Am\text{-}DDA)/\gamma\text{-}Fe_2O_3)_2(PSS/PAH\text{-}_{FITC})(PSS/PAH)$ poly electrolyte capsules a) Capsules with low concentration of $\gamma\text{-}Fe_2O_3$ nanoparticles. b) capsules with high concentration of $\gamma\text{-}Fe_2O_3$ nanoparticles. Left panels: Fluorescence images of green emitting dye. Central panels: optical transmission images. Right panels: corresponding overlay of both fluorescence and transmission channels. Scale bars correspond to 5 µm.

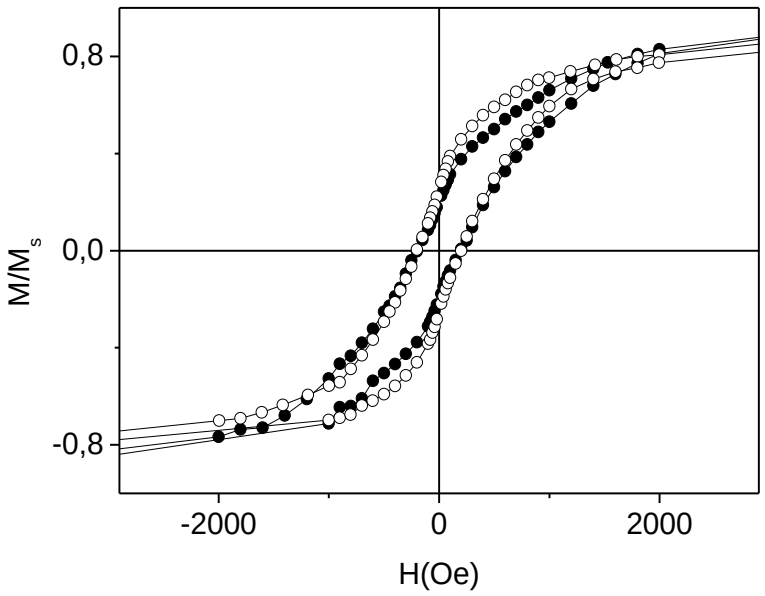

Figure 4: Normalized hysteresis curves of $\gamma\text{-}Fe_2O_3$ NPs in the wall of capsules (full circles) and freely dispersed (open circles).

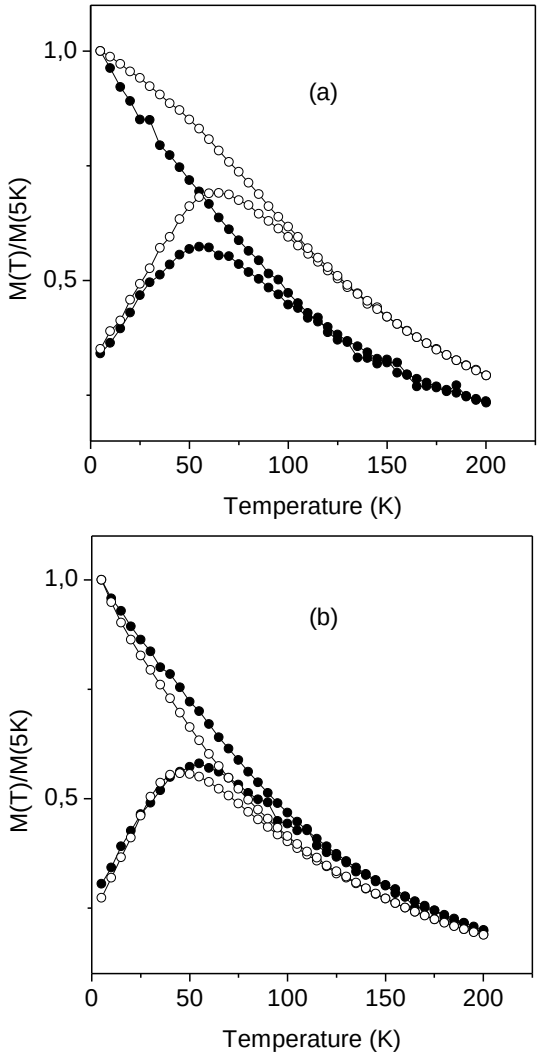

Figure 5: ZFC-FC characterization of γ-Fe_2O_3 NPs (a) in the wall of capsules (LbL) and (b) freely dispersed (FREE_NPS) at low (full circles) and high (open circles) concentrations. The curves are normalized to the values at T = 5 K

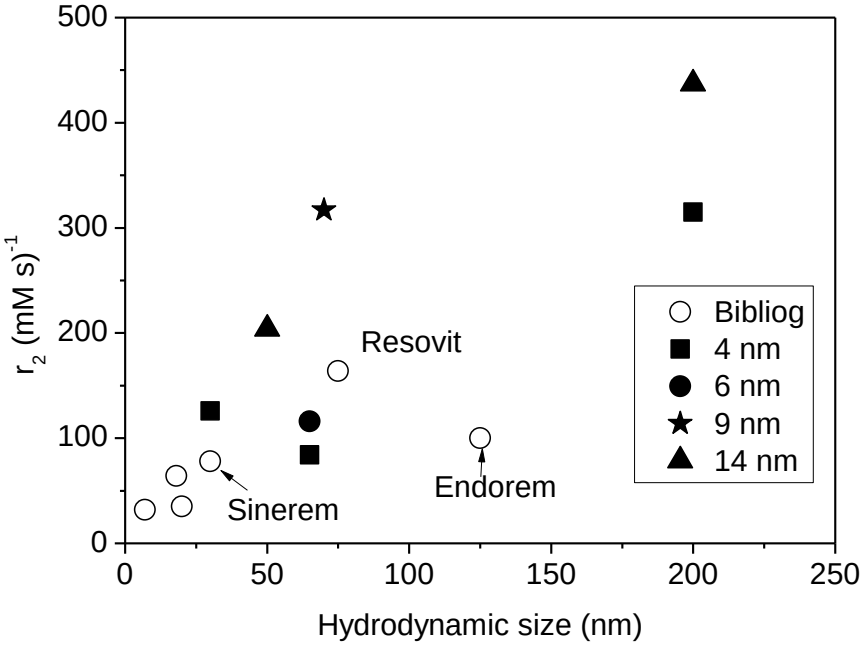

Figure 6: Transversal relaxivity values (r_2) for magnetic nanoparticles of magnetite with different particle size and aggregate size.

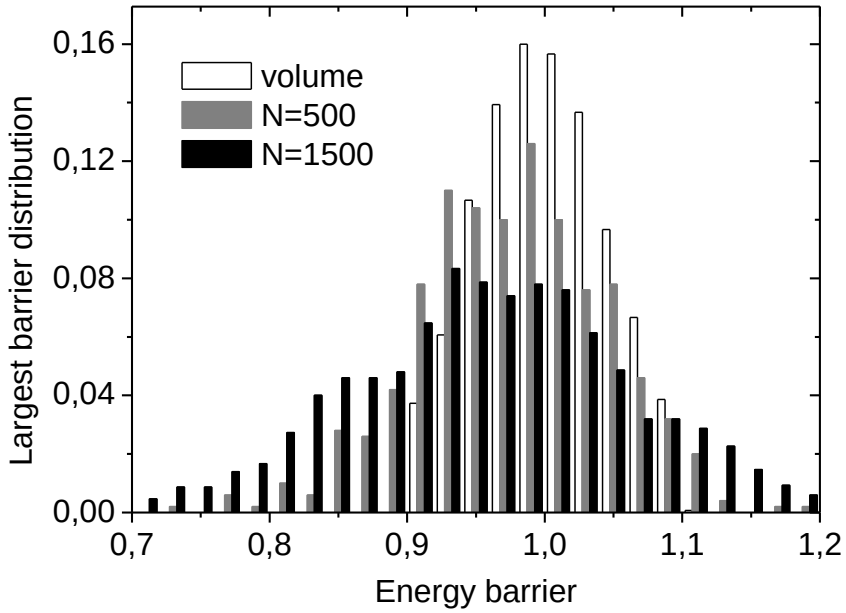

Figure 7: Distribution of volumes and energy barriers (normalized to the value K<V>) for a capsule of D=400 nm containing N=500 (packing fraction 3%) and N=1500 (packing fraction 9%) NPs.

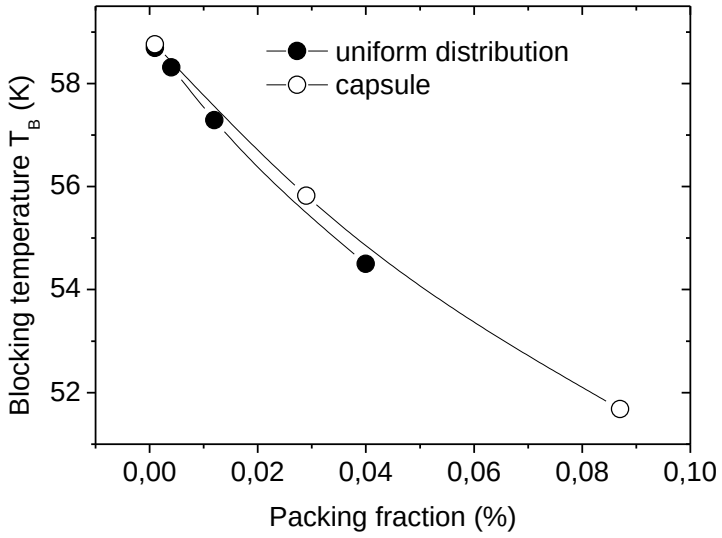

Figure 8: Blocking temperatures for an ensemble of uniformly distributed NPs and a capsule with D=400 nm, assuming the anisotropy value K=3.3 10^5 erg/cm^3 and low values of packing fractions.

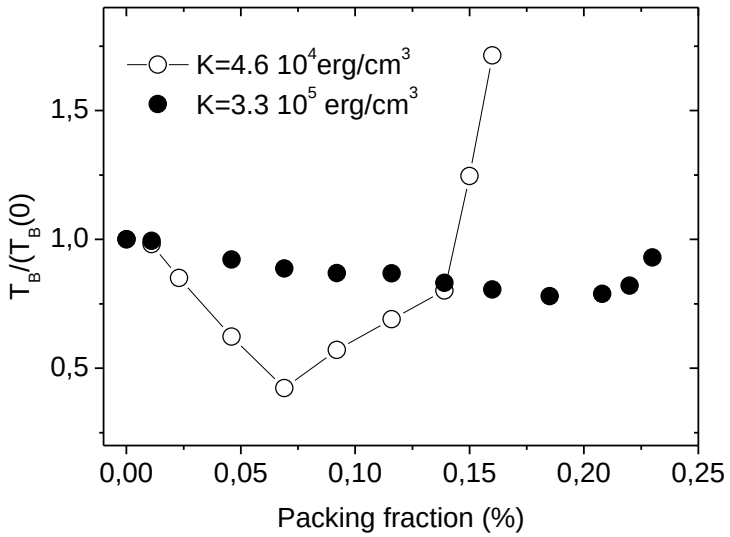

Figure 9: Blocking temperature (normalized to the non-interacting ensemble case) as a function of surface packing densities. This calculations are performed for a capsule with D=200 nm and two values of the anisotropy parameter.

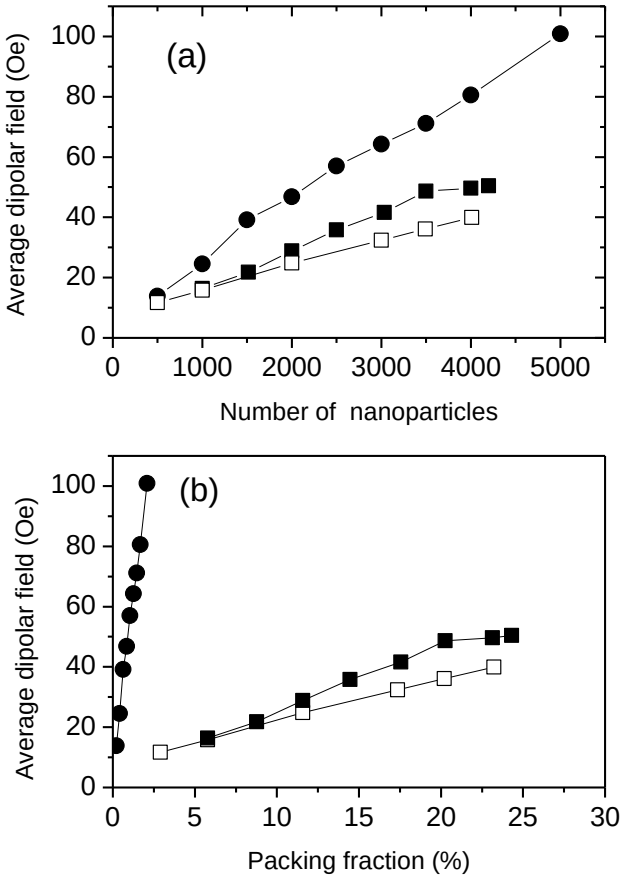

Figure 10: Average absolute value of the dipolar field in modeled systems as a function of (a) the number of NPs and (b) the packing fraction. (● free NPs with K= 3.3 10^5erg/cm^3; ■ capsules with K = 3.3 10^5 erg/cm^3 and □ capsules with K = 4.6 10^4 erg/cm^3)

References

1. E. K. U. Larsen, T. Nielsen, T. Wittenborn, H. Birkedal, T. Vorup-Jensen, M. H. Jakobsen, L. Ostergaard, M. R. Horsman, F. Besenbacher, K. A. Howard and J. Kjems, *ACS Nano*, 2009, 3, 1947-1951.
2. O. Gleeson, R. Tekoriute, Y. K. Gun'ko and S. J. Connon, *Chem.-Eur. J.*, 2009, 15, 5669-5673.
3. T. Atanasijevic, M. Shusteff, P. Fam and A. Jasanoff, *Proceedings of the National Academy of Sciences of the United States of America*, 2006, 103, 14707-14712.
4. I. Rodriguez, S. Perez-Rial, J. Gonzalez-Jimenez, J. M. Perez-Sanchez, F. Herranz, N. Beckmann and J. Ruiz-Cabello, *Journal of Pharmaceutical Sciences*, 2008, 97, 3637-3665.
5. L. M. Lacroix, D. Ho and S. H. Sun, *Current Topics in Medicinal Chemistry*, 2010, 10, 1184-1197.
6. M. Johannsen, U. Gneueckow, B. Thiesen, K. Taymoorian, C. H. Cho, N. Waldofner, R. Scholz, A. Jordan, S. A. Loening and P. Wust, *European Urology*, 2007, 52, 1653-1662.
7. A. Jordan, R. Scholz, P. Wust, H. Fahling and R. Felix, *JOURNAL OF MAGNETISM AND MAGNETIC MATERIALS*, 1999, 201, 413-419.
8. A. Villanueva, P. de la Presa, J. M. Alonso, T. Rueda, A. Martinez, P. Crespo, M. P. Morales, M. A. Gonzalez-Fernandez, J. Valdes and G. Rivero, *Journal of Physical Chemistry C*, 2010, 114, 1976-1981.
9. T. K. Jain, M. A. Morales, S. K. Sahoo, D. L. Leslie-Pelecky and V. Labhasetwar, *Mol. Pharm.*, 2005, 2, 194-205.
10. A. Ito, M. Shinkai, H. Honda and T. Kobayashi, *J. Biosci. Bioeng.*, 2005, 100, 1-11.
11. L. Gutierrez and F. J. Lazaro, *JOURNAL OF MAGNETISM AND MAGNETIC MATERIALS*, 2007, 316, 136-139.
12. X. Batlle and A. Labarta, *Journal of Physics D-Applied Physics*, 2002, 35, R15-R42.
13. V. Salgueirino-Maceira and M. A. Correa-Duarte, *Advanced Materials*, 2007, 19, 4131-4144.
14. R. Arshady, ed., *Microspheres, microcapsules & liposomes*, Citus, London, 1999.
15. P. de la Presa, T. Rueda, M. D. Morales, F. J. Chichon, R. Arranz, J. M. Valpuesta and A. Hernando, *Journal of Physical Chemistry B*, 2009, 113, 3051-3057.
16. Y. J. Chen, A. Bose and G. D. Bothun, *Acs Nano*, 2010, 4, 3215-3221.
17. A. Wooding, M. Kilner and D. B. Lambrick, *Journal of Colloid and Interface Science*, 1992, 149, 98-104.
18. U. I. Tromsdorf, N. C. Bigall, M. G. Kaul, O. T. Bruns, M. S. Nikolic, B. Mollwitz, R. A. Sperling, R. Reimer, H. Hohenberg, W. J. Parak, S. Forster, U. Beisiegel, G. Adam and H. Weller, *Nano Lett.*, 2007, 7, 2422-2427.
19. Y. M. Huh, Y. W. Jun, H. T. Song, S. Kim, J. S. Choi, J. H. Lee, S. Yoon, K. S. Kim, J. S. Shin, J. S. Suh and J. Cheon, *Journal of the American Chemical Society*, 2005, 127, 12387-12391.
20. N. Nasongkla, E. Bey, J. M. Ren, H. Ai, C. Khemtong, J. S. Guthi, S. F. Chin, A. D. Sherry, D. A. Boothman and J. M. Gao, *Nano Lett.*, 2006, 6, 2427-2430.
21. W. J. M. Mulder, G. J. Strijkers, G. A. F. van Tilborg, A. W. Griffioen and K. Nicolay, *NMR Biomed.*, 2006, 19, 142-164.
22. S. B. Seo, J. Yang, T. I. Lee, C. H. Chung, Y. J. Song, J. S. Suh, H. G. Yoon, Y. M. Huh and S. Haam, *Journal of Colloid and Interface Science*, 2008, 319, 429-434.
23. M. P. Morales, M. F. Bedard, A. G. Roca, P. de la Presa, A. Hernando, F. Zhang, M. Zanella, A. A. Zahoor, G. B. Sukhorukov, L. L. del Mercato and W. J. Parak, *Journal of Materials Chemistry*, 2009, 19, 6381-6386.
24. S. Aime, D. D. Castelli, D. Lawson and E. Terreno, *Journal of the American Chemical Society*, 2007, 129, 2430-+.
25. D. V. Berkov and N. L. Gorn, *Journal of Physics: Condensed Matter*, 2001, 13, 9369.
26. A. K. Gupta and M. Gupta, *Biomaterials*, 2005, 26, 3995-4021.
27. A. G. Roca, S. Veintemillas-Verdaguer, M. Port, C. Robic, C. J. Serna and M. P. Morales, *Journal of Physical Chemistry B*, 2009, 113, 7033-7039.

28. T. Hyeon, S. S. Lee, J. Park, Y. Chung and H. Bin Na, *Journal of the American Chemical Society*, 2001, 123, 12798-12801.
29. C. A. J. Lin, R. A. Sperling, J. K. Li, T. Y. Yang, P. Y. Li, M. Zanella, W. H. Chang and W. G. J. Parak, *Small*, 2008, 4, 334-341.
30. M. T. Fernandez-Arguelles, A. Yakovlev, R. A. Sperling, C. Luccardini, S. Gaillard, A. S. Medel, J. M. Mallet, J. C. Brochon, A. Feltz, M. Oheim and W. J. Parak, *Nano Letters*, 2007, 7, 2613-2617.
31. O. Kreft, A. M. Javier, G. B. Sukhorukov and W. J. Parak, *Journal of Materials Chemistry*, 2007, 17, 4471-4476.
32. A. Diaspro, D. Silvano, S. Krol, O. Cavalleri and A. Gliozzi, *Langmuir*, 2002, 18, 5047-5050.
33. G. F. Goya, T. S. Berquo, F. C. Fonseca and M. P. Morales, *JOURNAL OF APPLIED PHYSICS*, 2003, 94, 3520-3528.
34. O. Chubykalo-Fesenko and R. W. Chantrell, *JOURNAL OF APPLIED PHYSICS*, 2005, 97.
35. O. A. Chubykalo and R. W. Chantrell, *JOURNAL OF MAGNETISM AND MAGNETIC MATERIALS*, 2004, 272, E1169-E1171.
36. Q. A. Pankhurst, N. K. T. Thanh, S. K. Jones and J. Dobson, *Journal of Physics D-Applied Physics*, 2009, 42.

Supporting Information

Magnetic microcapsules for NMR imaging and drug delivery: Effect of magnetic nanoparticles spatial distribution and aggregation.

Azhar Zahoor Abbasi, Luc*i*a Gut*i*errez, Loretta L. del Mercato, Fernando Herranz, Oksana Chubykalo-Fesenko, Sabino Veintemillas-Verdaguer, Wolfgang J. Parak, M. Puerto. Morales, Jesús M Gonzalez, Antonio Hernando and Patricia de la Presa.

I) Synthesis of monodisperse hydrophobic maghemite (γ-Fe_2O_3) nanoparticles

I.1) Chemicals

I.2) Synthesis of γ-Fe_2O_3 nanoparticles

I.3) Absorption spectra of γ-Fe_2O_3 nanoparticles

I.4) Size distribution measurements using transmission electron microscopy (TEM)

I.5) X-ray diffraction of nanoparticles

I.1) Chemicals

Iron pentacarbonyl ($Fe(CO)_5$ 99.999% Sigma-Aldrich #481718), Octyl ether ($[CH_3(CH_2)_7]_2O$ 99% Sigma-Aldrich #249599), Oleic acid ($CH_3(CH_2)_7CH=CH(CH_2)_7COOH$ 90% Sigma-Aldrich #364525), Trimethylamine N-oxide dehydrate ($(CH_3)_3NO$ 98% Sigma-Aldrich #T0514), Toluene (C_7H_8 99.8% Sigma-Aldrich #244511), Methanol (CH_3OH 99.8% Sigma-Aldrich #322415), Chloroform ($CHCl_3$ $\geqslant$99% Sigma-Aldrich #372978)

I.2) Synthesis of γ-Fe_2O_3 nanoparticles

Monodisperse γ-Fe_2O_3 nanoparticles (NPs) were synthesized using published protocol by Hyeon and coworkers.[1] Briefly 10 mL of octyl ether and 1.28 g of oleic acid were mixed and degassed in three neck flask for 20 min. at 60^0C. After 20 min. temperature was increased up to 100^0C. At this stage 0.28 mL of iron petacarbonyl was injected and temperature was increased up to refluxing temperature (~295-300^0C). The solution was kept at this temperature for 1hour. During this time the initial yellow color of the solution changed to black. After one hour the solution was cooled to room temperature. Then 0.34 g of dehydrated trimethylamine oxide was added and temperature was increased up to 130^0C. The solution was kept at this temperature for two hours. During this time the black color of the solution changed into dark brown. After two hours again the solution's temperature was increased up to refluxing temperature in steps each of 15 ^{0}C/min. The solution was kept at refluxing temperature for another hour. During this time the solution's color again changed from dark brown to black. After one hour the reaction was stopped by removing the heating mantel. At room temperature 2-5 mL of toluene was added followed by the 25-30 mL of methanol. Particles were precipitated with a centrifuge at the speed of 1800 rpm. The supernatant was removed and the precipitate was again washed using toluene and methanol. The precipitate was then redispersed in 10-20 mL of toluene or alternatively in chloroform.

I.3) Absorption spectra of γ-Fe_2O_3 nanoparticles

Absorption spectra of synthesized γ-Fe_2O_3 nanoparticles were recorded using an UV/vis spectrometer (Agilent 8453 UV/vis absorbance spectrometer). The absorption spectrum of as synthesized γ-Fe_2O_3 dissolved in toluene is shown in Fig.SI-1.

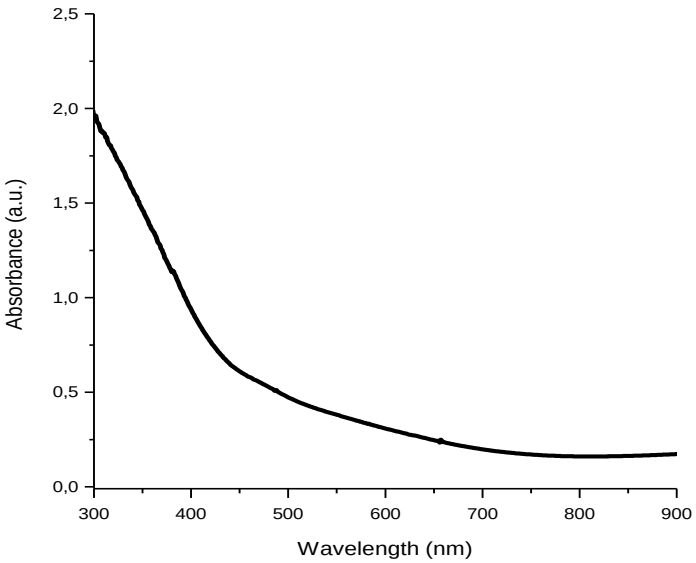

Figure SI-1: UV/vis absorption spectrum of γ-Fe_2O_3 particles dissolved in Toluene.

I.4) Size distribution measurements using transmission electron microscopy (TEM)

To analyze the size distribution and morphology of the synthesized nanoparticles a transmission electron microscope (TEM) was used for imaging. The TEM investigation was performed on a JEM 3010 high-resolution electron microscope (Jeol Ltd., Tokyo, Japan) operated at 300 kV. TEM samples were prepared by depositing the γ-Fe_2O_3 NPs on 300mesh copper grids covered with a thin carbon supporting film. The program Image J was used to derive the size distribution of particles from the TEM images. Fig. SI-2 shows one TEM image and the corresponding histogram of the size distribution as obtained using the Image J program. The average size distribution of nanoparticles was found to be is 10.8 nm with standard deviation σ=0.16.

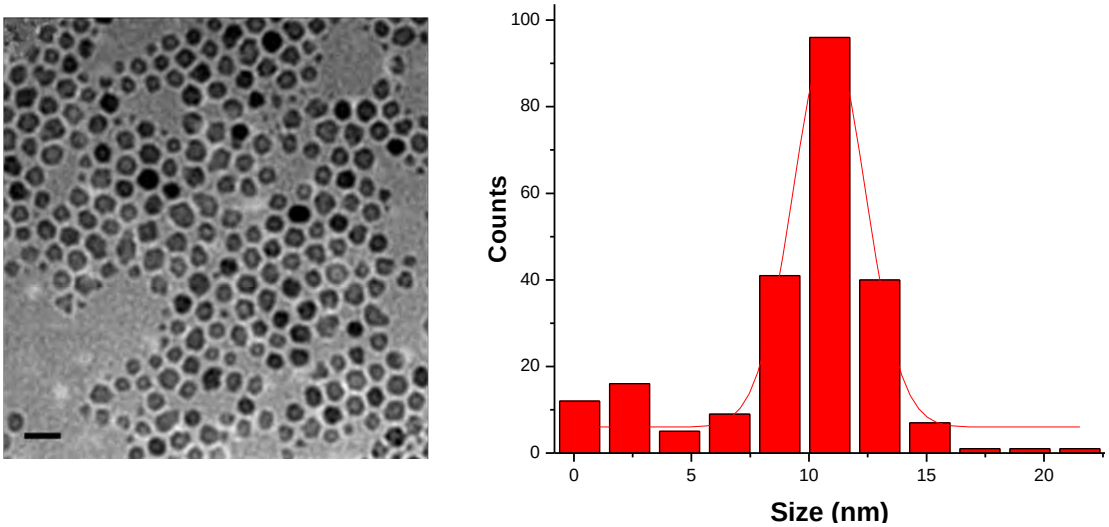

Figure SI-2: TEM image of γ-Fe_2O_3 nanoparticles dissolved in toluene. The scale bar corresponds to 20 nm. The histogram shows the distribution of detected diameters of the γ-Fe_2O_3 particles as obtained from the TEM images. Only the inorganic γ-Fe_2O_3 is visible, but not the organic coating on the particle surface. The size distribution is 10.8 nm with standard deviation σ=0.16.

I.5) X-ray diffraction (XRD)

The γ-Fe_2O_3 nanoparticles were analyzed for phase composition by X-ray powder diffraction (XRD). The XRD patterns were recorded with a Philips XPert PRO MPD system operating at 40 kV and 40 mA. The XRD scans were recorded over the 2θ range from 20–70^o, using Cu-K_α radiation (λ =1.54060 Å). The XRD pattern confirmed the formation of iron oxide nanoparticles in maghemite phase. The XRD peaks were compared with reported data of Hyeon [1] and coworkers for γ-Fe_2O_3 nanoparticles. The peaks match well with the reported data for γ-Fe_2O_3 confirming the formation of iron oxide nanoparticles in maghemite phase. The sample for XRD was prepared by washing the nanoparticle sample four times with methanol and toluene and finally drying of the precipitate under vacuum. The dried precipitate was then grinded using an agate mortar for 8-10 min. to get fine powder. The powder was then deposited on a XRD sample holder. Figure SI-3 shows the XRD pattern of iron oxide nanoparticles in maghemite phase.

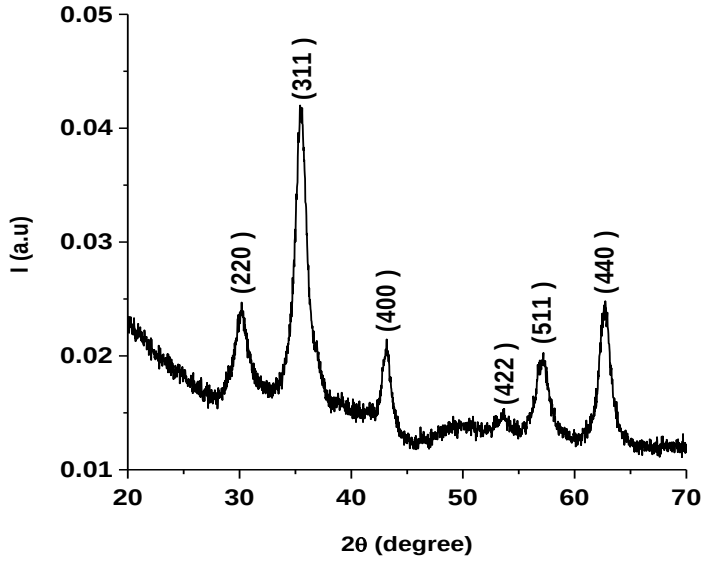

Figure SI-3: XRD pattern of γ-Fe_2O_3 nanoparticles.

II) Polymer coating of γ-Fe_2O_3 nanoparticles

II.1) Chemicals

II.2) Synthesis of amphiphilic polymer

II.3) Coating of γ-Fe_2O_3 using the amphiphilic polymer

II.1) Chemicals

Dodecylamine ($C_{12}H_{27}N$ 98% Sigma-Aldrich # D22,220-8), Tetrahydrofurane (THF) (C_4H_8O ≥99.9% Sigma-Aldrich #186562), poly(isobutylene-alt-maleic anhydride) (6 kDa/mol Sigma-Aldrich 531278), Chloroform ($CHCl_3$>=99%, Sigma-Aldrich #372978).

II.2) Synthesis of amphiphilic polymer

Synthesis of the amphiphilic polymer used for transferring the γ-Fe_2O_3 nanoparticles to aqueous solution was done using a published protocol.[2-3] Briefly 2.70 g (15 mmol) of dodecylamine powder was dissolved in 100mL THF in a round flask. When the dodeclyamine had dissolved well, the solution was poured into another round flask containing 3.084 g (20 mmol monomer) of poly(isobutylene-alt-maleicanhydride) powder. The mixture was sonicated until the solution was clear. In a next step this clear solution was heated under stirring condition at 55-60 ^{0}C for one hour. After one hour the solution was concentrated to 30-40 mL by evaporating the THF solvent to enhance the reaction between the maleic anhydride rings of poly(isobutylene-alt-maleicanhydride) and the amino groups of dodeclyamine. This solution was left stirring overnight. On the next day the solution was completely dried by evaporation and the remaining powder of the resulting amphiphilic polymer was redissolved in 40 mL chloroform to a final monomer concentration of 0.5 M.

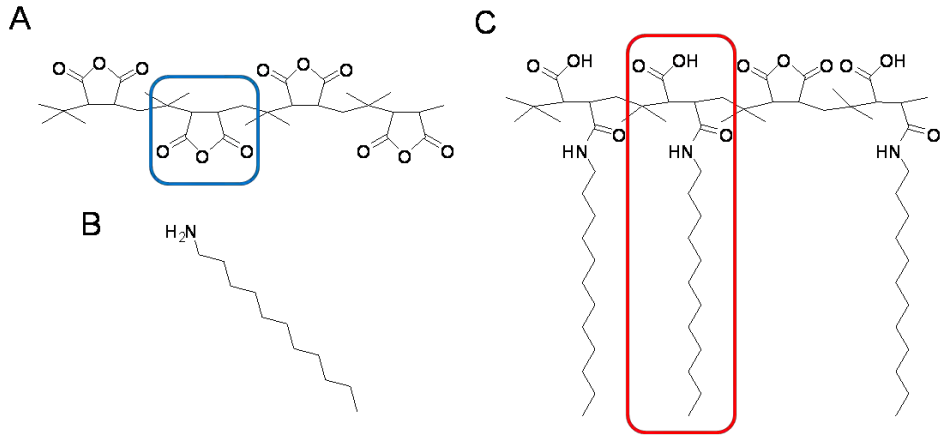

Figure SI-4: Structure of the amphiphilic polymer. A) Poly(isobutylene-alt-maleic anhydride) is used as hydrophilic backbone. The blue box shows one motif / monomer unit with a molecular weight of 154 g/mol. There are about 39 anhydride monomers in each polymer chain. B) Dodecylamine is used as hydrophobic side chain. C) The amphiphilic polymer was obtained by reaction of the hydrophilic backbone with hydrophobic side chains. The red box indicates one motif / monomer unit.

II.3) Coating of γ-Fe_2O_3 using the amphiphilic polymer

The polymer coating procedure was according to previous reports.[2-6] In this work we mixed solutions of amphiphilic polymer and hydrophobic γ-Fe_2O_3 NPs by a molar ratio of 100-200 polymer motifs per nm^2 of NP's effective surface area. The effective diameter D_{eff} of the NPs includes the hydrophobic surfactant shell around the inorganic cores and the inorganic core diameter itself. In the case of γ-Fe_2O_3 we assumed D_{eff} to be 11.9 nm. After mixing, the solvent was slowly evaporated under reduced pressure until the sample was completely dried. The remaining solid film in the flask was redissolved in SBB12 (sodium borate buffer, 50 mM, pH 12) under vigorous stirring until the solution turned clear. Hereby the amphiphilic polymer wrapped around the surface of the hydrophobic NPs and thus the coated NPs became soluble in SBB12 buffer. The polymer coated nanoparticles were then purified using HPLC (high performance liquid chromatography; Agilent 1100). We used a self-packed sephacryl S-300 HR column (GE Healthcare, Amersham Biosciences, #17-0599-10) or S-400 HR gel self-packed column (GE Healthcare, Amersham Biosciences, #17-0599-10). After the HPLC purification the eluted polymer coated γ-Fe_2O_3 NPs were concentrated by centrifuge filters (membrane: 100kDa Mw cut off PES, Sartorius Stedim, #VS2042) at ~2000 rpm. This was followed by additional filtering with 0.2 mm filters (Millipore) to get rid of any possible big aggregates. The purified samples were stocked in SBBS buffer (50 mM sodium borate, 100mM NaCl, pH 9.0).

III) Synthesis of micro capsules with hydrophilic γ-Fe_2O_3 nanoparticles in their wall

III.1) Chemicals
III.2) Synthesis of $CaCO_3$ cores
III.3) Layer by layer (LbL) assembly of polyelectrolytes on $CaCO_3$ cores and embedding of γ-Fe_2O_3 in the wall of capsules
III.4) Confocal laser scanning microscopy of hollow capsules
III.5) Transmission electron microscopy of hollow capsules (TEM)
III.6) Scanning electron microscopy of hollow capsules (SEM)
III.7) Inductive coupled plasma emission spectroscopy (ICP_OES)
III.8) Calculation of the number of γ-Fe_2O_3 nanoparticles per capsule

III.1) Chemicals

Poly(sodium 4-styrenesulfonate) (PSS, Mw ~70 kDa, Sigma-Aldrich #243051), poly(allylamine hydrochloride) (PAH, Mw ~56 kDa, Sigma-Aldrich #283223), poly(acrylamide-co-diallyl-dimethylammonium chloride) (P(Am-DDA, Mw 232.8 g/mol, Sigma-Aldrich #409081), calcium chloride dehydrate ($CaCl_2$, Sigma-Aldrich #223506), sodium carbonate (Na_2CO_3, Sigma-Aldrich #S7795), poly(fluorescein isothiocyanate allylamine hydrochloride) (PAH_{-FITC}, Mw ~56 kDa, Sigma-Aldrich #630209), ethylenediaminetetraacetic acid (EDTA, Sigma-Aldrich #E5134).

III.2) Synthesis of $CaCO_3$ cores

Microparticles of $CaCO_3$ were obtained from mixing solutions of calcium chloride ($CaCl_2$) and sodium carbonate (Na_2CO_3) under vigorous stirring.[7] Briefly, equal volumes (0.615 mL) of aqueous $CaCl_2$ and Na_2CO_3 solutions (0.33 M) and 0.77 mL of distilled water were mixed and thoroughly agitated on a magnetic stirrer for 30 s at room temperature. After agitation the mixture was left without stirring for 4 min at room temperature. The solution was then precipitated using centrifugation at 6000 rpm for 4 s. The supernatant was removed and precipitate was washed three times by adding 1 mL of distilled water and using the same centrifuge speed and time (i.e 600 rpm, 4 s) to remove the unreacted species. As last step the particles were washed with acetone and dried in vacuum.

III.3) Layer by layer (LbL) assembly of polyelectrolytes on $CaCO_3$ cores and embedding of γ-Fe_2O_3 in the wall of the capsules

Polyelectrolyte capsules were synthesized by using the layer by layer (LbL) technique on $CaCO_3$.[8] Briefly, the dried $CaCO_3$ cores were dispersed in 0.5 M NaCl solution containing negatively charged polymer PSS (2 mg/mL). The dispersion was sonicated and shaken for 12 minutes (2 min. sonication and 10 min. for shaking). After 12 minutes the particles were precipitated with centrifugation at a speed of 6000 rpm for 3-4 s and washed with distilled water three times to remove the excess and unreacted PSS. After three washing steps capsules were again dispersed in 0.5 M NaCl solution containing positively charged polymer PAH (2 mg/mL) for 12 minutes followed by three washing steps. After one more bi-layers of PSS and PAH one bi-layer of (PSS/P(Am-DDA)) was added. The strong positively charged polymer P(Am-DDA) was used using the same concentration (2 mg/mL) in 0.5 M NaCl solution. After addition of the (PSS/P(Am-DDA)) bi-layer the sample solution was divided into two parts. One part of the sample was then incubated in 1 mL of nanoparticle solution containing a low concentration of iron oxide nanoparticles for 12 minutes. The second part of the sample was incubated in 1 mL of nanoparticle solution with a high concentration of nanoparticles for 12 minutes. The reason for adding the strong positively charged polymer P(Am-DDA) before the addition of nanoparticles was to increase the attachment of polymer coated nanoparticles which were negatively charged. After nanoparticle addition again one bi-layer of (PSS/P(Am-DDA)) was added followed by the addition of one more layer of negatively charged nanoparticles at the respective concentrations. Finally two bi-layers of (PSS/PAH) were added. Hereby one layer contained PAH conjugated with FITC fluorophore (PAH_{-FITC}) to make the wall of the capsules fluorescent. In this way the morphology of the capsules could be observed with confocal microscopy after dissolution of the $CaCO_3$ cores. After addition of each layer the sample was sonicated for two minutes to reduce aggregation of $CaCO_3$ particles. The final structure of capsules was $(PSS/PAH)_2(PSS/P(Am\text{-}DDA)/\gamma\text{-}Fe_2O_3)_2(PSS/PAH_{-FITC})(PSS/PAH)$. In a next step, the $CaCO_3$ cores were removed by complexation with EDTA. Coated $CaCO_3$ particles were shaken for 2 min with 1 mL of an EDTA solution (0.2 M, pH 5.5), followed by centrifugation and redispersion in 1 mL of a fresh EDTA solution (0.2 M, pH 7). The obtained hollow microcapsules were washed five times with 1 mL distilled water. The microcapsules were finally stored as suspension in water at 4 ^{0}C.

III.4) Confocal laser scanning microscopy (CLSM) images of hollow capsules

After the dissolution confocal laser scanning microscopy (CLMS) was used to take images of the capsules. For this purpose the wall of the capsules had been made fluorescent by adding one layer of poly(fluorescein isothiocyanate allylamine hydrochloride) (PAH_{-FITC}) during the layer by layer assembly on the $CaCO_3$ cores. All the fluorescence images were taken by a confocal laser scanning microscope (CLSM 510 META, Zeiss, Germany). The Ar/Kr laser (488 nm) was used to excite the FITC. Samples were observed through a 100X/1.45 NA oil-immersion PLAN-FLUOAR objective. A 20 μL drop of sample was placed onto a cover glass and imaged in liquid.

III.5) Transmission electron microscopy of hollow capsules (TEM)

To see the distribution of γ-Fe_2O_3 in the wall of polyelectrolyte capsules transmission electron microscope (TEM) images were taken. For TEM analysis the samples were prepared by putting a drop with low concentration of capsules on a Formvar®/carbon coated TEM-grid (300 Mesh 3.05 mm Copper, Plano GmBH) and dried at room temperature before imaging. All the images were taken on JEM 3010 high-resolution electron microscope (Jeol Ltd., Tokyo, Japan) operating at an accelerating voltage of 300 kV.

III.6) Scanning electron microscopy of hollow capsules (SEM)

To see the morphology of the hollow polyelectrolyte capsules after the dissolution of the $CaCO_3$ core scanning electron microscopy (SEM) was performed. SEM analysis was performed on a JEOL JSM-7500F SEM at an operation voltage of 2.00 kV. For the SEM recording a drop with low concentration of capsules was placed on a glass cover and dried in vacuum before the SEM analysis.

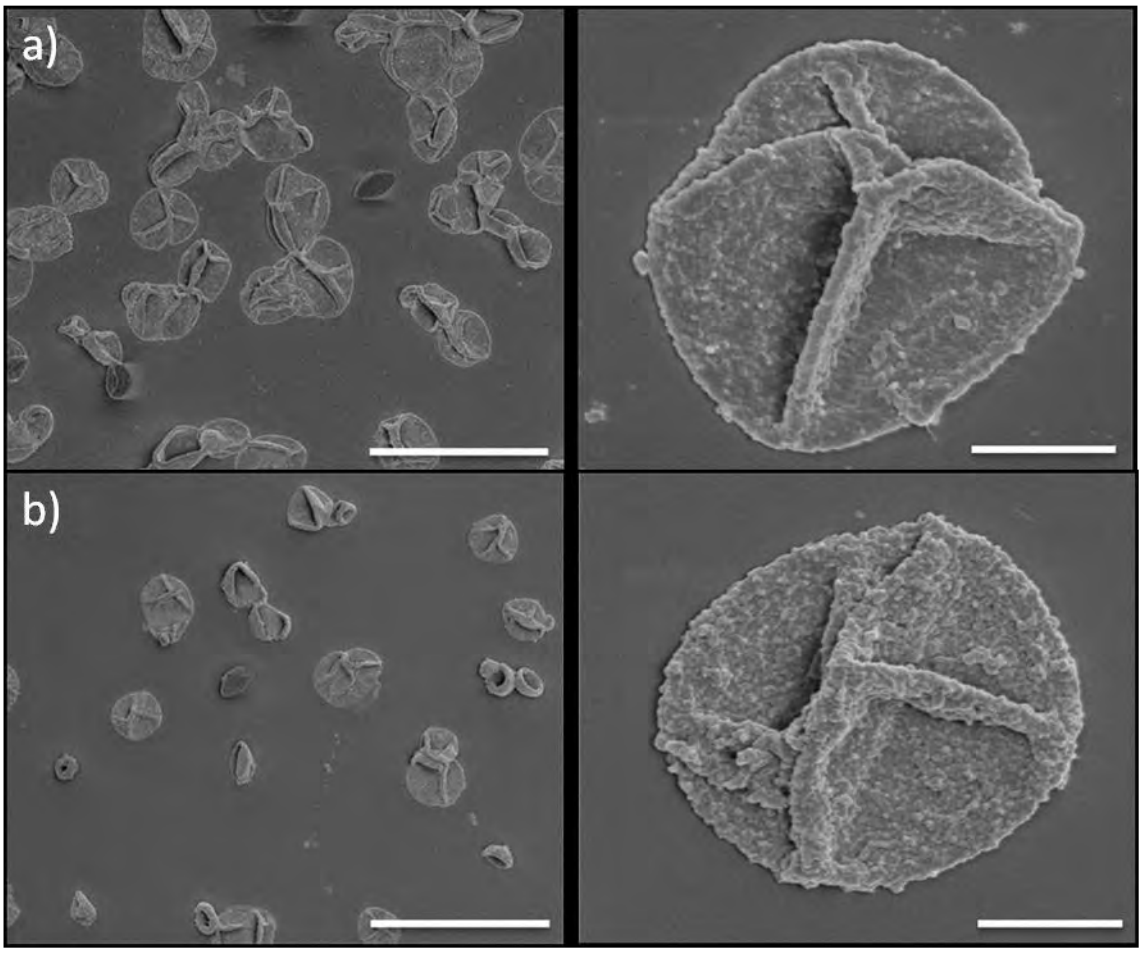

Figure SI-5: SEM images of $(PSS/PAH)_2(PSS/P(Am\text{-}DDA)/\gamma\text{-}Fe_2O_3)_2(PSS/PAH_{FITC})(PSS/PAH)$ polyelectrolyte capsules after core removal. a) Capsules with low concentration of γ-Fe_2O_3 nanoparticles. b) Capsules with high concentration of γ-Fe_2O_3 nanoparticles. Capsules collapse after core removal indicating the absence of the cores in their cavities. Scale bars represent 10 μm (left column), 1 μm (right column).

III.7) Inductive coupled plasma emission spectroscopy (ICP-OES)

The number of γ-Fe_2O_3 nanoparticles per capsules was calculated by using concentration of Fe in the capsule samples as obtained from Inductively Coupled Plasma Optical Emission Spectrometer (ICP-OES). ICP-OES measurements were performed on a PERKIN ELMER OPTIMA 2100 DV. For the ICP-OES measurements 0.1 mL of sample from the original stock was digested with 1 M concentrated nitric acid using 0.1 mL to oxidize the organic coating around the particles. Then 0.1 mL of 12 M hydrochloric acid was used to dissolve the iron oxide nanoparticles. The concentrations of iron obtained from ICP measurements were 0.932, 0.227 and 0.0532 mg/mL for the nanoparticles freely dispersed in SBBS buffer, and for high density and for low density of γ-Fe_2O_3 in the wall of polyelectrolyte capsules, respectively. We calculated that one 10.8 nm γ-Fe_2O_3 nanoparticle contains $2.61\text{x}10^4$ atoms of Fe. Using this number we calculated the total number of γ-Fe_2O_3 nanoparticles which was $(2.61\text{x}10^4)^{-1}$ times the total number of Fe atoms in the solution. We also determined the concentration of capsules for each sample by counting the number of capsules in an aliquot using the microscope in phase contrast mode. We found that each sample contained 10^8

capsules. Finally the number of γ-Fe_2O_3 NP per capsule was obtained by simply dividing the total number of γ-Fe_2O_3 NPs by the total number of capsules for each sample.

III.8) Calculation of the number of nanoparticles per capsule

III.8.1) Counting of the number of capsules

The number of capsules was determined by counting the number of capsules in an aliquot by using a hemocytometer chamber (cfg. Fig. SI-6) under a microscope in phase contrast mode. This was done by putting a drop of a diluted solution of capsules onto the chamber. The number of capsules deposited into the four regions marked by crossed double lines was then counted by using a 20X objective. Then the number of counted capsules in each region was averaged and multiplied by the volume of the capsule solution and by a factor of 10^4 (Formula: average n° of capsules x volume of capsule solution x 10^4). Finally, the obtained number is multiplied by the dilution factor used to dilute the stock solution of capsules. We found that each sample contains 10^8 capsules.

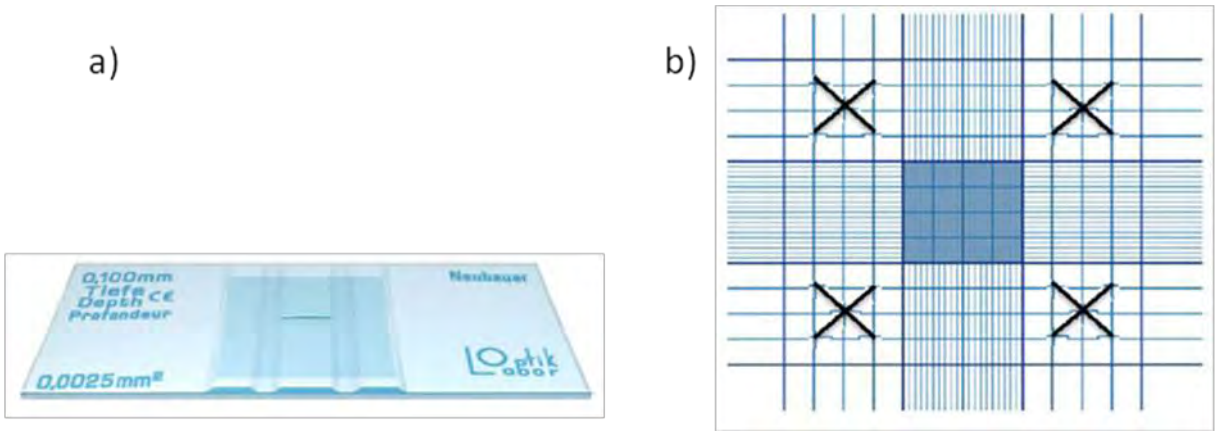

Figure SI-6: a) Hemocytometer chamber used for the counting of capsules b) Image of the chamber from the top showing the region with cross in which capsules were counted.

III.8.2) Calculation of the number of γ-Fe_2O_3 nanoparticles in each sample

To calculate the number of iron oxide nanoparticles for each sample, we measured the number of Fe atoms for each sample.[9] In the calculation we use the following symbols:

p: refers to particles

a: refers to atoms

u: refers to unit (one unit corresponds to two Fe and three O atoms)

$m_{a,Fe}$: refers to the mass of one Fe atom

$m_{a,O}$: refers to the mass of one O atom

$m_{u,Fe2O3}$: refers to the mass of one unit of Fe_2O_3 containing two Fe and three O atoms

ρ_{Fe2O3}: refers to the density of γ-Fe_2O_3

$V_{p,Fe2O3}$: refers to the volume of one γ-Fe_2O_3 nanoparticle (diameter 10.8 nm)

$m_{p,Fe2O3}$: refers to the mass of one γ-Fe_2O_3 nanoparticle (diameter 10.8 nm)

$N_{a,Fe}$: refers to the number of Fe atoms in one γ-Fe_2O_3 nanoparticle

$N_{u,Fe2O3}$: refers to the number of Fe_2O_3 units (two Fe and three O) per γ-Fe_2O_3 nanoparticle

$N_{p,Fe2O3}$: refers to the number of γ-Fe_2O_3 particles in the sample solution
N_{Fe} = number of detected Fe atoms within the sample solution
c_{Fe} = concentration of Fe atoms in sample solution
V = Volume of sample solution
N_{caps} = number of capsules in the sample solution
To calculate the number of γ-Fe_2O_3 nanoparticle for each sample in the first step we calculated the mass of one 10.8 nm γ-Fe_2O_3 using the formula $\mathbf{m_{p,Fe2O3} = \rho_{Fe2O3} \cdot V_{p,Fe2O3}}$, where $\mathbf{\rho_{Fe2O3}}$ is the density of γ-Fe_2O_3 which is **5.25g/cm^3** and $\mathbf{V_{p,Fe2O3}}$ is the volume of one γ-Fe_2O_3 nanoparticle calculated using the formula $\mathbf{V_{p,Fe2O3} = 4/3\ \pi\ r^3}$**.** Here **r** is the radius of the γ-Fe_2O_3 nanoparticles of 10.8 nm. The calculated volume $\mathbf{V_{p,Fe2O3}}$ is **6.6x10^{-19} cm^3**. Thus the mass of one γ-Fe_2O_3 nanoparticle **($\mathbf{m_{p,Fe2O3}}$)** was calculated to be **3.46x10^{-18} g**.
The total atomic mass of one Fe atom ($\mathbf{m_{a,Fe}}$) is **9.2x10^{-23} g.** The total atomic mass of one O atom **($\mathbf{m_{a,O}}$)** is **2.6x10^{-23} g**. The total mass of one unit of two Fe and three O atoms is **($\mathbf{m_{u,Fe2O3}}$)** is **2.2x10^{-22}** g. The total number of Fe_2O_3 units **($\mathbf{N_{u,Fe2O3}}$)** per particle was obtained by dividing the mass of one γ-Fe_2O_3 nanoparticle **($\mathbf{m_{p,Fe2O3}}$)** by the total mass of one unit of two Fe and three O atom**s ($\mathbf{m_{u,Fe2O3}}$)**. We found **1.3x10^4** units of two Fe and three O atoms per nanoparticle. Each unit contains two Fe atoms. Thus the total number of Fe atoms **($\mathbf{N_{a,Fe}}$)** in one γ-Fe_2O_3 nanoparticle is two times the total number of units with two Fe and three O atoms. In this way there are **2.6x10^4** Fe atoms in one γ-Fe_2O_3 nanoparticle of 10.8 nm diameter **($\mathbf{N_{a,Fe}}$).**

i) γ-Fe_2O_3 freely dispersed in SBBS buffer
From the ICP-OES measurements we got the concentration of Fe in the sample solution ($\mathbf{c_{Fe}}$): $\mathbf{c_{Fe}}$ = **1.67 x 10^{-5}mol / mL**. From the obtained Fe concentration $\mathbf{c_{Fe}}$ we got the total number of Fe atoms **($\mathbf{N_{Fe}}$)** within the sample by using the formula $\mathbf{N_{Fe} = c_{Fe} \cdot V \cdot N_A}$ with the Avogadro number $\mathbf{N_A}$ **= 6.02x10^{23} mol^{-1}**. The volume of the samples was **V = 1 mL** which lead to the number of Fe atoms in the sample of $\mathbf{N_{Fe}}$ **= 1.0x10^{19}**. As one γ-Fe_2O_3 particle contains **2.6x10^4 ($\mathbf{N_{a,Fe}}$)** Fe atoms the number of γ-Fe_2O_3 nanoparticle in the sample solution ($\mathbf{N_{p,Fe2O3}}$) was calculated by dividing $\mathbf{N_{Fe}}$ by $\mathbf{N_{a,Fe}}$. The calculated value was $\mathbf{N_{p,Fe2O3}}$ **= 3.8x10^{14}**.

ii) Calculation of number of γ-Fe_2O_3 particles per capsule for the low density sample
Knowing the concentration of Fe **($\mathbf{c_{Fe}}$)** for the sample we used the same method as described in i) to calculate the number of γ-Fe_2O_3 particles. Finally the number of γ-Fe_2O_3 nanoparticles per capsules was obtained by dividing the total number of γ-Fe_2O_3 nanoparticles in the sample with total number of capsules in the sample.
$\mathbf{c_{Fe}}$ = **9.5 x10^{-7}mol / mL** as determined with ICP-OES on sample **V = 1 mL**
$\Rightarrow$ $\mathbf{N_{Fe}}$**= 5.7x10^{17}** (number of Fe atoms in the sample)
$\Rightarrow$ $\mathbf{N_{p,Fe2O3}}$ **= 2.2x10^{13}** (number of γ-Fe_2O_3 particles in the sample)
$\mathbf{N_{caps}}$ **= 3.0 x10^8** (number of capsules in the sample as determined by counting)
$\Rightarrow$ $\mathbf{N_{p,Fe2O3}}$ **/** $\mathbf{N_{caps}}$ **= 2.2x10^{13} / 3.0 x10^8 = 7.15x10^4** (number of nanoparticles per capsule)

iii) Calculation of number of γ-Fe_2O_3 nanoparticles per capsule for the high density sample
Using the same method as in i) we calculated the number of γ-Fe_2O_3 NPs per capsules
$\mathbf{c_{Fe}}$ = **4.0 x10^{-6}mol / mL** as determined with ICP-OES on sample **V = 1 mL**

$\Rightarrow$ $\mathbf{N_{Fe} = 2.4x10^{18}}$ (number of Fe atoms in the sample)

$\Rightarrow$ $\mathbf{N_{p,Fe2O3} = 9.3x10^{13}}$ (number of γ-Fe_2O_3 particles in the sample)

$\mathbf{N_{caps} = 3.2\ x10^{8}}$ (number of capsules in the sample as determined by counting)

$\Rightarrow$ $\mathbf{N_{p,Fe2O3} / N_{caps} = 9.3x10^{13} / 3.2\ x10^{8} = 2.8x10^{5}}$ (number of nanoparticles per capsule)

III.8.3) Calculation of the packing fraction

The packing fraction for a low and high density of nanoparticles in the volume of the capsule wall was obtained by dividing the total volume of nanoparticles in each sample by the volume of the capsule walls in which the nanoparticles are distributed. First volume in which the nanoparticles are distributed was calculated. This was done by multiplying the thickness of the wall of capsules and the surface area of capsules. The thickness of one polyelectrolyte layer is ~1.5 nm.[10] The wall of each capsule is made of six bi-layers leading to a total thickness of the wall of 18 nm. The surface area of spherical capsules was calculated to be $\mathbf{4\pi r^2}$, where **r** is the radius of one capsules. The capsule radius is r = 1.9 μm as obtained from CLSM and TEM images of the hollow capsules (diameter D= 3.8 ± 0.5 μm). The obtained value for surface area of one capsule was $\mathbf{4.5x10^{-7}\ cm^2}$. This leads to a value for the volume of each capsule in which the nanoparticle are distributed of $\mathbf{8.16\ x10^{-13}\ cm^3}$. Next we calculated the total volume of the nanoparticles which was obtained by multiplying the volume of one γ-Fe_2O_3 nanoparticle of 10.8 nm diameter with the total number of nanoparticle per capsule. Finally the packing fraction was obtained by dividing the calculated total volume of nanoparticles by the obtained volume of the capsule wall in which the nanoparticle are distributed.

IV) Numerical modeling details

We consider an ensemble of nanoparticles which are described as interacting macrospins. The total energy of the system is the sum of the anisotropy, Zeeman, and dipolar-dipolar contributions:

$$E = -K\sum_i (\mathbf{m}_i\mathbf{e}_i)^2 V_i - M_s\sum_i (\mathbf{H}\mathbf{m}_i) M_s V_i - \frac{1}{2}M_s^2\sum_{i,j} V_i V_j\left[\frac{(\mathbf{m}_i\mathbf{m}_j)}{r_{ij}^3} - \frac{3(\mathbf{m}_i\mathbf{r}_{ij})(\mathbf{m}_j\mathbf{r}_{ij})}{r_{ij}^5}\right] \qquad (1)$$

Here m_i is the magnetic moment for the nanoparticle i, e_i is the anisotropy direction, K is the anisotropy constant, M_s is the saturation magnetization value, V_i is the nanoparticle volume, H is the applied field and r_{ij} is the vector connecting the position of the nanoparticle i with the nanoparticle j. We generate an ensemble of nanoparticles with a log-normal distribution having the most probable diameter D = 10 nm and 10% of the volume dispersion. The nanoparticles are distributed inside a cube in two geometries: (a) uniform volume distribution and (b) uniform distribution within a surface layer of 18 nm on a sphere with a given diameter (see Fig. SI-9). To avoid the edge effects, periodic boundary conditions were applied. We consider nanoparticles in a macrospin approximation with saturation magnetization values Ms = 400 emu/cm3 and two possible values of the anisotropies K= 4.6 104 erg/cm3 and K= 3.3 105 erg/cm3. The anisotropy axes are considered distributed randomly.

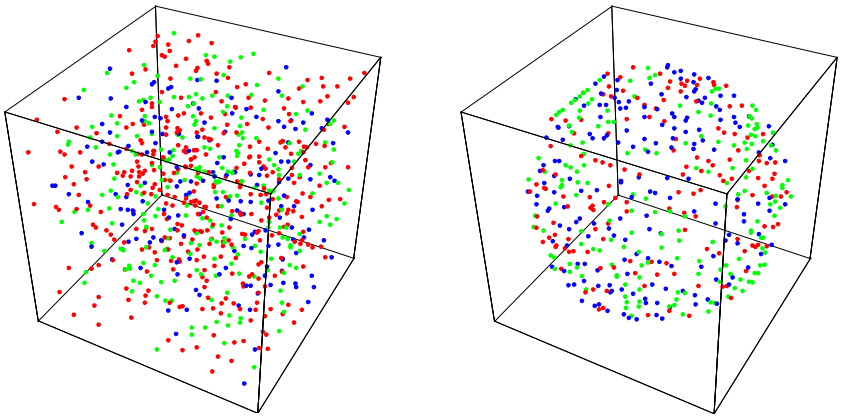

Figure SI-7: Modeled systems: (left) uniformly distributed nanoparticle ensemble (right) nanoparticles distributed on the surface of a capsule. Periodic boundary conditions are assumed.

The total energy of the system was minimized using the integration of the Landau-Lifshitz-Gilbert equation of motion. To prepare the initial state the system was slowly quenched under a decreasing applied field. The averaged dipolar field and energy barriers were evaluated in zero applied field. To evaluate energy barriers ΔE_B^i for low packing densities we used the Pfeiffer approximation.[11-12]

$$\Delta E^{i}{}_{Pf} = K_i V_i [1 - h^{i}{}_{\text{int}} / g_i(\phi)]^{k(\phi)}$$

$$\Delta E^{i}{}_{B} = \begin{cases} \Delta E^{i}{}_{Pf} & (m_i, h^{i}{}_{\text{int}}) < 0 \\ \Delta E^{i}{}_{Pf} + E^{2}_{i,\min} - E^{1}_{i,\min} & (m_i, h^{i}{}_{\text{int}}) > 0 \end{cases}$$

where the interaction field $h^{i}{}_{int}$ contains the local dipolar field, normalized to the anisotropy field $H_K{}^{i}=2K_i/Ms$. The function $g_i(\phi_i)$ depends on the angle between the local dipolar field and the anisotropy field and is defined as

$$g_i(\phi_i) = [\cos^{2/3}(\phi_i) + \sin^{2/3}(\phi_i)\ ]^{-3/2}$$
$$k_i(\phi_i) = 0.86 + 1.14 g(\phi_i)$$

The values $E^{1}{}_{i,\,min}$ and $E^{2}{}_{i,\,min}$ denote the two energy minima of the individual nanoparticle i ,evaluated by minimizing the total system energy. Note that each nanoparticle has two individual energy barriers and only the largest one is relevant for the blocking temperature. The Pfeiffer approximation is a local approximation for the individual energy barrier of each nanoparticle. It is valid for a relatively weak interaction strength of approximately 0.2 H_K.[13-14] For a larger packing fraction, the obtained energy barriers were corrected using the augmented Hessian method in a multidimensional space.[13-15]

To evaluate the blocking temperature we assume the Arrhenius-Neel law for the switching time of each nanoparticle:

$$\tau_i = \tau_0 \exp(-\Delta E^{i}_{B} / k_B T)$$

where k_B is the Bolzmann constant, T is the temperature and the reversal constant τ_0=9 10^{-13} s was taken from Ref [16]. For the measurement time approximately *1 ms* this corresponds to the blocking condition $\Delta E^{i}_{B} > 20.8\ k_B T$. The blocking temperature was defined from the condition that 90% of the nanoparticles are in the blocked state.

V. References

1. T. Hyeon, S. S. Lee, J. Park, Y. Chung and H. B. Na, *Journal of the American Chemical Society*, 2001, **123**, 12798-12801.
2. C.-A. J. Lin, R. A. Sperling, J. K. Li, T.-Y. Yang, P.-Y. Li, M. Zanella, W. H. Chang and W. J. Parak, *Small*, 2008, **4**, 334-341.
3. M. T. Fernández-Argüelles, A. Yakovlev, R. A. Sperling, C. Luccardini, S. Gaillard, A. S. Medel, J.-M. Mallet, J.-C. Brochon, A. Feltz, M. Oheim and W. J. Parak, *NanoLetters*, 2007, **7**, 2613-2617.
4. T. Pellegrino, L. Manna, S. Kudera, T. Liedl, D. Koktysh, A. L. Rogach, S. Keller, J. Rädler, G. Natile and W. J. Parak, *Nanoletters*, 2004, **4**, 703-707.
5. R. A. Sperling, T. Pellegrino, J. K. Li, W. H. Chang and W. J. Parak, *Adv. Funct. Mater.*, 2006, **16**, 943-948.
6. A. V. Yakovlev, F. Zhang, A. Zulqurnain, A. Azhar-Zahoor, C. Luccardini, S. Gaillard, J. M. Mallet, P. Tauc, J. C. Brochon, W. J. Parak, A. Feltz and M. Oheim, *Langmuir*, 2009, **25**, 3232-3239.
7. D. V. Volodkin, A. I. Petrov, M. Prevot and G. B. Sukhorukov, *Langmuir*, 2004, **20**, 3398-3406.
8. O. Kreft, A. Muñoz_Javier, G. B. Sukhorukov and W. J. Parak, *J. Mater. Chem.*, 2007, **17**, 4471-4476.
9. M. P. Morales, M. F. Bedard, A. G. Roca, P. de la Presa, A. Hernando, F. Zhang, M. Zanella, A. Z. Abbasi, G. B. Sukhorukov, L. L. del Mercato and W. J. Parak, *J. Mater. Chem.*, 2009, **19**, 6381-6386.
10. A. Diaspro, D. Silvano, S. Krol, O. Cavalleri and A. Gliozzi, *Langmuir*, 2002, **18**, 5047-5050.
11. H. Pfeiffer, *Physica Status Solidi a-Applied Research*, 1990, **122**, 377-389.
12. M. El-Hilo, R. W. Chantrell and K. O'Grady, *Journal of Applied Physics*, 1998, **84**, 5114-5122.
13. O. A. Chubykalo and R. W. Chantrell, *Journal of Magnetism and Magnetic Materials*, 2004, **272**, E1169-E1171.
14. O. Chubykalo-Fesenko, K. Guslienko, T. J. Klemmer, X. W. Wu, R. W. Chantrell and D. Weller, *Physica B-Condensed Matter*, 2006, **382**, 235-244.
15. O. Chubykalo-Fesenko and R. W. Chantrell, *Journal Of Applied Physics*, 2005, **97**.
16. G. F. Goya, T. S. Berquo, F. C. Fonseca and M. P. Morales, *Journal of Applied Physics*, 2003, **94**, 3520-3528.

Synthesis and characterization of ratiometric ion-sensitive polyelectrolyte capsules

Loretta L. del Mercato[1], Azhar Z. Abbasi[1], Wolfgang J. Parak[1,*]

[1] Fachbereich Physik and Wissenschaftliches Zentrum für Materialwissenschaften, Philipps Universität Marburg, Marburg (Germany)

Email: Wolfgang J. Parak (wolfgang.parak@physik.uni-marburg.de)

*Correspondence to Wolfgang J. Parak, Fachbereich Physik and Wissenschaftliches Zentrum für Materialwissenschaften, Philipps Universität Marburg, Marburg (Germany)

Supporting Information is available on the WWW under http://www.small-journal.com or from the author.

Keywords: Polymeric Capsules; Ion Sensing; Ratiometric Sensor; Fluorescence; Nanotechnology

Abstract

Micrometer-sized polyelectrolyte capsules are synthesized, which had ion-sensitive fluorophores embedded in their cavities. As the membranes of the capsules are permeable to ions, the fluorescence of the capsules changes with the ion concentration. In particular capsules sensitive for proton, sodium, potassium, and chloride ions are fabricated and their fluorescence response analyzed. In order to allow for ratiometric measurements additional fluorophores whose emission does not depend on the ion concentration and which are emitting at a different wavelength are co-embedded in the capsule cavities.

1. Introduction

Sensing analyte concentrations plays a pivotal role for numerous studies in the bio-medical field, ranging from cell biology to diagnostics. In cells there is a large difference in the concentration of ions, such as protons (H^+), sodium (Na^+), calcium (Ca^{2+}), potassium (K^+) and chloride (Cl^-), between the intracellular and extracellular environments. For instance, the concentration of K^+ is normally 30-50 times greater in the intracellular space compared to the extracellular, whereas the intracellular Na^+ concentration is lower than the extracellular.[1] Variations of any of these ions in the body or inhibition of their transport across the cell membranes can initiate processes which finally compromise cell viability leading to pathological disturbances.[2-6] Therefore, real-time measurements of the difference in the intra- and extracellular concentration of the aforementioned analytes may give crucial information about the activity, integrity and functionality of the cells.

In the last decades, many types of ion sensitive sensors, mainly based on optical detection, have been developed.[7-12] Fluorescence ion sensors are typically based on the feature of the sensor to reversibly change its optical properties upon chemical interaction with the corresponding analyte (i.e., fluorescence intensity changes, or spectral shifts in either absorption or emission spectra). The changes are used to determine the analyte concentration. Major advantages of this class of sensors over conventional electrochemical approaches include their fast response and their relatively intense signal, as well as the possibility to use simple instrumentation to read the output signals. Disadvantages lie on the potential cytotoxicity of the dye molecules purely injected into the cells, on the eventual inactivation of the dyes by sequestration into specific organelles or by their non-specific binding to proteins and other cell components. Moreover, it is hard to perform ratiometric measurements because the ratiometric probes (dyes which have dual excitation or emission peaks) are few and they are complicated to synthesize. Thus it is often required to inject into the cell a separate reference dye (a fluorescent dye which fluorescence is not affected upon different ion concentrations) to ensure accurate analysis of ions levels. Finally, by free injection of sensor probes into the cells it is difficult to measure several analytes in parallel. In order to circumvent some of these limitations, considerable research effort has been shifted towards the development of fluorescence sensors based on new strategies. One approach consists on combining the fluorescence indicators to nano- or micrometer sized particulate systems, such as solid particle matrices,[8, 13-16] liposomes,[17, 18] vesicles[19] or polyelectrolyte multilayer capsules,[12, 20-23] which act as carriers of the sensing component. As result, the fluorescent sensor is confined to a small volume, protecting it from the cellular environment, and conversely, protecting the cell from chemical pertubation by the sensor[24]. Also, by loading similar nano- and microparticle carriers with fluorophores sensitive to different ions, ion-sensitive probes having the same surface chemistry but which respond to different ions, can be made. This is in contrast to plain ion-sensitive dyes, of which dyes for different ions typically possess different chemical structure and therefore surface chemistry.

In this study, we describe the synthesis of ratiometric sensor systems based on polyelectrolyte microcapsules for sensing of H^+, Na^+, K^+ and Cl^- ions. We have chosen polyelectrolyte capsules as platform because of the possibility offered by such system to combine different functions for each individual sensor.[25-28] Each sensor consists of the indicator and the reference dye separately conjugated to dextran molecules and entrapped within the cavity of the multilayer capsule. Such configuration enables ratiometric measurements of each ion by measuring the ratio of the fluorescent indicator peak to the fluorescent reference dye peak. Similarly to NPs-based sensors, [7, 15, 29] the sensing mechanism is based on the permeation of analytes (ions) into the cavity of the capsules followed by their binding to the sensing element (Scheme 1). In this approach, a change of the fluorescence signal of the sensor is detected after its interaction to the analyte. The response of the free fluorescent probes has been compared to the probes after their linking to the dextran molecules as well as after their encapsulation in order to assess that the intermediate steps did not affect the activity of the indicators. The resulting capsules displayed a ratiometric output in solution detectable by both fluorescence spectroscopy and fluorescence microscopy.

2. Results

2.1. H^+-sensor capsules based on FITC as fluorescent indicator

Fluorescein isothiocyanate (FITC) displays pH-indicative properties.[30] The dye is characterized by a pK_a of ~6.5 and its ionization equilibrium leads to pH-dependent fluorescence over a range of 5 to 9.[30] **Figure 1** shows the fluorescence intensity ratio (g/r), obtained by fluorimetric cuvette measurements, for free (square), dextran-conjugated (circle) and encapsulated dextran-conjugated (triangle) FITC and AF594 with increasing pH values (2.0 to 11). For the sake of clarity, the form "green-yellow to red ratio" is hereinafter used to refer to all ratio measurements of FITC/AF594, whereas the abbreviation "I_g/I_r" is used to refer to all the fluorescence intensity ratios of FITC/AF594. The green-yellow to red ratio for each pH value has been calculated by dividing the fluorescence intensity at 520 nm (FITC, indicator dye) to the fluorescence intensity at 610 nm (AF594, reference dye) (the corresponding fluorescence emission spectra are displayed in **SI**, **Figure SI-8**). The resulting I_g/I_r has been plotted against corresponding pH values of buffer **(Figure 1)** and the data points fitted with a Boltzmann sigmoid function using the equation:

$$\frac{I_g}{I_r}(pH) = \frac{I_a - I_b}{1 + \exp\left(\frac{pH - pH_{inf}}{\Delta pH}\right)} + I_b \qquad \textbf{Eq. 1}$$

where I_g/I_r are the measured data points, I_a is the value of the I_g/I_r curve at low pH values which is considered as the acidic titration endpoint, and I_b is the value of the I_g/I_r curve at high pH values which is considered as the basic titration endpoint as well, pH_{infl} describes the point of inflection of the I_g/I_r curve, i.e. the pH value at which the slope of the curve is maximum.[8] From the fit of the I_g/I_r data, the fit parameters I_a, I_b, pH_{infl} and ΔpH were determined for each set of spectra (see also **SI**, **Figure SI-19**). The graphs reported in **Figure 1** show an increase

of the fluorescence intensity in the range between pH 2.0 and 11 for each analyzed system. The fluorescence response trend of FITC-/AF594-dextran was almost identical to those of free FITC and AF594 (see also fluorescence spectra in **SI**, **Figure SI-8**), indicating that the conjugation of the dye to amino-dextran does not impair the sensitivity of the dye. Furthermore, the fluorescence trend of encapsulated FITC-/AF594-dextran was almost comparable to the trend of free dyes and dextran-conjugated dyes. A point of inflection (pH_{infl}) of 4.9, 6.2 and 5.6 was found for the free dyes, dye-dextran conjugates and encapsulated dye-dextran conjugates, respectively. However, there are some changes in the intensity ratios of the FITC-dextran and AF594-dextran after encapsulation in comparison to the free and conjugated indicator dyes. These changes might reflect the presence of a higher concentration of FITC-dextran inside the capsules compared to AF594-dextran (see also **SI**, **Figure SI-8**). It has to be pointed out that the fluorimetric titration measurements of free dye and dye-dextran conjugates were performed by keeping the concentration of both the indicator and reference dyes constant in the investigated solutions (12.5 μM each). In this way, slight differences in the overall intensity of all the readings were mainly attributed to the small variations of the dye concentration during sample preparation and cuvette measurements. Instead, in the case of encapsulated samples, we analyzed capsules with a lower concentration of embedded dye-dextran conjugates (see **SI**, **Table 1**). For this reason, the three curves shown in **Figure 1** should be compared in terms of trend of the fluorescence and not in terms of intensity, since the last comparison is difficult because the concentration of dye-dextran conjugates inside the capsules is lower than the free and conjugated dyes in solution. Despite these changes in the intensity of the fluorescence, the difference in the g/r ratio of capsules is still efficiently detected in the whole investigated range. These results indicate that once loaded in the capsule cavities FITC-/AF504-dextran can efficiently senses different pH values in the surrounding bulk solution, thus making such capsules suitable for pH-sensing measurements.

The response of FITC-/AF594-dextran loaded capsules was then analyzed by fluorescence microscopy. For this purpose, a 20 μL drop of capsules was resuspended in a solution of buffer with the desired pH value and deposited onto a glass coverslip (see **SI, Figure SI-21**). Figure 2a shows the fluorescence response of the capsules in buffer solution at pH 5.0 and pH 9.0. As expected, the fluorescence of FITC-dextran decreases at acidic pH and increases at basic pH. In contrast, the red fluorescence of AF594-dextran remains constant at different pH values (the response of the capsules has been recorded over the whole pH range 2.0-11 and the corresponding data are reported in the **SI**, **Figure SI-22**). For homogeneity, the fluorescence signals of all ion-sensitive dyes (FITC, SNARF, SBFI, PBFI and amino-MQAE) are shown as false colors in green in all the microscopy images and the corresponding channel is abbreviated by using the letter "g". To quantify the pH-depending response of the FITC-/AF594-dextran loaded capsules, the fluorescence microscopy images were processed by ROI-analysis as described above (see Material and Methods). Some examples of measured ROIs are reported in **Figure 2a**. **Figure 2b** contains a plot of peak ratio (I_g/I_r) as a function of proton concentration obtained by quantifying the fluorescence intensity of green-yellow and

red signals. These were detected inside single capsules exposed to buffer solutions with pH from 2.0 to 11 (30 capsules were analyzed for each pH value). The I_g/I_r data points were again fitted with eq. 1 (fit parameters values are shown in the corresponding graph). According to the fluorescence images, the ratio-imaging data confirmed that there is a sigmoid relationship between FITC fluorescence increase and proton concentration. This analysis does not only confirm the previous data obtained by fluorimteric titration analysis of encapsulated dye-dextran conjugates (**Figure 1**, triangles), but also shows that ROI-analysis can be applied to quantify via software fluorescence changes of both, the indicator and the reference dyes embedded into the capsule cavities.

2.2. H^+-sensor capsules based on SNARF as fluorescent indicator

pH-sensitive capsules based on SNARF as indicator dye were also fabricated as alternative system to FITC-based sensor for pH-sensing. SNARF offers the advantage to perform ratiometric measurements without the requirement of a reference dye. Upon basification, SNARF typically exhibits a shift from yellow to red fluorescence (hereinafter abbreviated as "green-yellow to red ratio" and I_g/I_r). The pH-dependency of the fluorescence of free SNARF, SNARF conjugated to dextran and capsules loaded with SNARF-dextran was tested and evaluated by means of fluorescence spectroscopy and fluorescence microscopy. **Figure 3** shows the fluorescence intensity ratio (I_g/I_r), recorded by fluorimetric analysis of SNARF in solution (squares), SNARF-dextran in solution (circles) and SNARF-dextran loaded capsules (triangles) with increasing pH values (2.0 to 11). The green-yellow to red ratio for each pH value has been obtained by dividing the fluorescence intensity at 585 nm (I_g) by the fluorescence intensity at 640 nm (I_r) (the corresponding fluorescence spectra are displayed in **SI**, **Figure SI-9**). The results show that the SNARF dye conjugated to dextran, before and after encapsulation, can still sense different pH values in the surrounding bulk solution. Except for small differences in the overall intensity, the trends of the I_g/I_r ratios of free SNARF and SNARF-dextran, before and after encapsulation, are substantially the same (see also **SI**, **Figure SI-9**). The SNARF emission peaks are at approximately the same spectral position in both the solution and capsules (see also **SI**, **Figure SI-9**). A clear sigmoid curve as a function of proton concentration has been observed when I_g/I_r data points of every type of SNARF were fitted with eq. 1 **(Figure 3)**, only slight differences in the slope of the (I_g/I_r) versus pH curve can be observed. Additionally, the data reported in **Figure 3** demonstrate that the conjugation of the SNARF to dextran and its encapsulation did not significantly affect the sensitivity of the fluorophore. In contrast to the pH-sensitive capsules based on FITC as indicator dye and AF594 as reference dye, such sensor capsules are loaded with only one type of dye-dextran conjugate, the SNARF-dextran. In this way, the I_g/I_r ratio of SNARF capsules is calculated by measuring the fluorescence changes of only one dye.

Figure 4a shows the fluorescence images of SNARF-dextran loaded capsules in buffer solution at pH 5.0 and 9.0. Also in this case, the response of the capsules has been recorded over the whole pH range 2.0-11 (**SI**, **Figure SI-23**). As expected, the green-yellow fluorescence signal increases at acidic pH and decreases at basic pH. Differently, the red

fluorescence signal decreases at acidic pH and increases at basic pH. **Figure 4b** contains a plot of peak ratio (I_g/I_r) as a function of proton concentration obtained by quantifying the fluorescence intensity of SNARF-dextran loaded capsules at different pH values (some example of measured ROIs are reported in **Figure 4a**). Similarly to fluorimetric measurements (**Figure 3**), the ratio-imaging ROI analysis indicated a sigmoid relationship between SNARF fluorescence and proton concentration (fit parameter values are showed in the corresponding graph). These data are in agreement with previous results reported by Kreft *et al*. who studied the fluorescence response of SNARF-dextran conjugate loaded in the cavities of polyelectrolyte capsules inside living cells (*in vitro*).[22]

2.3. Na^+-sensor capsules based on SBFI as fluorescent indicator

The sodium sensitive dye, sodium-binding benzofuran isophthalate (SBFI), and the potassium sensitive dye, potassium-binding benzofuran isophthalate (PBFI), are two of the most widely used selective ion indicators for the fluorimetric determination of intracellular concentrations of Na^+ and K^+, respectively. These dyes consist of two benzofuran isophthalate fluorophores linked to the nitrogens of diaza-crown ether with a cavity size that confers selectivity for Na^+ and K^+, respectively.[31] The monovalent cations bind to the active site of the dye with a 1:1 stoichiometry. Upon binding, the excitation maxima of both PBFI and SBFI shift to shorter wavelengths, with changes in the intensity of the emission maximum. The ratio of the fluorescence signals obtained by exciting the indicator probe, SBFI or PBFI, and the reference dye, AF594, at 340 nm, while monitoring the fluorescence at 520 nm and 610 nm, was used to detect increasing concentrations of Na^+ or K^+, respectively. Because a certain degree of pH sensitivity of SBFI has been described in a cell-free *in vitro* system[32] all the ion-sensing measurements were performed by dissolving NaCl or KCl in Tris 0.05 M buffer solutions keeping the pH constant (7.5) while raising the ion concentration in the solution up to 0.14 M (see **SI**, **Figure SI-10**). **Figure 5** shows the fluorescence intensity ratio (I_g/I_r) of SBFI and AF594 in solution (squares), SBFI- and AF594-dextran in solution (circles), and SBFI- and AF594-dextran loaded capsules (triangles) as a function of Na^+ concentration. The green to red ratio for each Na^+ value has been obtained by dividing the fluorescence intensity at 520 nm (I_g) to the fluorescence intensity at 610 nm (I_r) (the corresponding fluorescence spectra are displayed in **Figure SI-11**). The resulting curves were fitted with an exponential function using the following equation:

$$\frac{I_g}{I_r}(c(Na^+)) = I_0 + \Delta I \cdot \left(1 - \exp^{-c(Na^+)/c_0}\right) \qquad \textbf{Eq. 2}$$

here I_0 is the offset , ΔI a scaling factor and c_0 [M] the decay constant. The fit parameters values are shown in the **Figure 5**. As expected, upon binding to Na^+ ions, the emission maxima of every type of SBFI increase. These changes are very clear in the control sample made of free SBFI/AF594 dyes (**Figure 5**, squares) (see also raw data in **SI**, **Figure SI-11**). Unlike pH-sensor capsules, the ratios of dye-dextran conjugates and encapsulated dye-dextran conjugates revealed some differences in terms of trends as well as intensities. In particular, after linking of the dyes to amino-dextran, SBFI-/AF594-dextran showed a lower intensity

compared to the free SBFI/AF594 in solution (concentration of the dyes in free and linked forms were kept constant during titration measurements, 12.5 μM). We assumed that the positive charges carried by the amino-dextran polymer (i.e., -NH_2 groups) influence the sensing properties of the dyes by repelling the sodium ions. It is known that the linking can influence the fluorescence of the indicator dyes. Recently, we have demonstrated that charges of nanoparticles (NPs) can affect the ion-sensing properties of NP-fluorophore systems.[8, 33] In particular, by studying proton sensing with SNARF fluorophores coupled to the surface of negatively charged Au NPs it was found that the local anionic concentration close to the NP surface, and thus in direct contact to SNARF linked onto the NPs surface, is lower than in the bulk.[8] This effect has been addressed to the negative charges of NPs (i.e., COO^- groups), which attract positively charged ions and repel negatively charged ions, according to the Debye Hückel theory.[34, 35] Thus, depending on the surface charge and the sensed ion, higher or lower local ion concentrations are present in the direct environment of the sensitive fluorophore as compared to bulk. As a result, the fluorophore detects the local ion concentration close to the NP surface, but not the bulk concentration. This model has been further validated by studying chloride sensing with the chloride sensitive dye amino-MQAE and a reference dye (cresyl violet) coupled to the surface of negatively charged Au NPs. It was found that by varying the distance between amino-MQAE and the negatively charged polymeric surface of the NPs through PEG spacers, the distance dependent charge effect on local chloride concentration could be adjusted.[33] SBFI-/AF594-dextran conjugates are positively charged because of the excess of -NH_2 groups onto the amino-dextran (see also **SI**, **Figure SI-6**) and thus, oppositely to NP-fluorophore systems, they might attract negatively charged ions while repelling positively charges ones. Consequently, the intensity of the fluorescence signal of dye-dextran conjugated should be reduced compared to the free dyes, of which fluorescence spectra have been recorded in absence of amino-dextran **(Figure 5)**. Upon encapsulation, the peak of SBFI in the blue-green becomes more intense and a small blue shift can be observed (**SI**, **Figure SI-11**). This might be due to some autofluorescence of the polyelectrolytes employed during the LbL step. To address this question, we have recorded the emission spectra of PSS and PAH by using the same excitation wavelength used for exciting SBFI dye. A clear emission spectrum has been found for PSS, whose emission maximum peak occurs at 385 nm and ends at around 500 nm (λ_{exc} = 340 nm), whereas no emission was detected by PAH (data not shown). Additional proof of the contribution of PSS to the analyzed spectra is given by the observation that the contribution from PSS was detected only in sensor capsules loaded with indicator dye excited at lower wavelengths where also PSS absorbs (340 nm for SBFI and PBFI, 350 nm for amino-MQAE). In fact, no contribution from PSS was detected in FITC-/AF594-dextran (λ_{exc} = 490 nm) or SNARF-dextran capsules (λ_{exc} = 540 nm). To overcome this limitation, an anionic polyelectrolyte without autofluorescence could be employed for capsule fabrication. However, the fluorescence response of encapsulated SBFI-/AF594-dextran increases from low to high concentration of sodium, which is crucial to distinguish between extra- and intracellular levels of Na^+ (**Figure 5**, triangles). **Figure 6a** shows the fluorescence images of SBFI-/AF594-dextran loaded capsules in buffer solution at 0 and 0.14 M Na^+ concentration. For some

capsules a higher concentration of the SBFI-dextran has been observed in the inner wall, probably due to a slight diffusion of the dextran from the cavities or to electrostatic attractions of the cargo to the inner anionic polyelectrolyte layer (PSS). Nevertheless, this phenomenon did not prevent the determination of different concentrations of sodium. It is not yet completely understood why the same type of amino-dextran linked to two different dyes behave in a different way inside the cavities. In particular, a good entrapment of the AF594-detxran is observed in all tested capsules, whereas partial filling of cavities with SBFI-dextran was observed in some capsules (**Figure 6a** and **SI**). Firstly, diffusion of the SBFI-dextran out of the capsules during LbL assembly and core removal procedure had been hypothesized. However, since the molecular weight of the dextran used for linking both types of dyes is the same (500 kDa), diffusion of only one type of dextran should be excluded. Secondly, adhesion of SBFI-dextran to the first PSS layer has been taken into account. Although the charge of both types of linked dextran is positive (see **SI**, **Table 1**), thus electrostatic interactions between the PSS layer and only one type of labeled dextran should be also ruled out. Hence, the different behavior between the two types of linked dextran could be addressed to a different efficiency of loading of the capsules during the first step of capsules synthesis ($CaCO_3$ co-precipitation, see Scheme 1 and **SI**). In fact, by mixing equal quantity of dextran-conjugated dyes, it was found that different concentrations of dyes were entrapped into the resulting $CaCO_3$ templates (see **Table 1**, **SI**). However, in case of sodium sensitive capsules, very similar quantities of the SBFI-dextran and of AF594-dextran were estimated in the resulting $CaCO_3$ particles (see **Table 1**, **SI**), which also leaves out this last assumption. The chemical structure of the linked fluorophores might also play a role on the entrapment of dextran. We are currently investigating this issue to address the above raised points in order to better understand the properties of these systems. It has to be pointed out that besides these observations, a clear difference in the overall SBFI fluorescence intensity could be observed between low and high Na^+ concentration, whereas the fluorescence intensity of the reference dye was constant. In **Figure 6b** a plot of the peak ratio (I_g/I_r) is reported as a function of the Na^+ ion concentration as obtained by quantifying the fluorescence intensity of green and red signals detected inside single capsules at different Na^+ concentrations (0 to 0.14 M) (some examples of measured ROIs are reported in **Figure 6a**). Notably, only capsules with cavities homogenously loaded with SBFI-dextran were used for the ROI analysis (see circles in **Figure 6a**). The I_g/I_r data points were plotted against the Na^+ concentration and fitted to eq. 2 (fit parameters values are shown in the corresponding graph). In line with the fluorescence images (**SI**, **Figure SI-24**), the ratio-imaging data indicate that there is almost an exponential increase relationship between SBFI fluorescence and Na^+ concentration. The detection limit of the capsules appears to be roughly 0.1 mM.

2.4. K^+-sensor capsules based on PBFI as fluorescent indicator

Figure 7 shows the results obtained for free PBFI and AF594 (squares), PBFI and AF594 conjugated to dextran (circles) and PBFI-dextran and AF594-dextran loaded into the capsule cavities (triangles). The I_g/I_r data points were plotted against the K^+ concentration and fitted again by using eq. 2 (however with $c(K^+)$ instead of $c(Na^+)$, fit parameters are shown in

Figure 7). Similarly to SBFI-/AF594-dextran loaded capsules, PBFI-/AF594-dextran capsules showed an exponential increase of fluorescence versus the K^+ concentration. Also in this case the intensity of the PBFI-/AF594 dyes after conjugation resulted lower than for the free dyes PBFI/AF594 (**Figure 7**, circles) (see also **SI**, **Figure SI-12b**). This trend might confirm the previous mechanism hypothesized for SBFI-/AF594-dextran based on the assumption that positively charged amino-dextran affects the sensing properties of PBFI by repelling potassium ions in the local environment. Also here, in the case of encapsulated PBFI-/AF594-dextran, emission maxima of PBFI shift to shorter wavelengths while increasing in intensity because of increasing K^+ concentration. As in the case of SBFI, PBFI fluorescence was elicited at 340 nm and measured from 400 nm to 670 nm (in order to detect also the red reference dye AF594). In this way, autofluroescence of PSS was once more detected during fluorimteric titration measurements of encapsulated PBFI-/AF594-dextran samples (**Figure 7**, triangles) (see also **SI**, **Figure SI-12c**).

The response of capsules loaded with both PBFI-dextran and AF594-dextran (PBFI-/AF594-dextran) was studied by fluorescence microscopy. **Figure 8a** shows two representative images of capsules in buffer solution at 0 and 0.14 M K^+ concentrations (all the images are reported in the **SI**, **Figure SI-25**). Similarly to sodium sensitive capsules, an increase of the fluorescence signal of the encapsulated potassium probe PBFI was also detected at high K^+ concentrations. This indicates the ability of these capsules to sense low and high concentrations of K^+. **Figure 8b** shows the plot of peak ratios (I_g/I_r) as a function of K^+ ion concentration (0 to 0.14 M) obtained by ROI analysis performed in the cavities of single capsules (some examples of measured ROIs are reported in **Figure 8a**). The graph shows that the fluorescence intensity of PBFI increases exponentially with increasing potassium concentration.

2.5. Cl^--sensor capsules based on MQAE as fluorescent indicator

The halide-sensitive fluorescent indicator amino-MQAE has been used to assemble capsules sensitive to Cl^- concentrations. Amino-MQAE belongs to the class of N-substituted quinoline compounds that are suited for determining $c(Cl^-)$ by measuring the quenching of fluorescence emission. The quenching results in an ion concentration-dependent fluorescence decrease without a shift in wavelength (see **SI**, **Figure SI-13**). The fluorescence spectra at varying chloride concentrations were recorded and the I_g/I_r ratio at 440/610 nm were plotted against the chloride concentrations. The data points of free dyes and dextran-conjugated dyes were fitted with an exponential decay function by using the following equation:[33]

$$\frac{I_g}{I_r}(c(Cl^-)) = I_0 + \Delta I \cdot \exp^{-c(Cl^-)/c_0} \qquad \textbf{Eq. 3}$$

where I_0 is the offset, ΔI is a scaling factor for the amplitude, and c_0 is the decay constant. The fit parameter values are shown in the **Figure 9**.

The fluorescence intensity ratio (I_g/I_r), shown in **Figure 9**, illustrates the quenching of amino-MQAE fluorescence by the presence of Cl^-, as measured at several concentrations of chloride ions in Tris 0.05 M buffer (pH 7.5). The fluorescence behavior of a mix of amino-MQAE and AF594 after conjugation to dextran (**Figure 9**, circles) resulted to be similar to the control (free amino-MQAE and AF594, **Figure 9**, squares). After co-loading amino-MQAE-dextran and AF594-dextran into the cavities of the capsules, the quenching of the sensor dye is reduced (**Figure 9**, triangles).

Chloride sensor capsules were fabricated by linking the amino-modified MQAE to a negatively charged carboxy dextran. Thus, similarly to the charge effect present for the amino-dextran in the SBFI and PBFI sensor systems, hereby chloride ions, which are negatively charged, can be electrostatically repulsed by the negatively charged dextran. This might explain the lower degree of quenching observed for encapsulated amino-MQAE-/AF594-dextran samples (**Figure 9**, triangles). Notably, similar results have been observed for amino-MQAE dye bound to the surface of negatively charged colloidal nanoparticles.[33] By adjusting the distance between the amino-MQAE dye and the negatively charged surface of polymer-coated Au NPs with PEG spacers of different length, the fluorescence quenching behavior of amino-MQAE upon presence of chloride ions could be tailored.

Unlike proton, sodium and potassium sensitive capsules which were loaded with 500 kDa dye-dextran conjugates, chloride sensitive capsules were obtained by loading amino-MQAE linked to a 12 kDa CM-dextran and AF594 linked to a 500 kDa amino dextran. CM-dextran of 500 kDa (CarboMer, Inc., #500939) was initially used for conjugating the amino-MQAE dye; however the conjugation reaction was not efficient because of the poor solubility of the high molecular weight compound in a variety of tested solvents (see **SI** for details). To overcome these solubility problems, we decided to conjugate the chloride sensitive dye to carboxy dextran of lower molecular weight (M_w = 12 kDa, Sigma, #86524). As expected, this choice reduced the filling efficiency of the capsule cavities because of the small molecular weight of the dextran. As a result, amino-MQAE-dextran partially diffused out of the capsules during LbL assembly as well as during core removal. Thus the data obtained should be carefully interpreted because diffusion of the sensor from the cavities of the capsules should also be taken into account. In **Figure 10a**, two fluorescent images of the capsules loaded with both amino-MQAE-dextran and AF594-dextran and imaged with 0 and 0.14 M Cl^- buffer solution, are reported. **Figure 10b** shows the ratio obtained by quantifying the fluorescence of the probe indicator and the reference dye with increasing concentration of Cl^-. According to the spectroscopic analysis (**Figure 9**, triangles) the sensitivity of the dye has been impaired, which makes the determination of c(Cl^-) practically impossible. Fluorimetric titration and microscopy results agree in the finding that the encapsulation corrupts the sensing of Cl^-. One strategy for solving the problem related to encapsulation of amino-MQAE might be the linking of the dye onto a dextran of higher molecular weight. To do this, a MQAE dye with carboxy reactive groups instead of amino reactive groups should be synthesized in order to

covalently bind it to a 500 kDa amino-dextran. This is the object of studies that are being currently performed in our laboratory and will be reported in due course.

3. Discussion

One advantage of capsules-based sensor systems consists on the possibility of loading a wide range of ion-sensitive fluorophores within their cavities by maintaining the external surface of the sensor platform identical. In this way, capsules will be taken up by the cells via the same uptake process, whereas their cavity will display different sensing properties. In this study, we have synthesized ion-sensitive polyelectrolyte capsules for optical ratiometric investigation of H^+, Na^+, K^+ and Cl^- ions *in vitro*. The indicator and reference dyes were separately linked to dextran cargo molecules to prevent the diffusion of the low molecular weight dyes out of the capsule cavities. By loading the cavities of the capsules with ratiometric dextran-labeled molecules, it was possible to optically determine the concentration of ions in the surrounding solution by recording the fluorescence intensity of the encapsulated dyes. From the fluorescence intensity of the indicator and reference dyes, the I_g/I_r ratio was calculated and plotted against the tested ion concentrations thus obtaining calibration curves for several analytes. The response of each sensor capsule measured by fluorimetric measurements was compared to the response of the corresponding free dye and dye-dextran conjugate **(Figures 1,3,5,7,and 9)**. It was found that upon encapsulation the response of the fluorophores is influenced by the charge of dextran. In particular, the sensitivity of SBFI and PBFI was negatively affected after their linking to amino-dextran (**Figures 5 and 7**, circles). These results are in agreement with recent studies in which we demonstrated that the response curve of ion sensitive dyes coupled to the external surface of charged gold NPs can be shifted when the dyes are close to a charged environment.[8] Furthermore, by varying the distance between the sensitive dye and the charged carrier NPs, the sensitivity of the indicator fluorescent probe can be tuned[33] thus confirming that charges play a crucial role on the ion sensing with organic fluorophore-NP hybrids. In this work, similar charge effects on the ion-sensing with fluorophore-dextran conjugates have been observed in terms of sensitivity (**Figures 5 and 7**, circles). Additional studies are being performed to gain deeper insight into the ion sensing mechanisms of organic fluorophores conjugated to charged molecules. However after encapsulation, the sensitivity of fluorophore-dextran conjugates increased again suggesting a positive effect of the encapsulation process on the indicator activity (**Figures 5 and 7**, triangles). Apart from some changes detected by fluorimetric measurements in the overall intensity ratios of encapsulated sensor dye to encapsulated reference dye, sensor capsules were able to sense different ion concentrations. By passing through the porous multilayer polyelectrolyte shell, ions such as H^+, Na^+ and K^+, are able to diffuse inside the cavities of the capsules where they interact with the embedded sensor dyes (**Figures 1,3,5,7**, triangles). In the case of Cl^- sensor capsules, diffusion of the low molecular weight amino-MQAE-dextran out of the capsules or hindering of the Cl^- ions to the sensor dye due to charge repulsion effects have been hypothesized to elucidate the reduced quenching of the encapsulated amino-MQAE-dextran under high concentrations of chloride (**Figure 7**, triangles). Future investigations will determine the validity of these proposals.

The fluorescence response of each sensor system has been analyzed also by fluorescence microscopy and quantified by ROI-analysis **(Figures 2,4,6,8,10)**. For this purpose, fluorescence images of the sensor and reference dyes, co-embedded within the cavities of the capsules, were separately recorded under different ion concentrations. By measuring the intensity of the fluorescence within definite regions of the capsules, ratiometric measurements of the sensors were performed. The obtained data showed the possibility to quantify the fluorescence response of the sensors via ROI-analysis. Current investigations are focused on the writing of a universal program able to simultaneously evaluate the fluorescence response of multiple sensor capsules via ROI-analysis for real-time measurements of ions.

4. Conclusions

In conclusion, we have described the synthesis of ratiometric ion-sensitive polyelectrolyte capsules sensitive for protons, sodium, potassium, and chloride ions. We have characterized their fluorescence response by titration fluorimetric measurements and fluorescence microscopy. pH-sensor capsules, based on FITC or on SNARF as fluorescent indicator, were able to efficiently sense different proton concentration after linkage of the dyes to amino-dextran molecules as well as after their encapsulation. In contrast, in the case of Na^+- and K^+-sensor capsules, the response of the fluorophores resulted to be influenced by the conjugation of the dyes to amino-dextran molecules. In particular, SBFI and PBFI dye fluorophores showed a lower intensity response after their linking to amino-dextran. We assumed that the positive charges carried by the amino-dextran polymer might influence the sensing properties of the covalently linked dyes (SBFI or PBFI) by affecting their interaction to the cations (Na^+ or K^+). However, an increase of the fluorescence signal of both the encapsulated SBFI-dextran and PBFI-dextran was detected at high Na^+ and K^+ concentrations, thus indicating the ability of the capsules to sense low, medium and high concentrations of these ions. In the case of chloride sensor capsules, we also observed a charge effect of the carboxy-dextran on the fluorescence response of the amino-MQAE indicator dye which resulted in a reduced quenching of the dye after its encapsulation. Notably, similar results have been observed for amino-MQAE dye bound to the surface of negatively charged colloidal nanoparticles.[33] Future work will focus on studying the influence of charges carried by dextran molecules and/or by polyelectrolyte layers on the sensing properties of the embedded fluorophores. The use of indicator dyes with different chemical structure as well as the use of different macromolecules as anchor components will be also investigated. The peculiar features of polyelectrolyte capsules systems, along with the possibility to modify their properties by manipulating their two compartments (cavities and walls), may provide several advantages for their use in future applications in intracellular biosensing. Experiments aimed at designing multilayer capsules which combine a barcode labeling system of the walls (by engineering the shell of every sensor type capsule with mixtures of different quantum dots) to the sensor activity of the cavities, are currently under investigation. By analyzing the fluorescence of the walls, it will be possible to distinguish between different sensor types possibly localized in different area of the cells. These studies are expected to allow for carrying multiplex real-time sensing measurements of different ions inside living cells.

5. Experimental Section

Materials: Poly(sodium 4-styrenesulfonate) (PSS, Mw ~70 kDa, #243051), poly(allylamine hydrochloride) (PAH, Mw ~56 kDa, #283223), calcium chloride dehydrate ($CaCl_2$, #223506), sodium carbonate (Na_2CO_3, #S7795), fluorescein 5(6)-isothiocyanate (Mw 389.38, #46950), carboxymethyl-dextran sodium salt (CM-dextran, Mw ~12 kDa, #86524), ethylenediaminetetraacetic acid calcium disodium salt (EDTA disodium salt, #ED2SC), 2-(N-Morpholino)ethanesulfonic sodium buffer 0.05 M at pH 6.0 (MES-Na, #M3671), N-(3-Dimethylaminopropyl)-N′-ethylcarbodiimide hydrochloride (EDC, Mw 191.71, #E7750), Tris(hydroxymethyl)aminomethane (Tris, #T1503), and glass vials (shorty vials, #Z106399) were purchased from Sigma-Aldrich. Alexa Fluor® 594 carboxylic acid, succinimidyl ester (AF594, Mw 819.85, #A-20004), PBFI tetraammonium salt (Mw 950.99, # P-1265MP), SBFI tetraammonium salt (Mw 906.94, #S-1262), 5-(and-6)-carboxy SNARF®-1 (SNARF, Mw 453.45, # C-1270), and amino dextran (AM-dextran, Mw ~500 kDa, #D7144) were obtained from Invitrogen. Carboxymethyl dextran (CM-dextran, Mw ~ 500 kDa, #500939) was bought from CarboMer, Inc (San Diego, CA 92196-1026 USA). All chemicals were used as received. Ultrapure water with a resistance greater than 18.2 MΩ cm was used for all experiments. The chloride sensitive quinolinium-derivate dye amino-MQAE, 2-(2-(6-Methoxyquinoliniumchloride)ethoxy)-ethanamin-hydrochloride (Mw 311.167), ((2-(2-(6-methoxyquinolininiumchloride)ethoxy)-ethanamine-hydrochloride (adopted from Invitrogen #E3101), was synthesized and kindly provided by Prof. Ulrich Koert, Faculty of Chemistry, Philipps University of Marburg (Germany).[33]

Synthesis of $CaCO_3$ particles loaded with Dextran: Five types of polyelectrolyte capsules were fabricated: pH-sensor capsules based on FITC or on SNARF as fluorescence indicators, Na^+-sensor capsules based on SBFI as fluorescence indicator, K^+-sensor capsules based on PBFI as fluorescence indicator, and Cl^--sensor capsules based on amino-MQAE as fluorescence indicator. For each capsule system, $CaCO_3$ microparticles were precipitated from solutions of calcium chloride ($CaCl_2$) and sodium carbonate (Na_2CO_3) under vigorous stirring.[36] The schematic illustration of the synthesis is reported in **Figure SI-5**. In a glass vial, equal volumes (615 µL) of aqueous $CaCl_2$ and Na_2CO_3 solutions (0.33 M) were mixed with 400 µl of a dextran solution labelled with a desired ion-indicator dye (usually 50 µM dye concentration), and with 370 µl of a dextran solution labelled with the reference dye AF594 (usually 50 µM dye concentration) as an internal standard (**Figure SI-5**,i). A detailed protocol for conjugation of amino-dextran and carboxy-dextran with fluorophores can be found in the Supporting Information (**SI**). The solution was thoroughly agitated on a magnetic stirrer (1000 rpm) for 30sec at room temperature (RT). After the agitation, the mixture was left without stirring for 4 min at RT. During this time, the amorphous $CaCO_3$ crystals generated by mixing the two supersaturated solutions of aqueous $CaCl_2$ and Na_2CO_3 are transformed into spherical and porous $CaCO_3$ particles. After this resting time, the resulting suspension was centrifuged at 6000 rpm for 5 s to sediment all the particles to the bottom of the vial. The supernatant was removed with a pipette and the particles were washed three times with 1 mL of Milli-Q water in order to remove unreacted species. Every washing step was performed by

centrifugation of the particles at 6000 rpm for 5 s, removal of the supernatant followed by addition of fresh Milli-Q water. In the last step, the particles were washed with 1 mL of acetone (≥99.5% for synthesis, #5025.6, Roth,) and after removal of the supernatant, air-dried in a dessicator at ~ 1mbar for 10-15 minutes. The resulting powder (stable against dissolution and recrystallization) was used directly for the LbL assembly of polylectrolytes or stored in dry and dark for several weeks. By using the above described protocol, spherical $CaCO_3$ particles with an average diameter ranging from 2.5-3.5 μm are typically formed. However some variability of size of the cores can be observed between different batches of microparticles (see also **SI**). This can be mainly addressed to small changes of some conditions, such as the temperature and the stirring speed, which turned out to be crucial parameters for the control of morphologies of $CaCO_3$. For instance, it was observed that by using cold solutions of $CaCl_2$ and Na_2CO_3 or by performing the co-precipitation step in an ice bath (T~4 ℃), the size of the $CaCO_3$ microparticles can be increased up to 5-10 μm. Conversely, by increasing the temperature (30 ℃) and the mixing speed (1200 rpm) particles of approximately 1 μm can be obtained.

LbL assembly of polyelectrolytes around $CaCO_3$ Particles loaded with Dextran: The $CaCO_3$ particles were then coated by multiple LbL assembly of oppositely charged polyelectrolytes (**Figure SI-5**, ii-iii). 20 mg of dextran-loaded $CaCO_3$ particles powder were weighted and dispersed in a 0.5M NaCl solution containing the polyanion PSS (2 mg mL^{-1}, pH 6.5). The dispersion was initially left for 2 minutes in a sonication bath and subsequently continuously shaken for 10 min at ~200 rpm to avoid precipitation of the particles on the bottom of the tube and aggregation. After this exposure time, the excess polyanion was removed by three centrifugation/washing steps with 1 mL of Milli-Q water (6000 rpm for 5 s. Subsequently, 1 mL of a 0.5M NaCl solution containing the polycation PAH (2 mg mL^{-1}, pH 6.5) was added and the dispersion was mixed as previously for 12 min, followed again by three centrifugation/washing steps with 1 mL of Milli-Q water (6000 rpm for 5 s). This procedure was repeated three times for each incubation step with a polyelectrolyte resulting in the deposition of 5 polyelectrolyte bi-layers on the dextran-loaded $CaCO_3$ particles. In a second step, the $CaCO_3$ template core was removed by complexation with EDTA (**Figure SI-5,** iv). Coated $CaCO_3$ particles were shaken for 2 min with 1 mL of EDTA solution (0.2M, pH 5.5) followed by gentle centrifugation at 1100 rpm for 8 minutes in order to settle down the template-free capsules. After that, the supernatant was removed and the capsules resuspended with 1 mL of a fresh EDTA solution (0.2 M, pH 7.0). This washing step was used to quickly adjust the pH of the suspension to neutral value. Additional details can be found in the **SI**. Afterward, the capsules were extensively washed (five times) with Milli-Q water (1 mL) by centrifuge steps at 1100 rpm for 8 minutes. Finally, the microcapsules were stored as suspension in 500 μL of Milli-Q water at 4 ℃. After core removal, the capsule number per volume was determined by direct counting by a hemocytometer chamber under a microscope. A drop of a diluted solution of capsules was added onto the chamber and the number of capsules deposited into the four regions marked by crossed double lines was counted by using a 20X objective. Then the number of counted capsules in each region was averaged and

multiplied by the volume of the capsule solution and by a factor of 10^4 (formula: average n ° of capsules x volume of capsule solution x 10^4). Finally, the obtained number is multiplied by the dilution factor used to dilute the stock solution of capsules. From each synthesis we typically obtained about 10^8 capsules/mL.

Absorbance and Fluorescence Spectroscopy: The concentration of the fluorophores was obtained by UV-vis spectroscopy (Agilent 8453 UV-vis absorbance spectrometer) by utilizing Lamberts-Beer's law (a detailed description is given in the **SI)**. The analyte-dependent fluorescence of each indicator was investigated for the free dye, the dye conjugated to dextran, and the encapsulated dye-dextran conjugate via fluorescence spectroscopy for calibration purposes. Fluorescence measurements were recorded using a Fluorolog (FL3-122) fluorescence spectrometer equipped 450-W Xenon short arc (Ushio-UXL-450S-O) with 450W as the source of excitation. The emitted light was observed at right angles to the excitation radiation. All of the spectra were recorded at RT under air. The indicator dyes FITC was excited at 490 nm, SNARF at 540 nm, SBFI and PBFI at 340 nm and the amino-MQAE at 350 nm. The reference dye AF594 was excited at the same wavelength used for each indicator. For example, for fluorimetric titration measurements of sodium, SBFI and AF594 were both excited at 340 nm, so that the ratios of emission of SBFI (increase of its emission upon increasing sodium concentration) and AF594 (stable emission, internal standard) could be obtained from one spectrum. The raw data for all presented results and all control measurements are provided in detail in the **SI**.

Fluorescence Microscopy: All images were recorded with a Zeiss Axiovert 200M microscope equipped with a mercury lamp (FluoArc, Zeiss) as source of light and a CCD camera (AxioCam HRm, Zeiss) as detector. Fluorescent imaging was performed with two sets of green and red fluorescence filters to separately detect the indicator and the reference dyes embedded into the capsule cavities. Capsules co-loaded with FITC- or SBFI- or PBFI- or amino-MQAE-dextran and AF594-dextran, were imaged by using the excitation filter F39-340 (BrightLine HC 340/26, AHF, Germany) with the emission filters F37-584 (BrightLine HC 510/84) and F42-601 (HQ 500 LP, AHF Germany) for green and red fluorescence, respectively. Capsules loaded with SNARF-dextran were imaged by using a different set of yellow and red fluorescence filters specific for the SNARF dye (exciter: BP515/30 nm; yellow emitter: BP580/25 nm; red emitter: BP640/25 nm, AHF, Germany). For each measurement in which ionic concentrations were detected by reading out the fluorescence of a capsule, a 20 µL drop of capsules was resuspended in a solution of buffer with the desired ion concentration and deposited onto a glass coverslip. After the capsules had settled down to the surface of the substrate two fluorescence images with the green and red filter set were recorded at fixed exposure time (the detailed description of the measurements is given in the **SI**). The obtained fluorescent images were processed using ImageJ v1.42m software (http://rsb.info.nih.gov/ij/) in order to perform the following ratio-imaging analysis: spherical-shaped regions of interest (ROIs) of the same size were drawn into the cavities of single capsules and the fluorescence intensities in both channels (green and red), under different ion

concentrations were measured by means of the image calculator. A total number of 30 individual capsules were analyzed per each measured concentration. For each measurement, a ROI of the same shape and size was measured into an area without capsules and the obtained value was subtracted from the overall intensity measured in the capsule cavities to correct for background interference. Quantitative fluorescence data were exported from ImageJ into Microsoft Excel software for further analysis.

Acknowledgements

The authors are grateful to Florian Dommerhausen from the group of Prof. Dr. Ulrich Koert for providing the amino-modified MQAE dye. This project was funded by the BMBF / ERANET -NEURON project NanoSyn. The authors are grateful to Markus Ochs, Carolin Ganas, Andreas Riedinger and Patrick Durkin for helpful discussions and proof-reading of the manuscript.

References

[1] V. B. Alberts, D. Bray, J. Lewis, M. Raff, K. Roberts, J. D. Watson, *Molecular biology of the cell*, 3rd ed., Garland Publishing Inc., New York, **1994**.

[2] M. Mall, A. Hipper, R. Greger, K. Kunzelmann, *Febs Letters* **1996**, *381*, 47.

[3] M. J. Stutts, C. M. Canessa, J. C. Olsen, M. Hamrick, J. A. Cohn, B. C. Rossier, R. C. Boucher, *Science* **1995**, *269*, 847.

[4] J. L. Farber, *Chemical Research in Toxicology* **1990**, *3*, 503.

[5] J. R. Inglefield, R. D. Schwartz-Bloom, *Journal of Neurochemistry* **1998**, *70*, 2500.

[6] A. J. Hansen, *Physiological Reviews* **1985**, *65*, 101.

[7] Y. E. Lee, R. Kopelman, R. Smith, *Annu Rev Anal Chem* **2009**, *2*, 57.

[8] F. Zhang, Z. Ali, F. Amin, A. Feltz, M. Oheim, W. J. Parak, *ChemPhysChem* **2010**, *11*, 730.

[9] A. Schulz, S. Hornig, T. Liebert, E. Birckner, T. Heinze, G. J. Mohr, *Organic & Biomolecular Chemistry* **2009**, *7*, 1884.

[10] E. Pringsheim, D. Zimin, O. S. Wolfbeis, *Advanced Materials* **2001**, *13*, 819.

[11] K. E. Sapsford, T. Pons, I. L. Medintz, H. Mattoussi, *Sensors* **2006**, *6*, 925.

[12] T. A. Duchesne, J. Q. Brown, K. B. Guice, S. R. Nayak, Y. M. Lvov, M. J. McShane, *Optical Diagnostics and Sensing of Biological Fluids and Glucose and Cholesterol Monitoring Ii* **2002**, *4624*, 66.

[13] T. Doussineau, S. Trupp, G. J. Mohr, *Journal Of Colloid And Interface Science* **2009**, *339*, 266.

[14] A. Graefe, S. E. Stanca, S. Nietzsche, L. Kubicova, R. Beckert, C. Biskup, G. J. Mohr, *Anal Chem* **2008**, *80*, 6526.

[15] M. Brasuel, R. Kopelman, J. W. Aylott, H. Clark, H. Xu, M. Hoyer, T. J. Miller, R. Tjalkens, M. A. Philbert, *Sensors And Materials* **2002**, *14*, 309.

[16] A. Burns, P. Sengupta, T. Zedayko, B. Baird, U. Wiesner, *Small* **2006**, *2*, 723.

[17] A. H. Ma, Z. Rosenzwieg, *Analytical Chemistry* **2004**, *76*, 569.

[18] T. Nguyen, Z. Rosenzweig, *Analytical and Bioanalytical Chemistry* **2002**, *374*, 69.

[19] Z. L. Cheng, C. A. Aspinwall, *Analyst* **2006**, *131*, 236.

[20] J. Q. Brown, K. B. Guice, M. J. McShane, *Proceedings of the Ieee Sensors 2003, Vols 1 and 2* **2003**, 111.

[21] M. J. Mc_Shane, J. Q. Brown, K. B. Guice, Y. M. Lvov, *J Nanosci Nanotechnol* **2002**, *2*, 411.

[22] O. Kreft, A. Muñoz_Javier, G. B. Sukhorukov, W. J. Parak, *Journal Of Materials Chemistry* **2007**, *17*, 4471.

[23] U. Reibetanz, D. Haloan, M. Brumen, E. Donath, *Biomacromolecules* **2007**, *8*, 1928.

[24] P. Rivera Gil, L. L. del Mercato, P. del Pino, A. Munoz Javier, W. J. Parak, *Nano Today* **2008**, *3*, 12.

[25] G. B. Sukhorukov, H. Mohwald, *Trends In Biotechnology* **2007**, *25*, 93.

[26] A. P. R. Johnston, C. Cortez, A. S. Angelatos, F. Caruso, *Current Opinion in Colloid & Interface Science* **2006**, *11*, 203.

[27] G. B. Sukhorukov, A. L. Rogach, M. Garstka, S. Springer, W. J. Parak, A. Muñoz-Javier, Oliver Kreft, A. G. Skirtach, A. S. Susha, Y. Ramaye, R. Palankar, M. Winterhalter, *SMALL* **2007**, *3*, 944.

[28] L. L. del_Mercato, P. Rivera-Gil, A. Z. Abbasi, M. Ochs, C. Ganas, I. Zins, C. Sönnichsen, W. J. Parak, *Nanoscale* **2010**, *2*, 458.

[29] E. J. Park, M. Brasuel, C. Behrend, M. A. Philbert, R. Kopelman, *Anal. Chem.* **2003**, *75*, 3784.

[30] R. Sjoback, J. Nygren, M. Kubista, *Spectrochimica Acta Part a-Molecular and Biomolecular Spectroscopy* **1995**, *51*, L7.

[31] K. Meuwis, N. Boens, F. C. De Schryver, J. Gallay, M. Vincent, *Biophys J* **1995**, *68*, 2469.

[32] A. Minta, R. Y. Tsien, *Journal of Biological Chemistry* **1989**, *264*, 19449.

[33] A. Riedinger, F. Zhang, F. Dommershausen, C. Röcker, S. Brandholt, G. U. Nienhaus, U. Koert, W. J. Parak, *SMALL* **2010**, *submitted*.

[34] P. Debye, E. Hückel, *Physikalische Zeitschrift* **1923**, *24*, 185.

[35] P. Debye, E. Hückel, *Physikalische Zeitschrift* **1923**, *24*, 305.

[36] D. V. Volodkin, A. I. Petrov, M. Prevot, G. B. Sukhorukov, *Langmuir* **2004**, *20*, 3398.

[37] G. T. Hermanson, *Bioconjugate Techniques*, 2nd ed., Academic Press, San Diego, **2008**.

[38] B. G. De_Geest, A. G. Skirtach, A. A. Mamedov, A. A. Antipov, N. A. Kotov, S. C. De Smedt, G. B. Sukhorukov, *Small* **2007**, *3*, 804.

[39] S. H. Hu, C. H. Tsai, C. F. Liao, D. M. Liu, S. Y. Chen, *Langmuir* **2008**, *24*, 11811.

[40] S. De Koker, T. Naessens, B. G. De Geest, P. Bogaert, J. Demeester, S. De Smedt, J. Grooten, *Journal of Immunology* **2010**, *184*, 203.

Figures

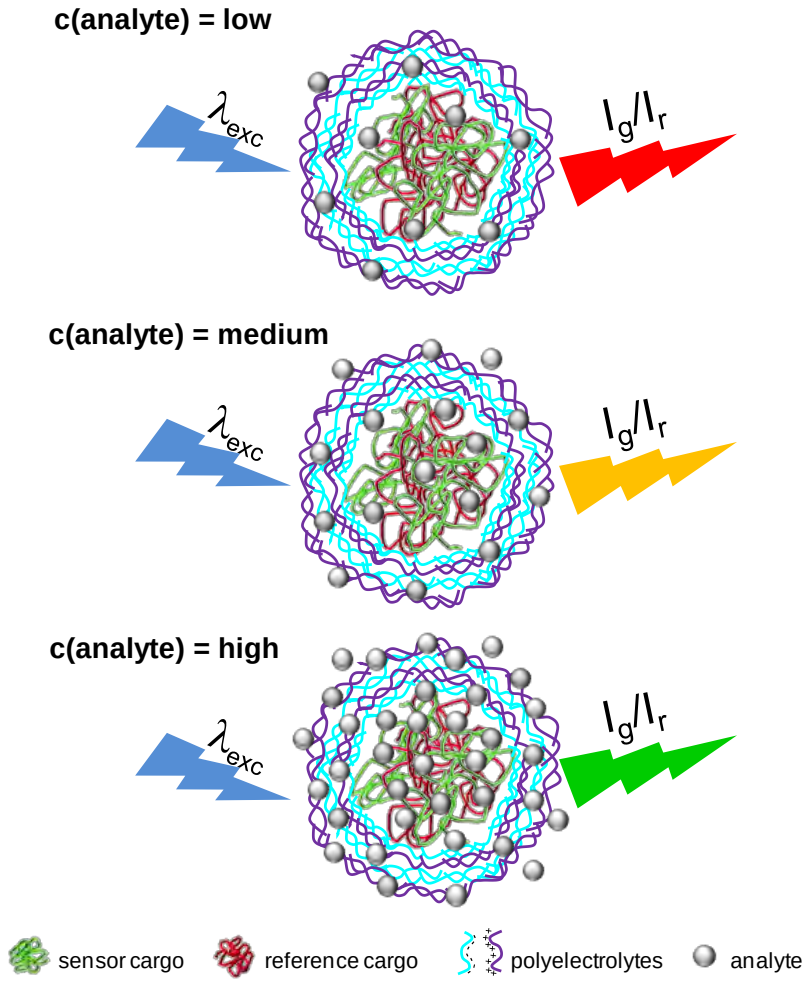

Scheme 1. Concept of a ratiometric fluorescent analyte sensor based on polyelectrolyte multilayer capsules. The indicator and the reference dyes are separately linked to macromolecules (i.e., dextran) and encapsulated in the cavity of the capsule. Because of the porous nature of the multilayer wall, small analytes (e.g., ions) diffuse in and out the cavities and virtually freely interact with the embedded fluorescent indicators. The analyte concentration is read-out as fluorescence ratio between the emission of the indicator probe and the emission of the reference dye (I_g/I_r). The use of both, indicator dyes and reference dyes, enables ratiometric fluorescent detection, which can correct for variations in excitation source intensity and minimizes the effects of photobleaching on quantitative measurements. For the sake of clarity only few layers are showed. Capsules are not drawn to scale.

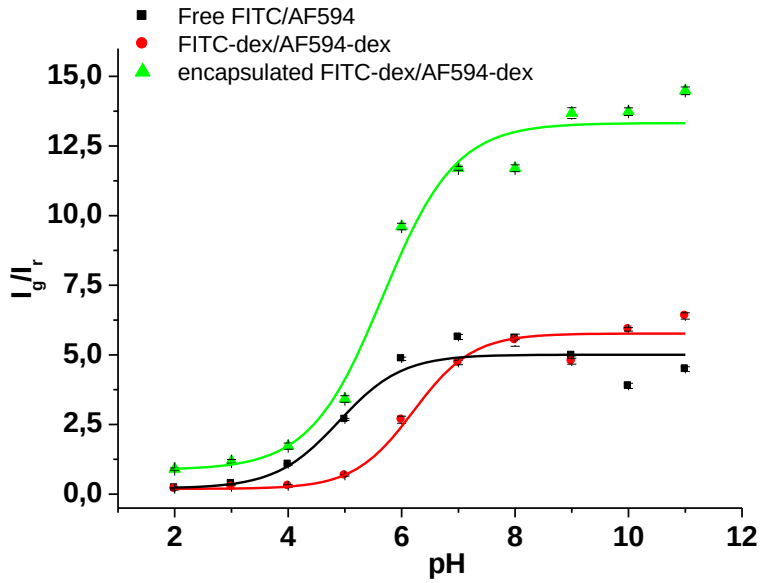

Figure 1. Comparison of fluorescence intensity ratio (g/r) of FITC and AF594 in solution (squares) to FITC-/AF594-dextran in solution (circles) and to FITC-/AF594-dextran loaded capsules in solution (triangles) with increasing pH values. The green-yellow to red ratios (g/r) of the fluorescence intensities at 520 nm (I_g) and 610 nm (I_r) are plotted versus the pH of the solution. All data represent the average of three replicate cuvette measurements at each concentration and the error bars show the standard deviation. Data points were fitted with a Boltzmann sigmoid function using eq. 1 (see **SI**).[8] The fit parameters used for the 3 curves are given in the table below. From these data the pK_a has been calculated (see **SI**, **Figure SI-19**)[8] and the following values have been obtained. The most important parameter for the pH-sensitivity is pK_a (based on pH_{infl}).

cuvette measurements	I_a	I_b	pH_{infl}	ΔpH	pK_a
free dye	0.21	5.01	4.9	0.56	4.9
dye bound to dextran	0.19	5.77	6.21	0.52	6.2
encapsulated dye	0.87	13.3	5.67	0.64	5.6

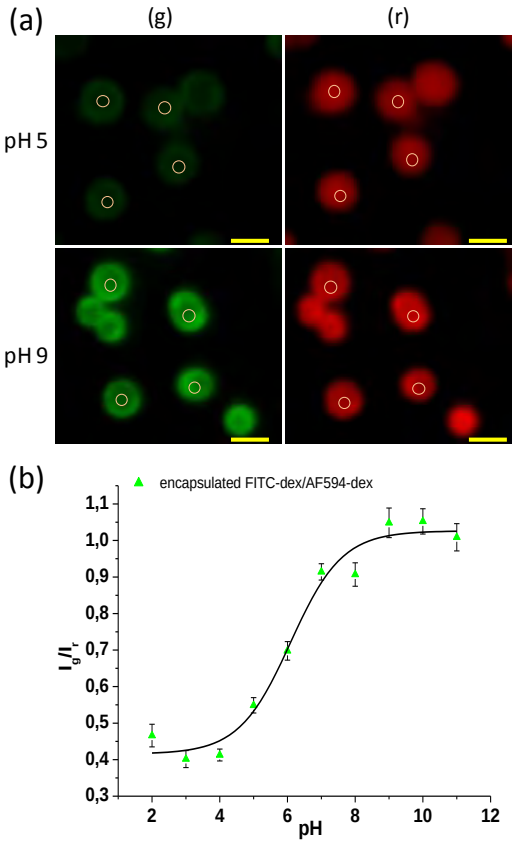

Figure 2. Ratio-imaging derived from ROI analysis performed in the cavity of single capsules simultaneously loaded with both FITC-dextran and AF594-dextran. (a) Example of ROI analysis showing fluorescence microscopy images as obtained with a green (g) and red (r) filter of capsules in buffer solution at pH 5.0 (top row) and pH 9.0 (bottom row) which are sedimented onto a glass coverslip. The circles indicate the ROIs drawn into the cavities that were used to measure the intensity of fluorescence in the green (I_g) and red channel (I_r) at different pH values. For simplicity, only the images of capsules at pH 5.0 and 9.0 are reported (see also **SI**, **Figure SI-22**) (scale bars 3 μm). (b) Fluorescence intensity ratio (I_g/I_r) obtained from images such as shown in (a). The (I_g/I_r) values correspond to the mean values of the ratios of the green and red fluorescence intensities as obtained for 30 capsules plotted versus the pH of the solution. Error bars correspond to the standard deviation. Data points were fitted again with a Boltzmann sigmoid function using the eq. 1.[8] The fit parameters are the following. The most important parameter for the pH-sensitivity is pK_a (based on pH_{infl}).

ROI measurements	I_a	I_b	pH_{infl}	ΔpH	pK_a
encapsulated dye	0.42	1.03	6.09	0.76	5.9

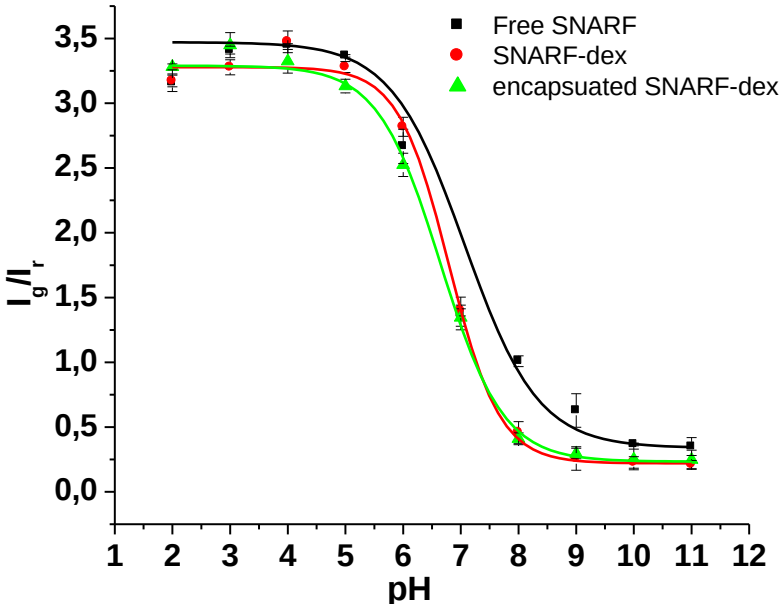

Figure 3. Comparison of fluorescence intensity ratio (I_g/I_r) of SNARF in solution (squares) to SNARF-dextran in solution (circles) and to SNARF-dextran loaded capsules (triangles) with increasing pH values. The green-yellow to red ratios (I_g/I_r) of the fluorescence intensities at 585 nm (I_g) and 640 nm (I_r) have been plotted versus the pH of the solution. All data points represent the average of three replicate cuvette measurements at each concentration and the error bars show the standard deviation. The data were fitted with a Boltzmann sigmoid function using eq. 1.[8] The fit parameters used for the 3 curves are given in the table below. From these data the pK_a of every form of SNARF were calculated (see **SI**, **Figure SI-20**)[8] to obtain the following values. The most important parameter for the pH-sensitivity is pK_a (based on pH_{infl}).

cuvette measurements	I_a	I_b	pH_{infl}	ΔpH	pK_a
free dye	3.47	0.34	7.07	0.64	7.0
dye bound to dextran	3.28	0.22	6.80	0.44	6.8
encapsulated dye	3.29	0.23	6.65	0.54	6.6

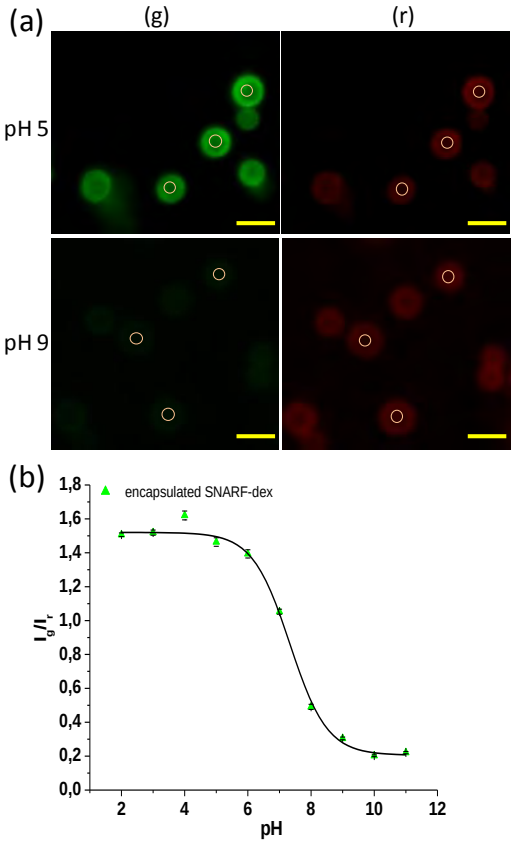

Figure 4. Ratio-imaging derived from ROI analysis of single SNARF-dextran loaded capsule. (a) Example of ROI analysis showing fluorescence microscopy images obtained with yellow (g) and red (r) fluorescence filters of SNARF-dextran loaded capsules in buffer solution at pH 5.0 (top row) and pH 9.0 (bottom row), which are sedimented onto a glass coverslip. The circles indicate the ROIs drawn into single capsules cavity that were used to measure the intensity of fluorescence in the yellow and red channel at different pH values. For simplicity, only the images of capsules at pH 5.0 and 9.0 are reported (see also **SI**, **Figure SI-23**) (scale bars 3 μm). (b) Fluorescence intensity ratio I_g/I_r obtained from images such as shown in (a). The I_g/I_r value corresponds to the mean value of the ratios of the yellow and red fluorescence intensities as obtained with 30 capsules and plotted versus the pH of the solution. Error bars correspond to the standard deviation between the individual capsules. Data points were fitted with a Boltzmann sigmoid function using the eq. 1.[8] The fit parameters used are given in the table below. The most important parameter for the pH-sensitivity is pK_a (based on pH_{infl}).

ROI measurements	I_a	I_b	pH_{infl}	ΔpH	pK_a
encapsulated dye	1.52	0.21	7.33	0.59	7.3

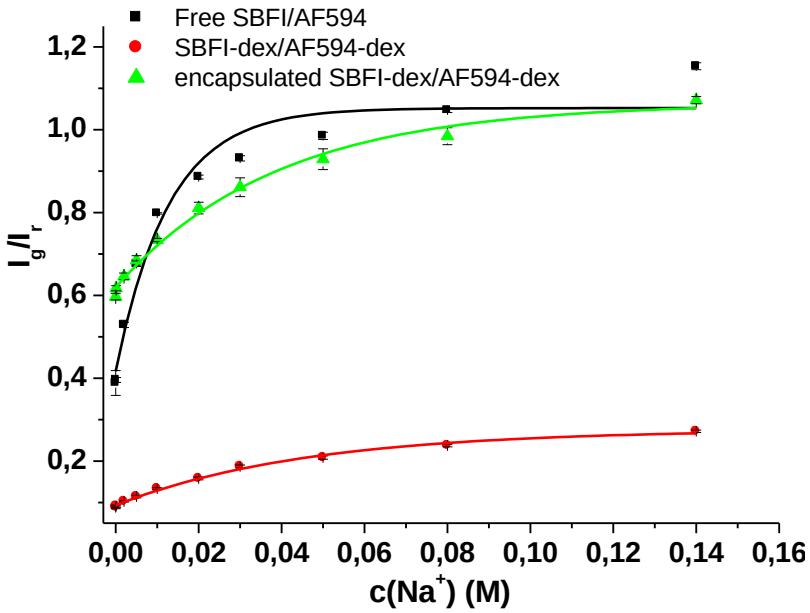

Figure 5. Comparison of fluorescence intensity ratio (I_g/I_r) of SBFI/AF594 in solution (squares) to SBFI-/AF594-dextran in solution (circles) and to SBFI-/AF594-dextran embedded in the capsules (triangles) with increasing Na^+ concentrations (pH 7.5). All values were averaged from three replicate scans at each concentration. Error bars show the standard deviation. Data points were fitted with eq. 2. The fit parameters used for the 3 curves are given in the table below. The important parameter for the Na^+-sensitivity is c_0.

cuvette measurements	I_0	ΔI	c_0[M]
free dye	0.42	0.64	0.013
dye bound to dextran	0.09	0.18	0.046
encapsulated dye	0.62	0.44	0.039

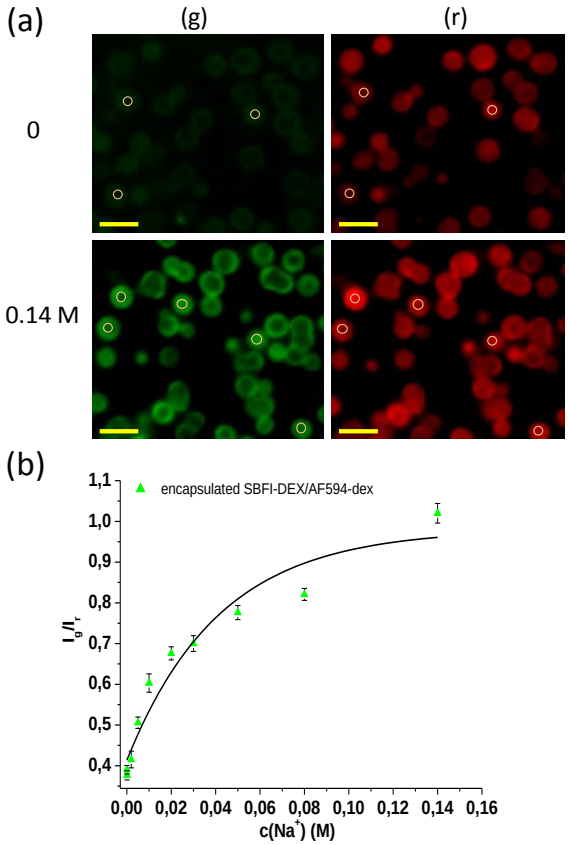

Figure 6. Ratio-imaging derived from ROI analysis performed in the cavity of single capsules simultaneously loaded with both SBFI-dextran and AF594-dextran. (a) Example of ROI analysis showing fluorescence microscopy images of capsules suspended in Tris 0.05 M buffer solution (pH 7.5) without (0) and with (0.14 M) Na^+. The circles indicate the ROIs drawn into the cavities that were used to measure the intensity of fluorescence in the green (I_g) and red channel (I_r) at different Na^+ concentrations. For simplicity, only the images of capsules at 0 and 0.14 M c(Na^+) are reported (see **SI**, **Figure SI-24**) (scale bars 3 μm). (b) Fluorescence intensity ratio I_g/I_r obtained from images such as shown in (a). The I_g/I_r value corresponds to the mean value of the ratios of the green and red fluorescence intensities plotted versus increasing c(Na^+) of the solution and fitted to a sigmoid curve. Error bars correspond to the standard deviation between 30 different capsules). Data points were fitted with eq. 2. The fit parameters used for the 3 curves are given in the table below. The important parameter for the Na^+-sensitivity is c_0.

ROI measurements	I_0	ΔI	c_0[M]
encapsulated dye	0.41	0.57	0.042

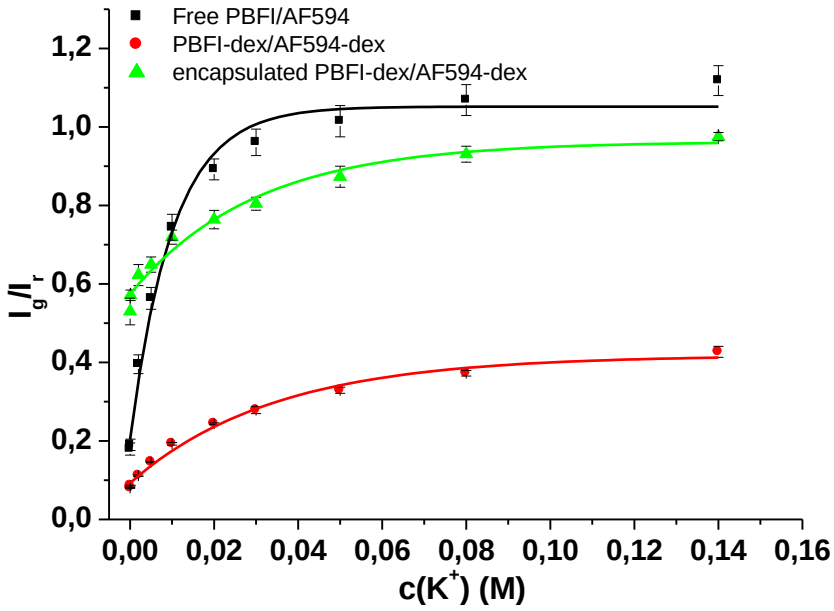

Figure 7. Comparison of fluorescence intensity ratio (I_g/I_r) of PBFI and AF594 in solution (squares) to PBFI-/AF594-dextran in solution (circles) and to PBFI-/AF594-dextran embedded inside capsules (triangles) with increasing K^+ concentration (pH 7.5). All values were averaged from three replicate scans at each concentration. Error bars show the standard deviation. Data points were fitted with eq. 2 (with $c(K^+)$ instead of $c(Na^+)$). The fit parameters used for the 3 curves are given in the table below. The important parameter for the K^+-sensitivity is c_0.

cuvette measurements	I_0	ΔI	c_0[M]
free dye	0.20	0.85	0.010
dye bound to dextran	0.09	0.32	0.034
encapsulated dye	0.57	0.39	0.030

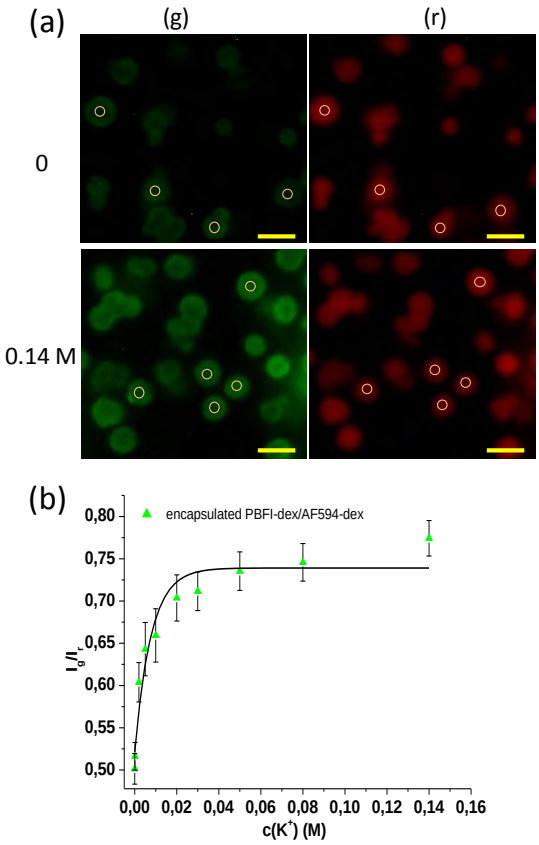

Figure 8 Ratio-imaging derived from ROI analysis performed in the cavity of single capsules simultaneously loaded with both PBFI-dextran and AF594-dextran. (a) Example of ROI analysis showing fluorescence microscopy images of capsules suspended in Tris 0.05 M buffer solution (pH 7.5) without (0) and with (0.14 M) K^+. The circles indicate the ROIs drawn into the cavities that were used to measure the intensity of fluorescence in the green and red channels at different K^+ concentrations. For simplicity, only the images of capsules at 0 and 0.14 M c(K^+) are reported (see **SI, Figure SI-25**) (scale bars 3 μm). (b) Fluorescence intensity ratio I_g/I_r obtained from images such as shown in (a). The I_g/I_r values correspond to the mean value of the ratios of the green and red fluorescence intensities plotted versus increasing K^+ of the solution and are fitted with a sigmoid curve. 30 capsules were analyzed and error bars correspond to the standard deviation between the individual capsules. Data points were fitted with eq. 2 (with c(K^+) instead of c(Na^+)). The fit parameters are given in the table below. The important parameter for the K^+-sensitivity is c_0.

ROI measurements	I_0	ΔI	c_0[M]
encapsulated dye	0.52	0.22	0.008

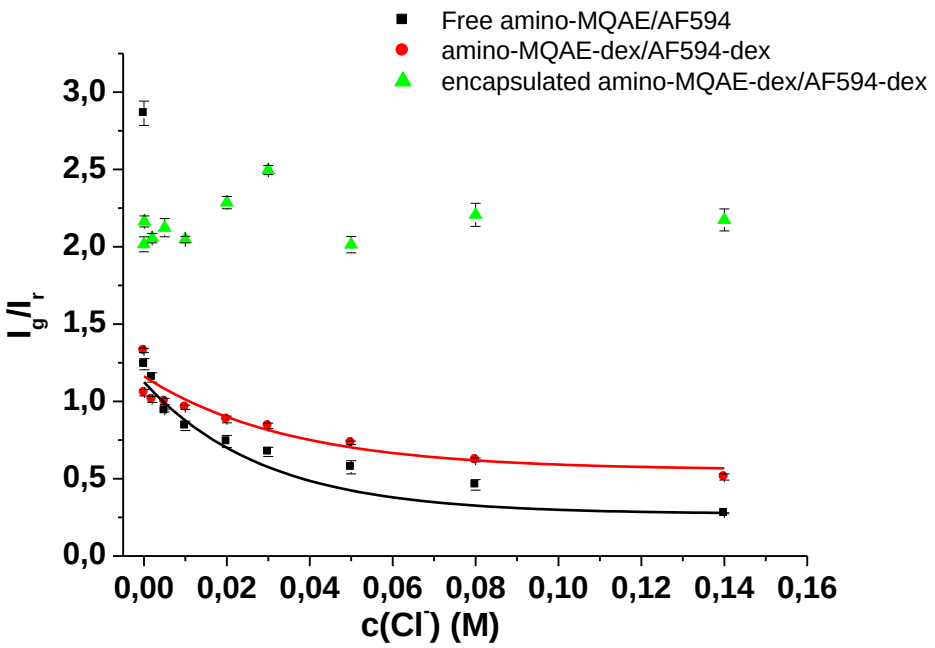

Figure 9. Comparison of fluorescence intensity ratio (I_g/I_r) of amino-MQAE and AF594 in solution (squares) to amino-MQAE-/AF594-dextran in solution (circles) and to amino-MQAE-/AF594-dextran embedded inside capsules (triangles) with increasing chloride concentration (pH 7.5). All values were averaged from three replicate scans at each concentration and error bars show the standard deviation. Data points were fitted with eq. 3. The fit parameters used for 2 curves are given in the table below. Encapsulated amino-MQAE/AF594-dextran data points were not fitted because of their non exponential behavior. The important parameter for the Cl^--sensitivity is c_0.

cuvette measurements	I_0	ΔI	c_0[M]
free dye	0.27	0.85	0.029
dye bound to dextran	0.56	0.61	0.035
encapsulated dye	-	-	-

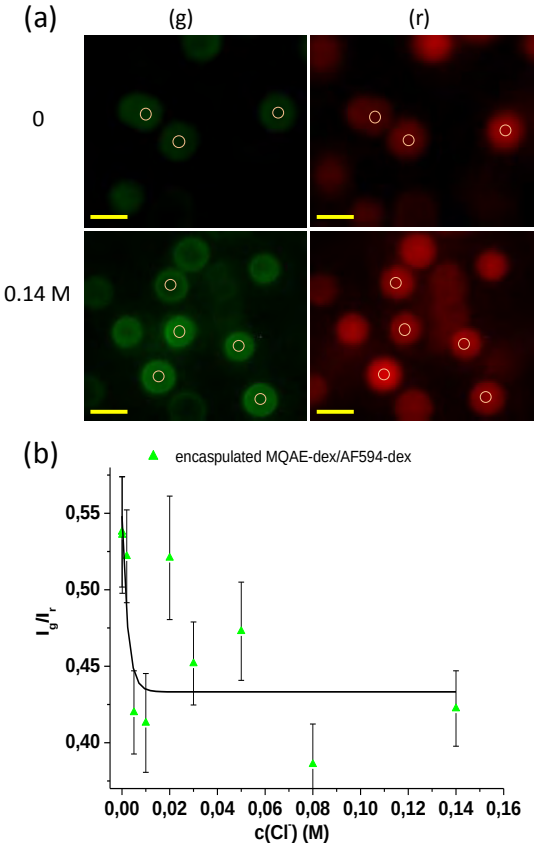

Figure 10. Ratio-imaging derived from ROI analysis performed in the cavity of single capsules simultaneously loaded with both MQAE-dextran and AF594-dextran. (a) Example of ROI analysis showing fluorescence microscopy images of capsules suspended in Tris 0.05 M buffer solution (pH 7.5) without (0) and with (0.14 M) Cl^-. The circles indicate the ROIs drawn into the cavities that were used to measure the intensity of fluorescence in the blue, here abbreviated as "g" and red (r) channels at different Cl^- concentrations. For simplicity, only the images of capsules at 0 and 0.14 M Cl^- concentration are reported (see **SI**, **Figure SI-26**) (scale bars 3 μm). (b) Fluorescence intensity ratio I_g/I_r obtained from images such as shown in (a). The I_g/I_r values correspond to the mean values of the ratios of the blue (I_g) and red (I_r) fluorescence intensities plotted versus increasing Cl^- of the solution. Error bars correspond to the standard deviation between the individual capsules, whereby 30 capsules were analyzed. Data points were fitted with eq. 3. The fit parameters used are given in the table below. The important parameter for the Cl^--sensitivity is c_0.

ROI measurements	I_0	ΔI	c_0[M]
encapsulated dye	0.43	0.11	0.002

Table of Content entry:

Ion-sensitive polyelectrolyte capsules for proton, sodium, potassium, and chloride are fabricated by embedding sensor dye molecules and reference dye molecules into their cavities. The fluorescence response of every sensor type is quantitatively evaluated by ratiometric fluorescence spectroscopy and ratiometric fluorescence microscopy measurements. Typically, the capsules are able to sense low, medium and high concentration of ions *in vitro*. In some conditions the read-out in ion sensing is affected by the surface charge of the macromolecules linked to the sensor dye molecules.

Table of Content figure:

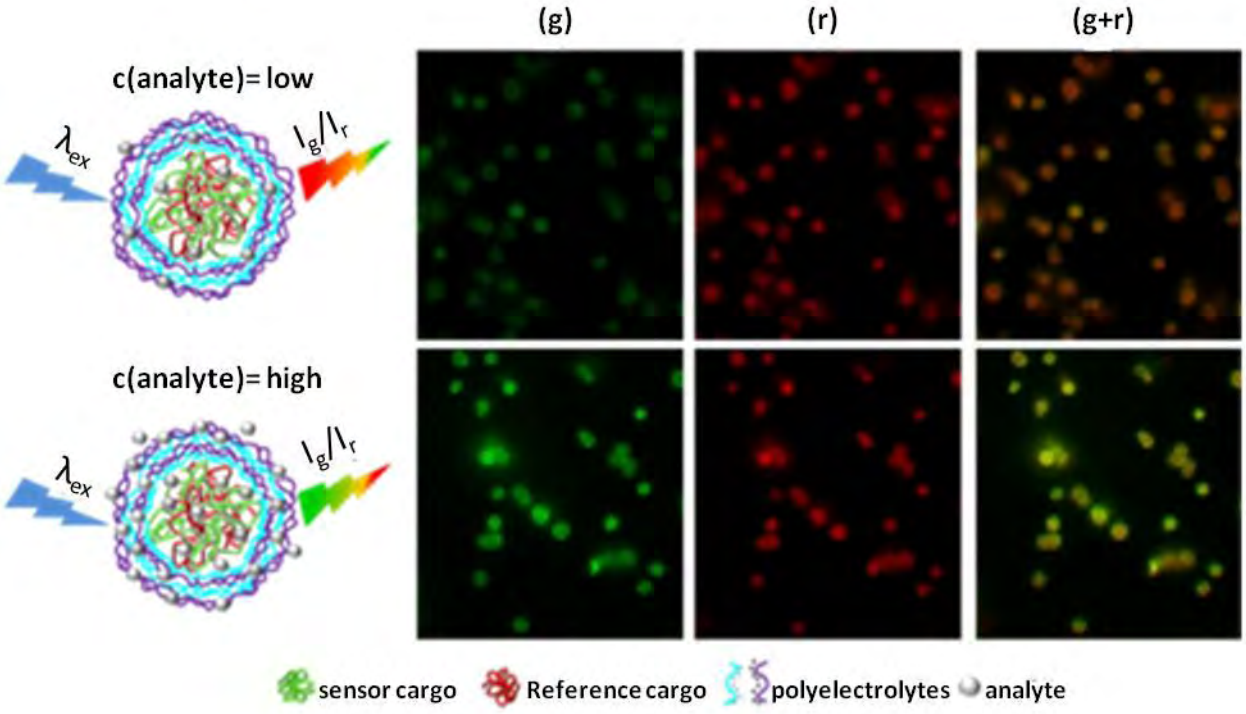

Keywords: Polymeric Capsules; Ion Sensing; Ratiometric Sensor; Fluorescence; Nanotechnology

Synthesis and characterization of ratiometric ion-sensitive polyelectrolyte capsules

Loretta L. del Mercato[1], Azhar Z. Abbasi[1], Wolfgang J. Parak[1,*]

[1] Fachbereich Physik and Wissenschaftliches Zentrum für Materialwissenschaften, Philipps Universität Marburg, Marburg (Germany)

Email: Wolfgang J. Parak (wolfgang.parak@physik.uni-marburg.de)

*Correspondence to Wolfgang J. Parak, Fachbereich Physik and Wissenschaftliches Zentrum für Materialwissenschaften, Philipps Universität Marburg, Marburg (Germany)

SUPPORTING INFORMATION

I) Long term motivation

The goal of our work consisted on using fluorescent indicators for K^+, Na^+, H^+ and Cl^- ions to build up ratiometric sensor systems based on polyelectrolyte microcapsules for multiple ion sensing inside living cells. We have chosen polyelectrolyte capsules as platform because of the possibility offered by such system to combine different functions for each individual sensor.[1-4] Indeed, the cavity can be loaded with the indicator probe, thus overcoming some of the main limitations of freely injected dyes (i.e., intracellular sequestration or inactivation, non-specific binding, toxicity). The semi-permeable wall plays two important functions: on the one hand it allows the diffusion of small analytes (e.g., ions) inside the cavities of the capsules, where the indicators are embedded. On the other hand it provides a barrier against the diffusion of high molecular weight components (e.g., proteins) inside the capsules, which would possibly affect the activity of the encapsulated indicator probes. Additionally, the wall of each sensor capsule can be further engineered by adding fluorescence molecules or quantum dots of different colors, thus in principle enabling multiplex real-time measurements of different ions inside living cells. Finally, by encapsulating also a reference dye, ratiometric fluorescence-based sensors can be effectively fabricated by rationing the fluorescence intensities of both indicator and reference dye.

Ratiometric sensors based on hollow polyelectrolyte microcapsules have been firstly reported by McShane *et al.*[5-7] In this work the authors loaded both, the bare indicator and the bare reference dyes into the shells of the capsules and then measured their sensing activity under different ion concentrations via fluorescence spectroscopy. The authors demonstrated that microcapsules may be used as chemical sensors for various analytes like potassium, sodium and oxygen through modification of the polyelectrolyte multilayer shells. In a different approach we have previously employed fluorescence microscopy as detection method for

measuring the answer of multifunctional ratiometric pH-sensor capsules inside living cells.[8] The capsule-based sensors were assembled by loading the ratiometric fluorescence probe seminaphtharhodafluor (abbreviated as SNARF, Invitrogen) into the cavities and pH-insensitive fluorophores into the shells of the capsules. In this way, two distinct compartments were individually utilized for sensing (cavity) and labeling (shell) purposes. In order to retain the sensor probes in the interior of the capsules, the SNARF molecules were covalently linked to a cargo macromolecule. In this way it was possible to distinguish between basic, neutral and acidic environments during the transition of the capsules from the alkaline cell medium to the acidic endosomal/lysosomal compartments.[8]

Thus, by loading different dextran-conjugate indicator and reference dyes together into the capsule cavities it is possible to design a set of ion sensitive capsules which undergo virtually the same interaction with cells. In this study, the fluorophores FITC and SNARF have been investigated as pH indicator probes, whereas the dyes SBFI, PBFI and amino-MQAE have been employed as Na^+, K^+ and Cl^- indicator probes, respectively. For non-ratiometric dyes (e.g., FITC, SBFI, PBFI and amino-MQAE) a reference dye was used (AF594) as internal standard to perform ratiometric determination of H^+, Na^+, K^+ and Cl^- ions. The indicator and the reference dye were separately conjugated to dextran molecules and entrapped within the cavity of the multilayer capsule. From the fluorescence intensity of the indicator and reference dyes, the I_g/I_r ratio was calculated and plotted against the tested ion concentrations thus obtaining calibration curves for several analytes. The response of each sensor capsule measured by fluorimetric measurements was compared to the response of the corresponding free dye and dye-dextran conjugate **(Figures 1,3,5,7,and 9)**. Notably, pH sensor capsules were analyzed in buffer solutions from pH 2.0 to pH 11, in 1 pH step, and K^+, Na^+ and Cl^- sensor capsules were tested in buffer solutions with ion concentrations varying from 0 M to 0.14 M in several steps. The aim of such measurements was to characterize the behavior of the capsules at numerous ion concentrations as well as to compare their trends to control samples (free dyes and dye-dextran conjugates). However, for sensing applications in living cells, the main prerequisite of the sensor would be dependent on its ability to distinguish between environments containing low (~0.01 M) or high (0.14 M) ion concentrations. Indeed, the extracellular concentration of Na^+ ions is estimated to be around 0.15 M, whereas its intracellular concentration is around 0.015 M. Similarly, the extracellular concentration of Cl^- ions is about 0.11 M and its intracellular concentration is around 0.007 M. Conversely, a low concentration of K^+ is found in the extracellular environment (~0.005 M) while an high concentration of this ion is found in the intracellular environment (~0.15 M).[9] These data indicate that the two environments are characterized by large difference on the concentration of these ions, thus sensor systems (e.g., polyelectrolyte capsules) able to detect such changes can be ideally suitable for ion-sensing inside cells. However, it has to be pointed out that for such measurements, crosstalk of the indicator probes to other ions should be taken into account. For example, MQAE shows crosstalk to other halogenides. It is well known that SBFI is also responsive for K^+ and vice versa.[10] In particular, SBFI is ~18-fold more selective for Na^+ than for K^+, whereas PBFI is only 1.5-fold more selective for K^+ than for Na^+. However, because there is normally about 10 times more K^+ than Na^+ in cells, it has been accepted from the scientific community that PBFI is suitable for intracellular potassium determinations. Following this approach, sensor capsules can still be suitable for intracellular measurements of ions by detecting between low and high ion concentrations. We are currently measuring the crosstalk between every capsules sensor and different ions in order to include a calibration for quantitative measurements of intra- and extracellular concentration ions.

Clearly, the key properties of the resulting hybrid sensor-based systems (such as sensitivity, selectivity, reversibility and stability) mainly depend on the characteristics of the available fluorescence probe indicators. Therefore, it is evident that the design and synthesis of novel fluorophores that allow for ratiometric sensing must be under continuous progress to enhance the final properties of the sensors. However, as explained the integration of fluorophores to nano- and micrometer-sized carrier systems brings in advantages compared to the plain fluorophores.

II) Description of the Analyte-Specific Fluorescent Indicators

II.1) *FITC, fluorescein 5(6)-isothiocyanate*
II.2) *SNARF, SNARF, 5-(and-6)-carboxy SNARF®-1*
II.3) *PBFI. tetraammonium salt and SBFI, tetraammonium salt*
II.4) *Amino-MQAE, 2-(2-(6-Methoxyquinoliniumchloride)ethoxy)-ethanamin-hydrochloride*

II.1) *FITC, fluorescein 5(6)-isothiocyanate*

FITC (Fluka, #46950) is an amine reactive derivative of fluorescein. FITC has a pK_a ~6.5 and its fluorescence is significantly reduced below pH 7.0, thus making this dye useful for intracellular measurements of pH. The fluorescence of the dye increases when the ambient pH changes from acidic to alkaline.

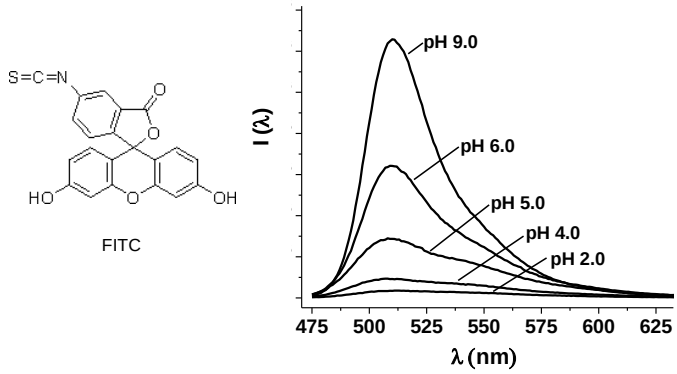

Figure SI-1. (Left) Chemical structure of the pH indicator FITC (*image taken from Sigma*). (Right) Fluorescence emission spectra of FITC under different pH (λ_{exc} = 490 nm; λ_{em} = 518 nm) (*Author recorded spectra*).

II.2) *SNARF, 5-(and-6)-carboxy SNARF®-1*

SNARF (Invitrogen, #C-1270) is a fluorescent ratiometric probe that allows pH quantification virtually independent of probe concentration and/or laser intensity. As a dual-emission pH indicator, the fluorescent probe. SNARF changes its fluorescence spectrum from green-yellow to red when the ambient pH changes from acidic to alkaline (pK_a of ~7.5). This pH dependence determines the ratio of the fluorescence intensities of the dye at two emission wavelengths - typically 580 nm and 640 nm. The ratio of intensities obtained at both wavelengths provides a quantitative measure of pH.

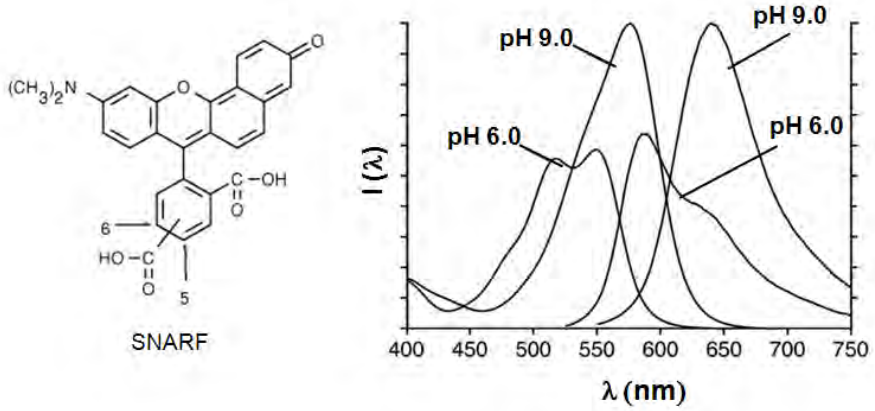

Figure SI-2. (Left) Chemical structure of the pH indicator SNARF. (Right) Absorption and fluorescence emission (excited at 514 nm) spectra of carboxy SNARF-1 in pH 9.0 and 6.0 buffers (λ_{exc}= 488 nm or 514 nm; λ_{em} = 580 nm/640 nm). *Images taken from Invitrogen*.

II.3) *PBFI. tetraammonium salt and SBFI, tetraammonium salt*
SBFI (Invitrogen, #S1262) and PBFI (Invitrogen, #P1265MP) are fluorescent indicators for sodium and potassium, respectively. The fluorescence of both PBFI and SBFI increase as $c(K^+)$ or $c(Na^+)$ increases, respectively. The K_d of SBFI for Na^+ is 11.3 mM in the presence of physiological concentrations of K^+ and 3.8 mM without K^+. SBFI is ~18 times more selective for Na^+ than for K^+.

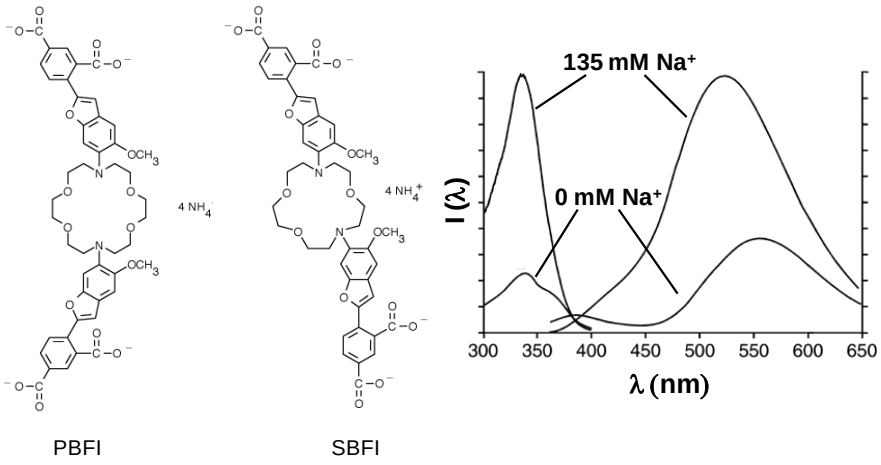

Figure SI-3. (Left) Chemical structures of the potassium (PBFI) and the sodium (SBFI) indicators. (Right) Fluorescence excitation (detected at 505 nm) and emission (λ_{exc}= 340 nm) spectra of SBFI in pH 7.0 buffer containing 135 mM or zero $c(Na^+)$. *Images taken from Invitrogen*.

II.4) *Amino-MQAE, 2-(2-(6-Methoxyquinoliniumchloride)ethoxy)-ethanamin-hydrochloride*
MQAE is a 6-methoxyquinolinium derivative and is a chloride-sensitive dye of which the fluorescence is quenched by chloride ions. The amino-modified MQAE dye has been provided by Florian Dommerhausen from the group of Prof. Dr. Ulrich Koert.[11]

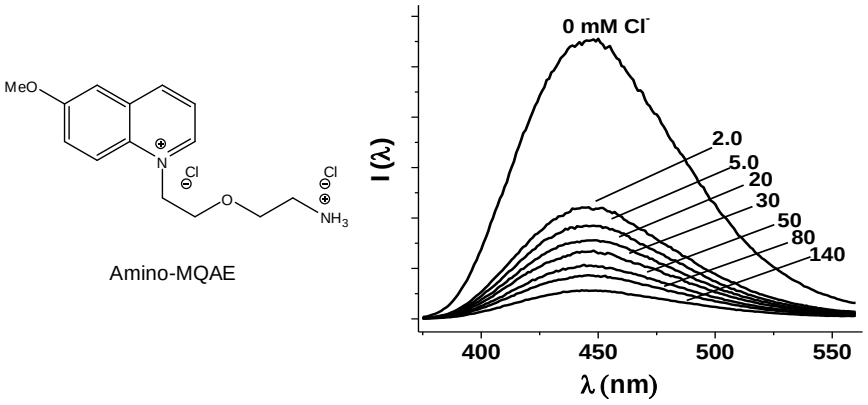

Figure SI-4. (Left) Chemical structure of the chloride sensitive quinolinium-derivate amino-MQAE.[11] (Right) Fluorescence emission spectra of amino-MQAE in increasing concentrations of c(Cl^-) (λ_{exc}= 350 nm; λ_{em} = 518 nm).

III) Conjugation of dyes to dextran and subsequent encapsulation

III.1) *Conjugation of amino- and carboxyl- reactive dyes to carboxy- and amino-dextran*
III.2) *Estimation of dye concentration*
III.3) *Scheme of the synthesis of LbL multilayer capsules based on $CaCO_3$ cores*
III.4) *Estimation of the amount of encapsulated dextran labeled molecules after synthesis of $CaCO_3$ microparticles*
III.5) *Estimation of the charge of different dextran labeled molecules*

III.1) *Conjugation of amino- and carboxyl- reactive dyes to carboxy- and amino-dextran*

The dyes were covalently linked to dextran molecules via simple coupling reactions between the dyes functionalized with carboxyl- (SBFI, PBFI, SNARF), amine- (MQAE) or isothiocyanate- (FITC) groups and the dextran, which contained either amine- or carboxyl-groups. This procedure prevents the diffusion of the low molecular weight dyes out of the capsule cavities. In this way the fluorescent indicator and the reference dye are kept inside the cavities and are able to sense the ion concentration of the surrounding bulk solution. In fact, as already described, the multilayer shell of the capsules acts as a porous membrane through which small molecules, such as ions, can travel in and out and can thus virtually freely interact with eventual probes encapsulated inside the capsule interior (Scheme 1).

The carboxyl containing fluorophores (SNARF, SBFI and PBFI) were reacted with free amino groups of AM-dextran 500 kDa (Invitrogen, # D-7144) by means of a condensation reaction to yield amide bonds. For this, a high excess molar ratio of water-soluble carbodiimide, EDC hydrochloride[12] was added to each reaction mixture. After forming an intermediate compound with the carboxylic moiety, the activated group is reactive towards the amines.[12] Similarly, the amino containing dye, amino-MQAE, was conjugated to carboxymethyl-dextran sodium salt (CM-dextran) 12 kDa (#86524, Sigma) by use of the EDC reaction. Carboxymethyl-dextran of 500 kDa (CarboMer, Inc., #500939) was initially used for conjugating the amino-MQAE dye. However the conjugation reaction was not efficient because of the poor solubility of the high molecular weight compound in a variety of tested solvents. In particular, small aliquots of CM-dextran 500 kDa (5 and 10 μM) were dispersed in SBB buffer pH 9.0, MES-Na buffers pH 7.0, DMSO and THF. In all cases the CM-dextran was not fully soluble and the formation of a gel-like solution was observed also after sonication at 40-50 ℃ for several hours (up to 10 hours). Therefore we decided to use the 12 kDa CM-dextran in order to overcome the solubility problems of the 500 kDa CM-dextran. However, this choice resulted in the partial loss of the cargo molecules from the cavities of the capsules because of the permeability of the capsules which allows molecules $\leq$70 kDa to diffuse through the multilayer wall. The details of the protocols used to conjugate CM-dextran and AM-dextran to amino- and carboxyl- reactive dyes are given below. The dye:polymer ratios in the labeling reaction are meant in number of molecules.

The SBFI and PBFI dyes were separately conjugated to 500 kDa AM-dextran by using a molar ratio of 25:1 (dye:polymer). 40 mg of AM-dextran (500 kDa) was dissolved in 8 mL of MES-Na buffer 0.05 M at pH 6.0 (2-(N-Morpholino)ethanesulfonic acid, #M3671, Sigma). Subsequently, 1 mL of 2 mM SBFI or 2 mM PBFI dye in Milli-Q water was added to the AM-dextran solution. Finally, 800 μL of 1 M EDC in MES-Na buffer 0.05 M at pH 6.0 was added to the reaction mixture (molar ratio 10000:1, EDC:dextran) and the resulting solution was incubated 2 hours under agitation (dark, room temperature). SNARF was conjugated to 500 kDa AM-dextran by using a molar ration of 35:1 (dye:polymer). 30 mg of AM-dextran (500 kDa) was dissolved in 6 mL of MES-Na buffer 0.05 M at pH 6.0 (2-(N-Morpholino)ethanesulfonic acid, #M3671, Sigma). Subsequently, 1.05 mL of 2 mM SNARF

dye in Milli-Q water was added to the AM-dextran solution. Finally, 600 μL of 1 M EDC in MES-Na buffer 0.05 M at pH 6.0 was added to the reaction mixture (molar ratio 10000:1, EDC:dextran) and the resulting solution was incubated 2 hours under agitation (dark, room temperature).
The amino-MQAE was conjugated to 12 kDa CM-dextran by using a molar ratio of 50:1 (dye:polymer). The reaction was carried out in the following way: 15 mg of CM-dextran (12 kDa) was dissolved in 1.25 mL of Sodium borate buffer 0.05 M at pH 9.0. Subsequently, 2.5 mL of 25 mM amino-MQAE dye in SBB pH 9.0 was added to the CM-dextran solution. Finally, 3.75 mL of 1 M EDC in SBB pH 9.0 was added to the reaction mixture (molar ratio 3000:1, EDC:dextran) and the resulting solution was incubated 2 hours under agitation (dark, room temperature).
The amine-reactive AF594, containing the active ester N-hydroxysuccinimide (NHS), was conjugated to AM-dextran by reacting the NHS ester with free amino groups on the dextran of 500 kDa by forming a stable, covalent amide bond. A molar ratio of 6:1 (dye:polymer) was used. The reaction was carried out in the following way: 50 mg of AM-dextran (500 kDa) was dissolved in 5 mL of Sodium borate buffer 0.05 M at pH 9.0. Subsequently, 50 μl of AF594 dye 12 mM, dissolved in DMSO 99.9%, was added to the AM-dextran solution and the resulting solution was incubated 2 hours under agitation (dark, room temperature).
FITC-dextran was obtained by reaction of the isothiocyanate group (NCS) of the dye with the free amino groups of AM-dextran 500 kDa by forming a stable thiourea bond (#09161: Bioconjugate Techniques). A molar ratio of 12:1 (dye:polymer) was used. The reaction was carried out in the following way: 50 mg of AM-dextran (500 kDa) was dissolved in 5 mL of Sodium borate buffer 0.05 M at pH 9.0. Subsequently, 100 μl of FITC dye 12 mM, dissolved in DMSO 99.9%, was added to the AM-dextran solution and the resulting solution was incubated 2 hours under agitation (dark, room temperature).
After 2 hours of incubation, all the solutions were extensively washed against with water (about 2 weeks) to remove non-reacted reagents by using centrifugal filter tubes (3000 rpm, 15 minutes each cycle). Filter units with a molecular weight cut-off of 30 kDa (Amicon Ultra-15, Cat. No. UFC903024; Millipore, Bedford, MA) were used to wash the labeled 500 kDa AM-dextran. To wash the labeled 12 kDa CM-dextran, centrifugal filter tubes with a molecular weight cut-off of 3 kDa were used. Washing was performed until no fluorescence signal in the downstream of the tubes was detectable by spectrometer analysis. The concentration of the dye was measured by absorbance spectrometer. Then the conjugated dextrans were stored protected from light at -20 ℃.

III.2) *Estimation of dye concentration*
From the Beer-Lambert Law ($A = \varepsilon * l * c$) and the maximum absorption peak (A) of each dye solution at given path length (l), the concentration (c) of the free and conjugated species of the dyes in aqueous suspensions were determined. For the AF594, SBFI, PBFI and SNARF dyes, we have used the available molar extinction coefficients (ε) reported from Invitrogen Company (AF594: 90,000 $cm^{-1}M^{-1}$ at 590 nm; PBFI and SBFI: 42,000 $cm^{-1}M^{-1}$ at 340 nm; SNARF: 27,000 $cm^{-1}M^{-1}$ at 540 nm). For amino-MQAE and for FITC dyes, we have determined the ε value by measuring the maximum absorption peak of aqueous dye suspensions at different known molar concentrations. Six concentrations were measured (0.01, 0.008, 0.006, 0.004, 0.002, 0.001 mM) and three readings for each concentration were recorded and averaged. The average absorption maxima values (A) were then plotted versus the concentration (c) to build a calibration curve. We determined the extinction coefficient (ε)

from the following equation $A = A_0 + \varepsilon * c$ by the linear fit function of the plotted values. ε values of 537,270 $cm^{-1}M^{-1}$ and 30,560 $cm^{-1}M^{-1}$ were determined for amino-MQAE and FITC, respectively.

III.3) *Scheme of the synthesis of LbL multilayer capsules based on $CaCO_3$ cores*

Figure SI-5 shows the main steps used in the synthesis of LbL multilayer capsules based on $CaCO_3$ cores. Steps 1 (core formation) and steps 4 (core removal) are the most important steps which may strongly influence the quality of the resulting capsules in terms of morphology and sensing properties.

Regarding step 1, after mixing equal quantities of $CaCl_2$ and Na_2CO_3 solutions, $CaCO_3$ cores with some variability of size can be observed, especially between different batches of microparticles. This can be mainly addressed to small changes of some conditions, such as the temperature and the stirring speed, which turned out to be crucial parameters for the control of morphologies of $CaCO_3$. For instance, it was observed that by using cold solutions of $CaCl_2$ and Na_2CO_3 or by performing the co-precipitation step in an ice bath (T~4 ℃), the size of the $CaCO_3$ microparticles can be increased up to 5-10 μm. Conversely, by increasing the temperature (30 ℃) and the mixing speed (1200 rpm) particles of approximately 1 μm can be obtained. These factors must be strictly controlled in order to produce batches of capsules with comparable properties for long-time studies in living cells.

Regarding step 4, we observed that the initial exposure of the microcapsules to a slightly acidic EDTA solution lead to a faster and complete decomposition of the $CaCO_3$ cores compared to their direct exposure to a neutral EDTA solution. The use of an acidic EDTA solution has been previously reported by others.[13-15] In particular, the dissolution of the cores appears to be very fast when EDTA is added onto microcapsules which cores have been pre-loaded with some dextran macromolecules. Instead, microcapsules prepared onto plain cores must be incubated for longer time (around 1 hour) with fresh solutions of EDTA to efficiently remove the templates. This different behavior might be due to some changes into the structure of the templates between filled and non-filled $CaCO_3$ particles.

During this step we also observed the partial diffusion of dye-dextran conjugates out of the cavities of some capsules. It was found that diffusion of dextran varies not only depending on its molecular weight but also on the chemical structure of the conjugated dye as well as on the reactivity of the dye. This phenomenon may affect the optical ratiometric imaging analysis of the sensors which is based on the study of the fluorescence changes of the sensor probes embedded in the cavities of the capsules. We tried to overcome diffusion of cargo by increasing the molecular weight of dextran up to 500 kDa. In this way we have limited the diffusion of dextran through the multilayer shell of 5 polyelectrolyte bi-layers (PSS/PAH) capsules.

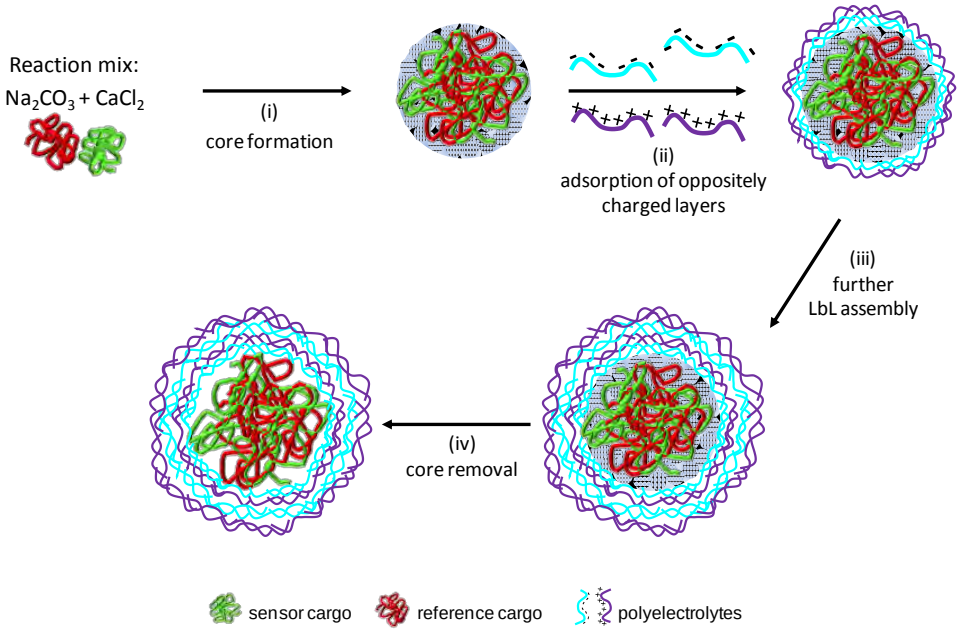

Figure SI-5. LbL assembly of a multilayer polyelectrolyte sensor capsule. (i) $CaCO_3$ microparticles are fabricated by co-precipitation from supersaturated $CaCl_2$ and Na_2CO_3 solutions. The fluorescent analyte-indicator and the reference dyes are covalently linked onto individual dextran polymers and are both encapsulated within the same $CaCO_3$ matrix by adding them during the particle formation process. (ii–iii) Oppositely charged polyelectrolytes are consecutively adsorbed around the spherical templates by electrostatic attractions. (iv) The original template is removed by dissolution to obtain a hollow capsule with encapsulated fluorescent indicator and reference dye. Capsules are not drawn to scale.

III.4) *Estimation of the amount of encapsulated dextran labeled molecules after synthesis of $CaCO_3$ microparticles*

UV/vis spectroscopy was used to measure the amount of dextran molecules loaded into $CaCO_3$ cores by monitoring the changes in the concentration of the dye molecules (sensor dyes and reference dye) covalently linked to the dextran molecules during each step of core synthesis.

For this purpose, an aliquot of the dye-dextran solution was used to measure the concentration of the dye molecules in the original stock solution (**Table 1**, c_i) before their loading into the $CaCO_3$ microparticles. After synthesis of $CaCO_3$ cores, the resulting microparticles were centrifuged and precipitated at the bottom of the tube. The supernatant solution, containing the excess dextran molecules not embedded into the cores, was removed and replaced by Milli-Q water to wash the spherical cores. An aliquot of the supernatant was used to measure the concentration of the dye molecules (**Table 1**, c_f). By subtracting the amount of the dextran molecules remained in the supernatant solution to the original amount added into the reaction mixture, the total amount of molecules actually encapsulated could be estimated (**Table 1**,c_{core}). During LbL coating of such $CaCO_3$ filled particles a partial loss of dextran cannot be excluded, thus the final quantity of dye-dextran conjugates into the cavities of the capsules might be further reduced.

Dye-Dex(500kDa)	c_i (μM)	c_f (μM)	c_{core} (μM)
FITC	10	4.34	5.66
Alexa	9.24	8.05	1.18
PBFI	10	7.55	2.45
SBFI	10	8.82	1.17
SNARF	9.62	6.53	3.0

Table 1. Calculation of the amount of embedded dye molecules conjugated to dextran after co-precipitation of $CaCO_3$ microparticles (c_i = initial concentration; c_f = supernatant concentration; c_{core} = concentration in the cores particles).

III.5) *Estimation of the charge of different dextran labeled molecules*
The charge of the labeled dextran molecules was measured by gel electrophoresis: a 10 μM aliquot of each labeled dextran was loaded on a 2% agarose gel and run for 1 hour at 100V in Tris-borate-EDTA (TBE) buffer 0.5 M. As expected, after labeling the overall charge of each AM-dextran remains positive, as can be seen by the migration of the polymers toward the negative electrode **(Figure SI-6)**.

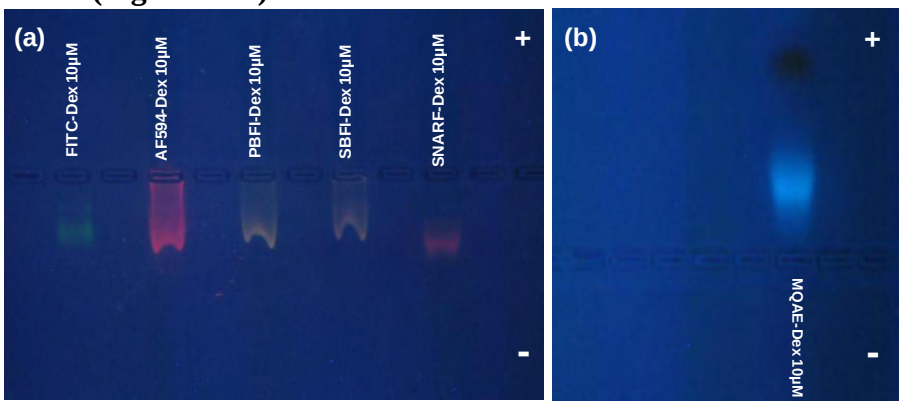

Figure SI-6: Gel electrophoresis of (a) AM-dextran (500 kDa) after linking to FITC, AF594, PBFI, SBFI or SANRF; (b) CM-dextran (12 kDa) after linking to amino-MQAE.

IV) Fluorescence spectra from cuvette measurements
IV.1) *Scheme of cuvette measurements*
IV.2) *FITC and AF594 mixtures*
IV.3) *SNARF*
IV.4) *SBFI and AF594 mixtures*
IV.5) *PBFI and AF594 mixtures*
IV.6) *Amino-MQAE and AF594 mixtures*
IV.7) *Reproducibility between different batches*

IV.1) *Scheme of cuvette measurements*
All Na^+, K^+ and Cl^- sensing measurements were achieved by dissolving NaCl or KCl in Tris 0.05 M buffer solutions, keeping the pH constant (7.5) while raising the ion concentration in the solution up to 0.14 M. All the pH-sensing measurements were recorded in commercial

standard buffers of different pH values (2.0-11) (#38741; #38742; #38743; #38744; #38745; #38745; #38747; #38748; #38749; #38750, Fluka, Sigma).
For analysis of free dye and dye-dextran conjugates, the final concentration of the indicator and reference dyes in the solution was kept constant (12.5 µM each) while changing the ion concentration. For example, to measure the response of SBFI (or SBFI-dextran) in a 0.14 M NaCl solution 10 µL of a 50 µM stock of FITC dye (or FITC-dextran) was added to 10 µL of a 50 µM stock of AF594 dye (or AF594-dextran). The resulting 20 µL of dyes was then diluted with 20 µL of 0.28 M NaCl solution (final concentration of the dyes = 12.5 µM, final concentration of NaCl = 0.14 M). For capsule analysis, 10µl of capsules loaded with the dextran-conjugated dyes was diluted in 10µl of ion-solutions containing the double amount of ion concentration respect to the desired final concentration.
pH-sensing measurements were performed by mixing the samples with an excess of buffer in a sample to buffer ratio of about 1:10. The pH of all final solutions was checked by a pH meter (Professional-Meter PP-50, Sartorius, equipped with a Mettler Toledo, InLab®Micro thin detector, for pH 2-11, electrolyte: 3 M KCl, Item code: T-LOQ, Item number: 51343160) before and after buffer addition as control.

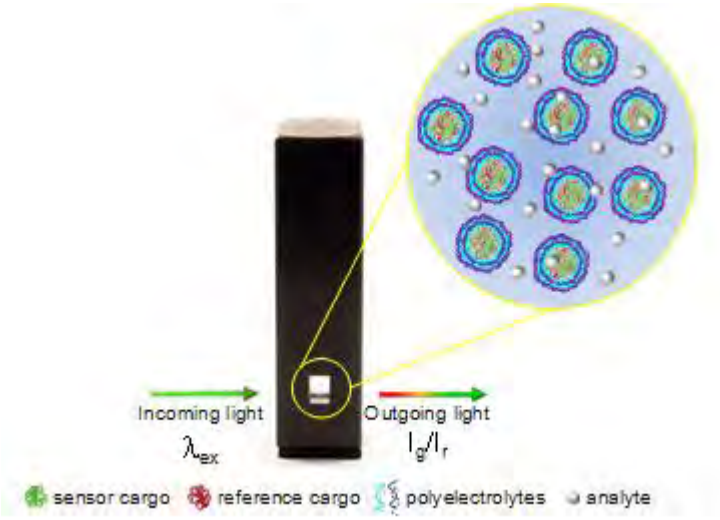

Figure SI-7. Schematic representation showing fluorescence spectroscopy measurements performed by adding the sensor capsules into a cuvette containing buffer with the desired ion concentration. The fluorescence intensity signal of both the indicator (I_g) and reference (I_r) dye were simultaneously recorded. The indicator dyes SBFI and PBFI were excited at 340 nm, amino-MQAE at 350 nm, FITC at 490 nm and SNARF at 540 nm. The reference dye AF594 was excited at the same wavelength used for each indicator (λ_{exc}). Ratiometric measurements of H^+, Na^+, K^+ and Cl^- ions were performed by measuring the ratio of the fluorescent indicator peak (I_g) to the fluorescent reference dye peak (I_r).

IV.2) *FITC and AF594 mixtures*

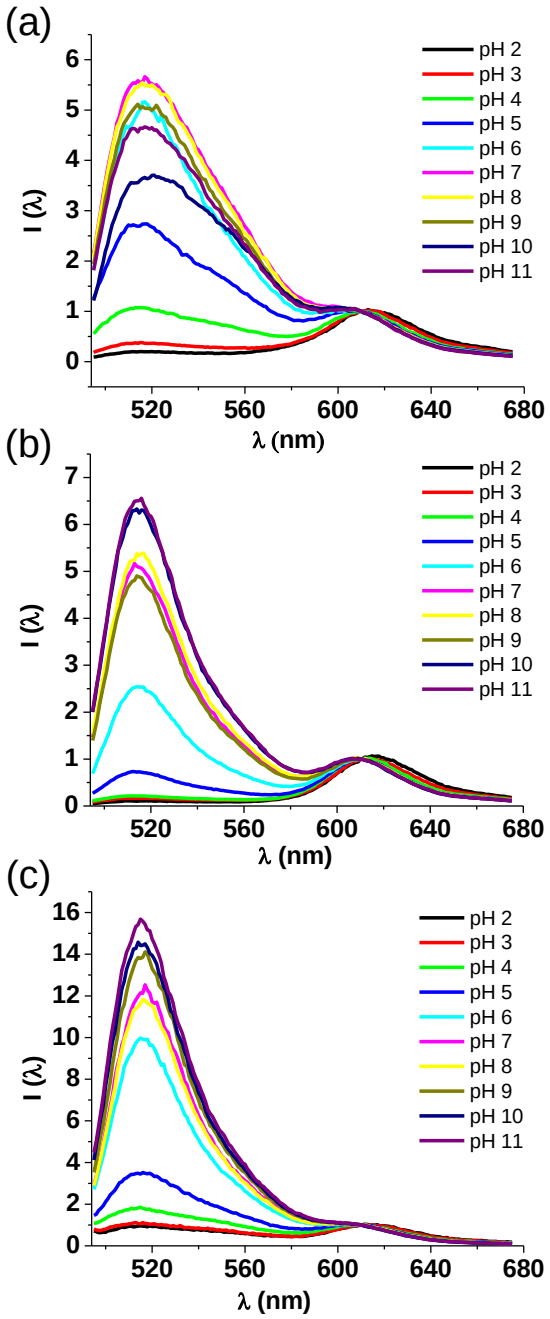

Figure SI-8. Fluorescence spectra (normalized to 610 nm) of (a) FITC and AF594 free in solution, (b) FITC-/AF594-dextran in solution and (c) FITC-/AF594-dextran embedded inside the capsules, with increasing pH values.

IV.3) *SNARF*

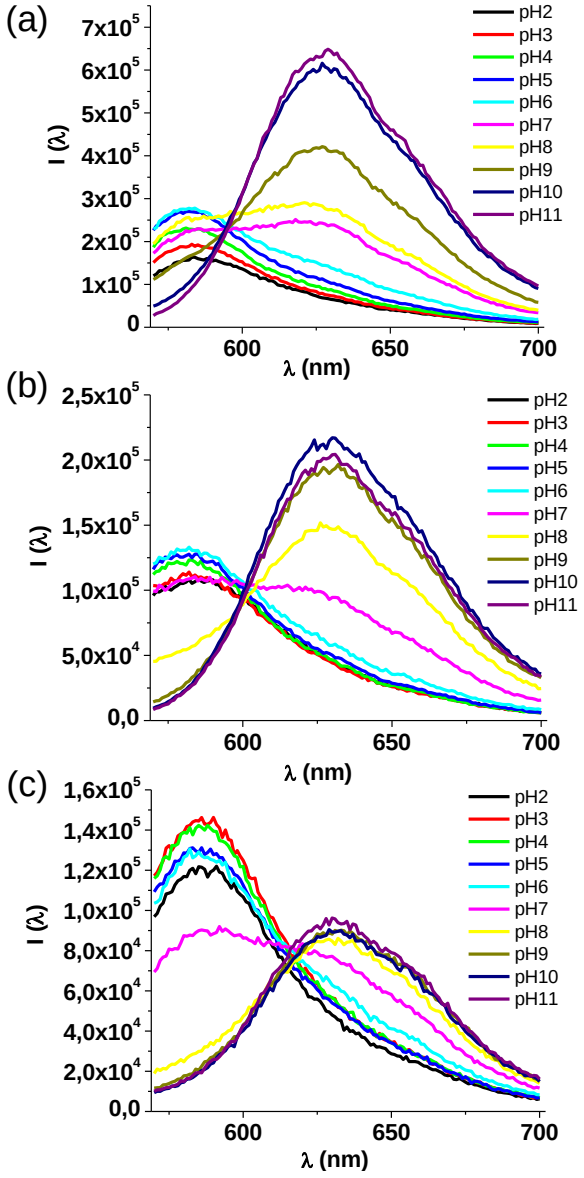

Figure SI-9. Fluorescence spectra of (a) SNARF free in solution, (b) SNARF-dextran in solution and (c) SNARF-dextran embedded inside the capsules, with increasing pH values.

IV.4) *SBFI and AF594 mixtures*

12.5 µM of free SBFI dye was mixed with NaCl stock solutions (1:1) in a 50 µL plastic tube and then transferred into a quartz cuvette for fluorimteric titration analysis. **Figure SI-10a** shows the fluorescence spectra of SBFI recorded at Na^+ concentrations from 0 M to 0.14 M. As expected, the fluorescence response of the indicator is sensitive to Na^+ ions. Subsequently, in order to measure the degree of pH sensitivity of SBFI, the free dye (12.5 µM) has been mixed with buffer solutions of different pH values (1:1) and with constant Na^+ concentration (~ 0.07 M). Changes in the emission wavelength or emission intensity of SBFI occurs over the whole investigated pH range (2.0-10) indicating a certain degree of pH sensitivity of the dye (λ_{exc} 340 nm).

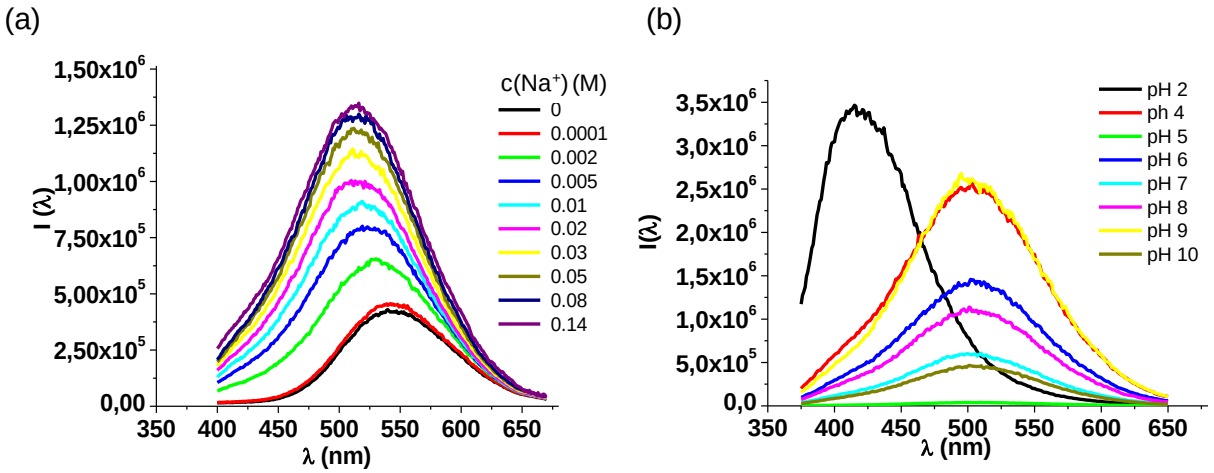

Figure SI-10. Fluorescence spectra of SBFI dye free in solution under different conditions. (a) Free SBFI (12.5 µM) in Tris 0.05 M buffer at constant pH value (pH = 7.6), with increasing sodium concentration (0-1.14 M). (b) Free SBFI (12.5 µM) at constant Na^+ concentration (~ 0.07 M) under different pH values.

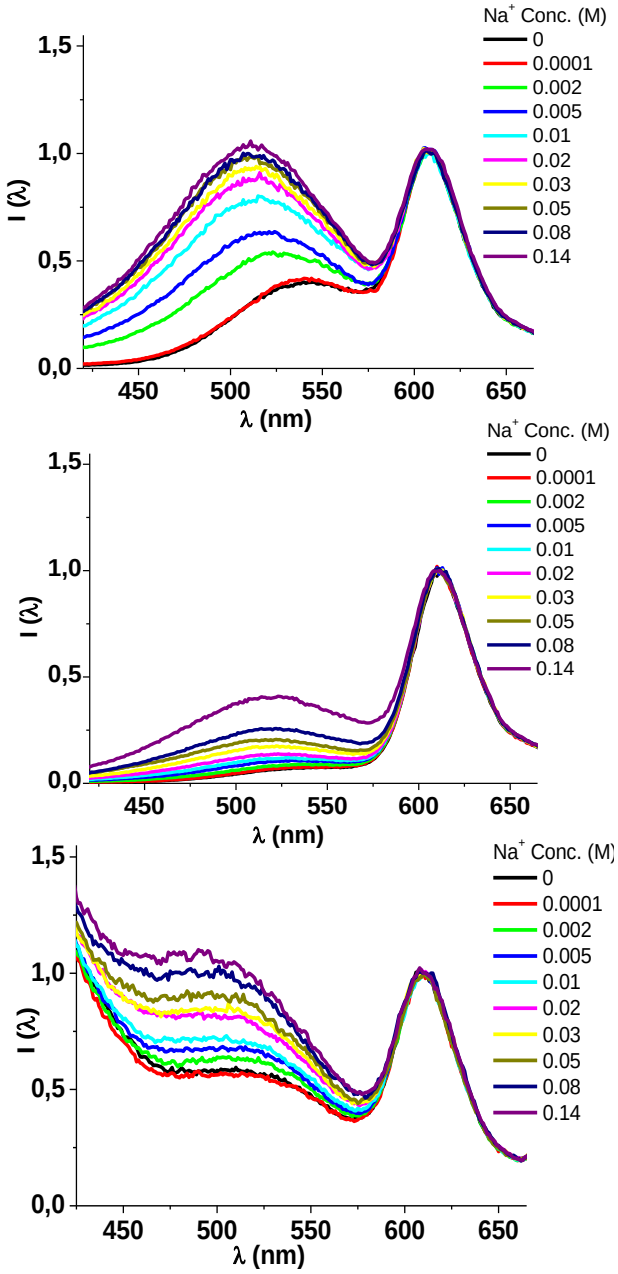

Figure SI-11. Fluorescence spectra (normalized to the emission peak at 610 nm) of (a) SBFI and AF594 dyes free in solution, (b) SBFI-/AF594-dextran in solution and (c) SBFI-/AF594-dextran embedded inside the capsules, with increasing sodium concentration.

IV.5) *PBFI and AF594 mixtures*

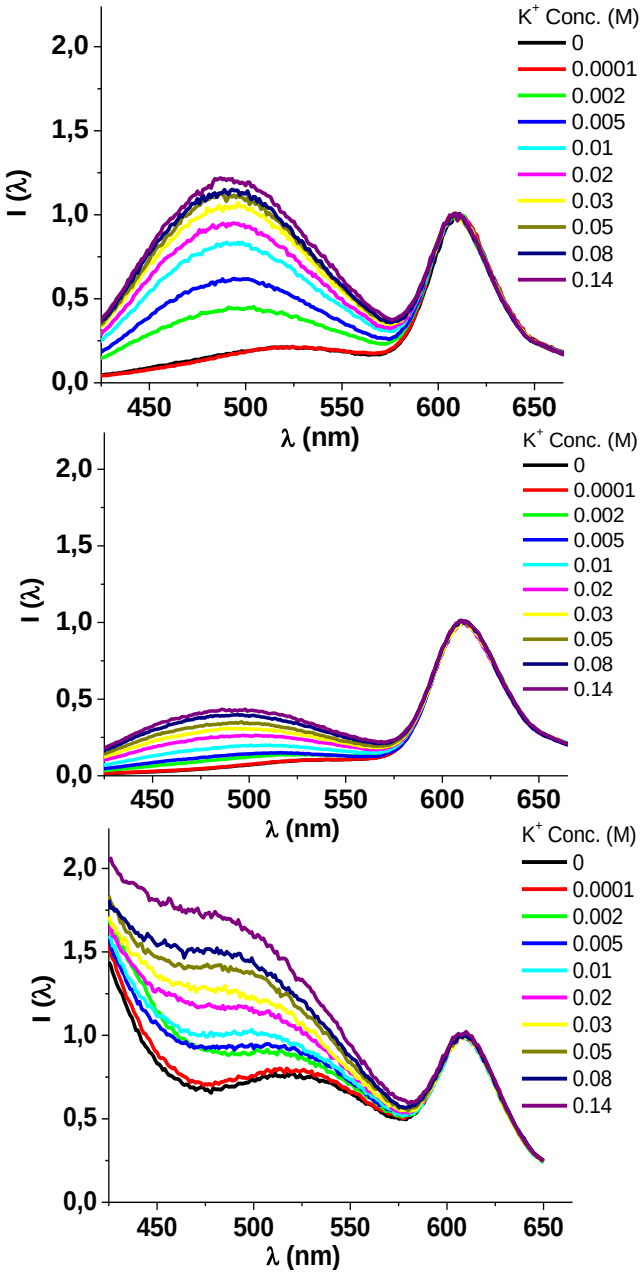

Figure SI-12. Fluorescence spectra (normalized to the emission maximum at 610 nm) of (a) PBFI and AF594 dyes free in solution, (b) PBFI-/AF594-dextran in solution and (c) PBFI-/AF594-dextran embedded inside the capsules, with increasing potassium concentration.

IV.6) *Amino-MQAE and AF594 mixtures*

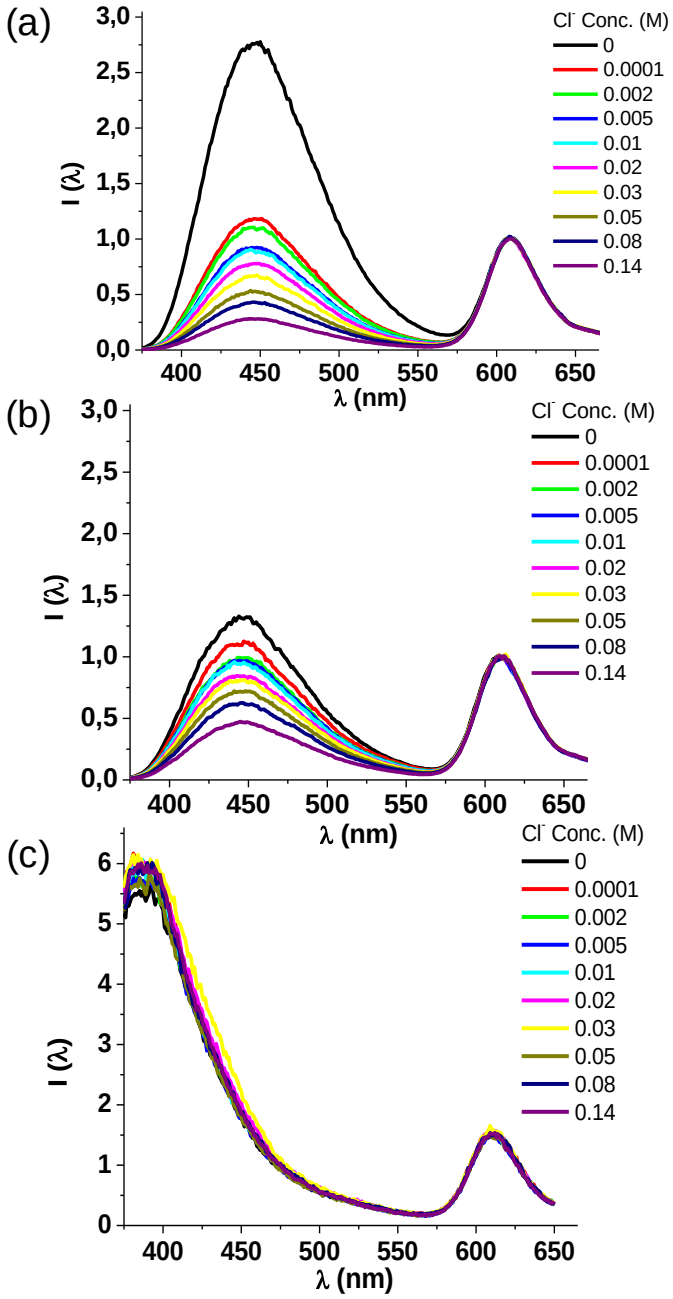

Figure SI-13. Fluorescence spectra (normalized to the emission peak at 610 nm) of (a) amino-MQAE and AF594 dyes free in solution, (b) amino-MQAE-dextran12 kDa and AF594-dextran500 kDa in solution, and (c) amino-MQAE-dextran12 kDa and AF594-dextran500 kDa both embedded inside the capsules, with increasing chloride concentration.

IV.7) *Reproducibility between different batches*

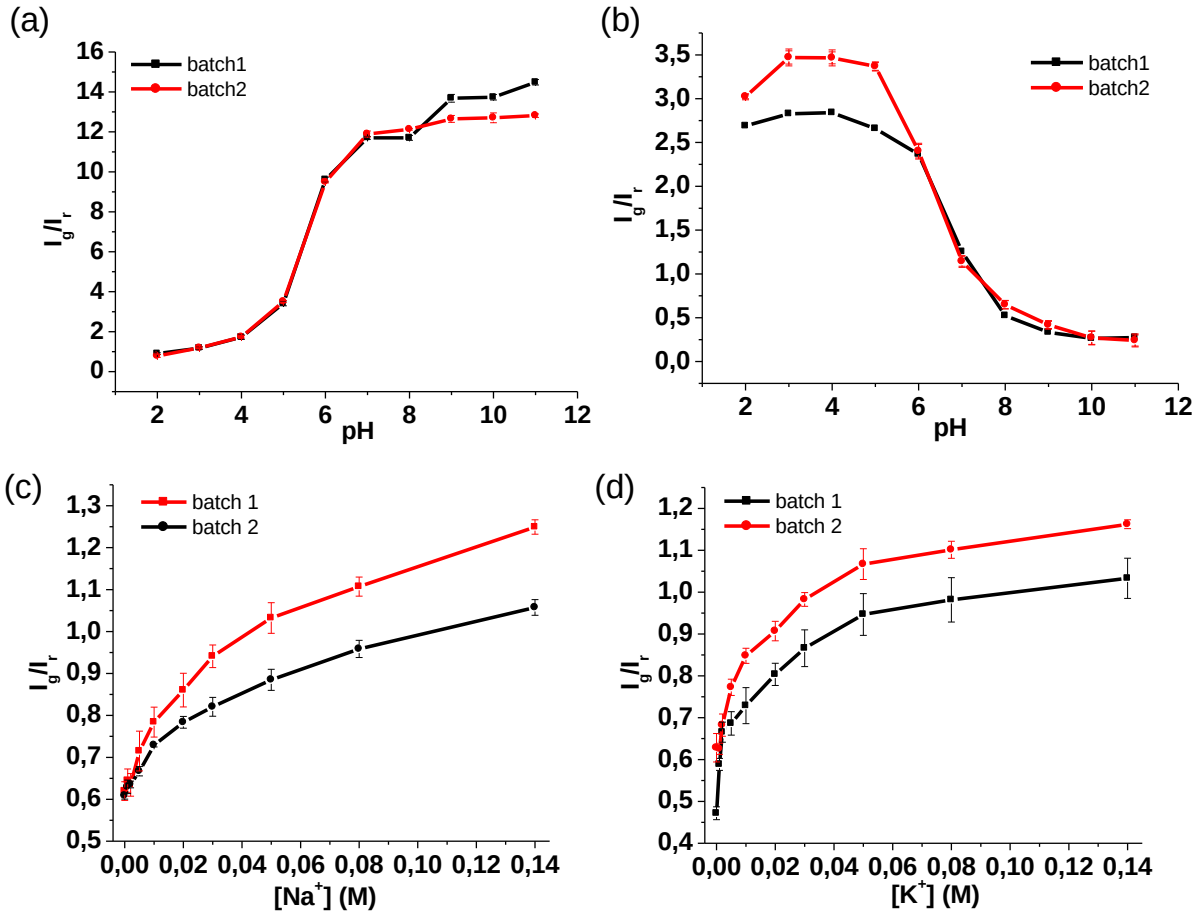

Figure SI-14. Comparison between the calibration curves of two different batches of each analyte fluorescent sensor. (a) pH-sensor capsules based on FITC as probe indicator. Green (I_g) and red fluorescence (I_r) was detected at 520 nm and 610 nm, respectively. (b) pH-sensor capsules based on SNARF as probe indicator. Green-yellow (I_g) and red fluorescence (I_r) was detected at 585 nm and 540 nm, respectively. (c) Na^+-sensor capsules based on SBFI as probe indicator. Green (I_g) and red fluorescence (I_r) was detected at 520 nm and 610 nm, respectively. (d) K^+-sensor capsules based on PBFI as probe indicator. Green (I_g) and red fluorescence (I_r) was detected at 520 nm and 610 nm, respectively. The I_g/I_r values have been plotted versus the H^+, Na^+ and K^+ concentration of the solution, respectively. For each batch all values were averaged from three replicate scans at each concentration. Error bars show the standard deviation. The raw data for these images are shown in **Figure SI-15 - Figure SI-18**.

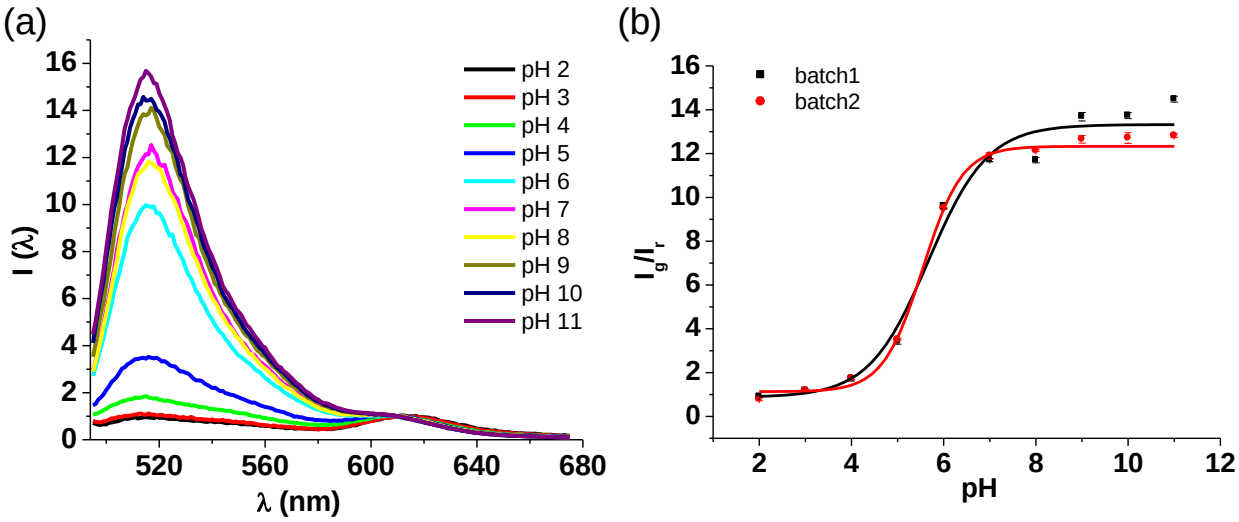

Figure SI-15. Comparison between the calibration curves of two different batches of pH-sensor capsules based on FITC as probe indicator. The I_g/I_r values have been plotted versus the pH of the solution. Error bars show the standard deviation (all values were averaged from three replicate scans at each concentration). The data were then fitted with a Boltzmann sigmoid function using eq. 1.[16] The fit parameters are given in the table. From these data the pK_a has been calculated (see **SI**, **Figure SI-20**).[16] The most important parameter for the pH-sensitivity is pK_a (based on pH_{infl}).

cuvette measurements	I_a	I_b	pH_{infl}	ΔpH	pK_a
encapsulated dye (batch 1)	0.87	13.33	5.66	0.64	5.7
encapsulated dye (batch 2)	1.13	12.33	5.54	0.43	5.5

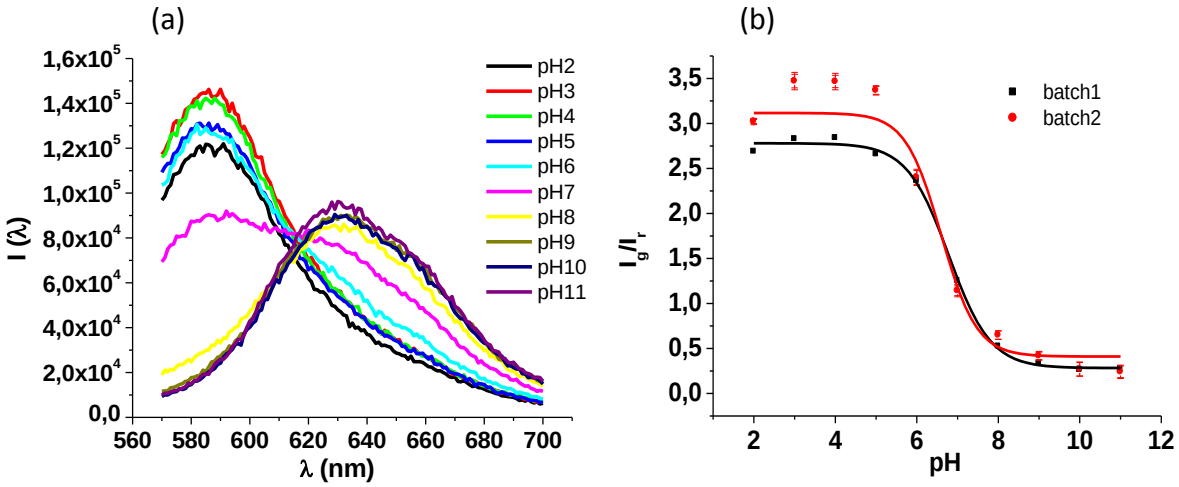

Figure SI-16. Comparison between the calibration curves of two different batches of pH-sensor capsules based on SNARF as probe indicator. The I_g/I_r values have been plotted versus the pH of the solution. Error bars show the standard deviation (all values were averaged from three replicate scans at each concentration). The data were then fitted with a Boltzmann sigmoid function using eq. 1.[16] The fit parameters are given in the table. From these data the pK_a has been calculated (see **SI**, **Figure SI-20**).[16] The most important parameter for the pH-sensitivity is pK_a (based on pH_{infl}).

cuvette measurements	Ia	Ib	pHinfl	ΔpH	pKa
encapsulated dye (batch 1)	2.78	0.28	6.78	0.51	6.8
encapsulated dye (batch 2)	3.11	0.41	6.59	0.43	6.6

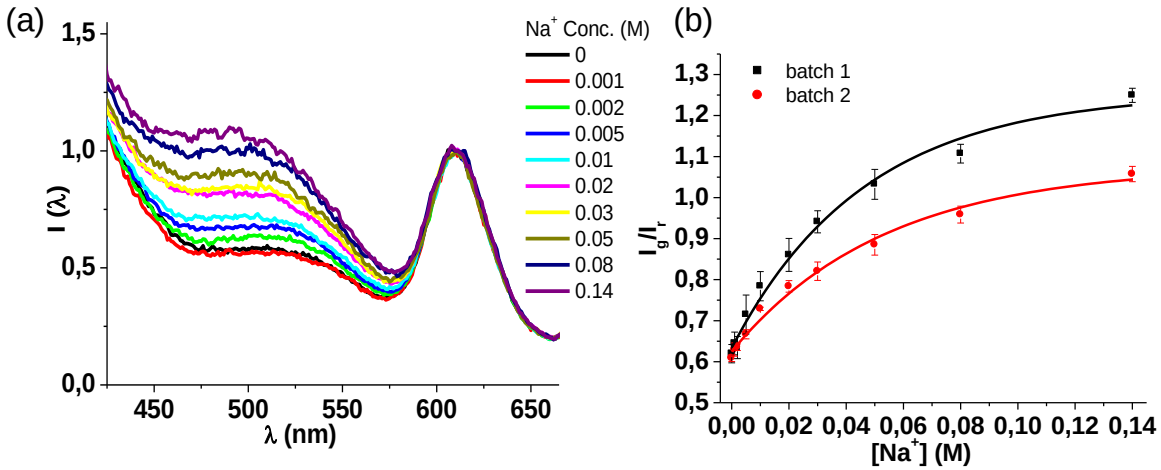

Figure SI-17. Comparison between the calibration curves of two different batches of Na^+-sensor capsules. The I_g/I_r values have been plotted versus increasing Na^+ of the solution (pH 7.5). Error bars correspond to the standard deviation between the individual capsules (SD, n = 30). Data points were fitted with eq. 2. The fit parameters used for the 3 curves are given in the table. The important parameter for the Na^+-sensitivity is c_0.

cuvette measurements	I0	ΔI	c_0[M]
encapsulated dye (batch 1)	0.63	0.62	0.046
encapsulated dye (batch 2)	0.62	0.45	0.053

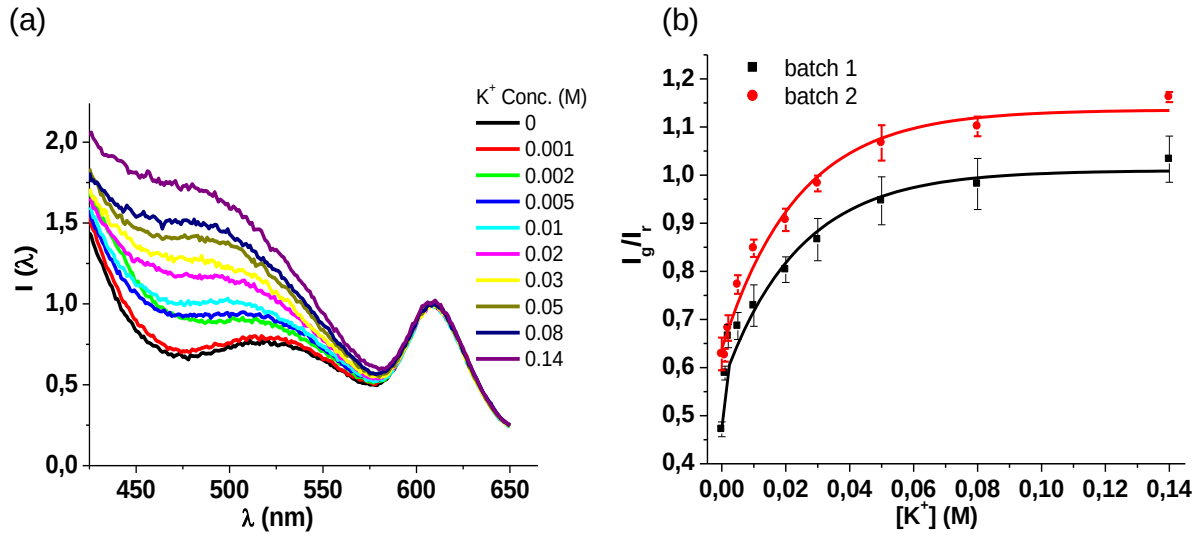

Figure SI-18. Comparison between the calibration curves of two different batches of K^+-sensor capsules. The I_g/I_r values have been plotted versus increasing K^+ of the solution (pH 7.5). Error bars correspond to the standard deviation between the individual capsules (SD, n = 30). Data points were fitted with eq. 2 (but with $c(K^+)$ instead of $c(Na^+)$). The fit parameters used for the 3 curves are given in the table. The important parameter for the K^+-sensitivity is c_0.

cuvette measurements	I_0	ΔI	c_0[M]
encapsulated dye (batch 1)	0.56	0.44	0.023
encapsulated dye (batch 2)	0.64	0.49	0.023

V) Calculation of pKa of pH sensitive fluorophores

V.1) *pKa value of free FITC, FITC-dextran and encapsulated FITC-dextran*

V.2) *pKa value of free SNARF, SNARF-dextran and encapsulated SNARF-dextran*

V.1) *pKa value of free FITC, FITC-dextran and encapsulated FITC-dextran*

For each sample fluorescence spectra I(λ) at an excitation wavelength of 490 nm was recorded in commercial standard buffers of different pH. Hereby the samples were mixed with buffer in a sample to buffer ratio of about 1:1. The pH of all final solutions was checked by a pH meter before and after buffer addition as control.

To calculate the pK_a values for free, conjugated and encapsulated FITC, firstly fluorescence spectra were recorded using an excitation wavelength of 490 nm **(Figure SI-8)**. For simplicity we explain the steps to calculate the pK_a for the free FITC **(Figure SI-19, a-d)**. The pK_a values for the other samples (i.e., dye-dextran conjugates and encapsulated dye-dextran conjugates) were calculated using the same approach.[16] For the calculation of the pK_a of free FITC, for each obtained spectrum the fluorescence intensities I_g= I(520 nm) and I_r = I(610 nm) were determined **(Figure SI-19a)**. The ratios of intensities I_g/I_r was calculated and plotted against the corresponding pH values of the buffer **(Figure SI-19b)**. The points of the I_g/I_r curve were then fitted with a Boltzmann-function **(Figure SI-19c)**.

$$\frac{I_g}{I_r}(pH) = \frac{I_a - I_b}{1 + \exp\left(\frac{pH - pH_{inf}}{\Delta pH}\right)} + I_b \qquad \textbf{Eq. 1}$$

Here I_g/I_r are the measured data points, I_a is the value of the I_g/I_r curve at low pH values which is considered as the acidic titration endpoint, and I_b is the value of the I_g/I_r curve at high pH values which is considered as the basic titration endpoint as well; pH_{infl} describes the point of inflection of the I_g/I_r curve, i.e. the pH value at which the slope of the curve is maximum. ΔpH is an indicator for the slope at the point of inflection.[16] From the fit of the I_g/I_r data the fit parameters I_a, I_b, pH_{infl} and ΔpH were determined for each set of spectra.

In the next step we applied eq. 4 to derive the pK_a value from these data:

$$pH = pK_a - \log\left(\frac{\frac{I_g}{I_r} - I_b}{I_a - \frac{I_g}{I_r}} \times \frac{I_{b,g}}{I_{a,g}}\right) \qquad \textbf{Eq. 4}$$

At the end the term –log(……) was calculated for all pH values from pH = 3.0 to pH = 9.0 and plotted versus pH (see **Figure SI-19d**). All the I_g/I_r values fitted with eq. 1 to yield as previously described the I_a, I_b, pH_{infl} and ΔpH. Using these parameters then gives an analytical formula for $I_g/I_r(pH)$. This was put in eq. 4. $I_{a,g}$ and $I_{b,g}$ are the absolute fluorescence intensities of FITC (green-yellow channel, λ = 520) nm at the pH values where the measured I_g/I_r values are the most approximate values to the fitted I_a and I_b values, respectively (in our case we took pH 3.0 and pH 9.0, respectively). $I_{a,g}$ and $I_{b,g}$ were directly derived from the original fluorescence spectra as shown in **Figure SI-8a**. The obtained curve -log(...) versus

pH is a linear function. We thus fitted the -log(...) versus pH curve with a linear function, of which the intercept corresponds to the pK_a value according to eq. 4.[16]

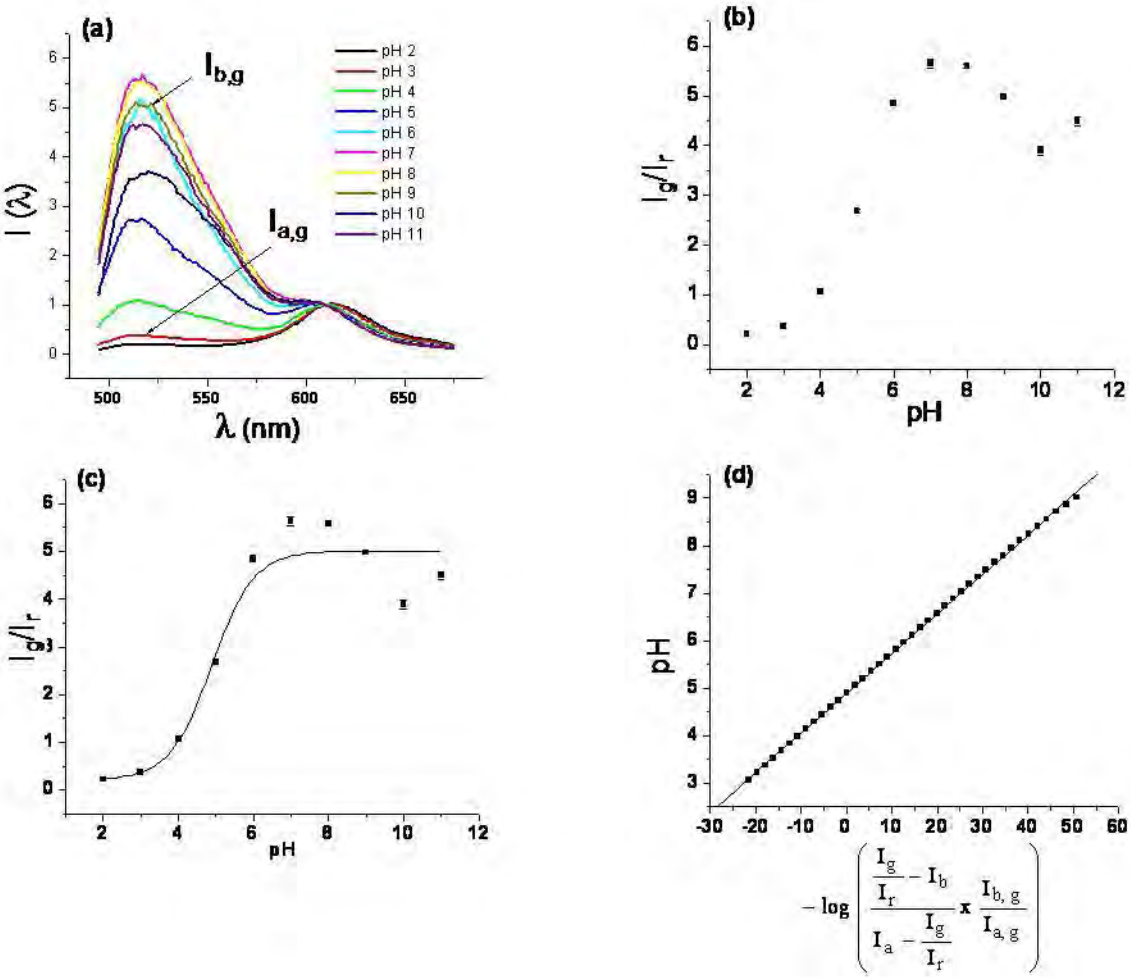

Figure SI-19. Calculation of the pK_a value for free FITC mixed with AF594. (a) Fluorescence spectra I(λ) at different pH of free FITC+AF594 recorded using an excitation of 490 nm. (b) The ratios I_g/I_r from the determined I_g = I(λ = 520 nm) and I_r = I(λ = 610 nm) values as obtained from the spectra at different pH shown in (a) were plotted versus the pH. (c) The I_g/I_r data points were fitted with the Boltzmann function given in eq. 1.[16] The fit delivered the fit parameters I_a = 0.21, I_b = 5.00 , pH_{infl} = 4.89, and ΔpH = 0.56. (d) The pH was plotted versus the function $-\log\left(\frac{\frac{I_g}{I_r}-I_b}{I_a-\frac{I_g}{I_r}}\times\frac{I_{b,g}}{I_{a,g}}\right)$. The values I_g/I_r (pH) were hereby derived from eq. 1 with the fit parameters as obtained in (c) and the $I_{a,g}$ and $I_{b,g}$ values were directly obtained from the original spectra shown in (a): $I_{a,g}$ = 0.3648 and $I_{b,g}$ = 5.5. Then the resulting data points were fitted with a linear function pH = pK_a + α*X with X =

$$-\log\left(\frac{\frac{I_g}{I_r}-I_b}{I_a-\frac{I_g}{I_r}}\,x\,\frac{I_{b,g}}{I_{a,g}}\right)$$

.[16] The linear fit derived the fit parameters pK_a = 4.9 and α=0.68. According to eq. 4 the intercept is the pK_a value for free FITC (+ AF594) which was determined to be 4.9. Using the same approach we calculated the pK_a of conjugated FITC-dextran (+ AF594-dextran) (6.2) and encapsulated FITC-dextran (+ AF594-dextran) (5.6).

V.2) *pKa value of free SNARF, SNARF-dextran and encapsulated SNARF-dextran*

To calculate the pKa value of SNARF, firstly we recorded the fluorescence spectra of three different samples of SNARF (free, conjugated and encapsulated) as shown in **Figure SI-9**. Here we explain the method to calculate the pK_a of free SNARF (**Figure SI-20a-d**) (the same approach was used to calculate the pK_a of conjugated and encapsulated SNARF).[16] To calculate the pK_a of free SNARF, for each obtained spectrum the fluorescence intensities I_g= I(585 nm) and I_r = I(640 nm) were determined **(Figure SI-20a)**. Then the ratio of intensities I_g/I_r was calculated and plotted against corresponding pH values of buffer **(Figure SI-20b)**. The data points of the I_g/I_r curve were then fitted with a Boltzmann-function eq.1 **(Figure SI-20c)**. Again from the Boltzmann function fit of the data I_g/I_r we obtained the fit parameters I_a, I_b, pH_{infl} and ΔpH for each set of spectra. In the next step we used eq. 4 to get the pK_a of SNARF. The term -log(……) was calculated for all pH values from pH = 5.0 to pH = 11 and plotted versus pH (see **Figure SI-20d**). Hereby all the I_g/I_r values were calculated with eq. 1 and the previously determined parameters I_a, I_b, pH_{infl} and ΔpH. Hereby $I_{a,r}$ and $I_{b,r}$ are the absolute fluorescence intensities of SNARF in the red channel (λ = 640 nm) at the pH values where the measured I_g/I_r values are the most approximate values to the fitted I_a and I_b values, respectively (here we took pH 5.0 and pH 10 respectively). $I_{a,r}$ and $I_{b,r}$ were directly derived from the original fluorescence spectra as shown in **Figure SI-9a**. The obtained curve -log(...) versus pH was a linear function, see eq. 4. We thus fitted the -log(...) versus pH curve with a linear function, of which the intercept corresponds to the pK_a value according to eq. 4.[16]

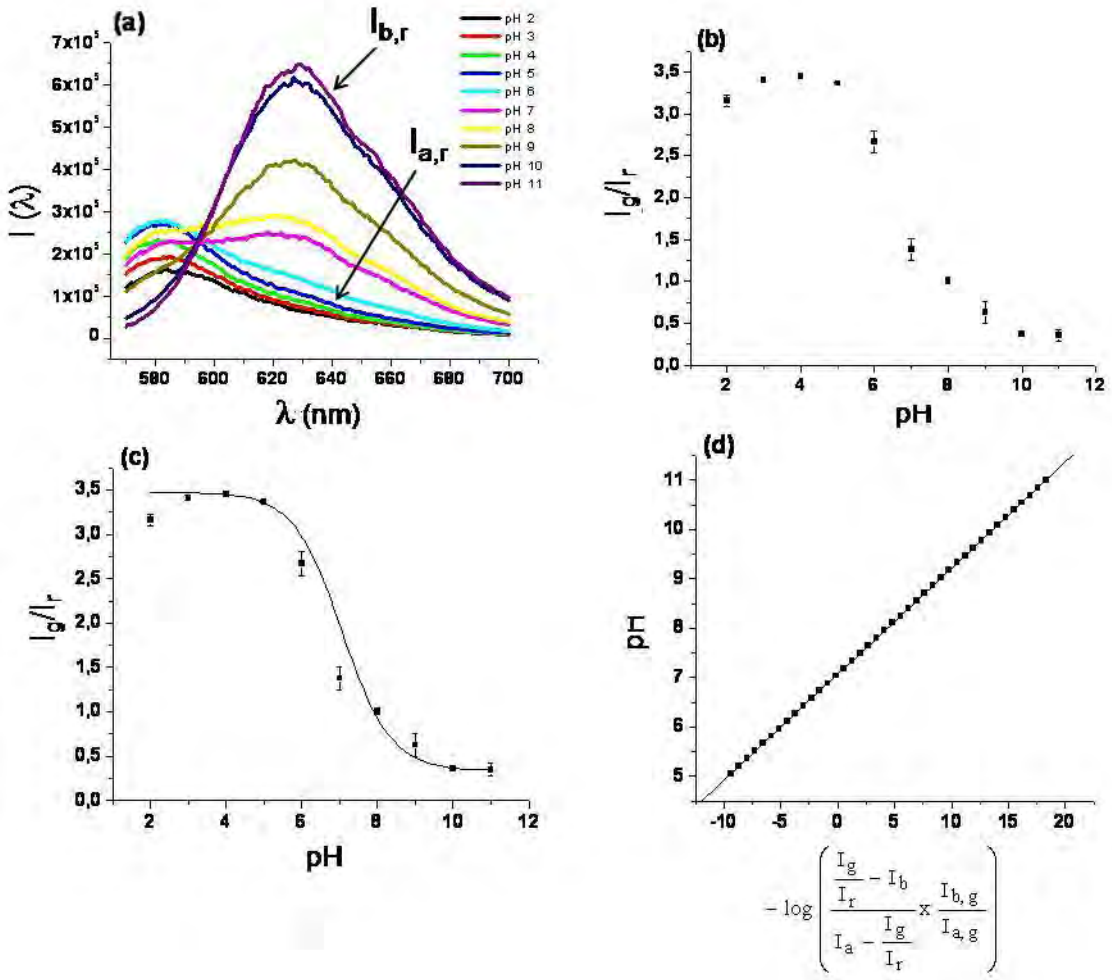

Figure SI-20. Calculation of the pKa value for free SNARF. (a) Fluorescence spectra of free SNARF recorded using excitation wavelength of 540 nm. (b) The ratios I_g/I_r determined from the values I_g and I_r which were obtained from the spectra at different pH shown in (a) were plotted versus the pH. (c) The I_g/I_r data points fitted with the Boltzmann function given in eq.1.[16] The fit delivered the fit parameters I_a = 3.47, I_b = 0.34, pH_{infl} = 7.07, and ΔpH = 0.64. (d) The function - log(...) was plotted versus pH. The values I_g/I_r were derived from eq. 1 with the fit parameters as obtained in (c) and the $I_{a,r}$ and $I_{b,r}$ values were directly obtained from the original spectra shown in (a): $I_{a,r}$ = 81610 and $I_{b,r}$ = 534190. Then the resulting data points were fitted with a linear function.[16] According to eq. 4 the intercept is the pK_a value for free SNARF which was determined to be 7.0. Using the same approach we calculated the pK_a of conjugated SNARF-dextran (6.8) and encapsulated SNARF-dextran (6.6).

VI) Microscopy images

VI.1) *False colors used for microscopy images*
VI.2) *Scheme of fluorescence microscopy measurements*
VI.3) *FITC and AF594 capules*
VI.4) *SNARF capsules*
VI.5) *SBFI and AF594 capsules*
VI.6) *PBFI and AF594 capsules*
VI.7) *Amino-MQAE and AF594 capsules*

VI.1) *False colors used for microscopy images*

For the sake of clarity the fluorescence signals of all the ion-sensitive dyes (FITC, SNARF, SBFI, PBFI and amino-MQAE) are showed as false colors in green in all the microscopy images.

VI.2) *Scheme of fluorescence microscopy measurements*

For microscopy ratiometric imaging, 10 µl of sensor capsules was diluted in 10 µl of ion-solutions containing the double amount of ion concentration respect to the desired final concentration. After seeding on glass, capsules were imaged by using a 100X/1.45 NA Planofluoar oil-immersion objective. Then per each ion concentration value, the green and red fluorescence images were taken. By overlaying the images of the green and red fluorescence, the response of the indicator dye can be directly analyzed.

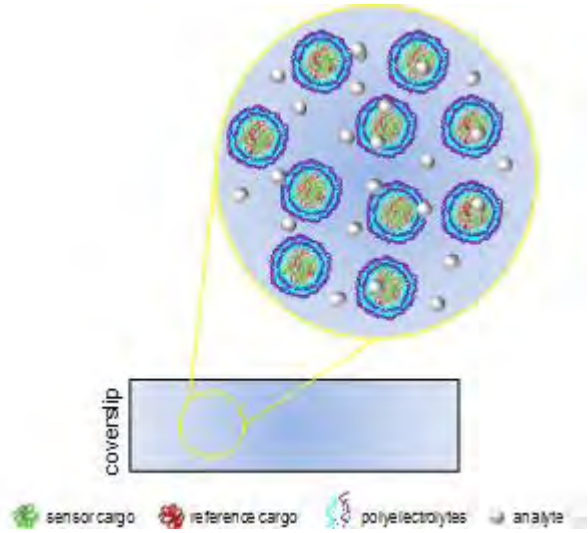

Figure SI-21. Schematic representation showing fluorescence microscopy measurements performed by depositing onto a glass coverslip a 20 µL drop of sensor capsules re-suspended in solutions of buffer with the desired ion concentration. A mercury lamp was used as source of light and a CCD camera was used as detector. After the capsules were settled to the surface of the substrate, two fluorescence images were recorded at fixed exposure time using two sets of filters to separately read out the fluorescence intensity of the indicator and the reference dyes embedded into the capsule cavities.

VI.3) *FITC and AF594 capsules*

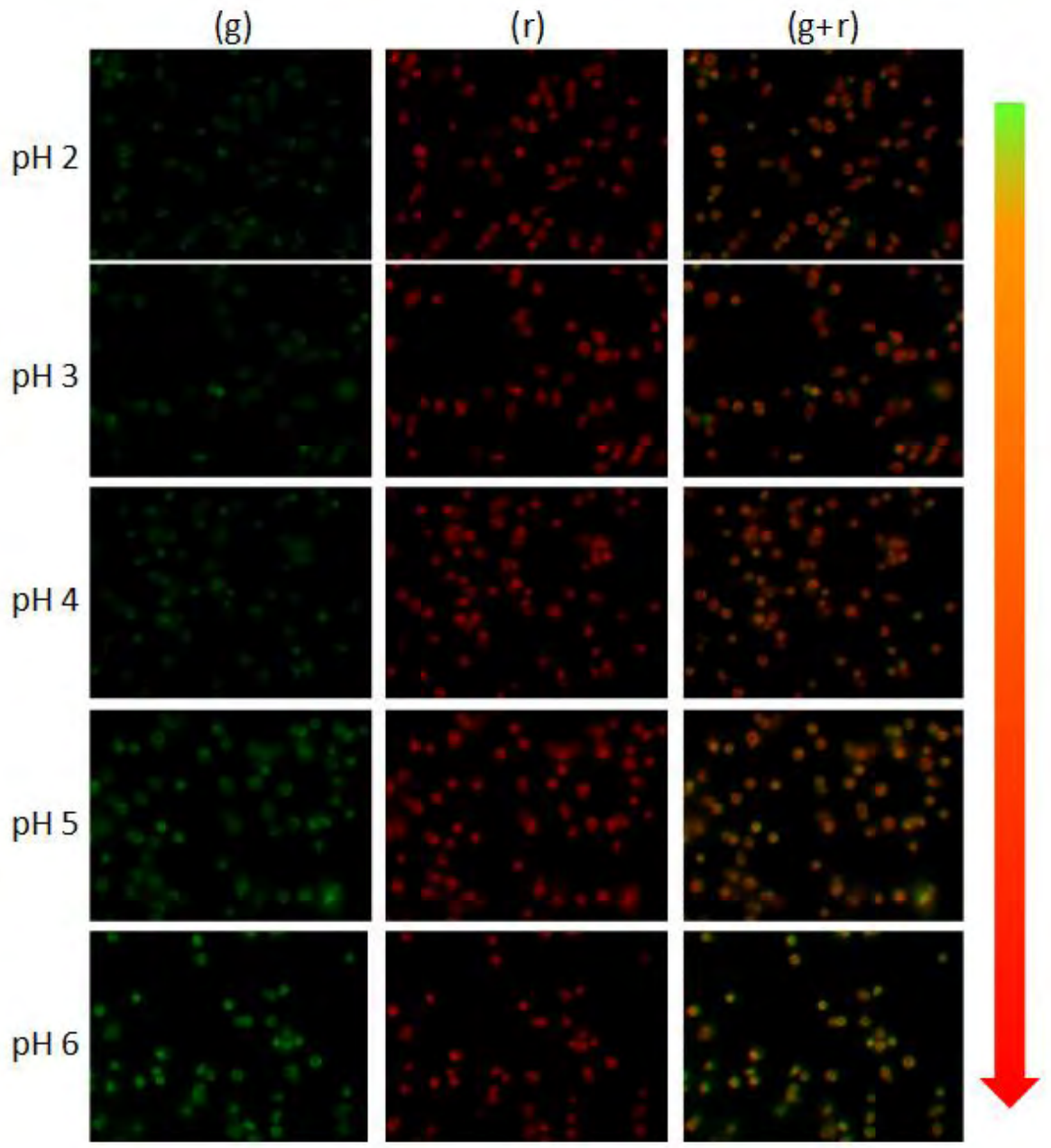

Figure SI-22. FITC-/AF594-dextran loaded capsules. Fluorescence microscopy images of FITC-/AF594-dextran loaded capsules under different pH values.

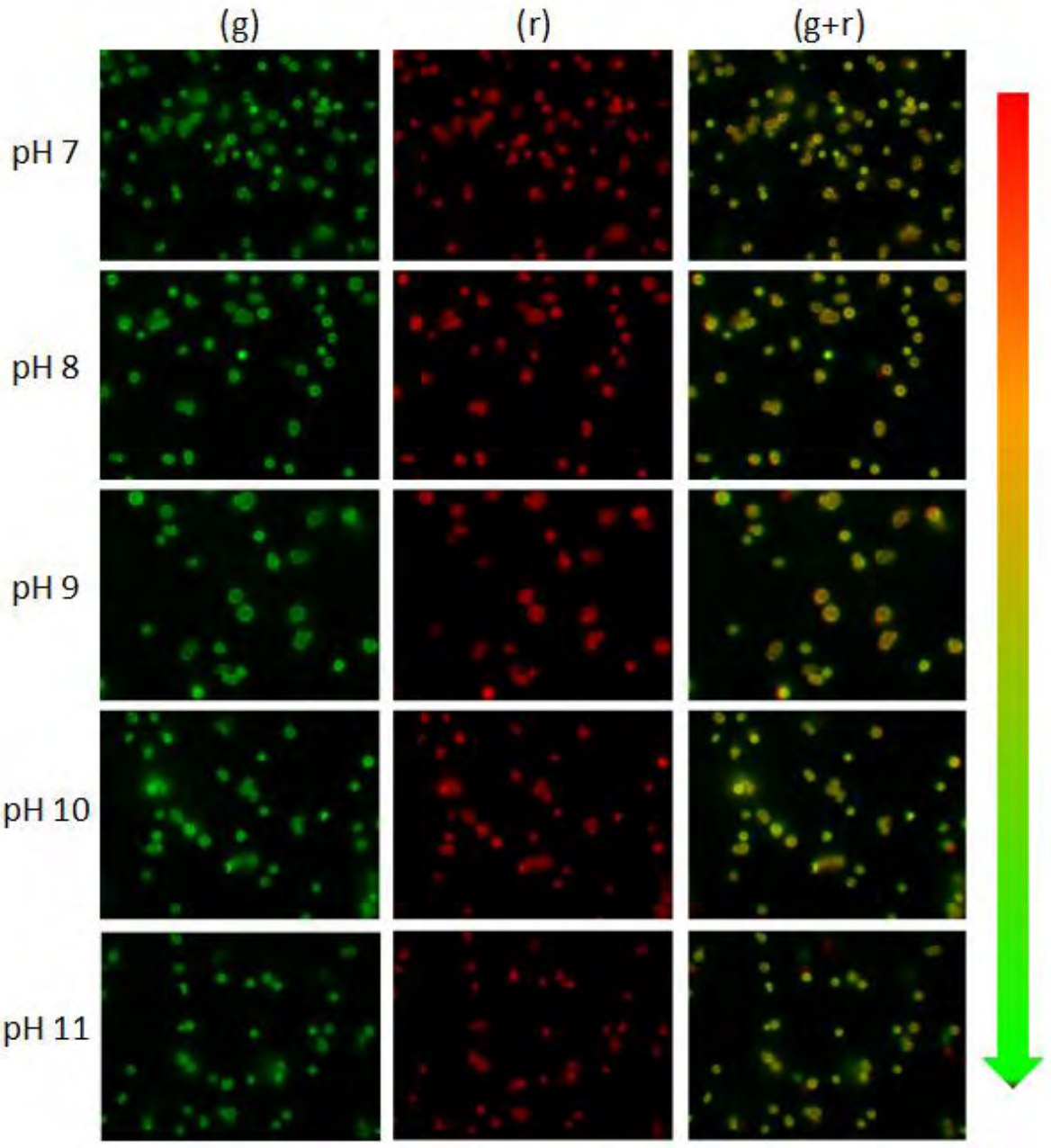

Figure SI-22. FITC-/AF594-dextran loaded capsules. Fluorescence microscopy images of FITC-/AF594-dextran loaded capsules under different pH values.

VI.4) *SNARF capsules*

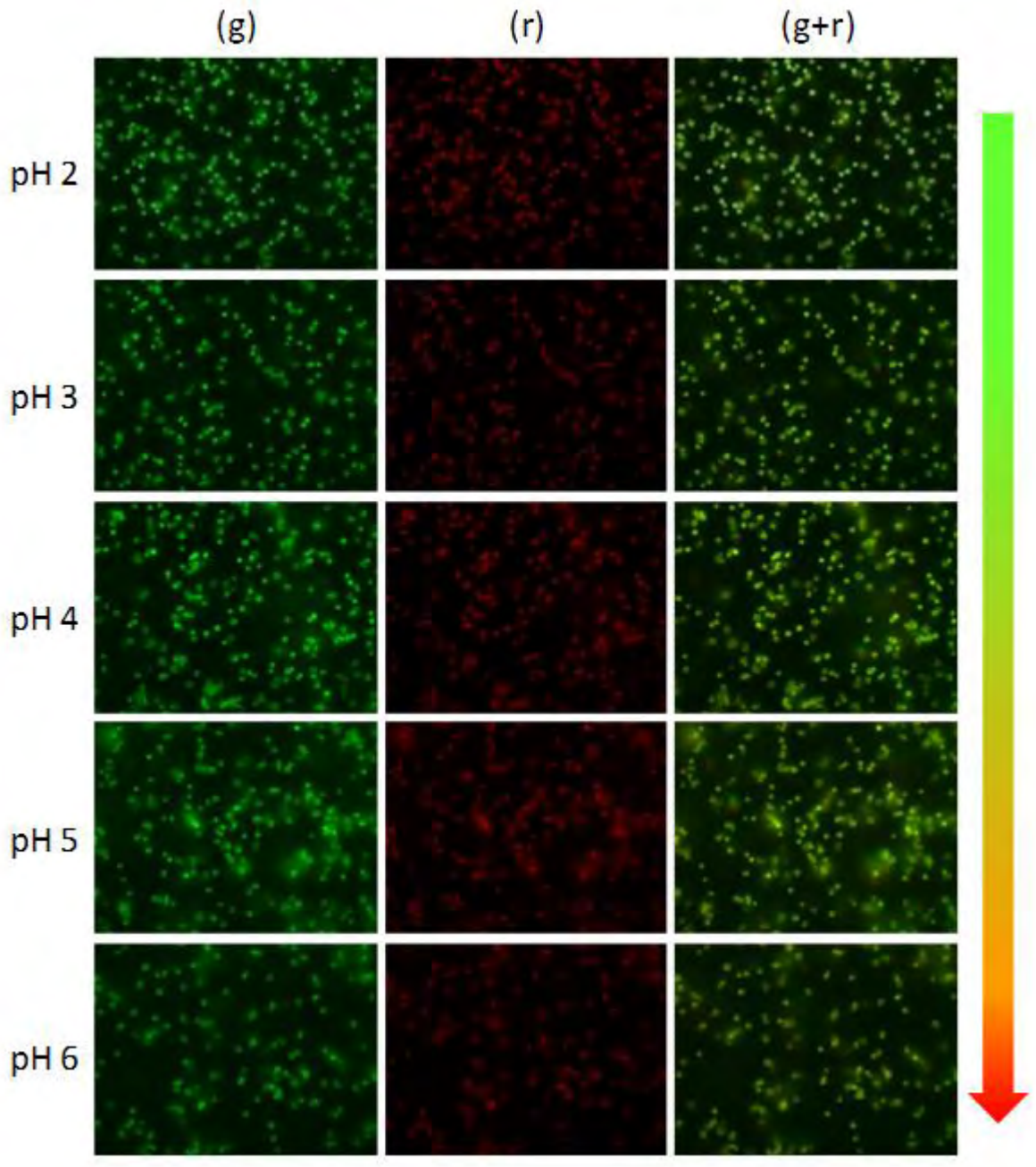

Figure SI-23. SNARF-dextran loaded capsules. Fluorescence microscopy images of SNARF-dextran loaded capsules under different pH values.

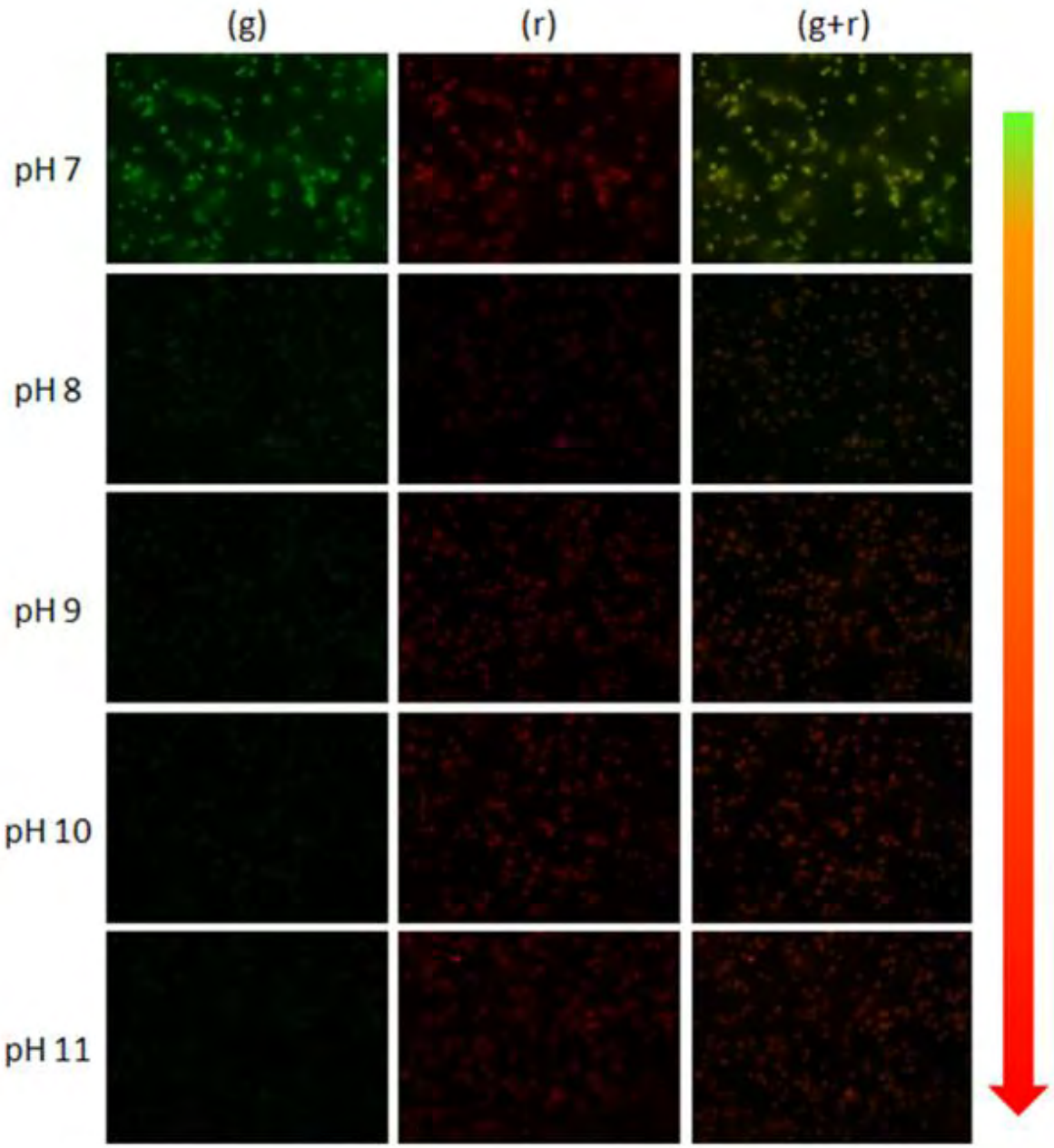

Figure SI-23. SNARF-dextran loaded capsules. Fluorescence microscopy images of SNARF-dextran loaded capsules under different pH values.

VI.5) *SBFI and AF594 capsules*

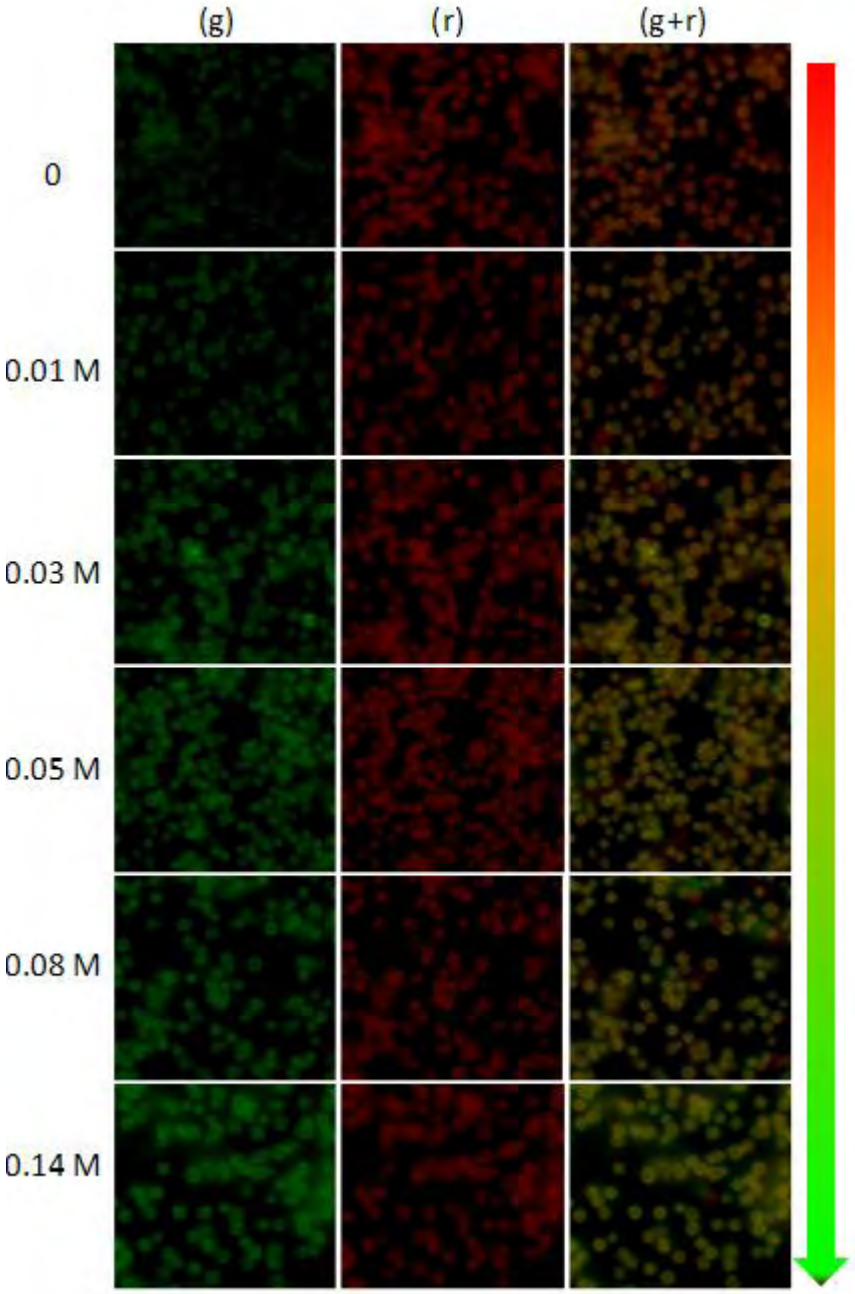

Figure SI-24. SBFI-/AF594-dextran loaded capsules. Fluorescence microscopy images of SBFI-/AF594-dextran loaded capsules under different Na^+ concentrations.

VI.6) *PBFI and AF594 capsules*

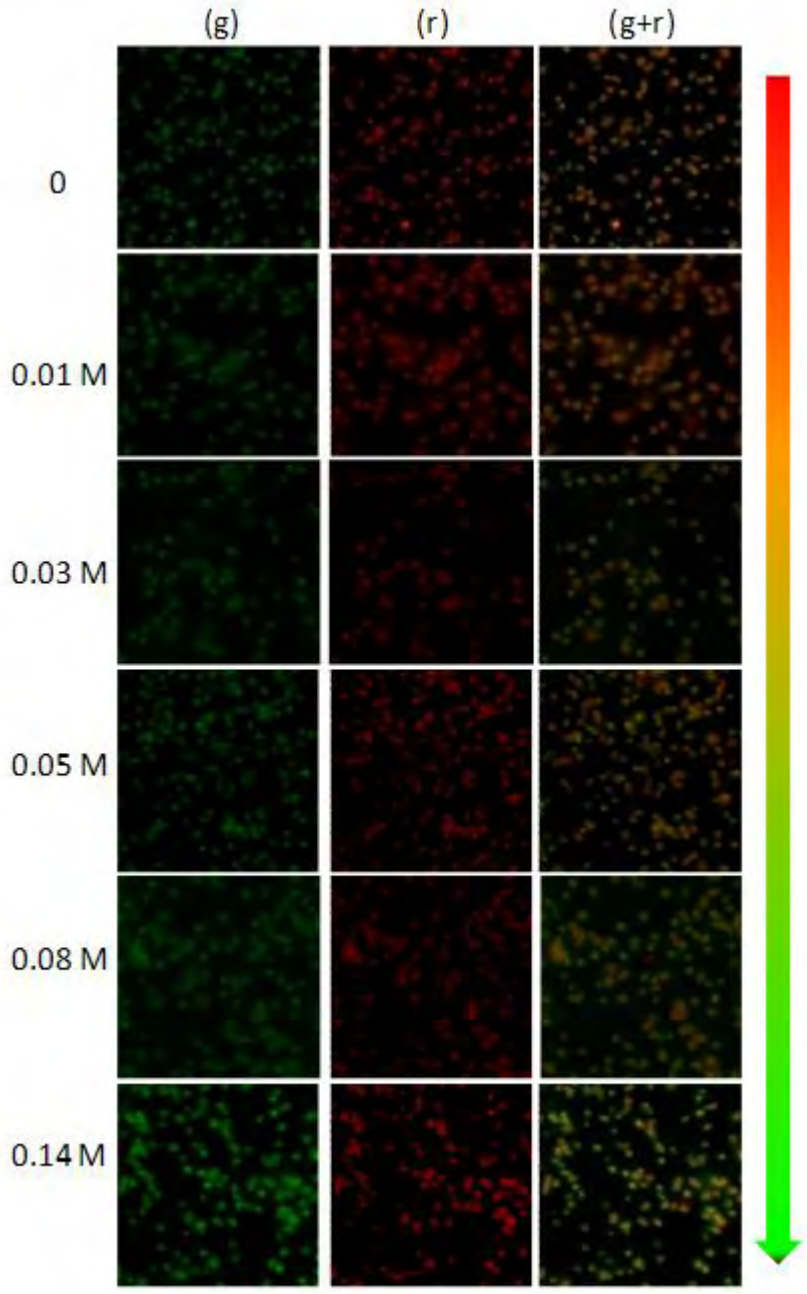

Figure SI-25. PBFI-/AF594-dextran loaded capsules. Fluorescence microscopy images of PBFI-/AF594-dextran loaded capsules under different K^+ concentrations.

VI.7) *Amino-MQAE and AF594 capsules*

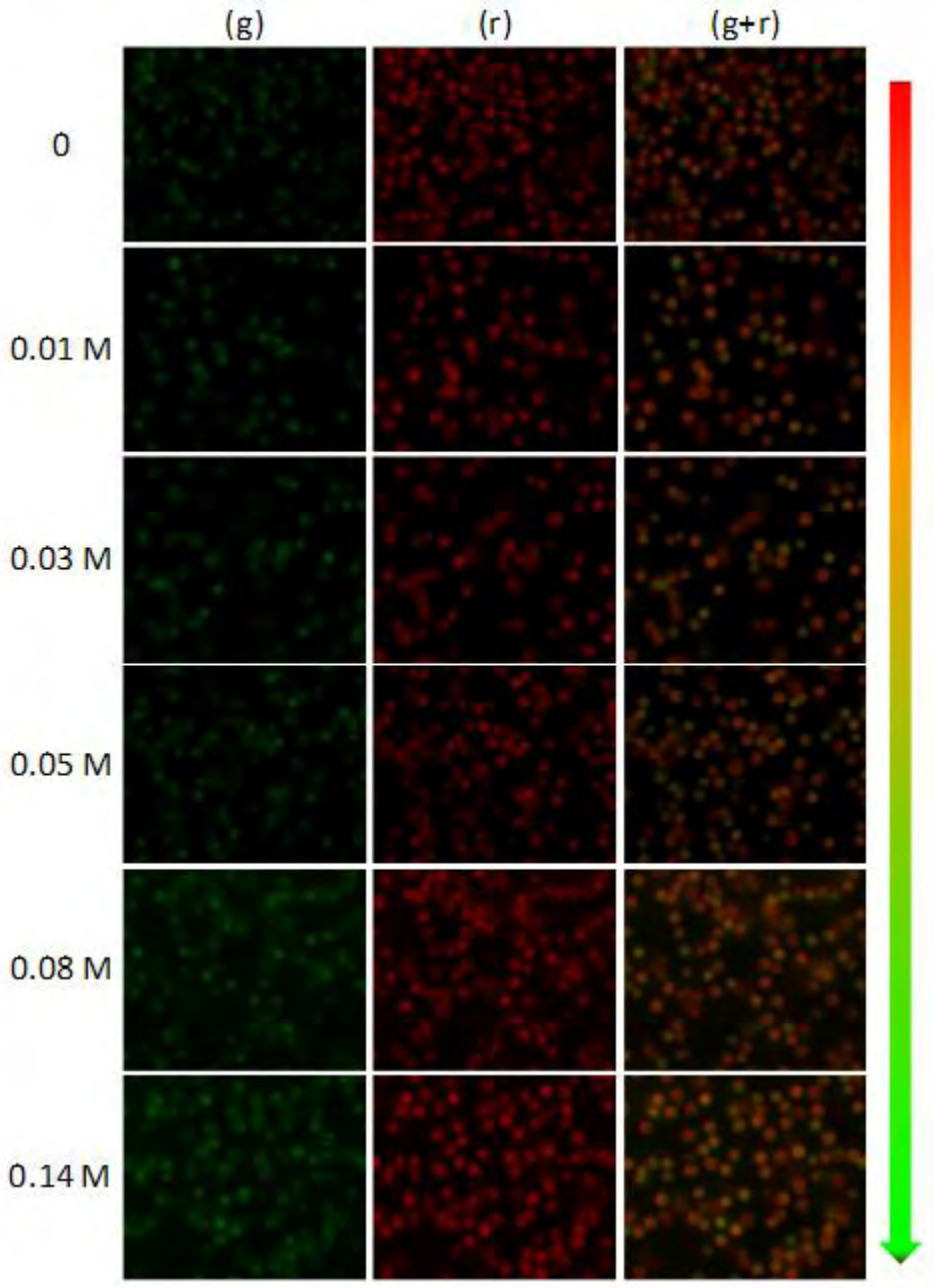

Figure SI-26. Amino-MQAE-/AF594-dextran loaded capsules. Fluorescence microscopy images of MQAE-/AF594-dextran loaded capsules under different Cl^- concentrations.

References

[1] G. B. Sukhorukov, H. Mohwald, *Trends In Biotechnology* **2007**, *25*, 93.
[2] A. P. R. Johnston, C. Cortez, A. S. Angelatos, F. Caruso, *Current Opinion in Colloid & Interface Science* **2006**, *11*, 203.
[3] G. B. Sukhorukov, A. L. Rogach, M. Garstka, S. Springer, W. J. Parak, A. Muñoz-Javier, Oliver Kreft, A. G. Skirtach, A. S. Susha, Y. Ramaye, R. Palankar, M. Winterhalter, *SMALL* **2007**, *3*, 944.
[4] L. L. del_Mercato, P. Rivera-Gil, A. Z. Abbasi, M. Ochs, C. Ganas, I. Zins, C. Sönnichsen, W. J. Parak, *Nanoscale* **2010**, *2*, 458.
[5] T. A. Duchesne, J. Q. Brown, K. B. Guice, S. R. Nayak, Y. M. Lvov, M. J. McShane, *Optical Diagnostics and Sensing of Biological Fluids and Glucose and Cholesterol Monitoring Ii* **2002**, *4624*, 66.
[6] J. Q. Brown, K. B. Guice, M. J. McShane, *Proceedings of the Ieee Sensors 2003, Vols 1 and 2* **2003**, 111.
[7] M. J. Mc_Shane, J. Q. Brown, K. B. Guice, Y. M. Lvov, *J Nanosci Nanotechnol* **2002**, *2*, 411.
[8] O. Kreft, A. Muñoz_Javier, G. B. Sukhorukov, W. J. Parak, *Journal Of Materials Chemistry* **2007**, *17*, 4471.
[9] V. B. Alberts, D. Bray, J. Lewis, M. Raff, K. Roberts, J. D. Watson, *Molecular biology of the cell*, 3rd ed., Garland Publishing Inc., New York, **1994**.
[10] K. Meuwis, N. Boens, F. C. De Schryver, J. Gallay, M. Vincent, *Biophys J* **1995**, *68*, 2469.
[11] A. Riedinger, F. Zhang, F. Dommershausen, C. Röcker, S. Brandholt, G. U. Nienhaus, U. Koert, W. J. Parak, *SMALL* **2010**, *submitted*.
[12] G. T. Hermanson, *Bioconjugate Techniques*, 2nd ed., Academic Press, San Diego, **2008**.
[13] B. G. De_Geest, A. G. Skirtach, A. A. Mamedov, A. A. Antipov, N. A. Kotov, S. C. De Smedt, G. B. Sukhorukov, *Small* **2007**, *3*, 804.
[14] S. H. Hu, C. H. Tsai, C. F. Liao, D. M. Liu, S. Y. Chen, *Langmuir* **2008**, *24*, 11811.
[15] S. De Koker, T. Naessens, B. G. De Geest, P. Bogaert, J. Demeester, S. De Smedt, J. Grooten, *Journal of Immunology* **2010**, *184*, 203.
[16] F. Zhang, Z. Ali, F. Amin, A. Feltz, M. Oheim, W. J. Parak, *ChemPhysChem* **2010**, *11*, 730.

De Novo Design of Supercharged, Unfolded Protein Polymers and their Assembly into Supramolecular Aggregates[a]

Anke Kolbe,[b] Loretta L. del Mercato,[b] Azhar Z. Abbasi, Pilar Rivera Gil, Sekineh J. Gorzini, Wim H.C.Huibers, Bert Poolman, Wolfgang J. Parak,* and Andreas Herrmann*

_____

A. Herrmann, A. Kolbe, S.J. Gorzini
Department of Polymer Chemistry, Zernike Institute for Advanced Materials, University of Groningen, Nijenborgh 4, 9747 AG Groningen, The Netherlands
Fax: +31 50 363 4400; E-mail: a.herrmann@rug.nl

W.J. Parak, L.L. del Mercato, A.Z. Abbasi, P. Rivera Gil
Fachbereich Physik and Wissenschaftliches Zentrum fuer Materialwissenschaften, Philipss Universitaet Marburg, Renthof 7, 35037 Marburg, Germany
Fax: +49 6421 28 27 034; E-mail: wolfgang.parak@physik.uni-marburg.de

B. Poolman, W.H.C. Huibers
Department of Biochemistry, Groningen Biomolecular Science and Biotechnology Institute & Zernike Institute for Advanced Materials, University of Groningen, Nijenborgh 4, 9747 AG Groningen, The Netherlands
Fax: +31 50 363 4165; E-mail: b.poolman@rug.nl

_____

Here we report for the first time the design and expression of highly charged, unfolded protein polymers based on elastin-like peptides (ELPs). Positively and negatively charged variants were achieved by introducing lysine and glutamic acid residues, respectively, within the repetitive pentapeptide units. Subsequently it was demonstrated that the monodisperse protein polyelectrolytes with precisely defined amino acid compositions, sequences and stereochemistries can be transferred into superstructures exploiting their electrostatic interactions. Hollow capsules were assembled from oppositely charged protein chains by using the layer-by-layer technique. The structures of the capsules were analyzed by various microscopy techniques revealing the fabrication of multilayer containers. Due to their low toxicity in comparison to other polyelectrolytes, supercharged ELPs are appealing candidates for the construction of electrostatically induced scaffolds in biomedicine.

Supporting information for this article is available at the bottom of the article's abstract page, which can be accessed from the journal's homepage at http://www.macros.wiley-vch.de, or from the author.

[b] Shared first authorship due to equal contribution.

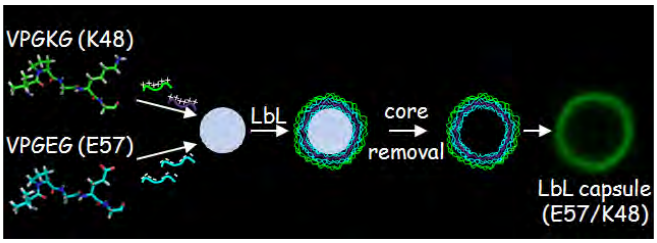

Introduction

Genetically encoded polypeptides with repetitive motifs have gained increasing attention in recent years due to their high potential for biotechnological and biomedical applications. This development was mainly fueled by progress in recombinant DNA technology allowing precise control of the structure of the resulting macromolecules.[1, 2] Important examples are silk-like,[3] collagen-like[4, 5] and elastin-like proteins (ELPs).[6] The latter are derived from a repeating motif within a hydrophobic domain of mammalian tropoelastin. The most common pentapeptide motif has the sequence $(VPGXG)_n$ with X being any guest amino acid except proline and n denoting the number of repeats.[7] The structural and physical properties of ELPs, such as their elastic/mechanical as well as thermoresponsive behavior, have been investigated.[8-10] Their ability to undergo a reversible phase transition at the so-called lower critical solution temperature (LCST) has been exploited for the purification of proteins[11] and DNA.[12] For tissue engineering purposes, ELPs were designed as thermally sensitive hydrogels that solidify when injected into the body.[13] Furthermore, their temperature responsiveness was utilized for drug delivery applications. In hyperthermia treatment, ELPs were accumulated in tumors[14] and the LCST-behavior was employed to induce micelle formation of block ELP structures.[15]

Results and Discussion

Design, Preparation and Characterization of Elastin-like Polypeptides

The choice of different guest amino acids within the ELP motif allows the precise control of LCST and the incorporation of chemical modifications.[16] Here, we took advantage of the flexibility of amino acid composition at the fourth position within the repeat to transform ELPs into unprecedented highly charged anionic and cationic polyelectrolytes. These structures of biosynthetic origin are much better defined than their chemically synthesized counterparts. To assess their viability in a common application for polyelectrolytes in a biomedical context, these materials were transformed into superstructures, i.e. hollow capsules, employing the electrostatic interactions of oppositely charged variants.

We thus decided to introduce lysine and glutamic acid residues in order to obtain highly positively and negatively charged polypeptide chains, respectively. Monomer units of the ELP gene encoded ten pentapeptide repeats (Val-Pro-Gly-Lys/Glu-Gly) and were multimerized using recursive directional ligation, as described by Chilkoti and co-workers.[10] ELPs with 48 positive (K48) or 57 negative (E57) charges were produced in *E. coli* and purified (Supporting Information). Protein yields were 1 and 5 mg per liter of bacterial cell

culture for K48 and E57, respectively. The purity of the products was analyzed by polyacrylamide gel electrophoresis and subsequent staining with either SimplyBlue™ SafeStain (Invitrogen) or copper(II) chloride (**Figure 1**). ELPs exhibited reduced electrophoretic mobilities compared to globular proteins, a finding widely observed with ELPs.[10] It was also observed that the negatively charged variant E57 was poorly stained with the SimplyBlue™ SafeStain as well as with Coomassie brilliant blue R-250 (data not shown). Staining with copper(II) chloride, however, led to a clear E57 protein band and a white K48 protein band against an opaque, whitish-blue background (Figure 1b). Analysis of the purified ELPs by mass spectrometry resulted in molecular weights that were in excellent agreement with the theoretical values (see Supporting Information). As expected,[17] the proteins K48 and E57 do not exhibit LCST behavior until 90 ℃ and show mainly random coil structure when dissolved in water (see Supporting Information).

Capsule Preparation and Characterization

After successful expression our next goal was to exploit the high net charges of K48 and E57 for self assembly of the ELP variants into supramolecular structures, namely multilayer polypeptide capsules, using a Layer-by-Layer (LbL) technique[18] (**Figure 2**). This technique is based on the consecutive assembly of oppositely charged polymers around a preformed charged spherical template[18] with typical diameter from a few hundred nm to a few μm. At the end of the LbL adsorption process, the cores can be successfully removed to obtain hollow and intact capsules. Polymer containers based on the LbL technique have recently attracted high interest for a variety of different applications, ranging from drug delivery systems and targeted gene therapy to biosensor devices.[19, 20] To date, capsules have been made of synthetic and biodegradable polyelectrolytes,[21, 22] comprising natural molecules such as oligonucleotides[23] and proteins,[24, 25] which demonstrates the high versatility of LbL assembly.

Using standard LbL preparation techniques[18] and employing supercharged proteins E57 and K48 as building blocks, we generated capsules exhibiting the following wall structure: (DEXS/pARG)(E57/K48)$_3$(E57/K48$_{AF488}$)E57, where DEXS denotes dextran sulfate and pARG poly(arginine), two charged biodegradable polymers made from naturally occurring monomers (see Supporting Information). The use of DEXS/pARG as a first bi-layer proved crucial to growing a stable multilayer (E57/K48) wall, providing a barrier against diffusion of the proteins into the porous $CaCO_3$ particle templates (see Supporting Information, Figure S6). For visualization purposes, one layer of K48 was fluorescence labeled with Alexa AF488 (see Supporting Information). Capsules were characterized with confocal laser scanning microscopy (CLSM), transmission electron microscopy (TEM) and scanning electron microscopy (SEM).

In **Figure 3** representative images of the capsules formed by supercharged proteins are shown. These images clearly demonstrate the existence of capsules with an empty interior and stable walls. Notably, the dissolution of the core is a critical step in the preparation of hollow capsules, as it may result in capsules breaking or swelling due to decomposition conditions (i.e., low pH) where the polymer wall may disaggregate. In view of that, the results reported in Figure 3 indicate that a hollow and stable wall remains when the inorganic core is dissolved.

Compared to capsules formed by standard synthetic polyelectrolytes, such as polystyrene sulfonate (PSS) and poly(allylamine hydrochloride) (PAH),[18] the walls of capsules based on supercharged proteins are rather porous (see Supporting Information, Figures S10, 12-13). This may be a result of the lower charge density of E57 and K48 compared to PSS and PAH (see Supporting Information, Table 1), which results in a higher mechanical pressure during the dissolution procedure. For instance, permeability tests performed on (E57/K48) capsules without cores showed the diffusion across the protein wall of the encapsulated dextran (500 kDa MW) (see Supporting Information, Figure S10), thus indicating the formation of large pores in the multilayer wall. This hypothesis was subsequently supported by TEM and SEM observation of capsules after core dissolution (see Supporting Information, Figures S12-13). At any rate, the two structural compartments of capsules, cavity and wall, are well defined and prove successful and stable assembly (Supporting Information, Figures S7 and S9).

Evaluation of In Vitro Cytotoxicity

Such capsules might be appealing containers for use in biomedicine. Since positively charged polymers are the most common source of toxicity in charged systems due to their interaction with anionic intracellular components,[26-28] the toxicity of K48 was investigated and compared to the other positive polyelectrolytes used for the synthesis of capsule controls (i.e. PLL, PAH, pARG). A fluorimetric metabolic assay employing NIH/3T3 embryonic fibroblast cells was utilized to assess cytotoxicity. The normalized fluorescence of Resorufin, a dye indicating metabolically active cells, was plotted against polyelectrolyte concentrations (**Figure 4**). The resulting dose response curves yielded the following polymer concentrations causing 50% cell death (LD50, mg mL^{-1}) in decreasing order of toxicity: PLL (LD50 = 0.007), PAH (LD50 = 0.009), pARG (LD50 = 0.015) and K48 (LD50 = 0.196). PLL, PAH and pARG exhibited similar dose response curves with similar LD50 values, whereas the curve for K48 was strongly shifted to higher concentration values. This indicates that lower concentrations of PLL, PAH and pARG than of K48 are able to induce cell death. K48 induces toxicity at the maximum concentration value used (1 mg mL^{-1}) and this effect was immediately mitigated by halving the dose. A plateau level of viability was reached at a concentration of 3.1×10^{-2} mg mL^{-1}.

Conclusion

In this work we demonstrated the expression of supercharged polypeptides consisting of repetitive motifs. As a result of incorporating a single charge per almost every repeat, unfolded polyelectrolytes were obtained that are perfectly defined regarding their number and distribution of charges, monomer composition, stereochemistry and dispersity, which is almost impossible by conventional polymerization techniques. With K48 for example, 1 positive charge per 5.7 amino acids was reached. ELPs with charged amino acids as guest residues have already been produced, but with much lower charge densities than reported herein.[16] So far only a single folded protein, Green Fluorescent Protein (GFP), was equipped with similar amounts and densities of charges.[29] However, within GFP the charges were by far not as equally distributed as in the ELP backbone. In this respect we demonstrated that the

concept of supercharging by genetic engineering can be extended to other peptide-based biopolymers. When comparing supercharged ELPs with naturally occurring polypeptides, we see that with K48 it was even possible to realize a charge density comparable to only a few naturally occurring unfolded proteins,[29, 30] all while using a minimal set of the amino acid alphabet.
It was further shown that the high number of charges of these de novo designed proteins could be exploited for the fabrication of supramolecular structures. Oppositely charged variants were transformed into multilayer capsules by electrostatic interactions employing the widely used Layer-by-Layer technique. Due to their low toxicity, supercharged proteins like the highly charged ELPs presented in this work promise to be a favorable alternative to their chemically synthesized counterparts in the context of biomedical scaffolds. In the future we will employ supercharged ELPs for the generation of other electrostatically induced polymeric architectures such as polyplexes and hydrogels with well defined network porosity.

Acknowledgements: Parts of the project were supported by an *ERC* starting grant (A.H.), and by the *BMBF ERA-NET* grant NanoSyn (W.J.P.). The research in the group of B.P. was supported by the *Netherlands Proteomics Centre (NPC*).

Received: ((will be filled in by the editorial staff)); Revised: ((will be filled in by the editorial staff)); Published online: ((will be filled in by the editorial staff));
DOI: ((will be filled in by the editorial staff))

Keywords: biomaterials; elastin like polypeptides; layer-by-layer assembly; polyelectrolytes; proteins

References

[1] R. Langer, D. A. Tirrell, *Nature* **2004**, *428*, 487.
[2] J. M. Dang, K. W. Leong, *Adv. Drug Del. Rev.* **2006**, *58*, 487.
[3] U. K. Slotta, S. Rammensee, S. Gorb, T. Scheibel, *Angew. Chem. Int. Ed.* **2008**, *47*, 4592.
[4] H. Y. Bai, K. Xu, Y. J. Xu, H. Matsui, *Angew. Chem. Int. Ed.* **2007**, *46*, 3319.
[5] H. Jia, C. Wong Po Foo, D. L. Kaplan, *Polym. Rev.* **2007**, *47*, 29.
[6] A. Chilkoti, T. Christensen, J. A. MacKay, *Curr. Opin. Chem. Biol.* **2006**, *10*, 652.
[7] K. Trabbic-Carlson, L. A. Setton, A. Chilkoti, *Biomacromolecules* **2003**, *4*, 572.
[8] J. Gosline, M. Lillie, E. Carrington, P. Guerette, C. Ortlepp, K. Savage, *Philos. Trans. Roy. Soc. London, B Biol. Sci.* **2002**, *357*, 121.
[9] L. L. del Mercato, G. Maruccio, P. P. Pompa, B. Bochicchio, A. M. Tamburro, R. Cingolani, R. Rinaldi, *Biomacromolecules* **2008**, *9*, 796.
[10] D. E. Meyer, A. Chilkoti, *Biomacromolecules* **2002**, *3*, 357.
[11] W. Y. Wu, C. Mee, F. Califano, R. Banki, D. W. Wood, *Nat. Protoc.* **2006**, *1*, 2257.
[12] U. L. Lao, J. Kostal, A. Mulchandani, W. Chen, *Nat. Protoc.* **2007**, *2*, 1263.
[13] H. Betre, L. A. Setton, D. E. Meyer, A. Chilkoti, *Biomacromolecules* **2002**, *3*, 910.
[14] M. R. Dreher, W. G. Liu, C. R. Michelich, M. W. Dewhirst, F. Yuan, A. Chilkoti, *Journal of the National Cancer Institute* **2006**, *98*, 335.
[15] T. A. T. Lee, A. Cooper, R. P. Apkarian, V. P. Conticello, *Adv. Mater.* **2000**, *12*, 1105.
[16] A. Girotti, J. Reguera, F. J. Arias, M. Alonso, A. M. Testera, J. C. Rodriguez-Cabello, *Macromolecules* **2004**, *37*, 3396.
[17] D. W. Lim, K. Trabbic-Carlson, J. A. MacKay, A. Chilkoti, *Biomacromolecules* **2007**, *8*, 1417.
[18] E. Donath, G. B. Sukhorukov, F. Caruso, S. A. Davis, H. Möhwald, *Angew. Chem. Int. Ed.* **1998**, *37*, 2202.
[19] M. F. Bedard, B. G. De Geest, A. G. Skirtach, H. Mohwald, G. B. Sukhorukov, *Adv. Colloid Interface Sci.* **2009**, *158*, 2.
[20] P. Rivera Gil, L. L. del Mercato, P. del Pino, A. Munoz Javier, W. J. Parak, *Nano Today* **2008**, *3*, 12.
[21] B. G. De Geest, R. E. Vandenbroucke, A. M. Guenther, G. B. Sukhorukov, W. E. Hennink, N. N. Sanders, J. Demeester, S. C. d. Smedt, *Adv. Mater.* **2006**, *18*, 1005.
[22] P. Rivera Gil, S. De Koker, B. G. De Geest, W. J. Parak, *Nano Lett.* **2009**, *9*, 4398.
[23] A. P. Johnston, L. Lee, Y. Wang, F. Caruso, *Small* **2009**, *5*, 1418.
[24] Y. Zhu, W. J. Tong, C. Y. Gao, H. Mohwald, *J. Mater. Chem.* **2008**, *18*, 1153.
[25] W. Qi, X. Yan, L. Duan, Y. Cui, Y. Yang, J. Li, *Biomacromolecules* **2009**, *10*, 1212.
[26] A. C. Hunter, *Adv. Drug Deliv. Rev.* **2006**, *58*, 1523.
[27] N. Seiler, F. Raul, *J. Cell. Mol. Med.* **2005**, *9*, 623.
[28] D. Fischer, Y. X. Li, B. Ahlemeyer, J. Krieglstein, T. Kissel, *Biomaterials* **2003**, *24*, 1121.
[29] M. S. Lawrence, K. J. Phillips, D. R. Liu, *J. Am. Chem. Soc.* **2007**, *129*, 10110.
[30] V. N. Uversky, J. R. Gillespie, A. L. Fink, *Prot. Struct. Funct. Gen.* **2000**, *41*, 415.

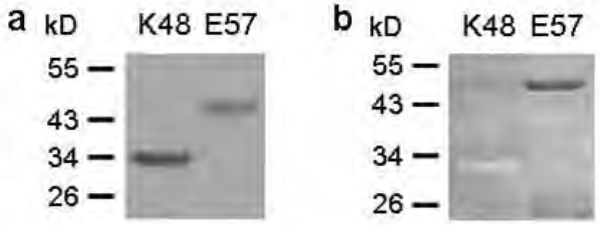

Figure 1. Purified ELP variants K48 and E57 examined by SDS-PAGE. a) 4-12% NuPAGE gel stained with SimplyBlue™ safe stain. K48: 2 µg, E57: 8 µg. b) 12% SDS-PAGE gel stained with a 0.3 M copper (II) chloride solution. K48: 2 µg, E57: 4 µg.

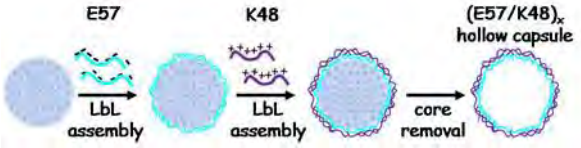

Figure 2. Schematic illustration of the multiple assembly of the two oppositely supercharged proteins onto spherical $CaCO_3$ porous microparticles via LbL assembly technique, and fabrication of a hollow protein-based capsule by dissolution of the template core. The turquoise lines represent the supercharged negative E57 ELP, the violet lines represent the supercharged positive K48 ELP. For simplicity, only two layers are shown. Capsules are not drawn to scale.

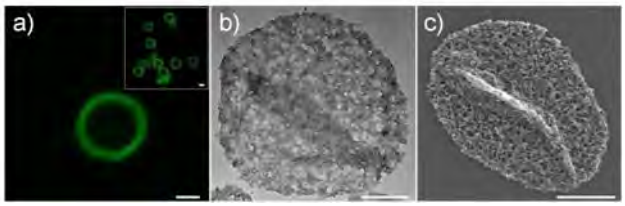

Figure 3. Structural analysis of capsules assembled by the supercharged proteins E57 and K48 after removal of the template cores. a) CLSM image of one capsule in aqueous solution whose wall had been labeled with Alexa Fluor 488. The inset shows a low resolution image of several capsules. Images demonstrate the particulate nature of the capsules. b) –c) TEM and SEM image of one capsule. As TEM and SEM are performed in vacuum capsules collapse, indicating the absence of the template core and thus an empty cavity. Scale bars represent 1 µm.

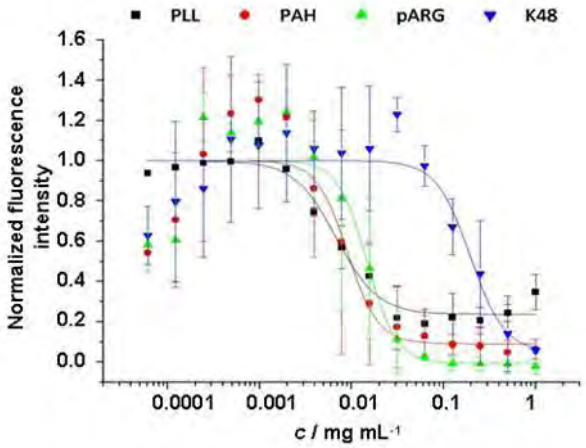

Figure 4. Comparison of the polyelectrolyte-induced toxicity on NIH/3T3 embryonic fibroblasts. Cells were incubated with the different polymers in a concentration range from 1 mg mL^{-1} to 6.1 x 10^{-5} mg mL^{-1} and some cells were left untreated as positive control for viability. Cell viability was assessed by an increase in the fluorescence signal and is given as mean of normalized intensities. The normalized fluorescent intensity is plotted against the concentration (c) and shows a sigmoidal concentration-toxicity relationship. PLL: poly-L-lysine; PAH: poly(allylamine hydrochloride); pARG: poly-L-arginine.

Table of Contents

Supercharged, unfolded protein polymers based on elastin-like peptides (ELPs) are designed and expressed by introducing positively and negatively charged amino acids, respectively, within the repetitive pentapeptide units. An example of their potential for the fabrication of supramolecular structures is presented in this work by the assembly of multilayer capsules.

Supporting Information for

De Novo Design of Supercharged, Unfolded Protein Polymers and their Assembly into Supramolecular Aggregates

Anke Kolbe, Loretta L. del Mercato, Azhar Z. Abbasi, Pilar Rivera Gil, Sekineh J. Gorzini, Wim H.C.Huibers, Bert Poolman, Wolfgang J. Parak, and Andreas Herrmann

Materials

E.coli XL1-Blue competent cells were purchased from Stratagene (La Jolla, CA). The pUC19 cloning vector, restriction endonucleases, T4 DNA ligase (LC), Fast AP™ thermosensitive alkaline phosphatase (Fast AP), and GeneJET™ Plasmid Miniprep kit were purchased from Fermentas (St. Leon-Rot, Germany). Digested DNA fragments were purifed using QIAquick® spin miniprep kits from QIAGEN, Inc. (Valencia, CA). The pET-25b(+) vector and *E.coli* BLR(DE3) competent cells were purchased from Novagen Inc. (Milwaukee, WI). Oligonucleotides were synthesized by biomers.net (Ulm, Germany). Bacto™ tryptone and BBL™ yeast extract were purchased from Becton, Dickinson and Co. (Sparks, MD). Potassium phosphate monobasic, potassium phosphate dibasic, sodium phosphate monobasic, sodium phosphate dibasic, sodium chloride, and glycerol were purchased from Merck KGaA (Darmstadt, Germany). Ampicillin and imidazole were purchased from Roth (Karlsruhe, Germany). Isopropyl ß-thiogalactopyranoside (IPTG) was purchased from Duchefa (Harlem, Netherlands). 3,5 dimethoxy-4-hydroxycinnamic acid and internal standards bovine serum albumin and trypsinogen were purchased from LaserBio Labs (Sophia-Antipolis, France). Poly(sodium 4-styrenesulfonate) (PSS, Mw ~70,000), poly(allylamine hydrochloride) (PAH, Mw ~56,000), poly(fluorescein isothiocyanate allylamine hydrochloride) (PAH_{FITC}, Mw ~56,000), poly-L-arginine (pARG, Mw> 70 kDa), dextran sulfate (DEXS, Mw ~10 kDa), poly-L-lysine hydrobromide (pLL, Mw 15,000 – 30,000 Da), calcium chloride dehydrate ($CaCl_2$), Sodium carbonate (Na_2CO_3) and ethylenediaminetetraacetic acid (EDTA) were purchased from Sigma-Aldrich. Alexa Fluor488, Alexa Fluor 594 carboxylic acid succinimidyl ester and amino dextran (Mw ~500,000) carboxylic acid succinimidyl ester were obtained from Molecular Probes (Invitrogen). All chemicals were used as received. Ultrapure water with a resistivity greater than 18.2 MΩ cm was used for all experiments.

Monomer gene synthesis and gene oligomerization

Construction of the monomer genes and subsequent multimerization were performed as described by Chilkoti and co-workers.[1] Briefly, a monomer gene was constructed from eight 5'-phosphorylated, PAGE-purified synthetic DNA oligonucleotides. For annealing, equimolar mixtures of the oligonucleotides in T4 DNA ligase buffer were heated to 94ºC and then slowly cooled down to 4ºC, yielding a double-stranded DNA cassette with *Eco*RI and *Hin*DIII compatible ends. pUC19 was digested with *Eco*RI and *Hin*DIII, dephosphorylated with Fast AP and run on a 1% agarose gel in TAE buffer (per 1L, 108 g Tris base, 57.1 mL glacial acetic acid, 0.05 м EDTA, pH 8.0). The vector band was cut out and purified using a spin column purification kit. The annealed oligonucletides were ligated to the linearized vector. For transformation, 200 µL of chemically competent *E.coli* XL1-Blue cells were combined with 5 µL of the ligation mixture and further treated according to the manufacturer's protocol.

Cells were spread on Lysogeni broth (LB) agar plates (for 1L, 10 g Bacto™ tryptone, 5 g BBL™ yeast extract, 5 g NaCl, 15 g agar) supplemented with 100 µg/mL ampicillin, and incubated over night at 37ºC. Colonies were picked and grown in 6 mL LB media (for 1L, 10 g Bacto™ tryptone, 5 g BBL™ yeast extract, 5 g NaCl) supplemented with 100 µg/mL ampicillin over night, and plasmids were isolated using the GeneJET Plasmid Miniprep kit. Positive clones were verified by plasmid digestion with *Eco*RI and *Hin*DIII and subsequent gel electrophoresis. The DNA sequence of putative inserts was further verified by DNA sequencing (SequenceXS, Leiden, The Netherlands).

Gene oligomerization was performed as described by Chilkoti and co-workers.[1] Positive clones were verified by plasmid digestion with *Eco*RI and *Hin*DIII and subsequent gel electrophoresis. The DNA sequences of putative inserts were further verified by DNA sequencing (SequenceXS, Leiden, The Netherlands). Gene sequences and respective amino acid sequences of K48 and E57 are shown in figure S1. As the recognition sites of the restriction enzymes *Pfl*MI and *Bgl*I have to be preserved, a valine residue instead of a lysine or glutamic acid residue is incorportated with every step of oligomerization.

a) Gene sequence of ELP K48

*Eco*RI *Pfl*MI
A ATT CAT ATG GGC CAC GGC GTG GGT GTT CCG GGC AAA GGT GTTCCGGGT AAA GGT GTG
G V G V P G K G V P G K G V

CCG GGC AAA GGT GTT CCT GGT AAA GGT GTG CCG GGT AAA GGT GTG CCG GGC AAA GGT
P G K G V P G K G V P G K G V P G K G

GTT CCT GGT AAA GGT GTG CCG GGT AAA GGT GTG CCG GGT AAA GGT GTA CCA GGT AAA
V P G K G V P G K G V P G K G V P G K

GGT GTT CCG GGT AAA GGC GTT CCG GGT AAA GGT GTG CCG GGC GTG GGT GTT CCG GGC
G V P G K G V P G K G V P G V G V P G

AAA GGT GTT CCG GGT AAA GGT GTG CCG GGC AAA GGT GTT CCT GGT AAA GGT GTG CCG
K G V P G K G V P G K G V P G K G V P

GGT AAA GGT GTG CCG GGC AAA GGT GTT CCT GGT AAA GGT GTG CCG GGT AAA GGT GTG
G K G V P G K G V P G K G V P G K G V

CCG GGT AAA GGT GTA CCA GGT AAA GGT GTT CCG GGT AAA GGC GTT CCG GGT AAA GGT
P G K G V P G K G V P G K G V P G K G

GTG CCG GGC GTG GGT GTT CCG GGC AAA GGT GTT CCG GGT AAA GGT GTG CCG GGC AAA
V P G V G V P G K G V P G K G V P G K

GGT GTT CCT GGT AAA GGT GTG CCG GGT AAA GGT GTG CCG GGC AAA GGT GTT CCT GGT
G V P G K G V P G K G V P G K G V P G

AAA GGT GTG CCG GGT AAA GGT GTG CCG GGT AAA GGT GTA CCA GGT AAA GGT GTT CCG
K G V P G K G V P G K G V P G K G V P

GGT AAA GGC GTT CCG GGT AAA GGT GTG CCG GGC GTG GGT GTT CCG GGC AAA GGT GTT
G K G V P G K G V P G V G V P G K G V

CCG GGT AAA GGT GTG CCG GGC AAA GGT GTT CCT GGT AAA GGT GTG CCG GGT AAA GGT
P G K G V P G K G V P G K G V P G K G

GTG CCG GGC AAA GGT GTT CCT GGT AAA GGT GTG CCG GGT AAA GGT GTG CCG GGT AAA
V P G K G V P G K G V P G K G V P G K

GGT GTA CCA GGT AAA GGT GTT CCG GGT AAA GGC GTT CCG GGT AAA GGT GTG CCG GGC
G V P G K G V P G K G V P G K G V P
*Bgl*I *Hind*III
GGG CTG GAA TA

b) Gene sequence of ELP E57

*Eco*RI *Pfl*MI
A ATT CAT ATG GGC CAC GGC GTG GGT GTT CCG GGC GAA GGT GTT CCG GGT GAA GGT GTG
G V G V P G E G V P G E G V

CCG GGC GAA GGT GTT CCT GGT GAA GGT GTG CCG GGT GAA GGT GTG CCG GGC GAA GGT
P G E G V P G E G V P G E G V P G E G

GTT CCT GGT GAA GGT GTG CCG GGT GAA GGT GTG CCG GGT GAA GGT GTA CCA GGT GAA
V P G E G V P G E G V P G E G V P G E

GGT GTT CCG GGT GTG GGC GTT CCG GGT GAA GGT GTG CCG GGC GAA GGT GTT CCG GGC
G V P G V G V P G E G V P G E G V P G

GAA GGT GTT CCG GGT GAA GGT GTG CCG GGC GAA GGT GTT CCT GGT GAA GGT GTG CCG
E G V P G E G V P G E G V P G E G V P

GGT GAA GGT GTG CCG GGC GAA GGT GTT CCT GGT GAA GGT GTG CCG GGT GTG GGT GTG
G E G V P G E G V P G E G V P G V G V

CCG GGT GAA GGT GTA CCA GGT GAA GGT GTT CCG GGT GAA GGC GTT CCG GGT GAA GGT
P G E G V P G E G V P G E G V P G E G

GTG CCG GGC GAA GGT GTT CCG GGC GAA GGT GTT CCG GGT GAA GGT GTG CCG GGC GAA
V P G E G V P G E G V P G E G V P G E

GGT GTT CCT GGT GAA GGT GTG CCG GGT GAA GGT GTG CCG GGC GTG GGT GTT CCT GGT
G V P G E G V P G E G V P G V G V P G

GAA GGT GTG CCG GGT GAA GGT GTG CCG GGT GAA GGT GTA CCA GGT GAA GGT GTT CCG
E G V P G E G V P G E G V P G E G V P

GGT GAA GGC GTT CCG GGT GAA GGT GTG CCG GGC GAA GGT GTT CCG GGC GAA GGT GTT
G E G V P G E G V P G E G V P G E G V

CCG GGT GAA GGT GTG CCG GGT GTG GGT GTG CCG GGT GAA GGT GTA CCA GGT GAA GGT
P G E G V P G V G V G V P G E G V P G E G

GTT CCG GGT GAA GGC GTT CCG GGT GAA GGT GTG CCG GGC GAA GGT GTT CCG GGC GAA
V P G E G V P G E G V P G E G V P G E

GGT GTT CCG GGT GAA GGC GTT CCG GGT GAA GGT GTG CCG GGC GAA GGT GTT CCG GGC
G V P G E G V P G E G V P G E G V P G

GAA GGT GTG CCG GGC GTG GGT GTT CCT GGT GAA GGT GTG CCG GGT GAA GGT GTG CCG
E G V P G V G V P G E G V P G E G V P

GGC GAA GGT GTT CCT GGT GAA GGT GTG CCG GGT GAA GGT GTG CCG GGT GAA GGT GTA
G E G V P G E G V P G E G V P G E G V
*Bgl*I
CCA GGT GAA GGT GTT CCG GGT GAA GGC GTT CCG GGT GAA GGT GTG CCG GGC GGG CTG
P G E G V P G E G V P G E G V P
*Hind*III
GAA TA

Figure S1. Genes and corresponding polypeptide sequences of **(a)** ELP K48 (lysine variant) and **(b)** ELP E57 (glutamic acid variant). Recognition sites for the restriction enzymes *Eco*RI, *Pfl*MI, *Bgl*I, and *Hind*III are underlined.

Expression vector construction

The expression vector pET 25b(+) (Novagen) was modified by cassette mutagenesis as described by Chilkoti and co-workers.[1] The DNA sequence spanning *Nde*I to *Eco*RI was exchanged for a sequence which incorporates a unique *Sfi* I recognition site and which encodes for an affinity tag consisting of six histidine residues (Fig. S2). The modified pET 25b(+) expression vector was digested with *Sfi*I, dephosphorylated and purified using a microcentrifuge spin column kit. The ELP gene was excised from the pUC19 vector by

digestion with *Pfl*MI and *Bgl*I, and the excised gene was purified by agarose gel extraction following gel electrophoresis. The linearized vector and ELP-encoding gene were ligated, transformed into XL1-Blue cells, and screened as described above.

Insert sequence of modified expression vector pET-25b(+)-SfiI-H6

*Nde*I *Sfi*I *Eco*RI

T ATG GGC GCG GGG CCG GGC TGG CCG CAC CAC CAC CAC CAC CAC TGA TAA GAA TT

M G A G P G W P H H H H H H * *

Figure S2. Sequence inserted into pET-25b(+) between recognition sites *Nde*I and *Eco*RI. The modified pET-25b(+)-SfiI-H6 vector contains a unique *Sfi*I recognition site to insert ELP genes into the vector, and sequence encoding for a hexa-histidine (H6) tag at the C-terminus of the expressed protein for affinity purification.

Protein expression and purification

E.coli BLR (DE3) cells (Novagen) were transformed with the pET expression vectors containing the respective ELP genes. For protein production, Terrific Broth medium (for 1L, 12 g tryptone and 24 g yeast extract) enriched with phosphate buffer (for 1L, 2.31 g potassium phosphate monobasic and 12.54 g potassium phosphate dibasic) and glycerol (4 mL per 1L TB), and supplemented with 100 µg/mL ampicillin was inoculated with an overnight starter culture to an initial OD_{600} of 0.1 and incubated at 37°C with orbital agitation at 250 rpm until OD_{600} reached 0.7. Protein production was induced by addition of IPTG to a final concentration of 1 mM. Cultures were then continued for an additional 4 h post-induction. Cells were subsequently harvested by centrifugation (7,000 x *g*, 20 min, 4ºC), resusupended in lysis buffer (50 mM sodium phosphate buffer, pH 8.0, 300 mM NaCl, 20 mM imidazole) to an OD_{600} of 100 and disrupted with a French Press. Cell debris was removed by centrifugation (40,000 x *g*, 90 min, 4ºC). Proteins were purified from the supernatant under native conditions by Ni-sepharose chromatography (GE Healthcare). Product-containing fractions were pooled and dialyzed against Ultrapure water (>18 MΩ). K48 was further purified by affinity chormatography using a Heparin HP column (GE Healthcare) and protein-containing fractions were dialyzed against Ultrapure water (>18 MΩ). Purified proteins were stored at -20ºC or lyophilized and stored at room temperature until further use.

Protein characterization

The concentrations of the purified ELPs were determined by measuring absorbance at 280 nm using a spectrophotometer (NanoDrop™, Thermo Scientific). Protein purity was analyzed by PAGE (poly(acrylamide) gel electrophoresis) on a 4-12% NuPAGE® Bis-Tris gel (Invitrogen) and subsequent staining of the gel with SimplyBlue™ SafeStain (Invitrogen). Furthermore, purified proteins were characterized by SDS-PAGE (SDS - sodium dodecyl sulfate) on a 12% polyacrylamide gel according to Laemmli[2] and subsequent copper (II) chloride staining as reported by Lee and coworkers.[3] Mass spectrometric analysis was performed using a 4800 Plus MALDI-TOF/TOF Analyzer (Applied Biosystems, Foster City, CA, USA). The samples were prepared in a recrystallized 3,5 dimethoxy-4-hydroxycinnamic acid matrix with the calibration standards bovine serumalbumin (MW = 66,429.9) for K48 and trypsinogen (MW = 23980.9) for E57. Mass spectra were recorded in positive ion mode with the 4000 Series Explorer Software, version 3.0 (Applied Biosystems, Foster City, CA, USA). The data were analyzed in Data Explorer, version 4.9 (Applied Biosystems, Foster City, CA, USA). The

masses determined by MALDI-TOF were 24,105 +/- 50 Da for K48 and 28,967 +/- 50 Da for E57, which is in excellent agreement with the calculated masses of 24,150.7 and 28,970.1 Da, respectively.

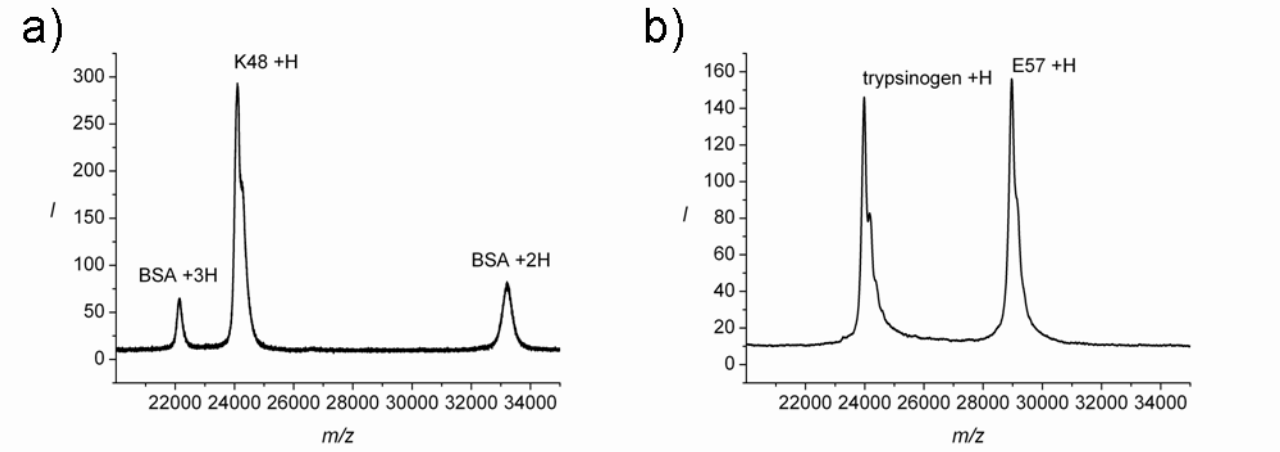

Figure S3. MALDI-TOF mass spectra of supercharged elastin-like proteins K48 and E57. a) Mass spectrum of K48 (m/z is 24,104.6) with internal standard bovine serum albumin (BSA; m/z is 22,135.5 for BSA +3H and m/z is 33,215.3 for BSA +2H). b) Mass spectrum of E57 (m/z is 28,967.1) with internal standard trypsinogen (m/z is 23,982.0). I = absolute intensity.

Analysis of secondary structure

Circular dicroism (CD) spectra were recorded using a Jasco-815 spectropolarimeter (Jasco, Japan). Measurements were carried out at room temperature with a cell path length of 1 mm. The polypeptide concentrations in Ultrapure water were 10 and 5 µM for K48 and E57, respectively. The CD sprectra of of both polypeptides showed a smaller trough at around 220 nm and a larger trough at around 200 nm (Fig. S4). This spectral behavior is usually interpreted to represent largely random coil structure with some contribution of α-helical segments.[4, 5]

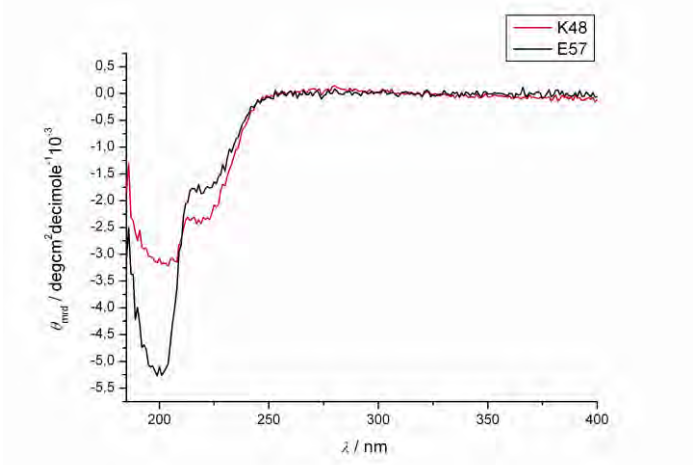

Fig. S4. Circular dicroism (CD) spectra of aqueous solutions of ELPs K48 (10 µM) and E57 (5µM). Data represent averages of 25 scans.

LCST behavior analysis

To characterize the ELP inverse temperature transition, the OD_{350} of K48 and E57 ELPs in ultrapure water at a concentration of 57 and 24 μM, respectively, were measured as a function of temperature on a Jasco V630 spectrophotometer. Measurements were performed between 20 and 90ºC by increasing the temperature every 10 min in 5ºC increments. No significant increase in the OD_{350} values for either of the ELP variants could be observed at any temperature measured. OD_{350} values were below 0.1 at all times. This finding is in line with published data, where the incorporation of increasing numbers of lysine or glutamic acid residues in ELPs led to an increase in the lower critical solution temperature (LCST) at neutral pH values.[6, 7]

Labelling of proteins

Alexa Fluor® 488 sulfodichlorophenol ester (AF488) was purchased from Molecular Probes (Invitrogen) and dissolved in DMF to a concentration of 10 mg/mL. To 3.15 mg of K48 in 0.1 M sodium carbonate buffer, pH 8.6, an equimolar amount of AF488 was added under vigorous stirring. After incubation for 2 h at room temperature under vigorous stirring, hydroxyamine solution (pH 8.6) was added to a final concentration of 0.14 M and incubated for additional 90 min at room temperature. Uncoupled dye was removed by size exclusion using an illustra NAP™-25 column (GE Healthcare) and 0.1 M sodium carbonate buffer (pH 8.6) as equilibration and elution buffer. Protein-containing fractions were pooled and dialyzed (cut-off 500 Da) against Ultrapure water (>18 MΩ). Protein concentration was determined using the following equation:

$$c\ [mg/mL] = (A_{280} - 0.11 * A_{495}) * MW_{K48}$$

where A_{280} and A_{495} are the absorbance values at 280 and 495 nm, respectively, and MW_{K48} is the molecular weigth of K48. The labelled protein ($K48_{AF488}$) was lyophilized and stored at room temperature until further use.

Cytotoxicity assay of positively charged polyelectrolytes (PEs)

NIH/3T3 embryonic fibroblasts were seeded in a 96-well-platte (Greiner by Sigma-Aldrich) at a cell density of 10^4 cells/well in 100 μL growth medium (DMEM-F12 Ham´s basal medium supplemeted with 10% calf serum, 1% L-glutamine and 1% penicilline/streptomycine whereby all material were provided by Sigma-Aldrich). The next day, the cells were incubated with the PEs under investigation (i.e. PLL, PAH, pARG, and K48) for 24h. A starting concentration of 1 mg/mL was used for each PE and consecutively halved until a final concentration of 6.1×10^{-5} mg/mL. All concentrations were done in duplicate. Cells that were not treated with any PE served as a positive control for viability. After 24 h, the cells were washed once with PBS, 100 μL of a 10% Resazurin (TOX-8 kit from Sigma-Aldrich) solution (in growth medium) were added to each well and incubated for 3 h at 37°C and 5% CO_2. Resazurin is a blue, non-fluorescent sodium salt, which is converted to resorufin by metabolically active cells. Resorufin is a pink, fluorescent sodium salt that accumulates outside the cells. This reduction process requires functional mitochondrial activity which is inactivated immediately after cell death. Fluorescence spectra were measured using a 96-microwell plate reader connected to a Fluorolog® spectrofluorometer (Jovin Yvon) at an excitation wavelength of 560 nm. The emission was recorded in the range of 572-650 nm with 1 nm resolution and a slit of 5 nm. Firstly, the mean of the intensities of the emission spectra of the duplicates was calculated and then, the maximum intensity values found in the range 578-585 nm were also averaged. The mean background signal (640-650 nm) was substracted from the mean maximum emission values and subsequently normalized with the maximum

fluorescence value obtained. The maximum fluorescence value corresponded not always to the untreated cells, probably due to the formation of hydroresorufin, a transparent nonfluorescent product which is formed upon further reduction of resorufin by viable cells.[8] The experiments were repeated three times for each PE. The means of the normalized fluorescence intensity values of the three experiments (I/Imax) were plotted against the different concentrations of the PEs. A sigmoidal distribution was obtained and fitted as a function of a logistic dose response curve which enables us calculating the PE concentration yielding 50% cell death (LD50).

Charges of positive and negative polyelectrolytes (PEs)

The main driving force in alternate LBL assembly of multilayer capsules is the electrostatic interaction between oppositely charged species. Hence, the charges per molecule of the two supercharged unfolded proteins K48 and E57, employed as component layer of ELPs-derived capsules, was calculated and compared to the number of charges per molecule of the other PEs used for the synthesis of capsules controls (i.e. PAH, pARG, PSS and DEXS) (Table 1). As expected, all the control PEs have a higher number of charges per molecule than the ELPs except for DEXS, which has around 27 charges per molecule. The µmol charges per 1 mg are also higher for all of the control PEs than for the ELPs.

PE	**full name**	**MW (average) [Da]**	**charges/ molecule at pH 7.0**	**µmol charges in 1 mg**
E57	ELP-glutamic acid	28,970	57	1.97
K48	ELP-lysine	24,150	48	1.99
DEXS	Dextran sulfate sodium salt from *Leuconostoc* spp.	6,500-10,000	27.79	3.37
pARG	Poly-L-arginine hydrochloride	70,000	498	7.11
PSS	Poly(sodium 4-styrenesulfonate)	70,000	339	4.84
PAH	Poly(allylamine hydrochloride)	56,000	605	10.8
pLL	poly-L-lysine hydrobromide	15,000-30,000	108	4.8

Table 1: Calculation of the charges per molecule and µmol charge per 1 mg of each PE (E57, K48, DEXS, pARG, PSS and PAH).

Capsule preparation

The negatively charged E57 and the positively charged K48 ELPs were alternatively assembled onto inorganic calcium carbonate ($CaCO_3$) microparticle templates for the preparation of hollow polypeptide microcapsules (Scheme S1). $CaCO_3$-based cores were used because compared to organic templates[9] they allow for the synthesis of capsules under mild conditions, as the $CaCO_3$ core material can be easily removed by complexation with ethylenediaminetetraacetic acid (EDTA) buffer.[10] Additionally, the encapsulation of biomacromolecules can be performed directly during the synthesis of the $CaCO_3$ microparticles by entrapping the cargo within the sacrificial template particles, owing to their high porosity.[10, 11] As control samples, capsules made of degradable and non-degradable

polylectrolytes were produced. Degradable capsules, susceptible to enzymatic degradation, were composed of dextran sulfate (DEXS) as the polyanion and of poly-L-arginine (pARG) as the polycation,[12] non-degradable capsules were made of poly(sodium 4-styrenesulfonate) (PSS) as the polyanion and of polyallylamine hydrochloride (PAH) as the polycation.

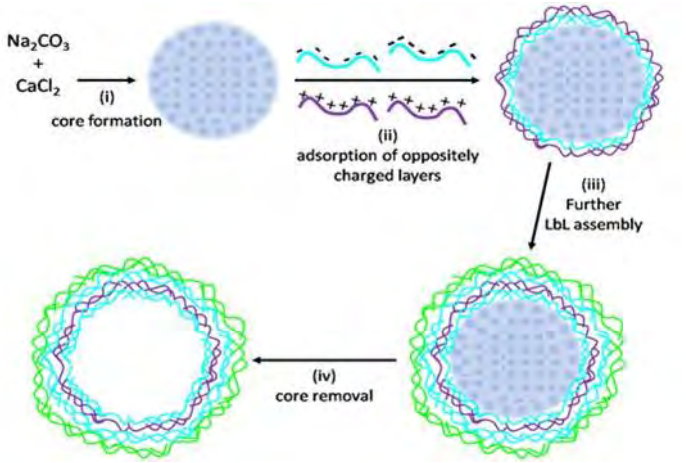

Scheme S5. Schematic representation of polyelectrolyte capsule fabrication by layer-by-layer (LbL) assembly. (i) Spherical $CaCO_3$ microparticles are fabricated by precipitation from supersaturated $CaCl_2$ and Na_2CO_3 solutions. (ii–iii) Oppositely charged polymer layers are consecutively adsorbed around the spherical templates by electrostatic attractions. (iv) The original template is removed by dissolution to obtain a capsule with an empty cavity. Only few layers of polyelectrolyte are shown, for sake of clarity. Capsules are not drawn to scale.

Preparation of $CaCO_3$ microparticles

For each capsule system, $CaCO_3$ microparticles were precipitated from solutions of calcium chloride and sodium carbonate under vigorous stirring.[10] Briefly, equal volumes (0.615 mL) of aqueous $CaCl_2$ and Na_2CO_3 solutions (0.33 M) were mixed in the presence of 5 mg/mL 500 kDa dextran and thoroughly agitated on a magnetic stirrer for 30 s at room temperature. After the agitation, the mixture was left without stirring for 4 min at room temperature. During this time precipitation of $CaCO_3$ occurs and spherical $CaCO_3$ particles with an average diameter ranging from 2.5-3.5 µm are formed. Dextran is integrated in the cores.[13] Subsequently, the precipitate was separated from the supernatant by centrifugation (6000x g, 6 s) and washed three times with pure water to remove unreacted species. In the last step, the particles were washed with acetone and air-dried. We incorporated dextran in the $CaCO_3$ cores, as dissolution of the cores including dextran by addition of EDTA was faster than that of cores without dextran. Naturally, in this way dextran remains in the capsule cavities after core dissolution. The whole powder obtained from one synthesis (about 20 mg) was employed for the LbL coating.

Fabrication of multilayer capsules

The resulting spherical cores were coated by sequential incubation of the particles in the corresponding polyanion and polycation solutions. Three different types of microcapsules made of different layer constituents were prepared by sequential adsorption of negatively charged and positively charged species on $CaCO_3$ microparticles (~20 mg per samples) to give the following shell architectures comprising 11 layers in total:

PSS/PAH - capsules: $(PSS/PAH)_3(PSS/PAH_{FITC})(PSS/PAH)PSS$,

DEXS/pARG - capsules: $(DEXS/pARG)_3(DEXS/pARG_{AF488})(DEXS/pARG)DEXS$, and

E57/K48 - capsules: $(DEXS/pARG)(E57/K48)_3(E57/K48_{AF488})E57$.

The adsorption of polyelectrolytes PSS, PAH, PAH_{FITC} and DEXS was conducted in 2 mg/mL solutions in 0.5 M NaCl, whereas the polyelectrolyte pARG and the positively charged and negatively charged proteins (K48 and E57, respectively) were suspended in 1 mg/mL solutions in 0.5 M NaCl. The pH of the polyelectrolyte solutions was adjusted to 6.5 by addition of NaOH, whereas the pH of the protein solutions was maintained neutral (~7.2-7.6). The adsorbing protocol started with the negatively charged polymer (PSS or DEXS). PAH_{FITC} (obtained from Sigma) and PAH_{AF488} (obtained by reacting NHS-ester modified Alexa488 to the amino groups of PAH or pARG) were used instead of non-labeled polycation for the eighth layer of the multilayer polymer shell, so that the capsules had a green emitting dye label in their walls. Similarly, $K48_{AF488}$ was used for the tenth layer of the protein capsules to label the capsule walls. After addition of each charged species, samples were continuously shaken for 12 min. The coated particles were then centrifuged at 6000x g for 6 s and the supernatant containing unabsorbed species was removed. This procedure was repeated three times after each absorption step. After each cycle the $CaCO_3$ suspension was resuspended with ultrasound pulses to prevent aggregation. At the end eleven layers were deposited for each capsule type, starting from the polyanion. We want to point out that in the case of the protein capsules the first two layers were DEXS and pARG in order to mechanically stabilize the capsules. As the capsule cavities include dextran, the first layer of dextran sulphate has the same constituency as the interior of the capsule cavity. Poly-L-arginine is a polypeptide and thus similar in nature to the following layers of supercharged proteins. Both DEXS and pARG are biodegradable.[12] After assembly of the capsule walls by LbL deposition the $CaCO_3$ core was removed by complexation with EDTA. Coated $CaCO_3$ particles were shaken for 2 min with 1 mL of an EDTA solution (0.2 M, pH 5), followed by centrifugation and redispersion in 1 mL of a fresh EDTA solution (0.2 M, pH 7). The thus obtained hollow microcapsules with some dextran in their cavities were washed five times with pure water with centrifugation at 1000 x *g* for 8 min. The microcapsules were finally stored as suspension in water at 4°C.

Capsule characterization

Confocal laser scanning microscopy (CLSM)

Fluorescent images were taken by a confocal microscope (LSM 510 META, Zeiss). The excitation wavelength was 488 nm. Samples were observed through a 100X/1.45 NA oil-immersion PLAN-FLUOAR objective. Capsules labeled with FITC and Alexa488 fluorescence were studied with the Ar/Kr laser 488 nm. A 20 μL drop sample was placed onto a cover glass and imaged in liquid.

The typical morphologies of core-shell microparticles after LbL assembly with the same number of layers but with different layer components are presented in Figure S5. In the three systems investigated the diameter of the microparticles was found to be in the range of 2-2.5

µm. As shown in the fluorescence channels, the fluorescence signal corresponding to the labeled layers, which had been added as tenth layer in the ELP capsules and as eighth layer in the biodegradable and non-degradable capsules, was detected only from the walls. This indicates that the layers were efficiently adsorbed around the spherical templates during the LbL assembly. As expected, the $CaCO_3$ cores were clearly visible in the corresponding transmission channels. By overlaying the fluorescent and transmission channels, the two compartments of the capsules, walls and cavities, were distinguished.

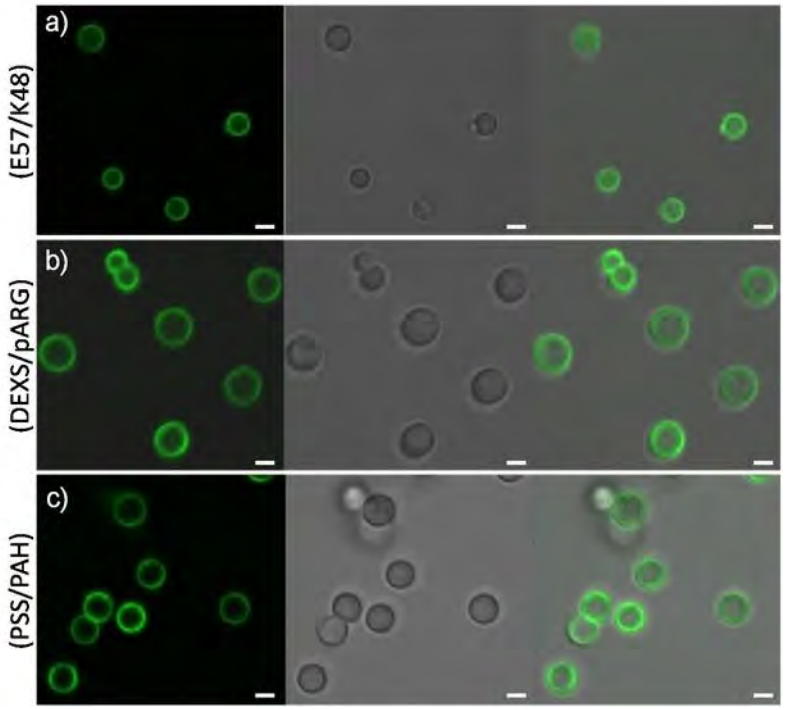

Figure S5. CLSM images of (a) $(DEXS/pARG)(E57/K48)_3(E57/K48_{AF488})E57$, (b) $(DEXS/pARG)_3(DEXS/pARG_{AF488})(DEXS/pARG)DEXS$ and (c) $(PSS/PAH)_3(PSS/PAH_{FITC})(PSS/PAH)PSS$ capsules before core removal. The capsule walls were labeled with AF488 (a, b) and FITC (c). Left panels: Fluorescence images of green emitting dyes. Central panels: optical transmission images. Right panels: corresponding overlay of both fluorescence and transmission channels. The fluorescence signal coming from the capsule walls can be seen whereas the spherical shape of $CaCO_3$ porous cores can be observed in the corresponding transmission images. Scale bars represent 1 µm.

In a previous experiment, protein capsules assembled by using E78 as first layer showed the diffusion of the fluorescent layer $K48_{AF488}$ inside the capsule cavity during the LbL steps (Fig. S6). Moreover after core removal, no spherical capsules were detected under fluorescent microscopy, thus confirming that both the E57 and the K48 polypeptides were mostly localized as complexes inside the $CaCO_3$ cores instead of alternately depositing at the template surface. It is worth noting that $CaCO_3$ microparticles are characterized by a high porosity which pores ranging from 20 to 60 nm.[10] This allows small molecules with a size of several nanometers to penetrate inside the templates during the LbL assembly. Thus, in order to prevent the diffusion of the ELP inside the cavities, we decided to start to build up the ELP multilayer shell after adsorption of one biodegradable bi-layer made up of (DEXS/pARG) polymers. This results in the final structure of E57/K48 - capsules: $(DEXS/pARG)(E57/K48)_3(E57/K48_{AF488})E57$.

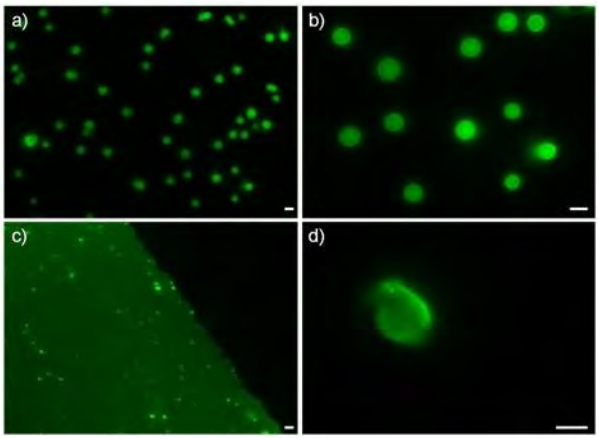

Figure S6. Fluorescence images of capsules consisting of 8-layers of $(K48/E57)_3(K48_{AF488}/E57)$ ELP polypeptides. $CaCO_3$ core-shell microparticles before (a-b) and after (c-d) core removal. Fluorescence signal from the capsules cavities indicated the diffusion of the $K48_{AF488}$ polypeptide inside the capsule interior during the LbL assembly (a-b). After core removal, no spherical capsules were visible under the fluorescence microscope (c-d), whereas a fluorescent carpet layer and small aggregates of particles were observed due to the release of the $K48_{AF488}$ out of the microparticles following the core dissolution. This confirmed that the E57 and K48 polypeptides were mostly localized inside the $CaCO_3$ cores instead of depositing on the wall. Scale bars represent 2 μm.

After following the core removal procedure, CLSM pictures were taken of the resulting capsules (Figures S7 and S8). Notably, the fluorescence signal in the ELP capsules was found to be still confined to the walls even after core removal, showing that the integrity of the multilayer polypeptide shell $(DEXs/pARG)(E76/K48)_3(E76/K48AF488)E76$ was not affected during the core dissolution. Instead, in some of the biodegradable capsules a slight diffusion of the labeled polymer $pARG_{AF488}$ inside the cavities was observed, owing to the above mentioned porosity of the $CaCO_3$ cores.[10] The absence of the cores was clearly detected in each capsule type sample, as shown in the transmission channels.

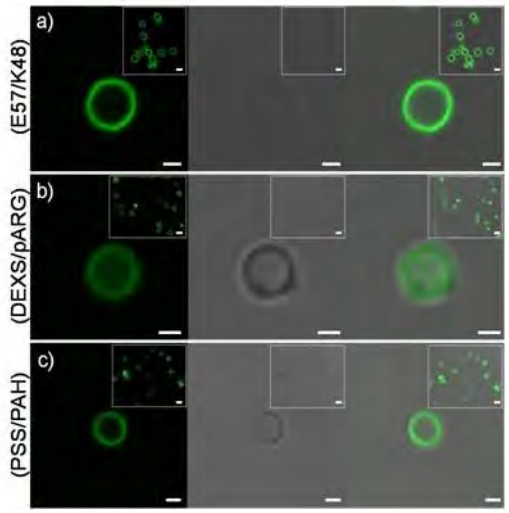

Figure S7. CLSM images of (a) $(DEXS/pARG)(E57/K48)_3(E57/K48_{AF488})E57$,
(b) $(DEXS/pARG)_3(DEXS/pARG_{AF488})(DEXS/pARG)DEXS$ and
(c) $(PSS/PAH)_3(PSS/PAH_{FITC})(PSS/PAH)PSS$ single capsule after core removal. The capsule walls were labeled with AF 488 (a, b) and FITC (c). The absence of the $CaCO_3$ cores can be clearly observed in the transmission images. Inset: CLSM images of several capsules showing spherical and intact capsules after core removal. Scale bars represent 1 μm.

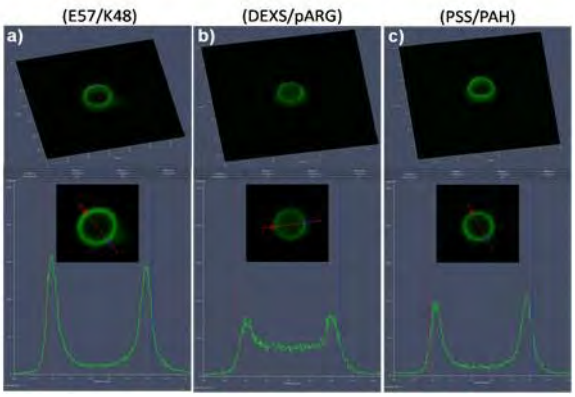

Figure S8. Three-dimensional CLSM image (Top row) and corresponding cross-section profiles (Bottom row) of single capsules after core removal. The graphs in the bottom show the intensity of the fluorescence along the red lines traced on the single capsule. The peaks are due to emission from the AF488 (a and b) and FITC (c) fluorophores on the capsule walls.

The efficient assembly of the protein layers was confirmed by the following control experiment: $CaCO_3$ particles were coated with 1 bi-layer of DEXS/$pARG_{AF488}$ and analyzed by CLSM before and after core removal (Figure S9). Before core removal, the typical morphology of capsules with a green-fluorescent labeled wall was observed (Figure S9, top row) (pARG labeled with the dye AF488 was used enabling characterization by CLSM). After core removal, no capsules were observed in the bulk solution indicating that capsules made of only 1 bi-layer are not stable against the dissolution conditions. The core removal treatment with EDTA solution resulted in dismantling of the (DEXS/pARG) bi-layer shell, which showed fluorescence only in the bulk solution (Figure S9, bottom row). In contrast, the multilayers of the (DEXS/pARG)(E57/K48)$_3$(E57/$K48_{AF488}$)E57-coated particles remained intact after exposure to EDTA (Figure S7). These data confirmed that the protein-based capsules prepared by LbL assembly of E57/K48 onto 1 bi-layer of (DEXS/pARG) were actually made of alternately assembly of the protein layers with the fluorescently labeled $K48_{AF488}$ as second-last layer.

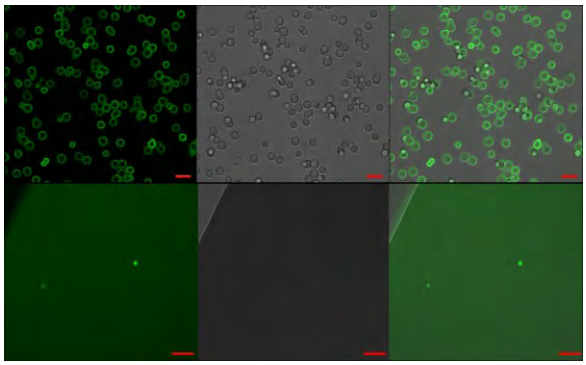

Figure S9. CLSM images of 1 bi-layer (DEXS/$pARG_{AF488}$) capsules before (top row) and after (bottom row) core removal. AF488-labeled pARG was used as fluorescent layer. Before core removal, $CaCO_3$ cores can be clearly observed in the transmission channel, whereas the green signal indicates the presence of the $pARG_{AF488}$ layer only in the wall. After core removal, no capsules are found out in the bulk solution, indicating the disassembly of the bi-layer wall during the core decomposition. Scale bar represents 5 μm.

Capsules permeability

In order to compare the permeability behavior of the protein-based capsules with the control capsules based on DEXS/pArg and PSS/PAH layers, dextran 500 kDa, labeled with AF594, was entrapped inside the cavities during the synthesis of the $CaCO_3$ cores. Figure S10 shows LSM images of the capsules before and after core removal. The wall of each capsule system was labeled with AF488. After core removal the diffusion of the dextran across the wall was observed in the (E57/K48) capsules whereas no diffusion was observed across the wall of control capsules. These data suggested the existence of large pores in the wall of supercharged protein-based capsules, as confirmed by further SEM and TEM analysis.

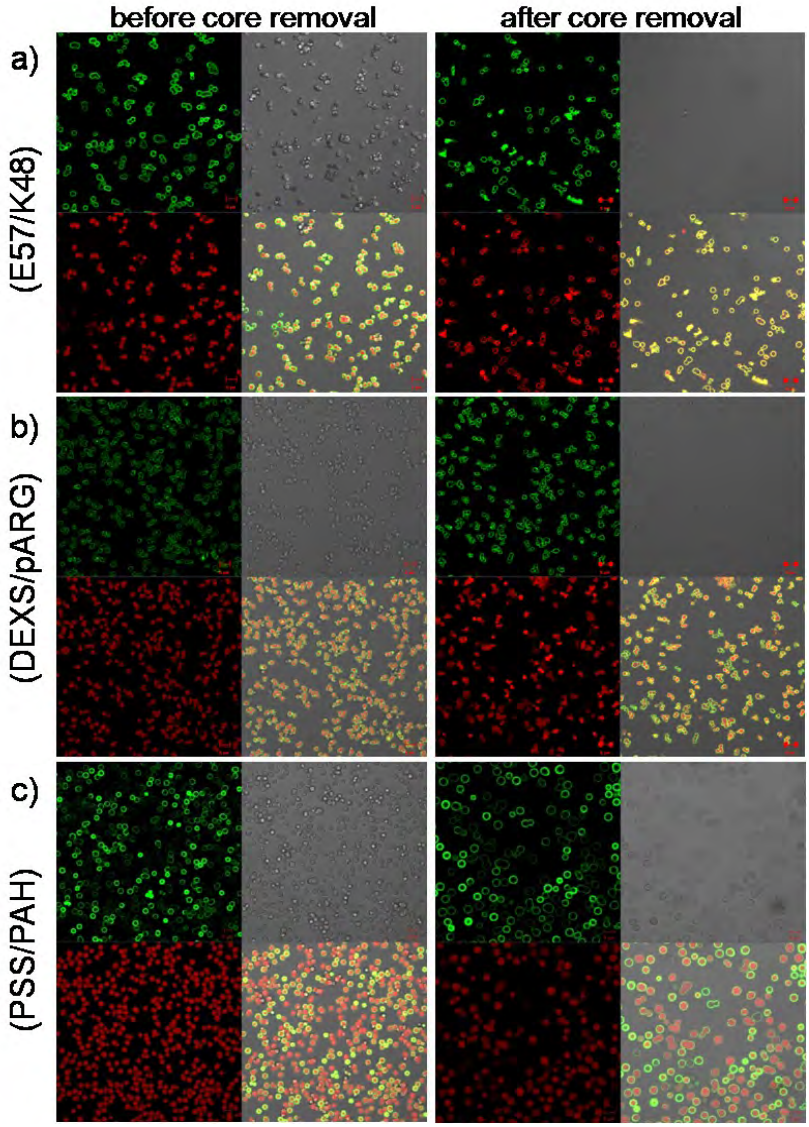

Figure S10. CLSM images of 11-layer (a) (E57/K48), (b) (DEXS/pARG) and (c) (PSS/PAH) capsules before and after core removal. The capsule cavities were loaded with 500 kDa dextran labeled with AF543, the capsule walls were labeled with AF488 (a, b) and FITC (c). The presence and the absence of the $CaCO_3$ cores can be clearly observed in the transmission images of each sample. After core removal the diffusion of the dextran outside was observed for the (E57/K48) capsules suggesting a higher porosity of the wall compared to the control capsules. Scale bars represent 5 µm.

Electron Microscopy

Protein capsules were then analyzed by Scanning Electron Microscopy (SEM) and Transmission Electron Microscopy (TEM) to gain deeper insight into the structure and morphology of the multilayer polypeptide wall, both before and after core removal, and to compare their properties to the control capsules. SEM micrographs were conducted with a JEOL JSM-7500F SEM at an operation voltage of 2.00 kV. A 10 µl drop sample was placed onto a cover glass, dried at room temperature, and sputtered with a platinum layer under vacuum for 90 s. TEM were recorded by using a JEOL 3010 TEM operating at an accelerating voltage of 300 kV. A 10 µl drop sample was placed on a Formvar®/carbon coated TEM-grid (300 Mesh 3.05 mm Copper, Plano GmBH) and dried at room temperature before imaging.
Figure S11 shows the SEM images corresponding to the core-shell microparticles previously presented in Figure S6. The images in the bottom row show a magnified area of the wall of the particles reported in the top row in which the surface texture of the particles can be appreciated. In general, protein-coated cores and (DEXS/pARG)-coated cores were characterized by a thick surface, suggesting that the polymers were densely packed into the multilayer shells. On the contrary, in the case of capsules made up of (PSS/PAH) polyelectrolytes, a highly porous surface was observed. This might be explained by the adsorption of the polylelctrolytes onto the very rough surface of the $CaCO_3$ microparticles which results in the formation of a very porous polyelectrolyte network of the capsule wall.[10] However, after dissolution of the templates, a porous network with clear holes was observed in the protein capsules sample (Fig. S12). These capsules correspond to the ones shown in Figure S7. A thick wall and a porous-like wall were detected in the biodegradable and non-degradable capsules.

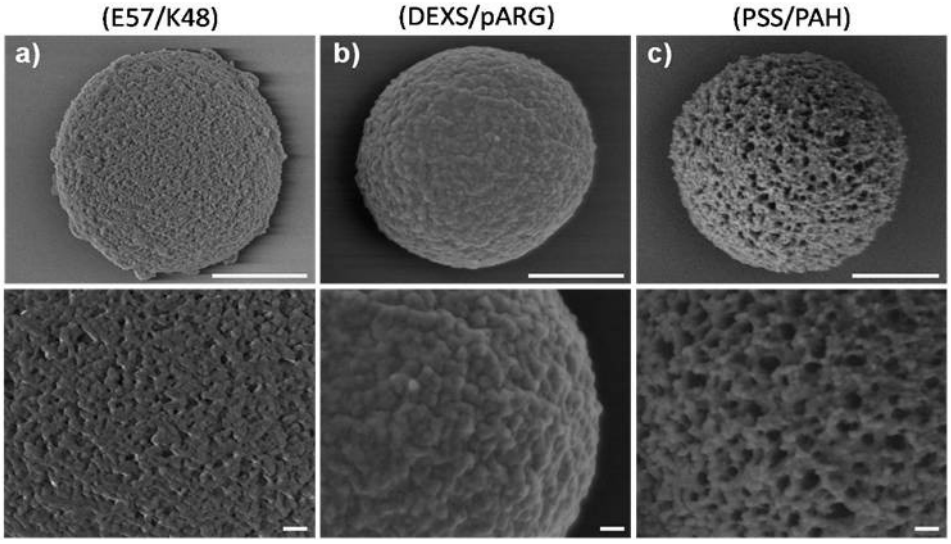

Figure S11. SEM images of $CaCO_3$ cores after coating
(a) $(DEXS/pARG)(E57/K48)_3(E57/K48_{AF488})E57$,
(b) $(DEXS/pARG)_3(DEXS/pARG_{AF488})(DEXS/pARG)DEXS$ and
(c) $(PSS/PAH)_3(PSS/PAH_{FITC})(PSS/PAH)PSS$. The typical spherical, porous-like structure of capsules templated on $CaCO_3$ cores can be observed. Scale bars represent 1 µm (top row), 100 nm (bottom row).

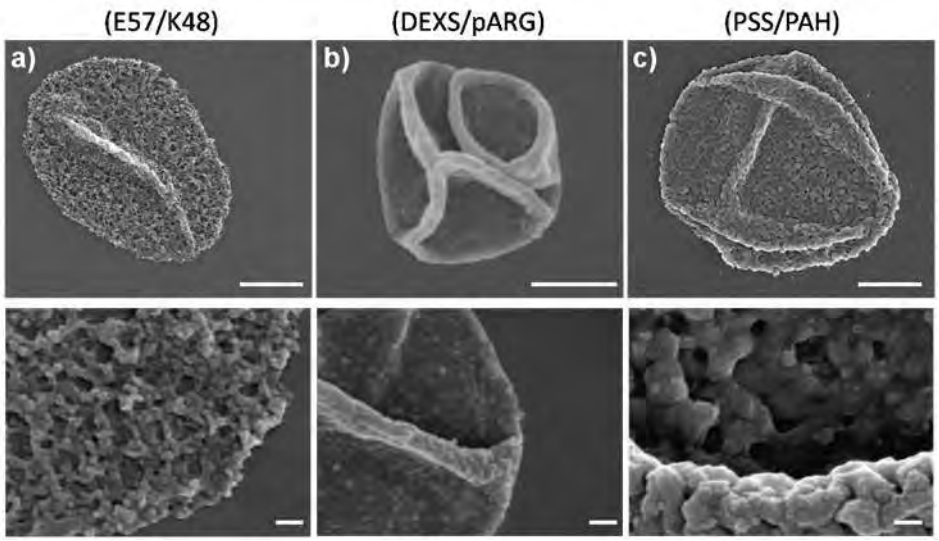

Figure S12. SEM images of
(a) (DEXS/pARG)(E57/K48)$_3$(E57/K48$_{AF488}$)E57,
(b)(DEXS/pARG)$_3$(DEXS/pARG$_{AF488}$)(DEXS/pARG)DEXS and
(c) (PSS/PAH)$_3$(PSS/PAH$_{FITC}$)(PSS/PAH)PSS capsules after core removal. Capsules collapse after core removal indicating the absence of the cores in their cavities. Scale bars represent 1 μm (top row), 100 nm (bottom row).

In line with the LSM and SEM data the walls of the protein capsules investigated under TEM were found to be more porous than biodegradable and non-degradable capsules (Fig. S13), indicating that the two investigated polypeptides, E57 and K48, formed thinner shells during the LbL assembly. Nonetheless we would like to point out that the porosity, and thus the permeability, of the protein capsules could be reduced by increasing the number of layers employed to grow the multilayer wall or by cross-linking the proteins after their adsorption onto the sacrificial core surfaces (i.e., by using glutaraldehyde as a cross-linker agent).[14, 15] Finally, the use of unfolded, supercharged proteins with higher number of charges per molecule (see Table 1) might be taken into account to build up a multilayer shell with stronger electrostatic attractions between each component layer.

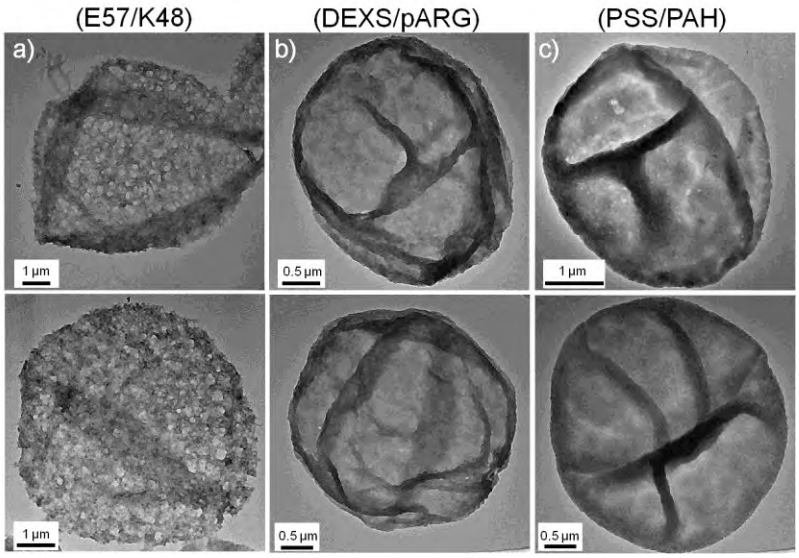

Figure S13. TEM images of
(a) (DEXS/pARG)$(E57/K48)_3(E57/K48_{AF488})$E57,
(b) (DEXS/pARG)$_3$(DEXS/pARG$_{AF488}$)(DEXS/pARG)DEXS and
(c) (PSS/PAH)$_3$(PSS/PAH$_{FITC}$)(PSS/PAH)PSS capsules after core removal. Capsules collapse after core removal indicating the absence of the cores in their cavities.

References

[1] D. E. Meyer, A. Chilkoti, *Biomacromolecules* **2002**, *3*, 357.
[2] U. K. Laemmli, *Nature* **1970**, *227*, 680.
[3] C. Lee, A. Levin, D. Branton, *Anal. Biochem.* **1987**, *166*, 308.
[4] M. Miao, C. M. Bellingham, R. J. Stahl, E. E. Sitarz, C. J. Lane, F. W. Keeley, *J. Biol. Chem.* **2003**, *278*, 48553.
[5] D. W. Urry, *J. Prot. Chem.* **1988**, *7*, 1.
[6] A. Girotti, J. Reguera, F. J. Arias, M. Alonso, A. M. Testera, J. C. Rodriguez-Cabello, *Macromolecules* **2004**, *37*, 3396.
[7] K. Trabbic-Carlson, L. A. Setton, A. Chilkoti, *Biomacromolecules* **2003**, *4*, 572.
[8] J. O'Brien, I. Wilson, T. Ortaon, F. Pognan, *Small* **2001**, *164*, 132.
[9] G. B. Sukhorukov, E. Donath, S. Davis, H. Lichtenfeld, F. Caruso, V. I. Popov, H. Möhwald, *Polymers for Advanced Technologies* **1998**, *9*, 759.
[10] D. V. Volodkin, A. I. Petrov, M. Prevot, G. B. Sukhorukov, *Langmuir* **2004**, *20*, 3398.
[11] G. B. Sukhorukov, D. V. Volodkin, A. M. Günther, A. I. Petrov, D. B. Shenoy, H. Möhwald, *J. Mater. Chem.* **2004**, *14*, 2073.
[12] B. G. De Geest, R. E. Vandenbroucke, A. M. Guenther, G. B. Sukhorukov, W. E. Hennink, N. N. Sanders, J. Demeester, S. C. d. Smedt, *Adv. Mater.* **2006**, *18*, 1005.
[13] O. Kreft, A. Muñoz Javier, G. B. Sukhorukov, W. J. Parak, *J. Mater. Chem.* **2007**, *17*, 4471.
[14] W. Qi, L. Duan, K. W. Wang, X. H. Yan, Y. Citi, Q. He, J. B. Li, *Adv. Mater.* **2008**, *20*, 601.
[15] Y. Zhu, W. J. Tong, C. Y. Gao, H. Mohwald, *J. Mater. Chem.* **2008**, *18*, 1153.

Synthesis and evaluation of gold nanoparticle-modified polyelectrolyte capsules under microwave irradiation for remotely controlled release for cargo

Loretta L. del Mercato[1], Edgar Gonzalez[2], Azhar Z. Abbasi[1], Wolfgang J. Parak[1,] Victor Puntes[2,]*

[1] Fachbereich Physik and Wissenschaftliches Zentrum für Materialwissenschaften, Philipps Universität Marburg, Marburg, Germany
[2] Institut Català de Nanotecnologia, Barcelona, Spain, and Institut Català de Recerca i Estudis Avançats (ICREA), Barcelona, Spain

* Victor.Puntes.icn@uab.es

Keywords: Polymeric Capsules; gold nanoparticles; MW irradiation; drug delivery; radiation controlled release

Abstract

The Layer-by-Layer fabrication of polyelectrolyte capsules with and without Au nanoparticles (NPs) embedded into their walls is reported. We have studied the behaviour of these capsules under microwave irradiation. Their properties have been investigated by transmission electron microscopy and dynamic light scattering measurements. We demonstrate that microwaves affect the structure of both capsules types by inducing remarkable damages into the multilayer wall. We also show that upon microwave exposure the walls of Au NP modified polyelectrolyte capsules undergo a rapid damage compared to capsules without NPs. These results indicate that microwaves can be used to simultaneously control the opening of numerous cargo-loaded capsules for drug delivery purposes.

Introduction

Layer-by-Layer (LbL) capsules have attracted high interest in the last layers as versatile platform for fabricating multifunctional carrier systems suitable for numerous applications ranging from drug delivery to medical diagnostic to biological sensing (Stuart, Huck et al. 2010). Polyelectrolyte capsules are fabricated by the stepwise LbL deposition of oppositely charged polymers around a charged spherical surface (Decher 1997). The multilayer build-up is electrostatically driven via the surface charge reversal which occurs after each adsorption step (Decher and Schlenoff 2002). Once the desired LbL composition is obtained, the original template can be removed to obtain hollow polymeric capsules (Donath, Sukhorukov et al. 1998; Sukhorukov, Donath et al. 1998). Since the layers of polyelectrolyte microcapsules are held together primarily by electrostatic forces, charged NPs (or other charged macromolecules) can be integrated into the polyelectrolyte network (Radt, Smith et al. 2004; Skirtach, Antipov et al. 2004; Bedard, Braun et al. 2008). So far different types of inorganic NPs have been introduced into multilayer polyelectrolyte walls in order to address different functions (Sukhorukov, Rogach et al. 2007; Rivera Gil, del Mercato et al. 2008; Bedard, De Geest et al. 2009).

The ideal polymer capsule carrier system for targeting release must be capable of hosting, protecting, transporting and releasing the embedded payload to the target site (e.g. tumors). Those tasks can be achieved by applying external physical stimuli capable to induce some changes into the structure of the wall of the capsules (i.e., formation of pores), so that the loaded drugs can freely diffuse outside. To this purpose, the wall of the capsules can be modified with inorganic NPs (NPs) in order to build up multilayer containers responsive to specific stimuli, such as light, magnetism, ultrasound, or microwaves.

Light irradiation has been employed to remotely open the wall of polymer capsules modified with metal NPs (Bedard, De Geest et al. 2009). Capsules with silver or gold NPs in their wall can be opened upon laser irradiation as a result of the temperature increase of the metal NPs upon light absorption. The viability of cells after photo-activated release has been investigated to probe for side effects (Muñoz_Javier, Pino et al. 2009). The obtained data have demonstrated the possibility to release cargo molecules into the cytosol of living cells without significantly impairing the cell viability on the time scale of hours (Palankar, Skirtach et al. 2009). Notably, this method allows for the controlled opening of individual capsules in single cells. Thus it appears to be mostly suitable for *in vitro* studies. In particular it has been employed for time-resolved investigation of stimulated reactions inside living cells.

For burst-like release, there is the need to develop a method which allows for remotely inducing the opening of a large number of capsules simultaneously. In this context, magnetism, ultrasound and microwave treatments applied to LbL NP-modified capsules have being considered as safe methods for *in vitro* and *in vivo* opening of capsules. Magnetic force has been used to localize and release encapsulated material from capsules modified with magnetic NPs (Lu, Prouty et al. 2005; Zebli, Susha et al. 2005; Hu, Tsai et al. 2008). For example, Fe-based NPs have been embedded within the walls of polyelectrolyte capsules (Lu, Prouty et al. 2005; Hu, Tsai et al. 2008). Such capsules were used for targeted drug delivery, in which capsules could be directed to target locations upon application of external magnetic field gradients (Zebli, Susha et al. 2005). The magnetic field induces the NPs to rotate, damaging the capsule wall. As a result the permeability of the wall is increased and the encapsulated substances are released (Gorin, Portnov et al. 2008). Compared to photo-activated release, magnetism has the potential advantage of being applied inside tissues to switch on the unloading of several capsules at the same time. Ultrasound has been employed to trigger the release of encapsulated material from polyelectrolyte multilayer capsules with both silver and gold NPs in their walls (De_Geest, Skirtach et al. 2007; Skirtach, De_Geest et al. 2007). When the capsules are subjected to ultrasound, cavitation and collapse of microbubbles from dissolved gases occur. The ultrasonic shock waves propagate through the liquid and cause high shear forces between the successive liquid layers. When such shear forces cleave through the membrane of the capsules, the membrane is torn apart and the capsules are destroyed (De_Geest, Skirtach et al. 2007). Notably, sonication was found to destroy both plain and NP-modified capsules. However NP containing capsules responded more sensitive to ultrasound exposure. It was postulated that at low frequency the temperature difference between the NPs and the medium will be in equilibrium, whereas at high frequency only a small portion of the surface will be affected by thermal waves. Similar frequency dependence is applicable to viscous losses, wherein extensive NP motion occurs at low frequency while little movement takes place at high frequencies. Thus, when the capsules were subjected to ultrasound, a morphological change of the capsule wall occurred which resulted in the disruption of the capsule membrane and release of encapsulated species.

Microwave (MW) radiation has also been investigated as an alternative strategy for *in vivo* controlled release of pharmaceutical compounds without the need for excessive heat, prolonged process and toxic reactants (Hallahan, Qu et al. 2001; Zhou, Sun et al. 2004; Martin, Craciun et al. 2008). Such method is based on the application of microwaves with shorter waves than ultrasound, to modify the molecular interactions between the organic molecules. The general concept is depicted in Figure 1.

Besides, Gorin *et al.* demonstrated that microwaves can be used to destroy polyelectrolyte microcapsules and that the effects of MW action depends on the capsules composition and on the frequency and power of radiation (Gorin, Shchukin et al. 2006). Especially, the destructive effect resulted to be particularly evident in capsules with embedded silver NPs in the polymer wall. The authors correlate the observed results to the high electric and thermal conductivity of silver, as well as to the MW induced heating of metal NPs and the adjacent regions of polymer walls (Gorin, Shchukin et al. 2006). However, it has to be kept in mind that the electromagnetic radiation is transformed into molecular vibrations between molecular dipoles, especially in water. Therefore, non-thermal effects can be of significant importance. Such NP–microwave interaction might be a promising approach to release encapsulated materials from polymeric microcapsules. However, to the best of our knowledge, the work of Gorin *et al.* is the only work reported so far using microwaves as external trigger to remotely destroy the wall of polyelectrolyte capsules.

In a different approach, the use of microwaves combined to gold NPs has been employed to locally and remotely manipulate protein aggregation (Kogan, Bastus et al. 2006; Araya, Olmedo et al. 2008). In particular, the effect of MWs and gold NPs linked to amyloidogenic proteins has been investigated to inhibit and reversed their spontaneous aggregation into amyloid fibrils and plaques. In this approach the local heat dissipated by gold NPs upon radiation with low Gigahertz electromagnetic fields was postulated and has been used to redissolve the amyloidogenic deposits (Kogan, Bastus et al. 2006; Araya, Olmedo et al. 2008). However, again, the energy balance indicated that the mechanism is not only due to the heating of the NPs induced by Foucault and Joule effects, since the administrated energy was not enough to break the polypeptide bonds. We also want to mention early work by Hamad-Schifferli et al. who used MW generated heat in Au NPs to melt double-stranded.

In this work, capsules, with and without gold NPs embedded in the multilayer wall, were fabricated and the effect of MW radiation was explored by comparing transmission electron microscopy (TEM) images and dynamic light scattering (DLS) data obtained before and after irradiation of the two different samples. The obtained results show that by combining weak microwave fields (~104 mW) and gold NPs, the wall of the capsules can be rapidly destroyed with moderate heat generation (~6.279 J) likely thanks to some conformational changes of the polyelectrolytes chains Au-NPs composites caused by MW radiation.

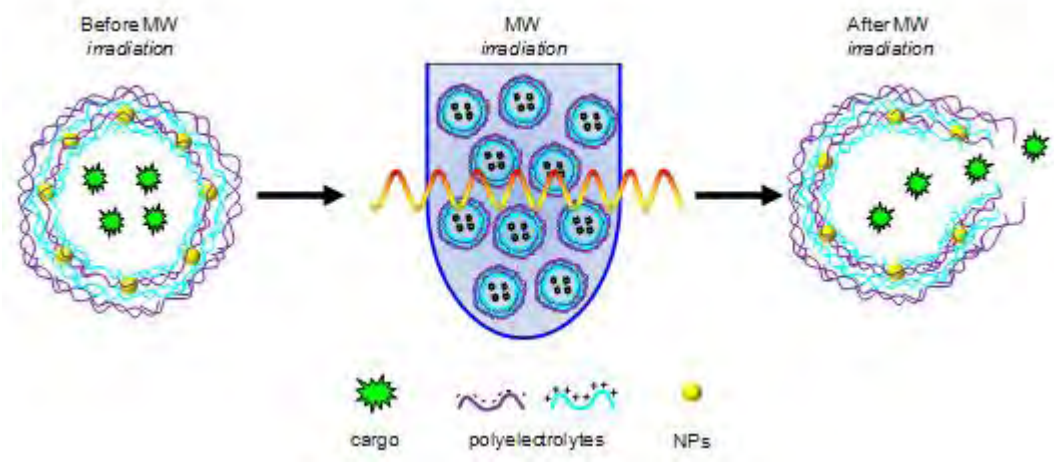

Figure 1. Schematic representation of the release of substances from Au NP-modified polyelectrolyte capsules. Capsules with Au NPs embedded in their walls are loaded with cargo molecules. After MW treatment, the wall of capsules undergoes rupture and releases the encapsulated substances

Results and Discussions

Two types of microcapsules were prepared (Scheme 1, **SI**), one was composed of 5 bi-layers of (PSS/PAH) polyelectrolytes (control sample) (Figure 2, top row), and the other was composed of 5 bi-layers of (PSS/PAH) polyelectrolytes containing Au NPs added after the eighth PAH layer (Figure 2, bottom row). The size and the morphological properties of both capsules types before and after exposure to MW irradiation were investigated via DLS and TEM analysis.

The average size of capsules in solution before MW irradiation resulted in 1.5 $\pm$ 0.1 μm (without Au NPs) an 2.0 $\pm$ 0.2 μm (with Au NPs) determined with DLS with a Malvern ZetaSizer. Note that the geometry of the capsule may underestimate the capsule diameter since this commercial DLS set-up is rather designed to analyze solid particles (Murdock, Braydich-Stolle et al. 2008).

The surface morphology of capsules has been analyzed by TEM before MW irradiation (Figure 2). The two capsule types showed a good structural integrity after core removal. As expected, a size enlargement was measured under TEM analysis because of the collapse of capsules upon the drying procedure. For $(PSS/PAH)_4$AuNP(PSS/PAH) capsules, the Au NPs were homogeneously dispersed in the polyelectrolyte wall and no defects, such as breaks or holes, were detected in the walls. Also an even distribution of Au NPs in the capsule walls was observed evidencing a good control on electrostatic interactions between the oppositely charged building blocks, i.e. the Au NPs and the polyelectrolytes. By using Inductive coupled plasma mass spectrometer (ICP-MS) analysis, a total number of 6.7×10^8 Au NPs per capsule was estimated. A detailed protocol for calculating the number of Au NPs per capsule can be found in the Supporting Information (SI).

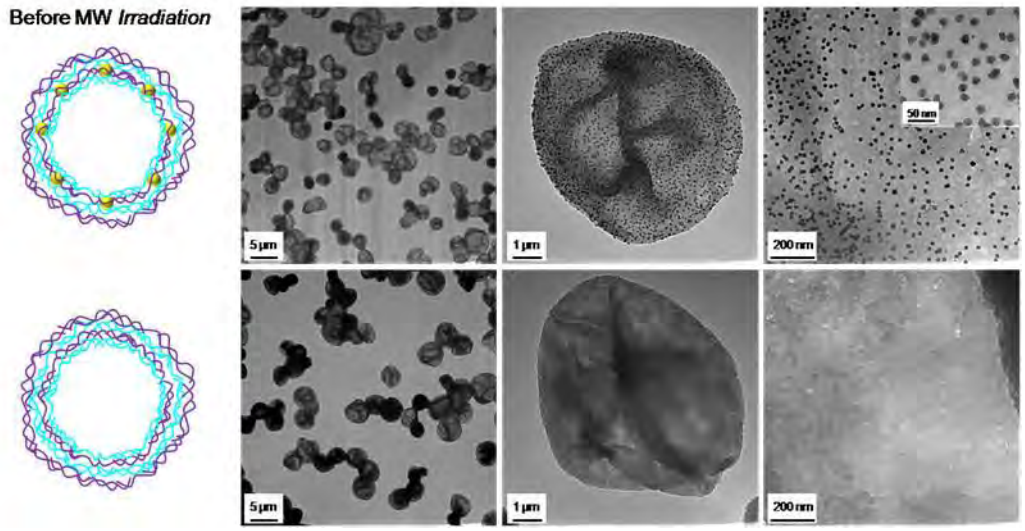

Figure 2. TEM images of 5 bi-layer $(PSS/PAH)_4$AuNP(PSS/PAH) (top row) and $(PSS/PAH)_5$ (bottom row) capsules before microwave (MW) treatment. The low magnification images show a large number of individual capsules with typical folds and creases due to drying of the capsules without cores in the cavities. The high resolution images are zoomed into the capsule walls and show the integrity of the multilayer wall after core removal. The inset show a higher magnification of the Au NPs embedded into the polymer matrix.

In Figure 3 the time evolution of equivalent capsules, with and without Au NPs, under irradiation followed by DLS measurements is shown. It is observed that as control samples

(capsules without Au NPs) were irradiated (up to 10 minutes) they progressively decreased in their size. A different behaviour was observed once polyelectrolyte-Au NP capsules were exposed to same electromagnetic (e/m) fields of 2.45 GHz, 104 mW. In this case, the mean capsule diameter decreased earlier and dramatically collapsed at shorter times (4 minutes).

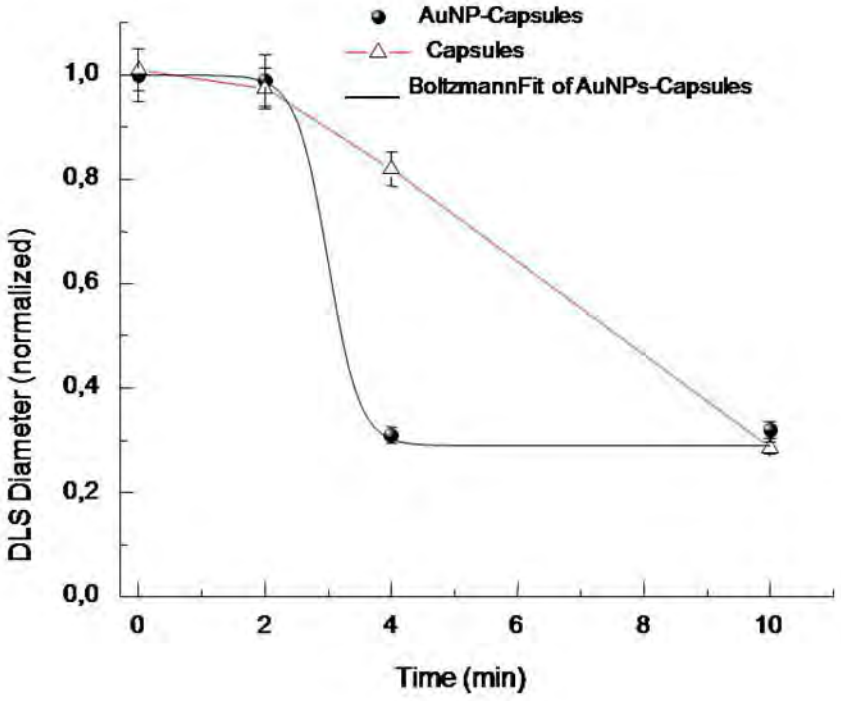

Figure 3. Capsule irradiation. (left) normalized DLS signal of the irradiated capsules containing Au NPs (spheres) and without NPs (triangles).

This phenomenon cannot be attributed to thermal-effects, i.e., Au NPs cannot act as local and remote energy sources increasing the temperature of the solution. Assuming that all the radiation is absorbed only by the Au NPs and considering the weakness of the employed radiation and the littleness of the Au NPs, temperature increase would be only of the order of few mK. In addition, since incoming photons have the frequency of a water absorption peak (absorption resonance frequency), no microwave photons are expected to significantly reach Au NPs, discarding therefore thermal heating by combined Foucault and Joule effects. Thermal effects of electromagnetic (e/m) fields on macromolecules, for instance, proteins, arise from heat generation by e/m energy absorption. However, significant "non-thermal" effects were noted, such as marked changes in the protein's secondary structure (denaturalization) relative to the zero-field state when proteins were irradiated by low power MW photons (English and Mooney 2007). This occurred primarily as a consequence of alignment of the protein's total dipole moment with the external field, although the dipolar alignment of water molecules in both the solvation layer and the bulk was also found to be influential. In fact, this swing effect produced by surrounding water dipoles dissipates energy which could break weak chemical bonds responsible for the protein ternary and quaternary structures and as hydrophobic or electrostatic interactions. This swing oscillation appears when MWs are produced in a resonating chamber and stationary waves are set. Water molecules absorb the incoming photons which resonate with their dipolar moments transducing the e/m wave into GHz vibrations. We think that such high frequency dipolar mechanical vibration is responsible for the observed capsule wreckage. When the Au NPs are inserted into the capsule walls the presence of the NPs in the structure has strong effects on

the resilience of the capsules to this dipolar oscillation. This might be due to the high surface charge of the small NPs (-45 mV surface charge, 10nm diameter), which could be more susceptible to the fluctuations of the dipolar field than the surrounding polymer, producing sheer forces. However, the high screening effects of charges present in solution and the fact that the NPs are buried within the electrolyte layers may attenuate this effect. Besides, respect to the mechanical vibration, as Au is almost 20 times denser then the capsule molecules, the impulse the Au NPs will experience due to the water vibrations and the capsule molecules (pushed by the water molecules) will be considerably smaller than that of neighbouring molecules inducing again sheer forces that may be the leading cause in the simultaneous breakage of many capsules at shorter times.

TEM microscopy also showed how the capsules where broken when microwaves were applied. In Figure 4 the TEM comparative analysis of capsules with (top row) and without (bottom row) Au NPs after MW irradiation is reported. As it can be observed, the wall of the capsules comprising Au NPs resulted to be significantly destroyed after MW exposure. In particular the formation of large pores into the polyelectrolyte multilayer wall was observed. Instead in the control sample (capsules without NPs), no evident effects could be observed as rupture of the capsules' walls, whereas a clear size reduction was noticed.

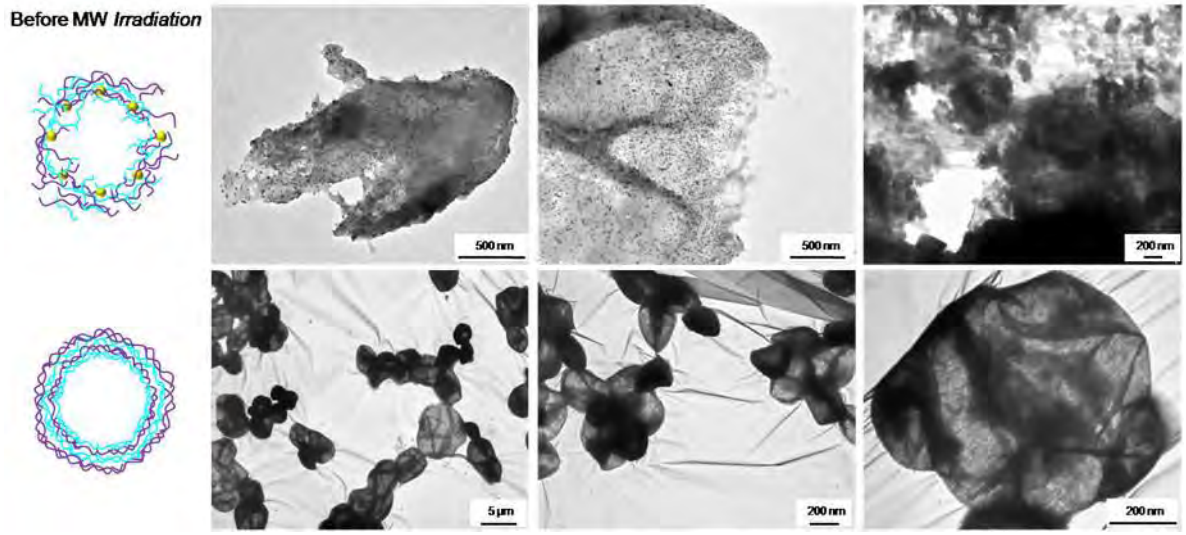

Figure 4. TEM images of 5 bi-layers $(PSS/PAH)_4$AuNP(PSS/PAH) (top row) and $(PSS/PAH)_5$ (bottom row) capsules after microwave treatment (irradiation time: 4 min). Top row: capsules with Au NPs are significantly damaged after irradiation. The high resolution image shows the Au NPs embedded into the polymer matrix of the capsules. Bottom row: capsules without Au NPs retain their integrity after irradiation.

The observation of the broken capsules and large pieces of capsule walls in the case of MW irradiated NP-containing capsules suggests that once a capsule is broken it rapidly collapses. The used irradiation was 2.45 GHz, 104 mW, which is able to heat 1.5 ml by 1 ℃ in 1 min. In this condition a (geometrically) coherent and polarized vibration induces an oscillation of the dipolar distribution via the water molecule dipoles to which highly charged molecules are susceptible, as the used electrolytes. This is complementary to the observed fact that the presence of the NPs in the capsules' walls increments their stability as had been observed when sonicating or vigorously shaking the capsules (data not shown) (Gorin, Shchukin et al. 2006). This means that NP modified capsules will be both, more robust and yet more susceptible to MW irradiation.

This is related to previous work where the use of microwaves was used to dehybridize DNA double strands attached to Au NPs or dissolve beta-amyloid deposits decorated with Au. In view of these results, the consideration of the Au NPs as antennas for micro-wave irradiation in water (highly microwave absorbing media) should be reviewed, because the above described non-thermal effects might be the responsible for the data observed in these publications. It is remarkable that random vibrations of the water molecules, as those produced by conventional thermal effects, surrounding the capsule walls, do not have this ability of perturbation as they are induced by static nodes in a resonating chamber.

Conclusion

Polyelectrolyte capsules containing gold NPs into their walls were fabricated via the LbL technique and their behaviour under MW irradiation was investigated with DLS and TEM analyses. The structure of the capsules' walls, comprising 5 bi-layers of (PSS/PAH) polyelectrolytes with integrated Au NPs, resulted significantly affected after 4 minutes of MW irradiation (2.45 GHz, 104 mW) due to the formation of large pores into the multilayer wall. It is assumed that capsules with Au NPs absorb more energy compared to capsules without NPs. Heating of a high number of NPs causes strong local surface defects and finally leads to collapse of the whole system after few minutes (4 minutes) of MW exposure. In the case of capsules without NPs, MW irradiation interacts with the dipole of water molecules and polyelectrolytes of the multilayer walls which are charged. After a certain time (10 minutes), the capsules break.

The obtained results show that MW irradiation can be used to induce a burst-like rupture of capsules by applying the field to microcapsules comprising Au NPs in their wall for a short period of time (4 minutes). Such a MW-sensitive microcapsule would permit a fast and remotely controlled opening and could be suggested as method for simultaneous opening of numerous cargo loaded capsules. In case a sustained release is desired, MW irradiation could be applied to capsules without Au NPs in order to induce a progressive rupture of the capsules.

Future investigations will be performed to tune the opening of the capsules under different conditions, e.g. by changing the irradiation parameters (such as the frequency and power of radiation), or the composition of the polymer capsules (such as the number of polyelectrolyte layers and the concentration of the Au NPs in the walls).

Acknowledgements
This work was supported by the BMBF / ERA-NET NEURON (WJP, project Nanosyn).

Supporting Information Available
Additional details for synthesis, irradiation and characterization measurements of polyelectrolyte capsules with and without Au NPs before and after MW irradiation are available free of charge via the Internet at http://xxxx.

Synthesis and evaluation of gold nanoparticle-modified polyelectrolyte capsules under microwave irradiation for remotely controlled release for cargo

Loretta L. del Mercato[1], Edgar Gonzalez[2], Azhar Z. Abbasi[1], Wolfgang J. Parak[1,] Victor Puntes[2,*]

[1] Fachbereich Physik and Wissenschaftliches Zentrum für Materialwissenschaften, Philipps Universität Marburg, Marburg, Germany
[2] Institut Català de Nanotecnologia, Barcelona, Spain, and Institut Català de Recerca i Estudis Avançats (ICREA), Barcelona, Spain

* Victor.Puntes.icn@uab.es

Supporting Information

I) Synthesis of microcapsules with and without Au nanoparticles into their wall
II) Microwave (MW) Irradiation
III) Dynamic Light Scattering (DLS)
IV) Transmission electron microscopy (TEM)
IV) Inductive coupled plasma mass spectroscopy (ICP-MS)

I) Synthesis of microcapsules with and without Au nanoparticles into their wall
I.1) Chemicals
I.2) Synthesis of $CaCO_3$ Particles
I.3) Layer by layer (LbL) assembly of polyelectrolytes on $CaCO_3$ cores and embedding of Au NPs in the wall of capsules

I.1) Chemicals

Poly(sodium 4-styrenesulfonate) (PSS, Mw ~70,000, # 243051), poly(allylamine hydrochloride) (PAH, Mw ~56,000, # 283223), poly(fluorescein isothiocyanate allylamine hydrochloride) (PAH_{FITC}, Mw ~56,000, # 630209), calcium chloride dehydrate ($CaCl_2$, # 223506), sodium carbonate (Na_2CO_3, #S7795), ethylenediaminetetraacetic acid (EDTA, #E5134) and dextran (M_w ~2000,000, # 95771) were purchased from Sigma-Aldrich. Citrate-coated gold nanoparticles (NPs) of 20nm diameter were obtained from BBI/TED Pella (Redding, Calif,USA). In order to improve their stability in buffer solution, the adsorbed citrate molecules were replaced by a phosphine (bis(p-sulfonatophenil)phenylphosphine dehydrate, dipotassium salt) (Zanchet, Micheel et al. 2001). The concentration of the Au NPs was determined by UV/vis spectroscopy by using the molecular extinction coefficient (1.13E+9 $M^{-1}Cm^{-1}$) of their absorption at the plasmon peak.

I.2) Synthesis of $CaCO_3$ Particles

$CaCO_3$ microparticles were precipitated from solutions of calcium chloride ($CaCl_2$) and sodium carbonate (Na_2CO_3) under vigorous stirring (Volodkin, Petrov et al. 2004). In a typical synthesis, equal volumes (0.615 mL of aqueous $CaCl_2$ and Na_2CO_3 solutions (0.33 M) were mixed in the presence of 5 mg/mL of the dextran and thoroughly agitated on a magnetic

stirrer for 30 s at room temperature. After the agitation, the mixture was left without stirring for 4 min at room temperature. Subsequently, the precipitate was separated from the supernatant by centrifugation (6000 rpm for 5 s) and washed three times with pure water to remove unreacted species. In the last step, the particles were washed with acetone and air-dried. We incorporated dextran in the $CaCO_3$ cores as dissolution of the cores including dextran by addition of EDTA was faster than that of cores without dextran. Naturally, in this way trace of dextran remain in the capsule cavities after core dissolution.

I.3) Layer by layer (LbL) assembly of polyelectrolytes on $CaCO_3$ cores and embedding of Au NPs in the wall of capsules

20 mg of dried $CaCO_3$ particles were weighted and dispersed in a 0.5M NaCl solution containing the polyanion PSS (2 mg mL^{-1}). The dispersion was continuously shaken for 12 min. The excess polyanion was removed by three centrifugation/washing steps with 1 mL of milli-Q water (6000 rpm for 5 s). Subsequently, 1 mL of a 0.5M NaCl solution containing the polycation PAH (2 mg mL^{-1}) was added and the dispersion was continuously shaken for 12 min, followed again by three centrifugation/washing steps (6000 rpm for 5 s). This procedure was repeated three times for each polyelectrolyte resulting in the deposition of ten polyelectrolyte layers around the $CaCO_3$ particles.

Two different types of microcapsules were produced: with and without Au NPs in the multilayer wall (Scheme 1). For capsules with Au NPs, the capsules were resuspended in a solution of phosphine-stabilized 20nm Au NPs (500 µL of 0.045 µM stock) following the deposition of the eighth layer (PAH). The final multilayer composition was $(PSS/PAH)_4AuNP(PSS/PAH)$. For capsules without Au NPs, the final multilayer composition was $(PSS/PAH)_5$.

In a second step, the $CaCO_3$ core was removed by complexation with EDTA buffer. Coated $CaCO_3$ particles were shaken for 2 min with 1 mL of an EDTA solution (0.2M, pH 5.0), followed by centrifugation (1200 rpm for 8 min) and redispersion in 1 mL of a fresh EDTA solution (0.2 M, pH 7.0). We observed that the initial exposure of the microcapsules to a slightly acidic EDTA solution lead to a faster and complete decomposition of the $CaCO_3$ cores compared to their direct exposure to a neutral EDTA solution, as previously reported by others (De_Geest, Skirtach et al. 2007; Hu, Tsai et al. 2008; De Koker, Naessens et al. 2010). Then the capsules were washed with 1 mL of neutral EDTA for quickly increasing the pH up to 7. To remove the dissolved ions, the thus obtained hollow microcapsules were gently washed three times centrifugation (1200 rpm for 6 minutes) and washings steps with 1 mL of fresh milli-Q water. The microcapsules were finally stored as suspension in water at 4 ℃. The microcapsules concentration was estimated to be $3.12x10^8$ microcapsules/mL. The capsule number per volume was determined by direct counting by a hemocytometer under a microscope. A drop of a diluted solution of capsules was added onto the chamber and the number of capsules in the volume defined by the hemocytometer was counted by using a 20X objective.

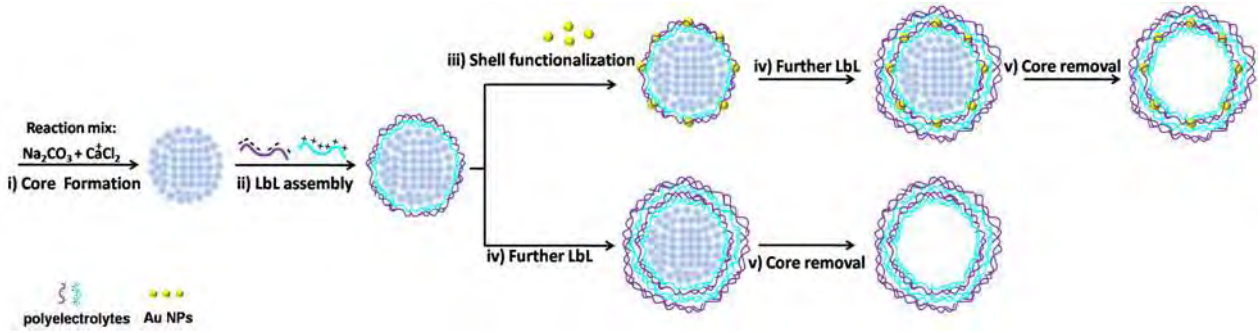

Scheme 1. Schematic illustration of the synthesis of a polyelectrolyte capsule with and without Au NPs embedded in the wall. i) A spherical $CaCO_3$ porous template is synthesized by mixing two solutions of Na_2CO_3 and $CaCl_2$. ii) The $CaCO_3$ particle is then coated via consecutive LbL deposition of oppositely charged polyelectrolytes to grow a multilayer polymer wall around the template. iii) The wall is functionalized by loading charged Au NPs onto an oppositely charged layer during the LbL assembly. iv) LbL of polyelectrolytes is repeated to obtain a stable multilayer wall on both capsules with and without Au NPs in the wall. v) The spherical template is removed to obtain a multilayer capsule with and without Au NPs in the walls. Capsules are not drawn to scale. Only few layers of polyelectrolyte and of NPs are shown for sake of clarity.

II) Microwave (MW) Irradiation

MW radiation was produced by a house customized RF microwave generator at 2.45 GHz. The sample was placed inside a resonating chamber for irradiation. In this condition, and for a sample volume of 1.5 mL, the temperature increases by 1^0C in a radiation time of one minute. The power administrated to the system is of 104 mW with a total thermal energy of 6.3 J every minute. An aqueous suspension (1 mL) of capsules with and without NPs containing $1.12x10^8$ capsules/mL was placed into a resonating chamber for irradiation. Samples were not shaken to avoid interference with mechanical disruption and an inner temperature probe was used to monitor the temperature variation at the sample position.

III) Dynamic Light Scattering

Measurements were made with a Malvern ZetaSizer Nano ZS Instrument operating at a light source wavelength of 532nm and a fixed scattering angle of 173 ° for detection. Aliquots of 0.8 mL of the colloidal NP solutions were placed into the specific cuvette and the software was arranged with the specific parameters of refractive index and absorption coefficient of the material and solvent viscosity. DLS allows for determining of the hydrodynamic diameter of colloidal particles. This is the diameter of the equivalent sphere with the same Brownian motion as the analyzed sample. The observed differences of the initial diameter between the DLS values of capsules with and without NPs are attributed to the different contrast of the different capsules under the measuring beam but with and without the presence of metallic (plasmonic) NPs.

IV) Transmission electron microscopy (TEM)

Polyelectrolyte capsules, with and without Au NPs into the multilayer walls, were analyzed by Transmission Electron Microscopy (TEM) after core removal by using a JEOL 3010 TEM operating at an accelerating voltage of 300 kV. A 10 µl drop sample was placed on a Formvar®/carbon coated TEM-grid (300 Mesh 3.05 mm Copper, Plano GmBH) and dried at room temperature before imaging.

V) Inductive coupled plasma mass spectroscopy (ICP-MS)

The number of Au NPs per capsules has been calculated by measuring the amount of Au ions per capsules as obtained from the Inductive coupled plasma mass spectrometer (ICP-MS). For the ICP-MS measurements 100 µL of capsule sample from the original stock was first digested with 20 µL of 12 M concentrated nitric acid to oxidize the organic coating around the NPs. Then 80 µL of 12 M hydrochloric acid was used to dissolve the Au NPs into Au ions. Concentration of Au determined from ICP-MS measurement was 2E-3 m mol/ml. We calculated that one Au NP of 20nm contains $2.4x10^5$ atoms of Au. Using this number we calculated the total number of Au NPs in the solution to be $2.4x10^5$ times smaller than the total number of Au ions in the solution. The concentration of capsules in a capsules sample of the same volume of 100 µl was determined to be 10^8 capsules per mL, by counting the number of capsules using the microscope in phase contrast mode. At the end the number of Au NPs per capsules was calculated by dividing the concentration of Au NPs and the number capsules in the solution. The obtained value was $7.29x10^3$ Au NPs per capsule. The calculation is given in details below.

p refers to nanoparticles
m_{aAu} = mass of 1 Au atom / ion
ρ_{Au} = density of Au
V_{pAu} = Volume of 1 Au NP (diameter 20nm)
m_{pAu} = mass of 1 Au NP (diameter 20nm)
N_{aAu}: refers to the number of Au atoms in one Au NP
N_{pAu}: refers to the number of Au NPs in the sample solution
N_{Au} = number of detected Au ions within the sample solution
c_{Au} = concentration of Au ions in the sample solution
V = Volume of sample solution
N_{caps} = number of capsules in the sample solution

To calculate the number of Au atoms per 20nm Au NP firstly we calculated the mass of one Au NP of 20nm (m_{pAu}) using the following formula: $m_{pAu} = \rho_{Au} \bullet V_{pAu}$. ρ_{Au} is the mass density of Au which is 19.3 g/cm^3. V_{pAu} is the volume of one Au NP calculated using the formula $V_{pAu} = 4/3\ \pi\ r^3$, whereby r is the radius of one Au NP. The calculated volume V_{pAu} is $4.1x10^{-18}$ cm^3. Using the above given ρ_{Au} and V_{pAu} values, the mass of one Au NP (m_{pAu}) was calculated to be $8.1x10^{-17}$ g. The total mass of one Au atom / ion (m_{aAu}) is $3.2x10^{-22}$. The number of Au atoms in one 20 nm Au NP was obtained by dividing the mass of one Au NP (m_{pAu}) by the total atomic mass of Au (m_{aAu}). We found $2.4x10^5$ atoms of Au in one 20nm Au NP (N_{aAu}).

With ICP-MS measurements we determined the concentration of Au ions in solution after dissolving the Au NPs: c_{Au} From the Au concentration c_{Au} we got the total number of Au atoms (N_{Au}) within sample by $N_{Au} = c_{Au} \bullet V \bullet N_A$ with the Avogadro number $N_A = 6.02x10^{23}$. The volume of the samples was V = 1 mL. In our experiments we got c_{Au} = 2E-3 mmol / 1 mL as result. From this concentration value we got the total number of Au atoms (N_{Au}) in this sample, which was $N_{Au} = 1.21x10^{18}$. Each Au NP contains $2.4x10^5$ (N_{aAu}) Au atoms. Thus the number of Au NPs in the sample solution (N_{pAu}) was calculated by dividing N_{Au} with $2.47x10^5$. This resulted in the value $N_{pAu} = 4.88x10^{12}$.

The number of capsules N_{caps} in the samples was counted to be $N_{caps} = 6.70x10^8$. Finally, the number of Au NPs per capsule was obtained by dividing the number of Au NPs (N_{pAu}) by the number of capsules (N_{caps}) in the sample. $N_{pAu}/N_{caps} = 4.88x10^{12} / 6.70x10^8 = 7.29x10^3$

References

Araya, E., I. Olmedo, et al. (2008). "Gold Nanoparticles and Microwave Irradiation Inhibit Beta-Amyloid Amyloidogenesis." Nanoscale Research Letters **3**(11): 435-443.

Bedard, M. F., D. Braun, et al. (2008). "Toward self-assembly of nanoparticles on polymeric microshells: Near-IR release and permeability." Acs Nano **2**(9): 1807-1816.

Bedard, M. F., B. G. De Geest, et al. (2009). "Polymeric microcapsules with light responsive properties for encapsulation and release." Adv Colloid Interface Sci.

De Koker, S., T. Naessens, et al. (2010). "Biodegradable Polyelectrolyte Microcapsules: Antigen Delivery Tools with Th17 Skewing Activity after Pulmonary Delivery." Journal of Immunology **184**(1): 203-211.

De_Geest, B. G., A. G. Skirtach, et al. (2007). "Ultrasound-triggered release from multilayered capsules." Small **3**(5): 804-808.

Decher, G. (1997). "Fuzzy nanoassemblies: Toward Layered Polymeric Multicomposites." Science **277**: 1232-1237.

Decher, G. and J. Schlenoff (2002). Multilayer Thin Films: Sequential Assembly of Nanocomposite Materials, Wiley VCH.

Donath, E., G. B. Sukhorukov, et al. (1998). "Novel Hollow Polymer Shells by Colloid-Templated Assembly of Polyelectrolytes." Angewandte Chemie International Edition **37**(16): 2202-2205.

English, N. J. and D. A. Mooney (2007). "Denaturation of hen egg white lysozyme in electromagnetic fields: a molecular dynamics study." J Chem Phys **126**(9): 091105.

Gorin, D. A., S. A. Portnov, et al. (2008). "Magnetic/gold nanoparticle functionalized biocompatible microcapsules with sensitivity to laser irradiation." Phys Chem Chem Phys **10**(45): 6899-905.

Gorin, D. A., D. G. Shchukin, et al. (2006). "Effect of microwave radiation on polymer microcapsules containing inorganic nanoparticles." Technical Physics Letters **32**(1): 70-72.

Hallahan, D. E., S. M. Qu, et al. (2001). "Radiation-mediated control of drug delivery." American Journal of Clinical Oncology-Cancer Clinical Trials **24**(5): 473-480.

Hu, S. H., C. H. Tsai, et al. (2008). "Controlled rupture of magnetic polyelectrolyte microcapsules for drug delivery." Langmuir **24**(20): 11811-8.

Kogan, M. J., N. G. Bastus, et al. (2006). "Nanoparticle-mediated local and remote manipulation of protein aggregation." Nano Letters **6**(1): 110-115.

Lu, Z., M. D. Prouty, et al. (2005). "Magnetic switch of permeability for polyelectrolyte microcapsules embedded with Co@Au nanoparticles." Langmuir **21**(5): 2042-50.

Martin, D., G. Craciun, et al. (2008). "Radiation exposure facilities for medical studies in vitro and vivo." Proceedings of the 11Th International Conference on Optimization of Electrical and Electronic Equipment, Vol I: 77-86

273.

Muñoz_Javier, A., P. d. Pino, et al. (2009). "Photoactivated release of cargo from the cavity of polyelectrolye capsules to the cytosol of cells." Langmuir **24**: 12517-12520.

Murdock, R. C., L. Braydich-Stolle, et al. (2008). "Characterization of nanomaterial dispersion in solution prior to in vitro exposure using dynamic light scattering technique." Toxicol Sci **101**(2): 239-53.

Palankar, R., A. G. Skirtach, et al. (2009). "Controlled Intracellular Release of Peptides from Microcapsules Enhances Antigen Presentation on MHC Class I Molecules." Small **5**(19): 2168-2176.

Radt, B., T. A. Smith, et al. (2004). "Optically Addressable Nanostructured Capsules." Advanced Materials **16**(23-24): 2184-2189.

Rivera Gil, P., L. L. del Mercato, et al. (2008). "Nanoparticle-modified polyelectrolyte capsules." Nano Today **3**(3-4): 12-21.
Skirtach, A. G., A. A. Antipov, et al. (2004). "Remote activation of capsules containing Ag nanoparticles and IR dye by laser light." Langmuir **20**(17): 6988-6992.
Skirtach, A. G., B. G. De_Geest, et al. (2007). "Ultrasound stimulated release and catalysis using polyelectrolyte multilayer capsules." Journal Of Materials Chemistry **17**(11): 1050-1054.
Stuart, M. A. C., W. T. S. Huck, et al. (2010). "Emerging applications of stimuli-responsive polymer materials." Nature Materials **9**(2): 101-113.
Sukhorukov, G. B., E. Donath, et al. (1998). "Stepwise polyelectrolyte assembly on particle surfaces: a novel approach to colloid design." Polymers for Advanced Technologies **9**(10-11): 759-767.
Sukhorukov, G. B., A. L. Rogach, et al. (2007). Nanoengineered polymer capsules: Tools for detection, controlled delivery and site specific manipulation.
Zebli, B., A. S. Susha, et al. (2005). "Magnetic Targeting and Cellular Uptake of Polymer Microcapsules Simultaneously Functionalized with Magnetic and Luminescent Nanocrystals." Langmuir **21**: 4262-4265.
Zhou, G. F., Y. P. Sun, et al. (2004). "In vivo antitumor and immunomodulation activities of different molecular weight Lambda-Carrageenans from Chondrus ocellatus." Pharmacological Research **50**(1): 47-53.

Relaxation times of colloidal iron platinum in polymer matrixes†‡

Maria Puerto Morales,*[a] Matthieu F. Bédard,[bc] Alejandro G. Roca,[a] Patricia de la Presa,[d] Antonio Hernando,[d] Feng Zhang,[e] Marco Zanella,[e] Abbasi Azhar Zahoor,[e] Gleb B. Sukhorukov,[c] Loretta L. del Mercato[e] and Wolfgang J. Parak*[ef]

Received 1st April 2009, Accepted 29th May 2009
First published as an Advance Article on the web 13th July 2009
DOI: 10.1039/b906455a

Colloidal magnetic iron platinum nanoparticles were embedded at different densities into the walls of polyelectrolyte multilayer capsules. Changes in their magnetic properties such as relaxivities as a function of average distances between the magnetic nanoparticles were investigated and their properties for magnetic resonance imaging discussed.

Introduction

Magnetic particles are interesting as contrast agents for magnetic resonance imaging (MRI). MRI is a non-invasive technique based on the variation of the water proton relaxation time from one tissue to another. Different chemical compounds have been used as contrast agents to enhance the contrast between normal and diseased tissues, to indicate organ function or blood flow.[1] Gadolinium (Gd)-based organometallic complexes provide high contrast for T_1-imaging, while iron (Fe)-containing nanoparticles have been proven to provide good contrast for T_2-imaging.[2,3] Magnetic particles provide good imaging contrast capabilities for MRI because the T_1 and T_2 relaxation times are very sensitive to changes in local field gradients created by the superparamagnetic particles that accelerate the loss of phase coherence of the spins of nearby protons contributing to the MR signal (*e.g.* from surrounding water molecules). Changes in the relaxation times T_1 and T_2 depends on both material composition and on the size of the particles.[4]

Size dependence of the nanoparticles has been extensively demonstrated, both experimentally and theoretically, since magnetic colloidal nanoparticles can be synthesized with excellent size distribution and shape control.[5–12] However, since the magnetic moments of magnetic nanoparticles are strongly affected by environmental factors, introducing such nanoparticles in a different environment may have serious implications on their MRI potential. In this sense, if individual colloidal nanoparticles aggregate to ill-defined complexes their contrast providing properties change significantly.[13] Magnetic nanoparticles can be embedded into matrixes in order to improve their contrast providing properties.[14] Whereas size dependence of contrasting has been investigated in much detail, there is only a limited number of studies available in which the inter-particle distance on contrasting is studied.[14] This is mainly due to the fact that it is technologically complicated to vary the mean inter-particle distance without changing other parameters such as the composition of the matrix in which the particles are embedded or the surface chemistry of the particles. In this study, we introduce polyelectrolyte capsules as a convenient matrix system which allows for the integration of colloidal nanoparticles at controlled nanoparticle density and thus provides a good system for studying the inter-particle distance dependent contrasting.

Polyelectrolyte capsules are constructed using the layer-by-layer assembly (LbL) approach according to which oppositely charged polymers are alternatively added to a charged surface.[15] Growth of a multilayered film is possible because each addition of a polyelectrolyte layer results in some uncompensated charges that permit an oppositely charged polymer to deposit.[16] Once the desired LbL composition is obtained, the colloidal template was decomposed resulting in hollow polymeric capsules.[17,18] As the different layers of polyelectrolyte microcapsules are held together primarily by electrostatic forces, charged nanoparticles (or other charged macromolecules) can be integrated into the polyelectrolyte network.[19–24] In this way capsules with magnetic Fe-based nanoparticles within their polyelectrolyte walls have been synthesized.[25–28] Such capsules were used for targeted drug delivery, in which capsules could be directed to target locations with magnetic field gradients.[27,29] Besides targeted delivery and visualization, magnetic nanoparticles were also used as an agent to remotely open microcapsules using an alternating magnetic field and inducing nanoparticles embedded in the capsule shell to rotate, damaging the latter and allowing the capsule to release encapsulated substances.[28] Microcapsule technology is also attractive due to the many physical parameters that can be finely-tuned, such as shell thickness and roughness. Capsules are due to their controlled step-by-step construction also an ideal matrix for

[a]*Instituto de Ciencia de Materiales de Madrid, CSIC, C/ Sor Juana Inés de la Cruz 3, Campus de Cantoblanco, 28049 Madrid, Spain. E-mail: Puerto@icmm.csic.es*
[b]*Max-Planck Institute of Colloids and Interfaces, Potsdam 14424, Germany*
[c]*School of Engineering and Materials Science, Queen Mary, University of London, London, UK E1 4NS*
[d]*Instituto de Magnetismo Aplicado, UCM-ADIF-CSIC, 28230 Las Rozas (Madrid), Spain*
[e]*Fachbereich Physik, Philipps Universität Marburg, Marburg, Germany. E-mail: wolfgang.parak@physik.uni-marburg.de*
[f]*Wissenschaftliches Zentrum für Materialwissenschaften, Philipps Universität Marburg, Marburg, Germany*

† This paper is part of a *Journal of Materials Chemistry* theme issue on inorganic nanoparticles for biological sensing, imaging, and therapeutics. Guest editor: Jinwoo Cheon.

‡ Electronic supplementary information (ESI) available: Additional data for the characterization of the FePt particles, and the determination of the number of FePt particles per capsule. See DOI: 10.1039/b906455a

changing the mean distance between magnetic particles. Charge–charge repulsion between nanoparticles which are deposited at the surface of a polyelectrolyte film helps maintain a homogeneous distribution in the final capsule construction.[22] In the work presented here capsules were loaded with three different concentrations of magnetic nanoparticles and their effect on T_1 and T_2 relaxation was compared to that of free nanoparticles.

Materials and methods

FePt nanoparticle synthesis

Synthesis of hydrophobic FePt nanoparticles. We followed the recipe previously reported by Sun *et al.*[5] Briefly, in a 50 ml three-neck flask, 10 ml of octyl ether, 95mg of platinum acetylacetonate and 195 mg of hexadecanediol were mixed under nitrogen atmosphere. Temperature was raised up to 100 °C until the solution turned into a clear translucent yellow color. Oleic acid (0.08 ml), oleyl amine (0.08 ml) and iron pentacarbonyl (0.06 ml) were quickly injected under vigorous stirring and the temperature was raised to 280 °C with a rate of 12 °C/min, then the solution was left at that temperature for 15 minutes before removing the heating mantle. Nanoparticles were then washed with a mixture of methanol and ethyl acetate and redispersed in fresh chloroform. The synthesis yielded nearly monodisperse nanoparticles which were characterized by transmission electron microscopy (TEM). In a next step the hydrophobic nanoparticles were transferred to aqueous solution by coating them with an amphiphilic polymer.

Synthesis of the amphiphilic polymer. The synthesis of the amphiphilic polymer has been reported previously.[30,31] Briefly, 2.70 g (15 mmol) of dodecylamine (DoCA, 98%, Sigma, # D22,220-8) was firstly dissolved in 100 ml tetrahydrofurane anhydrous (THF, ≥99.9%, Aldrich, #186562) in a round flask. After dodecylamine dissolved well, the solution was poured into another round flask with 3.084 g (20 mmol motifs, one polymer molecule has about 39 motifs) powder of poly(isobutylene-alt-maleic anhydride, average Mw ~6,000 g/mol, Sigma, #531278). This mixture was sonicated for several seconds (~20 s), and then heated to 55–60 °C for 1 hour under stirring conditions. Afterwards, the solution was concentrated to 30–40 ml by evaporation of THF solvent and left stirring overnight. Finally, the solution was completely dried by evaporation and redissolved in 40ml anhydrous chloroform to a final concentration of 0.5 M of polymer motifs.

Coating of the hydrophobic FePt particles with the amphiphilic polymer. The polymer coating procedure has been described previously.[30,31] Briefly, solutions of polymers were mixed with FePt nanoparticle solution in a round flask. The polymer was kept in excess by using 200 motifs per nm^2 of particle's surface to obtain the best size distribution. By slowly evaporating the solvents completely, the particles with polymer were redissolved in SBB (50 mM sodium borate, pH 12) buffer.

Purification of the water-soluble polymer coated FePt particles. Polymer coated FePt nanoparticles were purified by size exclusion chromatography using a Sephacryl S300 HR gel column (GE Healthcare, #17-0599-10) connected with a HPLC system (Agilent 1100). Before and after the purification, the polymer coated FePt nanoparticle samples were concentrated by ultrafilters (100kD MWCO, Millipore) followed by additional filtering with 0.2 μm filters (Millipore) to get rid of any possible big aggregates. The purified samples were stocked in SBBS buffer (50mM sodium borate, 100mM NaCl, pH 9.0) finally.

Capsule synthesis

Preparation of Silica Templates. The fabrication of $(PDADMAC/PSS)_4$ microcapsules was done on 4.78 μm silica particles (Microparticles GmbH, Germany) using the Layer-by-Layer deposition technique.[23] Typically, 1 mL of template SiO_2 particles solution were first cleaned from stabilizers in a sonication bath after resuspending them in a 1:1 solution of water and isopropanol.

LbL assembly of polyelectrolyte capsules. Solutions of poly(diallyldimethylammonium chloride) (PDADMAC, Sigma-Aldrich, 200–350 kDa) (2 mg/mL, 0.5 M NaCl) and poly(styrenesulfonate, sodium salt) (PSS, Sigma-Aldrich, 70 kDa) (2 mg/mL, 0.5 M NaCl) were prepared without further purification. Silica templates with an average diameter of 4.78 μm were treated alternatively with 3 layers of polyelectrolytes beginning with PDADMAC and ending with PDADMAC. At layers 3 and 5 (PDADMAC), SiO_2 templates were re-suspended in a mixture of water and polymer-coated FePt nanoparticles suspension with desired concentration, while gently stirring. A total of four PDADMAC/PSS bilayers of polyelectrolytes were used to coat the silica templates. Particles needed to be treated in a sonication bath after each step of assembly in order to reduce the tendency of the samples to aggregate. When the desired multilayer structure was obtained, the templates were dissolved in HF (0.3 M) solution, and the sample was then washed with water until the pH of the solution reaches above 5. In total, 3 types of polymeric microcapsules were prepared using three different concentrations of FePt nanoparticles (low, medium and high), moreover one sample made of capsules without FePt nanoparticles was fabricated as control. A schematic of the samples analyzed in this work are displayed in Fig. 1.

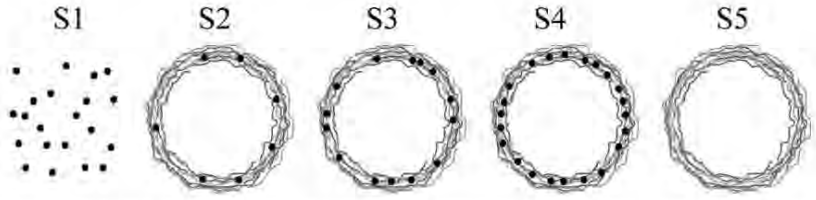

Fig. 1 Five different samples were prepared. Free FePt particles (S1), polyelectrolyte capsules with a low (S2), medium (S3), and high (S4) concentration of FePt particles, and polyelectrolyte capsules without FePt particles (S5).

Capsule characterization

Determination of Microcapsule Diameter. To visualize the microshells by laser scanning confocal microscopy (LSCM) the capsules were made fluorescent by the addition of a drop of 10^{-7} M solution of rhodamine 6G. A Leica TCS SP confocal scanning system (Leica, Germany) equipped with a 100x/1.4-0.7 oil immersion objective was used for measurements. The average capsule diameter for each sample was determined by measuring the wall-to-wall diameter at the largest point for at least 30 capsules per sample. The diameters were determined to be 4.9 μm ± 0.2, 4.8 μm ± 0.2, 5.0 μm ± 0.3 and 4.8μm ± 0.2 for samples S2 to S5, respectively. The diameters were therefore not significantly different.

Number of FePt nanoparticles per capsule. The concentration of capsules was directly determined by taking an aliquot of solution and counting the number of capsules with an optical microscope in phase-contrast mode and was determined to be around 10^9 capsules per mL. The counted numbers were generated by averaging the number of capsules contained in 6 aliquots of a dilution of each sample leading to a standard deviation of around 10%. The concentration of iron atoms in each sample was determined with elemental analysis. For this purpose samples were digested with nitric acid to oxidize the organic coating and then, with hydrochloride acid to dissolve the iron. The Fe concentration was then measured in a plasma emission spectrometer (ICP) PERKIN ELMER OPTIMA 2100 DV. We estimated that each FePt nanoparticle with a diameter of 3.2 ± 0.4 nm as determined by TEM comprises approximately 288 ± 91 Fe atoms.[32] Using this number the FePt nanoparticle concentration of each solution is 1/288-th of the measured iron concentration. By knowing the FePt nanoparticle and the capsule concentration of each solution the number of FePt nanoparticles embedded per capsule was determined, by assuming that all FePt nanoparticles were actually bound to the capsules. In this way we estimated the number of $2.6 \times 10^8 \pm 0.9 \times 10^8$, $3.2 \times 10^8 \pm 1.1 \times 10^8$, and $6.6 \times 10^8 \pm 2.3 \times 10^8$ FePt nanoparticles per polymer capsules for the samples S2, S3, and S4, respectively (cf. Table 1).

Structural characterization of capsules. Transmission electron microscopy (TEM) was done using a Zeiss Omega EM 912 at an operating voltage of 120 kV. Hereby the FePt nanoparticles provide strong contrast against the polymer layers.

Magnetic and relaxometric characterization

For each type of sample (S1–S5) a concentration series of different aliquots was done by dilution. The Fe concentration c(Fe) within each aliquot was determined with elemental analysis using a plasma emission spectrometer (ICP) as described above. Magnetic characterisation of the suspensions (0.1 ml) was carried out by means of a Quantum Design SQUID magnetometer in special closed sample holders. The magnetic characterization consists in hysteresis cycles at 5 Tesla and at 5 K. Relaxometric properties were also investigated for each aliquot by measuring T_1 and T_2 protons relaxation times at different dilutions. The relaxation time measurements were carried out in a MINISPEC MQ60 (Brucker) at 37 °C and a magnetic field of 1.5 T. From the graph of the Fe-concentration dependent relaxation times, the relaxivities r_1 and r_2 were determined for each type of sample.

Results and discussion

Structural analysis

Representative TEM images of capsules containing different concentrations of FePt nanoparticles are shown in Fig. 2 (upper row). The capsules, typically spherical in solution, appear with folds and creases in TEM imaging as a result of drying. The thin and light coloured folds seen in the centre of the capsule in sample S2 indicate that the shell is rather thin. On the other hand, the dark and thicker folds found in S4 indicate relatively thicker capsule walls. It was found by LSCM measurements that all the capsules are approximately the same diameter (~ 4.9 μm). A magnification of flat areas of capsules from each sample is shown in the lower row. The FePt particles are clearly visible as dark spots. From these images the increasing loading density from sample S2 to S3 and to S4 is also supported by the fact that folds in the dried capsules appear darker and thicker as FePt nanoparticle concentration increases. These observations agree well with the data obtained from elemental analysis. Furthermore the particles show a random distribution in the polymer matrix instead of forming regions of agglomerated particles.

Magnetic and relaxometric properties

Hysteresis curves at 5 T of 0.1 ml suspensions of capsules containing different concentrations of FePt nanoparticles were recorded and a section of the loops for samples S2 and S3 around ±2 Teslas is shown in Fig. 3. The inset in Fig. 3 shows the complete hysteresis loop for sample S3. Sample S4 shows similar magnetic behaviour as sample S3. Room temperature curves are unable to distinguish between capsules because of the low saturation magnetization values at that temperature (0.5 emu/g for pure FePt particles). The magnetic response depends strongly on the FePt concentration in the capsules. For low FePt concentrations (S2), a reversible magnetisation curve is obtained indicating superparamagnetic behaviour at 5 K and lower blocking temperatures. However, for high FePt concentrations (S3 and S4) a hysteresis loop is observed with a coercivity of 800 Oe. These results indicate an increase in the dipolar interactions between particles from sample S2 to sample S3 as expected when encapsulating more FePt particles in a similar size capsule. Saturation magnetisation is reached at lower field for sample S3 as a consequence of the stronger dipolar interactions and is about

Table 1 Number of FePt nanoparticles per capsule for samples S2, S3, S4

sample	S2	S3	S4
FePt NPs/capsule	$2.6 \times 10^8 \pm 0.9 \times 10^8$	$3.2 \times 10^8 \pm 1.1 \times 10^8$	$6.6 \times 10^8 \pm 2.3 \times 10^8$

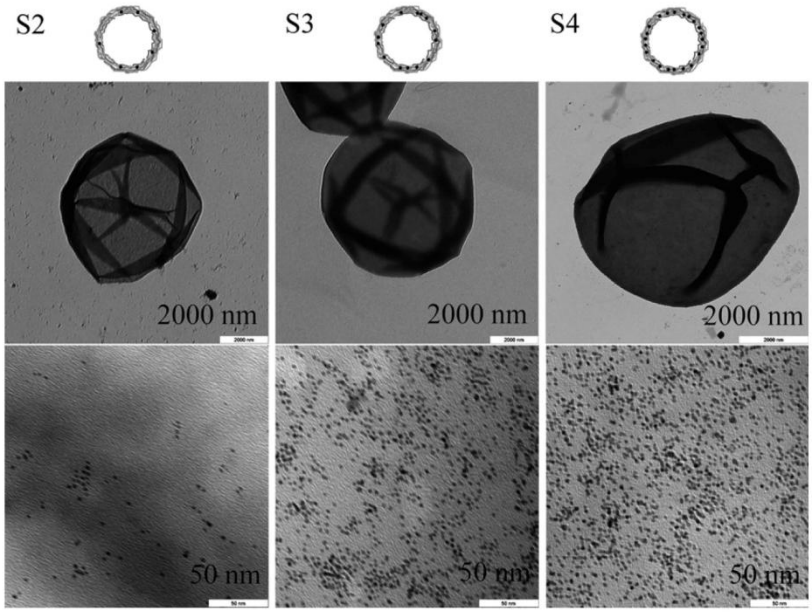

Fig. 2 TEM images in low and high resolution for samples S2, S3, and S4. The low magnification images show individual capsules. The high resolution images are zoomed into the capsule shells and show the distribution of the FePt particles in the capsule wall. The scale bars in the upper and lower row correspond to 2 μm and 50 nm, respectively.

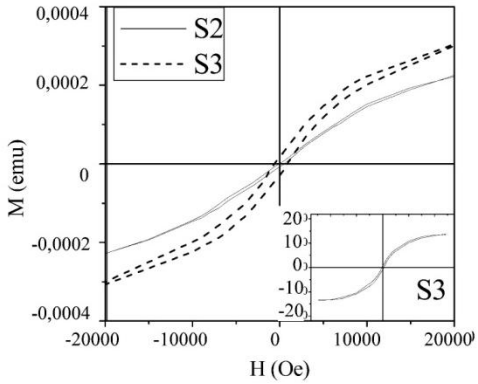

Fig. 3 Hysteresis loops at 5K for S2 and S3 suspensions containing different FePt nanoparticles per capsule.

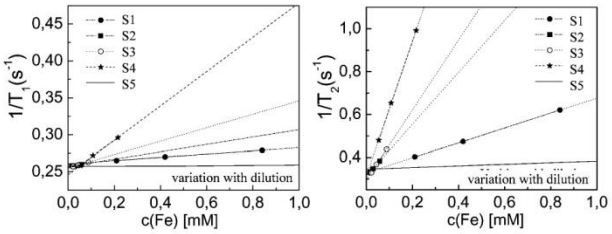

Fig. 4 T_1 and T_2 relaxation times for samples S1–S5 for different dilutions. Concentrations of each diluted aliquot were determined by the amount of iron (c(Fe)) by ICP.

Table 2 r_1 and r_2 relaxivities for samples S1–S4

sample	S1	S2	S3	S4
r_1 [mmol^{-1}s^{-1}]	0.021	0.045	0.092	0.230
r_2 [mmol^{-1}s^{-1}]	0.35	1.18	1.62	3.14
r_2/r_1	16.7	26.2	17.8	13.6

13 emu/g, much smaller than the saturation of FePt bulk but quite similar to the saturation of FePt NPs of same size.[33]

Magnetic interactions between particles are often significant and may even result in superferromagnetic ordering at low temperatures, *i.e.* ordering of the magnetic moments of particles which would be superparamagnetic if they were isolated.[34,35] This explains the magnetic behavior change from superparamagnetism for sample S2 (low concentration, almost isolated particles) to ferromagnetism for sample S3 (S4) (high concentration, interacting particles).

T_1 and T_2 relaxation times were measured for each of the samples for different concentrations by making a dilution series of each sample solidify with agar (5%) (see Fig. 4 and Table 2). For each concentration series the relaxivities $r_{1,2}$ ($s^{-1}mM^{-1}$) were determined according to eqn (1), where, $R_{1,2}$ are the relaxation rates obtained from the relaxation times ($1/T_{1,2}$ [s^{-1}]) and $R^0_{1,2}$ are the relaxation rates in the absence of contrast agent, *i.e.* the agar contribution.

$$R_{1,2} = R^{o}_{1,2} + r_{1,2} \cdot c(Fe) \quad (1)$$

From the data it is evident that embedding FePt particle changes the relaxation time, dependent of the FePt density in the capsule walls. All r_2 values for iron platinum particles are always well below the values for iron oxide magnetic nanoparticles (in agreement with the lower magnetic moment of FePt, 13 emu/g against ~60 emu/g for magnetite nanoparticles). The values for

r_2 are higher when the FePt particles are inside the capsules (S2, S3, S4) compared to the dispersed isolated FePt particles (S1). The r_2 values also increase with the degree of aggregation, *i.e.* $r_2(S2) < r_2(S3) < r_2(S4)$. This clearly demonstrates that relaxation times depend on the particle type (here: FePt), but also on the density in which they are embedded in a matrix.

Differences in relaxivity are due to local field gradients created by the superparamagnetic particles that accelerate the loss of phase coherence of the spins contributing to the MR signal.[1] Both magnetic moments and interactions (controlled by particle size and distribution) are the required parameters to understand the relaxivity data. The moment per FePt particle is expected to be the same in all capsules but interparticle interactions will modify the effective moment in each particle and therefore the field gradient around it affecting the relaxation of nearby water protons.

Relaxivity values for these FePt particles are two orders of magnitude smaller than r_2 values reported for commercial contrast agents based on iron oxide with similar particle size and hydrodynamic sizes of around 150 nm as Endorem. As the aggregate size decreases, r_2 is in these particles reduced from 120 $mmol^{-1}s^{-1}$ for 150 nm of hydrodynamic size to 65 $mmol^{-1}s^{-1}$ for 30 nm and 33 $mmol^{-1}s^{-1}$ for 7 nm.[36] However, for the FePt particles in capsules, r_2/r_1 values that are indicative of the effectiveness of the contrast, were similar or even higher than the value reported for the commercial iron oxide products ($r_2/r_1 = 2$ for 7nm aggregate size). Very high r_2 values (>200 $mmol^{-1}s^{-1}$) have been reported for other magnetic nanoparticles such as Manganese ferrites and Cobalt ferrites but the contribution from the aggregation state was unclear. It can be concluded that saturation magnetisation, aggregation state and spatial distribution determine the NMR contrast produced by magnetic nanoparticles.

Conclusions

The results of this study point out how important the interparticle distance for nanoparticle-based for magnetic contrast agents is. Bringing particles together by embedding them into a carrier matrix drastically increases the r_1 and r_2 relaxivities in magnetic resonance imaging. This fact should be taken into account for many studies in literature in which magnetic nanoparticles are suggested as contrast agents for in vivo magnetic resonance imaging. As a matter of fact the majority of magnetic nanoparticles used nowadays have limited colloidal stability. For this reason such particles tend to agglomerate in body fluids, such as blood, due to the present salt content. As shown in this study agglomeration or likewise controlled decrease of the average inter-particle distance can lead to significant changes in relaxation times. In other words, the magnetic properties of particles inside a body might differ greatly in comparison to the values measured under the laboratory conditions described in the present work. Therefore, in our opinion, without keeping exact track about the degree of agglomeration (for example with measurements of the hydrodynamic diameter of the particles[37]) data about relaxivities have to be interpreted with outmost care. As long as the degree of agglomeration is not exactly known and controlled, relaxivities are not stable but are likely to vary according to subsequent further increase of agglomeration upon incubation in body fluids.

Acknowledgements

The authors are grateful to Dr Andrei Skirtach, Dr Almudena Muñoz Javier, Dr Pablo del Pino, and Dr Oliver Kreft for helpful discussions. This work was supported by the German Research Foundation (DFG, SPP 1313), the European Commission (Nanointeract project), the Comunidad de Madrid S-0505/MAT/0194 and Reference Laboratory SOIMRM, and the Spanish Ministry of Science and Innovation MAT2008-01489 project.

References

1 A. E. T. Merbach, *The Chemistry of Contrast Agents in Medical Magnetic Resonance Imaging*, Wiley, New York, USA, 2001.
2 J. W. M. Bulte and D. L. Kraitchman, *NMR Biomed.*, 2004, **17**, 484.
3 M. G. Harisinghani, K. S. Jhaveri, R. Weissleder, W. Schima, S. Saini, P. F. Hahn and P. R. Mueller, *Clin. Radiol.*, 2001, **56**, 714.
4 Y. M. Huh, Y. W. Jun, H. T. Song, S. Kim, J. S. Choi, J. H. Lee, S. Yoon, K. S. Kim, J. S. Shin, J. S. Suh and J. Cheon, *J. Am. Chem. Soc.*, 2005, **127**, 12387.
5 S. Sun, C. B. Murray, D. Weller, L. Folks and A. Moser, *Science*, 2000, **287**, 1989.
6 M. Corti, A. Lascialfari, E. Micotti, A. Castellano, M. Donativi, A. Quarta, P. D. Cozzoli, L. Manna, T. Pellegrino and C. Sangregorio, *J. Magn. Magn. Mater.*, 2008, **320**, e320.
7 A. Figuerola, A. Fiore, R. Di Corato, A. Falqui, C. Giannini, E. Micotti, A. Lascialfari, M. Corti, R. Cingolani, T. Pellegrino, P. D. Cozzoli and L. Manna, *J. Am. Chem. Soc.*, 2008, **130**, 1477.
8 V. F. Puntes, D. Zanchet, C. Erdonmez and A. P. Alivisatos, *J. Am. Chem. Soc.*, 2002, **124**, 12874 12880.
9 S. Sun, H. Zeng, D. B. Robinson, S. Raoux, P. M. Rice, S. X. Wang and G. Li, *J. Am. Chem. Soc.*, 2004, **126**, 273.
10 S. Sun and H. Zeng, *J. Am. Chem. Soc.*, 2002, **124**, 8204.
11 E. V. Shevchenko, D. V. Talapin, A. L. Rogach, A. Kornowski, M. Haase and H. Weller, *J. Am. Chem. Soc.*, 2002, **124**, 11480.
12 F. Wetz, K. Soulantica, M. Respaud, A. Falqui and B. Chaudret, *Mater. Sci. Eng., C*, 2007, **27**, 1162.
13 A. G. Roca, S. Veintemillas-Verdaguer, M. Port, C. Robic, C. J. Serna and M. P. Morales, *J. Phys. Chem. B*, 2009, **113**, 7033.
14 U. I. Tromsdorf, N. C. Bigall, M. Kaul, O. T. Bruns, M. S. Nikolic, B. Mollwitz, R. A. Sperling, R. Reimer, H. Hohenberg, W. J. Parak, S. Förster, U. Beisiegel, G. Adam and H. Weller, *Nano Lett.*, 2007, **7**, 2422.
15 G. Decher, *Science*, 1997, **277**, 1232.
16 G. Ladam, P. Schaad, J. C. Voegel, P. Schaaf, G. Decher and F. Cuisinier, *Langmuir*, 2000, **16**, 1249.
17 G. B. Sukhorukov, E. Donath, S. Davis, H. Lichtenfeld, F. Caruso, V. I. Popov and H. Möhwald, *Polym. Adv. Technol.*, 1998, **9**, 759.
18 E. Donath, G. B. Sukhorukov, F. Caruso, S. A. Davis and H. Möhwald, *Angew. Chem., Int. Ed.*, 1998, **37**, 2201.
19 B. Radt, T. A. Smith and F. Caruso, *Adv. Mater.*, 2004, **16**, 2184.
20 A. G. Skirtach, A. A. Antipov, D. G. Shchukin and G. B. Sukhorukov, *Langmuir*, 2004, **20**, 6988.
21 M. F. Bédard, D. Braun, G. B. Sukhorukov and A. G. Skirtach, *ACS Nano*, 2008, **2**, 1807.
22 M. F. Bédard, A. Munoz-Javier, R. Mueller, P. del Pino, A. Fery, W. J. Parak, A. G. Skirtach and G. B. Sukhorukov, *Soft Matter*, 2009, **5**, 148.
23 G. B. Sukhorukov, A. L. Rogach, M. Garstka, S. Springer, W. J. Parak, A. Muñoz-Javier, Oliver Kreft, A. G. Skirtach, A. S. Susha, Y. Ramaye, R. Palankar and M. Winterhalter, *Small*, 2007, **3**, 944.
24 P. Rivera Gil, L. L. del Mercato, P. del Pino, A. Munoz Javier and W. J. Parak, *Nano Today*, 2008, **3**, 12.
25 Z. Lu, M. D. Prouty, Z. Guo, V. O. Golub, C. S. Kumar and Y. M. Lvov, *Langmuir*, 2005, **21**, 2042.
26 O. Kreft, A. G. Skirtach, G. B. Sukhorukov and H. Mohwald, *Adv. Mater.*, 2007, **19**, 3142.
27 D. A. Gorin, S. A. Portnov, O. A. Inozemtseva, Z. Luklinska, A. M. Yashchenok, A. M. Pavlov, A. G. Skirtach, H. Mohwald and G. B. Sukhorukov, *Phys. Chem. Chem. Phys.*, 2008, **10**, 6899.

28 S. H. Hu, C. H. Tsai, C. F. Liao, D. M. Liu and S. Y. Chen, *Langmuir*, 2008, **24**, 11811.
29 B. Zebli, A. S. Susha, G. B. Sukhorukov, A. L. Rogach and W. J. Parak, *Langmuir*, 2005, **21**, 4262.
30 C.-A. J. Lin, R. A. Sperling, J. K. Li, T.-Y. Yang, P.-Y. Li, M. Zanella, W. H. Chang and W. J. Parak, *Small*, 2008, **4**, 334.
31 M. T. Fernández-Argüelles, A. Yakovlev, R. A. Sperling, C. Luccardini, S. Gaillard, A. S. Medel, J.-M. Mallet, J.-C. Brochon, A. Feltz, M. Oheim and W. J. Parak, *Nano Lett.*, 2007, **7**, 2613.
32 X. W. Wu, C. Liu, L. Li, P. Jones, R. W. Chantrell and D. Weller, *J. Appl. Phys.*, 2004, **95**, 6810.
33 P. de la Presa, T. Rueda, A. Hernando, J. M. Ramallo-Lopez, L. J. Giovanetti and F. G. Requejo, *J. Appl. Phys.*, 2008, **103**, 103909.
34 M. El-hilo, K. Ogrady and R. W. Chantrell, *J. Magn. Magn. Mater.*, 1992, **109**, L164.
35 J. L. Dormann, L. Bessais and D. Fiorani, *J. Phys. C: Solid State Phys.*, 1988, **21**, 2015.
36 C. Corot, P. Robert, J. M. Idee and M. Port, *Adv. Drug Delivery Rev.*, 2006, **58**, 1471.
37 R. A. Sperling, T. Liedl, S. Duhr, S. Kudera, M. Zanella, C.-A. J. Lin, W. Chang, D. Braun and W. J. Parak, *J. Phys. Chem. C*, 2007, **111**, 11552.

Maria Puerto Morales[1,*], Matthieu F. Bédard[2,3], Alejandro G. Roca[1], Patricia de la Presa[4], Antonio Hernando[4], Feng Zhang[5], Marco Zanella[5], Abbasi Azhar Zahoor[5], Gleb B. Sukhorukov[3], Loretta del Mercato[5], Wolfgang J. Parak[5,6,*]

Relaxation times of colloidal iron platinum in polymer matrixes

[1] Instituto de Ciencia de Materiales de Madrid, CSIC, C) Sor Juana Inés de la Cruz 3, Campus de Cantoblanco, 28049 Madrid, Spain
[2] Max-Planck Institute of Colloids and Interfaces, Potsdam 14424, Germany
[3] School of Engineering and Materials Science, Queen Mary, University of London, London E1 4NS, UK
[4] Instituto de Magnetismo Aplicado, UCM-ADIF-CSIC, P.O. Box 155, 28230 Las Rozas (Madrid), Spain
[5] Fachbereich Physik, Philipps Universität Marburg, Marburg, Germany
[6] Wissenschaftliches Zentrum für Materialwissenschaften, Philipps Universität Marburg, Marburg, Germany
* corresponding authors: Puerto@icmm.csic.es, wolfgang.parak@physik.uni-marburg.de

Supporting Information

I) Synthesis of FePt nanoparticles
II) Embedding of FePt nanoparticles in polyelectrolyte capsules

I) Synthesis of FePt nanoparticles
I.1) Chemicals
I.2) FePt synthesis
I.3) Comments to nanoparticle synthesis
I.4) Absorption spectra of FePt nanoparticles
I.5) Size characterization with transmission electron microscopy (TEM)

I.1) Chemicals
Octyl ether (99%), 1,2 hexadecanediol (Tech 90%) and iron pentacarbonyl (99.99%), oleic acid (Tech90%), oleyl amine (Tech 70%) were purchased from Sigma, platinum acetylacetonate (98%) was purchased from ABCR chemicals. All solvents used for precipitation and re-dispersion of the particles (methanol, ethyl acetate, chloroform, toluene and hexane) were purchased as anhydrous solvents from Sigma.

I.2) FePt synthesis
For the synthesis of the iron platinum particles we followed the recipe previously reported by Sun [5]. In this synthesis method a combination of oleic acid and oleyl amine was used to stabilize the monodisperse FePt colloids and prevent oxidation. FePt particles were obtained by the reduction of $Pt(acac)_2$ (acac= acetylacetonate, $CH_3COCHCOCH_3$) by a diol and the decomposition of $Fe(CO)_5$ in high-temperature solutions. 1,2-hexadecanediol was used to reduce the $Pt(acac)_2$ to Pt metal. Briefly in a 50 ml three neck flask 10 ml of octyl ether, 95 mg of $Pt(acac)_2$ and 195 mg of 1,2 hexadecanediol were mixed under nitrogen atmosphere. The temperature was raised to 100 ℃ until the solution turned into clear translucent yellow color. A mixture of oleic acid (0.08 ml), oleyl amine (0.08 ml), and iron pentacarbonyl (0.06 ml) was injected quickly under vigorous stirring into the $Pt(acac)_2$ solution. The mixture solution was heated to 280 ℃ at a heating rate of 12 ℃/min. The solution was incubated at this temperature for 15 minutes. Finally the heating mantle was removed to stop the reaction. At room temperature particles were precipitated from the solution by addition of anhydrous methanol (15 ml) and a small quantity of ethyl acetate (2-3 ml) in order to prevent phase separation of the solvents. The supernatant was discarded, and the precipitate could be redispersed in chloroform, toluene or hexane. If the precipitation of these particles was performed at a moderate speed (800 rpm) the re-dispersed solution was stable for months

I.3) Comments to nanoparticle synthesis
During the synthesis $Pt(acac)_2$ and 1,2 hexadecanediol dissolve well in octyl ether at 100^0C giving a clear translucent yellow solution. Sometimes we observed that, under the same conditions, the above mentioned chemicals were not dissolving well in octyl ether. As final result it was not possible to get a clear translucent yellow solution at 100^0C. In particular the solution sometimes started making gel near 150^0C when it was cooled down after reaching 280^0C. To dissolve this gel we used small amounts of toluene and the particles were precipitated again (at room temperature) using methanol and finally redispersed in chloroform. Nevertheless after one day these particles started precipitating in chloroform indicating that they were no longer stable. We think that this problem is due to the 1,2hexadecandiol: we had used two packages of this chemical (chemical#1 Cat#21,374-8, Lot# S10101-462; chemical#2 Cat# 21,374-8 Lot# S42511-277) from the same manufacturer. For chemical #1 the synthesis was working well and we did not observe any gel formation, also the particles were stable after precipitation in chloroform for months whereas for chemical #2 the synthesis process was less efficient (gel formation and particle precipitation were observed sometimes as described above). In summary 1,2hexadecanediol is very critical for the FePt particle synthesis.

I.4) Absorption spectra of FePt nanoparticles

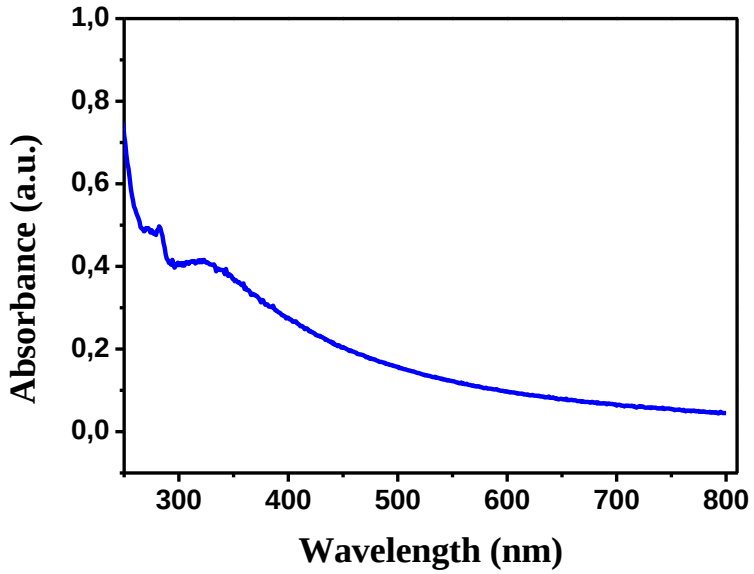

Figure SI-I.2.1: UV/vis absorption spectrum of FePt particles dissolved in chloroform.

I.5) Size characterization with transmission electron microscopy (TEM)

TEM analysis was carried out to characterize the morphology and the size distribution of the FePt nanoparticles. Here the nanoparticles dissolved in chloroform (before the polymer coating) are described. The average diameter of one FePt nanoparticle (only the inorganic FePt part, without the organic surfactant shell) was determined to be 3.16 ± 0.44 (3.2 ± 0.4) nm.

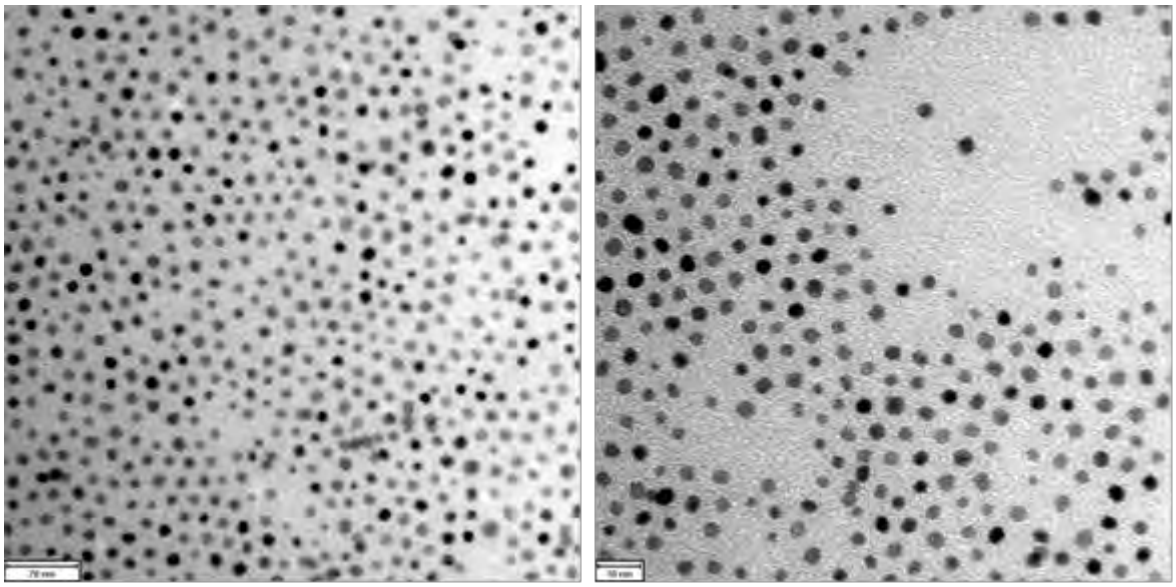

Figure SI-I.3.1: TEM images of FePt particles which had been dissolved in chloroform. The scale bars correspond to 20 and 10 nm.

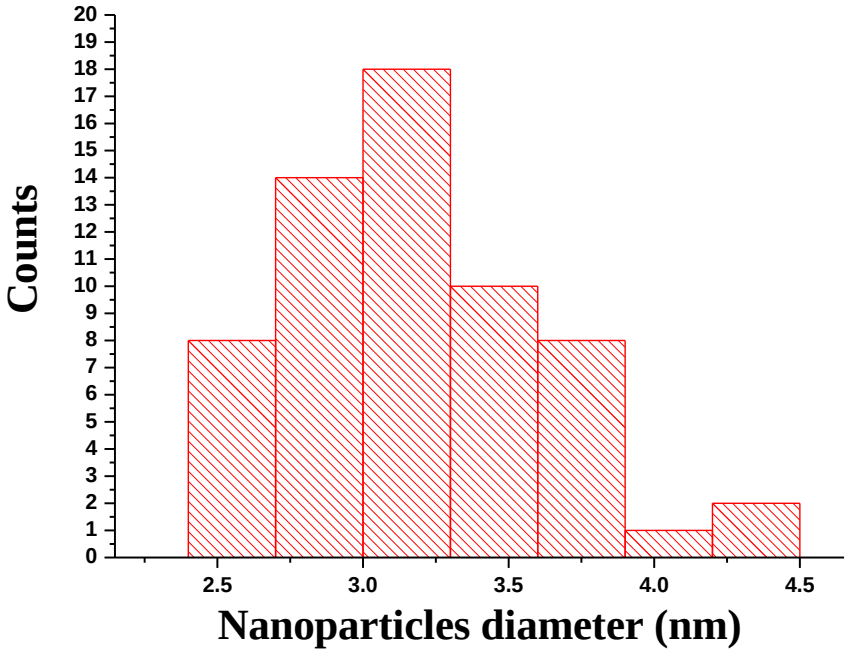

Figure SI-I.3.2: Histogram of the size distribution of the diameter of the FePt particles as obtained from the TEM images (3.2 ± 0.4 nm).

II) Embedding of FePt nanoparticles in polyelectrolyte capsules

Estimation of the number of FePt particles per capsule

To estimate the number of FePt nanoparticles per capsule, we calculated the number of Fe atoms per FePt nanoparticle (i), then we calculated the number of FePt nanoparticles in the sample solution (ii) and finally we calculated the number of FePt nanoparticles per capsule (iii). Below the legend used during the calculations is given.

a: refers to atoms
p: refers to particles
m^a_{Fe}: refers to the mass of 1 Fe atom
m^a_{Pt}: refers to the mass of 1 Pt atom
ρ_{FePt} : refers to density of FePt
V^P_{FePt}: refers to the volume of 1 FePt nanoparticle (diameter 3.16 ± 0.44 nm)
m^p_{FePt}: refers to the mass of 1 FePt nanoparticle (diameter 3.16 ± 0.44 nm)
m^a_{FePt}: refers to the mass of 1Fe + 1Pt atom
N^a_{FePt}: refers to the number of Fe atoms + number of Pt atoms in one FePt nanoparticle
N^a_{Fe}: refers to the number of Fe atoms per FePt particle
N^p_{FePt}: refers to the number of FePt particles in the sample solution
N_{Fe} = number of detected Fe atoms within the sample solution
c_{Fe} = concentration of Fe atoms in sample solution
V = Volume of sample solution
N_{caps} = number of capsules in the sample solution

(i) Calculation of the number of Fe atoms per FePt nanoparticle:

To calculate the number of Fe atoms per FePt nanoparticle firstly we calculated the mass of one FePt nanoparticle of 3.1 nm (m^{p}_{FePt}) using the following formula $\mathbf{m^{p}_{FePt} = \rho_{FePt} \bullet V^{p}_{FePt}}$, where $\mathbf{\rho_{FePt}}$ is the mass density of FePt which is **14 g/cm^3** as reported by Wu et al. [37] and $\mathbf{V^{p}_{FePt}}$ is the volume of one FePt nanoparticle calculated using the formula $\mathbf{V^{p}_{FePt} = 4/3\ \pi\ r^3}$, where **r** is the radius of one FePt nanoparticle. The calculated volume $\mathbf{V^{p}_{FePt}}$ is $\mathbf{1.65 \bullet 10^{-20}}$ **cm^3**. Using the above calculated $\mathbf{\rho_{FePt}}$ and $\mathbf{V^{p}_{FePt}}$ values, the mass of one FePt nanoparticle $\mathbf{(m^{p}_{FePt})}$ was calculated to be $\mathbf{2.31 \bullet 10^{-19}}$ **g**.

The total atomic mass of one Fe and one Pt atoms ($\mathbf{m^{a}_{FePt}}$) was obtained by adding the atomic mass of these two elements ($\mathbf{m^{a}_{FePt}: m^{a}_{Fe} + m^{a}_{Pt}}$). Given $\mathbf{m^{a}_{Fe}} = \mathbf{9.27 \bullet 10^{-23}}$ **g** and $\mathbf{m^{a}_{Pt}} = \mathbf{3.24 \bullet 10^{-22}}$ **g**, $\mathbf{m^{a}_{FePt}}$ is $\mathbf{4.17 \bullet 10^{-22}}$ **g**.

The number of Fe and Pt atoms in one 3.1 nm FePt nanoparticle was obtained by dividing the mass of one FePt nanoparticle ($\mathbf{m^{p}_{FePt}}$) with the total atomic mass of one Fe and one Pt atom ($\mathbf{m^{a}_{FePt}}$). We found 554 atoms of Fe and Pt in one FePt nanoparticle ($\mathbf{N^{a}_{FePt}}$). Since we assumed that there are 50% of Fe atoms and 50% Pt atoms in one FePt nanoparticle of 3.2 nm, the total number of Fe atoms in one FePt nanoparticle is $\mathbf{N^{a}_{Fe} = 277}$.

The error is directly correlated to the error in determining the volume of one FePt nanoparticle. As the diameter has been determined to be 3.16 ± 0.44 nm the volume $\mathbf{V^{p}_{FePt}}$ is 16,5 ± 6,0 nm^3. This corresponds to an error of 33%. In this way the accuracy in the number of Fe atoms in one FePt nanoparticle is $\mathbf{N^{a}_{Fe} = 277 \pm 91.}$

(ii) Calculation of the number of FePt nanoparticles in the sample solution (N^{p}_{FePt}):

From the ICP measurements we measured the Fe-concentration c_{Fe} for the capsules samples containing low (S2), medium (S3) and high (S4) concentration of FePt nanoparticles (see the capsule synthesis section). Moreover, the concentration of Fe of the original nanoparticle solution was measured (Control without capsules).

From the Fe concentration c_{Fe} we got the total number of Fe atoms (N_{Fe}) within each sample by $\mathbf{N_{Fe} = c_{Fe} \bullet V \bullet N_A}$ with the Avogadro number $\mathbf{N_A = 6.02 \bullet 10^{+23}}$.
The volume of the samples was **V = 2 ml**. Accuracy in the measurements is around 10%.

- Concentration of Fe atoms in S1 sample (Control: FePt particles without capsules)

  $\mathbf{c_{Fe} = 0.84 \bullet 10^{-3}}$ **mol / 2 ml**

  From this concentration value we got the total number of Fe atoms ($\mathbf{N_{Fe}}$) in this sample, which was $\mathbf{N_{Fe} = 5.06 \bullet 10^{+20}}$. As we know, one FePt particle contains 277 ± 91 ($\mathbf{N^{a}_{Fe}}$) Fe atoms, thus the number of FePt nanoparticle in the sample solution ($\mathbf{N^{p}_{FePt}}$) was calculated simply by dividing $\mathbf{N_{Fe}}$ with 277 and the calculated value was $\mathbf{N^{p}_{FePt} = 1.83 \bullet 10^{+18}}$.

- Concentration of Fe atoms in S2 sample (low capsule concentration)

  $\mathbf{c_{Fe} = 0.23 \bullet 10^{-3}}$ **mol / 2 ml**

  From this concentration value we got the total number of Fe atoms ($\mathbf{N_{Fe}}$) in this sample, which was $\mathbf{N_{Fe} = 1.39 \bullet 10^{+20}}$. The number of FePt nanoparticles in the solution thus was $\mathbf{N^{p}_{FePt}} = \mathbf{5.02 \bullet 10^{+17}}$.

- Concentration of Fe atoms in S3 sample (medium capsule concentration)

  $c_{Fe} = 0.44 \bullet 10^{-3}$ mol / 2 ml

  From this concentration value we got the total number of Fe atoms ($\mathbf{N_{Fe}}$) in this sample, which was $\mathbf{N_{Fe} = 2.65 \bullet 10^{+20}}$. The number of FePt nanoparticle in solution ($\mathbf{N^p_{FePt}}$) was $\mathbf{0{,}96 \bullet 10^{+18}}$.

- Concentration of Fe atoms in S4 sample (high capsule concentration)

  $c_{Fe} = 1.3 \bullet 10^{-3}$ mol / 2 ml

  From this concentration value we got the total number of Fe atoms ($\mathbf{N_{Fe}}$) in this sample, which was $\mathbf{N_{Fe} = 7.83 \bullet 10^{+20}}$. The number of FePt nanoparticles in the sample ($\mathbf{N^p_{FePt}}$) was $\mathbf{2.83 \bullet 10^{+18}}$.

Related to the accuracy in determining N^p_{FePt} the error of these values is around 30%.

(iii) Calculation of the number of FePt nanoparticles per capsule ($\mathbf{N^p_{FePt} / N_{caps}}$)

The number of capsules $\mathbf{N_{caps}}$ in the samples S2, S3, S4, and S5 (capsules without FePt) (with sample volume V = 2 ml) was counted

sample S2 : $\mathbf{N_{caps} = 1.8 \bullet 10^{+9}}$
sample S3: $\mathbf{N_{caps} = 2.8 \bullet 10^{+9}}$
sample S4: $\mathbf{N_{caps} = 4.1 \bullet 10^{+9}}$
sample S5: $\mathbf{N_{caps} = 2.8 \bullet 10^{+9}}$

Finally, the number of FePt nanoparticles per capsule was obtained by dividing the calculated number of FePt nanoparticles ($\mathbf{N^p_{FePt}}$) by the calculated number of capsules ($\mathbf{N_{caps}}$) in the original samples. Theses values ($\mathbf{N^p_{FePt}/N_{caps}}$) are reported in the Table 1 of capsule characterization section.

sample S2 : $\mathbf{N^p_{FePt}/N_{caps} = 5.02 \bullet 10^{+17} / 1.8 \bullet 10^{+9} = 2.8 \bullet 10^{+8}}$
sample S3: $\mathbf{N^p_{FePt}/N_{caps} = 0{,}96 \bullet 10^{+18} / 2.8 \bullet 10^{+9} = 3.4 \bullet 10^{+8}}$
sample S4: $\mathbf{N^p_{FePt}/N_{caps} = 2.83 \bullet 10^{+18} / 4.1 \bullet 10^{+9} = 6.9 \bullet 10^{+8}}$

As described above the major source of error is determination of the nanoparticle diameter due to the limited narrowness of the size distribution and in this way the amount of iron atoms per nanoparticle. Counting in FePt nanoparticles therefore has an error of around 33%, whereas error in counting capsules is associated to an error of 10%. Therefore errors in determination of $\mathbf{N^p_{FePt}/N_{caps}}$ are around 33%:

sample S2 : $\mathbf{N^p_{FePt}/N_{caps}} = \mathbf{(2.8 \pm 0.9) \bullet 10^{+8}}$
sample S3: $\mathbf{N^p_{FePt}/N_{caps} = (3.4 \pm 1.1) \bullet 10^{+8}}$
sample S4: $\mathbf{N^p_{FePt}/N_{caps} = (6.9 \pm 2.3) \bullet 10^{+8}}$

References:

1. A. E. T. Merbach, E., *The Chemistry of Contrast Agents in Medical Magnetic Resonance Imaging*, Wiley, New York, USA, 2001.
2. J. W. M. Bulte and D. L. Kraitchman, *Nmr In Biomedicine*, 2004, **17**, 484-499.
3. M. G. Harisinghani, K. S. Jhaveri, R. Weissleder, W. Schima, S. Saini, P. F. Hahn and P. R. Mueller, *Clinical Radiology*, 2001, **56**, 714-725.
4. Y. M. Huh, Y. W. Jun, H. T. Song, S. Kim, J. S. Choi, J. H. Lee, S. Yoon, K. S. Kim, J. S. Shin, J. S. Suh and J. Cheon, *Journal Of The American Chemical Society*, 2005, **127**, 12387-12391.
5. S. Sun, C. B. Murray, D. Weller, L. Folks and A. Moser, *Science*, 2000, **287**, 1989-1992.
6. M. Corti, A. Lascialfari, E. Micotti, A. Castellano, M. Donativi, A. Quarta, P. D. Cozzoli, L. Manna, T. Pellegrino and C. Sangregorio, *Journal Of Magnetism And Magnetic Materials*, 2008, **320**, E320-E323.
7. A. Figuerola, A. Fiore, R. Di Corato, A. Falqui, C. Giannini, E. Micotti, A. Lascialfari, M. Corti, R. Cingolani, T. Pellegrino, P. D. Cozzoli and L. Manna, *Journal Of The American Chemical Society*, 2008, **130**, 1477-1487.
8. V. F. Puntes, D. Zanchet, C. Erdonmez and A. P. Alivisatos, *J. Am. Chem. Soc.*, 2002, **124**, 12874-12880.
9. S. Sun, H. Zeng, D. B. Robinson, S. Raoux, P. M. Rice, S. X. Wang and G. Li, *Journal of the American Chemical society*, 2004, **126**, 273-279.
10. S. Sun and H. Zeng, *Journal of the American Chemical Society*, 2002, **124**, 8204-8205.
11. E. V. Shevchenko, D. V. Talapin, A. L. Rogach, A. Kornowski, M. Haase and H. Weller, *JACS*, 2002, **124**, 11480-11485.
12. F. Wetz, K. Soulantica, M. Respaud, A. Falqui and B. Chaudret, *Materials Science & Engineering C-Biomimetic And Supramolecular Systems*, 2007, **27**, 1162-1166.
13. A. G. Roca, S. Veintemillas-Verdaguer, M. Port, C. Robic, C. J. Serna and M. P. Morales, *J. Phys. Chem. B*, 2009, **in press**.
14. U. I. Tromsdorf, N. C. Bigall, M. Kaul, O. T. Bruns, M. S. Nikolic, B. Mollwitz, R. A. Sperling, R. Reimer, H. Hohenberg, W. J. Parak, S. Förster, U. Beisiegel, G. Adam and H. Weller, *Nanoletters*, 2007, **7**, 2422-2427.
15. G. Decher, *Science*, 1997, **277**, 1232-1237.
16. G. Ladam, P. Schaad, J. C. Voegel, P. Schaaf, G. Decher and F. Cuisinier, *Langmuir*, 2000, **16**, 1249-1255.
17. G. B. Sukhorukov, E. Donath, S. Davis, H. Lichtenfeld, F. Caruso, V. I. Popov and H. Möhwald, *Polymers for Advanced Technologies*, 1998, **9**, 759-767.
18. E. Donath, G. B. Sukhorukov, F. Caruso, S. A. Davis and H. Möhwald, *Angewandte Chemie International Edition*, 1998, **37**, 2202-2205.
19. B. Radt, T. A. Smith and F. Caruso, *Advanced Materials*, 2004, **16**, 2184-2189.
20. A. G. Skirtach, A. A. Antipov, D. G. Shchukin and G. B. Sukhorukov, *Langmuir*, 2004, **20**, 6988-6992.
21. M. F. Bedard, D. Braun, G. B. Sukhorukov and A. G. Skirtach, *Acs Nano*, 2008, **2**, 1807-1816.
22. M. F. Bedard, A. Munoz-Javier, R. Mueller, P. del Pino, A. Fery, W. J. Parak, A. G. Skirtach and G. B. Sukhorukov, *Soft Matter*, 2009, **5**, 148-155.
23. G. B. Sukhorukov, A. L. Rogach, M. Garstka, S. Springer, W. J. Parak, A. Muñoz-Javier, Oliver Kreft, A. G. Skirtach, A. S. Susha, Y. Ramaye, R. Palankar and M. Winterhalter, *SMALL*, 2007, **3**, 944-955.

24. P. Rivera Gil, L. L. del Mercato, P. del Pino, A. Munoz Javier and W. J. Parak, *Nano Today*, 2008, **3**, 12-21.
25. Z. Lu, M. D. Prouty, Z. Guo, V. O. Golub, C. S. Kumar and Y. M. Lvov, *Langmuir*, 2005, **21**, 2042-2050.
26. O. Kreft, A. G. Skirtach, G. B. Sukhorukov and H. Mohwald, *Advanced Materials*, 2007, **19**, 3142-+.
27. D. A. Gorin, S. A. Portnov, O. A. Inozemtseva, Z. Luklinska, A. M. Yashchenok, A. M. Pavlov, A. G. Skirtach, H. Mohwald and G. B. Sukhorukov, *Phys Chem Chem Phys*, 2008, **10**, 6899-6905.
28. S. H. Hu, C. H. Tsai, C. F. Liao, D. M. Liu and S. Y. Chen, *Langmuir*, 2008, **24**, 11811-11818.
29. B. Zebli, A. S. Susha, G. B. Sukhorukov, A. L. Rogach and W. J. Parak, *Langmuir*, 2005, **21**, 4262-4265.
30. C.-A. J. Lin, R. A. Sperling, J. K. Li, T.-Y. Yang, P.-Y. Li, M. Zanella, W. H. Chang and W. J. Parak, *Small*, 2008, **4**, 334-341.
31. M. T. Fernández-Argüelles, A. Yakovlev, R. A. Sperling, C. Luccardini, S. Gaillard, A. S. Medel, J.-M. Mallet, J.-C. Brochon, A. Feltz, M. Oheim and W. J. Parak, *NanoLetters*, 2007, **7**, 2613-2617.
32. P. de la Presa, T. Rueda, A. Hernando, J. M. Ramallo-Lopez, L. J. Giovanetti and F. G. Requejo, *Journal Of Applied Physics*, 2008, **103,** 103909.
33. M. El-hilo, K. Ogrady and R. W. Chantrell, *Journal Of Magnetism And Magnetic Materials*, 1992, **109**, L164-L168.
34. J. L. Dormann, L. Bessais and D. Fiorani, *Journal Of Physics C-Solid State Physics*, 1988, **21**, 2015-2034.
35. C. Corot, P. Robert, J. M. Idee and M. Port, *Advanced Drug Delivery Reviews*, 2006, **58**, 1471-1504.
36. R. A. Sperling, T. Liedl, S. Duhr, S. Kudera, M. Zanella, C.-A. J. Lin, W. Chang, D. Braun and W. J. Parak, *Journal of Physical Chemistry C*, 2007, **111**, 11552 -11559.
37. X. W. Wu, C. Liu, L. Li, P. Jones, R. W. Chantrell and D. Weller, *Journal of Applied Physics*, 2004, **95**, 6810-6812.

LbL multilayer capsules: recent progress and future outlook for their use in life sciences

Loretta L. del Mercato,*[a] Pilar Rivera-Gil,[a] Azhar Z. Abbasi,[a] Markus Ochs,[a] Carolin Ganas,[a] Inga Zins,[b] Carsten Sönnichsen[b] and Wolfgang J. Parak[a]

Received (in Zürich, Switzerland) 6th November 2009, Accepted 28th December 2009
First published as an Advance Article on the web 10th February 2010
DOI: 10.1039/b9nr00341j

In this review we provide an overview of the recent progress in designing composite polymer capsules based on the Layer-by-Layer (LbL) technology demonstrated so far in material science, focusing on their potential applications in medicine, drug delivery and catalysis. The benefits and limits of current systems are discussed and the perspectives on emerging strategies for designing novel classes of therapeutic vehicles are highlighted.

Introduction

In the last three decades nanotechnology has attracted great interest in nanomedicine. Recent reviews describe the current impact and future prospects of nanotechnology with respect to drug/gene delivery and other fields of nanomedicine such as biosensing.[1–4] The main objectives in developing controlled release are avoidance of biological barriers, increase of the *in vivo* efficiency of drugs and targeted drug administration.[1,5] In addition the development of sensitive, specific and stable sensors, which allow for real-time measurements of physiological levels of important molecular species directly in the site of disease, is highly desirable.[6,7] For these purposes, a wide variety of carriers based on different methods of preparation have been developed ranging from nano-materials (such as carbon nanotubes,[8,9] nanoparticles,[10–13] and nanocomposites[14]) to biomaterials (such as dendrimers,[15] liposomes,[16,17] block co-polymer micelles,[18] biodegradable polymers[19]). These materials show some attractive properties such as small size (1 to 100 nm), chemically tailorable physical properties, tunable shape and structural robustness. Nonetheless, in the last years great attention has been focused on the development of novel "multifunctional" platforms[4,20–22] which combine a variety of properties allowing for the simultaneous or sequential performance of multiple functions in single cells, including enzymatic catalysis, controlled release, directed drug delivery and sensing. The most important requirements of a multifunctional system include (i) increased longevity and stability of the carrier in the circulation, (ii) targeting to the site of the disease *via* both non-specific and specific mechanisms, (iii) stimuli sensitivity to the local environment of the pathological site (such as pH or temperature) or to externally applied stimuli (such as magnetic field, ultrasound, laser irradiation), (iv) enhanced intracellular delivery of the cargo/drug, (v) contrast agents for both intra-cellular imaging of the carrier and real-time measurement of certain analytes in the body.[20] In this context polyelectrolyte multilayer capsules fabricated *via* the Layer-by-Layer (LbL) technique[23] have emerged as an interesting platform for the assembly of multifunctional carrier systems.[24] LbL-based hollow multilayer polyelectrolyte microcapsules consist of two distinct compartments: the multilayer shell and the cavity. The shell is built up through the consecutive adsorption of oppositely charged species around a charged spherical template and is held together due to the strong electrostatic forces that take place between each component layer.[23,25] The cavity, which is obtained after removal of the sacrificial template, represents the main volume of the capsules in which chemical reactions can be performed[26,27] and in which a range of materials from small molecules[28,29] to macromolecules[30–32] can be encapsulated, thus protecting unstable cargo from the surrounding hostile environment, beside increasing their biodistribution and solubility. Thanks to the high versatility of the LbL technique, the two compartments can be easily manipulated to create different types

[a]*Fachbereich Physik and Wissenschaftliches Zentrum für Materialwissenschaften, Philipps Universität Marburg, Renthof 7, 35037 Marburg, Germany. E-mail: loretta.delmercato@physik.uni-marburg.de*
[b]*Institut für Physikalische Chemie, Universität Mainz, Jakob-Welder-Weg 11, 55128 Mainz, Germany*

Loretta L. del Mercato

Dr Loretta Laureana del Mercato received her MSc in Biotechnology from the University "Federico II" of Naples (Italy) in 2004. In 2007 she obtained her Ph.D. in Innovative Materials and Technologies from the National Nanotechnology Laboratory (NNL) of CNR-INFM, Lecce (Italy) with a thesis on "Nanoscale characterization of synthetic polypeptides for nanobiotechnology applications". Since February 2008, she has been a post-doctoral researcher in the Biophotonics group of Professor Wolfgang J. Parak in the Physics Department of the Philipps Universität of Marburg (Germany). Her current research interests include the synthesis, functionalization and characterization of carrier systems based on polyelectrolyte capsules for applications in the biomedical field.

of active systems with respect to specific application requirements. The general properties of LbL microcapsules regarding their synthesis, loading and release,[33–36] physicochemical[36,37] and mechanical[38] properties as well as their permeability,[33,34,39] have been comprehensively reviewed by many articles in the past few years. Therefore, in this review, we first provide a short overview of the main steps involved in the preparation and functionalization of LbL-derived capsules, then we give an overview about some of the very recent progress achieved by several groups on the design of novel composite microcapsules, focusing on their use as drug delivery vehicles, intracellular sensors, and microreactor containers. Finally, we discuss the benefits and limits of current systems and we try to highlight the perspectives of the emerging strategies based on these systems for designing novel classes of therapeutics vehicles.

LbL-derived capsules: preparation and functionalization

LbL adsorption of oppositely charged species around submicrometre and micrometre-sized charged colloidal particles is a multi-step process which allows the fabrication of multilayer polyelectrolyte capsules for a wide range of applications. The technique is based on LbL adsorption of oppositely charged polymers on colloidal templates, followed by core dissolution.[23,25] Fig. 1 summarizes the main steps involved in the assembly of a multilayer polyelectrolyte capsule, based on a spherical porous template, in which more components with different functions have been combined at separate regions (cavity, wall and external surface of the capsule) to create a single object capable of performing multiple functions simultaneously.[40] As can be observed, the properties of the capsules can be varied at each step employing building blocks with different properties. For example, by using templates of different diameter (from 60 nm to 10 μm), the size of the resulting capsules can be tuned,[25,32,37,41] whereas by using different types of component layers, such as synthetic polyelectrolytes,[25,42] charged and not charged biopolymers,[43–47] the chemical properties of the multilayer shell can be tailored. Moreover the multilayer shell can be modified by simultaneously loading charged inorganic nanoparticles to yield capsules responsive to specific external stimuli.[48–51] Finally the surface of the capsules can be decorated to give low-fouling capsules by the adsorption of a poly(ethylene glycol)-based layer[52,53] or targeted capsules through the coupling of specific recognition elements (*e.g.*, antibodies).[54] In the following the range of materials used so far for each step of fabrication and their main properties are described.

The main classes of decomposable templates used for LbL assembly of capsules have been extensively reviewed in previous articles.[37,39,40] Briefly, capsules have been fabricated by using organic (*i.e.*, polystyrene latex,[55] melamine formaldehyde,[25] silicon dioxide[37]) or inorganic templates[41,56,57] (*i.e.*, $MnCO_3$, $CaCO_3$ $CdCO_3$) dissolvable in acidic or aqueous solvents, respectively. The choice of the initial core influences significantly the properties of the capsules such as their size distribution and the strategy used for loading the active molecules like dyes and drugs inside the cavities.[29,58,59] For instance, capsules based on organic cores are typically characterized by a good monodispersity and their cavities can be filled after the dissolution of the core by changing the permeability of the multilayer shell through variations in pH,[60–62] solvent polarity,[63] ionic strength[64,65] or temperature[59,64] (post-loading method). Instead

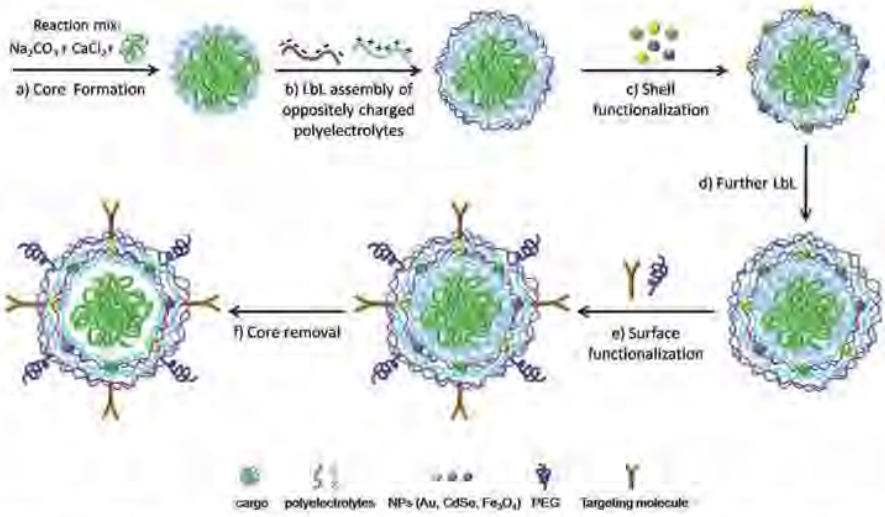

Fig. 1 Schematic illustration of the synthesis of a multifunctional polyelectrolyte capsule *via* LbL assembly. (a) A spherical $CaCO_3$ porous template is synthesized by mixing two solutions of Na_2CO_3 and $CaCl_2$ in presence of the cargo molecules (such as drugs, genes or proteins). The cargo molecules are embedded in the pores of the template. (b) The filled $CaCO_3$ particles are then coated *via* consecutive LbL deposition of oppositely charged polyelectrolytes to grow a multilayer polymer shell around the template. (c) The shell can be functionalized by loading charged NPs (such as metal, fluorescent and magnetic NPs) onto an oppositely charged layer during the LbL assembly. (d) LbL of polyelectrolytes is repeated to obtain a stable multilayer shell. (e) Additional surface functionalization to improve cellular uptake (*e.g.* targeting moieties) or *in vivo* longevity (*e.g.* conjugation of PEG) can be performed *via* electrostatic or covalent binding of molecules to the outer surface. (f) Finally the spherical template is removed to obtain a multilayer capsule with cargo molecules inside its cavity. Capsules are not drawn to scale. Only few layers of polyelectrolyte and of NPs are shown for sake of clarity.

capsules based on porous inorganic cores, such as carbonate crystals, can be directly loaded by mixing the cargo molecules with the porous templates, followed by the LbL coating with polyelectrolytes pairs (pre-loading method).[32,56] Because after the dissolution process some oligomers of the original core material can partially remain adsorbed within the shell,[66] capsules based on biocompatible templates, such as porous $CaCO_3$,[58] mesoporous silica[32] or polylactides microparticles (PLGA, PLA),[67] are typically preferred especially for biological applications.

Beside the choice of the cores, also the choice of the shell components plays a pivotal role in the LbL assembly since it directly influences the biocompatibility and degradability of the capsules inside living organisms. On one hand, capsules made of intracellular biodegradable shell components such as polyaminoacids (*i.e.* poly-L-arginine), synthetic polymers (*i.e.* poly(hydroxypropyl)methacrylamide dimethylaminoethyl (p(HPMA-DMAE))[47] or chitosan[43,45,68] are very useful for biomedical applications related to the delivery of active compounds such as genes, proteins or drugs inside living organisms.[69] On the other hand, biocompatible but not "easily" degradable polyelectrolytes are necessary for other applications like sensing inside cells *i.e.* determination of the intracellular ion concentration of different organelles.[70] For such applications the synthetic bio-incompatible polylelectrolytes sodium poly(styrene sulfonate, sodium salt) (PSS), poly(allylamine hydrochloride) (PAH) and polydiallyl dimethyl ammonium chloride (PDADMAC) have been widely used up to now.[59,71] The challenge for these capsule-based systems might rely on the ability of synthesizing biocompatible capsules stable enough in the different environments inside the different organelles so that they can accurately inform about the local environment of the capsules.

The capsule wall can be functionalized to impart optical, magnetic and photothermal properties to microcapsules by introducing during the LbL process inorganic charged nanoparticles (NPs)[48–51] through the use of electrostatic interactions (Fig. 2). The shell modification with different types of nanoparticles allows for addressing important functions such as the labelling, the targeting and the controlled opening of the capsules which are essential for using these systems as carriers for drug delivery and sensing applications. For example, by modifying the walls of the capsules with fluorescent nanoparticles non invasive optical detection of the capsules inside living organisms can be performed.[72–74] By incorporating magnetic nanoparticles to fluorescent capsules (*e.g.*, functionalized with organic dye molecules or light-emitting quantum dots), capsules with dual-imaging functionalities, magnetic resonance (MR) imaging and luminescent properties, can be produced for their use as biomarkers *in vitro* and *in vivo*.[75–77] Additionally, magnetic NPs-modified capsules can be externally manipulated using magnetic fields for directing and accumulating capsules to the target region (*e.g.*, cancer cells) before delivering the chemotherapeutic drugs. For instance, by using Fe_3O_4-particle-modified capsules a specific accumulation and high local concentration of the NPs-modified capsules was observed along a magnetic field gradient and their internalization by breast cancer cells *in vitro*.[78] Finally by embedding gold, silver and magnetic NPs into the capsule walls, the release of encapsulated drug molecules from the cavities can be achieved upon exposure to an external physical trigger such as electromagnetic or sound waves.[49,50,79,80] In a recent work, the laser irradiation of gold-modified capsules has been used to locally heat the metal NPs and to perturb the integrity/permeability of the walls of the capsules inducing the release of cargo from the cavities of single capsules to the cytosol of the cells.[71] Gold nanorods (Au NRs)[81,82] have been also employed as absorbing elements of the capsule walls for light-controlled release of encapsulated material.[83] Like Au NPs, charged Au NRs can be embedded within the multilayer shell during the LbL deposition of oppositely charged layers around the sacrificial template[84] (Fig. 2b and Fig. 3b). The use of gold nanorods allows producing capsules with near-infrared absorbing properties whose opening can be induced by using laser wavelength which corresponds to the tissue transparency window (800–900 nm). Capsules with such properties might be very promising for biomedical applications. Fig. 3a shows the mechanism of photoactivated release of cargo from the cavity of a polyelectrolyte capsule containing Au NRs in the walls: laser irradiation leads to local heating of the metal nanorods and subsequent opening of small pores within the capsule wall. In Fig. 3c is reported the effect of the laser irradiation of a FITC-dextran loaded capsule with the following multilayer shell $(PSS/PAH)_3(PSS/AuNRs)(PAH/PSS)_2$. Before laser illumination, the intact capsule retains the green cargo inside the cavity (phase contrast and green channel images). During laser illumination the irradiated capsule is deformed because of the heating of the Au NRs. After switching-off the laser the capsule shell appears damaged, as it can be observed in the phase contrast image, and the partial release of the fluorescent cargo can be noticed in the corresponding fluorescent channel. Alternatively to laser irradiation

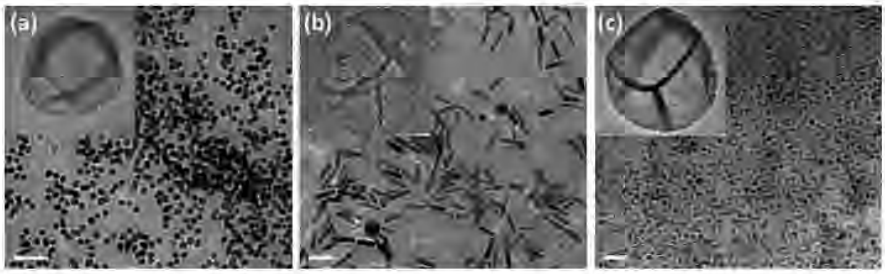

Fig. 2 Functionalization of polyelectrolyte capsules with inorganic nanoparticles incorporated in the multilayer shell. Typical TEM images of (a) Au NPs, (b) Au NRs and (c) Fe_3O_4 NPs embedded inside the multilayer shell of hollow $(PSS/PAH)_4$ capsules. Insets show the single nanoparticles-modified capsules. Scale bars represent 50 nm.

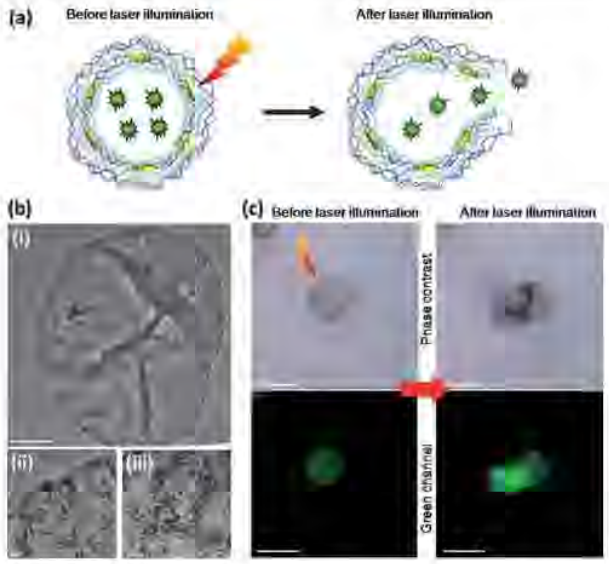

Fig. 3 Laser-opening of FITC-dextran loaded capsule with Au NRs embedded in the capsule wall. (a) Schematic representation of the geometry of a capsule with green dextran as cargo (green stars) encapsulated inside the cavity and Au NRs (yellow rods) embedded in the wall: laser irradiation of Au NRs-capsule (left) leads to local heating of the metal NRs and subsequent rupture of the capsule wall (right). (b) Representative TEM image of a single Au NRs-capsule (i) (scale bar 1 μm). (ii-iii) Two high-resolution images of the multilayer wall of the capsule shown in (i) (Scale bars 50 nm). (c) Effect of near-IR laser irradiation (830 nm) of a single Au NRs-capsule loaded with FITC-dextran. Before laser illumination: the capsule retains the green cargo inside the cavity. After laser illumination: the multilayer wall of the capsule is damaged (phase contrast) and the partial release of the green cargo throughout the small pores of the wall is observed (green channel) (scale bars 5 μm).

methods, ultrasound treatment of gold-doped capsules has been used to mechanically disintegrate the capsule walls.[85] In a different approach, high-frequency magnetic field (HFMF) has been proven to trigger the release of drugs from microcapsules prepared by loading Fe_3O_4 NPs into the walls.[86]

Capsules made of new components as layers

Besides conventional polyelectrolytes, a variety of substances have been investigated in the last years to construct capsules through LbL assembly. Generally these capsules display improved permeability properties and especially new features such as biocompatibility, degradability and controlled destructability, making them attractive for applications in the fields of pharmacology, medicine and cosmetics *etc.* In this section we describe some of the recent strategies exploited by several groups to fabricate LbL-derived capsules made of new combinations of building blocks (polymeric micelles, polysaccharides, proteins, liposome and oligonucleotides) as integral components of the capsules wall.

Hollow microcapsules containing polymeric micelles in their walls have been fabricated by alternating assembly of PAH and poly(styrene-b-acrylic acid) (PS-b-PAA) micelles on $MnCO_3$ microparticles.[87] In such a system, the micelles serve as hydrophobic reservoirs with a high loading capacity in the shells while the LbL shell provides the micelles with additional support and protection. Besides their potential use as a drug delivery vehicle, these capsules may also provide an alternative option to serve as bioreactors and biosensors.[87]

Iron-heparin hollow sub-micrometre capsules have been fabricated by alternating deposition of oppositely charged ferric ions(III) and heparin (a highly-sulfated glycosaminoglycan widely used as anticoagulant[88]) onto the surface of the polystyrene latex (PS) particles, followed by removal of the PS templates by dissolution.[89] The resulting capsules displayed longer anticoagulant activity in *in vitro* and *in vivo* assays compared with the same dose of an aqueous solution of heparin,[89] suggesting their potential use as injectable anticoagulant vehicles in the bloodstream.

Single-component degradable capsules based on poly(methacrylic acid) (PMA) cross-linked *via* disulfide linkages have been assembled and loaded with the protein transferrin[90] and oligonucleotides.[91] These capsules undergo a reversible swelling in response to changes in external pH, and degrade in the presence of a physiological concentration of a natural thiol-containing peptide (*i.e.*, glutathione)[92] releasing the cargo molecules in a reducing environment.

Disulfide bonds (S–S) have also been employed to cross-link the shell of protein-based microcapsules leading to capsules which are destroyable by organisms and cells. For example, bovine serum albumin (BSA) mono-component hollow microcapsules were fabricated by desolvation of BSA onto $MnCO_3$ microparticles followed by cross-linking with disulfide-containing dithiobis(succinimidylpropionate) (DSP) and subsequent core removal.[93] Destruction of the BSA microcapsules was achieved under the treatment with a reductive agent ($NaBH_4$) and with a further treatment of ultrasonication, indicating that these microcapsules are stabilized not only by S–S covalent bonds but also by other non-covalent forces (*i.e.*, hydrophobic forces and hydrogen bonds).[93] In another work, hemoglobin (Hb) microcapsules crosslinked by glutaraldehyde (GA) were fabricated through covalent LbL assembly onto $MnCO_3$ microparticles.[94] In this approach, the use of GA to crosslink proteins has been shown to lead to significant improvements in the permeability of Hb capsules in contrast to polyelectrolyte capsules.[94] In a further work, CF0F1-proteoliposomes, previously prepared by incorporating the chloroplastic F0F1-ATP synthase (CF0F1-ATP) into liposomes, were mixed with a suspension of Hb capsules leading to the adsorption of lipids on the capsule surface and the assembly of CF0F1-ATP synthase onto the capsule shells. The resulting lipid-coated Hb microcapsules were successfully used to synthesize ATP.[95]

Enzymatic proteins have been also used as layers to grow multilayer shells capable of performing specific reactions. Qi *et al.*, fabricated glucose-sensitive microcapsules from the LbL assembly of Hb and glucose oxidase (GOD) followed by cross-linking of the protein layers with GA.[96] The formation of hydrogen peroxide (H_2O_2) upon processing glucose, catalyzed by GOD and Hb, indicated that the proteins were still enzymatically active after their immobilization in the multilayer. In addition, the author observed a glucose-stimulated enhancement of the wall permeability probably due to the decrease in the local pH and the loosening of the multilayer structure. In a further work,

the author employed this pH dependent behaviour to control the release of insulin molecules encapsulated inside glucose-sensitive multilayer shells.[97] Briefly, GOD and catalase (CAT) were assembled onto insulin particles alternately *via* GA cross-linking. As expected, the release ratio of insulin from the protein multilayers was observed to linearly increase in response to addition of external glucose because of the increased permeability of the capsule wall[97] (Fig. 4). The described approach is interesting because it represents a proof of concept for potential applications of biocatalytic capsules sensitive to specific analytes for the controlled release of drugs.

Recently, the technologies of liposomes and LbL assembly have been combined to fabricate polyelectrolyte-coated magnetic liposomes with the aim of protecting the lipid bilayer with a polyelectrolyte multilayer shell, thus avoiding their fusion. Lately, superparamagnetic nanoparticles were encapsulated in liposomes and the resulting charged liposomes were used as templates for the stepwise LbL adsorption of the polyelectrolytes PAH and PSS. These polyelectrolyte-coated magnetic liposomes could be delivered to living cells and manipulated by applying an external magnetic field.[98] In a different approach, Caruso and co-workers combined liposomes and polyelectrolyte capsules to fabricate so-called capsosomes, a hybrid platform in which the properties/advantages of the two systems are merged. The capsosomes were formed through initial coating of silica cores with a precursor of PAH, followed by adsorption of 50 nm-sized DOPC liposomes and subsequent layering of PSS and PAH[99] (Fig. 5). However, since electrostatic interactions alone showed to provide insufficient affinity between liposomes and the underlying polymer surface, the authors developed a modified protocol in which cholesterol-modified polymers were used as noncovalent anchors for the loading of liposomes into the capsules. In this work the enzyme β-lactamase has been preloaded into the liposomes before their entrapment inside the polymer capsules and the presence of the active enzyme within

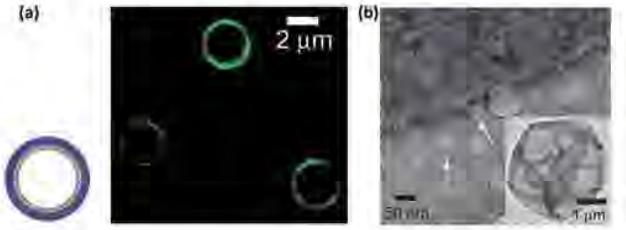

Fig. 5 Typical morphology of (PAH/liposomes$_{NBD}$/(PSS/PAH)$_4$/PSS) capsosome. (a) Scheme of the geometry of a capsosome with liposome embedded in its wall, CLSM image and (b) negative stained TEM image of capsosomes. The black arrows identify structurally intact liposomes, while the white arrows indicate areas where the liposomes have been displaced. The inset shows a complete capsosome. [Adapted from ref. 99.]

the as-prepared capsosomes has been confirmed by quantitative enzymatic reaction.[100] The main novelty of the presented approach consists on the synthesis of a hybrid microreactor system which contains numerous liposome subcompartments (about 8×10^3) in which different enzymatic reactions might be carried out simultaneously.

The use of DNA as shell component has also been demonstrated recently.[101] Multilayer DNA shells were formed by alternately depositing diblock oligonucleotides containing two different regions (one of which is complementary to the adsorbed single-stranded block in the film, whereas the second region is free for hybridization in the subsequent layer). In a related work the authors developed a method to encapsulate various nucleic acids inside degradable polyelectrolyte capsules.[91] Capsules entirely composed of DNA (as cargo and as shell constituents) could be of particular interest because they are biodegradable, biocompatible, and their physicochemical properties (*e.g.*, size, permeability, structure and shrinkage) can be finely controlled by base pairing of the nucleotides.

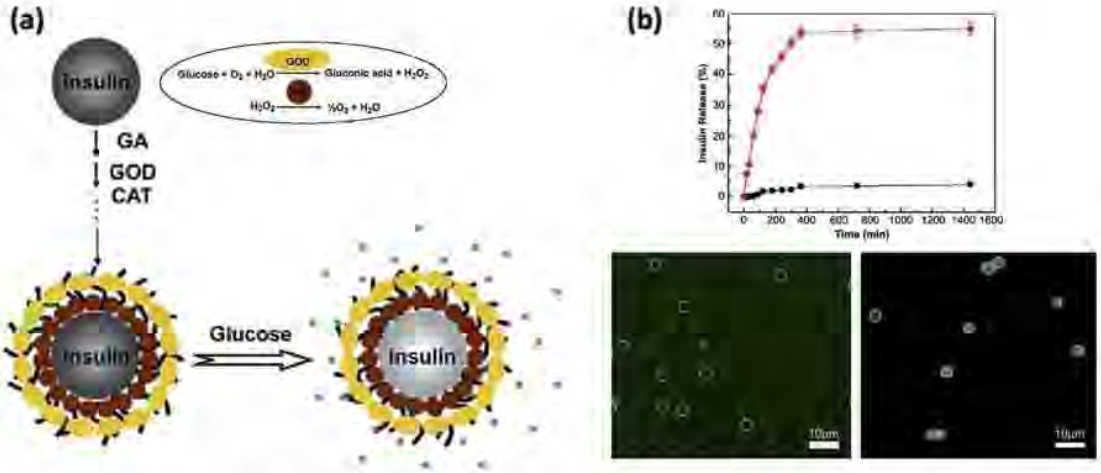

Fig. 4 Controlled release of insulin from glucose-sensitive enzyme multilayer shells. (a) Schematic representation of coupled reactions of glucose oxidase (GOD) and catalase (CAT) assembled onto insulin particles followed by the enhanced permeability of the capsule for release of insulin. (b) Top: Release profiles of coated insulin particles before (black line) and after (red line) external application of glucose solution, respectively. Bottom: CLSM images of (CAT/GOD)$_5$ microcapsules mixed with FITC dextran (2000 kDa): (i) before and (ii) after adding glucose solution. [Adapted from ref. 97.]

Biostability in physiological environments

One of the main problems of charged systems is that they are easily cleared from the organism by serum protein adsorption (opsonization) and subsequent phagocytosis. Covalent linkage of PEG (poly(ethylene glycol)) or other hydrophilic polymers to the surface of several carrier systems have displayed to reduce their non-specific uptake by the cells (including cells from the mononuclear phagocyte system) due to their enhanced low-fouling properties.[20,102–104] Since the main stabilizing forces in polyelectrolyte capsules are electrostatic interactions, the efficient binding of a PEG corona to the surface of the capsule has to be carried out by previous linkage of PEG to highly charged substances like polyelectrolytes. In this way, modified PEG can be strongly and stably attached to charged surfaces by electrostatic interactions. Modifying the surface of the polyelectrolyte multilayer capsules by adding polyelectrolyte (*i.e.* poly(L-lysine))-*graft*-PEG molecules has been a successful strategy to resist protein adsorption and therefore opsonization.[52,105–107] As mentioned before, the main forces that stabilize LbL assembled systems are based on electrostatic interactions. This makes such systems very sensitive to environmental conditions such as changes in the ionic strength of the medium or in the temperature and thus susceptible to disassembly. Although systems assembled in this way can be tailored to take advantage of these properties, for some biomedical applications this can be an important limitation. Recent approaches have developed capsules whose synthesis combines the electrostatic forces *via* LbL assembly and covalent cross-linking *via* click chemistry.[108] This versatile approach has several advantages: (i) low charged polyelectrolytes can be now incorporated to the LbL (after incorporation of covalent bonds); (ii) linkage groups that remain unreacted can be easily post-functionalized; (iii) due to the mild, non-harmful conditions of the click chemistry, sensitive cargo (easy denaturizable active molecules like protein, nucleic acids) can be incorporated.[106] Nevertheless, post-functionalization of the capsule surface is still an important feature under investigation. With click chemistry, all reactions are catalyzed by copper, thus leading to cytotoxic effects,[106] although very recently a metal-catalyst-free approach has been developed to introduce functional groups to the multilayer of the capsules.[109]

Cytotoxicity

Regarding the cytotoxicity of the capsules, although not yet well studied, the main sources for toxicity come obviously from the polyelectrolytes composing the wall as well as from the functionalities embedded in the cavity and/or in the wall.[40] The magnitude of the cytotoxic effect of the capsules is primarily concentration- and time-dependent.[69,110] Additionally, the intrinsic chemical properties of the positively charged polyelectrolyte (polycation) turned out to make them effective triggers of mitochondrial-mediated cell death (apoptosis/necrosis).[111,112] Due to their positive charge, polycations cause cellular membrane damage with subsequent activation of signalling pathways that end up with mitochondrial depolarization and generation of reactive oxygen species resulting in cell death. In this regard, together with the molecular weights, the cationic charge density of the polycations are key parameters for the interaction with cell membrane and cell damage.[113,114] Furthermore, polycations containing (poly)amine functionalities may result in an increased interaction with anionic intracellular components that also lead to oxygen-independent cell death.[115] In this regard, a reduction of the cytotoxicity could be obtained by using materials that are already present in the cells *i.e.* lipids and proteins as natural polyions. Owing to their amphiphilic character, cellular lipids can aggregate in aqueous solution into spherically closed bilayer structures due to hydrophobic interactions. When the aqueous solution contains a charged protein, a self-assembly process that combines electrostatic interactions and hydrophobic forces occurs in the immiscible interface. The result is the adsorption of proteins and lipids onto the interface of emulsion droplets and the formation of a multilayer elastic shell.[116] Despite the compatibility of these biomimetic capsules and the potential to incorporate molecular functionalities like channels or receptors, the main approach of this technique still relies in controlling the size of the capsules and the unwanted degradation of the system.

Applications in medicine

One of the possible contributions of LbL-derived multilayer capsules to medicine is their use as biocompatible multifunctional composite carrier systems that are sensitive to remote guidance and activation for local release of cargo molecules (*i.e.* drugs) inside target cells/tissues.[40] Due to the high versatility of the LbL technique, not only hydrophilic molecules can be loaded but also hydrophobic molecules (*i.e.* many therapeutical drugs) have been efficiently encapsulated and released thus overcoming the obstacles of hydrophobicity.[117] To date it is a fact that polyelectrolyte multilayer capsules of different sizes (from nanometre to micrometre) are taken up by living cells.[69,118] The incorporation of the capsules occurs spontaneously and is non-cell specific. Therefore the addition of low-fouling polymers which posses protein-repellent qualities is required besides targeting features toward the design of novel vehicles for targeted drug delivery *in vivo*. For instance, microcapsules coated with a layer of PEG-grafted polyelectrolytes have been shown to escape clearance by the mononuclear phagocytic system.[52,105,106] As previously described, the release of the transported cargo molecules can occur under exposure to external stimuli (*e.g.*, light- or ultrasound-treatment of nanoparticles modified capsules) or more challenging, by using the conditions of the local environment of the capsules (*i.e.* intracellularly).[68,97] Recent publications have proven the use of biodegradable capsules for the delivery of pro-drugs inside the cells.[47,119] Pro-drugs are the non-active form of a medicament that needs to be enzymatically hydrolysed to release the active form of the drug. Fig. 6 shows a capsule-based system sensitive to enzymatic degradation at two distinct positions.[119] Both the capsule wall and the encapsulated cargo (in this case a pro-drug) are easily degraded by proteases located inside the cells. The intracellular degradation of the capsule wall leads to the release of the pro-drug and enables activation of the drug through enzymatic cleavage. Furthermore, sustained release of the cargo molecules is obtained by the continuous enzymatic digestion of the capsule membrane.[119] In this way, several main requirements for drug delivery are achieved. The incorporation of highly environmental-sensitive

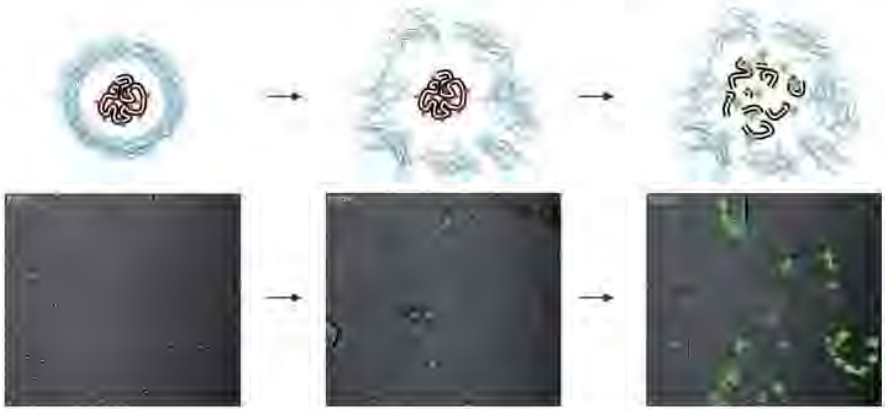

Fig. 6 Cargo release and activation mediated by intracellular degradation of capsules. Capsule walls are of DEXS/pARG and the cavity is filled with a fluorogenic substrate for proteases (DQ-OVA™). Upon cellular internalization, the capsule wall is actively degraded enzymatically, this lead specific enzymes to reach the cargo proteins (ovalbumine, OVA). When OVA is structurally intact, the fluorescence of the dyes conjugated to ovalbumine are quenched. On the contrary, when OVA is enzymatically cleavaged the quenching effect is relieved and a bright green fluorescence appears. As a result of the cleavage of OVA, single dye-labeled peptides are released out of the capsule. [Adapted from ref. 119.]

cargos (*i.e.* pro-drug or proteins) inside the capsule protects both the cargo from unwanted degradation and healthy cells from the action of the drug. Since less concentration of the drug could be administered in order to reach therapeutic concentrations, the side effects would be reduced. Thus, the intracellular degradation would enable the controlled release of cargo over a long period of time locally.

Anticancer drugs such as doxorubicin (DOX) have been demonstrated to be released upon changes in the pH of a solution.[120] Since the location of the capsules seems to be in acidic compartments,[70] by choosing the right materials that provide a good compromise between swelling and stiffness, drugs can be released from the capsules over time in a controlled manner self-regulated by the intracellular conditions. The low pH of the acidic vesicles where the capsules are transported causes swelling of the multilayer[121] with an initial rapid release of the drug due to high differences in the drug concentration between the bulk and the capsule cavity and followed by a plateau. The release can continue over a period of time until degradation of the capsule has been finalized or the entire amount of drug has been released. *In vivo* studies have demonstrated that this might be possible by using DOX-loaded biodegradable polyelectrolytes alternatively attached to doped $CaCO_3$-carboxylmethyl cellulose (CMS) templates. After chemical removal of the $CaCO_3$, CMS forms a complex with DOX and is stabilized in the capsule cavity. Direct injection of the loaded-capsules to the tumor of a mouse, led to a sustained release of DOX for 4 weeks, probably due to a non-favorable thermodynamic process at low pH, and resulted in a reduction of the tumor.[45]

The LbL approach appears to be a helpful technique not only for anticancer therapy but also for vaccination. One of the main challenges in vaccination is the efficient delivery of effective doses and the co-delivery of adjuvants with the antigen in order to generate sufficient immune response. Self-exploding microcapsules made of a semi-permeable polyelectrolyte multilayer around a sugar-based hydrophilic microgel core (size around 10 μm) have emerged as a "single shot" delivery system for the release of antigens in multiple pulses.[122] Due to the large size of the core, smaller carriers can be incorporated in the gel. Because of the semi-permeable conditions of the wall, water can penetrate causing a strong swelling of the gel that finally leads to the rupture of the microcontainer followed by the "shooting" of the smaller carriers that are able to propagate in water faster than if they were in solution. This is of special importance when the species has to be released in viscous medium. By tuning the density of the microgel, the resistance to disruption can be modulated and the microcontainers are able to release cargo (*i.e.* vaccines) at different times.

Conclusion/outlook

In this review we have highlighted some of the recent progresses of designing and utilizing novel types of multifunctional LbL-based multilayer capsules. LbL-assembled capsules are very versatile platforms which can be used to encapsulate, to store and to delivery cargo molecules. Their selective permeability allows to load not only different types of molecules, ranging from ions to macromolecules, but also to perform chemical reactions inside the interior. In addition, they can be easily functionalized with various natural molecules or inorganic nanoparticles to create multifunctional materials with hybrid properties.

Nowadays several *in vitro*[45,118,123–125] and *in vivo* studies[45,89] have established the use of these capsules as carriers in living systems. Notably, capsules with different physicochemical properties have been produced for different applications ranging from simultaneous imaging and delivery of biologically active molecules,[72–74] to intracellular sensing and bio-reactors.[26,27,70,96,126,127] Capsules modified by metal nanoparticles capable of protecting molecules in their cavities and release them by light irradiation, have been fabricated and characterized.[71,80] As an alternative to active release mechanisms, biocompatible controlled-release by using capsules made of biodegradable polymer shells which are gradually decomposed within the cellular environment, have been demonstrated.[47,119]

Nevertheless, there are still some challenges left to be overcome for further development of LbL capsules systems for drug

delivery and therapeutic purposes. In particular, the preparations of capsules need to be improved in terms of particles dispersion and aggregation as well as new efficient methods for the large-scale production have to be developed since production of capsules is often time-consuming and at the laboratory scale. In addition there is a need for more generally applicable strategies to efficiently encapsulate water-soluble low molecular weight drugs, in fact most capsule shells show pores size around 10 nm which are often the reason of fast diffusion of the cargo out of the cavities. Regarding this issue, the recent data obtained by Song and colleagues are promising: the authors showed the efficient entrapment of a small drug procainamide hydrochloride (PrH), molecular weight 271.79, inside (PDADMAC/PSS) capsules by heat treatment and shrinking of the capsules.[28]

The cellular uptake pathway and the degradation/release kinetics have to be intensively investigated for optimization of these systems in biological applications. The cytotoxicity and immune response of capsules need to be evaluated in more detail for clinical application. Also future improvements in developing new molecules and in studying new active targeting and controlled release mechanisms are essential in order to assemble new complex functional systems transferrable to the clinic. For example, the development of capsules with multiple compartments able to simultaneously transport multiple therapeutics agents in pathological sites would be very promising for tumors/cancer therapies. Such systems could then co-deliver anticancer drugs and small interfering RNA (siRNA) to inhibit genetic components of the tumors. It is expected that the cooperation between different scientific communities (bioengineers, chemists, physicists, biologists, bio-nanotechnologists) might be the best approach to overcome the limits of the available current systems by designing novel materials capable of fulfilling the needs of different communities.

Acknowledgements

This work was supported by the BMBF within the ERANET Neuron framework.

References

1 R. Langer and D. A. Tirrell, *Nature*, 2004, **428**, 487 492.
2 O. C. Farokhzad and R. Langer, *ACS Nano*, 2009, **3**, 16 20.
3 M. Ferrari, *Nat. Rev. Cancer*, 2005, **5**, 161 171.
4 J. Peteiro-Cartelle, M. Rodríguez-Pedreira, F. Zhang, P. Rivera Gil, L. L. del Mercato and W. J. Parak, *Nanomedicine*, 2009, **4**, 967 979.
5 D. Peer, J. M. Karp, S. Hong, O. C. FaroKHzad, R. Margalit and R. Langer, *Nat. Nanotechnol.*, 2007, **2**, 751 760.
6 A. Merkoçi, Biosensing Using Nanomaterials, *Wiley Series In Nanoscience and Nanotechnology*, 2009.
7 R. Freeman, R. Gill, I. Shweky, M. Kotler, U. Banin and I. Willner, *Angew. Chem., Int. Ed.*, 2009, **48**, 309 313.
8 S. J. Son, X. Bai and S. Lee, *Drug Discovery Today*, 2007, **12**, 657 663.
9 S. J. Son, X. Bai and S. B. Lee, *Drug Discovery Today*, 2007, **12**, 650 656.
10 E. Boisselier and D. Astruc, *Chem. Soc. Rev.*, 2009, **38**, 1759 1782.
11 M. Arruebo, R. Fernandez-Pacheco, M. R. Ibarra and J. Santamaria, *Nano Today*, 2007, **2**, 22 32.
12 L. Zhang, F. X. Gu, J. M. Chan, A. Z. Wang, R. S. Langer and O. C. Farokhzad, *Clin. Pharmacol. Ther.*, 2008, **83**, 761 769.
13 R. A. Sperling, P. Rivera_Gil, F. Zhang, M. Zanella and W. J. Parak, *Chem. Soc. Rev.*, 2008, **37**, 1896 1908.
14 J. H. Adair, T. Li, T. Kido, K. Havey, J. Moon, J. Mecholsky, A. Morrone, D. R. Talham, M. H. Ludwig and L. Wang, *Mater. Sci. Eng., R*, 1998, **23**, 139 242.
15 H. L. Crampton and E. E. Simanek, *Polym. Int.*, 2007, **56**, 489 496.
16 Y. Malam, M. Loizidou and A. M. Seifalian, *Trends Pharmacol. Sci.*, 2009, **30**, 592 599.
17 A. Samad, Y. Sultana and M. Aqil, *Curr. Drug Delivery*, 2007, **4**, 297 305.
18 K. Kataoka, A. Harada and Y. Nagasaki, *Adv. Drug Delivery Rev.*, 2001, **47**, 113 131.
19 Y. Yang, W. Jia, X. Qi, C. Yang, L. Liu, Z. Zhang, J. Ma, S. Zhou and X. Li, *Macromol. Biosci.*, 2004, **4**, 1113 1117.
20 V. Torchilin, *Eur. J. Pharm. Biopharm.*, 2009, **71**, 431 444.
21 S. A. Corr, Y. P. Rakovich and Y. K. Gun'ko, *Nanoscale Res. Lett.*, 2008, **3**, 87 104.
22 E. Tasciotti, X. W. Liu, R. Bhavane, K. Plant, A. D. Leonard, B. K. Price, M. M. C. Cheng, P. Decuzzi, J. M. Tour, F. Robertson and M. Ferrari, *Nat. Nanotechnol.*, 2008, **3**, 151 157.
23 G. Decher, *Science*, 1997, **277**, 1232 1237.
24 G. B. Sukhorukov, A. L. Rogach, M. Garstka, S. Springer, W. J. Parak, A. Muñoz-Javier, Oliver Kreft, A. G. Skirtach, A. S. Susha, Y. Ramaye, R. Palankar and M. Winterhalter, *Small*, 2007, **3**, 944 955.
25 E. Donath, G. B. Sukhorukov, F. Caruso, S. A. Davis and H. Möhwald, *Angew. Chem., Int. Ed.*, 1998, **37**, 2201 2205.
26 L. Dähne, S. Leporatti, E. Donath and H. Mohwald, *J. Am. Chem. Soc.*, 2001, **123**, 5431 5436.
27 D. G. Shchukin and G. B. Sukhorukov, *Adv. Mater.*, 2004, **16**, 671 682.
28 W. Song, Q. He, H. Möhwald, Y. Yang and J. i. L, *J. Controlled Release*, 2009, **139**, 160 166.
29 F. Caruso, W. J. Yang, D. Trau and R. Renneberg, *Langmuir*, 2000, **16**, 8932 8936.
30 R. Georgieva, S. Moya, M. Hin, R. Mitlohner, E. Donath, H. Kiesewetter, H. Mohwald and H. Baumler, *Biomacromolecules*, 2002, **3**, 517 524.
31 F. Caruso, D. Trau, H. Möhwald and R. Renneberg, *Langmuir*, 2000, **16**, 1485 1488.
32 A. M. Yu, Y. J. Wang, E. Barlow and F. Caruso, *Adv. Mater.*, 2005, **17**, 1737.
33 G. B. Sukhorukov, A. Fery, M. Brumen and H. Mohwald, *Phys. Chem. Chem. Phys.*, 2004, **6**, 4078 4089.
34 G. Sukhorukov, A. Fery and H. Möhwald, *Prog. Polym. Sci.*, 2005, **30**, 885 897.
35 Bruno G. De Geest, Niek N. Sanders, Gleb B. Sukhorukov, Joseph Demeestera and S. C. D. Smedt, *Chem. Soc. Rev.*, 2007, **36**, 636 649.
36 A. P. R. Johnston, C. Cortez, A. S. Angelatos and F. Caruso, *Curr. Opin. Colloid Interface Sci.*, 2006, **11**, 203 209.
37 C. S. Peyratout and L. Dähne, *Angew. Chem., Int. Ed.*, 2004, **43**, 3762 3783.
38 A. Fery and R. Weinkamer, *Polymer*, 2007, **48**, 7221 7235.
39 A. Antipov and G. B. Sukhorukov, *Adv. Colloid Interface Sci.*, 2004, **111**, 49 61.
40 P. Rivera Gil, L. L. del Mercato, P. del Pino, A. Munoz Javier and W. J. Parak, *Nano Today*, 2008, **3**, 12 21.
41 G. B. Sukhorukov, D. V. Volodkin, A. M. Günther, A. I. Petrov, D. B. Shenoy and H. Möhwald, *J. Mater. Chem.*, 2004, **14**, 2073 2081.
42 W. J. Tong and C. Y. Gao, *Polym. Adv. Technol.*, 2005, **16**, 827 833.
43 G. Berth, A. Voigt, H. Dautzenberg, E. Donath and H. Mohwald, *Biomacromolecules*, 2002, **3**, 579 590.
44 X. P. Qiu, S. Leporatti, E. Donath and H. Mohwald, *Langmuir*, 2001, **17**, 5375 5380.
45 Q. Zhao, B. Han, Z. Wang, C. Gao, C. Peng and J. Shen, *Nanomedicine*, 2007, **3**, 63 74.
46 A. M. Yu, I. R. Gentle and G. Q. Lu, *J. Colloid Interface Sci.*, 2009, **333**, 341 345.
47 B. G. De Geest, R. E. Vandenbroucke, A. M. Guenther, G. B. Sukhorukov, W. E. Hennink, N. N. Sanders, J. Demeester and S. C. d. Smedt, *Adv. Mater.*, 2006, **18**, 1005 1009.
48 F. Caruso, A. S. Susha, M. Giersig and H. Möhwald, *Adv. Mater.*, 1999, **11**, 950 953.
49 A. G. Skirtach, A. A. Antipov, D. G. Shchukin and G. B. Sukhorukov, *Langmuir*, 2004, **20**, 6988 6992.

50 A. S. Angelatos, B. Radt and F. Caruso, *J. Phys. Chem. B*, 2005, **109**, 3071 3076.
51 Z. Lu, M. D. Prouty, Z. Guo, V. O. Golub, C. S. Kumar and Y. M. Lvov, *Langmuir*, 2005, **21**, 2042 2050.
52 R. Heuberger, G. Sukhorukov, J. Vörös, M. Textor and H. Möhwald, *Adv. Funct. Mater.*, 2005, **15**, 357 366.
53 C. R. Kinnane, K. Wark, G. K. Such, A. P. R. Johnston and F. Caruso, *Small*, 2009, **5**, 444 448.
54 C. Cortez, E. Tomaskovic-Crook, A. P. R. Johnston, B. Radt, S. H. Cody, A. M. Scott, E. C. Nice, J. K. Heath and F. Caruso, *Adv. Mater.*, 2006, **18**, 1998 2003.
55 F. Caruso, *Chem. Eur. J.*, 2000, **6**, 413 419.
56 D. V. Volodkin, N. I. Larionova and G. B. Sukhorukov, *Biomacromolecules*, 2004, **5**, 1962 1972.
57 A. A. Antipov, G. B. Sukhorukov, S. Leporatti, I. L. Radtchenko, E. Donath and H. Möhwald, *Colloids Surf., A*, 2002, **198–200**, 535 541.
58 D. V. Volodkin, A. I. Petrov, M. Prevot and G. B. Sukhorukov, *Langmuir*, 2004, **20**, 3398 3406.
59 K. Köhler and G. B. Sukhorukov, *Adv. Funct. Mater.*, 2007, **17**, 2053 2061.
60 T. Mauser, C. Dejugnat and G. B. Sukhorukov, *Macromol. Rapid Commun.*, 2004, **25**, 1781 1785.
61 Z. An, H. Möhwald and J. Li, *Biomacromolecules*, 2006, **7**, 580 585.
62 G. B. Sukhorukov, A. A. Antipov, A. Voigt, E. Donath and H. Mohwald, *Macromol. Rapid Commun.*, 2001, **22**, 44 46.
63 Y. Lvov, A. A. Antipov, A. Mamedov, H. Möhwald and G. B. Sukhorukov, *Nano Lett.*, 2001, **1**, 125 128.
64 C. Y. Gao, S. Leporatti, S. Moya, E. Donath and H. Mohwald, *Chem. Eur. J.*, 2003, **9**, 915 920.
65 A. A. Antipov, G. B. Sukhorukov and H. Mohwald, *Langmuir*, 2003, **19**, 2444 2448.
66 C. Y. Gao, S. Moya, H. Lichtenfeld, A. Casoli, H. Fiedler, E. Donath and H. Möhwald, *Macromol. Mater. Eng.*, 2001, **286**, 355 361.
67 D. B. Shenoy, A. A. Antipov, G. B. Sukhorukov and H. Mohwald, *Biomacromolecules*, 2003, **4**, 265 272.
68 Y. Itoh, M. Matsusaki, T. Kida and M. Akashi, *Biomacromolecules*, 2008, **9**, 2202 2206.
69 S. De Koker, B. G. De Geest, C. Cuvelier, L. Ferdinande, W. Deckers, W. E. Hennink, S. De Smedt and N. Mertens, *Adv. Funct. Mater.*, 2007, **17**, 3754 3763.
70 O. Kreft, A. Muñoz_Javier, G. B. Sukhorukov and W. J. Parak, *J. Mater. Chem.*, 2007, **17**, 4471 4476.
71 A. Muñoz Javier, P. d. Pino, M. Bedard, A. G. Skirtach, D. Ho, G. Sukhorukov, C. Plank and W. J. Parak, *Langmuir*, 2008, **24**, 12517 12520.
72 A. Rogach, A. Susha, F. Caruso, G. Sukhorukov, A. Kornowski, S. Kershaw, H. Möhwald, A. Eychmüller and H. Weller, *Adv. Mater.*, 2000, **12**, 333 337.
73 N. Gaponik, I. L. Radtchenko, M. R. Gerstenberger, Y. A. Fedutik, G. B. Sukhorukov and A. L. Rogach, *Nano Lett.*, 2003, **3**, 369 372.
74 N. Gaponik, I. L. Radtchenko, G. B. Sukhorukov, H. Weller and A. L. Rogach, *Adv. Mater.*, 2002, **14**, 879 882.
75 S. Mornet, S. Vasseur, F. Grasset and E. Duguet, *J. Mater. Chem.*, 2004, **14**, 2161 2175.
76 C. Corot, P. Robert, J. M. Idee and M. Port, *Adv. Drug Delivery Rev.*, 2006, **58**, 1471 1504.
77 V. I. Shubayev, T. R. Pisanic and S. H. Jin, *Adv. Drug Delivery Rev.*, 2009, **61**, 467 477.
78 B. Zebli, A. S. Susha, G. B. Sukhorukov, A. L. Rogach and W. J. Parak, *Langmuir*, 2005, **21**, 4262 4265.
79 A. G. Skirtach, C. Dejugnat, D. Braun, A. S. Susha, W. J. Parak, H. Möhwald and G. B. Sukhorukov, *Nano Lett.*, 2005, **5**, 1371 1377.
80 M. F. Bédard, D. Braun, G. B. Sukhorukov and A. G. Skirtach, *ACS Nano*, 2008, **2**, 1807 1816.
81 C. Sönnichsen, T. Franzl, T. Wilk, G. von Plessen, J. Feldmann, O. Wilson and P. Mulvaney, *Phys. Rev. Lett.*, 2002, **88**, 077402.
82 A. Henkel, A. Jakab, G. Brunklaus and C. Sonnichsen, *J. Phys. Chem. C*, 2009, **113**, 2200 2204.
83 A. G. Skirtach, P. Karageorgiev, B. G. De_Geest, N. Pazos-Perez, D. Braun and G. B. Sukhorukov, *Adv. Mater.*, 2008, **20**, 506 510.
84 T. V. Bukreeva, B. V. Parakhonskiy, I. V. Marchenko, B. N. Khlebtsov, N. G. Khlebtsov, O. V. Dementieva, M. N. Savvateev, L. A. Feigin and a. M. V. Kovalchuk, *Nanotechnol. Russ.*, 2008, **3**, 85 93.
85 A. G. Skirtach, B. G. De_Geest, A. Mamedov, A. A. Antipov, N. A. Kotov and G. B. Sukhorukov, *J. Mater. Chem.*, 2007, **17**, 1050 1054.
86 S. H. Hu, C. H. Tsai, C. F. Liao, D. M. Liu and S. Y. Chen, *Langmuir*, 2008, **24**, 11811 11818.
87 Y. Zhu, W. J. Tong, C. Y. Gao and H. Mohwald, *Langmuir*, 2008, **24**, 7810 7816.
88 R. Lever and C. P. Page, *Nat. Rev. Drug Discovery*, 2002, **1**, 140 148.
89 L. Yu, Y. G. Gao, X. L. Yue, S. Q. Liu and Z. F. Dai, *Langmuir*, 2008, **24**, 13723 13729.
90 A. N. Zelikin, J. F. Quinn and F. Caruso, *Biomacromolecules*, 2006, **7**, 27 30.
91 A. N. Zelikin, Q. Li and F. Caruso, *Angew. Chem., Int. Ed.*, 2006, **45**, 7743 7745.
92 A. N. Zelikin, Q. Li and F. Caruso, *Chem. Mater.*, 2008, **20**, 2655 2661.
93 Y. Zhu, W. J. Tong, C. Y. Gao and H. Mohwald, *J. Mater. Chem.*, 2008, **18**, 1153 1158.
94 L. Duan, Q. He, X. H. Yan, Y. Cui, K. W. Wang and J. B. Li, *Biochem. Biophys. Res. Commun.*, 2007, **354**, 357 362.
95 W. Qi, L. Duan, K. W. Wang, X. H. Yan, Y. Citi, Q. He and J. B. Li, *Adv. Mater.*, 2008, **20**, 601 605.
96 W. Qi, X. Yan, L. Duan, Y. Cui, Y. Yang and J. Li, *Biomacromolecules*, 2009, **10**, 1212 1216.
97 W. Qi, X. H. Yan, J. B. Fei, A. H. Wang, Y. Cui and J. B. Li, *Biomaterials*, 2009, **30**, 2799 2806.
98 J. F. Pereira da Silva Gomes, A. Rank, A. Kronenberger, J. Fritz, M. Winterhalter and Y. Ramaye, *Langmuir*, 2009, **25**, 6793 6799.
99 B. Städler, R. Chandrawati, K. Goldie and F. Caruso, *Langmuir*, 2009, **25**, 6725 6732.
100 B. Städler, R. Chandrawati, A. D. Price, S. F. Chong, K. Breheney, A. Postma, L. A. Connal, A. N. Zelikin and F. Caruso, *Angew. Chem., Int. Ed.*, 2009, **48**, 4359 4362.
101 A. P. R. Johnston, E. S. Read and F. Caruso, *Nano Lett.*, 2005, **5**, 953 956.
102 L. van Vlerken, T. Vyas and M. Amiji, *Pharm. Res.*, 2007, **24**, 1405.
103 G. Prencipe, S. M. Tabakman, K. Welsher, Z. Liu, A. P. Goodwin, L. Zhang, J. Henry and H. J. Dai, *J. Am. Chem. Soc.*, 2009, **131**, 4783 4787.
104 V. C. F. Mosqueira, P. Legrand, A. Gulik, O. Bourdon, R. Gref, D. Labarre and G. Barratt, *Biomaterials*, 2001, **22**, 2967 2979.
105 U. Wattendorf, O. Kreft, M. Textor, G. B. Sukhorukov and H. P. Merkle, *Biomacromolecules*, 2008, **9**, 100 108.
106 C. J. Ochs, G. K. Such, B. Stadler and F. Caruso, *Biomacromolecules*, 2008, **9**, 3389 3396.
107 A. J. Khopade and F. Caruso, *Langmuir*, 2003, **19**, 6219 6225.
108 B. G. De Geest, W. Van Camp, F. E. Du Prez, S. C. De Smedt, J. Demeester and W. E. Hennink, *Chem. Commun.*, 2008, 190 192.
109 L. A. Connal, C. R. Kinnane, A. N. Zelikin and F. Caruso, *Chem. Mater.*, 2009, **21**, 576 578.
110 C. Kirchner, A. M. Javier, A. S. Susha, A. L. Rogach, O. Kreft, G. B. Sukhorukov and W. J. Parak, *Talanta*, 2005, **67**, 486 491.
111 A. C. Hunter, *Adv. Drug Delivery Rev.*, 2006, **58**, 1523 1531.
112 D. Fischer, Y. X. Li, B. Ahlemeyer, J. Krieglstein and T. Kissel, *Biomaterials*, 2003, **24**, 1121 1131.
113 T. Bieber, W. Meissner, S. Kostin, A. Niemann and H. P. Elsasser, *J. Controlled Release*, 2002, **82**, 441 454.
114 W. T. Godbey, K. K. Wu and A. G. Mikos, *J. Biomed. Mater. Res.*, 1999, **45**, 268 275.
115 N. Seiler and F. Raul, *J. Cell. Mol. Med.*, 2005, **9**, 623 642.
116 J. B. Li, H. Mohwald, Z. H. An and G. Lu, *Soft Matter*, 2005, **1**, 259 264.
117 K. Wang, Q. He, X. Yan, Y. Cui, W. Qi, L. Duana and J. Li, *J. Mater. Chem.*, 2007, **17**, 4018 4021.
118 A. Muñoz Javier, O. Kreft, M. Semmling, S. Kempter, A. G. Skirtach, O. Bruns, P. del Pino, M. F. Bedard, J. Rädler, J. Käs, C. Plank, G. Sukhorukov and W. J. Parak, *Adv. Mater.*, 2008, **20**, 4281 4287.
119 P. Rivera-Gil, S. De Koker, B. G. De Geest and W. J. Parak, *Nano Lett.*, 2009, **9**, 4398 4402.

120 X. L. Yang, X. Han and Y. H. Zhu, *Colloids Surf., A*, 2005, **264**, 49 54.
121 C. Déjugnat and G. B. Sukhorukov, *Langmuir*, 2004, **20**, 7265 7269.
122 B. G. De Geest, M. J. McShane, J. Demeester, S. C. De Smedt and W. E. Hennink, *J. Am. Chem. Soc.*, 2008, **130**, 14480 14482.
123 Y. J. Wang, V. Bansal, A. N. Zelikin and F. Caruso, *Nano Lett.*, 2008, **8**, 1741 1745.
124 Z. H. An, K. Kavanoor, M. L. Choy and L. J. Kaufman, *Colloids Surf., B*, 2009, **70**, 114 123.
125 M. Semmling, O. Kreft, A. Muñoz Javier, G. B. Sukhorukov, J. Käs and W. J. Parak, *Small*, 2008, **4**, 1763 1768.
126 M. J. McShane, J. Q. Brown, K. B. Guice and Y. M. Lvov, *J. Nanosci. Nanotechnol.*, 2002, **2**, 411 416.
127 U. Reibetanz, D. Haloan, M. Brumen and E. Donath, *Biomacromolecules*, 2007, **8**, 1927 1933.

Anal Bioanal Chem (2010) 396:1095–1103
DOI 10.1007/s00216-009-3347-y

ORIGINAL PAPER

Evaluation of quantum dots applied as switchable layer in a light-controlled electrochemical sensor

Zhao Yue · Waqas Khalid · Marco Zanella · Azhar Zahoor Abbasi · Andrea Pfreundt · Pilar Rivera Gil · Kirsten Schubert · Fred Lisdat · Wolfgang J. Parak

Received: 9 October 2009 /Revised: 15 November 2009 /Accepted: 24 November 2009 /Published online: 30 December 2009

Abstract Gold electrodes with switchable conductance are created by coating the gold surface with different colloidal quantum dots. For the quantum dot immobilization, a dithiol compound was used. By polarizing the electrode and applying a light pointer, local photocurrents were generated. The performance of this setup was characterized for a variety of different nanoparticle materials regarding drift and signal-to-noise ratio. We varied the following parameters: quantum dot materials and immobilization protocol. The results indicate that the performance of the sensor strongly depends on how the quantum dots are bound to the gold electrode. The best results were obtained by inclusion of an additional polyelectrolyte film, which had been fabricated using layer-by-layer assembly.

Zhao Yue and Waqas Khalid contributed equally to this study.

Z. Yue · W. Khalid · M. Zanella · A. Z. Abbasi · A. Pfreundt · P. Rivera Gil · W. J. Parak
Department of Physics, Philipps University Marburg, 35037 Marburg, Germany

Z. Yue
Department of Electronics, Nankai University, 300071 Tianjin, China

K. Schubert · F. Lisdat
Biosystems Technology, University of Applied Sciences Wildau, 1574 Wildau, Germany

W. J. Parak (✉)
Wissenschaftliches Zentrum für Materialwissenschaften, Philipps University Marburg, 35037 Marburg, Germany
e-mail: wolfgang.parak@physik.uni-marburg.de

Keywords Light-addressable potentiometric sensor · Quantum dots · Photocurrent

Introduction

In standard sensor arrays, each active spot typically needs to be connected with one individual wire. As the number of required wires of an $n \times n$ sensor matrix scales with n^2, sensor arrays with a large number of active spots are technologically challenging [1]. For this reason, several research groups have worked toward sensors in which the active spot where the measurement takes place is selected via optical illumination instead of hardware wiring. The basic idea of such a light-addressable potentiometric sensor (LAPS) is rather simple [2, 3]. The original surface of a LAPS electrode comprises a semiconductor and insulator layer. Due to the bad conductivity of the insulator, no DC current flow is possible. However, if parts of the device are optically illuminated with a modulated light source, the local AC conductivity goes up due to the creation of electron-hole pairs. This creates a local short circuit which and thus defines the active spot, where an AC photocurrent can flow [1, 3]. By scanning a light pointer along the sensor surface, any site can be selectively defined as active spot at which the measurement is supposed to take place [4–7].

By immobilizing different enzymes at distinct locations of the sensor surface, different enzymatic reactions could be detected by subsequently switching the light pointer to the different locations to read out the respective electrochemical signal via measurement of the local photocurrent [8–17]. The lateral resolution, i.e., the size of the smallest possible active spot which can be achieved, is on the order of a few micrometers to a few tens of micrometers. This is

due to that fact that light-generated electron-hole pairs can laterally diffuse within the semiconductor layer [18] and that photocurrent can flow wherever free charge carriers are available [19–26]. Better spatial resolution should be obtained by preventing lateral movement of free charge carriers within the semiconductor layer. This might be achieved by using a semiconductor layer, which is composed out of a lot of small semiconducting islands distributed along the sensor surface, which are not electrically connected. We have recently created a prototype of such a device by coating the surface of a gold electrode with a film of discrete colloidal semiconductor nanoparticles (quantum dots (QDs)) [27–29]. We were able to demonstrate the principle of obtaining a light-generated and concentration-dependent photocurrent, but we have not investigated the spatial resolution of the device yet.

Besides being a light-modulated switch for conductance, the colloidal semiconductor nanoparticles can uptake or deliver electrons from the environment [30–33]. We have demonstrated this by using the redox protein cytochrome *c* and a low molecular weight substrate (superoxide) in solution above a nanoparticle-covered gold electrode [28]. Although the protein was not directly linked to the nanoparticle layer, we were able to record changes in the photocurrent due to electron transfer from the substrate via the protein to the nanoparticles and then to the gold electrode. This could be also shown for high molecular weight, enzymatic reaction partners of cytochrome *c* such as nitrate reductase [34]. Since a direct tunnelling of electrons between the active centers of enzymes to colloidal nanoparticles has also been shown for first examples [34–36], this may open a new field of research where direct protein electrochemistry can be combined with light-triggered readout of electrodes for analytical purpose.

However, here we want to address a different aspect. In our prototype, light-generated DC photocurrent is achieved by a semiconductor layer only (see Fig. 1), in contrast to the AC photocurrent of the original LAPS, which also involves an insulator layer. Such spatially resolved DC photocurrent by selective illumination of different parts of the sensor surface has been already demonstrated before [37]. DC current can flow, as in case of illumination, and the semiconductor layer has enhanced conductivity compared to the situation without illumination. As in the literature, a huge variety of different colloidal semiconductor nanoparticles are reported [38, 39], and the major aim of the present report was to investigate the dependence of the material of the nanoparticle on some characteristic parameters of the device. We have thus to point out that in this report, the device is not used for the actual sensing of analytes, as we did not integrate any sensitive layer. This report is about the characterization of the construction of the device with the goal of improving stability and signal-to-noise ratio of the readout.

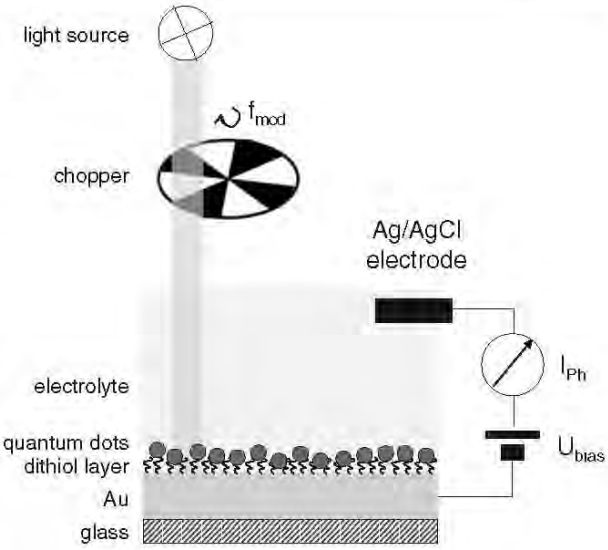

Fig. 1 A gold chip (glass coverslip with film of evaporated Au; the Ti layer between Au and glass which solely promotes adhesion of Au on glass is not drawn) is coated with a layer of dithiols onto which colloidal QDs have been adsorbed. A bias voltage U_{bias} is applied between the gold chips and a reference electrode in the electrolyte above the gold chip. The gold chip is illuminated with a light source with power P_{Illum}, and the corresponding DC current $I_{Ph(DC)}$ is measured in dependence of the bias voltage. The illumination can be optionally modulated with a chopper of frequency f_{mod}. In this case, the amplitude $\langle I_{Ph(AC)} \rangle$ of the modulated photocurrent is measured with a lock-in amplifier. The *angle brackets* indicate that the lock-in converts the modulated AC current $I_{Ph(AC)}$ in a DC current $\langle I_{Ph(AC)} \rangle$, which corresponds to the amplitude of the modulated AC current

Materials and methods

Semiconductor nanoparticles (QDs) were grown via thermal decomposition of precursors under the presence of organic surfactant molecules following published procedures. In particular, we synthesized spherical CdSe [40], CdSe/ZnS [41], CdS [42], and CdTe particles and rod-shaped CdSe [42] and stored them in toluene.

Particles were immobilized on glass chips, which had been covered with a 100-nm-thick evaporated Au film on top of a 20 nm Ti layer (which was used as adhesion mediator of the Au film) in the following way: Initially, Au electrodes were sonicated in ethanol and acetone for 5 min each, and then they were cleaned by using cyclic voltammetry in 1 M NaOH for 15–20 min and later in 500 mM H_2SO_4 for 25–30 min. After cleaning the electrodes, the following method was adopted for immobilizing the nanoparticles. The cleaned Au electrodes were incubated in 50 mM 1,4 benzene-dithiol for 40 h. Then the electrodes were

rinsed with toluene to remove excess of 1,4 benzene-dithiol. We now applied three different methods of immobilization. In the first case, the Au electrodes were simple incubated in QD solutions for 48 h. Again the electrodes were rinsed with toluene to remove excess of unbound QDs. In the second case, the Au electrodes were spin-coated with QD solution, and a QD film formed by evaporation of the toluene. In the third case, QDs were brought to the Au electrodes by spin coating, as described in the second case. After this, 10 bilayers of PSS/PAH (sodium poly(styrene sulfonate)/poly(allylamine hydrochloride)) were place on top of the QD layer by layer-by-layer assembly [43].

The prepared chips were put into a home-built measurement cell. A bias voltage U_{bias} was applied using a home-built potentiostat between the gold film as working electrode and an Ag/AgCl reference electrode (#MF-2078, RE-6 Reference Electrode, BASi, Warwickshire, UK) the bath solution on top of the sensor surface. As bath solution of 0.1 M phosphate buffer pH 7.5 at 25 °C with 50 mM of a Fe(III)/Fe(II) redox couple (potassium ferri-/ferrocyanide) were used. Light of a Xenon lamp (PTI Model A-1010 Arc Lamp Housing, UXL-75Xe Xenon lamp from USHIO, Japan, powered by PTI LPS-220) was focused to the surface of the particle covered gold film with a lens to a spot with around 3 mm diameter (23 mW; local illumination power P_{illum}, as detected with a photometer (Fieldmaster photometer coherent)), and the corresponding photocurrent I_{Ph} was recorded. In order to achieve better signal-to-noise ratio, the light pointer was modulated with a mechanical chopper (modulation frequency f_{mod}), leading to an AC photocurrent of the same frequency. By using a lock-in amplifier, the amplitude of this photocurrent $I_{Ph,mod}$ was determined [44].

Results and discussion

The schematic diagram of the electrode arrangement is given in Fig. 1. QDs were first attached to the Au electrode by chemisorption to the dithiol layer present on the Au surface. Binding is thought to happen by a local ligand exchange in which the TOPO ligand on the nanoparticle surface (from the particle synthesis) is partly replaced by binding to the dithiol layer [45, 46]. We do not have evidence that the nanoparticle layer on top of the dithiol layer is nicely ordered. However quartz crystal microbalance measurements with CdSe/ZnS nanoparticles immobilized by a similar incubation protocol indicate coverage in the range of a monolayer. In order to get more homogeneous QD layers, the QDs were alternatively immobilized by spin coating instead of mere incubation in QD solution. As a third variation, we added a polymer film formed by layer-by-layer adsorption of oppositely charged polyelectrolytes on top of the QD layer as formed by spin coating. This permeable polymer film is thought to stabilize the QD layer.

Illumination of QDs generates electron-hole pairs as free charge carriers [47]. In Fig. 2, cyclic voltammograms of QD-coated Au chips without and under constant illumination are shown. No redox peaks of the Fe(III)/Fe(II) couple are visible. This indicates sufficient passivation of the surface of the Au electrode with the dithiol layer. Under illumination, the conductivity of the QDs is increased, and thus, the current $I_{Ph,DC}$ in the voltammograms is higher under illumination than in the case without illumination. In other words, upon turning the light on and off, the current $I_{Ph,DC}$ changes accordingly. This is the principle which potentially allows for spatially resolved measurements. At any selectively illuminated position, the current $I_{Ph,DC}$

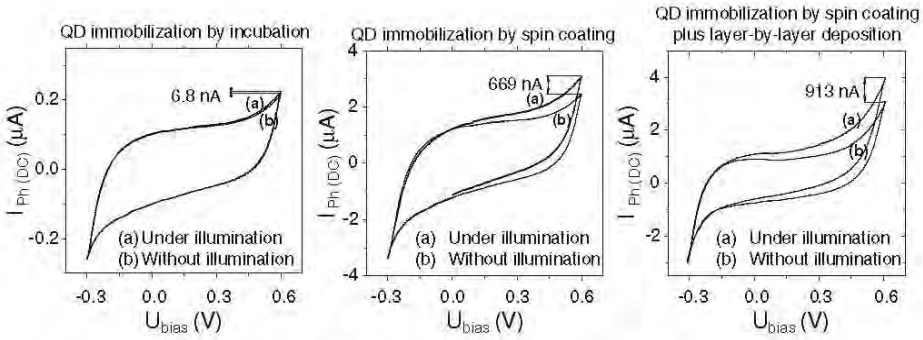

Fig. 2 A variable bias voltage U_{bias} was applied with triangular shape in cyclic voltammetry with a sweep rate of 50 mV/s for the $I_{Ph(DC)}$ measurements. The current I_{Ph} was recorded depending on the cyclically applied bias voltage. Three different surfaces were examined: (1) gold chips coated with CdS (λ_{green}=342 nm, whereby λ is the wavelength of the first exciton peak of CdS the QDs) immobilized by incubation, (2) gold chips coated with QDs immobilized by spin coating, and (3) gold chips which with QDs immobilized by spin coating and layer-by-layer deposition. As electrolyte of 0.1 M phosphate buffer with 50 mM ferri-/ferrocyanide was used. The first voltammogram was recorded with constant illumination (P_{Illum}=23 mW, f_{mod}=0), the second one without illumination (P_{Illum}=0). The resulting DC current $I_{Ph(DC)}$ is plotted versus the applied bias voltage U_{bias}

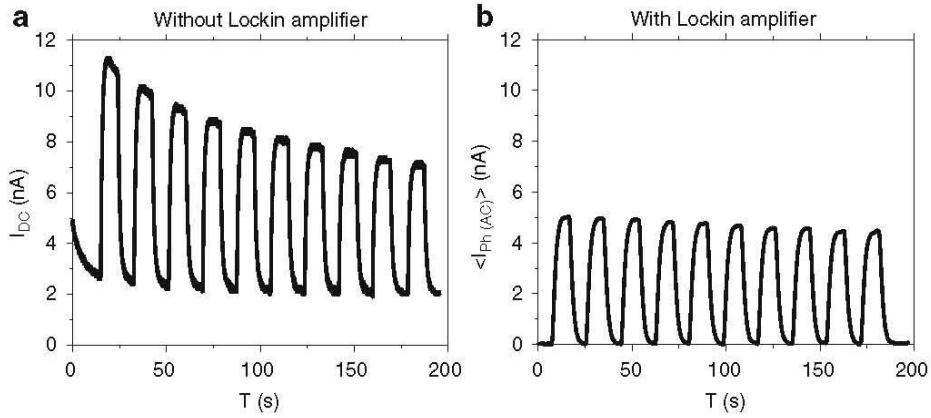

Fig. 3 A constant bias voltage U_{bias}=200 mV was applied to gold chips with CdS QDs (λ_{green}=342 nm, whereby λ is the wavelength of the first exciton peak of CdS QDs) immobilized via spin coating. The chips were in contact with 0.1 M phosphate buffer, pH 7.5. **a** The light was switched on (P_{Illum}=23 mW) and off (P_{Illum}=0) in intervals of 10 s each, and the photocurrent $I_{Ph(DC)}$ was recorded against time. Note that the change in current upon switching on and off the light pointer is significantly higher than the constant background current, which is due to bypassing the QD switch. **b** The light was modulated (f_{mod}=23.8 Hz) and switched on (P_{Illum}=23 mW) and off (P_{Illum}=0) in intervals of 10 s each, and the amplitude of the resulting photocurrent <$I_{Ph(AC)}$> was recorded against time with a lock-in amplifier

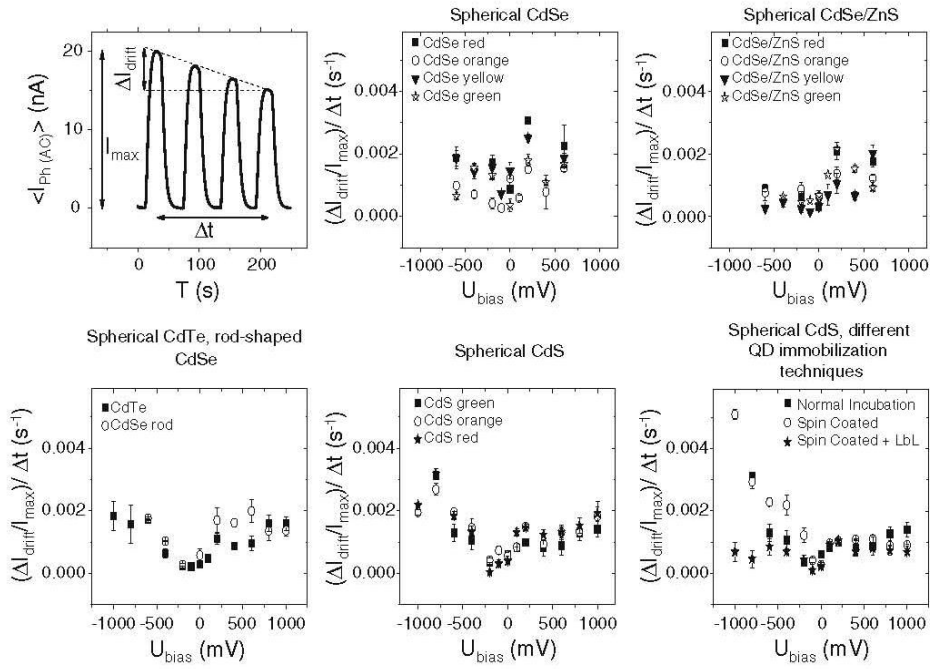

Fig. 4 A constant bias voltage U_{bias} was applied to gold chips with immobilized QDs. The chips were in contact with 0.1 M phosphate buffer, pH 7.5. The chips were illuminated with modulated light (f_{mod}=23.8 Hz), and the amplitude of the resulting photocurrent <$I_{Ph(AC)}$> was determined with a lock-in amplifier. Within the time interval Δt of a few minutes, the light source was four times switched on (P_{Illum}=23 mW) and off (P_{Illum}=0), whereby time traces of <$I_{Ph(AC)}$> were recorded. From these data, the influence of drift on the photocurrent was derived as $(\Delta I_{drift}/I_{max})/\Delta t$. Here I_{max} is the initial amplitude of the photocurrent <$I_{Ph(AC)}$>, and ΔI_{drift} is the loss in current during the time interval Δt. $(\Delta I_{drift}/I_{max})/\Delta t$ values at different applied bias voltages U_{bias} obtained on chips with nanoparticles made out of different materials are displayed: spherical CdSe λ_{red}=588 nm, λ_{orange}=560 nm, λ_{yellow}=532 nm, and λ_{green}=515 nm; spherical CdSe/ZnS λ_{red}=596 nm, λ_{orange}=570 nm, λ_{yellow}=540 nm, and λ_{green}=521 nm, rod-shaped CdSe λ_{rods}=665 nm; spherical CdTe λ=441 nm; spherical CdS λ_{red}=426 nm, λ_{orange}=369 nm, and λ_{green}=342 nm; whereby λ is the wavelength of the first exciton peak of the respective QDs. The QDs were immobilized to the Au electrode by incubation. Only in the last image was a comparison of different immobilization methods given. Spherical CdS QDs (λ_{green}=342 nm) were immobilized by incubation, immobilized by spin coating, and immobilized by spin coating and layer-by-layer deposition, respectively. The values are the average of measurements performed on different devices at different days and their standard deviation as *error bar*

would increase in dependence on the electrode potential applied. To directly measure the difference in current $\Delta I_{Ph,DC}=I_{Ph,DC}^{(illuminated)}-I_{Ph,DC}^{(dark)}$ without the background DC current, the lock-in technique can be advantageously employed. For this purpose, the light is periodically turned on and off with the modulation frequency f_{mod}, and the amplitude of the thus modulated photocurrent $<I_{Ph,AC}>\propto\Delta I_{Ph,DC}$ is detected. In Fig. 3, photocurrent measurements under modulated illumination are shown. As expected, the amplitude of the modulated photocurrent roughly corresponds to the difference in DC current with and without illumination. The lock-in technique has the advantage to remove the DC background current (i.e., $<I_{Ph,AC}^{(dark)}>=0$) and thus part of the initial drift, and it reduces the noise level. Thus the lock-in technique should be very useful for spatially resolved measurements.

The aim of this study was now to investigate the influence of the material of the QDs and the way of their immobilization on the photocurrent behavior. As can be seen in Fig. 2, QD layers made by spin coating (with or without additional polymer film) lead to significantly higher currents. In the experiments with QD layers made by incubation and spin coating (without the additional polymer film), a decrease of the photocurrent can be seen in the first subsequent measurements. One explanation might be a loss of QDs upon measurements. No significant loss in photocurrent upon repetitive measurements was seen in the case of spin-coated QDs with additional layer-by-layer assembly of a polymer film on top of them. These data already indicate that incubation of the QDs on the gold electrode plays a crucial role in the performance of the device. The data shown in Fig. 2 suggest that immobilization of QDs with spin coating increases the amount of detectable photocurrent and that the additional polymer film above the QD layer shows some stabilizing effect.

For more detailed analysis, three parameters were tested for chips prepared with different nanoparticles and with different immobilization methods: drift of the photocurrent, noise level of the photocurrent, and influence of the illumination intensity onto the photocurrent. We used

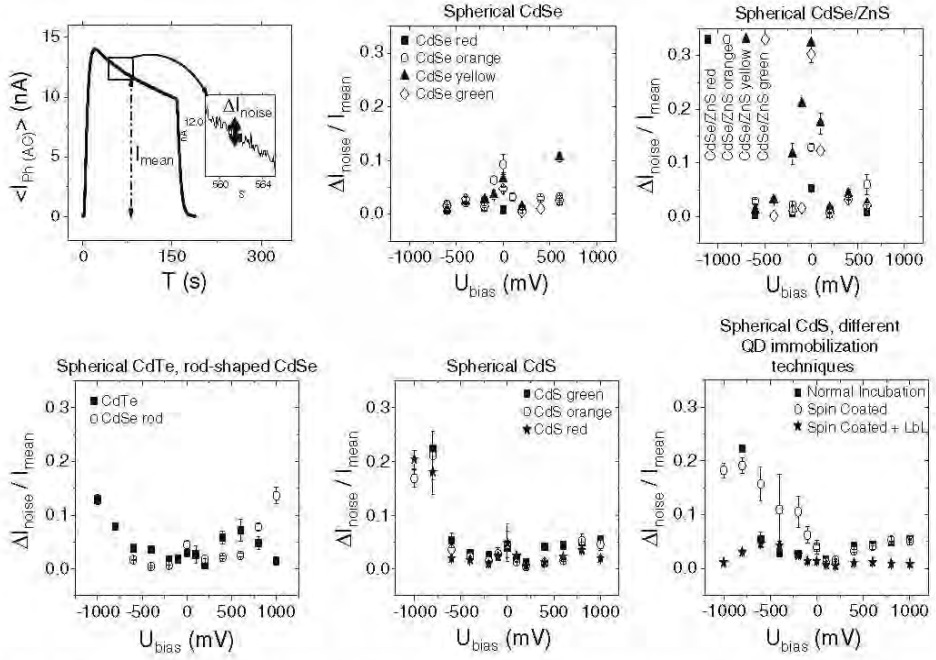

Fig. 5 A constant bias voltage U_{bias} was applied to gold chips with immobilized QDs. The chips were in contact with 0.1 M phosphate buffer, pH 7.5. The chips were illuminated with modulated light (f_{mod}=23.8 Hz), and the amplitude of the resulting photocurrent $<I_{Ph(AC)}>$ was determined with a lock-in amplifier. Following the determination of drift, the signal-to-noise ratio was determined for all different chips and bias voltages. The light source was switched on (P_{Illum}=23 mW), and the mean amplitude of the photocurrent I_{mean} and the height of fluctuations ΔI_{noise} was determined. Using these data, we derived the relative noise level as $\Delta I_{noise}/I_{mean}$. The graphs show the $\Delta I_{noise}/I_{mean}$ values as obtained for several bias voltages U_{bias} on chips with nanoparticles made out of different materials: spherical CdSe λ_{red}=588 nm, λ_{orange}=560 nm, λ_{yellow}=532 nm, and λ_{green}=515 nm; spherical CdSe/ZnS λ_{red}=596 nm, λ_{orange}=570 nm, λ_{yellow}=540 nm, and λ_{green}=521 nm; rod-shaped CdSe λ_{rods}=665 nm; spherical CdTe λ=441 nm; spherical CdS λ_{red}=426 nm, λ_{orange}= 369 nm, and λ_{green}=342 nm; whereby λ is the wavelength of the first exciton peak of the respective QDs. The QDs were immobilized to the Au electrode by incubation. Only in the last image was comparison of different immobilization methods given. Spherical CdS QDs (λ_{green}= 342 nm) were immobilized by incubation, immobilized by spin coating, and immobilized by spin coating and layer-by-layer deposition, respectively. The values are the average of measurements performed on different devices at different days and their standard deviation as *error bar*

spherical CdSe, CdS, CdTe, and CdSe/ZnS particles and rod-shaped CdS particles. For probing the mode of immobilization, spherical CdS particles were immobilized with QDs by mere incubation, with spin coating, and spin coating with additional adsorption of a layer-by-layer assembled polymer film. As the photocurrent is dependent on the applied electrode polarization, the experiments were done at different bias voltages U_{bias}. All measurements were performed in triplicate for the different chips. The measurement cycle and the results for the different QD materials and incubation methods are summarized in Figs. 4, 5, and 6.

We first characterized drift, as it was found that during the first light pulses, the photocurrent shows a running in behavior. In order to characterize this drift, the chips were investigated with the following cycle: Firstly, the light source which was modulated with a chopper was four times switched on and off, while the amplitude of the photocurrent was measured. The change in the amplitude of the photocurrent I_{drift} during this cycle was determined and normalized to the maximum amplitude I_{max}, and the time interval Δt in which the light was switched on and off four times. In this way, we got $(\Delta I_{drift}/I_{max})/\Delta t$ as parameter for the temporal stability of the sensor readout. As can be seen from the results presented in Fig. 4 for all investigated nanoparticles, there was drift in the amplitude of the photocurrent over time. The effect is particularly pronounced when rather large photocurrents are generated, i.e., under highly negative and highly positive polarization ($U_{bias}<<0$ and $U_{bias}>>0$; see Fig. 4). The initial drift behavior is obviously a general property of this system and not dependent on the nature of the QDs. As all QDs have their first exciton peak between 300 and 600 nm, illumination with a Xenon lamp with continuous spectrum facilitates excitation of electron-hole pairs in all cases. In contrast, we found an influence of the immobilization method on the stability of the photocurrent. Coating of the QD layer with a layer-by-layer assembled polymer film drastically reduced drift compared to the other modes of QD immobilization, in particular for negative polarization ($U_{bias}<<0$). We speculate that the creation or saturation of surface states at the QD surface may appear as one reason for this time-dependent behavior. Another reason might be the loss of QDs from the electrode surface. The fact that the photocurrent is more stable upon the presence of a polymer film on top of the QDs

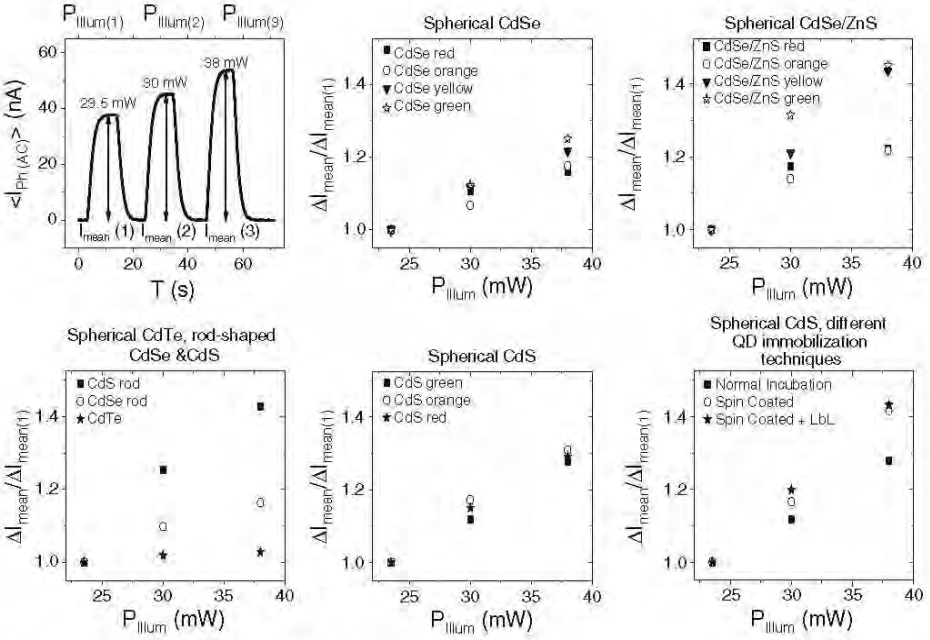

Fig. 6 A constant bias voltage U_{bias}=200 mV was applied to gold chips with immobilized QDs. The chips were in contact with 0.1 M phosphate buffer, pH 7.5. The chips were illuminated with modulated light (f_{mod}=23.8 Hz), and the amplitude of the resulting photocurrent $<I_{Ph(AC)}>$ was determined with a lock-in amplifier. The light source was turned on three times for several tens of seconds with different illumination power (P_{Illum}=23, 30, and 38 mW), and the corresponding mean value I_{mean} of the amplitude of the photocurrent $<I_{Ph(AC)}>$ was determined. From the three data points, $\Delta I_{mean(i)}/\Delta I_{mean(1)}$ (i=1, 2, 3) was determined. These values are plotted for chips made with different QDs: spherical CdSe λ_{red}=588 nm, λ_{orange}=560 nm, λ_{yellow}=532 nm, and λ_{green}=515 nm; spherical CdSe/ZnS λ_{red}=596 nm, λ_{orange}=570 nm, λ_{yellow}=540 nm, and λ_{green}=521 nm; rod-shaped CdSe λ_{rods}=665 nm; spherical CdTe λ=441 nm; spherical CdS λ_{red}=426 nm, λ_{orange}=369 nm, and λ_{green}=342 nm; whereby λ is the wavelength of the first exciton peak of the respective QDs. The QDs were immobilized to the Au electrode by incubation. Only in the last image was a comparison of different immobilization methods given. Spherical CdS QDs (λ_{green}=342 nm) were immobilized by incubation, immobilized by spin coating, and immobilized by spin coating and layer-by-layer deposition, respectively

suggests that this polymer film reduces loss of QDs from the electrode. In all cases, drift was strongest in the beginning of measurements. This offers the possibility to perform a preconditioning with several light pulses before a stable photocurrent is generated. After equilibration, stable photocurrents can be generated rather for a long time. For example, permanent illumination of a QD electrode with CdSe/ZnS nanoparticles for 1 h resulted only in a current decrease of about 10%.

Second, in order to characterize the noise behavior, the modulated light source was switched on, and fluctuations in the recorded amplitude of the photocurrent ΔI_{noise} were recorded. Normalization of the noise to the average amplitude (i.e., the mean value) of the photocurrent I_{mean} led to the noise level $\Delta I_{noise}/I_{mean}$. Results are presented in Fig. 5. Noise is highest for very negative bias voltages, where also high photocurrents are flowing. $\Delta I_{noise}/I_{mean}$ also peaks around $U_{bias} \approx 0$. This is due to the fact that the mean photocurrent I_{mean} is very low at this point. Again, the biggest influence is the mode of QD immobilization. QDs immobilized by spin coating with addition polymer film on top of them showed the lowest noise profile, in particular at very low and very high bias.

Third, for the investigation of the light power influence, the modulated light was turned on and off three times with different illumination intensities P_{Illum}, and the respective mean amplitudes of the photocurrent I_{mean} were determined. In all cases, the photocurrent rose linearly with the illumination power; see Fig. 6. This indicates that the variation in charge carrier generation inside the QDs can be followed by the electron transfer reaction to the electrode in all cases. Thus, this step seems to be not the limiting one at least for the light intensities tested.

Comparison of all three parameters for the chips with QDs of different materials does not lead to highly significant different values. This can be understood by the fact that in this study we were using white-light illumination in a spectral range at which all QDs sufficiently absorb light. On the other hand, we found an improvement upon addition of a polymer film on top of the QD layer. This film reduced initial drift and noise, in particular at very negative bias voltages. In all cases, the stability and the signal-to-noise ratio of the photocurrent were best for small positive and negative bias voltages of only a few hundred millivolts. This suggests the operation range for future measurements.

Conclusions

Using QDs as light-controlled switch for spatially resolved measurements has been demonstrated to be a feasible concept. In this work, we have investigated drift, i.e., missing stability in the sensor readout after preparation, to be one important shortcoming of the sensor. This effect is likely to be caused intrinsically by the sensor readout. Photocurrents are thought to oxidize or reduce the QDs and respective surface states as well the interconnecting dithiol layer. Also a loss of QDs from the sensor surface cannot be ruled out. We have demonstrated that the addition of a polymer film on top of the QDs can significantly reduce as well initial current drift as noise. This might be due to the fact that the polymer film prevents loss of the underlying QDs from the Au electrode. Also the changed chemical environment by the polymer might change the filling up of surface states or might reduce particle–particle communication. In terms of using the device for detection of analytes, the presence of the polymer film will impose certain restrictions. While similar polymer films have been demonstrated to be permeable for small analytes [48, 49], certainly bigger molecules would not be able to reach the QDs as they would not be able to penetrate the polymer film. However, this also could be turned to an advantage. Enzymes can be conveniently integrated in the polymer film in between the different layers [50, 51]. This would offer a convenient way to immobilize enzymes directly on top of the QD layer. Small analytes as substrate could permeate the network of the polymer film, reach the enzymes, and get processed to the product, which would be finally detected as local photocurrent. By immobilization of different enzymes at different regions of the sensor surface, the advantage of the possibility of spatially resolved measurements could be finally put into practice.

Acknowledgments This work was funded by the German Research Foundation (DFG grants Pa 794/3-1 and Li 706/2-1).

References

1. George M, Parak WJ, Gaub HE (2000) Highly integrated surface potential sensors. Sens Actuators, B 69:266–275
2. McConnell HM, Owicki JC, Parce JW, Miller DL, Baxter GT, Wada HG, Pitchford S (1992) The cytosensor microphysiometer: biological applications of silicon technology. Science 257:1906–1912
3. Owicki JC, Bousse L, Hafeman D, Kirk GL, Olson JD, Wada HG, Parce JW (1994) The light-addressable potentiometric sensor: principles and biological applications. Annu Rev Biophys Biomol Struct 23:87–113
4. Engström O, Carlsson A (1983) Scanned light technique for the investigation of insulator–semiconductor interfaces. J Appl Physi 54:5245–5251
5. Löfdahl M, Eriksson M, Lundström I (2000) Chemical images. Sens Actuators, B 70:77–82
6. Lundström I, Erlandsson R, Frykman U, Hedborg E, Spetz A, Sundgren H, Welin S, Winquist F (1991) Artificial 'olfactory' images from a chemical sensor using a light-pulse technique. Nature 352:47–50
7. Schoning MJ, Wagner T, Wang C, Otto R, Yoshinobu T (2005) Development of a handheld 16 channel pen-type LAPS for electrochemical sensing. Sens Actuators, B 108:808–814

8. Hafeman DG, Parce JW, McConnell HM (1988) Light-addressable potentiometric sensor for biochemical systems. Science 240:1182–1185
9. Adami M, Piras L, Lanzi M, Fanigliulo A, Vakula S, Nicolini C (1994) Monitoring of enzymatic activity and quantitative measurements of substrates by means of a newly designed silicon-based potentiometric sensor. Sens Actuators, B 18–19:178–182
10. Bousse L, Kirk G, Sigal G (1990) Biosensors for detection of enzymes immobilized in microvolume reaction chambers. Sens Actuators, B 1:555–560
11. Bousse L, Owicki JC, Parce JW (1992) Biosensors with microvolume reaction chambers. Chemical Sensor Technology 4:145–166
12. Eklund SE, Taylor D, Kozlov E, Prokop A, Cliffel DE (2004) A microphysiometer for simultaneous measurement of changes in extracelular glucose, lactate, oxygen, and acidification rate. Anal Chem 76:519–527
13. Ismail ABM, Yoshinobu T, Iwasaki H, Sugihara H, Yukimasa T, Hirata I, Iwata H (2003) Investigation on light-addressable potentiometric sensor as a possible cell–semiconductor hybrid. Biosens Bioelectron 18:1509–1514
14. Lee WE, Thompson HG, Hall JG, Bader DE (2000) Rapid detection and identification of biological and chemical agents by immunoassay, gene probe assay and enzyme inhibition using a silicon-based biosensor. Biosens Bioelectron 14:795–804
15. Piras L, Adami M, Fenu S, Dovis M, Nicolini C (1996) Immunoenzymatic application of a redox potential biosensor. Anal Chim Acta 335:127–135
16. Poghossion A, Yoshinobu T, Simonis A, Ecken H, Lüth H, Schöning MJ (2001) Penicillin detection by means of field-effect based sensors: ENFET, capacitive EIS sensor or LAPS? Sens Actuators, B 78:237–242
17. Stein B, George M, Gaub HE, Behrends JC, Parak WJ (2003) Spatially resolved monitoring of the cellular metabolic activity with a semiconductor-based biosensor. Biosens Bioelectron 18:31–41
18. Bousse L, Mostarshed S, Hafeman D, Sartore M, Adami M, Nicolini C (1994) Investigation of carrier transports through silicon wafers by photocurrent measurements. J Appl Physi 75:4000–4008
19. George M, Parak WJ, Gerhardt I, Moritz W, Kaesen F, Geiger H, Eisele I, Gaub HE (2000) Investigation of the spatial resolution of the light-addressable potentiometric sensor (LAPS). Sens Actuators, A 83:149–249
20. Parak WJ, Hofmann UG, Gaub HE, Owicki JC (1997) Lateral resolution of light addressable potentiometric sensors: an experimental and theoretical investigation. Sens Actuators, A 63:47–57
21. Moritz W, Gerhardt I, Roden D, Xu M, Krause S (2000) Photocurrent measurements for laterally resolved interface characterization. Fresenius' J Anal Chem 367:329–333
22. Ito Y (1998) High-spatial resolution LAPS. Sens Actuators, B 52:107–111
23. Moritz W, Yoshinobu T, Finger F, Krause S, Martin-Fernandez M, Schöning MJ (2004) High resolution LAPS using amorphous silicon as the semiconductor material. Sens Actuators, B 103:436–441
24. Nakao M, Inoue S, Oishi R, Yoshinobu T, Iwasaki H (1995) Observation of microorganism colonies using a scanning-laser-beam pH-sensing microscope. J Ferment Bioeng 79:163–166
25. Nakao M, Inoue S, Yoshinobu T, Iwasaki H (1996) High-resolution pH imaging sensor for microscopic observation of microorganisms. Sens Actuators, B 34:234–239
26. Yoshinobu T, Iwasaki H, Ui Y, Furuichi K, Ermolenko Y, Mourzina Y, Wagner T, Näther N, Schöning MJ (2005) The light-addressable potentiometric sensor for multi-ion sensing and imaging. Methods 37:94–102
27. Stoll C, Kudera S, Parak WJ, Lisdat F (2006) Quantum dots on gold: electrodes for photoswitchable cytochrome *c* electrochemistry. Small 2:741–743
28. Stoll C, Gehring C, Schubert K, Zanella M, Parak WJ, Lisdat F (2008) Photoelectrochemical signal chain based on quantum dots on gold—sensitive to superoxide radicals in solution. Biosens Bioelectron 24:260–265
29. Schubert K, Khalid W, Yue Z, Parak WJ, Lisdat F (2009) Quantum-dot-modified electrode in combination with NADH-dependent dehydrogenase reactions for substrate analysis. Langmuir. doi:10.1021/la902499e
30. Kucur E, Bucking W, Arenz S, Giernoth R, Nann T (2006) Heterogeneous charge transfer of colloidal nanocrystals in ionic liquids. ChemPhysChem 7:77–81
31. Kucur E, Riegler J, Urban GA, Nann T (2003) Determination of quantum confinement in CdSe nanocrystals by cyclic voltammetry. J Chem Phys 119:2333–2337
32. Zayats M, Willner I (2008) Photoelectrochemical and optical applications of semiconductor quantum dots for bioanalysis. Adv Biochem Eng Biotechnol 109:255–283
33. Willner I, Baron R, Willner B (2007) Integrated nanoparticle–biomolecule systems for biosensing and bioelectronics. Biosens Bioelectron 22:1841–1852
34. Katz E, Zayats M, Willner I, Lisdat F (2006) Controlling the direction of photocurrents by means of CdS nanoparticles and cytochrome *c*-mediated biocatalytic cascades. Chem Commun 1395–1397
35. Xiao Y, Patolsky F, Katz E, Hainfeld JF, Willner I (2003) "Plugging into enzymes": nanowiring of redox enzymes by a gold nanoparticle. Science 299:1877–1881
36. Ju HX, Liu SQ, Ge BX, Lisdat F, Scheller FW (2002) Electrochemistry of cytochrome *c* immobilized on colloidal gold modified carbon paste electrodes and its electrocatalytic activity. Electroanalysis 14:141–147
37. Licht S, Myung N, Sun Y, Light A (1996) Addressable photoelectrochemical cyanide sensor. Anal Chem 68:954–959
38. Kudera S, Carbone L, Carlino E, Cingolani R, Cozzoli PD, Manna L (2007) Synthesis routes for the growth of complex nanostructures. Physica E-Low-Dimensional Systems & Nanostructures 37:128–133
39. Kumar S, Nann T (2006) Shape control of II–VI semiconductor nanomaterials. Small 2:316–329
40. Reiss P, Bleuse J, Pron A (2002) Highly luminescent CdSe/ZnSe core/shell nanocrystals of low size dispersion. Nano Lett 2:781–784
41. Dabbousi BO, Rodriguez-Viejo J, Mikulec FV, Heine JR, Mattoussi H, Ober R, Jensen KF, Bawendi MG (1997) (CdSe) ZnS core-shell quantum dots: synthesis and characterization of a size series of highly luminescent nanocrystallites. J Phys Chem B 101:9463–9475
42. Kudera S, Carbone L, Casula MF, Cingolani R, Falqui A, Snoeck E, Parak WJ, Manna L (2005) Selective growth of PbSe on one or both tips of colloidal semiconductor nanorods. Nano Lett 5:445–449
43. Decher G (1997) Fuzzy nanoassemblies: toward layered polymeric multicomposites. Science 277:1232–1237
44. Uchida H, Zhang WY, Katsube T (1996) High speed chemical image sensor with digital LAPS system. Sens Actuators, B 34:446–449
45. Hu K, Brust M, Bard AJ (1998) Characterization and surface charge measurement of self-assembled CdS nanoparticle films. Chem Mater 10:1160–1165
46. von Holt B, Kudera S, Weiss A, Schrader TE, Manna L, Parak WJ, Braun M (2008) Ligand exchange of CdSe nanocrystals

probed by optical spectroscopy in the visible and mid-IR. J Mater Chem 18:2728–2732
47. Bakkers EPAM, Reitsma E, Kelly JJ, Vanmaekelbergh D (1999) Excited-state dynamics in CdS quantum dots adsorbed on a metal electrode. J Phys Chem B 103(14):2781–2788
48. Kreft O, Muñoz_Javier A, Sukhorukov GB, Parak WJ (2007) Polymer microcapsules as mobile local pH-sensors. J Mater Chem 17:4471–4476
49. Beissenhirtz MK, Scheller FW, Lisdat F (2004) A superoxide sensor based on a multilayer cytochrome *c* electrode. Anal Chem 76:4665–4671
50. Caruso F, Schüler C (2000) Enzyme multilayers on colloid particles: assembly, stability, and enzymatic activity. Langmuir 16:9595–9603
51. Lisdat F, Dronov R, Mohwald H, Scheller FW, Kurth DG (2009) Self-assembly of electro-active protein architectures on electrodes for the construction of biomimetic signal chains. Chem Commun 274–283

Wrapping Nanocrystals with an Amphiphilic Polymer Preloaded with Fixed Amounts of Fluorophore Generates FRET-Based Nanoprobes with a Controlled Donor/Acceptor Ratio

Aleksey V. Yakovlev,[†,‡,§,∥,○] Feng Zhang,[⊥,○] Ali Zulqurnain,[⊥] Abbasi Azhar-Zahoor,[⊥] Camilla Luccardini,[†,‡,§,∥] Stéphane Gaillard,[#] Jean-Maurice Mallet,[#] Patrick Tauc,[▽] Jean-Claude Brochon,[▽] Wolfgang J. Parak,*[,⊥] Anne Feltz,*[,∥] and Martin Oheim*[,†,‡,§]

INSERM, U603, Paris F-75006, France, CNRS UMR 8154, Paris F-75006, France, Laboratory of Neurophysiology and New Microscopies, University Paris Descartes, 45 rue des Saints Pères, Paris F-75006, France, ENS-CNRS, UMR 8544, Laboratoire de Neurobiologie, Département de Biologie, Ecole Normale Supérieure, 46 rue d'Ulm, Paris F-75005, France, Department of Physics, Biophotonics, Philipps University of Marburg, Renthof 7, Marburg D-35037, Germany, ENS-CNRS, UMR 8642, Glycoscience, Département de Chimie, Ecole Normale Supérieure, 24 rue Lhomond, Paris F-75231, France, and ENS-CNRS, UMR 8113, Laboratoire de Biotechnologies et Pharmacologie génétique Appliquée (LBPA), Ecole Normale Supérieure de Cachan, 61 avenue du President Wilson, Cachan F-94235, France

Received November 19, 2008. Revised Manuscript Received December 22, 2008

Colloidal nanocrystal (NC) donors wrapped with a polymer coating including multiple organic acceptor molecules are promising scaffolds for fluorescence resonance energy transfer (FRET)-based nanobiosensors. Over other self-assembling donor−acceptor configurations, our preloaded polymers have the virtue of producing compact assemblies with a fixed donor/acceptor distance. This property, together with the possibility of stoichiometric polymer loading, allowed us to directly address how the FRET efficiency depended on the donor/acceptor. At the population level, nanoprobes based on commercial as well as custom CdSe/ZnS donors displayed the expected dose-dependent rise in transfer efficiency, saturating from about five ATTO dyes/NC. However, for a given acceptor concentration, both the intensity and lifetime of single-pair FRET data revealed a large dispersion of transfer efficiencies, highlighting an important heterogeneity among nominally identical FRET-based nanoprobes. Rigorous quality check during synthesis and shell assembly as well as postsynthesis sorting and purification are required to make hybrid semiconductor−organic nanoprobes a robust and viable alternative to organic or genetically encoded nanobiosensors.

Introduction

With their large absorbance permitting blue-shifted excitation remote from acceptor direct excitation, size-dependent tunable narrow emission, longer excited-state lifetime, and better photostability compared to organic chromophores, semiconductor nanocrystals (NCs) are potent donors for building fluorescence resonance energy transfer (FRET)-based nanoprobes.[1−7] Such nanosensors have been successfully used to detect toxins,[8] probe enzymatic activity,[9] screen for enzyme inhibitors,[10] or measure ion concentration.[11−13] In addition to offering new possibilities for ultrasensitive analyte detection, functionalized NCs provide an ideal platform for the attachment of multiple fluorophores, thereby increasing the FRET efficiency[2,4,12,14−17] or permitting the design of polyvalent sensors through acceptor multiplexing.[8,13,17,18]

In the past, nanoprobe assembly has typically involved a compromise between sensor performance and colloidal stability (reviewed in refs 19 and 20). Compact donor/acceptor assemblies

* Corresponding authors. E-mail: anne.feltz@ens.fr (A.F.); martin.oheim@univ-paris5.fr (M.O.); wolfgang.parak@physik.uni-marburg.de (W.J.P.)
† INSERM, U603.
‡ CNRS UMR 8154.
§ University Paris Descartes.
∥ ENS-CNRS, UMR 8544, Laboratoire de Neurobiologie, Département de Biologie.
⊥ Philipps University of Marburg.
ENS-CNRS, UMR 8642, Glycoscience, Département de Chimie.
▽ ENS-CNRS, UMR 8113, Laboratoire de Biotechnologies et Pharmacologie génétique Appliquée (LBPA).
○ These authors contributed equally.

(1) Willard, D. M.; Carillo, L. L.; Jung, J.; Van Orden, A. *Nano Lett.* **2001**, *1*, 469–474.
(2) Tran, P. T.; Goldman, E. R.; Anderson, G. P.; Mauro, J. M.; Mattoussi, H. *Phys. Status Solidi B* **2002**, *229*, 427–432.
(3) Medintz, I. L.; Goldman, E. R.; Lassman, M. E.; Mauro, J. M. *Bioconjugate Chem.* **2003**, *14*(5), 909–918.
(4) Clapp, A. R.; Medintz, I. L.; Mauro, J. M.; Fisher, B. R.; Bawendi, M. G.; Mattoussi, H. *J. Am. Chem. Soc.* **2004**, *126*(1), 301–310.
(5) Alphandéry, E.; Walsh, L. M.; Rakovich, Y.; Bradley, A. L.; Donegan, J. F.; Gaponik, N. *Chem. Phys. Lett.* **2004**, *388*, 100–104.
(6) Fernandez-Arguelles, M. T.; Yakovlev, A.; Sperling, R. A.; Luccardini, C.; Gaillard, S.; Medel, A. S.; Mallet, J. M.; Brochon, J. C.; Feltz, A.; Oheim, M.; Parak, W. J. *Nano Lett.* **2007**, *7*(9), 2613–2617.
(7) Lu, H.; Schöps, O.; Waggon, U.; Niemeyer, C. M. *J. Am. Chem. Soc.* **2008**, *130*, 4815–4827.
(8) Goldman, E. R.; Clapp, A. R.; Anderson, G. P.; Uyeda, H. T.; Mauro, J. M.; Medintz, I. L.; Mattoussi, H. *Anal. Chem.* **2004**, *76*, 684–688.
(9) Xu, C.; Xing, B.; Rao, J. *Biochem. Biophys. Res. Commun.* **2006**, *344*, 931–935.
(10) Shi, F.; Rosenzweig, N.; Roszenzweig, Z. *Anal. Chem.* **2007**, *79*, 208–214.
(11) Snee, P. T.; Somers, R. C.; Nair, G.; Zimmer, J. P.; Bawendi, M. G.; Nocera, D. G. *J. Am. Chem. Soc.* **2006**, *128*(41), 13320–13321.
(12) Pons, T.; Medintz, I. L.; Wang, X.; English, D. S.; Mattoussi, H. *J. Am. Chem. Soc.* **2006**, *128*(47), 15324–15331.
(13) Suzuki, M.; Husimi, Y.; Komatsu, H.; Suzuki, K.; Douglas, K. T. *J. Am. Chem. Soc.* **2008**, *130*(17), 5720–5725.
(14) Patolsky, F.; Gill, R.; Weizmann, Y.; Mokari, T.; Banin, U.; Willner, I. *J. Am. Chem. Soc.* **2003**, *125*(46), 13918–13919.
(15) Kim, J. H.; Stephens, J. P.; Morikis, D.; Ozkan, M. *Sens. Lett.* **2004**, *2*, 85–90.
(16) Levy, M.; Cater, S. F.; Ellington, A. D. *ChemBioChem* **2005**, *6*, 2163–2166.
(17) Medintz, I. L.; Clapp, A. R.; Brunel, F. M.; Tiefenbrunn, T.; Uyeda, H. T.; Chang, E. L.; Deschamps, J. R.; Dawson, P. E.; Mattoussi, H. *Nat. Mater.* **2006**, *5*(7), 581–589.
(18) Clapp, A. R.; Medintz, I. L.; Uyeda, H. T.; Fisher, B. R.; Goldman, E. R.; Bawendi, M. G.; Mattoussi, H. *J. Am. Chem. Soc.* **2005**, *127*, 18212–18221.
(19) Medintz, I. L. *Trends Biotechnol.* **2006**, *24*(12), 539–542.

10.1021/la8038347 CCC: $40.75
Published on Web 01/27/2009

favor high FRET efficiencies, but additional coating layers increasing their effective size have to be introduced to preserve solubility and colloidal stability. Also, polyethylene glycol (PEG), which is widely used for this purpose,[21,22] introduces a microenvironment that may restrict the access of the analyte to the acceptor on the NC surface. Conversely, the *post hoc* attachment of the acceptor to the already coated and functionalized NC considerably increases donor/acceptor separation and impairs FRET efficiency.

A factor that has limited sensor performance is that acceptor binding and NC coating have been usually considered as two independent steps. By far, most sensor geometries have in common that FRET is modulated by reversibly or irreversibly displacing the acceptor from the NC donor.[10,17] More recently, a pH sensitive donor/acceptor FRET pair has been described where the acceptor is tethered on the NC surface and analyte binding/unbinding modulates the overlap integral between donor photoluminescence (PL) emission and acceptor excitation and thus modifies the FRET efficiency.[11,13] However, upon analyte binding, most fluorescent indicators change fluorescence through a modulation of their quantum efficiency rather than their absorbance. Thus, in hybrid FRET-based nanoprobes built from such probes, the amount of acceptor fluorescence varies with analyte concentration, but the transfer efficiency is actually constant.

To benefit from the large spectrum of available ion indicators and purpose-tailored fluorescent probes, we designed FRET sensors that incorporate the acceptor directly into an amphiphilic polymer coating. We have previously shown that these probes minimize the acceptor/donor distance, thus permit high transfer efficiencies, and outperform conventional sensors in which the acceptor is added *post hoc*, after synthesis of the amphiphilic coat by surface functionalization.[6]

In the present work, we preloaded the polymer shell with variable amounts of acceptor to study the impact of changing the acceptor/donor ratio (A/D) at a fixed donor/acceptor distance. Taking donor quenching, shortening of the donor lifetime, or an increase in the sensitized acceptor fluorescence as a readout, we demonstrate that the detected transfer efficiency increases with the number of dye molecules but starts to saturate for as little as five acceptor dyes per NC donor. While population measurements closely followed the expected result for a multiple-acceptor transfer mechanism, single-pair FRET (spFRET) recordings revealed a large heterogeneity among nanoprobes, with respect to both their donor quenching and sensitized acceptor fluorescence, and the excited-state lifetime. Our study provides important guidelines for designing FRET-based nanobiosensors and highlights the importance of single-molecule experiments to reveal inner-batch heterogeneity and select for the best FRET sensors.

Materials and Methods

Nanocrystal Synthesis. Four kinds of NCs were used in the current experiments and included Evident NCs (Evidots 560, Evident Technologies, Inc., ED-C11-Tol-0560), Invitrogen NCs (Qdot 565 ITK organic quantum dots, #Q21731MP), and two batches of homemade NCs: one was CdSe without the ZnS shell, and the other was CdSe/ZnS. For Table 1, we determined for each batch the absorption/emission spectra, permitting the direct comparison of the extinction coefficients. Therefore, we could estimate the core size for all four kinds of NCs using the same calibration curve, neglecting the ZnS shell thickness (values in ref 23 are reported for the inorganic core only). Concentrations were determined by absorption measurements, using Beer–Lambert's law.

Table 1. Specifications of the Four Kinds of Nanocrystals Used

	1st peak[a]	$\varepsilon^{(peak)}$	D_i	D_e	A_s
Evident NCs	531	82 325.8	2.7	5.1	177.2
Invitrogen NCs	543	99 040.0	2.9	5.3	186.6
homemade CdSe/ZnS	535	87 334.1	2.8	5.2	180.1
homemade CdSe	523	73 683.1	2.6	5.0	172.0

[a] 1st peak, first exciton absorption peak (nm), obtained by UV–vis spectrometry; $\varepsilon^{(peak)}$, extinction coefficient at its first exciton peak (cm^{-1} M^{-1}), extracted according to ref 23; D_i, diameter of inorganic core (nm), extracted according to ref 23; D_e, effective diameter = $D_i + 2 \times 1.2$ (thickness of TOPO shell) (nm); A_s, surface area of NC = $4\pi(D_e/2)^2$ (nm^2).

Stoichiometric ATTO–Polymer Embedding. The polymer coating procedure has been described elsewhere.[6,24] Briefly, solutions of different ATTO–polymer ratio were mixed with NC-containing chloroform solution. For the three batches of Evident NCs and the Invitrogen Qdots used, a ratio of 100 polymer motifs per nm^2 of the NC surface was used in the coating process. For the homemade NC batches, we used 50 polymer motifs per nm^2. In contrast to previous protocols,[25] no cross-linker was used in this step. The ATTO–polymer-coated NCs were finally redissolved in borate buffer (sodium borate, 50 mM, pH 12.0).

Donor–Acceptor Ratios. We estimate that 25% of active maleic anhydride rings can react with other molecules containing amino groups. Using a derivate of ATTO with an amino group (abs/em = 597/615 nm, ATTO-TEC GmbH, Germany), the dye was first dissolved in anhydrous chloroform upon sonication, and its concentration was determined by absorption measurements, assuming an extinction coefficient at 597 nm in chloroform of 120 000 M^{-1} cm^{-1}. To obtain different ratios of ATTO dye embedded in polymer, ATTO solution was mixed with polymer solution as detailed in the text in % (mol/mol) of ATTO to maleic anhydride rings. The mixture was left overnight at room temperature and at least three-times concentrated to dryness and redissolved to enhance the reaction efficiency. Finally, the polymer concentration was determined either from the final solvent volume or from the calculated ATTO concentration determined by UV–vis spectrometry. The absorption spectrum of ATTO was not affected by the polymer (data not shown).

Purification. All solutions of the functionalized and assembled NCs were concentrated by ultrafiltering (100 kDa MW cutoff, Millipore) and filtered on 0.2 μm filters (Millipore). Gel electrophoresis on 2% agarose (UltraPure, Invitrogen #15510027) in 0.5× TBE buffer (44.5 mM Tris-borate and 1 mM EDTA, pH 8.3; Sigma-Aldrich, #T3913) was used for purification and run at 100 V for 80–100 min. The separated bands of empty micelles (faster band, red color) and particles (slow band, green or yellow colors) were cut by distinguishing the different colors under the UV lamp.[6] The samples were extracted from the cut bands sealed in dialysis membranes (50 kD, Spectrolabs, #132544) by elution and finally concentrated again by 100 kD ultrafiltration.

Overlap Integrals, Quantum Yields, and Calculated Förster Distances and FRET Efficiencies. We assembled FRET-based nanoprobes by wrapping a central NC donor with an amphiphilic polymer coat into which were included during synthesis ATTO molecules at a stoichiometry ratio (Figure 1A). The choice of these FRET pairs was guided by the requirements (i) to have bright enough NC donors to obtain detectable single-pair FRET (spFRET), (ii) to optimize the overlap between NC photoluminescent emission and ATTO absorption, and (iii) to maximize separation of the donor and acceptor emission spectra to permit dual-color FRET detection.

(20) Somers, R. C.; Bawendi, M. G.; Nocera, D. G. *Chem. Soc. Rev.* **2007**, *3*, 579–591.
(21) Ballou, B.; Lagerholm, B. C.; Ernst, L. A.; Bruchez, M. P.; Waggoner, A. S. *Bioconjugate Chem.* **2004**, *15*(1), 79–86.
(22) Yu, W. W. *J. Am. Chem. Soc.* **2007**, *129*(10), 2871–2879.
(23) Yu, W. W.; Qu, L.; Guo, W.; Peng, X. *Chem. Mater.* **2003**, *15*(14), 2854–2860.
(24) Lin, C. A.; Sperling, R. A.; Li, J. K.; Yang, T. Y.; Li, P. Y.; Zanella, M.; Chang, W. H.; Parak, W. J. *Small* **2008**, *4*(3), 334–341.
(25) Pellegrino, T.; Manna, L.; Kudera, S.; Liedl, T.; Koktysh, D.; Rogach, A. L.; Keller, S.; Rädler, J.; Natile, G.; Parak, W. J. *Nano Lett.* **2004**, *4*(4), 703–707.

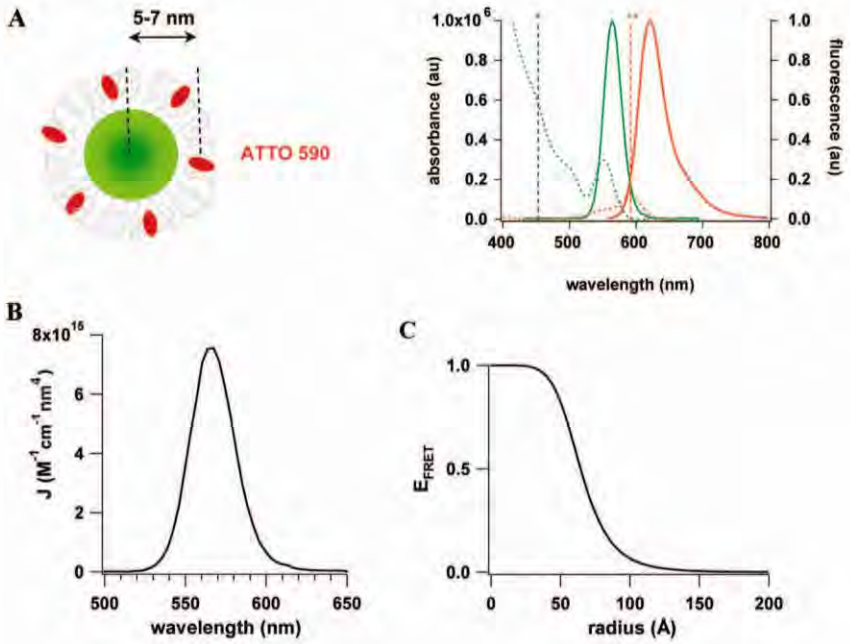

Figure 1. Overlap integrals, quantum yields, and calculated Förster distances and transfer efficiencies between Evident NC donors and ATTO590 dye: (A) Left: Cartoon showing the polymer-wrapped nanocrystal (NC)/ATTO dye assembly. Right: Absorbance (dotted) and normalized emission spectra (solid) of NC donor (green) and ATTO acceptor (red). Asterisk and double asterisk identify 450 and 590 nm wavelengths used for donor and direct (acceptor) excitation. (B) Calculated overlap integral and (C) FRET efficiency, assuming a r^6 dipole−dipole coupling. Förster radius R_F = 64.5 Å; $J = 7.75218 \times 10^{15}$ M^{-1} cm^{-1} nm^4.

We note that there is considerable uncertainty in the molar extinction ε of the NC donors, as different sources give different extinction coefficients (e.g., for Invitrogen NC at 543 nm, the manufacturer's data and measured data differ by a factor of 2; and similar discrepancies were observed by others[23,26] and might represent batch-to-batch variability). For consistency, all numbers reported were derived from the same calibration curve.[23,26]

We calculated the overlap integral

$$J = \int \mathrm{d}\lambda\, F_D(\lambda)\, \varepsilon_A(\lambda)\lambda^4 \tag{1}$$

which quantifies the normalized and dimensionless spectral overlap between donor emission $F_D(\lambda)$ and acceptor absorbance, $\varepsilon_A(\lambda)$, and R_0 the Förster radius, which is defined as the distance between the donor and acceptor that yields 50% energy-transfer efficiency (in $Å^6$),

$$R_0^{\,6} = 8.8 \times 10^{23} \kappa^2 n_D^{-4} Q_D J \tag{2}$$

Here, Q_D is the photoluminescence quantum yield of the NC donor in the absence of an acceptor, n_D is the refractive index of the medium (here, 1.33 for water at ~590 nm), and $\kappa^2 = 2/3$ is the orientation factor, assuming random orientation between the NC and ATTO dipoles.

We derived the transfer efficiency from the quenching of donor photoluminescence, or decrease in donor lifetime in the presence of the acceptor, according to

$$E^{(a)} = 1 - F_{DA}/F_D \tag{3a}$$

or from the sensitized acceptor fluorescence,

$$E^{(b)} = \frac{\varepsilon_A(\lambda_D)}{\varepsilon_D(\lambda_D)}\left(\frac{F_{DA}(\lambda_A)}{F_A(\lambda_A)} - 1\right) \tag{3b}$$

where λ_D and λ_A denote the donor and acceptor excitation wavelength, $\varepsilon_D(\lambda)$ is the donor absorbance at wavelength λ (and likewise for the acceptor), and $F_D(\lambda)$ is the donor fluorescence at wavelength λ. We finally used the decrease in donor lifetime in the presence of acceptor,

$$E^{(c)} = 1 - \tau_{DA}/\tau_D \tag{3c}$$

as a readout for estimating the FRET efficiency.

Finally, assuming a Förster-type (dipole−dipole) interaction between donor and acceptor, and N as the number of acceptors per donor

$$E(N, r) = N/\left(N + (r/R_0)^6\right) \tag{3d}$$

Estimate of the Donor−Acceptor Ratio. Absorption spectra were obtained on a UV−vis spectrometer (Agilent Technologies). ATTO absorption at 450 nm is negligible to that of the NCs. Conversely, all NC samples hardly absorb at the ATTO absorption peak (597 nm). Thus, measuring the absorbance at 450 and 597 nm, respectively, allowed the determination of [NC] and [ATTO]. All spectra were corrected for background with a blank run.

Fluorescence emission spectra were recorded upon 450 nm (donor excitation) or 590 nm (direct acceptor excitation) on a Fluorolog-3 spectrofluorometer (HORIBA Jobin Yvon, Japan) and were corrected for the instrument response.

After gel electrophoresis, we estimated the number of ATTO dyes per NC donor in the purified samples by the six following steps (Figure 2).

1. The three reference absorption spectra were measured: sample (1), NC−polymer; sample (2), NC−polymer−ATTO 1%; and sample (3), ATTO−polymer 1% in the absence of NC (EP).
2. From Lambert−Beer's law ($A = -\log_{10}(I/I_0) = \varepsilon cL$), using $\varepsilon_{597} = 120\,000\ M^{-1}\ cm^{-1}$ of ATTO dye at absorption maximum, the concentration of ATTO in sample (2) was estimated as 1.03 μM.
3. The spectrum of sample (3) was scaled up to match the measured absorption maximum of sample (2) at the ATTO absorption maximum. This scaled spectrum is referred to as sample (3)′ in the following. For the example shown in Figure 2, the scaling factor was 0.9789 (0.12082/0.12342), from the measured absorption of samples (2) and (3) at 597 nm (Figure 2B).

(26) Striolo, A.; Ward, J.; Prausnitz, J. M.; Parak, W. J.; Zanchet, D.; Gerion, D.; Milliron, D. J.; Alivisatos, A. P. *J. Phys. Chem. B* **2002**, *106*(21), 5500–5505.

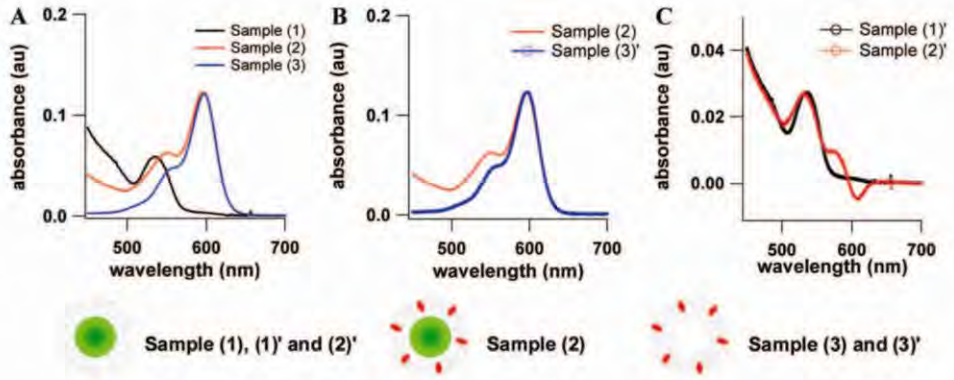

Figure 2. Estimation of the number of ATTO/NC. (A) Samples (1), (2), and (3) indicate absorbance spectra of purified, polymer-coated Evident NC, 1% ATTO−polymer-coated Evident NC, and 1% ATTO−polymer micelles (EP), respectively. (B) and (C) describe the scaling procedure. See text for details.

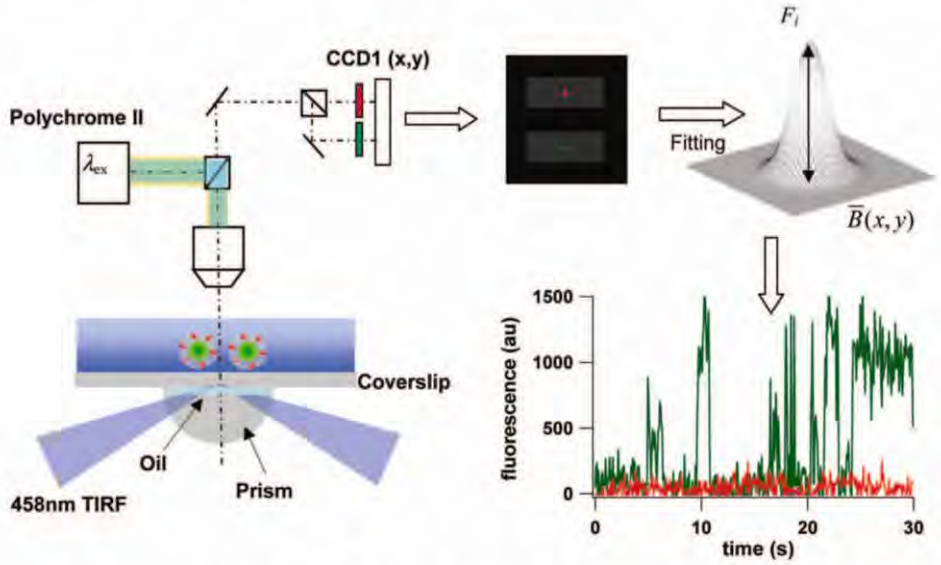

Figure 3. Schematic representation of the setup used for spFRET detection and subsequent data analysis. spFRET was detected on an upright fluorescence microscope fitted for combined epifluorescence and total internal reflection fluorescence (TIRF). We used the "prism-type" configuration, with an external prism and coverslip made of Schott SUPRASIL 311 coupled through a thin layer of ultralow autofluorescence immersion oil. Fluorescence was detected through a water immersion objective and directed, after the splitting of donor (green) and acceptor (red) fluorescence and appropriate filtering, on an electron-multiplying charge-coupled device (CCD) detector. Dual-color images containing a single FRET pair were excised and submitted to a PSF-fitting routine for the measurement of background $\bar{B}(x,y)$and spot Fi fluorescence (see Materials and Methods). Traces at the bottom right show blinking fluorescence of a naked NC and the corresponding trace in the red channel.

4. Next, we subtracted the spectrum of sample (3)′ from that of sample (2), thus obtaining a difference spectrum (called (2)′) indicative of the absorption of the NC alone, after subtraction of the ATTO component (Figure 2C). The obtained spectrum compares favorably with a scaled version of spectrum (1), termed sample (1)′ in Figure 2C.
5. From (2)′, the first exciton peak of polymer-coated NCs is measured at 532 nm with an amplitude 0.02731, so that we can calculate the concentration of polymer-coated NCs in sample (2) as 0.33 μM, again using Beer−Lambert's law and assuming $\varepsilon_{max} \sim 82\,000\ M^{-1}\ cm^{-1}$ at the first exciton peak.
6. Finally, the number of ATTO per NC is obtained by dividing the concentrations of ATTO and NCs, 1.03/0.33 = 3.1.

Single-Particle FRET (spFRET) Detection. For spFRET and TSCSPC (time- and space-correlated single-photon counting) measurements, glass coverslips (25 × 10 mm, Menzel, Braunschweig, Germany) were prepared for imaging by successive sonication in absolute ethanol, acetone, HNO_3, and 6 N KOH solutions for 20 min and subsequently washed three times with Milli-Q water. To remove unwanted autofluorescence, they were cured with UV light emitted from a HBO50 lamp during 30 min.

NCs were diluted 100 times from a ~0.2 μM stock in 50 mM borate buffer at pH 9.0. Droplets of 10 μL were dispersed on coverslips and allowed to dry. The coverslips were subsequently washed three times to remove free dye, micelles, and nonattached complexes. NCs remained stably attached to the glass surface in aqueous solution during several hours. For TSCSPC experiments, these coverslips were mounted on microscope slides (76 × 26 × 1 mm LLR2, CML, Nemours, France) and sealed with colorless nail varnish. All samples were stored in the dark at +4 °C until observation.

spFRET measurements were carried out on a custom upright microscope equipped for combined epifluorescence and prism-type evanescent-field excitation (Figure 3, left). Polychrome II (TILL Photonics, Gräfelfing, Germany) provided narrowband (18 nm fwhm intensity) polychromatic epifluorescence excitation which was used for localizing and focusing at the glass surface and for the recording of fluorescence excitation spectra.

For evanescent-field excitation, the beam of a multiline Ar^+-ion laser (<5mW at 458 nm impinging on the sample, Reliant 150, Laser Physics, Milton Green, Cheshire, U.K.) was directed at an oblique angle at a ultralow autofluorescence hemicylindrical prism (Suprasil-311, Bernhard Halle Nachfahren, Berlin, Germany).

Penetration depth depended on the angle of incidence of the laser beam and was of the order of 150 nm throughout.

Fluorescence was detected through a LUMFL 60×/1.1-NA water immersion lens (Olympus, Hamburg, Germany) and spectrally separated into a donor and acceptor fluorescence channel (W-view, Hamamatsu, Hamamatsu City, Japan), and directed on a QuantEM 512SC electron-multiplying charge-coupled device (CCD) camera (16 μm × 16 μm pixel size, Photometrics, Tucson, AZ). Images were acquired and analyzed with MetaMorph (Molecular Devices, Sunnyvale, CA). Acquisition rates were 5 or 10 Hz, with exposure times of 75−100 ms for imaging.

For point-spread function fitting and FRET quantification, we first averaged 400−500 image frames of a time-lapse movie and identified regions of interest (ROIs) containing a single NC donor. Individual NCs were recognized by their intensity and blinking; see, for example, Figure 3.

To improve the signal-to-noise ratio, we used a point-spread function (PSF) fitting approach. We used this approach (i) to localize corresponding objects in the donor and acceptor channel and correct for subpixel shift between the color channels, and (ii) to measure the background, amplitude, and width for of spots in the donor and acceptor channel. Image subregions (7 × 7 pixel) were excised from the dual-color fluorescence images and fitted with a two-dimensional (2-D) Gaussian (IGOR, Wavemetrics, Lake Oswego, OR),

$$F(x_i, y_i) = \bar{B}(x, y) + F_i \exp\left[-\frac{1}{2}\left(\left(\frac{x - x_i}{\delta_x}\right)^2 + \left(\frac{y - y_i}{\delta_y}\right)^2\right)\right] \quad (4)$$

where (x_i, y_i) and δx and δy are the center position and widths of the 2-D Gaussian and $\bar{B}(x,y)$ is the average background in the ROI of interest. For each batch, we report F_i for 20−30 ROIs per coverslip and average over at least three different coverslips.

On 458 nm evanescent-wave excited dual-color fluorescence images of single NCs, we proceeded analogously. We first extracted from the acceptor image ROIs containing a single fluorescent spot and transferred these ROIs onto the donor image. Pairs were retained if they represented detectable acceptor fluorescence as well as donor blinking, indicating a single NC donor at the origin of the detected acceptor fluorescence. Thus, our choice is biased toward bright FRET pairs with negligible donor quenching and moderate duty cycles.

Time- and Space-Correlated Single-Photon Counting (TSCSPC) Measurements. Shortening of the donor fluorescence lifetime in the presence of the acceptor or ingrowth of acceptor lifetime has been used here to quantify FRET efficiencies.[6,12] Lifetime measurements provide an intensity-independent readout of FRET efficiency, which is important when dealing with dim objects as in the present case. Here, we used TSCSPC to reveal the heterogeneity of donor photoluminescence decays within a given batch of NCs. Donor decays were recorded on a Leica SP2 inverted microscope equipped with a Leica TCSP2 confocal scan head (Leica, Solms, Germany). Donor photoluminescence was excited at 802 nm with a femtosecond-pulsed Ti:sapphire laser (100−200 fs, 80 MHz, MaiTai, Spectra Physics, Newport, CA), collected through a HQ 560/40m emission band-pass (Chroma Technology) to reject acceptor fluorescence, and detected on a microchannel plate (MCP) imaging detector (Hamamatsu R3809U-50, Japan). A TCSPC board (SPC-730, Becker & Hickl, Berlin, Germany) was used for the acquisition of both excitation light pulse and fluorescence emission. Typical durations to accumulate enough photons were 2000 s. The time scaling was 37.4 ps/channel, and 4096 channels were used. The instrument response following the laser pulse (100 ps, fwhm) was recorded by detecting the light scattered by a water solution. The large 2PEF cross sections of NC donors permitted the use of low average power (~1 μW). With a 2PEF cross section of ~7000 GM for 525−CdSe−ZnS NCs and ~100 GM for ATTO594, we expect the donor to be the predominantly excited species.[27]

The MCP detector allowed spatially resolved decay measurements (1.5 μm/pixel in the object plane). Binning increased the signal-to-noise ratio, at the expense of spatial resolution. In the later case, the measured decay is the ensemble average of all the NCs present in the binned megapixel. Analysis of the fluorescence decay used either the maximum entropy method[28] or a sum-of-exponentials method implemented in the Becker & Hickl SPCImage software. With the maximal entropy method, we obtained three lifetimes for all samples. Two shorter lifetimes were in the range of 0.2−0.3 ns and 0.8−0.9 ns, and a third longer lifetime component was of the order of 13−21 ns. The sum-of-exponentials method which only gave access to the two shorter lifetimes because of its 10 ns time window is more restrictive, since both χ^2 and the number of exponentials are fixed. We systematically rejected fits with $\chi^2 > 1.2$. The latter approach therefore yields lifetime values similar to those obtained in cuvette measurements, but with the additional information of the spatial distribution. Therefore, histograms of τ values could be obtained by sampling donor lifetimes at different regions of the coverslip.

Results and Discussion

For the synthesis of our NC−ATTO FRET system, an amphiphilic polymer was built by linking a hydrophobic side chain to a backbone of poly(isobutylene-alt-maleic anhydride), as previously described.[6,24] We chose the conditions so that 75% of the anhydride monomers reacted with one dodecyl hydrophobic chain, leaving the remaining 25% vacant for other couplings

As an acceptor fluorophore, we incorporated ATTO590-NH_2 dye (ex/em = 594/624 nm, extinction $\varepsilon_{594} = 120\,000\ M^{-1}\ cm^{-1}$, quantum yield $\phi = 0.8$, fluorescence lifetime $\tau = 3.7$ ns; see Figure 1 for details) by amide linkage to the vacant anhydride monomer positions. By systematically changing the stoichiometric ratio during synthesis, a series of amphiphilic polymers with increasing concentrations of ATTO dye from 0.01% up to 4% (referring to the percentage of anhydride rings in the polymer which are linked to ATTO dye molecules) were preassembled and, upon opening in aqueous medium of the still vacant anhydride which frees negatively charged carboxyl groups, used to colloidally stabilize NCs. We used as donors either EviDots 560 (Evident Technologies), QDot 565 ITK (organic quantum dots, Invitrogen), or homemade CdSe/ZnS and CdSe only nanocrystals.[29,30]

After core−shell assembly, colloidal NCs were purified by gel electrophoresis as described earlier,[31] thereby separating empty polymer micelles (EP) from coated and dye-loaded NCs [6]

Thus, controlling sensor assembly, we investigated how the FRET efficiency varied with the acceptor/donor ratio. Samples synthesized with acceptor varying from 0.01% to 4% were prepared from a *same* batch of NC donors, working either at the same concentration of ATTO dye (Figure 4A, B) or at the same concentration of NCs (Figure 4C, D), adjusting their concentrations so as to obtain identical absorbance at either 597 or 450 nm, respectively (see Materials and Methods). Donor excitation at 450 nm resulted in detectable fluorescence from both Evident NCs and ATTO590, despite the only negligible direct excitation of the acceptor (Figure 4A, C), thus indicating the transfer of excitation from the NC donor to the ATTO acceptor. As expected from a multiple-acceptor system, the yellow-green peak NC

(27) Clapp, A. R.; Pons, T.; Medintz, I. L.; Delehanty, J. B.; Melinger, J. S.; Tiefenbrunn, T.; Dawson, P. E.; Fisher, B. R.; O'Rourke, B.; Mattoussi, H. *Adv. Mater.* **2007**, *19*, 1921–1926.

(28) Brochon, J. C. *Numerical computer methods*, Part B; Academic Press: San Diego, CA, 1994; Vol. *240*, pp 262−311.

(29) Dabbousi, B. O.; Rodriguez-Viejo, J.; Mikulec, F. V.; Heine, J. R.; Mattoussi, H.; Ober, R.; Jensen, K. F.; Bawendi, M. G. *J. Phys. Chem. B* **1997**, *101*(46), 9463–9475.

(30) Reiss, P.; Bleuse, J.; Pron, A. *Nano Lett.* **2002**, *2*(7), 781–784.

(31) Parak, W. J.; Gerion, D.; Zanchet, D.; Woerz, A. S.; Pellegrino, T.; Micheel, C.; Williams, S. C.; Seitz, M.; Bruehl, R. E.; Bryant, Z.; Bustamante, C.; Bertozzi, C. R.; Alivisatos, A. P. *Chem. Mater.* **2002**, *14*(5), 2113–2119.

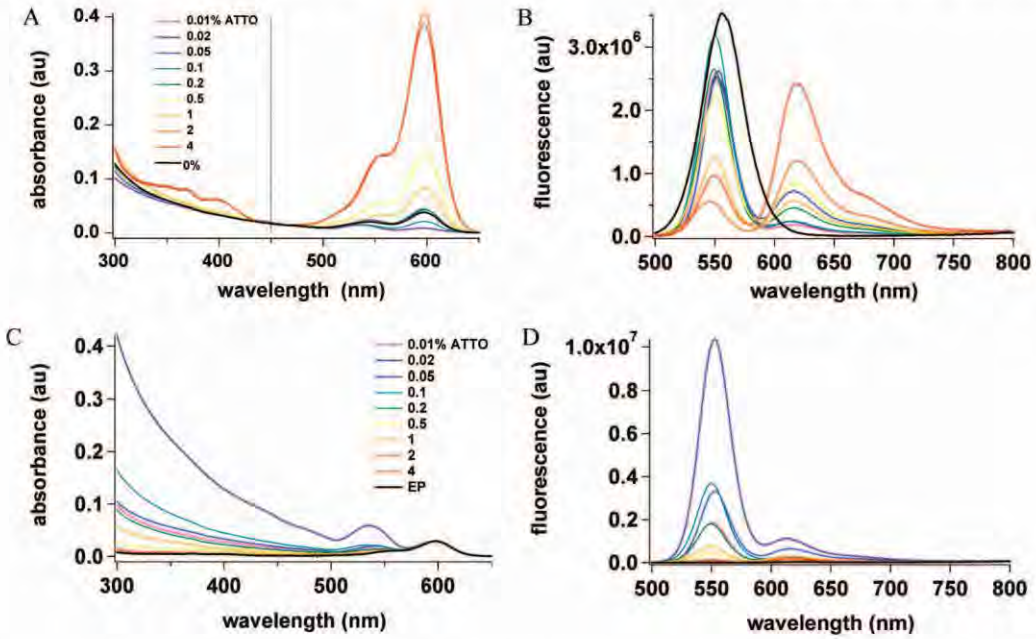

Figure 4. Dependence of normalized absorbance (left) and fluorescence emission (right) on acceptor concentration. A single batch of Evident nanocrystal (NC) donors was coated with ATTO−polymers with an ATTO load increasing from 0.01% to 4%. The percentage refers to the ratio of ATTO molecules to the number of anhydride rings making up the polymer backbone. EPs are empty polymer micelles (2% ATTO) extracted by gel electrophoresis,[6] and Evident NC (0% ATTO) denotes the polymer-coated bare donor, in the absence of acceptor fluorophores. For fluorescence spectra, conditions where adjusted by dilution/concentration of the samples so as to have the same concentration of NCs (absorbance measured at 450 nm, panel (A)) or of ATTO dye (absorbance measurement at 597 nm, panel (C)). (B) and (D) show the corresponding fluorescence emission spectra of the same samples as in (A) and (C) upon donor excitation at 450 nm. Note the increasing transfer of energy from the donor (emission peaking at 560 nm) to the acceptor, ATTO 590 (with 622 nm peak emission) upon increasing the concentration of the later.

emission systematically decreased with increasing ATTO concentration, illustrating the dose-dependent quenching of donor PL emission.[32] We observed a concomitant increase in the ATTO dye emission, indicating the energy absorbed by the donor sensitized acceptor fluorescence in a concentration-dependent manner. Notably, for an equal amount of donor, the total energy that was radiatively emitted as donor PL and acceptor fluorescence (i.e., the area of the spectrum) stayed roughly constant over the entire range of ATTO concentration, indicating that the addition of ATTO does not increase the fraction of dark reactions relaxing NC excitation states compared to bare NCs.

We next experimentally determined the actual acceptor/donor ratio, by successively comparing the absorbance of pairs of polymer−ATTO/NC−polymer−ATTO and NC−polymer/NC−polymer−ATTO. The concentration of ATTO in polymer was directly read off from its absorbance at 594 nm. Since ATTO was preloaded to the polymer before NC coating and NCs only negligibly absorb at 594 nm,[6] the absorbances of ATTO in polymer and in coated NCs could be scaled (see Materials and Methods). Subtracting the two latter spectra generates an artificial compound NC−polymer spectrum that closely reproduces the measured NC−polymer spectrum, with the exception of two small antiphasic deviations suggesting a slight peak shift of the donor or acceptor when conjugated (see Figure 2 in Materials and Methods). Conversely, the amount of NCs included in the NC−polymer−ATTO complexes was directly estimated from absorbance measurements at 450 nm where ATTO absorbance is negligible compared to that of the NCs. The acceptor/donor ratio is then given by the ratio of the measured amounts of ATTO and NCs. From these measurements, we estimate that varying between 0% and 4% the number of monomers building up the polymer resulted in embedding 0−20 molecules of ATTO dye per NC. For example, NCs prepared with "1%" ATTO−polymer contained, on average, five ATTO dye acceptors (see Figure 5A).

Using this stoichiometry calibration, we next quantified these notions by graphing evolution with A/D of the NC peak emission at 565 nm, as well as the sensitized donor fluorescence at 627 nm peak according to eq 3a (Figure 5B, left). From these data, we calculated the FRET efficiency E using either donor quenching or sensitized acceptor fluorescence as a parameter (Figure 5B, right). As expected for multiacceptor FRET, we observe an initial dependence of E on the number of acceptors and a plateau of ~0.65 for >5 acceptors.

How does this observation compare with theory? If we fit eq 3d, $E(N,r) = N/(N+(r/R_0)^p)$ with the experimental data while keeping $p = 6$ fixed, we find $r/R_0 = 1.11 \pm 0.04$, close to 0.77−1.08 predicted from ref 33. Two independent experiments confirmed these bulk cuvette measurements. First, single-pair FRET (spFRET) data obtained from individual NCs images on total-internal reflection fluorescence images (open squares in Figure 5B right) showed the same dependence of donor PL on the A/D ratio ($r/R_0 = 1.09 \pm 0.23$), indicating that our population average was not biased through the existence of bright subpopulations, NC aggregation, or low spectrometer sensitivity. Conversely, the presence of a dielectric interface in evanescent-wave excited fluorescence does only marginally, if at all, affect FRET. Letting both p and r/R_0 run freely in fits of $E(N,r)$ gave 5.6145 ± 1.9 and 1.09 ± 0.34 as best fit parameters. Nevertheless, the dispersion of the data would have allowed other suitable combinations of p and r/R_0 with $p \in (2, 6.5)$ to produce a similar precision (see gray trace in Figure 5B right)

(32) Schmelz, O.; Mews, A.; Basché, T.; Herrmann, A.; Müllen, K. *Langmuir* **2001**, *17*, 2861–2865.

(33) Sperling, R. A.; Liedl, T.; Duhr, S.; Kudera, S.; Zanella, M.; Lin, C.-A. J.; Chang, W. H.; Braun, D.; Parak, W. J. *J. Phys. Chem. C* **2007**, *111*, 11552–11559.

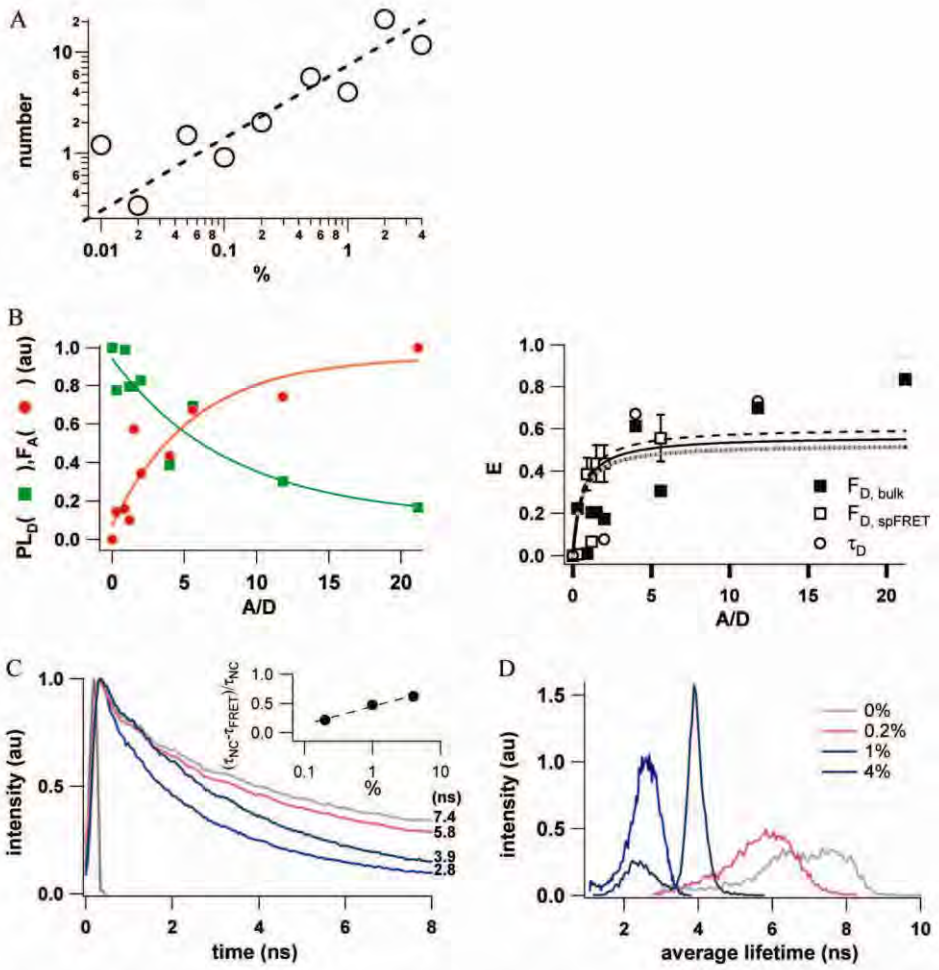

Figure 5. FRET efficiency of the Evident NC/ATTO system as a function of the polymer/ATTO stoichiometry and the number of ATTO molecules actually bound per NC. (A) Log−log plot of the measured relationship between percentages of ATTO included during polymer synthesis and ATTO molecules actually decorating the central NC donor. Points show mean values for three batches. Slope is 4−5. (B) Left: evolution with acceptor/donor ratio (A/D) of donor photoluminescence (PL_D, green rectangles) and sensitized donor fluorescence (F_A, red dots), measured as the peak of spectral donor and acceptor emission at 565 and 627 nm, respectively. Solid lines are to guide the eye. Right: transfer efficiency E as a function of A/D, measured from bulk cuvette photospectrometry, single-donor PL on TIRF images, or average donor lifetime obtained from time- and space-correlated single-photon counting (TSCSPC) measurements. (C) Examples of time-dependent fluorescence recordings for EviDot560 donors with different number of ATTO dye as indicated. Numbers denote average lifetimes calculated according to the maximum-entropy method. Pixel bin was 2 × 2, and total integration time was 2000s. (D) Average lifetime histograms for the different Evident NC samples shown in panel (B). Histograms are normalized to equal area. Note the broad and skewed lifetime distributions, even for bare NCs without ATTO dye.

Second, two-photon excitation time- and space-correlated single-photon counting (TSCSPC) showed a pronounced decrease in donor lifetimes for NC/ATTO assemblies compared with unconjugated NCs (Figure 5C). As expected, excited-state lifetimes dropped with increasing number of ATTO acceptors. Mean average decay times $\langle\tau\rangle$ for bare polymer-coated NCs were around 7 ns, whereas the maximal embedding of 20 dye molecules ("4%") reduced this value to 2.5 ns. Thus, time-resolved fluorescence independently corroborates our bulk and spFRET intensity data that FRET provides an efficient alternative route for donor relaxation, yielding, for $p = 6$ and high N, a limiting $E_{fit}^{\infty} = 1 - \tau_{DA}/\tau_D = 0.55$, very similar to the 0.51 from bulk and 0.59 TIRF measurements.

Fluorescence lifetime imaging microscopy (FLIM) analysis also allowed us to obtain spatially resolved donor fluorescence decays from FRET nanoprobes immobilized at a low density on a glass coverslip. Figure 5C quantifies the effect of increasing acceptor concentration in terms of distributions of single-pixel donor lifetimes. Even without acceptor, the distribution is relatively large and skewed to the short end. Although the effective pixel size (1.5 × 1.5 μm in the object plane) of our microchannel plate detector prohibited the detection of spFRET from individual nanoprobes (1 pixel containing some 1−5 NCs), the spatial sampling was fine enough to reveal an important heterogeneity of donor lifetimes within a given batch of NC donor and ATTO concentration. The spread of $\langle\tau\rangle$ was not due to pixel noise, because pixel binning resulted in average values reproducing the distribution means of single data (Figure 5C right). Thus, FLIM suggests that donor PL is influenced by factors other than FRET alone and probably linked to sample aging, aggregation, or photodegradation.

In the present work, we stoichiometrically embedded hydrophobic dye molecules in amphiphilic polymer micelles. Using these preassembled micelles to wrap NCs shells, we control the mean number of ATTO acceptor molecules bound per NC donor from 0 to 20. In this range, the intrinsic properties of the NC−ATTO dye complex as measured by the intensity and lifetime of the donor decreased monotonously with ATTO concentration. Our results provide the direct experimental demonstration that,

at a fixed A/D distance, multiacceptor FRET provides an efficient means to increasing the sensitivity of FRET-based nanoprobes.

Polymer wrapping is a rigid process, thereby fixing the donor/acceptor distance. However, a narrow distribution of the distances within the polymer shell critically depends on the tight wrapping of the NC central donor with the polymer coat. In this context, it is important to note that our experimental data are the size measurements derived from the hydrodynamic radii.[33] However, we can be sure that the inclusion of ATTO (at any percentage) does not change the geometry of the polymer shell, as the hydrodynamic radii are independent of the ATTO percentage. Also, donor/acceptor distance should fall within the smaller and bigger limits defined by the middle of the polymer shell and the outside of the polymer shell, respectively. However, we cannot exclude that the polymer shell detaches with time, resulting in a potentially larger distribution.

Irrespective of the precise distribution of donor/acceptor distances, our result of a monotonic dependence of the FRET efficiency on the acceptor concentration is different from the bell-shaped dependence of the FRET efficiency on the A/D ratio observed for a CdTe/Rhodamine B system,[5] where the drop in transfer efficiency at acceptor excess may reflect acceptor/acceptor or donor/donor interactions in the densely packed film used, similar to what has been suggested for crowded environments, where significant excitation transfer can occur via states that are optically dark.[34]

Emission-based FRET detection works best within a limited range of molar acceptor/donor ratios.[35] Although FLIM-FRET[36] is less restricted in this respect, the measurement of E and the estimation of interacting versus noninteracting species are simplified when the donor and acceptor are present at fixed molar ratios. Stoichiometric inclusion by preloading polymers permits one to tailor FRET pairs through a chemical variable that can be controlled during synthesis and nanoprobe assembly. It therefore adds a degree of freedom to nanosensor assembly beyond the existing choice of spectrally suitable donors and acceptors and tuning their separation distances through the use of molecular linkers. The capacity to fine tune the transfer efficiency will be of particular importance for sensors that derive their contrast from changes in donor/acceptor spectral overlap, where an E value close to 0.5 would maximize sensitivity, or for ratiometric constant-distance polymer-shell sensors for which one might want to find conditions that go along with incomplete donor quenching yet detectable acceptor fluorescence.

The observed heterogeneity among nominally identical NC donors complicates calibrated analyte sensing and implies that checkpoints need to be introduced at critical points of synthesis and sensor assembly. Alternatively, microfluidic postsynthesis recognition and sorting might provide more homogeneous sensor performance.[37] Thus, although FRET-based hybrid NC/fluorophore assemblies hold important promises for being the next generation of nanobiosensors, to work in nanoscale biological environments, the technique still needs further development.

Acknowledgment. This work was supported by the *Groupement d'intérêt Publique - Agence Nationale de la Recherche Programme Nanosciences et Nanotechnologies* (GIP-ANR PNANO, Grant No. ANR-05-NANO-051 "NanoFRET" to J.-M.M., A.F., M.O., and W.J.P.) and, in parts, by the European Union (Grant Nos. FP6-2004-013880 "Single-motor FLIN", FP6-2005-019481 "From FLIM to FLIN", and FP6-2006-037897 "AUTOSCREEN" to M.O.) and the German Research Foundation DFG (W.J.P., SPP 1313 PA 794/4-1). A.V.Y., C.L., and S.G. were postdoctoral fellows funded by the *Centre National de la Recherche* (CNRS), the *Fondation pour la Recherche Médicale* (FRM), and GIP-ANR, respectively. The authors thank Ralph Sperling and Marco Zanella for discussion.

Supporting Information Available: Synthesis of the polymer and preparation of homemade nanocrystals, estimation of photoluminescence quantum yields of NC donors, electrophoretic purification of NC−ATTO complexes, ensemble FRET measurements in cuvette, FRET efficiency as a function of donor/acceptor ratio, and single-particle FRET (spFRET) data and TSCSPC FLIM data for Invitrogen NCs (Qdot565) and homemade CdSe/ZnS as well as CdSe NCs. This material is available free of charge via the Internet at http://pubs.acs.org.

LA8038347

(34) Zimet, D. B.; Thevenin, B. J.-M.; Verkman, A. S.; Shohet, S. B.; Abney, J. R. *Biophys. J.* **1995**, *68*, 1592–1603.
(35) Barney, C.; Danuser, G. *Biophys. J.* **2003**, *84*, 3992–4010.
(36) Becker, W.; Bergmann, A.; Hink, M. A.; König, K.; Benndorf, K.; Biskup, C. *Microsc. Res. Tech.* **2004**, *63*, 58–66.
(37) Chang, J.-Y.; Yang, C.-H.; Huang, K.-S. *Nanotechnology* **2007**, *18*, 305305.

Acknowledgements

I thank Almighty God for giving me courage and determination to complete this research work.

I would like to express my deepest gratitude towards my supervisor Wolfgang Parak for his excellent supervision, constant guidance, valuable advices as well as his encouragement and patience throughout the course of this research.

I want to acknowledge my minor supervisors Marco and Loretta for their help and guidance during their stay in group. I am also very grateful for the friendship, encouragement and hands-on help given by the present and former lab fellows. Special thanks to Markus, Sumaira and Carolin for the proof-reading of thesis.

I would like to say thanks to Steffi and Frau Thomas for helping in administrative stuff and extend my thanks to Andreas for helping computer related problem and in ordering of chemicals. I am very grateful to Dr. Schaper and Michael for their help and guidance during my work in Material Science Centre, Em&M laboratory.

I want to say thanks to all our collaborators who invested time in different projects.

I would also like to acknowledge Higher Education Commission of Pakistan (HEC) and Deutsche Akademischer Austtausch Dienst (DAAD) for the fellowship.

I convey special thanks to Zulqurnain, Faheem, Samia and Imran for their nice company and making beautiful memories in Wherda 17 during last three years.

Where would I be without my family? My heartfelt pleasure to my parents, brothers and sisters for their love, support, encouragement and understanding throughout my studies. Thanks to all of you. Special thanks to my amiable sister Farhat who has been listening to my long calls when I was missing my family.

Last but not the least, I would like to give my cordial appreciation to my dear fiancée Hina who has accompanied me in this dissertation with her support and encouragement. I couldn't have done it without her, too.

Finally, I would like to thank everybody who was important to the successful realization of dissertation, as well as expressing my apology that I could not mention personally one by one.

Azhar Zahoor Abbasi

Academic career

2007-2010	Philipps Universität Marburg (Germany), AG. Bio photonic (Prof. Wolfgang J. Parak) PhD student. Field of research: Synthesis and applications of nanoparticles.
2004-2006	Quaid-i-Azam University Islamabad (Pakistan), Master of Philosophy in Physics.
2002-2004	Quaid-i-Azam University Islamabad (Pakistan), Master of Science in physics.
2000-2002	Punjab University Lahore (Pakistan), Bachelor of Science.
1998-2000	Board of Intermediate and Secondary Education Rawalpindi (Pakistan). Higher Secondary Certificate.